

# **Spectral properties and breathing dynamics of a few-body trapped bosonic mixture**

**Dissertation**

**zur Erlangung des Doktorgrades**

**an der Fakultät für Mathematik, Informatik und Naturwissenschaften**

**Fachbereich Physik**

**der Universität Hamburg**

**vorgelegt von  
Maxim Pyzh**

**Hamburg  
2022**

Gutachter/innen der Dissertation:

Prof. Dr. Peter Schmelcher  
Prof. Dr. Michael Thorwart

Zusammensetzung der Prüfungskommission:

Prof. Dr. Daniela Pfannkuche  
Prof. Dr. Peter Schmelcher  
Prof. Dr. Michael Thorwart  
Prof. Dr. Henning Moritz  
Dr. Tim Laarmann

Vorsitzende der Prüfungskommission:

Prof. Dr. Daniela Pfannkuche

Datum der Disputation:

04.10.2022

Vorsitzender Fach-Promotionsausschusses PHYSIK:

Prof. Dr. Wolfgang J. Parak

Leiter des Fachbereichs PHYSIK:

Prof. Dr. Günter H. W. Sigl

Dekan der Fakultät MIN:

Prof. Dr. Heinrich Graener

Dedicated to my beloved family  
for their endless love, support and encouragement.



## ABSTRACT

---

Interacting few-body systems are the fundamental building blocks of many-body theories. Few-body physics is exciting by itself and, importantly, it often benefits our understanding of many-body physics as well. The latter is challenging to solve numerically owing to the exponential scaling of the Hilbert space dimension with increasing number of particles. For that reason, certain approximations need to be made and effective models are obtained. However, the validity of these models is usually limited to weak interactions. In contrast, few-body problems are tractable to head-on numerical approaches at any strength of interactions, and in certain cases even allow for analytical solutions.

In this regard, we explore the few-body physics of a binary mixture subject to a species-selective confinement with a special emphasis on impurity physics. Impurities can significantly modify their environment and can be used as a sensitive probe of intrinsic properties of the host medium. The actual impact of inter-particle interactions is very sensitive to the shape of external potentials. We pay particular attention to account for inter-particle correlations by using the state-of-the-art numerical technique, the multi-layer multi-configuration time-dependent Hartree method. We classify the ground states in different parameter spaces, which serves as a starting point for subsequent analysis of the system's breathing dynamics. The corresponding collective excitations are being used in modern cold-atom experiments for diagnostics of single-species condensates and we want to check their utility for binary mixtures. We propose that our results on stationary properties and dynamics can be verified experimentally using quantum gas microscopy, which we adapt to non-lattice trapped sparse-density systems.

The final part of the thesis is dedicated to a fundamental topic, potentially relevant for many areas of science which deal with the matrix eigenvalue problem. Explicitly, we aim at characterizing structural properties of eigenstates and -energies. To this end, we employ two recent concepts from spectral graph theory: vertex pair cospectrality and isospectral reduction. The former concept imposes local parity on eigenvectors, even in absence of pair exchange symmetries. We reveal that the corresponding eigenvectors have additional structure beyond parity, which can be inferred by analysing the powers of a graph's matrix. The latter concept is a spectrum-preserving decimation procedure to reduce the graph size to a certain subsystem. The reduced graph might feature additional symmetries, which are absent in the unreduced version and for that reason are called latent. We show that a certain class of spectral degeneracies can be explained by latent symmetries of a graph.



## ZUSAMMENFASSUNG

---

Wechselwirkende Wenigteilchensysteme sind die grundlegenden Bausteine von Vielteilchentheorien. Die Physik von wenigen Teilchen ist an sich schon sehr spannend und, was noch bedeutender ist, sie trägt oft auch zu einem besseren Verständnis von Vielteilchenphysik bei. Letztere ist numerisch schwer zugänglich, da die Dimension des Hilbert-Raums mit zunehmender Teilchenzahl exponentiell ansteigt. Aus diesem Grund müssen bestimmte Näherungen vorgenommen werden, um effektiven Modelle abzuleiten. Die Gültigkeit dieser Modelle ist jedoch in der Regel auf schwache Wechselwirkungen beschränkt. Im Gegensatz dazu sind Wenigteilchenprobleme bei beliebiger Stärke der Wechselwirkungen mit numerischen Ansätzen lösbar. In bestimmten Fällen sind sogar analytische Formulierungen möglich.

In diesem Zusammenhang untersuchen wir die Wenigteilchenphysik einer binären Mischung, die in einer komponenten-abhängigen Falle gefangen ist, mit besonderem Schwerpunkt auf der Physik der Fremdatome. Fremdatome können ihre Umgebung erheblich beeinflussen und dienen als empfindliche Sonde für intrinsische Eigenschaften des umgebenden Mediums. Die tatsächliche Auswirkung der Wechselwirkungen zwischen den Teilchen ist sehr von der Form der externen Falle abhängig. Besonderes Augenmerk legen wir auf die Charakterisierung der Auswirkungen von Korrelationen, indem wir eine state-of-the-art numerische Methode verwenden, die Multi-Layer Multi-Configuration Time-Dependent Hartree Method for Mixtures. Wir klassifizieren die Grundzustände in verschiedenen Parameterräumen, die anschließend als Ausgangspunkt für die Atmungs-dynamik dienen. Die entsprechenden kollektiven Anregungen werden in modernen Kaltatomexperimenten zur Diagnose von aus einer Komponente bestehenden Kondensaten verwendet, und wir wollen ihren Nutzen für binäre Mischungen überprüfen. Wir schlagen vor, dass unsere Ergebnisse zu stationären Eigenschaften und zur Dynamik experimentell unter Verwendung der Quantengasmikroskopie verifiziert werden können, die wir an nicht gittergebundene Systeme mit geringer Dichte anpassen.

Im letzten Teil der Arbeit widmen wir uns einem grundlegenden Thema von potentieller Relevanz für viele Bereiche der Naturwissenschaften, die sich mit dem Matrixeigenwertproblem beschäftigen. Explizit geht es um die Charakterisierung der strukturellen Eigenschaften von Eigenzuständen und -energien. Zu diesem Zweck verwenden wir zwei neue Konzepte aus der spektralen Graphentheorie: Vertexpaar-Kospektralität und isospektrale Reduktion. Das erste Konzept erzwingt eine lokale Parität der Eigenvektoren, auch wenn es keine Austauschsymmetrien gibt. Wir zeigen, dass die entsprechenden Eigenvektoren eine zusätzliche Struktur über die Parität hinaus aufweisen. Diese lässt sich aus der Analyse der Potenzen einer Matrix ableiten. Das zweite Konzept ist ein spektrumerhaltendes Reduzierungsverfahren um die Größe eines Graphen auf ein bestimmtes Teilsystem

zu reduzieren. Der reduzierte Graph kann zusätzliche Symmetrien aufweisen, die in der originalen Version nicht vorhanden sind und deshalb als latent bezeichnet werden. Wir zeigen, dass eine bestimmte Klasse von spektralen Entartungen durch latente Symmetrien eines Graphen erklärt werden kann.



## PUBLICATIONS

---

This cumulative thesis is based on the following publications [MP1–MP7]:

### PUBLICATIONS COVERED BY THIS THESIS

- <sup>MP1</sup>M. Pyzh, S. Krönke, C. Weitenberg, and P. Schmelcher, “Spectral properties and breathing dynamics of a few-body Bose–Bose mixture in a 1D harmonic trap,” *New J. Phys.* **20**, 015006 (2018).
- <sup>MP2</sup>M. Pyzh and P. Schmelcher, “Breathing dynamics of the few-body Bose polaron in a species-selective harmonic trap,” *Phys. Rev. A* **105**, 043304 (2022).
- <sup>MP3</sup>M. Pyzh and P. Schmelcher, “Phase separation of a Bose-Bose mixture: Impact of the trap and particle-number imbalance,” *Phys. Rev. A* **102**, 023305 (2020).
- <sup>MP4</sup>M. Pyzh, K. Keiler, S. I. Mistakidis, and P. Schmelcher, “Entangling Lattice-Trapped Bosons with a Free Impurity: Impact on Stationary and Dynamical Properties,” *Entropy* **23**, 290 (2021).
- <sup>MP5</sup>M. Pyzh, S. Krönke, C. Weitenberg, and P. Schmelcher, “Quantum point spread function for imaging trapped few-body systems with a quantum gas microscope,” *New J. Phys.* **21**, 053013 (2019).
- <sup>MP6</sup>C. V. Morfonios, M. Pyzh, M. Röntgen, and P. Schmelcher, “Cospectrality preserving graph modifications and eigenvector properties via walk equivalence of vertices,” *Linear Algebra Appl.* **624**, 53–86 (2021).
- <sup>MP7</sup>M. Röntgen et al., “Latent Symmetry Induced Degeneracies,” *Phys. Rev. Lett.* **126**, 180601 (2021).

In addition, I participated in the following projects [MP8–MP11] not covered by this thesis:

### FURTHER PUBLICATIONS

- <sup>MP8</sup>M. Röntgen et al., “Designing pretty good state transfer via isospectral reductions,” *Phys. Rev. A* **101**, 042304 (2020).
- <sup>MP9</sup>M. Röntgen, M. Pyzh, C. V. Morfonios, and P. Schmelcher, “On symmetries of a matrix and its isospectral reduction,” *arXiv preprint arXiv:2105.12579* (2021).
- <sup>MP10</sup>D. J. Bosworth, M. Pyzh, and P. Schmelcher, “Spectral properties of a three-body atom-ion hybrid system,” *Phys. Rev. A* **103**, 033303 (2021).
- <sup>MP11</sup>C. V. Morfonios, M. Röntgen, M. Pyzh, and P. Schmelcher, “Flat bands by latent symmetry,” *Phys. Rev. B* **104**, 035105 (2021).

## DECLARATION OF PERSONAL CONTRIBUTIONS TO [MP1–MP7]

The idea for [MP1] emerged from my master thesis, though it is not based on the results of this thesis. The project was conducted almost entirely by myself, including the numerical work and the interpretation of the results. Dr. Sven Krönke provided valuable assistance in many technical aspects and contributed significantly to the presentation of our results. I also wrote the major part of the manuscript, subsequently edited and improved by all the co-authors. Dr. Christof Weitenberg supplied the section with an experimental proposal.

The projects [MP2, MP3] were conducted entirely by myself, including the specification of research questions, the numerical work and the interpretation of the results. I prepared the manuscript, subsequently edited and improved by my supervisor, Prof. Dr. Peter Schmelcher.

The idea for [MP4] was suggested by Dr. Kevin Keiler, and together with Dr. Simeon I. Mistakidis and myself, we worked out the concept. Dr. Kevin Keiler and myself did the numerical work. The analysis of stationary properties was conducted by myself. The dynamical studies were done by Dr. Kevin Keiler. I wrote the major part of the manuscript. Dr. Kevin Keiler supplied the section on dynamics and Dr. Simeon I. Mistakidis wrote the introductory part. The manuscript was subsequently edited and improved by all the co-authors.

The project [MP5] was invoked by Dr. Christof Weitenberg, and together with Dr. Sven Krönke and myself, we worked out the concept as well as the research strategy. The development of the theoretical framework was initiated and guided by Dr. Sven Krönke. I performed the numerical work, identified limitations of the framework and suggested a machine-learning assisted method to partially overcome these limitations, tested its performance and provided estimates of the experimental effort. The manuscript was prepared by joint efforts of Dr. Christof Weitenberg, Dr. Sven Krönke and myself, subsequently edited and improved by all the co-authors.

The project [MP6] emerged from a close collaboration of Dr. Christian Morfonios, M. Sc. Malte Röntgen and myself. The manuscript was also prepared by our joint efforts, subsequently edited and improved by our supervisor, Prof. Dr. Peter Schmelcher.

The project [MP7] was conducted in equal parts by Dr. Christian Morfonios, M. Sc. Malte Röntgen and myself. Dr. Nikolaos Palaiodimopoulos, Prof. Dr. Fotios Diakono and Prof. Dr. Peter Schmelcher provided valuable feedback on group-theoretical aspects of this work. The manuscript was also prepared by joint efforts of Dr. Christian Morfonios, M. Sc. Malte Röntgen and myself, subsequently edited and improved by all the co-authors.

In all cases, I had regular discussions with all the co-authors, in particular with my supervisor Prof. Dr. Peter Schmelcher.

# CONTENTS

---

1	Roadmap of this Thesis	1
<b>I Few-Body Physics with Mixtures of Ultracold Atoms</b>		
2	Few-Body Trapped Bosonic Mixture	5
3	Theoretical Description of Binary Mixtures	9
3.1	Exact Diagonalization	10
3.2	Time-Independent Basis for Initial Value Problems	11
3.3	Family of Hartree Methods	13
3.3.1	Time-Dependent Hartree Fock	13
3.3.2	Multi-Layer Multi-Configuration Time-Dependent Hartree Method	15
3.3.3	Convergence and Density Operators	18
4	Ground State Classification	21
4.1	Inhomogeneous 1D Bose gas	22
4.2	Bose-Bose Mixture	24
4.3	Preface: Eigensystem of a 2+2 harmonic mixture	31
4.4	Preface: Bose polaron in a harmonic trap	32
4.5	Preface: Bose polaron in a species-selective trap	33
5	Breathing dynamics	35
5.1	Collective modes	35
5.2	Breathing modes	36
5.3	Single species	38
5.4	Two species	39
5.5	Preface: Breathing response of a Bose mixture	39
5.6	Preface: Breathing response of a Bose polaron	41
6	Quantum Gas Microscope	43
6.1	Technical aspects	44
6.2	Preface: Quantum Point Spread Function	46
<b>II Spectral graph theory</b>		
7	Spectral graph theory in physics	51
7.1	Graphs	52
7.2	Cospectrality and Local Parity of Eigenvectors	53
7.3	Preface: Generator of cospectral Graphs	56
7.4	Isospectral Reduction and Latent Symmetries	58
7.5	Preface: Latent Symmetries Induced Degeneracies	61
<b>III Contributions, Summary and Outlook</b>		
8	Scientific Contributions	65
	Spectral properties and breathing dynamics of a few-body Bose–Bose mixture in a 1D harmonic trap [MP1]	67
	Breathing dynamics of the Bose polaron in a species-selective harmonic trap [MP2]	85

Phase separation of a Bose-Bose mixture: Impact of the trap and particle-number imbalance [MP3]	103
Entangling Lattice-Trapped Bosons with a Free Impurity: Impact on Stationary and Dynamical Properties [MP4]	119
Quantum point spread function for imaging trapped few-body systems with a quantum gas microscope [MP5]	139
Cospectrality preserving graph modifications and eigenvector properties via walk equivalence of vertices [MP6]	157
Latent Symmetry Induced Degeneracies [MP7]	191
9 Summary and Outlook	205
9.1 Stationary properties of a Bose mixture	205
9.2 Breathing dynamics of a Bose mixture	207
9.3 Quantum Gas Microscopy of trapped gases	209
9.4 Spectral graph theory in physics	210
Bibliography	213

## ACRONYMS

---

1D	one-dimensional
BEC	Bose-Einstein condensate
CF	composite fermionization
CoM	center-of-mass
CS	compressed sensing
DVR	discrete variable representation
FF	full fermionization
GPE	Gross-Pitaevskii equation
HF	Hartree-Fock
MCTDH-X	multi-configuration time-dependent Hartree method
ML-MCTDH-X	multi-layer multi-configuration time-dependent Hartree method for mixtures of bosons and fermions
NN	neural network
PS	phase separation
PSF	point spread function
QGM	quantum gas microscope
SMF	species mean-field
SNR	signal-to-noise ratio
SPF	single-particle function
TF	Thomas-Fermi
TG	Tonks-Girardeau



## ROADMAP OF THIS THESIS

---

In this thesis, our goal is to investigate few-body phenomena and interaction-induced correlation effects in a few-body binary mixture of bosons experiencing a species-selective inhomogeneous one-dimensional trap. Our works can be categorized in four topics: i) characterization and classification of ground states; ii) study of breathing dynamics; iii) quantum gas microscopy of trapped few-body systems and iv) recent insights from spectral graph theory contributing to a better understanding of matrix eigenvalue problems. The thesis is structured as follows.

In Chapter 2, we introduce our physical system. To characterize its stationary and dynamical properties, we use the multi-layer multi-configuration Hartree method. It is an ab-initio variational approach to simulate many-body dynamics in the weak-to-intermediate correlation regimes. The ground state can be obtained by imaginary time propagation, one can treat particles of mixed statistics and it has a rich toolbox of state analysis. Details of the method are discussed in Chapter 3.

In Chapter 4, we investigate stationary properties of our mixture. Identifying distinct regimes of a physical system is an important first step towards developing a deeper understanding of its intrinsic attributes and dynamical behaviour. In [MP1], our objective is to obtain and analyse the low-energy spectrum of a miniature problem with non-trivial particle statistics, the 2+2 mixture in a harmonic trap. We solve it by exact diagonalization in a relative-coordinates frame to define a correlation-tailored basis which greatly facilitates the method's convergence. Furthermore, the alternative frame reveals additional symmetries otherwise hidden in the laboratory frame. In [MP3], we explore the miscible-immiscible phase boundary. In particular, we quantify to which extent the conventional separation criterion for homogenous systems is violated by trap inhomogeneity, particle number imbalance and interaction-induced correlations. We evidence several possibilities for the two components to separate and provide a simple criterion to determine which configuration is energetically more favourable. In [MP4], we study ground states for a different trap combination, namely a lattice-trapped medium coupled to a free impurity. We identify parameter regions where the interplay between trap geometry and interactions leads to substantial perturbations with a sizeable amount of entanglement.

In Chapter 5, we use the above ground states as initial states for subsequent breathing dynamics. The system is set in motion by quenching the harmonic trap frequency. The ensuing dynamics is monitored by recording the time evolution of the reduced one-particle density. The breathing oscillations of a single-species condensate are known to display a two-frequency beating: one frequency is constant while the other interaction-sensitive and serves as a valuable diagnostics tool in experiments. Our goal is to verify

whether the utility of breathing excitations can be extended to binary mixtures. In [MP1], for a 2+2 mixture we identify three interaction-sensitive frequencies. It matches the number of interaction parameters, and we analyse the amplitudes of individual excitations across different interaction regions. In a follow-up work [MP2], we extend our studies to a particle-imbalanced case. We find that a species-asymmetric quench protocol allows to excite an additional beyond-mean-field mode whose amplitude is particularly sensitive to the amount of deposited entanglement.

In [MP1–MP4], the reduced one- and two-particle densities are crucial quantities to classify ground-state regimes, record the dynamical response and access the expectation value of many relevant observables. Naturally, we were concerned whether our results could be verified experimentally, which is the subject of Chapter 6. For this we would require single-atom sensitivity to access inter-particle correlations and high spatial resolution to resolve variations in position space. The recent invention of a pinning lattice combined with fluorescence imaging, the so-called quantum gas microscope, fulfils these two requirements and is readily available in modern laboratories. However, so far they have been utilized primarily in lattice-trapped systems. In [MP5], we propose to extend this concept to non-lattice trapped atoms. The idea is to bypass the limitations of lattice constant resolution by shifting the relative position of the pinning lattice potential. The imaging process is mapped to a convolution of the reduced density with an imaging filter, which we call the quantum point spread function. The resulting distortions can be partially removed by a machine-learning-assisted deconvolution procedure.

In Chapter 7, we zoom out from the field of ultracold atoms and concern ourselves with a fundamentally broad topic of practical significance for many areas of science dealing with the matrix eigenvalue problem. Our ideas are rooted in recent developments in spectral graph theory. Symmetries are known to simplify the numerical treatment of eigenvalue problems by imposing restrictions on the structure of eigenvectors. Strikingly, eigenvectors might have an elegant structure even in the absence of conventional symmetries, such as local parity on two eigenvector components, a phenomenon called vertex pair cospectrality. In [MP6], we identify further relations among components of an eigenvector by analysing the powers of the corresponding matrix. This work provides a theoretical framework for generating cospectral graphs, which is a hot topic in spectral graph theory, and it laid the foundation for a systematic construction and manipulation of flat bands in tight-binding systems. In [MP7], we analyse symmetries of an effective matrix obtained by a decimation procedure, called isospectral reduction. It reduces the size of a matrix to a dedicated subsystem while preserving the eigenvalue spectrum. Surprisingly, effective matrices can feature symmetries, which are not present in their unreduced version and for that reason are called latent symmetries. Importantly, they can be of great use in explaining spectral degeneracies in a visually interpretable way.

Our published works are listed in Chapter 8. Finally, we provide a summary and discuss promising directions for future research in Chapter 9.



Part I

FEW-BODY PHYSICS WITH MIXTURES OF  
ULTRACOLD ATOMS



Many-body systems [1] are challenging to solve. An analytical treatment is only possible for a fraction of problems or in some limiting cases. There exist effective models and perturbative expansions, but their validity is limited to weak or strong interactions and extensions are thus highly desirable. In particular, the regime of intermediate interactions is not yet fully understood. While it is amenable to numerical techniques, the exponential growth of the Hilbert space dimension with an increasing number of particles represents a major bottleneck which restricts their use to *few-body* systems, comprised of up to tens or hundreds of particles.

The microscopic physics of a few interacting particles [2] serves as a major building block of many-body theories. Physical insights gained by analysing few-body systems are indeed very useful to improve our current understanding of many-body physics [3–7]. However, even though few-body phenomena play an important role in large ensembles of particles, many-body systems may display quite different physical properties. One way to better understand these discrepancies and how they come to be is by studying the few- to many-body transition.

The field of *ultracold atoms* [8] is an ideal platform to systematically pursue this bottom-up approach. Since the first experimental realization of Bose-Einstein condensate (BEC) in dilute alkali gases in 1995 [9, 10], significant progress has been achieved in the manipulation of ultracold samples. Nowadays, the state-of-art experiments are able to:

- dynamically tailor the trapping geometry, including the effective dimensionality, by employing holographic optical tweezers with a spatial light modulator or acousto-optic deflectors [11, 12];
- tune the interactions via Fano-Feshbach resonances [13] by varying an external magnetic field;
- prepare multi-component systems of bosons and/or fermions by utilizing different hyperfine states or isotopes of the same element, even combining distinct elements;
- select a designated number of particles with a high fidelity [14–19];
- detect single atoms [20, 21] and perform high-resolution imaging of the particles' distribution with a quantum gas microscope (QGM) [22–27].

Note that the degree of flexibility depends on the chosen elements. Owing to this exquisite control over system parameters, ultracold atoms have been used over the past two decades as quantum simulators of condensed matter

and high energy physics [28]. Typical models, such as Heisenberg or Hubbard models, can be prepared and investigated in a well-controlled environment. In recent years, the research focus has increasingly expanded towards real-world applications in quantum computing, information processing and quantum metrology. From the above, it is undoubtedly a promising route to explore the physics of mesoscopic systems, increasing the complexity one particle at a time.

How does one actually prepare a few-body system in modern laboratories? One can distribute the particles uniformly over a shallow lattice (superfluid regime) and then suppress the inter-well tunnelling by a non-adiabatic increase of the lattice depth (Mott regime), thus freezing the instantaneous particle distribution at each lattice site [29]. One ends up with many independent realizations of a few-body system with an average statistics of a few particles per lattice site. The so-called super-lattice allows to manipulate simultaneously the shape of every well by varying the relative phase between the underlying sub-lattices [30]. Furthermore, a targeted redistribution of particles among wells has been demonstrated [31, 32]. Alternatively, an optical tweezer can be loaded with either an already pre-cooled few-body sample [33] or a thermal macroscopic ensemble, subsequently reduced to a few particles by tilting the trapping potential allowing the hot atoms to escape (evaporative cooling) [34]. For fermions, the above spilling mechanism allows for a full control of system's quantum state owing to the Pauli's exclusion principle [14–19].

A few-body system is characterized by a sparse particle density. Strikingly and counter-intuitively, in quasi-one-dimensional (1D) trapping geometries, realized by a strong transverse confinement, a lower density implies stronger interactions in contrast to higher dimensions [35]. It comes as no surprise that in recent years the physics of 1D ultracold atoms has triggered a lot of fundamental research interest [36–38]. By now it is recognized that correlations are largely enhanced in 1D, such that sophisticated numerical techniques are necessary for an accurate characterization of system properties, such as the multi-layer multi-configuration time-dependent Hartree method for mixtures of bosons and fermions (ML-MCTDH-X) [39–41] for continuous traps or the density matrix renormalization group (DMRG) [42–44] for discrete lattices.

Correlations acquire an additional flavour in *binary mixtures* of bosons, fermions and mixed particle statistics [38, 45, 46]. One differentiates among intra- and inter-component correlations. The former are primarily affected by species-internal parameters, such as intra-component interactions and external traps. When distinguishable particles become coupled, they produce an induced potential for each other, and there is a build-up of inter-component correlations caused by the entanglement [47]. It has a direct consequence for the internal structure of each component and standard intuition is often insufficient to predict how the two types of correlations affect each other. As a result of this complex interrelation, binary mixtures exhibit a rich set of spatial configurations such as bound clusters and segregated interfaces [38, 46].

In this thesis, we explore the domain of sizeable inter-particle correlations for a few-body two-component mixture of ultracold bosons confined to a **1D** geometry. A special emphasis is put on particle number imbalance, especially impurity problems as well as the inhomogeneity and species-selectivity of the external trap. Impurity physics is a hot topic linked to the polaron problem in condensed matter physics [48]. A highly particle-imbalanced mixture with a BEC background, termed the Bose polaron [49], can be mapped to a well-known Fröhlich model [50]: the electron is replaced by an impurity atom, while the role of phonons is played by the Bogoliubov excitations of the condensate. As opposed to solid state physics, the platform of ultracold atoms allows to examine the polaron phenomenon with exquisite control over system parameters, e. g., the coupling can be set to arbitrary values by Feshbach [13] or confinement induced resonances [51–54]. In particular, one can explore physical phenomena emerging beyond the validity of the weak-coupling Fröhlich paradigm [55–57]. The trap inhomogeneity strongly affects the intra-component correlations and quantizes the energy spectrum making continuum-based approaches quantitatively unreliable. The species-selective shaping of the external trap allows for a flexible way to manipulate the overlap region among the two components, which has a sizeable impact on the amount of entanglement the composite system may hold.

Formally, we consider a mixture of two *components* (*species*), denoted  $A$  and  $B$ . Each *component*  $\sigma \in \{A, B\}$ , also called *species*, consists of  $N_\sigma$  bosons of equal mass  $m$ , which can be experimentally realized by two different hyperfine states [58–67]. The particles are confined to a quasi-**1D** geometry [14–19, 68–71] by a tight harmonic trap in two spatial (transverse) directions and experience a species-selective trapping potential  $V_\sigma(x)$  [72, 73] along the remaining (longitudinal) direction. We operate in the limit of zero temperature, where particle interactions are completely determined by a single parameter, the s-wave scattering length  $a_s$  [74]. When the range of interaction is small compared to the inter-particle distance, as is the case for dilute quantum gases, one can replace the true potential by a mathematically convenient model potential [75]. A common choice is the zero-range contact potential  $g\delta(r)$  [76] with  $g$  the interaction strength and  $r$  the inter-particle distance. We distinguish between intra-component and inter-component interactions of strength  $g_\sigma$  and  $g_{AB}$ , respectively. Experimentally, they can be tuned independently by a combination of Feshbach [13] and confinement induced resonances (CIR) [51–54]. Thus, we arrive at the following Hamiltonian:

$$H = \sum_{\sigma} H_{\sigma} + H_{AB}, \quad (2.1)$$

$$H_{\sigma} = \sum_{i=1}^{N_{\sigma}} \left[ -\frac{\hbar^2}{2m} \partial_{x_i^{\sigma}}^2 + V_{\sigma}(x_i^{\sigma}) \right] + g_{\sigma} \sum_{i<j}^{N_{\sigma}} \delta(x_i^{\sigma} - x_j^{\sigma}), \quad (2.2)$$

$$H_{AB} = g_{AB} \sum_{i=1}^{N_A} \sum_{j=1}^{N_B} \delta(x_i^A - x_j^B), \quad (2.3)$$

where  $\hbar$  is the Planck constant and  $x_i^\sigma$  the position of the  $i$ -th particle from component  $\sigma$ . We consider two distinct parabolic traps with a frequency ratio  $\eta$  in [MP<sub>1</sub>–MP<sub>3</sub>] while in [MP<sub>4</sub>] we combine a five-well trap with a box potential. Furthermore, we focus on particle-imbalanced mixtures, where  $A$  is the majority and  $B$  the impurity species.

This chapter introduces numerical methods for solving the initial value problem  $i\hbar\partial_t|\Psi(t)\rangle = \hat{H}|\Psi(t)\rangle$  for a trapped few-body Bose-Bose mixture described by Eq. (2.1). The reduced dimensionality greatly enhances interaction-induced correlations [36, 37], further complicated by the shape of an external confinement [77]. Moreover, a binary mixture harbours two different types of correlations, the intra- and inter-component ones. Understanding their interplay is an exciting yet challenging task [47]. We aim at an accurate description of stationary properties and dynamics by taking all the relevant correlations into account. In particular, we want to extract the impact of correlations by comparing converged simulations to mean-field results. Unfortunately, sizeable correlations come with a great computational cost. The exponential scaling of the Hilbert space dimension with increasing number of particles limits our analysis to few-body system sizes. Nevertheless, such systems are experimentally accessible [14–19, 29–34], exhibit many exciting phenomena [2, 46], such as the Efimov effect [6], and provide valuable physical insights which might improve our current understanding of the many-body systems [3–5, 7].

In the following, we first discuss two well-established techniques for solving the time-dependent Schrödinger equation: exact diagonalization in Section 3.1 and expansion w. r. t. time-independent basis in Section 3.2. We emphasize the sensitivity of such approaches to a particular choice of basis functions and their inflexibility to describe a time-evolving subspace of the complete Hilbert space. This brings us to the family of Hartree methods which are based on an adaptive time-dependent basis. In Section 3.3 we describe why these methods have been so successful over the past years. We open our overview with the ‘grandparent’, the mean-field Hartree-Fock (HF), in Section 3.3.1. Of particular relevance for the field of ultracold atoms is the Gross-Pitaevskii equation (GPE), a mean-field ansatz to describe weakly correlated bosons. Then in Section 3.3.2 we discuss the descendants of HF: the multi-configuration and the multi-layer extensions. The former takes into account interaction-induced correlations while the latter represents an efficient way to describe mixtures of indistinguishable particles. The wave function expansion is given explicitly for the bosonic mixture studied in this work. We conclude this chapter in Section 3.3.3 with a discussion on the scaling properties of our method and elaborate on the significance of reduced density operators for evaluating the accuracy of simulations as well as for describing physical properties of our system [MP1–MP5].

Before we start, let us briefly comment that there are many other sophisticated methods available, such as the quantum monte carlo (QMC) [78, 79] and the density matrix renormalization group (DMRG) [42–44], particularly successful for the description of 1D continuous and lattice systems with

short range interactions [36]. However, we do not aim at comparing these methods to ours in terms of efficiency or interpretability. In this thesis, we concentrate exclusively on physical aspects of a bosonic mixture.

### 3.1 EXACT DIAGONALIZATION

Solving  $|\Psi(t)\rangle = e^{-\frac{i}{\hbar}\hat{H}t} |\Psi(0)\rangle$  with a time-independent Hamiltonian  $\hat{H}$  is equivalent to solving the underlying eigenvalue problem  $\hat{H} |E_k\rangle = E_k |E_k\rangle$ . Once the eigenstates and the eigenenergies of  $\hat{H}$  are known, the initial population of eigenstates  $c_k = \langle E_k | \Psi(0) \rangle$  can be evaluated and the state evolution is given simply by  $|\Psi(t)\rangle = \sum_k c_k e^{-\frac{i}{\hbar}E_k t} |E_k\rangle$ . Such an approach was employed for a weakly perturbed ground state in our work [MP1]. The eigenstates  $|E_k\rangle$  and corresponding eigenenergies  $E_k$  can be obtained by representing  $\hat{H}$  as a matrix in some truncated user-defined basis and diagonalizing it. This is an approximate method. The *exact* diagonalization refers to the situation when the basis size is sufficiently large to consider the eigenenergies of interest to be converged.

How does one choose a suitable basis for a many-body wave function? The one particle Hilbert space  $\mathcal{H}$  is spanned by so-called single-particle functions (SPFs)  $\{|\varphi_j\rangle\}$ . The Hilbert space of  $N$  particles is spanned by a tensor product of individual one particle Hilbert spaces, i. e.,  $\mathcal{H}^N = \otimes_{i=1}^N \mathcal{H}_i$ . Consequently, the many-body state can be expanded as follows:

$$|\Psi\rangle = \sum_{j_1 \dots j_N}^{s_1 \dots s_N} c_{j_1 \dots j_N} |\varphi_{j_1}\rangle \dots |\varphi_{j_N}\rangle. \quad (3.1)$$

In principle, any two particles may have distinct SPFs and the total number of SPFs may also differ. For simplicity, we assume a single set for all particles and just control the set size  $s$ , which affects the accuracy of our representation.

In case the particles are *indistinguishable*, such as bosons or fermions, only a subspace of the above  $N$ -body Hilbert space matters. Moreover, the set of SPFs needs to be the same for every particle. An additional symmetrization  $\hat{S}^\epsilon$  is necessary, such that the many-body wave function becomes symmetric (for bosons  $\epsilon = +1$ ) or antisymmetric (for fermions  $\epsilon = -1$ ) w. r. t. an exchange of any two particles. The operator  $\hat{S}_N^\epsilon = \frac{1}{\sqrt{N!}} \sum_{\pi \in S_N} \epsilon^{\text{sign}(\pi)} P_\pi$ , when acting on a single product state, creates a superposition of all possible ( $N!$ ) particle permutations<sup>1</sup>. The factor  $\epsilon^{\text{sign}(\pi)}$  is relevant only for fermions and gives the parity of a permutation  $\pi$ . A properly symmetrized and subsequently renormalized product state is termed a *Fock state* or a *number state*  $|n_1, \dots, n_s\rangle \equiv |\vec{n}\rangle$  encoding the distribution of particles over an orthonormal set of SPFs and fulfilling  $\sum_i n_i = N$ . Consequently, the many-body wave function of bosons or fermions needs to be expanded as follows:

$$|\Psi\rangle = \sum_{\vec{n}} c_{\vec{n}} |\vec{n}\rangle. \quad (3.2)$$

The bosonic (fermionic) number state is also called a permanent (determinant)

<sup>1</sup>  $S_N$  is the symmetric group over a set  $X = \{1, \dots, N\}$ ,  $\pi : X \rightarrow X$  a re-indexing of particle labels and  $P_\pi$  the corresponding permutation matrix.



In case of dealing with  $K$  different flavours of indistinguishable particles the basis becomes a tensor product of Fock states:

$$|\Psi\rangle = \sum_{\vec{n}^{(1)} \dots \vec{n}^{(K)}} c_{\vec{n}^{(1)} \dots \vec{n}^{(K)}} |\vec{n}^{(1)}\rangle \dots |\vec{n}^{(K)}\rangle \equiv \sum_{\vec{n}} c_{\vec{n}} |\vec{n}\rangle. \quad (3.3)$$

Note that for  $K = N$  Eq. (3.3) reduces to Eq. (3.1) and for  $K = 1$  it reduces to Eq. (3.2). In the following, we employ the notation  $|\vec{n}\rangle$  to denote the basis of the most general case from Eq. (3.3), i. e., a tensor product of distinguishable Fock states.

The Hamilton matrix  $\langle \vec{n} | H | \vec{m} \rangle$  can be now constructed and subsequently diagonalized. This gives us expansion coefficients for each eigenstate. The convergence is controlled by the total number  $s$  of SPFs. The Hilbert space dimension grows exponentially as  $s^N$  for distinguishable particles,  $\frac{(N+s-1)!}{N!(s-1)!}$  for bosons and  $\frac{s!}{N!(s-N)!}$  for fermions. Importantly, since the set of SPFs is not complete, the particular choice of basis functions strongly affects the convergence. Clearly, it is an impossible task to guess the best performing set of SPFs in a general setting. In most cases it is physically motivated, e. g., by solving the problem of non-interacting particles, which is a set of independent one-body problems.

Typically, systems of around four particles are treated with this method [80–83], though it highly depends on the degree of inter-particle correlations induced by interactions. A coordinate transformation to a relative frame  $\vec{x} \rightarrow \vec{r}$  might turn out useful. In particular, it changes the meaning of correlations: the relative coordinates  $r_i$  play now the role of ‘particles’ [MP1]. The relative frame basis may easily account for major correlations of the laboratory frame and vice versa [84].

### 3.2 TIME-INDEPENDENT BASIS FOR INITIAL VALUE PROBLEMS

Another somewhat similar way to solve the initial value problem is to use an a priori fixed number state basis with time-dependent coefficients, thus skipping the calculation of eigenstates outlined in the previous section:

$$|\Psi(t)\rangle = \sum_{\vec{n}} c_{\vec{n}}(t) |\vec{n}\rangle. \quad (3.4)$$

By applying any of the equivalent time-dependent variational principles (Lagrangian, McLachlan or Dirac-Frenkel) [85], one arrives at a set of coupled time-differential equations for the coefficients  $c_{\vec{n}}(t)$ .

As opposed to the exact diagonalization, this method can deal with time-dependent Hamilton operators, though it also suffers from the representation problem. To explain why, let us introduce the notion of an *active* Hilbert space (Fig. 3.1). It is a hyperplane of a finite and, generally, time-dependent dimension  $d(t)$  encapsulated within the complete Hilbert space. Clearly, at any point in time it can be represented by  $d(t)$  appropriately chosen basis vectors. Now, as the time evolves, the active space may rotate within the Hilbert space traversing from one subspace to another. Meanwhile, the active space dimension may even grow or shrink, though

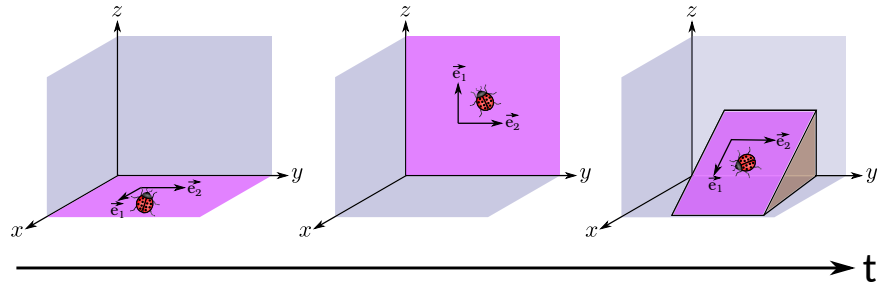


Figure 3.1: Illustration of an active space. Assume a three-dimensional Hilbert space spanned by a time-independent basis  $\{\vec{e}_x, \vec{e}_y, \vec{e}_z\}$ . Suppose a quantum system (represented by a bug) undergoes a dynamical evolution on a two-dimensional hyperplane (active space indicated by a magenta colour). The hyperplane may look different at different times, such that all basis vectors are required to describe the full time evolution. An adaptive time-dependent basis composed of two vectors  $\{\vec{e}_1, \vec{e}_2\}$  allows for a sparser representation of the ongoing dynamics.

it is bounded by  $d_{\max} = \max_t d(t)$  for a finite time interval  $t \in [0, T]$ . A time-independent basis can be optimized only once, e. g., for the initial state, i. e., it is properly rotated and truncated at a dimension large enough to incorporate the initial active space  $d(0)$ . However, in general it will become less appropriate over time. This means that a larger number of additional SPFs will be required.

For illustrative purposes, let us provide an another example. Imagine a wave-packet with a constant support (active space) moving along some axis with a constant velocity. Initially, we provide a finite-size grid of points which for a short time window perfectly resolves all the features of this wave-packet (optimized fixed basis). At some point the wave packet will reach the grid boundary and the theoretical description becomes inaccurate. To simulate the long-time dynamics a large grid would be necessary, although only a fraction of grid points are 'active' at any point in time [86].

$$\begin{array}{ccccccccc}
 \begin{bmatrix} v_1 \\ v_2 \\ 0 \\ 0 \end{bmatrix} & \rightarrow & \begin{bmatrix} v_1 \\ v_2 \\ v_3 \\ 0 \end{bmatrix} & \rightarrow & \begin{bmatrix} 0 \\ v_2 \\ v_3 \\ 0 \end{bmatrix} & \rightarrow & \begin{bmatrix} 0 \\ v_2 \\ v_3 \\ v_4 \end{bmatrix} & \rightarrow & \begin{bmatrix} 0 \\ 0 \\ v_3 \\ v_4 \end{bmatrix} \\
 t = 0 & & t_1 & & t_2 & & t_3 & & T
 \end{array}$$

Illustration of an active space: At  $t = 0$  the active space has a finite dimension  $d = 2$ . As the time goes by it grows and shrinks in dimension. At a final time  $T$  it ends up in a subspace orthogonal to the initial one.

This poses the following question: why not use an adaptive time-dependent basis which provides a sparse representation for the instantaneously relevant subspace of the total Hilbert space?

## 3.3 FAMILY OF HARTREE METHODS

The idea of a time-dependent basis is actually quite old [87–90]. It all started with only a single adaptive basis function, the Time-Dependent HF Method. It aimed to approximate a system of interacting fermions. The extension to bosons and distinguishable particles is straightforward. However, it is a mean-field method. To account for particle-induced correlations, the basis size has to be increased admitting multiple configurations: the multi-configuration time-dependent Hartree method (MCTDH-X)<sup>2</sup> [91–96]. Among recent developments there is the ML-MCTDH-X [39, 40]. As the name suggests, it can deal with multi-component mixtures of mixed particle statistics and is thus particularly suited for several tasks addressed within this thesis. In the following, we provide a historical viewpoint on the ideas behind ML-MCTDH-X, introduce the terminology used in our publications and discuss several technical aspects of the method.

## 3.3.1 Time-Dependent Hartree Fock

The time-dependent HF is a variational method for solving the initial value problem  $i\hbar\partial_t |\Psi(t)\rangle = \hat{H} |\Psi(t)\rangle$ . It has played an important role in molecular [97] and nuclear [98] physics for a long time providing reasonable approximations whenever *interaction-induced* inter-particle correlations could be considered small during the time evolution. Importantly, for indistinguishable particles the correlations, induced by the particle-exchange symmetry, are fully accounted for.

The many-body wave function of  $N$  (in)distinguishable particles is assumed to be a number state  $|\vec{n}\rangle_t$  composed of  $s$  time-dependent SPFs  $|\varphi_j(t)\rangle$ :

$$|\Psi(t)\rangle = |\vec{n}\rangle_t. \quad (3.5)$$

By applying the time-dependent variational principle [85], one arrives at a set of  $s$  coupled time-differential equations for the SPFs.

**RELAXATION:** If the real time evolution is replaced by an imaginary time-evolution [99], one arrives at an upper bound for the ground state, given that it has a finite overlap  $c_0 \neq 0$  with the initial wave function:

$$e^{-\hat{H}t} |\Psi(0)\rangle = \sum_{k=0} c_k e^{-E_k t} |E_k\rangle = e^{-E_0 t} \left[ c_0 |E_0\rangle + \sum_{k=1} c_k e^{-\gamma_k t} |E_k\rangle \right] \quad (3.6)$$

where  $\gamma_k = E_k - E_0$  is the decay rate of the  $k$ -th eigenstate. Note that the state norm decays and thus a renormalization after each time step is required.

<sup>2</sup> Originally, MCTDH was developed only for distinguishable particles [91, 92]. Later it was extended to bosons MCTDH-B [93] and fermions MCTDH-F [94]. The abbreviation MCTDH-X unites all three cases.

**SELF-CONSISTENT FIELD METHOD:** HF is called a mean-field theory [97]. To help understand why, let us change the viewpoint to the time-independent Schrödinger equation  $\hat{H}|\Psi\rangle = E|\Psi\rangle$ . One can get an upper bound approximation for the ground state using the Rayleigh–Ritz method [100]. To this end, the expected energy  $\langle\Psi|\hat{H}|\Psi\rangle$  of the HF ansatz is minimized w. r. t. SPFs. One arrives at a system of coupled *non-linear* differential equations for the SPFs:  $\hat{F}[\{\varphi_j\}]|\varphi_j\rangle = \epsilon_j|\varphi_j\rangle$ . Note that the one-body Fock operator  $\hat{F} = H_1 + H_{mf} + H_{ex}$  is non-linear. Apart from a linear term  $H_1$ , it has an averaged potential term  $H_{mf}$  induced by all the other orbitals (mean-field) and an exchange term  $H_{ex}$  for indistinguishable particles (correlations from particle exchange symmetry).

The HF equations are solved in a self-consistent manner using an iterative procedure. First, an initial basis of SPFs is chosen, usually motivated by the corresponding one-body problem of independent particles. Then a loop follows: i) the Fock operator is represented as a matrix in the current single-particle basis; ii) its eigenstates, obtained by diagonalization, replace the basis used in the previous step. The loop is terminated when the variation of energy drops below a pre-defined threshold. The mean-field potential experienced by the particles becomes consistent with the one they produce. Coming back to the initial value problem, the time-evolution of SPFs is dictated in a similar way by the instantaneous mean-field and exchange terms [98].

**GROSS-PITAEVSKII EQUATION:** For fermions, there is no ambiguity regarding which number state configuration to choose: because of the Pauli exclusion principle each particle needs a distinct SPF. For bosons, there are many possibilities regarding the number of SPFs and the distribution of particles among them. Which configuration will provide the best mean-field approximation?

In the field of ultracold atoms there is a particularly famous HF ansatz for bosons, the GPE [101–103]. At ultracold temperatures a weakly interacting BEC is assumed to be nearly condensed [104], i. e., all particles occupy the lowest-energy SPF of the non-interacting one-particle problem  $\langle\hat{n}_0\rangle \sim N$ . This suggests a number state configuration with just a single orbital  $|\vec{n}\rangle = |N\rangle$ . The variation principle gives a non-linear time-differential equation for the one SPF  $|\varphi\rangle$ , which is an effective one-body problem:

$$i\hbar\partial_t\varphi(x,t) = \left[ -\frac{\hbar^2}{2m}\partial_{x^2} + V(x) + g(N-1)|\varphi(x,t)|^2 \right] \varphi(x,t). \quad (3.7)$$

The last term in the parenthesis is a non-linear mean-field term caused by the s-wave contact interaction  $\propto \delta(x_i - x_j)$ . Note the absence of the exchange term, since no symmetrization is needed. For stationary solutions,  $i\hbar\partial_t\varphi(x,t)$  is replaced by  $\mu\varphi(x,t)$  with  $\mu$  the Lagrange multiplier which determines the normalization of  $\varphi(x,t)$ . It is tempting to think of  $\mu$  as the energy per particle except it double-counts the interaction energy, i. e., the total energy is given by  $E = N\mu - gN(N-1)/2 \int dx|\varphi(x,t)|^4$ .

*In the literature, it is common to use a different norm and a large particle limit  $\langle\varphi|\varphi\rangle = N \gg 1$*

To account for weak perturbations of a condensate fraction the renowned Bogoliubov approach can be used [8, 105, 106]. A suitable transformation leads to a description in terms of non-interacting quasi-particles, called phonons, which represent elementary excitations inside the condensate. GPE has been quite successful at describing the dynamics of particular BEC excitations, such as solitons and vortices [8]. When correlations are significant, the GPE displays often an anomalous behaviour, such as a dynamical instability manifested through symmetry breaking [107].

For a trapped bosonic system, especially at a sizeable strength of interactions, e. g., the Tonks-Girardeau (TG) gas of fermionized bosons [108, 109] or the Mott phase in lattice systems [110, 111], the GPE ansatz is not necessarily the optimal mean-field approximation. Instead, one might consider a different number state configuration (with multiple occupied orbitals) [112–118].

### 3.3.2 Multi-Layer Multi-Configuration Time-Dependent Hartree Method

The major drawback of HF is the complete ignorance of inter-particle correlations induced by interactions. The advanced MCTDH-X method combines the rigorousness of Eq. (3.4) and the flexibility of Eq. (3.5) by making both the expansion coefficients and the basis functions time-dependent [91–96]:

$$|\Psi(t)\rangle = \sum_{\vec{n}} c_{\vec{n}}(t) |\vec{n}\rangle_t. \quad (3.8)$$

Now, the adaptive basis comprises many configurations which can capture a *moderate* amount of interaction-induced correlations. Still, also MCTDH-X is subject to the infamous exponential growth of the Hilbert space dimension with the increasing number of particles  $s^N$ . However, the base  $s$  of this scaling can be considerably reduced [92] as compared to a time-independent basis Eq. (3.4), i. e., much less SPFs are generally required making larger systems numerically accessible. Thus, the quantum dynamics of mesoscopic systems hosting  $N \sim \mathcal{O}(10^1 - 10^4)$  particles has been successfully demonstrated [119–125]. An improved relaxation scheme allows to obtain the  $n$ -th eigenstate directly, i. e., bypassing the calculation of energetically lower eigenstates [95, 96]. This opens the possibility to analyse also the static properties of a given system.

We finally arrive at the final relevant extension, the ML-MCTDH-X [39–41] employed in [MP2–MP4]. The Multi-Layer (ML) concept [126] was first introduced in the context of distinguishable particles. Even though a correlated many-body wave function cannot be approximated by a single product state, it can still be reasonably well represented as a product state of grouped coordinates. The wave function may be thus expanded by partitioning the physical degrees of freedom into weakly correlated groups of strongly correlated particle coordinates. This scheme can be repeated several times tailoring the ansatz to system-specific correlations [127]. In particular, it allows to combine distinguishable and indistinguishable degrees of freedom. Each group  $\sigma$  of indistinguishable particles  $x_i^\sigma$  (a species) is merged into

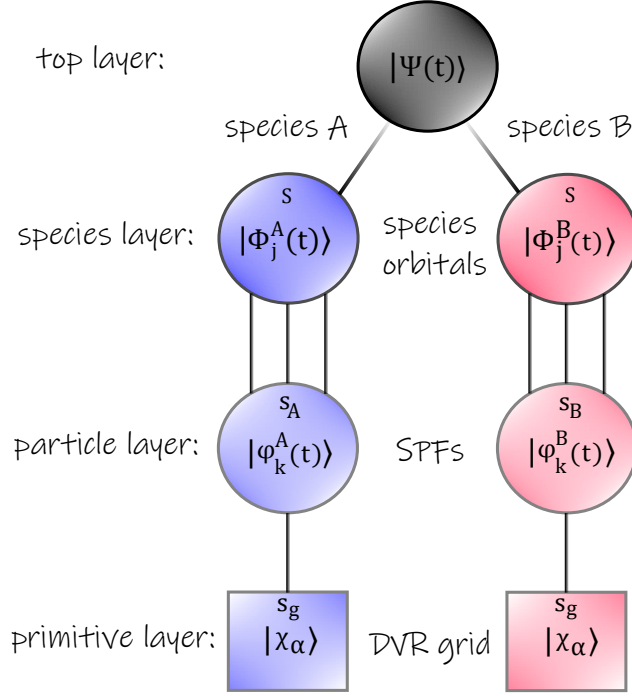


Figure 3.2: The Multi-Layer structure for a two-component Bose-Bose mixture.

a single logical coordinate  $q_\sigma = \vec{x}^\sigma$ . In the first step (top layer), the many-body wave function is expanded in terms of product states for the logical coordinates  $q_\sigma$ . Explicitly, for a mixture of two distinguishable species  $A$  and  $B$ , the top layer expansion takes the following form:

$$|\Psi(t)\rangle = \sum_{i,i'}^S A_{ii'}(t) |\Phi_i^A(t)\rangle |\Phi_{i'}^B(t)\rangle. \quad (3.9)$$

It is reminiscent of an **MCTDH-X** expansion for distinguishable particles, except here instead of **SPFs** we have so-called *species orbitals*  $|\Phi_i^\sigma(t)\rangle$ , each depending on many particle coordinates.

In the second step (species layer), each species orbital  $|\Phi_i^\sigma(t)\rangle$  is expanded according to Eq. (3.8), i. e., in terms of  $N_\sigma$ -body Fock states determined by  $s_\sigma$  time-dependent **SPFs**  $|\varphi_j^\sigma(t)\rangle$ :

$$|\Phi_i^\sigma(t)\rangle = \sum_{\vec{n}^\sigma | N_\sigma} C_{i;\vec{n}^\sigma}^\sigma(t) |\vec{n}^\sigma\rangle_t. \quad (3.10)$$

Note that expanding the wave function directly into multi-species product states  $|\vec{n}^A\rangle |\vec{n}^B\rangle$ , as is done in **MCTDH-XX** [128–130], results in a huge amount of coefficients. Assuming an equal number of particles  $N_\sigma = N$  and an equal number of **SPFs**  $s_\sigma = s$ , the amount of expansion coefficients is  $\left(\frac{(N+s-1)!}{N!(s-1)!}\right)^2$ . In contrast, we get only  $S^2 + 2S \frac{(N+s-1)!}{N!(s-1)!}$  coefficients by the top layer segmentation, given in Eq. (3.9), which has a much more favourable scaling.

Finally, in the last step (particle layer), each **SPF**  $|\varphi_j^\sigma(t)\rangle$  is expanded in terms of a time-independent spatial grid. For efficiency reasons one uses a

discrete variable representation (DVR) basis [131, 132]. It is a comparatively large set of  $s_g \gg s_\sigma$  time-independent SPFs  $|\chi_\alpha\rangle$ :

$$|\varphi_j^\sigma(t)\rangle = \sum_\alpha d_{j,\alpha}^\sigma(t) |\chi_\alpha\rangle. \quad (3.11)$$

The DVR has two useful properties. First, each grid function is represented in terms of analytical functions and thus admits exact expressions for one-body operators appearing in the time-differential equations. Second, each grid function is an eigenstate of the position operator  $\hat{x}$  and thus is highly localized around the corresponding eigenvalue  $\chi_\alpha(x_\beta) \propto \delta_{\alpha,\beta}$ .

**COUPLED GROSS-PITAEVSKII EQUATIONS:** Choosing  $s_\sigma = 1$  (implying  $S = 1$ ) amounts to a mean-field ansatz describing a weakly interacting two-component bosonic mixture at zero temperature [8]. The variation principle gives a system of coupled non-linear time-differential equations for the two SPFs  $|\varphi^A\rangle$  and  $|\varphi^B\rangle$ :

$$\begin{aligned} i\hbar\partial_t |\varphi^A\rangle_t &= \left[ H_1^A + g_A(N_A - 1)\rho_1^A(x, t) + g_{AB}N_B\rho_1^B(x, t) \right] |\varphi^A\rangle_t, \\ i\hbar\partial_t |\varphi^B\rangle_t &= \left[ H_1^B + g_B(N_B - 1)\rho_1^B(x, t) + g_{AB}N_A\rho_1^A(x, t) \right] |\varphi^B\rangle_t, \end{aligned} \quad (3.12)$$

*In the literature, it is common to use a different norm and a large particle limit  $\langle\varphi^\sigma|\varphi^\sigma\rangle = N_\sigma \gg 1$*

with the one-body term  $H_1^\sigma = -\frac{\hbar^2}{2m}\partial_x^2 + V_\sigma(x)$  and the reduced one-body density  $\rho_1^\sigma(x, t) = |\varphi^\sigma(x, t)|^2$  for the component  $\sigma$ . The mean-field terms come from the intra- and inter-component contact interactions. For stationary solutions  $i\hbar\partial_t |\varphi^\sigma\rangle_t$  is replaced by  $\mu_\sigma |\varphi^\sigma\rangle_t$  with  $\mu_\sigma$  the Lagrange multiplier of  $\sigma$  species which determines the normalization of  $\varphi^\sigma(x, t)$ . The total energy is:

$$E = \sum_\sigma N_\sigma \mu_\sigma - g_\sigma \frac{N_\sigma(N_\sigma - 1)}{2} \int dx [\rho_1^\sigma(x, t)]^2 - g_{AB} \int dx \prod_\sigma N_\sigma \rho_1^\sigma(x, t).$$

Similar to the single-component case,  $\mu_\sigma$  is not a chemical potential due to the miscounting of interaction energies.

**SPECIES MEAN-FIELD:** Choosing  $S = 1$  amounts to a species mean-field (SMF) ansatz describing a non-entangled two-component bosonic mixture. In particular, the inter-component correlations are completely neglected. Consequently, the particles of one component experience a mean-field potential produced by the density of the other component. Contrarily to coupled GPEs, the intra-component correlations are still accounted for by a multi-configurational expansion on the species layer:

$$\begin{aligned} i\hbar\partial_t |\Phi^A(t)\rangle &= \left[ H_A + g_{AB} \sum_i^{N_A} \rho_1^B(x_i^A, t) \right] |\Phi^A(t)\rangle, \\ i\hbar\partial_t |\Phi^B(t)\rangle &= \left[ H_B + g_{AB} \sum_i^{N_B} \rho_1^A(x_i^B, t) \right] |\Phi^B(t)\rangle, \end{aligned} \quad (3.13)$$

where  $H_\sigma$  is defined as in Eq. (2.1),  $|\Phi^\sigma(t)\rangle$  is a species orbital from Eq. (3.10) and  $\rho_1^\sigma(x, t)$  the reduced one-body density (defined below). Importantly, the SMF potential can sometimes greatly modify the fragmentation level of each component as compared to a decoupled mixture at  $g_{AB} = 0$ .

As a last remark, let us mention some recent improvements and developments for the Hartree methods.

**RESTRICTED ACTIVE SPACE:** Not all number state configurations  $|\vec{n}\rangle_t$  are relevant at all times judged by the magnitude of the corresponding expansion coefficients  $c_{\vec{n}}(t)$ . Monitoring their values during the time evolution allows to reduce the number of active configurations, known as the RAS-MCTDH [133, 134].

**SECOND QUANTIZATION REPRESENTATION:** ML-MCTDH-SQR [135] is based on the second quantization formalism. The many-body wave-function is represented by tensor products of single mode Fock spaces, i. e.,  $\mathcal{F} = \otimes_i^s |n_i\rangle$ . The  $s$  orbitals constitute distinguishable degrees of freedom, each spanned by a single-mode Fock space  $\{|n\rangle\}_{n=0,\dots,N}$ . This change of viewpoint is particularly suited for lattice problems.

### 3.3.3 Convergence and Density Operators

The accuracy of simulations is controlled by the numerical parameters  $\{S, s_\sigma, s_g\}$ . The parameter  $s_g$  determines the Hilbert space dimension, while  $S$  and  $s_\sigma$  truncate this space to a numerically feasible dimension. Moreover, the parameter  $s_\sigma$  is primarily responsible for inter-particle correlations within the component  $\sigma$ , while  $S$  controls the level of inter-species correlations.

The time-independent grid with  $s_g$  SPFs sets the stage for upcoming truncations. For a two-component bosonic mixture it would amount to  $\prod_\sigma \frac{(N_\sigma + s_g - 1)!}{N_\sigma!(s_g - 1)!}$  configurations. Considering that  $s_g \sim \mathcal{O}(10^2)$  this is a huge space.

Now we perform the first truncation by choosing  $s_\sigma \ll s_g$  adaptive SPFs arriving at  $\prod_\sigma \frac{(N_\sigma + s_\sigma - 1)!}{N_\sigma!(s_\sigma - 1)!}$  configurations, which is a considerable reduction. The time-independent grid should be dense enough to resolve spatial variations of adaptive SPFs and large enough to account for the maximal spatial extent of the system during the dynamical evolution. To fulfil the above requirements, we use a harmonic DVR (high density of grid points at the centre) with  $n_g = 151$  for parabolic external traps in [MP2, MP3] and a sine DVR (equally spaced) with  $n_g = 225$  for finite systems with hard-wall boundary conditions in [MP4]. The cost we pay for the truncation are the  $n_g \sum_\sigma s_\sigma \sim \mathcal{O}(10^3)$  additional expansion coefficients for the adaptive SPFs from Eq. (3.11).

The top layer expansion allows to further reduce the number of configurations to  $S^2 \sim \mathcal{O}(10^1)$ . Again, the cost one has to pay for the truncation are the  $S \sum_\sigma \frac{(N_\sigma + s_\sigma - 1)!}{N_\sigma!(s_\sigma - 1)!}$  expansion coefficients for species orbitals from Eq. (3.10).



The latter represents a major bottleneck for accessing bosonic mixtures of many particles. Increasing  $N_\sigma$  should be compensated by decreasing  $s_\sigma$  to keep the number of coefficients reasonably small, meaning that less intra-species correlations can be accounted for.

Whether a simulation has converged or not depends on the observable under consideration. To evaluate the expectation value of a  $n$ -body observable  $\hat{O}_n$ , a converged reduced  $n$ -body density operator  $\hat{\rho}_n = \text{Tr}_{N-n}[\hat{\rho}]$  is sufficient:  $\langle \hat{O}_n \rangle = \text{Tr}[\hat{O}_n \hat{\rho}] = \text{Tr}[\hat{O}_n \hat{\rho}_n]$ . A crucial evidence, that  $\hat{\rho}_n$  has converged, is obtained by monitoring the eigenvalues  $0 \leq m_j \leq 1$  (sorted in descending order and fulfilling  $\sum_j m_j = 1$ ) of its spectral decomposition

$$\hat{\rho}_n = \sum_j m_j |m_j\rangle \langle m_j| \quad (3.14)$$

as  $\{S, s_\sigma\}$  are incrementally increased. The eigenvalues  $m_j$  (-vectors  $|m_j\rangle$ ) of a density operator are often called *natural populations (orbitals)*. The smallest eigenvalue serves as an important indicator for considering a simulation as being converged on the  $n$ -body level. Usually, a value below  $10^{-6}$  is considered reasonably small. Additionally, natural populations have to display an exponential decay as a function of the eigenvalue index [39]. Of course, the above criteria is just a rule of thumb. In practice, the convergence of any observable is carefully verified as a function of numerical parameters.

Most observables of interest are either one- or two-body operators. In case of a two-component bosonic mixture, the crucial quantities are the reduced one- and two-body density operators of species  $\sigma$ , denoted as  $\hat{\rho}_1^\sigma$  and  $\hat{\rho}_2^\sigma$ , respectively, as well as the inter-species two-body density operator  $\hat{\rho}_2^{AB}$ . They are defined as follows:

$$\hat{\rho}_n^\sigma(t) = \text{Tr}_{N_\sigma - n_\sigma} \text{Tr}_{N_{\sigma^*}} [\hat{\rho}(t)], \quad (3.15)$$

$$\hat{\rho}_2^{AB}(t) = \text{Tr}_{N_A - 1} \text{Tr}_{N_B - 1} [\hat{\rho}(t)], \quad (3.16)$$

where  $\sigma^* \neq \sigma$  is the opposite component. They are not only useful to evaluate expectation values or to judge on the convergence of a simulation, but provide also valuable physical insights. Thus,  $\rho_1^\sigma(x, x') = \langle x | \hat{\rho}_1^\sigma | x' \rangle$  (the one-body density matrix) characterizes the coherence properties of component  $\sigma$ , while its diagonal  $\rho_1^\sigma(x)$  (the one-body density) is the probability distribution to find a single  $\sigma$  particle at position  $x$ . The diagonal of  $\hat{\rho}_2$  in spatial representation  $\rho_2(x, y) = \langle x, y | \hat{\rho}_2 | x, y \rangle$  (the two-body density matrix) characterizes the probability distribution of measuring two particles at different locations  $x$  and  $y$ .

**ENTANGLEMENT AND FRAGMENTATION:** An important measure of inter-component correlations is contained in the reduced  $N_\sigma$ -body density operator  $\hat{\rho}^\sigma(t) = \text{Tr}_{N_{\sigma^*}} [\hat{\rho}(t)]$  of species  $\sigma$  obtained by integrating out all  $N_{\sigma^*}$  particles of the other component  $\sigma^* \neq \sigma$ . Importantly,  $\hat{\rho}^A$  and  $\hat{\rho}^B$  share the same set of natural populations  $m_j$ . In particular,  $m_0 \approx 1$ , i. e., a pure state, implies an absence of entanglement between the two components. For

an entangled bipartite mixture, we employ the von Neumann entropy to quantify the degree of entanglement:

$$S_{vN} = - \sum_j m_j \log(m_j). \quad (3.17)$$

In a similar way, one can look at the species fragmentation entropy  $S_{vN}^\sigma$  by using natural populations of the reduced one-body density  $\hat{\rho}_1^\sigma$ .

In this chapter, we provide a brief overview of the variety of ground state regimes which can be realized in a Bose-Bose mixture. Gaining an understanding of the lowest energy eigenstate as a function of tunable parameters and classifying different regimes associated with distinct properties is an important first step to investigate any physical system. In several of our works [MP1, MP3, MP4], we focus on static properties of quasi-1D mixtures with a species-dependent confinement, primarily the parabolic one. The trap inhomogeneity is one of the major ingredients in our studies. Homogeneous ultracold gases can be often solved analytically via the famous Bethe ansatz [136, 137]. However, most experimental studies rely on an external confinement, such as a harmonic or a lattice potential. It adds an additional complexity to the problem, such that analytical results can be only obtained in some limiting cases. In-between these regimes a numerical treatment becomes necessary and we employ handy methods from the previous chapter, suitable to address such a problem.

We start our discussion with a single-component 1D Bose gas in Section 4.1. In particular, we cover: i) the mean-field BEC regime with almost every particle being condensed into the same lowest-energy orbital, ii) the Thomas-Fermi (TF) many-particle limit where the condensate becomes a mirror reflection of its external trap, iii) the strongly correlated TG gas of impenetrable bosons which disguise themselves as fermions and iv) its energetic counterpart at attractive interactions, the highly excited metastable super TG gas.

All of the above regimes can be also found in a 1D binary mixture of bosons. As long as the two components are only weakly coupled they are miscible. However, with increasing repulsion they undergo a *phase segregation*, which is discussed in Section 4.2. We derive a rough estimate for the critical coupling marking the transition in a homogeneous case. However, its exact value and the immiscible configuration are extremely sensitive to internal parameters of each species  $\sigma$  such as the external trap  $V_\sigma$ , mass  $m_\sigma$ , particle number  $N_\sigma$  and intra-component interaction strength  $g_\sigma$ . We review three segregated regimes in a harmonic trap for a species-symmetric mixture except for different  $g_\sigma$ : i) the core-shell phase separation (PS) with one component surrounded on both sides by the second, ii) the entangled composite fermionization (CF) with hard-core repulsion among particles from different components and iii) the full fermionization (FF), an analogue of TG which can be mapped to a discrete spin chain model. At attractive inter-component couplings, one can observe heterogeneous molecules and realize an interesting beyond mean-field phenomenon, called quantum droplet. Finally, we outline our own contributions in Sections 4.3 to 4.5, where we extend and complement the existing studies on static properties

of a Bose-Bose mixture. We pay a particular attention to species-selective external traps and particle number imbalance.

#### 4.1 INHOMOGENEOUS 1D BOSE GAS

When there is no coupling between the components in Eq. (2.1), i. e.,  $g_{AB} = 0$ , each component can be solved separately. Let us briefly recapitulate some relevant regimes which can be found in a single-component 1D Bose gas: BEC, TF, TG and super Tonks. We assume that the gas is at zero temperature, has a finite number of particles  $N$ , the transverse motion is frozen out and the longitudinal motion is subject to a harmonic confinement  $V(x) = \frac{1}{2}m\omega^2x^2$ .

A detailed discussion on the physics of low dimensional trapped gases can be found in [36, 138] for bosons and [37] for fermions. Before we start, let us rescale Eq. (2.2) (without  $\sigma$  label) to harmonic oscillator units, i. e.,  $l_\omega = \sqrt{\hbar/m\omega}$  for length and  $\hbar\omega$  for energy:

$$H = \sum_{i=1}^N \left[ -\frac{1}{2}\partial_{x_i}^2 + \frac{1}{2}x_i^2 \right] + \alpha \sum_{i<j}^N \delta(x_i - x_j), \quad (4.1)$$

with the dimensionless interaction parameter  $\alpha = \frac{mgl_\omega}{\hbar^2}$ . At repulsive interactions  $\alpha > 0$  there are three regimes [138] depicted in Fig. 4.1:

1. BEC at  $\alpha \ll 1$  and  $N \ll 1/\alpha$ ,
2. TG at  $\alpha \gg 1$  and  $N \ll \alpha^2$ ,
3. TF otherwise, in particular at a sufficiently large  $N$ .

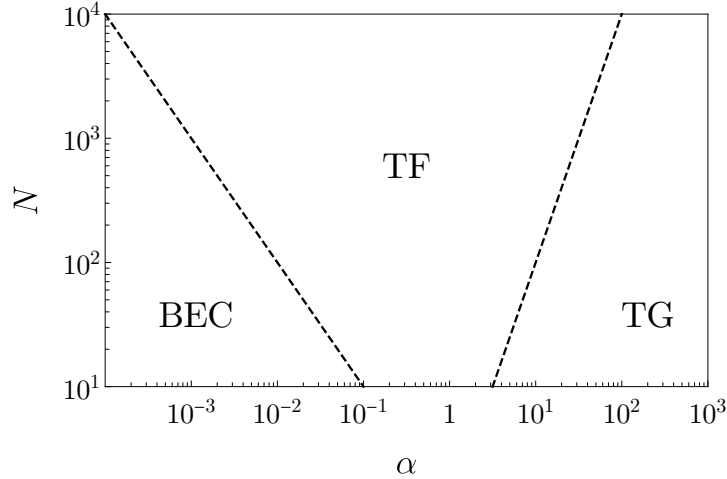


Figure 4.1: Ground state regimes in a finite-size 1D Bose gas under harmonic confinement as a function of an effective interaction strength  $\alpha$  and particle number  $N$ .

**BOSE-EINSTEIN GAS:** **BEC** [139, 140] is a phase (transition) which occurs when a gas of  $N$  non-interacting bosons is cooled down to an extremely low temperature ( $\mathcal{O} \sim \text{nK}$ ) [9, 10]. Below the critical temperature  $T_c$ , the population  $N_0$  of the lowest energy one-particle orbital  $|\varphi_0\rangle$  grows linearly with  $N$  for a sufficiently large  $N$ . One says the state is macroscopically occupied. Especially, in the limit  $T = 0$  all particles become *condensed*, i. e.,  $N_0 = N$ .

For finite size interacting systems, as in Eq. (4.1), the condensate fraction  $N_0/N$  corresponds to the largest eigenvalue  $m_0$  of a spectrally decomposed one-body density operator  $\hat{\rho}_1$  from Eq. (3.14) [104]. When the condensate fraction  $m_0 = N_0/N \approx 1$ , we are in the **BEC** regime. The ground state one-body density has a Gaussian profile and can be obtained from Eq. (3.7). Otherwise the condensate is called *fragmented* [141]. The degree of fragmentation can be quantified by the depletion  $1 - m_0$  or the von-Neumann entropy  $S_{vN}$  from Eq. (3.17).

**THOMAS FERMI GAS:** The gas becomes weakly interacting beyond a sufficiently large number of particles [142–144]. In a **TF** gas, the **GPE** framework Eq. (3.7) without the kinetic term can be applied. The ground state one-body density is just a reflection of the external potential across a constant line defined by the Lagrange multiplier  $\mu > 0$ :

$$N\rho_1(x) = \begin{cases} n_0 \left(1 - \frac{x^2}{R_{TF}^2}\right) & \text{for } |x| \leq R_{TF} \\ 0 & \text{otherwise} \end{cases} \quad (4.2)$$

with the **TF** radius  $R_{TF} = \sqrt{2\mu}$ , peak density  $n_0 = \mu/\alpha$  and chemical potential  $\mu = \left(\frac{3N\alpha}{4\sqrt{2}}\right)^{2/3}$  obtained from the normalization condition  $\int dx |\varphi(x)|^2 = 1$ .

**TONKS GIRARDEAU GAS:** At an infinite repulsion,  $\alpha = +\infty$ , one arrives at a highly correlated **TG** phase [108, 109] which was experimentally confirmed in [70, 71]. In this limit, the bosons display hard-core boundary conditions, meaning that the many-body wave function vanishes whenever the positions of any two particles coincide, i. e.,  $\Psi(\vec{x}) = 0$  if  $x_i = x_j$  for any particle pair  $(i, j)$ . This reminds of the Pauli exclusion principle. Moreover, the energy spectra of impenetrable bosons and non-interacting fermions are the same. In fact, an eigenstate of non-interacting fermions  $\Psi_F(\vec{x})$  and of hard core bosons  $\Psi_B(\vec{x})$  are intimately related via the so-called Bose-Fermi mapping  $\Psi_B(\vec{x}) = A(\vec{x})\Psi_F(\vec{x})$ , where  $A(\vec{x}) = \prod_{i<j} \text{sign}(x_i - x_j)$  ensures the bosonic exchange symmetry.

The ground state fulfils  $\Psi_B = |\Psi_F|$ . In a harmonic trap the ground state of  $N$  non-interacting fermions is an anti-symmetrized product state  $|\vec{n}\rangle$  composed of  $N$  **SPFs** with  $n_i = 1$ . The **SPFs** are harmonic oscillator

eigenstates. Applying symmetrization leads to a Bijl-Jastrow pair product form [145]

$$\Psi_B(\vec{x}) = C_N \left( \prod_{i<j}^N |x_i - x_j| \right) e^{-\sum_i x_i^2/2} \quad (4.3)$$

with a normalization constant  $C_N$ . The one-body density is identical to that of non-interacting fermions  $\rho_1(x) = \sum_{j=0}^{N-1} |\varphi_j(x)|^2$  with  $N$ -humps, though the humps blur out with an increasing number of particles leading to a ‘polished’ bell-shape density profile. There are also some striking differences to fermions. Thus, hard-core bosons have a larger condensed fraction [146, 147]. Moreover, the momentum distribution  $\rho_1(k)$  is a narrow peak with a  $1/k^4$  tail [148] as opposed to fermions which displays a broad  $N$ -hump profile.

**ATTRACTIVE GAS:** At attractive values of interaction,  $\alpha < 0$ , the ground state is a  $N$ -body bound state, followed by excited cluster-type bound states [149, 150]. Even higher in energy, there are gas-like eigenstates with fermionic properties. One such state can be accessed by preparing a **TG** gas at  $\alpha = +\infty$  and then traverse the Feshbach resonance to  $\alpha = -\infty$ . One ends up in a metastable gas-like state predicted theoretically [151, 152] and confirmed experimentally [153]. This phase is called a super Tonks gas, because correlations are stronger and more short ranged than in the **TG** gas.

#### 4.2 BOSE-BOSE MIXTURE

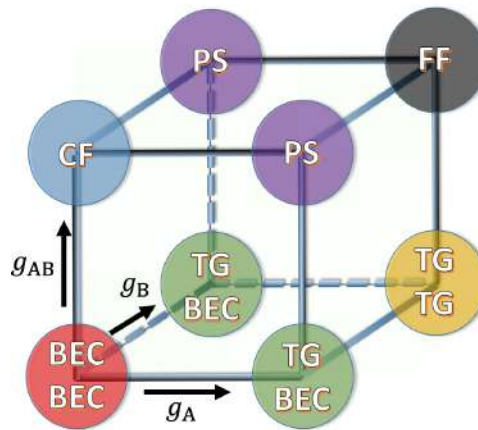


Figure 4.2: Ground state regimes in a two-component Bose mixture as a function of repulsive interactions. Reprinted figure from [81]. DOI: <https://doi.org/10.1088/1367-2630/16/10/103004>.

Now, we consider a **1D** Bose mixture in a harmonic trap (Fig. 4.2). When the two components are only weakly coupled, we are in the miscible regime. Thus, the single-component phases can coexist. In particular, at repulsive couplings three limiting cases can be identified:

- **BEC-BEC** at  $g_{AB} = 0$  and  $g_{\sigma} = 0$

- **BEC-TG** at  $g_{AB} = 0$  and  $g_{A(B)} = +\infty$  and  $g_{B(A)} = 0$
- **TG-TG** at  $g_{AB} = 0$  and  $g_\sigma = +\infty$

When the two components are strongly repulsive, we end up in the immiscible regime. Three distinct configurations can be identified:

- **core-shell PS** at  $g_{AB} = +\infty$  and  $g_{A(B)} = +\infty$  and  $g_{B(A)} = 0$
- **CF** at  $g_{AB} = +\infty$  and  $g_\sigma = 0$
- **FF** at  $g_{AB} = +\infty$  and  $g_\sigma = +\infty$

Let us discuss these regimes in more detail.

**PHASE SEPARATION:** First, we derive a commonly used immiscibility criterion valid for homogeneous mixtures having a large number of particles  $N_\sigma \gg 1$  [154]. To this end, we consider a finite box potential of extension  $L$ , i. e.,  $V_\sigma(x) = 0$  for  $x \in [0, L]$  and infinite outside. We assume a **TF** regime for both components implying weak correlations and negligible kinetic energy. The densities are obtained by solving the stationary coupled **GPEs** from Eq. (3.12). The total energy is given by:

$$E \approx \sum_\sigma g_\sigma \frac{N_\sigma^2}{2} \int_0^L dx [\rho_1^\sigma(x)]^2 + g_{AB} \int_0^L dx \prod_\sigma N_\sigma \rho_1^\sigma(x). \quad (4.4)$$

When the components are miscible, each density is spread over the whole interval  $L$ , meaning  $\rho_1^\sigma(x) = 1/L$  for all  $x \in [0, L]$ . The total energy in a miscible configuration amounts to:

$$E_M = \frac{1}{2L} (g_A N_A^2 + g_B N_B^2 + 2g_{AB} N_A N_B). \quad (4.5)$$

When the components are separated, each density occupies only a segment of length  $L_\sigma$ , such that  $L_A + L_B = L$ . Suppose  $A$  is left-separated, i. e.,  $\rho_1^A(x) = 1/L_A$  for  $x \in [0, L_A]$  and zero otherwise. Then  $B$  is right-separated, i. e.,  $\rho_1^B(x) = 1/L_B$  for  $x \in [L - L_B, L]$  and zero otherwise. The total energy in the immiscible configuration, i. e.,  $\rho_1^A(x)\rho_1^B(x) = 0$ , amounts to:

$$E_{PS} = \frac{1}{2} \left( g_A \frac{N_A^2}{L_A} + g_B \frac{N_B^2}{L_B} \right). \quad (4.6)$$

Minimizing this energy w. r. t.  $L_\sigma$  and keeping in mind the constraint  $L_A + L_B = L$ , we obtain optimal partitioning  $L_\sigma = L \left[ 1 + \sqrt{\frac{g_{\sigma'}}{g_\sigma} \frac{N_{\sigma'}}{N_\sigma}} \right]^{-1}$  with  $\sigma' \neq \sigma$  and can rephrase the above expression for  $E_{PS}$  as:

$$E_{PS} = \frac{1}{2L} (g_A N_A^2 + g_B N_B^2 + 2\sqrt{g_A g_B} N_A N_B), \quad (4.7)$$

which can be now easily compared to  $E_M$ . In particular, the two components become segregated when  $E_{PS} < E_M$  or, equivalently,  $\sqrt{g_A g_B} < g_{AB}$ . This is the immiscibility criterion for a homogeneous two-component Bose mixture.

The phase segregation has been extensively investigated over the past years both experimentally and theoretically [60, 154–162]. In particular, the trapping geometry strongly affects the immiscibility criterion outlined above along with the shape of segregated density distributions.

Thus, in a harmonic trap the ground state may undergo a *core-shell PS*: one species occupies the trap centre (the core) while the other component is pushed to the edges of the first component (the shell). Depending on the intra-component parameters we can get either *ABA* or *BAB* configurations. The overlap region between the two density profiles decreases with increasing repulsion  $g_{AB}$ . The state is non-generate and the least entangled among the segregated phases. In particular, it can be well matched by a species mean-field ansatz.

When the two components compete for the energetically low trap centre, usually one of the component gets the upper hand and forms the core. However, there are situations, when both components have equal energy arguments for occupying the trap centre and the winner cannot be decided. This brings us to the next segregated phase, the *CF*.

**COMPOSITE FERMIONIZATION:** Let us assume for simplicity a mixture with symmetric components, i. e.,  $\vec{x}^A \leftrightarrow \vec{x}^B$ . When the intra-component interactions are absent ( $g_\sigma = 0$ ) and the two components are strongly repelling each other ( $g_{AB} = +\infty$ ), one reaches a regime of *CF* [163, 164]. Note that a mixture of non-symmetric components also has a *CF* limit, though at a particular ratio of asymmetry parameters [MP3]. Similar to *TG*, the many-body eigenstates display hard-core boundary conditions, i. e.,  $\Psi(\vec{x}^A, \vec{x}^B) = 0$  if  $x_i^A = x_j^B$  for any pair of distinguishable particles. Owing to this resemblance, a pair product ansatz from Eq. (4.3) can be adapted to the *CF* ground state:

$$\Psi(\vec{x}^A, \vec{x}^B) \propto \left( \prod_i^{N_A} \prod_j^{N_B} |x_i^A - x_j^B| \right) e^{-\sum_i (x_i^A)^2/2} e^{-\sum_i (x_i^B)^2/2}. \quad (4.8)$$

Numerical simulations indicate two major natural populations for the reduced one-body density operator [80] and substantial entanglement between the components [MP3].

This regime displays multiple peculiar properties. The ground state is actually two-fold degenerate [MP1] and emerges out of two eigenstates with an opposite global reflection parity, meaning  $\vec{x}^\sigma \rightarrow -\vec{x}^\sigma$ . In particular, the degenerate manifold can be chosen to have a definite global parity, if appropriately rotated by a unitary transformation. At  $1/g_{AB} \ll 1$  but finite, with a numerically resolvable energy gap, we expect the quasi-degenerate eigenstates to have a definite global parity. Thus, the one-body density  $\rho_1^\sigma(x)$  displays two reflection symmetric humps and looks the same for both components (see Fig. 4.3 [top]). This overlapping conveys an impression of a miscible phase, which is unusual given the strong repulsion. The two components are indeed segregated, which can be evinced by the two-body density matrices. Thus, the inter-component two-body density matrix  $\rho_2^{AB}(x, y)$  is depleted along the diagonal  $x = y$  (see Fig. 4.3 [bottom row



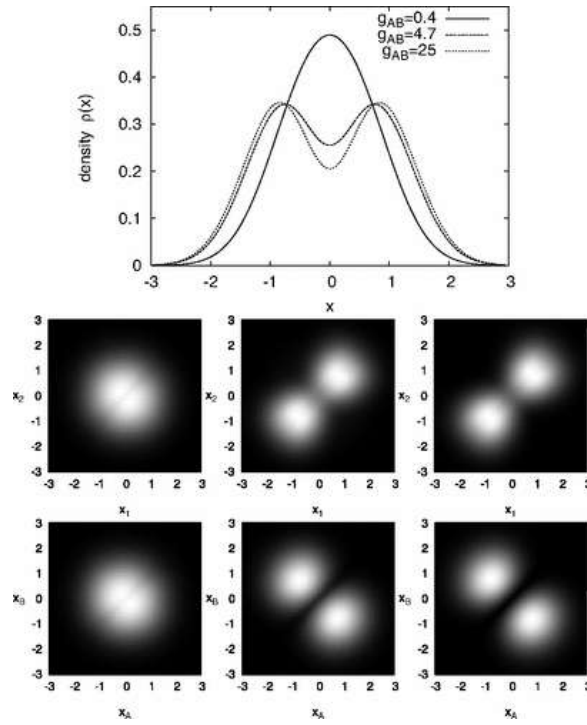


Figure 4.3: CF of a 2+2 mixture at  $g_\sigma = 0.4$ . One body density  $\rho_1^\sigma(x)$  [top], intra-component two-body density matrix  $\rho_2^\sigma(x_1, x_2)$  [middle row] and inter-component two-body density matrix  $\rho_2^{AB}(x^A, x^B)$  [bottom row] at three different couplings  $g_{AB} \in \{0.4, 4.7, 25\}$  [columns]. Last column is the characteristic pattern of CF. Reprinted figure with permission from [163]. Copyright (2008) by the American Physical Society. DOI: <https://doi.org/10.1103/PhysRevA.78.013629>.

on the right]), meaning there is zero probability of finding two particles of different species at the same location. In fact, judged by the anti-diagonal pattern of the density plot, two distinguishable particles are most likely to be found on opposite sides of the harmonic trap. Meanwhile, particles of the same component bunch together on the same side of the harmonic trap, as indicated by the diagonal pattern in the intra-component two-body density matrix  $\rho_2^\sigma(x, y)$  (see Fig. 4.3 [middle row on the right]).

Based on these observations, a two-mode approximation has been suggested [163]  $|\Psi\rangle \approx \frac{1}{\sqrt{2}} (|\Psi_L^A\rangle |\Psi_R^B\rangle \pm |\Psi_R^A\rangle |\Psi_L^B\rangle)$  with  $|\Psi_L^\sigma\rangle = |N_\sigma, 0\rangle$  and  $|\Psi_R^\sigma\rangle = |0, N_\sigma\rangle$  for a left and right localized Gaussian-type states, respectively. The advantage of this viewpoint is that each species orbital is a mean-field state. Naturally, a mean-field ansatz for the whole mixture is unable to describe the two configurations at the same time. Thus, only one configuration with ‘broken’ parity symmetry can be obtained by solving the coupled GPEs. Importantly, the symmetry breaking takes place already at intermediate values of  $g_{AB}$  [MP3] providing evidence for the failure of an uncorrelated ansatz.

**FULL FERMIONIZATION:** In the limit when all interactions become infinitely repulsive  $g_{AB} = +\infty$  and  $g_\sigma = +\infty$ , the mixture can be mapped to

a system of  $N = N_A + N_B$  non-interacting fermions [165]. Similar to **TG** and **CF** we can replace the effect of interactions by hard-core boundary conditions  $\Psi(\vec{x}) = 0$  if  $x_i = x_j$  for any pair of particles and  $\vec{x} = (\vec{x}^A, \vec{x}^B)$ . As in the **TG** case, we can employ the Bose-Fermi mapping to construct the ground state from a properly symmetrized determinant, i. e.,  $\Psi(\vec{x}) = A(\vec{x})\Psi_F(\vec{x}) = |\Psi_F(\vec{x})|$  with  $A(\vec{x}) = \prod_{i < j} \text{sign}(x_i - x_j)$ . However, as opposed to **TG**, here the ground state is  $\frac{N!}{N_A!N_B!}$ -fold degenerate. There is a particularly insightful choice of basis for this manifold, the so-called *snippets* [166, 167].

To better understand what snippets are, let us consider  $N$  distinguishable particles with an infinite  $\delta$  repulsion in a longitudinal potential  $V(z)$ . Since the particles are impenetrable, they are ordered and can be written as a label sequence  $|\sigma_1, \dots, \sigma_N\rangle$  with  $\sigma_i$  the particle label. E. g., for  $N = 3$  there are six ways of ordering:  $|ABC\rangle, |ACB\rangle, |BAC\rangle, |BCA\rangle, |CAB\rangle$  and  $|CBA\rangle$ . Thus, we can partition the whole space  $\mathbb{R}^N$  into  $N!$  configuration sectors  $C_\pi = \{\vec{x} \in \mathbb{R}^N | x_{\pi(1)} < \dots < x_{\pi(N)}\}$  with  $\pi$  a permutation of particles. Within each sector, the many-body wave-function obeys the Schrödinger equation of  $N$  non-interacting particles and it vanishes at the sector boundaries. A snippet state  $|\pi\rangle$  is a symmetrized fermionic state restricted to a particular sector  $C_\pi$ :

$$\langle \vec{x} | \pi \rangle = \sqrt{N!} \theta(x_{\pi(1)}, \dots, x_{\pi(N)}) |\langle \vec{x} | \Psi_F \rangle|, \quad (4.9)$$

where  $\theta(x_{\pi(1)}, \dots, x_{\pi(N)}) = 1$  if  $x_{\pi(1)} < \dots < x_{\pi(N)}$  and zero otherwise. The basis is orthonormal by construction  $\langle \pi | \pi' \rangle = \delta_{\pi, \pi'}$  and each state  $|\pi\rangle$  is a ground state of  $N$  distinguishable impenetrable particles.

Coming back to the Bose mixture, we now need to unite those sectors, which correspond to an exchange of indistinguishable particles, i. e., we symmetrize w. r. t. each species. E. g., for  $N_A = 2$  and  $N_B = 1$  there are only three configurations:  $|AAB\rangle, |ABA\rangle$  and  $|BAA\rangle$ , the same as the degeneracy level. Let  $|e\rangle$  refer to a many-body state of  $N$  distinguishable impenetrable particles with a default ordering  $x_1 < \dots < x_N$ . Then, we can construct all three eigenstates from the snippet basis as follows:

- $|AAB\rangle = \frac{1}{\sqrt{2}} (|e\rangle + |\pi_{1,2}\rangle)$
- $|ABA\rangle = \hat{\pi}_{2,3} |AAB\rangle$
- $|BAA\rangle = \hat{\pi}_{1,3} |AAB\rangle$

with  $\pi_{i,j}$  exchanging the positions of particles  $i$  and  $j$ .

For large but finite interactions,  $1/g_\sigma \ll 1$  and  $1/g_{AB} \ll 1$ , one can do zeroth order degenerate perturbation theory for the ground state manifold and derive an effective Hamiltonian  $H_{eff}$ :

$$\begin{aligned} H_{eff} = E_F \mathbb{1} - 2 \sum_{\sigma} \sum_i^{N-1} \frac{C_i}{g_\sigma} |\sigma\rangle_i |\sigma\rangle_{i+1} \langle \sigma|_i \langle \sigma|_{i+1} \\ - \sum_i^{N-1} \frac{C_i}{g_{AB}} (|A\rangle_i |B\rangle_{i+1} + |B\rangle_i |A\rangle_{i+1}) (\langle A|_i \langle B|_{i+1} + \langle B|_i \langle A|_{i+1}), \end{aligned} \quad (4.10)$$

where  $E_F$  is the ground state energy of  $N$  non-interacting fermions in a potential  $V(z)$ ,  $C_i = \frac{N! \hbar^4}{m^2} \int dx_1 \cdots dx_N \delta(x_i - x_{i+1}) \theta(x_1, \dots, x_N) \left| \frac{\partial \Psi_F}{\partial x_i} \right|^2$  and  $|\sigma\rangle_i$  refers to the label at index  $i$ .

By identifying  $|A\rangle \leftrightarrow |\uparrow\rangle$  and  $|B\rangle \leftrightarrow |\downarrow\rangle$ , one finds:

$$\begin{aligned}\sigma_x &= |A\rangle \langle B| + |B\rangle \langle A|, & \sigma_y &= -i |A\rangle \langle B| + |B\rangle \langle A|, \\ \sigma_z &= |A\rangle \langle A| - |B\rangle \langle B|, & \mathbb{1} &= |A\rangle \langle A| + |B\rangle \langle B|.\end{aligned}$$

We can now formulate Eq. (4.10) as a spin chain Hamiltonian  $H_{sp}$  [168–172]:

$$\begin{aligned}H_{sp} &= -\frac{1}{2g_{AB}} \sum_i^{N-1} C_i \left[ \sigma_x^{(i)} \sigma_x^{(i+1)} + \sigma_y^{(i)} \sigma_y^{(i+1)} \right] \\ &\quad - \frac{1}{2} \left( \frac{1}{g_A} + \frac{1}{g_B} - \frac{1}{g_{AB}} \right) \sum_i^{N-1} C_i \sigma_z^{(i)} \sigma_z^{(i+1)} \\ &\quad + \left[ E_F - \frac{1}{2} \left( \frac{1}{g_A} + \frac{1}{g_B} + \frac{1}{g_{AB}} \right) \sum_i^{N-1} C_i \right] \mathbb{1} \\ &\quad - \frac{1}{2} \left( \frac{1}{g_A} - \frac{1}{g_B} \right) \sum_i^{N-1} C_i \left[ \sigma_z^{(i)} + \sigma_z^{(i+1)} \right].\end{aligned}$$

The third term  $\propto \mathbb{1}$  is just an energy offset and can be ignored. The fourth term is an inhomogeneous magnetic field. Assuming  $V(z) = 0$  gives  $C_i = C$  and the field becomes homogenous. Since the total magnetization is conserved, the field has no effect, so we discard it.

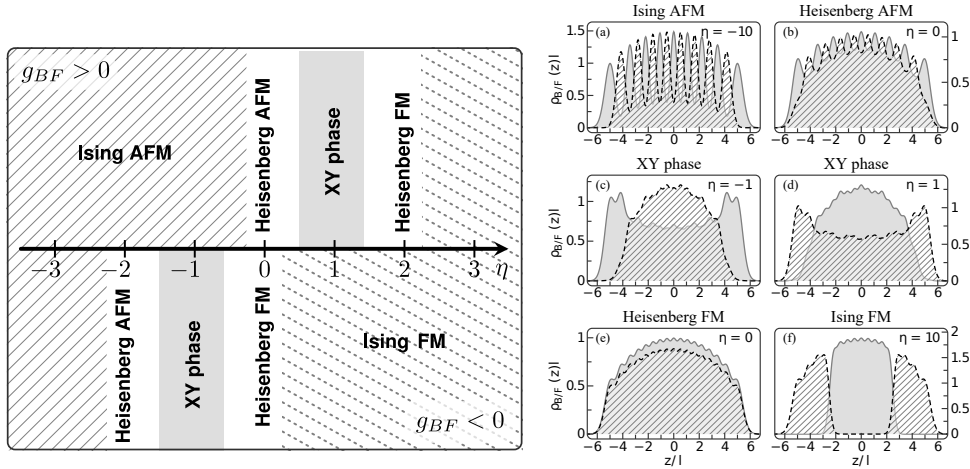


Figure 4.4: Phase diagram [left] and one-body densities  $\rho_1^\sigma(x)$  [right] of a Bose mixture at strong repulsive interactions. Reprinted figures with permission from [171]. Copyright (2017) by the American Physical Society. DOI: <https://doi.org/10.1103/PhysRevA.95.043630>.

If we further transform  $\sigma_x^{(i)} \rightarrow (-1)^i \sigma_x^{(i)}$  and  $\sigma_y^{(i)} \rightarrow (-1)^i \sigma_y^{(i)}$ , we arrive at the XXZ Heisenberg model in the absence of a magnetic field:

$$H_{XXZ} = J_{xy} \left[ \sum_i^{N-1} \sigma_x^{(i)} \sigma_x^{(i+1)} + \sigma_y^{(i)} \sigma_y^{(i+1)} + (1 - \eta) \sigma_z^{(i)} \sigma_z^{(i+1)} \right]$$

with  $J_{xy} = \frac{C}{2g_{AB}}$  and  $\eta = \frac{g_{AB}}{g_A} + \frac{g_{AB}}{g_B} = 1 - \frac{J_z}{J_{xy}}$ . The Hamiltonian has a very rich phase diagram (see Fig. 4.4): Heisenberg (Anti-)Ferromagnet, Ising (Anti-)Ferromagnet and XY phase. Different phases can be accessed by changing the sign and ratio of the coupling strengths.

**ATTRACTIVE COUPLING:** Finally, we would like to mention a particularly interesting phenomenon occurring in attractive mixtures ( $g_{AB} < 0$ ) of weakly repulsive components ( $g_\sigma > 0$ ), namely *quantum droplets* [173]. They display some peculiar properties and have been recently confirmed in experiments [59, 67, 174]. In free space they neither disperse nor collapse but remain self-bound. They are characterized by a saturation density  $\rho_*$ . As the number of particles is increased, the droplet first becomes denser while its spatial extension remains constant. After the threshold value  $N_*$  has been reached, the excess particles migrate to the density edges, causing a growth of the droplet's size while keeping the density fixed (see Fig. 4.5).

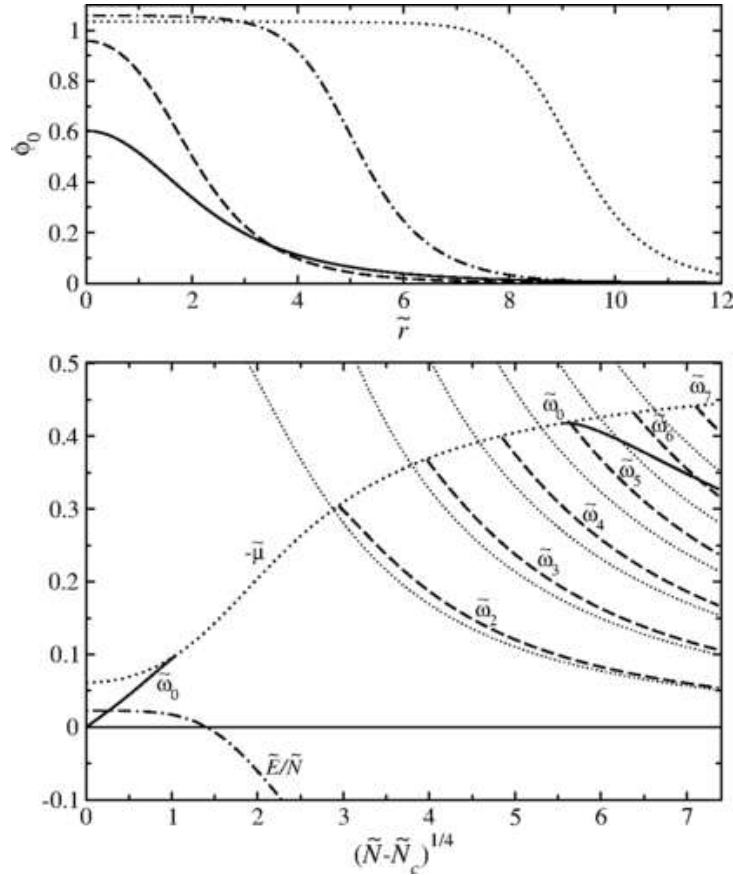


Figure 4.5: Top: The wave function of quantum droplet versus radial coordinate (both in rescaled units) for an increasing number of particles (indicated by the growing area under the curve). Reprinted figure with permission from [175]. Copyright (2015) by the American Physical Society. DOI: <https://doi.org/10.1103/PhysRevLett.115.155302>.

Droplets are possible because of beyond-mean field effects. Assume a homogeneous mixture in a miscible regime and introduce a residual mean-field coupling  $\delta g = g_{AB} + \sqrt{g_A g_B}$ . The GPE becomes unstable at  $\delta g < 0$

predicting a collapse of the condensate wave-function [176]. However, in the vicinity of  $\delta g \approx 0$  correlations become indispensable and a first order beyond-mean field correction to the GPE needs to be introduced, the Lee-Huang-Yang (LHY) term [175, 177, 178]. The residual mean-field and the LHY terms display different dependencies on the coupling constants and scaling with the condensate density  $\rho(x)$ . The trap dimensionality plays also a crucial role: in 3D the mean field term can be made attractive while the LHY term is repulsive; in 1D it is the other way around. Hence, one can tune the two contributions independently until they balance each other out. Thus, attractive forces which localize the particles become stabilized by repulsive forces. The collapse can be avoided and finite size quantum droplets are formed.

Another notable study [179] addresses the behaviour of attractively coupled TG mixture, i. e.,  $g_{AB} < 0$  and  $g_\sigma = +\infty$ . At intermediate couplings a molecular TG is formed, i. e., bound pairs composed of distinguishable particles, followed by condensation of these pairs at strong couplings and, beyond a critical value, the mixture undergoes a collapse.

#### 4.3 PREFACE: EIGENSYSTEM OF A 2+2 HARMONIC MIXTURE

In [MP1] we consider a few-body binary mixture with two bosons per species confined in a 1D harmonic trap. The work can be divided in two subtopics: the properties of the low-energy spectrum and the breathing dynamics. The latter shall be discussed in Section 5.5. Here, we proceed with the analysis of stationary properties.

To solve the eigenvalue problem, we employ the exact diagonalization method (Section 3.1) in a correlated product basis of relative-frame coordinates. Inspired by the analytical solution of a single-component two-body problem derived in [180], we perform a transformation to a coordinate frame  $\tilde{Y} = \{R_{cm}, R_{AB}, r_A, r_B\}$  composed of i) the centre-of-mass  $R_{cm} = \frac{1}{N_A+N_B} \sum_{i,\sigma} x_i^\sigma$ , ii) the relative intra-species distance  $r_\sigma = x_1^\sigma - x_2^\sigma$  and iii) the inter-component distance  $R_{AB} = \frac{1}{N_A} \sum_i x_i^A - \frac{1}{N_B} \sum_i x_i^B$ . Using product states of symmetrized parabolic functions, Eq. (2.2) becomes diagonal and Eq. (2.3) is the only non-diagonal matrix. As opposed to a straightforward expansion in terms of Fock states constructed from harmonic oscillator orbitals [81], our basis incorporates exactly the correlations induced by the intra-species interactions. As a result, we achieve a faster convergence w. r. t. the basis size.

Apart from technical improvements to solve the given Hamiltonian, we analysed the underlying symmetries in both frames. They have strong implication for observed degeneracies, explain avoided crossings and allow a convenient categorization of eigenstates into symmetry classes thereby promoting a symmetry-induced block-diagonalization.

In the laboratory frame, there is i) a bosonic exchange symmetry  $\hat{S}_\sigma$  for two indistinguishable particles, ii) the global coordinate reflection  $\hat{P}_X$ , i. e.,  $x_i^\sigma \rightarrow -x_i^\sigma$ , iii) in a species-symmetric case  $g_A = g_B$  the exchange of particle

labels  $\hat{S}_{AB}$ , i. e.,  $x_i^\sigma \rightarrow x_i^{\bar{\sigma}}$ , and iv) in a totally symmetric case  $g_A = g_B = g_{AB}$  any exchange of particles  $\hat{S}_{ij}$ .

In the relative frame, we discover additional symmetries: i) the parity of individual relative coordinates  $\hat{P}_{Y_i}$ , i. e.,  $Y_i \rightarrow -Y_i$  and ii) in a species-symmetric case  $g_A = g_B$  the exchange  $r_A \leftrightarrow r_B$ . Some of the above symmetries are by far not obvious from the laboratory frame perspective, as they involve improper rotations of the four-dimensional coordinate space. The spherical or cylindrical coordinates serve in fact the same purpose, namely to make the symmetries of the laboratory frame more obvious/simple from the mathematical point of view. The question arises whether further abstract symmetry transformations of the particles coordinates exist with an intuitive interpretation in a suitably-chosen coordinate frame, beyond what is currently known in physics. In a somewhat related spirit, in Section 7.4 we discuss yet another kind of hidden symmetries, called latent, revealed not by a coordinate transformation, but by a spectrum preserving subsystem partitioning.

#### 4.4 PREFACE: BOSE POLARON IN A HARMONIC TRAP

In [MP3] we investigate the process of phase separation in a Bose polaron setup, i. e., an impurity coupled to a medium composed of multiple atoms (see Eq. (2.1)). The miscible-immiscible transition is one of the key features in composite mixtures. For instance, it is of experimental relevance in the context of sympathetic cooling [181, 182], lies at the heart of dynamical domain formation [183–185] and allows for peculiar vortex patterns [186, 187].

We choose a harmonic species-selective external confinement with a trap ratio  $\eta = \omega_B/\omega_A$ . In addition, we vary the particle number imbalance  $N_B/N_A$  and the coupling strength  $g_{AB}$ . For simplicity, we assume a non-interacting medium ( $g_A = 0$ ). As we have already mentioned in Section 4.2, the miscible-immiscible phase boundary is by far not trivial. Furthermore, not much attention has been paid to characterize the boundaries among distinct types of phase segregation.

We classify phases according to the one-body density shapes discussed in Section 4.2. For weak-to-intermediate repulsive interactions we anticipate the miscible phase, the CF and two types of the core-shell PS with either the medium or the impurity occupying the trap centre, BAB and ABA, respectively. To differentiate among the four possibilities, we use

$$\Delta_\sigma = \frac{\rho_1^\sigma(x=0)}{\max_x \rho_1^\sigma(x)}, \quad (4.11)$$

which tells us whether species  $\sigma$  is at the centre of its trap ( $\Delta_\sigma = 1$ ). We remark that for a mean-field ansatz, instead of the CF which is an entangled state, we expect a configuration with a broken parity symmetry.

Our major finding is that at the miscible-immiscible phase boundary the type of phase segregation is determined by a critical trap ratio  $\eta_c$ :

$$\sqrt{1/\eta_c} = \sqrt[3]{N_B/N_A}, \quad (4.12)$$

which is derived from the energy competition of the two species to occupy the trap centre. To this end, we employ an effective Hamiltonian for the species  $\sigma$  featuring an induced potential determined by the density shape of the fellow component  $\bar{\sigma}$ :

$$V_{\text{eff}}^{\sigma}(x) = g_{AB} N_{\bar{\sigma}} \rho_1^{\bar{\sigma}}(x). \quad (4.13)$$

At weak couplings (the miscible regime), the effective potential is a scaled ground state of the quantum harmonic oscillator. Thus, the total potential is a harmonic trap with a central barrier, which grows in height with increasing  $g_{AB}$ . When the ground state energy of the effective potential turns below the barrier height, the species will depart from the trap centre and form two parity symmetric humps, i. e., it separates.

For  $\eta \gg \eta_c$  we predict the *ABA* core-shell **PS**, at  $\eta \approx \eta_c$  the **CF** and for  $\eta \ll \eta_c$  the *BAB* core-shell **PS**. This conforms well with our intuition:  $\eta \gg \eta_c$  corresponds to a tightly localized and robust impurity, whereas at  $\eta \ll \eta_c$  it is delocalized and easy to perturb. At  $\eta = \eta_c$  neither species can prevail to stay at the trap centre, so none of them does, which leads to the **CF**. With an increasing number of majority atoms,  $\eta_c$  tends to extremely high values implying a static impurity.

In addition, we provide estimate values for all phase boundaries and identify hints for the existence of tri-critical points, i. e., isolated points in the phase diagram, where three phases become adjacent. Furthermore, we link the critical trap ratio  $\eta_c$  to high values of the entanglement  $S_{vN}$ . This helps us to reveal a *latent* **CF** disguised as a core-shell **PS**. Indeed, the two-body density matrices confirm typical signatures of the **CF**: localization of a single component on either side of the trap and the separation of the two species to opposite sides.

#### 4.5 PREFACE: BOSE POLARON IN A SPECIES-SELECTIVE TRAP

In [MP4] we study the interplay between a finite-lattice trapped majority component (the medium) and an impurity confined in a box potential. Our goals are to find parameter regions with a potentially interesting behaviour, to segregate the mean-field effects and to characterize the impact of correlations.

In a decoupled regime ( $g_{AB} = 0$ ), the medium can reside in a superfluid-like phase or in an insulating-like phase depending on the lattice depth and intra-component interactions [188], whereas the impurity is localized at the trap centre and is spatially extended over a broad region.

First, we identify non-trivial parameter regions where the coupling strength  $g_{AB}$  leads to substantial structural differences when compared to a decoupled mixture. To this end, we employ the fidelity  $F(\hat{\rho}, \hat{\sigma})$  [189] to measure the distance between two quantum states described by density operators  $\hat{\rho}$  and  $\hat{\sigma}$ :

$$F(\hat{\rho}, \hat{\sigma}) = \left( \text{Tr} \sqrt{\sqrt{\hat{\rho}} \hat{\sigma} \sqrt{\hat{\rho}}} \right)^2 = F(\hat{\sigma}, \hat{\rho}). \quad (4.14)$$

We evaluate the fidelity for the ground state of a decoupled mixture and of a mixture with a finite coupling strength  $g_{AB}$ . We do so at different levels: the (pure) many-body states  $\hat{\rho}$  and (mixed) single-particle states  $\hat{\rho}_1^\sigma$ . On the many-body level, apart from the anticipated phase segregation at strong positive couplings, we find two further peculiar regimes, where the inter-component coupling greatly perturbs the many-body state of a decoupled mixture: a weakly interacting medium in a deep lattice with an attractive coupling to the impurity (regime I) and an attractively interacting medium coupled repulsively to the impurity with  $-g_A \approx g_{AB}$  (regime II). Although the overall impact looks diminished at the single-particle level, the fidelity of the medium displays similar signatures as the fidelity of the many-body state. However, in the immiscible regime the medium is almost unaffected by the impurity presence, whereas the impurity is strongly perturbed, namely it is pushed away from spatial regions occupied by the majority component leading to the core-shell PS. Thus, the fidelity of the impurity captures well the onset of phase segregation.

Second, we analyse the inter-component entanglement  $S_{vN}$  and the fragmentation entropy  $S_{vN}^\sigma$  of each species (defined in Section 3.3.3). This step allows us to differentiate between mean-field effects and correlation-induced phenomena. In the regime I, there is practically no entanglement or fragmentation present, i. e., a mean-field ansatz would be appropriate, even though the interactions are of a moderate strength. The fragmentation of the medium is completely destroyed by the attractive coupling to the impurity and the state becomes highly localized implying the formation of a many-body bound state. Interestingly, prior to this collapse we evidence states with a moderate amount of correlations. In the regime II, both the entanglement and fragmentation are extremely high. We suspect droplet-like states.

Third, we look at the one-body density functions  $\rho_1^\sigma(x)$  and two-body correlation distributions:  $\rho^{AA}(r)$  characterizing the probability for two majority particles to be at a distance  $r$  from each other and  $\rho^{AB}(r)$  characterizing the probability for a majority particle to be at a distance  $r$  from the impurity. In particular, we compare these quantities to their non-entangled counterparts, obtained assuming a SMF product ansatz. This allowed us to spatially resolve the impact of correlations on measurable quantities. Overall, we find that entanglement accelerates the process of phase segregation at repulsive couplings and counteracts the process of localization at attractive couplings.



After having developed a good understanding of ground state regimes which can be encountered in a trapped Bose gas/mixture (Chapter 4), we proceed with the investigation of collective low-energy excitations. In the early years after the experimental realization of a BEC, collective excitations of a trapped gas were among the first aspects to be tested experimentally [190–192] in order to benchmark effective theoretical models available at that time [193–196], such as the hydrodynamical and GPE approaches. Excellent agreement between theory and experiments have been found in the regime of a weakly-correlated macroscopic condensate [197].

The immense progress in experimental techniques allowed to extend these studies to regimes with sizeable correlations such as the transition from BEC to TG in a 1D geometry [69, 153, 198–200] or the BEC-BCS crossover [201–203] in a trapped Fermi mixture. The strong sensitivity of collective modes to the shape of interactions and trapping geometry along with the ability to measure them with high-accuracy, employing modern imaging tools such as the correlation-based principal component analysis (PCA) [204], open the road to use collective modes as a sensitive diagnostics: to verify at which regime the system has been prepared [69, 153, 203, 205]; to access mean kinetic, potential and repulsive energies and other key observables [206]; to perform high-precision measurements of the scattering length or the trapping frequency [207] and to extract the screening parameter and the particle charge in complex plasmas [208]. The utility of low-energy collective modes for trapped particles has been compared to absorption/emission spectroscopy used for molecular systems [209].

In this chapter, we want to discuss a particular type of collective modes, namely the breathing mode [209], focussing on harmonically trapped particles in 1D at zero temperature. In Section 5.1 we introduce the notion of collective modes through the lens of one-body density and a particular quench protocol employed in this work. Then, in Section 5.2 we characterize key features of a breathing mode. Section 5.3 contains major findings related to a single-species Bose gas. Finally, we address how a partial distinguishability of particles enriches the breathing response in a two-component Bose mixture in Section 5.4. In Sections 5.5 and 5.6 we outline our own contributions focussing on few-body mixtures and beyond mean-field effects.

## 5.1 COLLECTIVE MODES

We consider an equilibrated ultracold ensemble of  $N$  interacting particles (bosons or fermions) subject to an external confinement. At a time  $t = 0$ , the dynamics is triggered by a sudden but weak quench of a system parameter, which can be formulated as a perturbation  $\epsilon\hat{Q}$  with  $\epsilon \ll 1$ . The pre-quench

and post-quench Hamiltonians,  $\hat{H}_0$  and  $\hat{H}$  respectively, are related as  $\hat{H}_0 = \hat{H} + \epsilon\hat{Q}$ .

In the following, we are interested in the low-energy *collective* excitations participating in the dynamics. Collective implies that every particle performs the same motion. As the particles are indistinguishable, the problem can be reduced to a spatial monitoring of the time-evolving one-body density  $\rho_1(x, t)$ . As explained in Section 3.3.3, it is obtained by tracing out the many-body density  $\hat{\rho}(t)$ . The latter will be represented in the basis of post-quench eigenstates  $|E_j\rangle$  such that  $\hat{\rho}(t) = \sum_{j,k} c_j c_k e^{-\frac{i}{\hbar}(E_j - E_k)t} |E_j\rangle \langle E_k|$  with real overlap coefficients  $c_j = \langle E_j | \Psi(0) \rangle$  for the initial state  $|\Psi(0)\rangle$ , which is the ground state of  $\hat{H}_0$ . Given the above representation, the one body-density  $\rho_1(x, t)$  can be now decomposed as follows:

$$\rho_1(x, t) = \sum_j c_j^2 \rho_1^{(j,j)}(x) + 2 \sum_{j>k} c_j c_k \rho_1^{(j,k)}(x) \cos(\Omega_{j,k}t), \quad (5.1)$$

with transition densities  $\hat{\rho}_1^{(j,k)} = \text{Tr}_{N-1} [|E_j\rangle \langle E_k|]$  and frequencies  $\Omega_{j,k} = (E_j - E_k)/\hbar$ . The first term in Eq. (5.1) is a time-independent background density while the second term contains multiple oscillatory contributions for every eigenstate pair  $(j, k)$  which is populated ( $c_j c_k \neq 0$ ), each with a characteristic spatial modulation profile  $\rho_1^{(j,k)}(x)$ .

To evaluate the overlap coefficients  $c_j$ , it is convenient to view the initial state as a weakly perturbed ground state  $|E_0\rangle_\epsilon$  of the post-quench Hamiltonian  $\hat{H}$ . Using the non-degenerate perturbation theory, we arrive at a first order correction:

$$|E_0\rangle_\epsilon = c \left( |E_0\rangle + \epsilon \sum_{j \neq 0} \frac{\langle E_j | \hat{Q} | E_0 \rangle}{E_0 - E_j} |E_j\rangle \right), \quad (5.2)$$

with a constant  $c$  to normalize the state. Obviously, large energy gaps  $E_0 - E_j$  strongly suppress the population of higher energy eigenstates, while transition matrix elements  $\langle E_j | \hat{Q} | E_0 \rangle$  may filter out states of a particular symmetry. Given that  $\epsilon$  is sufficiently small, we may simplify Eq. (5.1):

$$\rho_1(x, t) \approx c_0^2 \rho_1^{(0,0)}(x) + 2 \sum_j c_j c_0 \rho_1^{(j,0)}(x) \cos(\Omega_{j,0}t), \quad (5.3)$$

where we neglected terms  $c_j c_k \propto \epsilon^2$ , i. e., when both  $j \neq 0$  and  $k \neq 0$ . In particular, every frequency corresponds now to an energy gap w. r. t. the ground state  $|E_0\rangle$ .

The density evolution may be further abstracted as  $\rho_1(x, t) = f(x) + \sum_n f_n(x) \cos(\Omega_n t)$  with distinct oscillation frequencies  $\Omega_n$ , i. e., summarizing contributions stemming from eigenstate pairs having the same energy gap. Each  $f_n(x) \cos(\Omega_n t)$  will be called a *collective mode* characterized by a mode profile  $f_n(x)$  and a mode frequency  $\Omega_n$ .

## 5.2 BREATHING MODES

When the perturbation operator corresponds to a weak quench of the trapping frequency  $\omega_0 = \omega + \eta$  in a harmonic confinement, i. e.,  $\hat{Q} = m\omega \sum_i x_i^2$ ,

the resulting dynamics observed in the one-body density resembles a respiratory motion, i. e., a periodic contraction and expansion of the density variance:

$$\sigma^2(t) = \int dx (x - \bar{x}_t)^2 \rho_1(x, t) = \frac{1}{N} \langle \sum_i x_i^2 \rangle_t - \frac{1}{N^2} \langle \sum_i x_i \rangle_t^2 \quad (5.4)$$

with mean  $\bar{x}_t = \int dx x \rho_1(x, t)$ . Collective excitations as registered by oscillations of the density variance  $\sigma^2(t)$  are known as *breathing modes*.

As the external confinement is reflection symmetric around the origin ( $x = 0$ ), only states of the same parity (even or odd) can be coupled by  $\hat{Q}$ . This implies  $\langle \sum_i x_i \rangle_t = 0$ . Thus,  $\sigma^2(t)$  is proportional to the expected value of the perturbation  $\langle \hat{Q} \rangle_t$  and we call  $\hat{X}^2 = \sum_i x_i^2$  the *breathing operator*.

*breathing is synonymous to monopole and compressional*

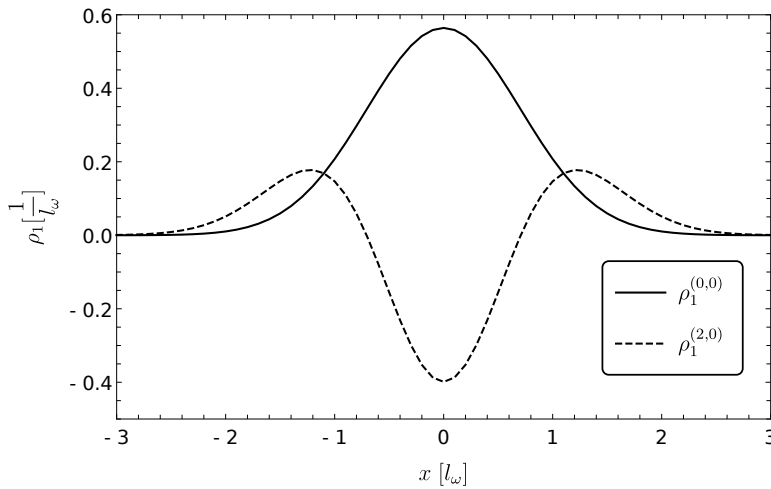


Figure 5.1: Single particle breathing. The background density  $\rho_1^{(0,0)}(x)$  and the modulation profile  $\rho_1^{(2,0)}(x)$ .

To provide some intuition as to why the density ‘breathes’, let us consider a single particle. To simplify the notation, we employ harmonic oscillator units of the post-quench operator, i. e.,  $H = -\frac{1}{2} \frac{\partial^2}{\partial x^2} + \frac{1}{2} x^2$ . The spectrum is equidistantly spaced  $E_k = k + 1/2$  and the spatial projection of eigenstates is  $E_k(x) = \frac{1}{\sqrt{2^k k!}} \frac{1}{\sqrt{\pi}} \exp(-\frac{x^2}{2}) H_k(x)$  with  $H_n(x)$  the physicists’ Hermite polynomial. The selection rule for allowed transitions mediated by the perturbation operator is  $\Delta n = \pm 2$ . Thus, starting initially with the ground state  $|E_0\rangle$ , we populate only the state  $|E_2\rangle$ . The breathing frequency is  $\Omega_{2,0} = (E_2 - E_0) = 2$  in units of  $\omega$ . The background and modulation densities are sketched in Fig. 5.1. As one can see, the static background  $\rho_1^{(0,0)}(x)$  is a Gaussian. Depending on the sign of the cosine function, the modulation profile  $\rho_1^{(2,0)}(x)$  can either i) expand the Gaussian by depleting the central region and simultaneously enhancing the outer regions or ii) compress the Gaussian via the reverse process.

## 5.3 SINGLE SPECIES

For  $N$  interacting particles the situation is slightly different with  $\langle \sum_i x_i^2 \rangle_t$  having two breathing frequencies instead of one. To gain a better understanding, it will be useful to replace particle coordinates (laboratory frame) with the center-of-mass (CoM)  $R_{cm} = \frac{1}{N} \sum_i x_i$  and relative distances  $r_j$ , e. g., the Jacobi coordinates (CoM frame). Then, the transformed Hamiltonian separates in two independent parts  $H = H_{cm} + H_{rel}$ , each with its own breathing frequency labelled  $\Omega_{cm}$  and  $\Omega_{rel}$  respectively.

The CoM Hamiltonian  $H_{cm}$  is a ‘single-particle’ harmonic oscillator with a frequency  $\omega$ . Thus, it features a single breathing mode with a universal (interaction-independent) frequency  $\Omega_{cm} = 2$  characterizing modulations of the CoM variance as measured by the breathing operator  $\langle \hat{R}_{cm}^2 \rangle$ . As a side remark, the expression  $N^2 \langle \hat{R}_{cm}^2 \rangle = \langle \sum_i x_i^2 \rangle + 2 \langle \sum_{i<j} x_i x_j \rangle$  indicates that the expectation  $\langle \sum_{i<j} x_i x_j \rangle$ , which depends on a two-body density  $\hat{\rho}_2$ , eliminates the relative frequency  $\Omega_{rel}$  from  $\langle \sum_i x_i^2 \rangle$ .

The Hamiltonian  $H_{rel}$  contains all the relative coordinates  $r_j$  and, importantly, the interaction term of  $H$ . The breathing operator  $\langle \sum_{i<j} d_{ij}^2 \rangle$  with  $d_{ij} = x_i - x_j$  excludes  $R_{cm}^2$  contribution. Thus, it probes exclusively the breathing of relative distances. The corresponding mode frequency  $\Omega_{rel}$  is very sensitive to the shape and strength of interactions.

Breathing mode frequencies are known in some limiting cases. In particular, we want to highlight the sensitivity of breathing modes to the shape and strength of interaction potentials by mentioning some common long-range and short-range repulsive interactions. We restrict our discussion to 1D systems as all of our studies have been carried out completely in 1D. For repulsive dipolar interaction  $\propto 1/r^3$ ,  $\Omega_{rel}$  decreases monotonically from 2 to  $\sqrt{3}$  as the interaction parameter is increased [210]. For repulsive Coulomb interaction  $\propto 1/r$ ,  $\Omega_{rel}$  increases monotonically from 2 to  $\sqrt{5}$  as the interaction parameter is increased [211, 212].

For repulsive short-range contact-type interaction, the behaviour is not monotonic anymore. For a BEC ( $g = 0$ ) and TG ( $g = +\infty$ ) there is just a single breathing frequency  $\Omega = 2$ , since both limits have an equally spaced spectrum of a quantum harmonic oscillator, i. e.,  $\Omega_{cm}$  and  $\Omega_{rel}$  are degenerate. In the TF regime, the relative motion breathing frequency attains its global minimum  $\Omega_{rel} = \sqrt{3}$ . In-between those regimes an approximation for  $\Omega_{rel}$  can be derived semi-analytically via weighted moments and sum rules [213] or numerically by a modified GPE approach [200].

The  $\Omega_{rel}(g)$  curve does also depend on the number of particles and correlations must be often included for an accurate description [214–216]. In particular, the two-body problem can be solved analytically and has already provided many fruitful insights [180, 217–219]. For mesoscopic systems  $N < 100$ , the global minimum lies above the TF value, i. e.,  $\min \Omega_{rel}(g) > \sqrt{3}$ . As the number of particle is increased, the plateau around the minimum broadens and the value approaches its TF limit. Additionally, the CoM breathing mode becomes increasingly suppressed because its amplitude scales as  $1/N$  [214].

## 5.4 TWO SPECIES

The breathing response becomes even more complex for two distinct components. Although more challenging to solve and analyse, the partial distinguishability of particles makes the spectrum richer and opens many exciting possibilities.

Elementary excitations of a binary bosonic mixture in a harmonic confinement have been studied primarily in 3D using a Bogoliubov approach [220–224]. Recently, the breathing dynamics of a Bose polaron in 1D has been realized experimentally [225, 226] with a particular emphasis on the impurity motion. Let us summarize major findings of the above studies, as they will be useful also in our setting. First, since there are two flavours of particles, it is possible to excite in-phase or out-phase oscillations of the two components by a suitable quench of external traps. Second, the inter-component coupling has a strong impact on the eigenenergies and thus also on the excitation frequencies. Generally, at a repulsive (attractive) coupling the frequencies of low energy excitations experience a negative (positive) shift. Some might even become imaginary, thereby indicating the onset of phase segregation and symmetry breaking. Third, there are species-type modes dominating the collective behaviour within a single component and modes synchronizing particles of both species.

As we have already evidenced in Chapter 4, interaction-induced correlations have a sizeable impact on static properties of a binary mixture, especially near the miscible-immiscible phase boundary. Hence, we anticipate sizeable differences between the mean-field and exact few-body dynamics. From the single-component discussion, we expect the universal CoM mode to be also present in the mixture setting, assuming the post-quench trap frequencies  $\omega_\sigma$  are equal, i. e., when the CoM coordinate is separable. In addition, at weak inter-component interactions one anticipates that each species will feature a characteristic intra-component breathing with a frequency  $\Omega_{rel}^\sigma$ , particularly sensitive to the intra-component interaction parameter  $g_\sigma$ . Naturally, they are likely to be shifted due to the inter-component coupling  $g_{AB}$ . Thus, we might consider to take a separate look at the breathing operator of each species  $\langle X_\sigma^2 \rangle_t = \langle \sum_i^{N_\sigma} (x_i^\sigma)^2 \rangle_t$  and classify the excited modes accordingly.

## 5.5 PREFACE: BREATHING RESPONSE OF A BOSE MIXTURE

In [MP1] we study the dynamical response of a stationary few-body binary mixture composed of two bosons per species upon slightly quenching the trap frequency of the mutual 1D parabolic confinement. To simulate the dynamics, we employ the eigenstates and eigenenergies obtained by exact diagonalization in a relative-frame coordinate system already mentioned in Section 4.3.

Our major finding is that a binary mixture exhibits a breathing motion with up to four frequencies depending on the intra- and inter-component interaction strengths. It is thus richer than a single-species case and demon-

strates that a sophisticated many-body treatment yields more frequencies than a mean-field theory. For a weakly coupled mixture ( $g_{AB} \ll 1$ ), there is a characteristic frequency for each coordinate of the relative frame  $\vec{Y} = \{R_{cm}, R_{AB}, r_A, r_B\}$ , i. e., a breathing observable  $\langle \hat{Y}_i^2 \rangle_t$  oscillates with a single frequency. We label them  $\{\Omega_{cm}, \Omega_{AB}, \Omega_A, \Omega_B\}$  respectively. For a species-symmetric case ( $g_A = g_B$ ), the relative coordinates degenerate, meaning that  $\langle \hat{r}_A^2 \rangle_t = \langle \hat{r}_B^2 \rangle_t$ . Consequently, only three frequencies appear  $\{\Omega_{cm}, \Omega_{AB}, \Omega_+\}$ .

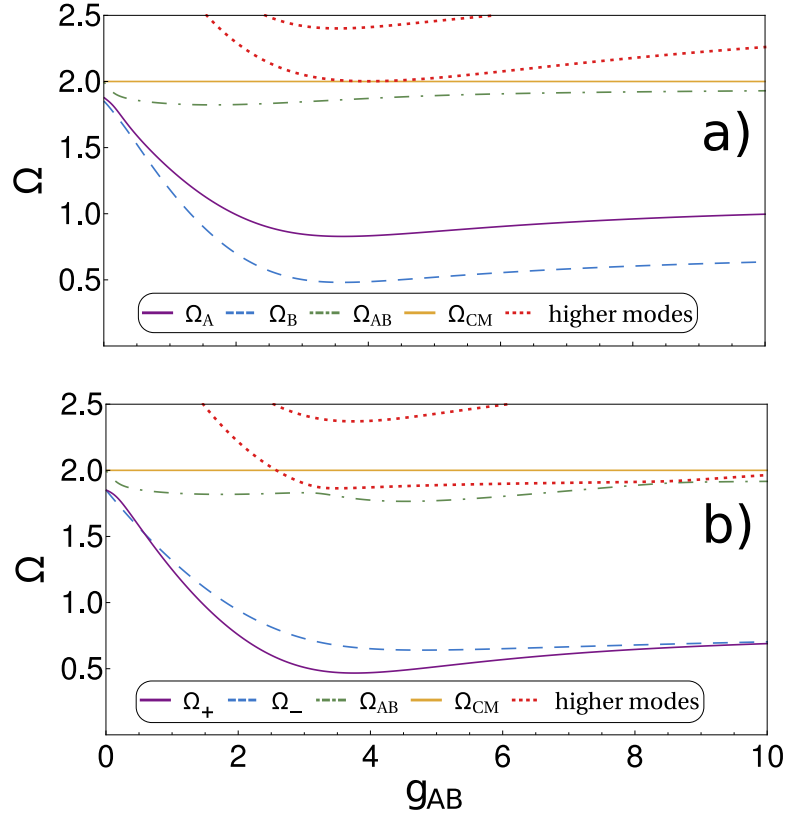


Figure 5.2: Breathing frequencies  $\Omega$  of a 2+2 bosonic mixture in a harmonic trap: a)  $g_A = 1$  and  $g_B = 2$ , b)  $g_A = g_B = 2$ . Adapted figures from [MP1]. DOI: <https://doi.org/10.1088/1367-2630/aa9cb2>.

We analyse the dependence of these frequencies on interactions (Fig. 5.2). The centre-of-mass Hamiltonian decouples and corresponds to a single-particle harmonic oscillator. Thus, the corresponding breathing observable  $\langle \hat{R}_{cm}^2 \rangle_t$  oscillates with a universal frequency  $\Omega_{cm} = 2$ . The relative distance modes  $\Omega_\sigma$  ( $\Omega_+$ ) are very sensitive to the intra-component interaction  $g_\sigma$ . With increasing  $g_{AB}$  they first quickly decay and then grow monotonically with a slow rate, though they do not recover back to the value of a decoupled mixture at  $g_{AB} = 0$ . The inter-species mode  $\Omega_{AB}$  behaves in a similar way as the relative motion mode of a single-species condensate [214]: in the limiting cases  $g_{AB} = 0$  and  $g_{AB} = \infty$  it degenerates with the  $\Omega_{cm}$ . However, in a two component mixture it might experience a bending in the vicinity of an avoided crossing at intermediate  $g_{AB}$ .

In addition, we monitor to which extent a given mode contributes to the oscillation of each relative-frame breathing observable. Thus, the monochrome breathing turns into multi-mode oscillations at intermediate  $g_{AB}$ . Importantly,  $\Omega_{AB}$  dominates over all other modes. In the **CF** and **PS** regimes, the oscillations become again monochrome. As opposed to the weakly-correlated miscible regime, the breathing observables  $\langle \hat{R}_{AB}^2 \rangle_t$  and  $\langle \hat{p}_\sigma^2 \rangle_t$  oscillate now with the same frequency  $\Omega_{AB}$ , whereas  $\Omega_\sigma$  ( $\Omega_+$ ) no longer contribute.

## 5.6 PREFACE: BREATHING RESPONSE OF A BOSE POLARON

In [MP2] we extend our previous studies on the breathing dynamics of a binary mixture in several ways. First, the setup has slightly changed. Now, we consider a few-body *Bose polaron*, i. e., an impurity  $B$  coupled to a medium  $A$  consisting of five-to-ten bosons, in a *species-selective* parabolic confinement with a trap ratio  $\eta = \omega_B/\omega_A$ . Second, we quench only the impurity trap, whereas the medium is set in motion indirectly by being coupled to the impurity. This is a notable difference to the species-symmetric quench protocol we considered before, as it allows for the pre-quench ground state to populate post-quench eigenstates of different **CoM** parity.

Since the total number of particles has been increased, the exact diagonalization is not up to the task any more. We use an alternative approach to extract the excitation frequencies, namely by simulating the time-evolution of a many-body state with **ML-MCTDH-X** (Section 3.3.2) and sampling breathing observables of interest at a given rate  $\Delta t$ . We differentiate between the impurity breathing  $\langle \hat{x}_B^2 \rangle_t$  and the medium breathing  $\langle \hat{x}_A^2 \rangle_t$ . A compressed sensing (**CS**) algorithm [227, 228] is applied to extract the frequencies of oscillations and their amplitudes. It is an alternative to Fourier transformation, particularly suited for time signals which are sparse in the frequency domain. This condition is well met for a weakly perturbed ground state. The prior information allows us to enhance the resolution in the frequency domain beyond limitations of the total evolution time. We have been very impressed by its capabilities to reduce the numerical effort. In our case, to obtain spectral information with a desired resolution  $\Delta\omega = 0.01$  would normally take around one year, which we acquired within just one month!

Equipped with sophisticated numerical tools, we study the breathing response for equal traps ( $\eta = 1$ ) at several values of the interaction strength  $g_A$  of the medium (attractive and repulsive). To our surprise, the outcome is quite different from what we saw in the particle-balanced Bose mixture. First, the universal **CoM** frequency  $\Omega_{cm}$  is barely populated. Second, the medium mode  $\Omega_A$  is still characterized by a strong sensitivity to medium-internal parameters,  $g_A$  and  $N_A$ , though in contrast to the particle-balanced case it is extremely flattened as a function of the medium-impurity interaction strength  $g_{AB}$ . Third, the frequency  $\Omega_B$  is obviously absent, because an internal-motion mode requires at least two particles. The inter-component mode  $\Omega_{AB}$  preserves its qualitative behaviour, i. e., in the limiting cases  $g_{AB} = 0$  and  $g_{AB} = \infty$  it degenerates with the  $\Omega_{cm}$ . In addition, we observe

strong sensitivity to some parameter variations such as the particle-number ratio  $N_B/N_A$  and the medium interaction strength  $g_A$ .

What is fundamentally new is the presence of yet another breathing frequency  $\Omega_{hs}$ . We call it the *hybrid sloshing* mode, because it can be traced back to an oscillatory motion between the ground state  $|N_A\rangle |1\rangle$  and a doubly excited eigenstate  $|N_A - 1, 1\rangle |0, 1\rangle$  of a Bose polaron at zero interactions. We note that this is not a simultaneous sloshing within each component, which would be a superposition of two states:  $|N_A - 1, 1\rangle |1\rangle$  and  $|N_A\rangle |0, 1\rangle$ . In fact, neither of components performs a sloshing if judged by the formal definition, i. e.,  $\langle \hat{x}_A \rangle_t = \langle \hat{x}_B \rangle_t = 0$ . At a finite coupling, the excited state can be classified by odd CoM and even global parity. The breathing frequency is a monotonically decaying function of the medium-impurity coupling parameter  $g_{AB}$ . We could not observe it in [MP1] for a species-symmetric quench, because of symmetry-dictated selection rules forbidding such a state from being populated. Thus, it is not a feature of the Bose polaron system, but of the quench protocol. Importantly, we find that the entanglement among the two components is indispensable for the mode existence. In particular, if one approximates the many-body wave function by a SMF ansatz, i. e., ignoring all entanglement effects, the mode disappears completely. Furthermore, we find that its contribution grows with increasing  $g_{AB}$ . So does the entanglement entropy.

In addition, we study the breathing response for a localized ( $\eta > 1$ ) and a delocalized ( $\eta < 1$ ) impurity, while the medium is assumed to be non-interacting ( $g_A = 0$ ). Even though the CoM coordinate is inseparable, we still evidence a monotonically decaying entanglement-sensitive breathing frequency.

Finally, we look at the breathing response of the first excited state at  $\eta = 1$ . As opposed to the ground state, it is of odd global parity. As the two subspaces of even and odd global parity are decoupled from each other, we have been curious to find out how the global parity affects the breathing dynamics. It turns out, the excitation spectra are almost identical. The major difference is an additional low-frequency mode. The reason for its existence can be understood as follows. At  $g_{AB} = 0$ , the first excited state is two-fold degenerate, whereas at finite  $g_{AB}$  the degeneracy is split. The employed quench protocol populates the former energy siblings across all  $g_{AB}$  values.



In the field of ultracold gases there are plenty of tools for extracting information from a many-body system. The interaction between light and matter is the key ingredient for probing ultracold samples and can be realized in multiple elegant ways [229, 230].

Early experiments recorded the intensity of a (near)-resonant laser beam after its passage through a sample of atoms, observing spatial variations of the shadow image on a CCD sensor (*absorption imaging*). A more advanced approach is based on separation of the transmitted light field into a phase-shifted scattered component and unaffected background light. By independent manipulation of the two parts an interference pattern can be generated, which allows to reconstruct the phase information (phase-contrast *dispersive imaging*). Alternatively, one can gather the light emitted by the sample (*fluorescence imaging*). Only a fraction of emitted photons can be gathered by a detector which makes the signal several orders of magnitude weaker. However, it has the notable advantage of being almost free of background noise, implying a high signal-to-noise ratio (SNR) as opposed to the transmitted light which is plagued by sizeable fluctuations of the laser beam intensity. Either way, the instantaneous intensity image of trapped atoms can be converted to the ('in-situ') one-body density  $\rho_1(x)$ , while letting the gas expand freely in space prior to imaging ('time-of-flight') translates to recording the momentum distribution  $\rho_1(k)$  instead.

The ultimate feature sought to be improved in an imaging apparatus is its spatial resolution, as it allows to differentiate subtle structural and dynamical variations in a physical system [231, 232]. Of particular interest is achieving a resolution which allows the detection of individual particles, which is vital for improving our current theoretical understanding of highly correlated phases of matter [1]. A great number of impressive accomplishments have been reached in modern experiments so far in the pursuit of these goals.

The imaging resolution of a probe of wavelength  $\lambda$  is bounded from below by a classical diffraction limit  $R \approx 0.61\lambda/\text{NA}$  known as the Rayleigh criterion with NA ( $\mathcal{O} \sim 1$ ) the numerical aperture of the imaging apparatus. The Rayleigh criterion is the minimum distance at which two incoherent point sources can be still distinguished. Each point source appears as a spread object on the imaging plane (point spread function (PSF)). Under aberration-free circumstances, it has the shape of an Airy function. Its full-width half-maximum (FWHM) determines the spatial resolution and the whole imaging process can be described mathematically as a convolution of the point source distribution with the PSF of the imaging system. Whilst the above-mentioned imaging methods already possess a resolution down

to several  $\mu\text{m}$ , they do not reach the diffraction limit due to heating by the probe pulse and imperfections in the imaging components.

The diffraction limit can be overcome by a non-linear optical response of matter to a spatially varying light field [233]. Recently, a super-resolution of tens of nanometres has been demonstrated [234, 235]. By using an optical control lattice with an adjustable position one can i) pump the illuminated fraction of particles into a state addressable by probe light [234] or ii) realize a position-dependent dark-state in a three-level system [235]. In particular, it allowed to observe density variations inside a single site of a physical lattice. Even non-demolition measurements [236, 237] have been suggested based on a dispersive coupling of the readout state to a cavity, enabling a real-time scanning of density fluctuations with sub-wavelength resolution. However, even though the above schemes have breached the classical diffraction limit, they lack the ability to locally identify individual particles at high density regimes. In sparse samples, high-fidelity single-atom detection and manipulation have been already demonstrated [20, 238–243]. A high resolution can be also achieved by a scanning electron microscope: an electron beam with a diameter  $\sim 150\text{nm}$  can be moved across a gas of neutral atoms to create ions which are subsequently extracted by a static electric field and detected by a channeltron [244, 245]. Unfortunately, the single-atom detection efficiency is only around  $\sim 20\%$ .

The advent of QGMs for bosons [22, 23] and fermions [24–27] has revolutionized detection in high density settings with sizeable correlations. It allows to identify individual atoms locally with a near-unit fidelity and at the same time offers a sub-micron resolution  $\sim 0.5\mu\text{m}$ . The QGMs are predominantly used for studying lattice systems, e. g., interaction-induced phase transitions [246, 247] and the many-body localization [248, 249] in Hubbard models. Importantly, projective measurements of site occupations provide access to correlation measures: antiferromagnetic spin correlations [250–252], hidden string order [253, 254] and entanglement entropy [255, 256].

## 6.1 TECHNICAL ASPECTS

QGM is a two step imaging process. The atoms are first pinned inside a deep optical lattice followed by occupation readout with fluorescence imaging.

An optical lattice can be created by the interference of two counter-propagating laser beams [257, 258] with frequency  $\omega$  leading to a periodic intensity pattern  $I(x) \propto |\vec{E}(x)|^2 \propto \sin^2(kx)$  with a lattice constant  $a = \pi/k = \lambda/2$  corresponding to the distance of two neighbouring minima. Neutral atoms exposed to this electric field become polarized. The interaction between the light field  $\vec{E}$  and the induced dipole moment  $\vec{d}$  results in an effective potential [259]  $V(x) = -\langle \vec{d}\vec{E}(x) \rangle \propto \alpha I(x)$  experienced by atoms with polarizability  $\alpha \propto 1/\Delta$  and laser detuning  $\Delta = \omega - \omega_0$  w. r. t. an atomic transition  $\omega_0$ . This is a second-order perturbative correction to the ground state energy (Stark shift). The atoms are attracted to the maxima of the lattice potential for a red-detuned laser ( $\Delta < 0$ ) or to the minima for

a blue-detuned laser ( $\Delta > 0$ ). By using additional lasers in perpendicular directions, two- or three-dimensional regular lattices can be realized. The lattice depth can be adjusted by changing the laser power and even the lattice constant may be dynamically adapted to the experimental needs either by tuning the laser wavelength or the angle between the two interfering beams [260, 261].

Attaining single atom sensitivity with near-unit fidelity requires a high SNR at the detector. Fluorescence imaging is perfectly suited for this purpose. Nevertheless, a sizeable number of photon scattering events per atom  $\mathcal{O}(10^4)$  need to take place. To maintain sub-wavelength resolution, the atoms should stay at their sites during the imaging process despite a massive amount of heating. For that reason, the lattice needs to be extremely deep, typically  $\sim 10^3 E_R$  with  $E_R = \frac{\hbar^2(2\pi)^2}{2m\lambda^2}$  the recoil energy, corresponding to several Watts of laser power. Additionally, during imaging the atoms are cooled down using various techniques: bright molasses [22, 23], Raman side-band [25, 27] or electromagnetically induced transparency [24, 26] cooling. There is an unfortunate side effect to this procedure: whenever more than two atoms occupy a single site of a pinning lattice, light-assisted collisions lead to formation of molecules. For bosons, this amounts to losses of particle pairs from the trap. Thus, QGMs detect the parity of the number of atoms (even or odd) at each lattice site [22, 23, 262]. Recently, it has been shown for Yb atoms that cooling can be avoided: the atomic sample was exposed to light for shorter times [263, 264] while maintaining high SNR.

The numerical aperture of the imaging apparatus for QGMs is typically  $\text{NA} \leq 0.8$  [22–27], meaning that the spatial resolution  $R > 3\lambda/4$  exceeds the distance between two lattice sites  $a \sim \lambda/2$ . Given high SNR and a prior knowledge about the discrete spacing among atoms, a deconvolution algorithm can deblur the detector image and recover the lattice features. Then, it is straightforward to distinguish between zero or one occupancy at each lattice site.

It is not surprising that QGM is primarily used to study physics in a lattice potential: the physical lattice can be easily switched into the imaging modus by increasing the laser power. Each measurement translates into a projection on some number state configuration in the lowest-band Wannier basis. However, the physical and imaging lattices may be different [265], allowing to oversample the physical lattice. This opens the possibility to eventually overcome the above mentioned limitation of fluorescence imaging to detect only the parity of the number of atoms on each site of the pinning lattice. Moreover, freezing of a large scale extended system after time-of-flight expansion has been demonstrated [266]. In that regard, it would be useful to generalize this scheme to arbitrary external traps. In particular, freezing and measuring of one-particle density structures on the scale of the pinning lattice constant might be challenging. We undertake this investigation in [MP5] to reveal limitations and eventual difficulties that might be encountered.

## 6.2 PREFACE: QUANTUM POINT SPREAD FUNCTION

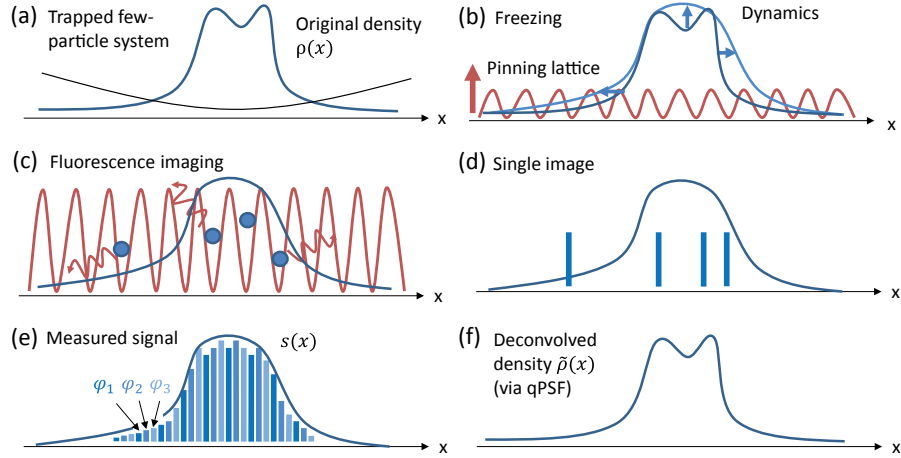


Figure 6.1: Imaging protocol. Reprinted figure from [MP5]. DOI: <https://doi.org/10.1088/1367-2630/ab1ae7>.

The ultimate goal of our measurement protocol, sketched in Fig. 6.1, is to obtain a highly-resolved  $n$ -particle distribution  $\rho_n(x_1, \dots, x_n)$  of a sparse-density many-body system confined by an external potential of arbitrary shape. In [MP5], we focus on the one-body density  $\rho_1(x)$  in 1D traps. It serves as the first step to verify the viability of our measurement protocol: to identify advantages, possible limitations and technical drawbacks.

Once an ensemble of atoms has been prepared in its ground state or has undergone some dynamical evolution, the instantaneous (pre-measurement) one-body density  $\rho_1(x)$  (Fig. 6.1a) is recorded in iterative manner by repeating a two-step sequence. In the first step (Fig. 6.1b), one switches off the external trap and tunes the strength of inter-particle interactions to a negligible value using a Feshbach resonance. At the same time, a pinning lattice with an inter-well spacing  $a_l$  and a phase off-set  $\varphi$  is ramped up to freeze the motion of particles. As a side effect, the pre-measurement density distribution becomes distorted in the process. In the second step, we read-out the distribution of particles over the lattice sites by fluorescence imaging (Fig. 6.1c). At a low-density regime the probability for two atoms to end up at the same lattice site is strongly suppressed. Thus, we neglect losses attributed to light-assisted collisions [23, 246]. A possible measurement outcome is illustrated in Fig. 6.1d. The procedure is repeated many times until the ensemble average has converged to the post-measurement distribution  $s(x_{n;\varphi})$  sampled at discrete values  $x_{n;\varphi} = na_l + \varphi$  with a resolution  $a_l$  (Fig. 6.1d). Importantly, the resolution of the signal  $s(x)$  can be further improved if we repeat the ensemble averaging procedure at several different phase off-sets  $\varphi_i$  of the lattice (Fig. 6.1e).

We have been able to formulate the measurement procedure, which gives the post-measurement distribution  $s(x)$ , in a very compact and convenient

way as a 2D convolution of the pre-measurement one-body density matrix  $\rho_1(x, x')$  with a 2D filter  $Q(x, x')$ :

$$(Q * \rho_1)(x, x) = \int dy dy' Q(x - y, x - y') \rho_1(y, y') \equiv s(x). \quad (6.1)$$

The filter  $Q(x, x')$  depends only on parameters of the ramp protocol. We call it the quantum PSF, in analogy to classical imaging devices [267, 268].

After acquiring the post-measurement density  $s(x)$ , we want to recover the pre-measurement one  $\rho_1(x)$  (Fig. 6.1f). A straightforward deconvolution procedure is not helpful here, because the signal  $s(x)$  represents just the diagonal of a 2D convolution  $s(x, x')$ . Although measuring the off-diagonal elements of the coherence matrix has been proposed [269], the feasibility has yet to be demonstrated.

Does it mean that our quest for a sub-lattice resolution is doomed or is it still possible to (partially) remove these distortions using our knowledge of the imaging procedure? Upon a careful inspection of lattice ramp parameters, we observed that quantum PSF can be shaped into an elongated Gaussian. This motivated us to approximate the signal  $s(x)$  as a 1D convolution of the pre-measurement density  $\rho_1(x)$  with a 1D filter  $q(x)$ :

$$s(x) \approx (q * \rho_1)(x) = \int dy q(x - y) \rho_1(y). \quad (6.2)$$

Unfortunately, taking the diagonal  $q(x) = Q(x, x)$  as a filter for 1D deconvolution does not perform well, in terms of recovering the original density. Instead, we came up with an advanced two-step recovery algorithm.

In the first step, we obtain  $q(x)$  using a machine learning technique. There is a vast body of literature on this exciting field of modern research encompassing all areas of science. We recommend [270] to learn some basics, [271] to get familiar with the state of the art programming library TensorFlow, and [272] for learning some advanced topics. For our purposes, we apply a simple convolutional neural network (NN). This type of networks are particularly suited for solving image-based tasks. We generate a sample of  $n_t$  physically relevant examples with an analytically known one-body density matrix  $\rho_1^{(j)}(x, x')$ . Then, we apply 2D convolution with an exact filter  $Q(x, x')$  to obtain the corresponding post-measurement density  $s^{(j)}(x)$ . The pre-measurement density  $\rho_1^{(j)}(x)$  serves as the input for the NN. The post-measurement density  $s^{(j)}(x)$  is the desired output of the NN. By minimizing the square distance between the desired output  $s^{(j)}(x)$  and the network generated output  $(\rho_1^{(j)} * q)(x)$  we let the network learn our filter  $q(x)$ :

$$\min_q \frac{1}{n_t} \sum_{j=1}^{n_t} \int dx |(Q * \rho_1^{(j)})(x, x) - (q * \rho_1^{(j)})(x)|^2. \quad (6.3)$$

After the NN has achieved a high performance on the training test, we verify our model's capability to generalize by applying it to a validation set, i. e., pairs of inputs and outputs not contained in the training data. Importantly, the validation set contains samples of correlated particles, whereas the training set is composed only of single-particle examples. The learned filter

passed the test with great performance. In the second step of the density reconstruction, we apply a 1D deconvolution [267, 268] with the learned filter  $q(x)$  choosing one of the many available libraries.

Finally, we tested our measurement protocol on several few-body systems trapped either in a harmonic or in a box potential. Whenever local density variations  $\sigma$  are on a larger scale than the lattice spacing  $a_l$ , the reconstruction step is not needed, because of small distortions caused by the lattice ramp. When the variations become comparable to the lattice spacing,  $\sigma \in [0.5, 2]a_l$ , the reconstruction works great and removes most of dynamical artefacts. For  $\sigma < 0.5a_l$ , the distortions become too large to be reasonably recovered. Furthermore, we tested the experimental feasibility by estimating the effort required to obtain the one-body density with a reasonable accuracy.

To summarize, our work proposes a measurement protocol for high-resolution imaging of the one-particle density in non-lattice trapped systems. In order to achieve a sub-lattice resolution, the position of the lattice needs to be shifted relative to the trapped system. The measurement protocol can be modelled as 2D convolution with a quantum PSF. A sophisticated deconvolution algorithm allows to recover the initial density, as long as local structures are larger than half a lattice spacing.

Part II

SPECTRAL GRAPH THEORY





A graph is a way to visualize a set of elements and a particular type of relation or interaction between them. This level of abstraction makes graphs a highly interdisciplinary tool finding applications in sociology, finances, logistics, informatics, biology, chemistry and physics [273–275]. For example, a graph may represent friendships among users of a social media platform such as Facebook, roads between cities, a web of neurons interlinked by synapses, chemical bonds among atoms forming a molecule or a system of masses connected by springs.

In this chapter we would like to convey our own motivation to study physical systems through the lens of graph theory. Can we learn something new by depicting them as graphs? Each discipline has its own viewpoint on a graph representation and developed corresponding tools to answer particular questions. We think it is worthwhile to look beyond the scope of one's own field. The change of perspective might reveal some fruitful insights and, eventually, open new unexpected research directions.

In Section 7.1 we introduce the formal definition of a graph and some key ideas necessary to understand our contributions. In particular, the duality between graphs and matrices forms a natural bridge which connects previous chapters to the world of networks. Once equipped with a basic understanding of graph theory, we dive deeper into the subfield of spectral graph theory [276–278]. There, one attempts to relate the eigenvectors and eigenvalues of a graph to its topology and global properties. E. g., eigenvector centrality [279, 280] quantifies the number and quality of connections for each element in a network, while the abundance of small symmetry motifs in a graph manifests itself as singularities in the spectral density. Among recent developments, we are particularly excited about vertex cospectrality and isospectral reduction.

Cospectrality of a vertex pair (Section 7.2) has a flavour of mystery. It imposes a parity relation among two components of any eigenvector. A permutation symmetry of a graph is known to induce such a relation. The issue is that many graphs have eigenvectors with such parity without any exchange symmetries behind it. We shed light on this peculiar property. In our contribution (Section 7.3) we show that these eigenvectors have even more structure than just parity. Furthermore, we develop a novel generator of cospectral graphs, a hot topic in spectral graph theory.

Isospectral reduction (Section 7.4) is a way to compress the size of a graph to a dedicated subset of vertices while preserving the energy spectrum. Surprisingly, the reduced graph might feature symmetries not present in its original version. In our contribution (Section 7.5) we demonstrate that these hidden symmetries are able to explain spectral degeneracies in a graph which does not have any conventional symmetries.

## 7.1 GRAPHS

Historically, graph theory has been the domain of pure mathematicians, a mere notion of curiosity rather than means of deriving real-world applications, such as the ‘seven bridges of Königsberg’ puzzle<sup>1</sup>. Nowadays, in the era of big data and high-performance computing, many fields of science benefit from and contribute to the developments in graph theory. Graph theory profited a lot from the arsenal of tools developed in the physical community, especially in statistical physics [274, 275]. A variety of graph optimization problems can be formulated as finding the ground state of an Ising Hamiltonian [281] we have already encountered in the context of a strongly interacting Bose mixture (Section 4.2). To get a taste of this complex yet exciting field we recommend some excellent books on this topic [282–285].

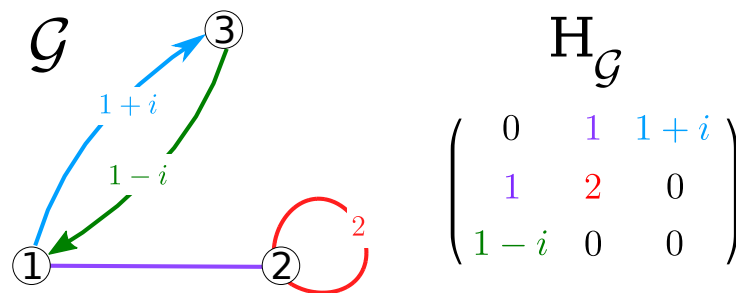


Figure 7.1: Duality between a graph and a square matrix.

Formally, in discrete mathematics a *graph*  $\mathcal{G}$ , also called a *network*, is a structure with two basic elements: a vertex set  $\mathcal{V}$  and an edge set  $\mathcal{E} \subseteq \mathcal{V} \otimes \mathcal{V}$ . In short notation,  $\mathcal{G} = (\mathcal{V}, \mathcal{E})$ . Typically, a graph is represented by a diagram (Fig. 7.1 on the left). The *vertices*  $v_i \in \mathcal{V}$ , also called sites or nodes, are depicted as points or circles. The *edges*  $(v_i, v_j) \in \mathcal{E}$ , also referred to as couplings or links, are drawn as arrow curves connecting vertex pairs with the arrow pointing from  $v_i$  towards  $v_j$ . By default, all edges are assumed to be of equal significance. However, depending on the problem a scalar weight  $w_{ij} \in \mathbb{C}$  might be attached to the corresponding edge  $(v_i, v_j)$  (“weighted edge”). Whenever  $v_i$  and  $v_j$  are symmetrically connected, i. e.,  $(v_i, v_j) \in \mathcal{E}$ ,  $(v_j, v_i) \in \mathcal{E}$  and  $w_{ij} = w_{ji}$ , the two directed edges are replaced by a single curve without any arrows (“undirected edge”). An edge  $(v_i, v_i)$  connecting vertex  $v_i$  to itself is depicted as a loop. For the graph in Fig. 7.1, we have  $\mathcal{V} = \{1, 2, 3\}$  and  $\mathcal{E} = \{(1, 1), (1, 2), (2, 1), (1, 3), (3, 1)\}$  with the corresponding edge weights  $\mathcal{W} = \{2, 1, 1, 1+i, 1-i\}$ .

We remark that the geometrical arrangement of vertices in Euclidean space is arbitrary and not a part of the graph definition. Naturally, one desires a graph drawing that is easy to read and understand. There are multiple metrics regarding the aesthetics of graph drawings [286, 287], such as minimizing the number of edge crossings or maximizing the orthogonality

<sup>1</sup> Back in 1736 in the city of Königsberg, now Kaliningrad, there was a conundrum about whether it is possible to cross the city using all of seven bridges only once. The mystery was solved by Euler who laid the foundation of today’s graph theory.

of edges. The final choice depends on the question asked and the personal taste. Our preference is to maximize the perception of graph symmetries.

A fundamentally important property of graphs is their correspondence to square matrices. Specifically, for a  $N \times N$  matrix  $\mathcal{H}_G$  the basis vectors  $|\phi_i\rangle$  correspond to vertices  $v_i$ , while the matrix elements  $h_{ij}$  are mapped to edges  $(v_i, v_j)$  with weights  $w_{ij} = h_{ij}$  and  $h_{ij} = 0$  implying no edge, e. g., see Fig. 7.1.

At this point one might ask: why does one need to draw a matrix as a graph? Our answer to this: because the topology of graph's relations determines its function such as the spread of information or the robustness to perturbations. What a better tool to recognize some regularities or to reveal some patterns than the human eye, a remarkable tool for visual analysis coupled with the creativity element of the brain to produce innovative conjectures which can then be systematically tested using the sophisticated tools of linear algebra. A picture is often worth a thousand words and can convey information in an enlightening or evocative way. Surely, for large networks containing billions of elements such a picture might be rather confusing. For that reason, one attempts to approach large complex networks with a bottom-up perspective, i. e., by first developing an understanding of smaller graphs. This has the same spirit as the previous chapters on few-body systems in the attempt to learn more about the many-body behaviour. For that reason we believe that graphs and matrices complement each other giving rise to a symbiotic relationship: linear algebra provides efficient tools to approach many graph-related problems, which then provide information about the structure and function of the underlying matrix.

In physics, we are often confronted with matrices, usually in the context of solving the eigenvalue problem  $\hat{H} |\Psi_j\rangle = E_j |\Psi_j\rangle$ . So far, we dealt with this problem on several occasions. To this end, the system operator  $\hat{H}$  is represented as a matrix by choosing a finite basis set<sup>2</sup>, i. e.,  $\langle \phi_i | \hat{H} | \phi_j \rangle = h_{ij}$ , which is subsequently diagonalized. Here, we use novel developments from spectral graph theory, namely cospectrality and isospectral reduction, to gain information about the eigenstates and eigenvalues of a matrix before the diagonalization step is done.

## 7.2 COSPECTRALITY AND LOCAL PARITY OF EIGENVECTORS

It is well-known that geometrical symmetries greatly simplify the treatment of physical systems in terms of interpretability and computational complexity. In the previous chapters, the global-reflection symmetry of the harmonic trap allowed the notion of even and odd parity eigenstates. This helped us a lot for clarifying the breathing response of a Bose mixture and to reduce the numerical effort by block-diagonalizing the Hamiltonian.

<sup>2</sup> Sometimes, the basis is motivated by the underlying physics, e. g., internal coordinates of a mass-spring system when solving for the vibrational modes of a molecule or localized atomic orbitals to obtain the electronic band structure of the tight-binding model. More often though, the basis is selected for its numerical convenience, such as analyticity, or is motivated by an intuition, such as splitting an operator into two parts  $\hat{H} = \hat{H}_0 + \hat{H}_1$ , containing a solvable term  $\hat{H}_0$  and a perturbative term  $\hat{H}_1$ .

In a randomly generated graph symmetries are rare, even more so when the edges are heterogeneous (non-uniform). Many real-world networks are by far not random, but rather ‘small-worlds’<sup>3</sup> [288] with a lot of structure, patterns and symmetries. Typically, they display an asymmetric core (the skeleton) and a large number of relatively small symmetric motifs attached to it [289–292]. It is a hot topic of current research to figure out how these motifs emerge, what shapes they typically take and what effect they have for the network function. In particular, we are interested in identifying relations between symmetries and spectral properties of a graph [276–278]. For example, sharp peaks are very common in the spectral density of a real-world network indicating highly degenerate eigenvalues, which can be often traced to the symmetries of a graph.

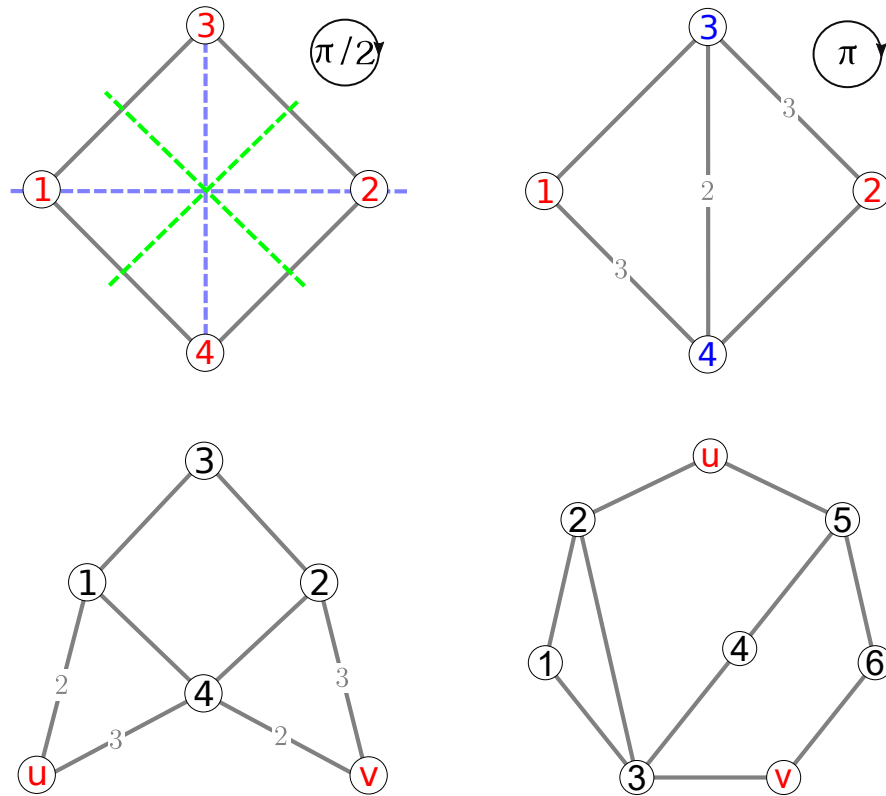


Figure 7.2: All the eigenvectors of depicted graphs have a definite parity among red (blue) coloured vertices. Permutation symmetries impose parity relations for graphs in the first row. There are no permutation symmetries for graphs in the second row.

The geometrical symmetry of a graph  $\mathcal{G}$  is a structure-preserving transformation of a graph onto itself, known as the graph *automorphism*. Formally, it is a permutation of vertices  $\pi : \mathcal{V} \rightarrow \mathcal{V}$ , such that whenever two nodes are joined by an edge, so are their images, i. e.,  $(v_i, v_j) \in \mathcal{E} \Leftrightarrow (\pi(v_i), \pi(v_j)) \in \mathcal{E}$ . On the matrix level, the above mapping corresponds to a permutation ma-

<sup>3</sup> A network having the small-world property is characterized by i) the neighbours of a given vertex are very likely to be adjacent to each other and ii) the distance between any two vertices is on average short compared to the size of the network.

trix<sup>4</sup>  $P_\pi$  acting as a symmetry transformation on  $\mathcal{H}_G$ , i. e.,  $P_\pi^{-1}H_G P_\pi = H_G$ . In the following, we employ the cycle notation for permutations, e. g., for a graph with four vertices  $\mathcal{V} = \{1, 2, 3, 4\}$  the permutation  $\pi = (1, 3, 2)(4)$  implies a 3-cycle  $\pi(1) = 3$ ,  $\pi(3) = 2$ ,  $\pi(2) = 1$  and a 1-cycle  $\pi(4) = 4$ . For brevity, we drop fixed points of a permutation, i. e., 1-cycles. For example, we abbreviate  $(1, 3, 2)(4)$  as  $(1, 3, 2)$ .

Graph automorphisms have a huge impact on the eigenvectors of the corresponding matrix. For the highly symmetric graph in Fig. 7.2 (first row on the left) we have in total seven permutation symmetries. One part of them can be interpreted ‘geometrically’ as reflections along dashed lines:  $(1, 2)$ ,  $(3, 4)$ ,  $(1, 4)(2, 3)$  and  $(1, 3)(2, 4)$ . The other part as rotations by  $\pi/2$  ( $(1, 3, 2, 4)$ ),  $\pi$  ( $(1, 2)(3, 4)$ ) and  $3\pi/2$  ( $(1, 4, 2, 3)$ ). All the eigenvectors  $\vec{\varphi}^{(k)}$  have a very beautiful structure, namely any pair of eigenvector components either fulfils or in case of degeneracies can be chosen to fulfil  $|\varphi_i^{(k)}| = |\varphi_j^{(k)}|$ . In fact, just a single automorphism is enough to induce a relation among eigenvector components, e. g., see Fig. 7.2 (first row on the right), where the only automorphism  $(1, 2)(3, 4)$  imposes  $|\varphi_1^{(k)}| = |\varphi_2^{(k)}|$  and  $|\varphi_3^{(k)}| = |\varphi_4^{(k)}|$ .

In contrast, the second row graphs in Fig. 7.2 have no automorphisms, yet their eigenvectors feature local parity on the red coloured vertices. What is the reason behind this mysterious structure of eigenvectors? The explanation has been provided by graph theoreticians: it turns out, the red vertices, labelled as  $u$  and  $v$ , are what they call *cospectral* [293, 294]. Vertex cospectrality turns out to be an important ingredient to realize a high-efficiency state transfer between two qubits of a quantum network [MP8, 295].

Cospectrality has many facets. We want to discuss a few of them which we think are particularly illuminating. First, what does it have to do with the spectrum? It turns out the vertex-deleted sub-graphs<sup>5</sup>  $\mathcal{G}/u$  and  $\mathcal{G}/v$ , share the same spectrum, i. e.,  $\sigma(\mathcal{G}/u) = \sigma(\mathcal{G}/v)$  (cospectral graphs). It is not surprising for the left graph in the second row of Fig. 7.2, where the vertex-deleted sub-graphs are the same. It is not obvious at all for the right graph in the second row of Fig. 7.2. Cospectral graphs have drawn a lot of attention in the attempt to answer the question of when the spectrum of a graph uniquely determines its topology [296–301]. Learning from the spectral information is also a relevant topic in physics and chemistry where methods such as absorption and emission spectroscopy are used to draw conclusion about the composition and physical structure of matter.

Another peculiarity of the cospectral pair  $u$  and  $v$  is the relation  $(H^k)_{uu} = (H^k)_{vv}$  valid for all matrix powers  $k$ . In graph language, the powers of a matrix have a very convenient interpretation in terms of walks. This viewpoint was very helpful and enlightening for us. A walk of length  $k$  is a sequence of  $k$  edges  $\{e_1, \dots, e_k\}$  where the out-vertex of an edge  $e_i$  coincides with the in-vertex of the follow-up edge  $e_{i+1}$ . The weight of a

<sup>4</sup> The matrix elements of  $(P_\pi)_{i,j}$  are obtained from the identity matrix by a permutation of rows, i. e.,  $(P_\pi)_{i,j} = \delta_{\pi(i),j}$  with  $\delta_{i,j}$  the Kronecker delta.

<sup>5</sup> A sub-graph  $\mathcal{G}/S$  is a graph obtained from  $\mathcal{G} = (\mathcal{V}, \mathcal{E})$  by removing the vertex subset  $S \subset \mathcal{V}$  and the corresponding edges  $(v_i, v_j) \in \mathcal{E}$  if  $v_i \in S$  or  $v_j \in S$ .

walk amounts to the product of individual weights of participating edges, i. e.,  $\prod_i^k w(e_i)$ . For an unweighted graph,  $(H^k)_{ij}$  gives the total number of distinct walks of length  $k$  starting at vertex  $i$  and terminating at vertex  $j$ . For a weighted graph,  $(H^k)_{ij}$  is the sum over corresponding walk weights. Thus, vertex pair cospectrality can be interpreted as a symmetry of walks.

Lastly, there is an orthogonal symmetry  $Q$ , i. e.,  $Q^{-1}H_GQ = H_G$ , responsible for the local parity of eigenvectors  $|\varphi_u^{(k)}| = |\varphi_v^{(k)}|$  on the two cospectral sites.  $Q$  is a hybrid block-symmetry with a geometrically interpretable block and a general transformation block unrelated to permutations. Specifically,  $Q$  performs a 2-cycle permutation on the cospectral sites, i. e.,  $q(u) = v$  and  $q(v) = u$ , and a weighted linear mixing involving the remaining vertices. The former imposes local parity on  $u$  and  $v$ . As a final remark, it can be easily verified, based on the above mentioned properties, that in the first row graphs in Fig. 7.2 any two vertices of the same colour are cospectral. Thus, local parity relations among eigenvector components are generally caused by orthogonal block symmetries  $Q$  having a permutation block, while the conventional vertex-exchange symmetries  $P_\pi$  is a subset of these.

### 7.3 PREFACE: GENERATOR OF COSPECTRAL GRAPHS

When we first stumbled upon eigenvectors with local parity in the absence of geometric symmetries, we were eager to investigate this phenomenon in more detail. But where does one get such exotic examples? There is a rich literature on generating pairs of graphs having the same spectrum, such as the Godsil-McKay switching [293] and its several generalizations [302, 303], the graph product [304], cousin vertices [305], the partial transpose [306], cloning [307] and overgraph extensions [308]. However, the available tools have been rather restricted with multiple subtle conditions to be fulfilled.

To be of practical relevance, we yearned for a LEGO kit to systematically generate arbitrarily large cospectral networks, ideally with inhomogeneous, tunable edge weights. To this end we created a database [MP8] of connected graphs with uniform edges having up to eleven vertices and without any automorphisms. This set was searched for graphs having at least one pair of cospectral vertices<sup>6</sup>. The filtered database, composed of millions of examples, turned out to be extremely useful on our graph journey.

Given that cospectrality is a symmetry of walks, we thought about symmetry-preserving perturbations of a graph  $\mathcal{G}$  with cospectral vertices  $u$  and  $v$  [MP6]. One such perturbation can be realized by coupling an ‘impurity’ vertex  $c$  to a subset  $M \subseteq \mathcal{V}$  with uniform edges, see Fig. 7.3 (top). Whenever successful, we looked at the matrix powers  $H^k$ . After some large-

<sup>6</sup> To check whether a pair of vertices is cospectral, one needs to verify  $(H^k)_{uu} = (H^k)_{vv}$  across all powers of a matrix, which seems to be an unfeasible task. Luckily, the Cayley-Hamilton theorem states that a square matrix fulfils its own characteristic polynomial. Thus, it is sufficient to verify the equality only for the first  $n - 1$  powers of a square matrix with  $n$  the matrix order.

scale analysis on the database we discovered a pattern, namely whenever

$$\sum_{z \in M} (H^k)_{uz} = p \sum_{z \in M} (H^k)_{vz} \neq 0 \quad (7.1)$$

was fulfilled with  $p = \pm 1$ , a perturber vertex  $c$  could be connected uniformly to  $M$  without breaking the vertex cospectrality, see Fig. 7.3 (middle). Using the walk interpretation of matrix powers mentioned in Section 7.2, Eq. (7.1) implies that the cumulative amount of walks leading from  $u$  to  $M$  is the same as from  $v$  to  $M$  for any walk length. We termed  $M$  as a (uniform) *multiplet*. Importantly, the newly coupled vertex  $c$  becomes also a multiplet, namely a singlet, i. e.,  $(H^k)_{uc} = p(H^k)_{vc}$ . This allows us in the next step to connect an arbitrarily large subsystem  $\mathcal{G}'$  to  $c$  without violating the cospectrality relation of  $u$  and  $v$ , see Fig. 7.3 (bottom). Later, we generalized multiplets to be non-uniform, i. e., the perturber might be connected with weighted edges, and established interconnections among existing multiplets as yet another form of perturbation allowing to alter the topology of the initial graph.

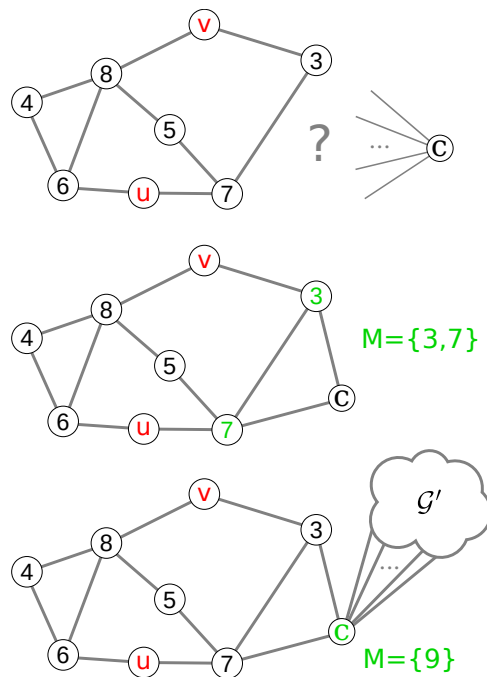


Figure 7.3: Top: Given a graph with a cospectral vertex pair  $\{u, v\}$ , is there a way to connect a perturber vertex  $c$  without destroying the underlying cospectrality? Middle: There are vertex subsets, called multiplets  $M$  defined in Eq. (7.1), which allow for such a symmetry-preserving perturbation, e. g.,  $M = \{3, 7\}$  is a multiplet w. r. t.  $\{u, v\}$  in the depicted graph. Bottom: The added vertex  $c$  becomes a singlet, i. e., a multiplet composed of a single vertex. A singlet allows in the next step to connect an arbitrarily large graph exclusively to it without breaking the cospectrality of  $\{u, v\}$ .

Furthermore, we observed that eigenvectors obey a certain relation on the multiplet set  $M$  depending on the local parity on  $u$  and  $v$ . For  $p = +1$

the negative-parity eigenvectors fulfil  $\sum_{m \in M} \varphi_m = 0$ , i. e., the sum of vector components vanishes on this set. The same is true for  $p = -1$  and the positive-parity eigenvectors. We note that Eq. (7.1) can not be simultaneously fulfilled for  $p = +1$  and  $p = -1$  if  $M$  is fixed. This implies that each multiplet  $M$  poses a restriction either on even or odd eigenstates. The relation among eigenvector components becomes modified with scalar vertex-dependent weights in the generalized version of multiplets. Overall, we have been very impressed by the amount of structure in the eigenvectors.

As a direct application, we used these insights to construct flat bands in tight-binding lattice systems [MP11]. A flat band relies on compact localized states, i. e., eigenstates with a compact spatial support [309, 310]. In the simplest case, they are localized inside a single unit cell, and with zero amplitude outside. We start with a disconnected lattice where the unit cell is a graph with a cospectral vertex pair. In the next step, following the rules in [MP6] we interconnect adjacent unit cells periodically while preserving the cospectrality inside each individual cell. At the same time, taken any cell as a reference, all the vertices outside are made singlets. Owing to the multiplet condition for eigenvectors mentioned above, a cell-internal *negative-parity* eigenstate will vanish on all singlets, i. e., it is not perturbed by the interconnection. Thus, it is also an eigenstate of the connected lattice and is localized. The shifted duplicate of this state occurs in every other unit cell, thus yielding a highly-degenerate flat band.

#### 7.4 ISOSPECTRAL REDUCTION AND LATENT SYMMETRIES

Another useful graph-theoretical tool we want to discuss is isospectral reduction of graphs [311]. Real-world networks are usually large and have a complex topology making their analysis a challenging task. It would be of advantage to have ways allowing us to shrink a graph  $\mathcal{G}$  to a smaller version  $\mathcal{G}_S$  with less vertices while preserving some of its fundamental properties. In particular, we are interested in keeping the energy spectrum  $\sigma(\mathcal{G}) = \{\lambda \in \mathbb{C} \mid \det(H_{\mathcal{G}} - \lambda \mathbb{1}) = 0\}$ . For matrices with scalar entries, this is an impossible task. The matrix of a reduced graph will be of a lower dimension. By the fundamental theorem of algebra it will have less eigenvalues than the original graph<sup>7</sup>. But what if, in the process of dimensionality reduction, the entries of the shrunk matrix would become functions  $m(\lambda)$  of the spectral parameter  $\lambda$ ? The spectrum of the reduced graph  $\sigma(\mathcal{G}_S) = \{\lambda \in \mathbb{C} \mid \det(H_{\mathcal{G}_S}(\lambda) - \lambda \mathbb{1}) = 0\}$  would be capable of holding more eigenvalues than its dimension. E. g., the following matrix

$$R_{\{1,2,3,4\}} = \begin{pmatrix} \frac{4}{\lambda} & 0 & \frac{6+\lambda}{\lambda} & 1 \\ 0 & \frac{9}{\lambda} & \frac{6+\lambda}{\lambda} & 1 \\ \frac{6+\lambda}{\lambda} & \frac{6+\lambda}{\lambda} & \frac{13}{\lambda} & 0 \\ 1 & 1 & 0 & 0 \end{pmatrix}$$

<sup>7</sup> A polynomial of degree  $n$  with complex coefficients has exactly  $n$  complex roots (counting multiplicities). The degree of the characteristic polynomial of a square matrix equals the order of that matrix.



has six eigenvalues and is depicted as a graph in Fig. 7.4 on the right.

To arrive at such a representation, let us partition the vertex set  $\mathcal{V}$  of a graph into two disjoint parts  $S$  and  $\bar{S}$ , i. e.,  $\mathcal{V} = S \cup \bar{S}$  and  $S \cap \bar{S} = \emptyset$ . The set  $S$  is the target set we want to keep while the complement  $\bar{S}$  contains vertices to be discarded in the reduction process. We can view the corresponding matrix  $H_G$  as two subsystems,  $H_{SS}$  and  $H_{\bar{S}\bar{S}}$ , coupled via  $H_{S\bar{S}}$  and  $H_{\bar{S}S}$ :

$$H_G = \begin{pmatrix} H_{SS} & H_{S\bar{S}} \\ H_{\bar{S}S} & H_{\bar{S}\bar{S}} \end{pmatrix}. \quad (7.2)$$

Isospectral reduction [312]  $R_S(\lambda)$  of the above matrix over the set  $S$  is defined as:

$$R_S(\lambda) = H_{SS} - H_{S\bar{S}}(H_{\bar{S}\bar{S}} - \lambda \mathbb{1})^{-1}H_{\bar{S}S}. \quad (7.3)$$

Importantly, the matrix elements of  $R_S(\lambda)$  are rational functions  $p(\lambda)/q(\lambda)$  with polynomials  $p(\lambda)$  and  $q(\lambda)$  having complex coefficients. E. g., the graphs in Fig. 7.4 are obtained by reducing the first graph in the second row of Fig. 7.2 over  $S = \{u, v\}$  and  $S = \{1, 2, 3, 4\}$ . They have the same energy spectrum as the original graph and, moreover, the eigenvectors of reduced matrices are related to their full-size counterparts<sup>8</sup> [313]. Such a reduction can be performed in multiple steps  $S_1 \supset \dots \supset S_n$ . The order does not affect the final outcome, which is equivalent to a right away reduction over the terminal set  $S_n$ .

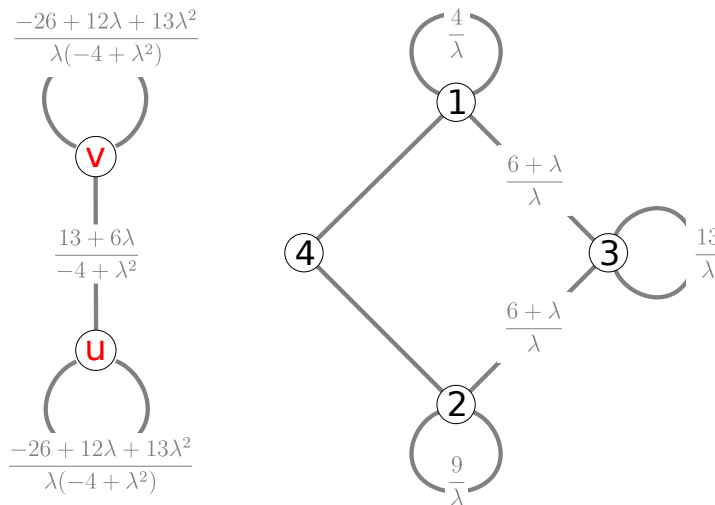


Figure 7.4: Isospectral reduction of the first graph in the second row of Fig. 7.2. Left: Reduction over  $S = \{u, v\}$ . Right: Reduction over  $S = \{1, 2, 3, 4\}$ . Both graphs have the same spectrum.

Isospectral reduction is a relatively young research branch of graph theory. So far, it has been applied to several problems including the dynamics in networks with time-delayed interactions [314, 315], improved estimates for the eigenvalues of a matrix [316] and the stability of pseudo-spectra to

<sup>8</sup> If  $\varphi$  is an eigenvector of  $H$  and its eigenvalue  $\lambda$  is not contained in the spectrum of the sub-matrix  $H_{\bar{S}\bar{S}}$ , then the projection  $\varphi_S$  is an eigenvector of  $R_S$  to the same eigenvalue.

perturbations in the context of linear mass-spring networks [317]. Isospectral reduction is intimately related to the famous Schur complement [318]. Moreover, the technique has been known in the physics community in the context of *renormalization group theory* used to describe the physics of atoms and molecules interacting with quantized electromagnetic fields [319, 320]. A decimation procedure, known as the Feshbach-Schur projection method, allows to derive an effective Hamiltonian, the same as Eq. (7.3), describing a subsystem  $S$  'dressed' by an environment  $\bar{S}$ . The impact of the environment is carried by the so-called *self-energy* [321]  $\Sigma_{SS}(\lambda) = H_{S\bar{S}}(H_{\bar{S}\bar{S}} - \lambda\mathbb{1})^{-1}H_{\bar{S}S}$ . The self-energy can be well understood by applying the interpretation of walks mentioned in the previous section, i. e., it describes the process of a single-link jump from  $S$  to  $\bar{S}$ , a multi-step propagation<sup>9</sup> in  $\bar{S}$  and, finally, a single-link back jump from  $\bar{S}$  to  $S$ .

What fascinates us the most about isospectral reduction is the notion of latent symmetries [324]. A *latent* symmetry is a geometrical symmetry of the reduced graph, i. e., an automorphism of  $R_S$ . For any automorphism present in  $\mathcal{G}$ , there is at least one set of latently symmetric vertices. However, not every latent symmetry can be traced back to an automorphism in  $\mathcal{G}$ . Thus, it is an extension of conventional permutation symmetries. As an example, compare the left graph in the second row of Fig. 7.2, having no automorphisms, to its reduction over  $S = \{u, v\}$  in Fig. 7.4 (on the left), which does have a 2-cycle permutation  $(u, v)$ . Since the eigenvectors of the reduced graph  $R_S$  are projections of original eigenvectors  $\varphi^{(k)}$  on the corresponding set  $S$ , as was shown in [313], we get yet another way to explain local parity of eigenvectors on cospectral vertices, i. e.,  $|\varphi_u^{(k)}| = |\varphi_v^{(k)}|$ . This is no coincidence: for a real symmetric matrix the cospectrality of a vertex pair  $S = \{u, v\}$  is equivalent to isospectral reduction over  $S$  being a  $2 \times 2$  bisymmetric matrix [325].

Latent symmetry can be analysed at different scales to infer how deep it is hidden within a network. One can define a visibility measure  $\mathcal{M} = \max_T (|T| - |S|) / (|\mathcal{V}| - |S|)$ . Formally, one needs to identify the largest superset  $T$ , satisfying  $S \subseteq T \subseteq \mathcal{V}$ , for which the isospectral reduction  $R_T$  reveals a permutation symmetry on the set  $S$ . In the limiting cases,  $T = \mathcal{V}$  implies visible in the unreduced graph  $\mathcal{G}$  ( $\mathcal{M} = 1$ ), while  $T = S$  signifies not revealed when reducing over any larger subset ( $\mathcal{M} = 0$ ).

Latent symmetries have been shown to exist in real-world networks [324]. Importantly, they determine a number of functional and structural properties of a graph the same way the conventional symmetries do, i. e., they are of equal or maybe even of a greater importance for the network. To demonstrate the power of this formalism, let us discuss one of our own ideas, where spectral degeneracies, seemingly accidental, can be explained by latent symmetries.

<sup>9</sup> A matrix inverse can be expanded in terms of matrix powers using the Cayley-Hamilton theorem [322, 323].

## 7.5 PREFACE: LATENT SYMMETRIES INDUCED DEGENERACIES

Symmetries play an important role in physics and chemistry. For the majority of problems, the theoretical treatment reduces at some point to a matrix description. Matrix diagonalization is one of the most expensive numerical operations having a complexity of  $\mathcal{O}(n^3)$  where  $n$  is the matrix dimension. Any methods allowing to partition a matrix into decoupled blocks are extremely valuable as they speed up calculations and make larger system sizes accessible. Group theory is one of the oldest techniques for this purpose. Explicitly, a group of symmetry operations commuting with a given Hamiltonian allows to switch to an efficient representation by a similarity transformation, where symmetry-adapted basis functions belonging to different symmetries are not coupled by the Hamiltonian. Furthermore, the degeneracy of eigenvalues is closely related to the representation theory. In particular, *non-abelian*<sup>10</sup> symmetry groups are known to induce degeneracies in the energy spectrum.

Conventionally, the symmetries one is looking for have a geometrical interpretation, such as the molecular point group in chemistry or the space group in crystallography. However, there are plenty of systems, where such symmetries alone do not suffice to explain all the multiplicities of energy eigenvalues. Whenever this happens, the degeneracy is called accidental because Schur's lemma does not constrain eigenvalues belonging to distinct irreducible representations to be different. It may well be that by accident, they happen to coincide for no particular reason. The prime examples are the molecular potential energy surfaces intersecting at some isolated points of a multidimensional parameter space. Actually, we observed a similar type of degeneracy in the spectrum of the 2+2 Bose mixture [MP1] as the coupling parameter was varied.

On the other hand, it is tempting to think that we overlook some higher order symmetry. In fact, the history of quantum mechanics knows a couple of examples where such was a case [326–328]: the hydrogen atom where the spherical symmetry group  $SO(3)$ , associated with the conservation of the total angular momentum, accounts only for the degeneracy in the quantum number  $m$  of the  $z$ -projection of the angular momentum, but not for the degeneracy in the quantum number  $l$  of the total angular momentum. The mystery was resolved by a higher dimensional symmetry group  $SO(4)$  and an additional conserved quantity, being the Runge-Lenz vector. Another fruitful example is the well-known isotropic harmonic oscillator, where for instance in 2D the cylindrical symmetry  $SO(2)$  would allow only for two-fold degenerate eigenvalues, whereas the degeneracy of the  $n$ -th excited state is in fact proportional to the number of ways  $n$  can be decomposed into a sum of two positive integers, which is  $n + 1$ . It turned out that the special unitary group  $SU(2)$ , a supergroup of  $SO(2)$ , is responsible for observed degeneracies.

In our work [MP7], we provide our own viewpoint on degeneracies being accidental. We argue that in some cases, the degeneracies might be

<sup>10</sup> A group of symmetries is called non-abelian if some of its elements do not commute.

explained in terms of latent symmetries, i. e., conventional symmetries of an effective Hamiltonian obtained by isospectral reduction. The major benefit of this approach as compared to other effective descriptions is that the spectrum of the initial model remains largely<sup>11</sup> preserved and is encoded in the self-energy which depends on the spectral parameter  $\lambda$ .

Thus, whenever an isospectrally reduced matrix can be similarity transformed into  $m$  non-equivalent irreducible blocks by group theory arguments, the  $j$ -th block will be either a  $\lambda$ -function multiple of an identity matrix, i. e.,  $b_j(\lambda)\mathbb{1}_{d_j}$  or a direct sum of  $d_j$  copies of a  $\lambda$ -dependent matrix  $B_j(\lambda)$ , i. e.,  $\bigoplus^{d_j} B_j(\lambda)$ , where  $d_j$  is the dimension of the irreducible representation. In the next step, we solve either  $b_j(\lambda) - \lambda = 0$  or  $\det(B_j(\lambda) - \lambda) = 0$ . Each solution will be an eigenvalue of  $R_S$ , but also of the initial matrix  $H$ , and it will occur  $d_j$ -times!

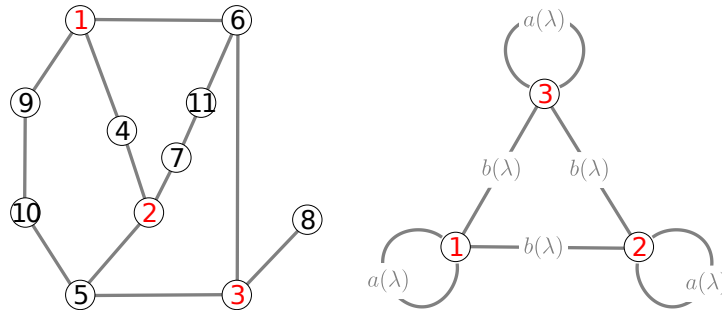


Figure 7.5: Hidden symmetry group behind degeneracies. Left: A graph with two-fold degeneracies but no permutation symmetries. Right:  $C_{3v}$  symmetry of a reduced graph  $R_S(\lambda)$  with  $S = \{1, 2, 3\}$ .

For a sneak-peak, see Fig. 7.5. The graph on the left has no permutation symmetries. Nevertheless, it has two doubly degenerate eigenvalues:  $-1$  and  $2$ . The reduced graph on the right features the symmetry group  $C_{3v}$ . As the group is non-abelian, it enforces blocks with degenerate entries. Explicitly, we perform a similarity transformation  $T$ , which gives

$$T^{-1}R_S(\lambda)T = \begin{pmatrix} b_1(\lambda) & 0 & 0 \\ 0 & b_1(\lambda) & 0 \\ 0 & 0 & b_2(\lambda) \end{pmatrix}. \quad (7.4)$$

We evidence a structural degeneracy of  $b_1(\lambda) = 1 + 2/\lambda$ . The equation  $b_1(\lambda) - \lambda = 0$  has two solutions:  $\lambda = -1$  and  $\lambda = 2$ , thus giving rise to the two degeneracies of the original graph in Fig. 7.5. Latent symmetry is a step beyond conventional tools of symmetry analysis and it offers alternative ways to interpret spectral degeneracies of physical models.

<sup>11</sup> The energy spectrum of the reduced matrix  $R_S$  from Eq. (7.3) is composed of eigenvalues of the original matrix  $H$  (including multiplicities). However, in case an eigenvalue of  $H$  happens to be also an eigenvalue of the sub-matrix  $H_{\bar{S}\bar{S}}$ , it will be not contained in the spectrum of  $R_S$ , i. e.,  $\sigma(R_S) = \sigma(H) - \sigma(H_{\bar{S}\bar{S}})$  with  $\sigma$  denoting a multi-set of eigenvalues.

Part III

CONTRIBUTIONS, SUMMARY AND OUTLOOK



SCIENTIFIC CONTRIBUTIONS

---

In this chapter we list our publications [MP1–MP7].







## OPEN ACCESS

RECEIVED  
12 July 2017REVISED  
21 October 2017ACCEPTED FOR PUBLICATION  
23 November 2017PUBLISHED  
10 January 2018Original content from this work may be used under the terms of the [Creative Commons Attribution 3.0 licence](https://creativecommons.org/licenses/by/4.0/).

Any further distribution of this work must maintain attribution to the author(s) and the title of the work, journal citation and DOI.



## PAPER

## Spectral properties and breathing dynamics of a few-body Bose–Bose mixture in a 1D harmonic trap

Maxim Pyzh<sup>1,4</sup>, Sven Krönke<sup>1,2</sup>, Christof Weitenberg<sup>3</sup> and Peter Schmelcher<sup>1,2</sup><sup>1</sup> Zentrum für Optische Quantentechnologien, Universität Hamburg, Luruper Chaussee 149, D-22761 Hamburg, Germany<sup>2</sup> The Hamburg Centre for Ultrafast Imaging, Universität Hamburg, Luruper Chaussee 149, D-22761 Hamburg, Germany<sup>3</sup> Institut für Laserphysik, Universität Hamburg, D-22761 Hamburg, Germany<sup>4</sup> Author to whom any correspondence should be addressed.E-mail: [mpyzh@physnet.uni-hamburg.de](mailto:mpyzh@physnet.uni-hamburg.de) and [pschmelc@physnet.uni-hamburg.de](mailto:pschmelc@physnet.uni-hamburg.de)**Keywords:** collective excitations, breathing mode, low-dimensional systems, few-body systems, strong interactions, bosonic mixtures

## Abstract

We investigate a few-body mixture of two bosonic components, each consisting of two particles confined in a quasi one-dimensional harmonic trap. By means of exact diagonalization with a correlated basis approach we obtain the low-energy spectrum and eigenstates for the whole range of repulsive intra- and inter-component interaction strengths. We analyse the eigenvalues as a function of the inter-component coupling, covering hereby all the limiting regimes, and characterize the behaviour in-between these regimes by exploiting the symmetries of the Hamiltonian. Provided with this knowledge we study the breathing dynamics in the linear-response regime by slightly quenching the trap frequency symmetrically for both components. Depending on the choice of interactions strengths, we identify 1 to 3 monopole modes besides the breathing mode of the centre of mass coordinate. For the uncoupled mixture each monopole mode corresponds to the breathing oscillation of a specific relative coordinate. Increasing the inter-component coupling first leads to multi-mode oscillations in each relative coordinate, which turn into single-mode oscillations of the same frequency in the composite-fermionization regime.

## 1. Introduction

The physics of ultra-cold atoms has gained a great boost of interest since the first experimental realization of an atomic Bose–Einstein condensate [1, 2], where research topics such as collective modes [3–5], binary mixtures [6, 7] and lower-dimensional geometries [8–10] were in the focus right from the start. In most of the experiments on ultra-cold gases the atoms are but weakly correlated and well described by a mean-field (MF) model, the well-known Gross–Pitaevskii equation (GPE), or in case of mixtures by coupled GPEs [11–13]. Bose–Bose mixtures exhibit richer physics compared to their single component counterpart. For instance, different ground state profiles can be identified depending on the ratios between the intra- and inter-species interaction strengths, being experimentally tunable by e.g. Feshbach resonances (FRs) [14]; the miscible, immiscible symmetry-broken (SB) or immiscible core–shell structure, also called phase separation (PS) [15–17]. Comparing the experimentally obtained densities to numerical MF calculations [18, 19] provides a sensitive probe for precision measurements of the scattering lengths or, if known, the magnetic fields used to tune them [16]. Another possibility to access the interaction regime and thus the scattering lengths is by exciting the system and extracting the frequencies of low-lying excitations [20]. In contrast to a single-species case the collective modes of mixtures exhibit new exciting phenomena: doublet splitting of the spectrum containing in-phase and out-of-phase oscillations, mode-softening for increasing inter-component coupling, onset of instability of the lowest dipole mode leading to the SB phase as well as minima in the breathing mode frequencies w.r.t. interaction strength [21–23].

The breathing or monopole mode, characterized by expansion and contraction of the atomic density, has in particular proven to be a useful tool for the diagnostics of static and dynamical properties of physical systems. It

is sensitive to the system's dimensionality, spin statistics as well as form and strength of interactions [24–27]. In the early theoretical investigations on quasi-one-dimensional single-component systems [28] it was shown that different interaction regimes can be distinguished by the breathing mode frequency, which has been used in experiments [10, 29, 30]. Furthermore, the monopole mode provides indirect information on the ground state [31], its compressibility [32] and the low-lying energy spectrum such that an analogy has been drawn to absorption/emission spectroscopy in molecular physics [27].

From a theoretical side, those of the above experiments which are concerned with quasi-1D set-ups are in particular interesting, since correlations are generically stronger, rendering MF theories often inapplicable. Here, confinement induced resonances (CIR) [8] can be employed to realize the Tonks–Girardeau limit [33, 34], where the bosons resemble a system of non-interacting fermions in many aspects. While this case can be solved analytically [35, 36], strong but finite interactions are tractable only to numerical approaches, which limits the analysis to few-body systems. For instance, a profound investigation of the ground state phases of a few-body Bose–Bose mixture [37, 38] showed striking differences to the MF calculations: for coinciding trap centres, a new phase with bimodal symmetric density structure, called composite fermionization (CF), is observed while SB is absent for any finite inter-component coupling. Only in the limit of infinite coupling the ground state becomes two-fold degenerate enabling to choose between CF and SB representations [39], while the MF theory predicts the existence of SB already for finite couplings. This observation accentuates the necessity to include correlation effects.

In this work we solve the time-independent problem of the simplest Bose–Bose mixture confined in a quasi-1D HO trap with two particles in each component, covering the whole parameter space of repulsive intra- and inter-species interactions, thereby complementing the analysis of some previous studies [39–41]. To accomplish this, an exact diagonalization method based on a correlated basis is introduced. We unravel how the distinguishability of the components renders the spectrum richer and complexer compared to a single component case [42]. Furthermore, these results are used to investigate the breathing dynamics of the composite system. While the breathing spectrum of a single component was recently investigated comprehensively in [43–49], reporting a transition from a two mode beating of the centre of mass  $\Omega_{\text{CM}}$  and relative motion  $\Omega_{\text{rel}}$  frequencies for few atoms to a single mode breathing for many particles, the breathing mode properties of few-body Bose–Bose mixtures are not characterized so far. For this reason, we analyse the number of breathing frequencies and the kind of motion to which they correspond in dependence on the intra- and inter-component interaction for the binary mixture at hand.

This work is structured as follows. In section 2 we introduce the Hamiltonian of the system. In section 3 we perform a coordinate transformation to construct a fast converging correlated basis. Using exact diagonalization with respect to this basis we study in section 4 the low-lying energy spectrum for various interaction regimes. Section 5 is dedicated to the breathing dynamics within the linear response regime. An experimental realization is discussed in section 6 and we conclude the paper with a summary and an outlook in section 7.

## 2. Model

We consider a Bose–Bose mixture containing two components, which are labelled by  $\sigma \in \{A, B\}$ , confined in a highly anisotropic harmonic trap. We assume the low temperature regime, where the inter-particle interactions may be modelled via a contact potential, and strong transversal confinement allowing us to integrate out frozen degrees of freedom leading to a quasi-1D model. Our focus lies on a mixture of  $N_\sigma = 2$  particles, which have the same mass  $m_\sigma \equiv m$  and trapping frequencies  $\omega_{\sigma,\perp} \equiv \omega_\perp$ ,  $\omega_{\sigma,\parallel} \equiv \omega$  in the transversal, longitudinal direction, respectively. This can be realized by choosing different hyperfine states of the same atomic species. By further rescaling the energy and length in units of  $\hbar\omega$  and  $a_{\text{ho}} = \sqrt{\hbar/(m\omega)}$  one arrives at the dimensionless Hamiltonian:

$$H = \sum_{\sigma} H_{\sigma} + H_{AB}, \quad (1)$$

with the single-component Hamiltonians  $H_{\sigma}$

$$H_{\sigma} = \sum_{i=1}^2 \left( -\frac{1}{2} \frac{\partial^2}{\partial x_{\sigma,i}^2} + \frac{1}{2} x_{\sigma,i}^2 \right) + g_{\sigma} \delta(x_{\sigma,1} - x_{\sigma,2}), \quad (2)$$

and inter-component coupling  $H_{AB}$

$$H_{AB} = g_{AB} \sum_{i,j=1}^2 \delta(x_{A,i} - x_{B,j}), \quad (3)$$

where  $g_{\alpha} \approx (2a_{\alpha}^{3\text{D}}\omega_{\perp})/(\omega a_{\text{ho}})$  with  $a_{\alpha}^{3\text{D}}$  the 3D s-wave scattering length and  $\alpha \in \{A, B, AB\}$  are effective (off-resonant) interaction strengths.

### 3. Methodology: exact diagonalization in a correlated basis

To obtain information on the low-energy excitation spectrum we employ the well-established method of exact diagonalization [50]. However, instead of taking bosonic number states w.r.t. HO eigenstates for the underlying basis as done in e.g. [40], we pursue a different approach by using a correlated atom-pair basis. This allows us to study arbitrary intra-component interactions  $g_\sigma$  (even infinity) exactly, whereas HO number states are much more inefficient in handling strong intra-component interactions. At the same time our method converges quickly for inter-component couplings  $g_{AB} \leq 10$  requiring at most 700 basis states. In comparison, a straightforward treatment in the laboratory frame requires typically  $\sim 10^5$  HO number states for obtaining converged ground-state results [38]. For even larger  $g_{AB}$  couplings, the chosen basis becomes less appropriate such that our basis size has then to be significantly increased in order to obtain accurate results. Going, however, beyond  $g_{AB} = 10$  would not give qualitatively new physical phenomena. Essentially all effects of the strong-coupling regime can be investigated by studying the crossover from  $g_{AB} = 0$  to  $g_{AB} = 10$ .

Actually, the idea of choosing optimized basis sets to speed up the convergence with respect to the size of basis functions can be also seen in the context of the potential-optimized discrete variable representation [51]. Here, one employs eigenstates of conveniently constructed one-dimensional reference Hamiltonians in order to incorporate more information on the actual Hamiltonian into the basis compared to the standard DVR technique [52, 53]. Another approach, stemming from nuclear physics, uses an effective two-body interaction potential instead of an optimized basis for solving ultra-cold many-body problems [54–56].

In order to construct a tailored basis, which already incorporates intra-component correlations, we apply a coordinate transformation to the relative frame  $\hat{Y} \equiv (R_{CM}, R_{AB}, r_A, r_B)^T$  defined by:

- total CM coordinate

$$R_{CM} = \sum_\sigma \sum_{i=1}^2 x_{\sigma,i}/4,$$

- relative CM coordinate

$$R_{AB} = \sum_{i=1}^2 x_{A,i}/2 - \sum_{i=1}^2 x_{B,i}/2,$$

- relative coordinate for each  $\sigma$  component

$$r_\sigma = x_{\sigma,1} - x_{\sigma,2}.$$

In this frame, the Hamiltonian (1) attains the following form:

$$H = H_{R_{CM}} + H_{R_{AB}} + \sum_{\sigma=A,B} H_{r_\sigma} + g_{AB} H_1. \quad (4)$$

Here, the total CM separates,  $H = H_{R_{CM}} + H_{rel}$ , and is simply governed by a harmonic oscillator (HO) Hamiltonian with mass  $M = 4$ :

$$H_{R_{CM}} = -\frac{1}{8} \frac{\partial^2}{\partial R_{CM}^2} + 2R_{CM}^2, \quad (5)$$

featuring the spectrum  $E_n^{CM} = n + 1/2$  with  $n \in \mathbb{N}_0$ . The remainder of the Hamiltonian can be decomposed as  $H_{rel} = H_0 + g_{AB} H_1$ , where  $H_0 = H_{R_{AB}} + \sum_\sigma H_{r_\sigma}$  can be solved analytically and  $H_1$  couples the eigenstates of  $H_0$ :

$$H_{R_{AB}} = -\frac{1}{2} \frac{\partial^2}{\partial R_{AB}^2} + \frac{1}{2} R_{AB}^2, \quad (6)$$

$$H_{r_\sigma} = -\frac{\partial^2}{\partial r_\sigma^2} + \frac{1}{4} r_\sigma^2 + g_\sigma \delta(r_\sigma), \quad (7)$$

$$H_1 = \sum_{i,j=1}^2 \delta \left( R_{AB} + (-1)^i \frac{r_A}{2} + (-1)^j \frac{r_B}{2} \right). \quad (8)$$

So  $H_{R_{AB}}$  is a HO Hamiltonian of mass  $M = 1$  and  $H_{r_\sigma}$  leads to the Weber differential equations<sup>5</sup> for its eigenstates with delta-function constraint. The corresponding solutions are normalized as well as symmetrized parabolic

<sup>5</sup>  $f''(r) + (\mu + \frac{1}{2} - \frac{1}{4}r^2)f(r) = 0$  with  $r \in \mathbb{R}$  and  $\mu \in \mathbb{R}$ .

cylinder functions<sup>6</sup> (PCF)  $\varphi_n^\sigma(r_\sigma) \propto D_{\mu(g_\sigma, n)}(|r_\sigma|)$  of the relative coordinate with  $\mu(g_\sigma, n)$  being a real valued quantum number depending on the intra-component interaction strength  $g_\sigma$  and the excitation level  $n \in \mathbb{N}_0$ , which is obtained by solving a transcendental equation stemming from the delta-function constraint [57]:

$$g_\sigma = -2^{\frac{3}{2}} \frac{\Gamma(\frac{1-\mu}{2})}{\Gamma(-\frac{\mu}{2})}. \quad (9)$$

Now to diagonalize  $H_{\text{rel}}$  we choose the eigenvectors of  $H_0$  as basis states and label them as  $|k, l, m\rangle$  with  $k, l, m \in \mathbb{N}_0$ . Their spatial representation and corresponding eigenenergies read:

$$\langle R_{AB}, r_A, r_B | k, l, m \rangle = \Phi_k^{AB}(R_{AB}) \varphi_l^A(r_A) \varphi_m^B(r_B), \quad (10)$$

$$E_{k,l,m}^{(0)} = k + \mu(g_A, l) + \mu(g_B, m) + \frac{3}{2}, \quad (11)$$

where  $\Phi_k^{AB}$  are HO eigenstates of  $H_{R_{AB}}$ . We note that all  $\varphi_l^\sigma(r_\sigma)$  are of even parity because of the bosonic nature of the particles of each component.

The main challenge now is the calculation of the matrix elements of  $H_1$ , which are complicated 2D integrals at first sight and need to be tackled numerically. In the [appendix](#) we provide a circumvention of this problem via the Schmidt decomposition [58], allowing us to replace one 2D integral by multiple 1D integrals, which results in faster computation times. In quantum chemistry, the algorithm for achieving such a representation is known as POTFIT [59]. In the [appendix](#), we moreover point out several symmetries which can be utilized for efficiently evaluating these 1D integrals and discuss in detail, why our computational strategy is much more efficient than the direct evaluation of the 2D integrals for the problem at hand.

To summarize, the coordinate transformation to the chosen relative frame (i) decouples the CM motion and (ii) naturally guides us to employ the analytically known eigenstates of  $H_0$  as the basis states in order to incorporate intra-component correlations into our basis.

## 4. Stationary properties

By means of the correlated basis introduced above and an efficient strategy for calculating the Hamiltonian matrix to be diagonalized, we can easily obtain the static properties of our system for arbitrary intra-component interaction strengths  $g_\sigma$  and inter-component coupling  $g_{AB} \leq 10$ . The most representative choices of interaction strengths ( $g_A, g_B, g_{AB}$ ) are the subject of this section and in order to get a deeper understanding of the spectral properties a thorough discussion of the symmetries of  $H$  is necessary.

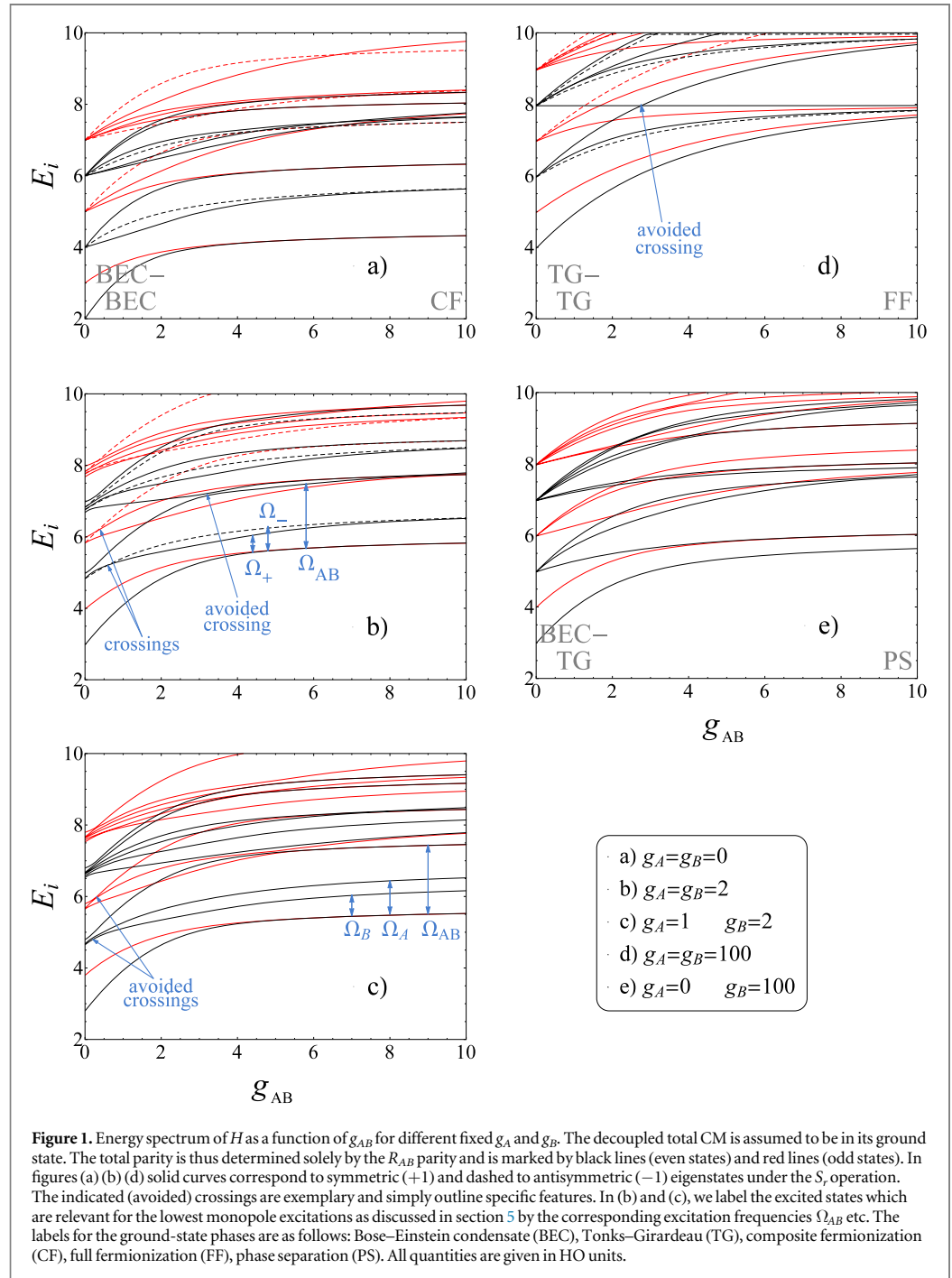
### 4.1. Symmetry analysis

In the laboratory frame, there are only a few obvious symmetries: (i) the total parity  $P_{\text{tot}}$  (i.e. simultaneous replacement of all coordinates  $x_{\sigma,i}$  by  $-x_{\sigma,i}$ ), (ii) an interchange of the two  $A$  particles  $S_A$  or of the two  $B$  particles  $S_B$ , (iii) in the case of equal intra-component couplings  $g_A = g_B$  a simultaneous interchange of two  $A$  particles with two  $B$  particles  $S_{AB}$  and (iv) given all couplings to be equal, the exchange  $S_{ij}$  of any two particles being labelled by  $i, j$ . In the relative frame though, additional symmetries become apparent. The total Hamiltonian  $H$  commutes with each individual parity operator  $P_{Y_i}$  of the relative frame coordinates ( $P_{Y_i}$  replaces  $Y_i$  by  $-Y_i$  while leaving the other coordinates of the relative frame invariant). In these regards, we note that  $P_{R_{AB}}$  does not commute with the individual terms in equation (8) but only with the whole sum of these four terms. The eigenvectors of  $P_{r_\sigma}$  are restricted to even parity because of the bosonic character of our components, corresponding to the  $S_\sigma$  operation. In contrast to the former operations, the symmetry transformations  $P_{R_{\text{CM}}}$  and  $P_{R_{AB}}$  are highly non-trivial in the laboratory frame involving improper rotations of the four-dimensional coordinate system. Due to the decoupling of  $H_{R_{\text{CM}}}$  it is sufficient to consider only the ground state of the total CM motion, which is of even  $R_{\text{CM}}$  parity, in the following. Then, the parity of the  $R_{AB}$  degree of freedom completely determines the total parity of the eigenstates. Finally, a further symmetry arises if one chooses equal intra-component interaction strengths  $g_\sigma$ . In this case, the Hamiltonian  $H$  is invariant under an exchange of the relative coordinates  $r_A \leftrightarrow r_B$ , which we define as the  $S_r$  transformation in the following. Contra-intuitively,  $S_r$  is not the same as the  $S_{AB}$  transformation. In total, the chosen relative frame indicates a set of additional symmetries, which are hidden in the laboratory frame.

### 4.2. Energy spectra

In figure 1 we show the total energy spectrum as a function of  $g_{AB}$  for various fixed values of  $g_A$  and  $g_B$ . The total CM is assumed to be in its ground state. Figure 1(a) depicts the non-interacting intra-component scenario

<sup>6</sup>  $D_\mu(|r|) = 2^{\frac{\mu}{2}} e^{-\frac{r^2}{4}} U\left(-\frac{1}{2}\mu, \frac{1}{2}, \frac{1}{2}r^2\right)$  with  $U(a, b, x)$  denoting the Tricomi's hypergeometric function.



$g_\sigma = 0$ . For  $g_{AB} = 0$  the Hamiltonian represents two uncoupled non-interacting bosonic species and we will label this regime as BEC–BEC following the nomenclature of [40]. The eigenenergies are integers with equal spacings of  $\hbar\omega$ , which is 1 in our units. In this limit the PCFs are even HO eigenstates of mass  $m = 1/2$ . The eigenenergies are thus  $E_{\text{tot}} = E_{n=0}^{\text{CM}} + E_{k,l,m}^{(0)} \equiv E_{0,k,l,m}^{(0)} = k + 2l + 2m + 2$ .

For  $g_{AB} = 0$ , the  $i$ th eigenenergy corresponding to only even (odd)  $R_{AB}$ -parity eigenstates is  $(i + 2)/(2!i!)$  fold degenerate with  $i \in \mathbb{N}_0$ . Already a small inter-component coupling lifts all these degeneracies such that branches of eigenenergies arise. In the following, we label these resulting branches as the  $i$ th even or odd  $R_{AB}$ -parity branch, respectively. Note that this grouping of the energy levels into branches will be used in the following for all values of  $g_{AB}$  and in particular for the analysis of the breathing dynamics in section 5. As we further increase the inter-component coupling strength, we observe that states corresponding to branches of

opposite  $R_{AB}$ -parity incidentally cross, as they are of different symmetry and consequently not coupled by the  $H_1$  perturbation.

For very strong  $g_{AB}$  values, i.e. in the CF limit [37, 38], we observe a restoration of degeneracies, but in a different manner, namely the lowest states merge pairwise forming a two-fold degeneracy. In this regime the two components spatially separate for the ground state, where one component locates on the left side of the trap, while the other is pushed to the right side due to the strong inter-component repulsion. The two-fold degeneracy of the ground state reflects actually the two possible configurations:  $A$  left  $B$  right and  $A$  right  $B$  left. This behaviour can be observed in the relative frame densities, discussed later in this section. Another striking peculiarity for  $g_{AB} \rightarrow \infty$  are non-integer eigenvalues and unequal energy spacings, meaning that for CF no ‘TG-like’ mapping to a non-interacting HO system exists.

A very similar analysis concerning this specific choice of interactions ( $g_\sigma = 0$  and arbitrary  $g_{AB}$ ) was performed in [39], where an effective interaction approach was employed to greatly improve the convergence properties of exact diagonalization in order to access properties of a Bose–Bose mixture with up to  $N = 10$  particles. However, the analysis only covered a single line of the  $(g_A, g_B, g_{AB})$  parameter space. Another similar work [40] deals with the system’s properties for an even wider range of intra- and inter-component interactions, however the main focus lies on the ground state properties. Here, we extend the analysis of [39, 40] by studying both the ground state and the low-lying excitations for weak, strong as well as intermediate interactions  $g_\sigma$ .

In figure 1(b) we show the impact of moderate but symmetric intra-component interactions of strength  $g \equiv g_\sigma = 2$ . Already in the uncoupled regime ( $g_{AB} = 0$ ) we observe fewer degeneracies compared to the  $g_\sigma = 0$  case. Nevertheless, we group the eigenstates into branches of even/odd  $R_{AB}$ -parity also for finite  $g_\sigma$  by continuously following the eigenenergies to the  $g_\sigma \rightarrow 0+$  limit. The reason for the reduced degeneracies is that the PCFs are not HO eigenstates anymore, while the PCFs of both components coincide pairwise. The eigenenergies read  $E_{0,k,l,m}^{(0)} = k + \mu(g, l) + \mu(g, m) + 2$ . To roughly estimate the energetic ordering it is sufficient to know that the real-valued quantum number  $\mu(g, n)$  fulfills for  $0 < g < \infty$  the following relations:

- $2n < \mu(g, n) < 2n + 1$
- $\mu(g, n) + 1 < \mu(g, n + 1) < \mu(g, n) + 2$

meaning that a single excitation of the relative motion  $r_\sigma$  is energetically below a double excitation of the  $R_{AB}$  degree of freedom. E.g. the first even  $R_{AB}$ -parity branch in the uncoupled non-interacting regime (BEC–BEC in figure 1(a)) contains three degenerate states:  $|2, 0, 0\rangle$ ,  $|0, 1, 0\rangle$  and  $|0, 0, 1\rangle$  (equation (10)). By choosing finite  $g_\sigma$  values  $|2, 0, 0\rangle$  acquires a higher energy than  $|0, 1, 0\rangle$  and  $|0, 0, 1\rangle$  leading to reduced degeneracies in the spectrum. Another striking feature is the appearance of additional crossings between states of the same  $R_{AB}$ -parity due to the  $S_r$  symmetry. States, which possess different quantum numbers concerning the  $S_r$  transformation ( $+1$  or  $-1$ ), are allowed to cross as they ‘randomly’ do throughout the  $g_{AB}$  variation. Of course, such crossings are also present in the previous non-interacting case, it being also component-symmetric. An avoided crossing between a state of the first even  $R_{AB}$ -parity branch and a state of the second even  $R_{AB}$ -parity branch is worth mentioning, which is present for all values of  $g_\sigma$  (see the exemplary arrow in figures 1(b) or (d)). States of the same symmetry obviously do not cross according to the Wigner-von Neumann non-crossing rule [60].

In figure 1(c) we asymmetrically increase the intra-component interactions  $g_\sigma$  as compared to the non-interacting case, namely to  $g_A = 1$  and  $g_B = 2$ . For the uncoupled scenario ( $g_{AB} = 0$ ) all the degeneracies are lifted, because now PCFs of the  $A$  and the  $B$  components are different. The energy is  $E_{0,k,l,m}^{(0)} = k + \mu(g_A, l) + \mu(g_B, m) + 2$ . The energetic state ordering is far from obvious, which becomes apparent upon closer inspection of the  $\mu(g, n)$  function. E.g. consider again the first even  $R_{AB}$ -parity branch. Its lowest energy state is a single excitation of  $r_B$ , followed by a single excitation of  $r_A$ . The highest energy of this branch corresponds to a double  $R_{AB}$  excitation. The ordering pattern for higher order branches is even more complicated. For intermediate values of  $g_{AB}$  we observe that crossings from the previous scenario (with  $g_\sigma = 2$ ) between states of the same  $R_{AB}$ -parity are replaced by avoided crossings because of the broken  $S_r$  symmetry. The strong coupling regime displays less degeneracies as compared to the component-symmetric cases of figures 1(a) and (b) with the two-fold ground state degeneracy remaining untouched.

In figure 1(d) we choose very strong intra-component interaction strengths  $g_\sigma = 100$ . When the  $g_{AB}$ -coupling is absent, we have two hard-core bosons in each component. The system can thus be mapped to a two-component mixture of non-interacting fermions [35, 61] and will be referred to as TG–TG limit. The PCFs become near degenerate with odd HO eigenstates, which again leads to integer-valued eigenenergies  $E_{0,k,l,m}^{(0)} \approx k + 2l + 2m + 4$  with equal spacings and the same degree of (near-)degeneracies as in the non-interacting case (figure 1(a)). The limit of strong inter-component coupling displays a completely different structure of the spectrum. The so-called full fermionization (FF) [36] phase can be mapped to a non-interacting ensemble of four fermions with the ground state energy  $N^2/2 = 8$ . However, in contrast to the single-

component case of four bosons, we need to take into account that the components are distinguishable. Thus, the degeneracy of the ground state is expected to be  $N!/(N_A!N_B!) = 6$ -fold and corresponds to the different possibilities of ordering the laboratory frame coordinates while keeping in mind the indistinguishability of particles of each component. This limit of all interactions strengths going to infinity can be treated analytically by using the so-called ‘snippet’ basis [62, 63].

For strong but finite couplings, i.e.  $1/g_\alpha \ll 1$ , recent research also unveiled the existence of a mapping to an effective spin-chain model by employing perturbation theory with respect to the ‘snippet’ basis. Various intriguing ground-state configurations have been revealed depending on the ratio and the sign of the interaction parameters: Heisenberg antiferromagnet (AFM)/ferromagnet (FM), Ising AFM/FM and XY phase [64–68]. Such a mapping is applicable not only for Bose–Bose mixtures, but also Bose–Fermi and Fermi–Fermi mixtures may be treated with this approach.

The last case we discuss is the highly asymmetric case  $g_A = 0$  and  $g_B = 100$  in figure 1(e). For  $g_{AB} = 0$  (BEC–TG) one expects, based on the previous considerations, integer eigenvalues  $E_{0,k,l,m}^{(0)} \approx k + 2l + 2m + 3$  and thus equal spacings as for the cases  $g_\sigma = 0$  and  $g_\sigma = 100$  depicted in figures 1(a) and (d), because the PCF of the  $A$  component is an even HO eigenstate and the PCF of the  $B$  component is degenerate with an odd HO eigenstate. Very peculiar is the strong coupling case, where we observe a non-degenerate ground state, the so-called PS phase [40], where the  $A$  component occupies the centre of the harmonic trap, while the  $B$  component, in order to reduce its intra-component interaction energy, forms a shell around the  $A$  component.

### 4.3. Relative-frame densities

Let us now inspect the relative-frame probability densities  $\rho_1(Y_i)$  instead of the usually studied one-body densities  $\rho_1(x_\sigma)$  of the laboratory frame as e.g. in [40]. We will see that these quantities can be used to identify regions of most probable relative distances and provide a more detailed picture of particle arrangements than their laboratory frame counterparts. Moreover, in the quench dynamics study, the subject of the next section, an occupation of a certain eigenstate of  $H$  will lead to the breathing oscillation of only one relative-frame density, making it possible to connect different breathing modes to specific relative motions within the system, at least for the weakly coupled case  $g_{AB} \ll 1$ .

We define these quantities as follows:

$$\rho_1^{(j)}(Y_i) = \int \prod_{p \neq i} dY_p |\langle \vec{Y} | E_j \rangle|^2, \quad (12)$$

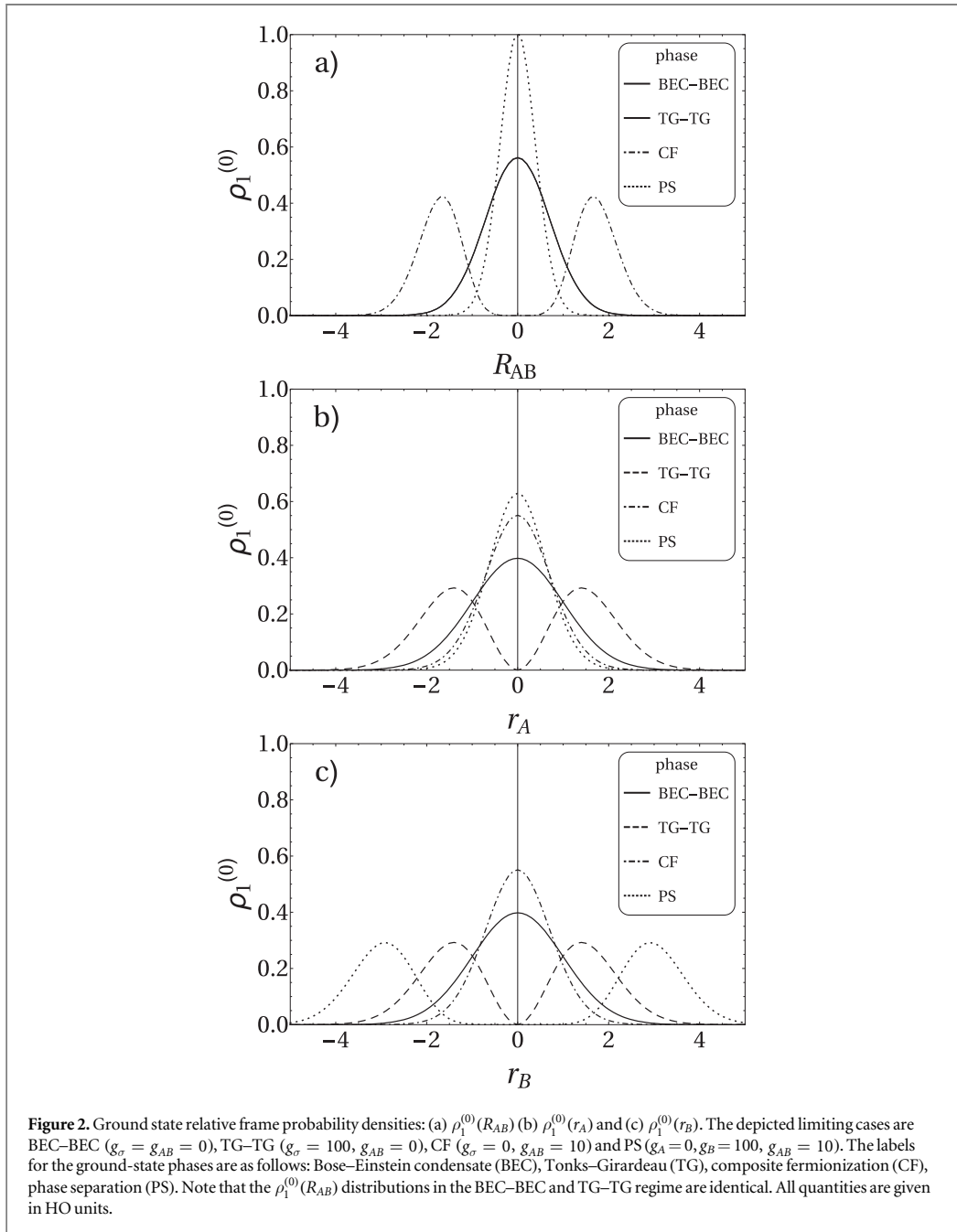
where  $|E_j\rangle$  is the  $j$ th eigenstate of  $H$  and we trace out all the degrees of freedom of the relative frame  $\vec{Y}$  except for one.

Let us compare our results concerning the ground state densities for some limiting cases to the ones obtained in [40]. In figure 2 we show the densities for all the degrees of freedom except for  $R_{CM}$ , which trivially obeys a Gaussian distribution. In the BEC–BEC case all the densities are characterized by a Gaussian density profile, since the Hamiltonian consists of completely decoupled HOs for each degree of freedom.

When the  $g_{AB}$  coupling is turned off, the ground state is known analytically:  $\Phi_0^{AB}(R_{AB}) \varphi_{\mu(g_A,0)}^A(r_A) \varphi_{\mu(g_B,0)}^B(r_B)$ . Thus, by tracing out the  $r_\sigma$  coordinates we acquire the same  $\rho_1^{(0)}(R_{AB})$  for arbitrary intra-component interactions, which explains the identical distributions for the BEC–BEC and TG–TG phase in figure 2(a). While the PCF  $\varphi_{\mu(g_\sigma,0)}^\sigma(r_\sigma)$  is identical to the HO ground state for  $g_\sigma = 0$ , for any finite positive  $g_\sigma$  it splits into two symmetric peaks with a cusp at the origin, which tends to zero as  $g \rightarrow \infty$  [57]. In this limit it becomes equivalent to the modulus of the first excited HO eigenstate, which explains the shape of the TG-curves in figures 2(b), (c). We remark that going beyond  $g_\sigma = 100$  does not induce substantial changes on the densities, which justifies our interpretation of this parameter regime as TG limit.

The CF phase is in some sense a complete counter-part to the TG–TG case. Now  $\rho_1^{(0)}(R_{AB})$  features two maxima and a minimum in between, a result of  $A$  and  $B$  strongly repelling each other. This feature is blurred in the one-body density distributions  $\rho_1^{(0)}(x_\sigma)$  of the laboratory frame and one needs to additionally consider the two-body density function  $\rho_2^{(0)}(x_A, x_B)$  to verify this behaviour [37]. The density distribution of  $\rho_1^{(0)}(r_\sigma)$  is more compressed compared to the BEC–BEC case due to the tighter confinement induced by the other component.

Finally, the PS phase corresponds to a core–shell structure, where  $\rho_1^{(0)}(R_{AB})$  and  $\rho_1^{(0)}(r_A)$  show a more pronounced peak, while  $\rho_1^{(0)}(r_B)$  obeys a bimodal distribution with two density peaks being much further apart than both in the CF and in the TG–TG case. This can be understood in the following way: firstly, the fact that  $A$  locates in the trap centre and not the other way around is because  $B$  needs to minimize its repulsive intra-component interaction energy by separating its particles. Secondly, the need to minimize the repulsive inter-component energy pushes the  $B$  particles even further along the harmonic trap at the cost of increased potential energy until these two energies balance themselves out. The two  $A$  particles are compressed to closer distances as compared to the BEC–BEC case because of a tighter trap induced by  $B$ , while at the same time  $A$  modifies the HO



potential to a double well for  $B$ . This results in stronger localization of particles, which leads to a more pronounced peak in the  $R_{AB}$  distribution.

## 5. Breathing dynamics

The spectral properties discussed above can be probed by slightly quenching a system parameter such that the lowest lying collective modes are excited. Here, we focus on a slight quench of the trapping frequency in order to excite the breathing or monopole modes being characterized by a periodic expansion and compression of the atomic density. While in the single-component case two lowest lying breathing modes of in general distinct frequencies exist, being associated with a motion of the CM and the relative coordinates [24, 43], respectively,



the number of breathing modes, their frequencies and the associated ‘normal coordinates’<sup>7</sup> are so far unknown for the more complex case of a binary few-body mixture and shall be the subject of this section.

Experimentally, breathing oscillations can be studied by measuring the width of the  $\sigma$  species density distribution  $\int dx_\sigma x_\sigma^2 \rho_1(x_\sigma, t)$  where we have omitted the subtraction of the mean value  $\int dx_\sigma x_\sigma \rho_1(x_\sigma, t)$  squared, which vanishes due to the parity symmetry. From a theoretical point of view, it is fruitful to define a breathing observable as  $\sum_{\sigma, i} x_{\sigma, i}^2$ , whose expectation value is essentially the sum of the widths of the  $A$  and the  $B$  component.

To study the breathing dynamics we will perform a slight and component-symmetric quench of the HO trapping frequency, where our HO units will be given with respect to the post-quench system. The initial state for this quench scenario is the ground state  $|\Psi(t=0)\rangle = |E_0\rangle_{\omega_0}$  of the pre-quench Hamiltonian  $H(\omega_0)$  with harmonic trapping frequency  $\omega_0 \gtrsim 1$ , where  $H(\omega_0)$  is obtained from equation (1) by multiplying the harmonic potential terms with the pre-factor  $\omega_0^2$ . At time  $t=0$  a sudden quench is performed to  $\omega=1$ . The time evolution is thus governed by the post-quench Hamiltonian  $H$  (see equation (1)) as follows:

$$|\Psi(t)\rangle = e^{-iHt}|E_0\rangle_{\omega_0} \approx \sum_{j=0}^n c_j e^{-iE_j t} |E_j\rangle, \quad (13)$$

where  $|E_j\rangle \equiv |E_j\rangle_\omega$  and  $c_j = \langle E_j|E_0\rangle_{\omega_0}$  is the overlap between the initial state and the  $j$ th eigenstate  $|E_j\rangle$  of the post-quench Hamiltonian  $H$ . Since both the pre- and post-quench Hamiltonian are time-reversal symmetric, we assume their eigenstates and thereby also the overlap coefficients  $c_j$  to be real-valued without loss of generality. A small quench ensures that  $|c_0| \approx 1$  and only the  $n$  lowest excited states are of relevance. Symmetry considerations further reduce the number of allowed contributions. E.g. states of odd  $R_{CM}$ -parity or odd  $R_{AB}$ -parity have zero overlap with  $|E_0\rangle_{\omega_0}$ , because the initial state is of even  $R_{CM}$ - and  $R_{AB}$ -parity and the quench does not affect any of the symmetries discussed in the previous section. Similarly, in the component-symmetric case  $g_A = g_B$ , states, which are antisymmetric w.r.t. the  $S_r$  operation, have no overlap with the pre-quench ground state being symmetric under  $S_r$ .

For the weakly coupled regime, the relative-frame coordinates turn out to be extremely helpful for characterizing the participating breathing modes. Therefore, we study in particular the reduced densities of the relative-frame coordinates. Employing the expansion in post-quench eigenstates from equation (13), their time-evolution may be approximated within the linear-response regime as

$$\rho_1(Y_i, t) \approx c_0^2 \rho_1^{(0)}(Y_i) + 2 \sum_{j=1}^n c_0 c_j \rho_1^{(0,j)}(Y_i) \cos(\Delta_j t), \quad (14)$$

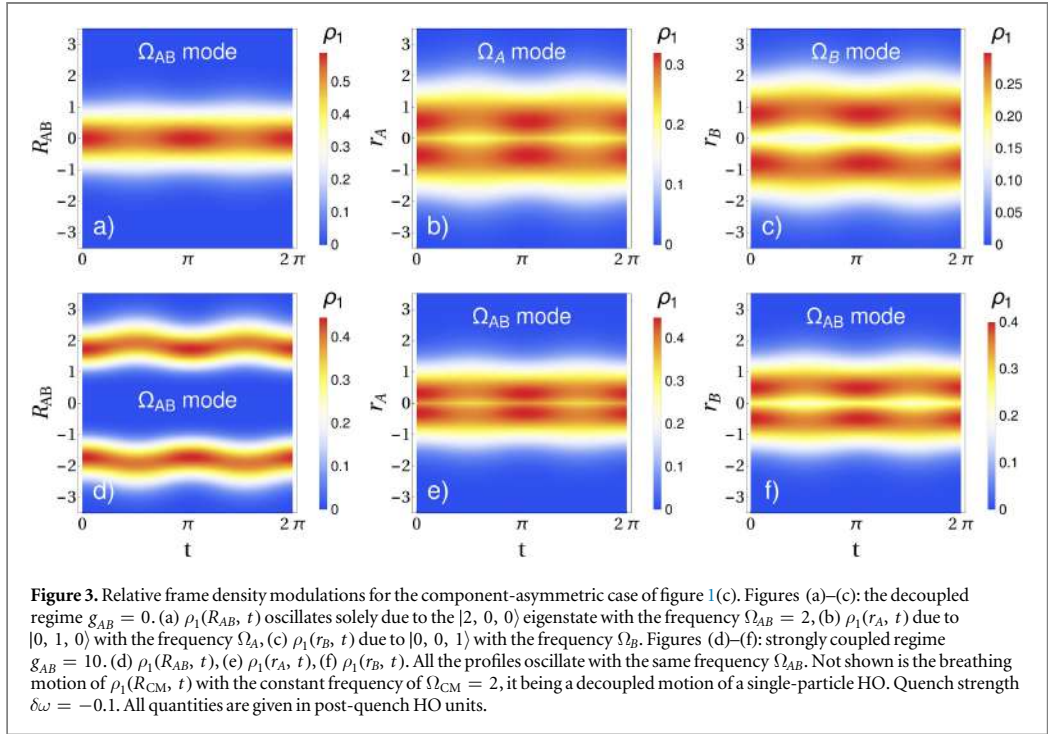
neglecting terms of the order  $c_i c_j$  for  $i, j > 0$ . So  $\rho_1(Y_i, t)$  can be decomposed into the stationary background  $\rho_1^{(0)}(Y_i)$  and time-dependent modulations of the form  $\rho_1^{(0,j)}(Y_i) = \int \prod_{p \neq i} dY_p \langle \vec{Y}|E_0\rangle \langle E_j|\vec{Y}\rangle$ , further called transition densities, with oscillation frequency  $\Delta_j = E_j - E_0$ . Below we discuss how to calculate the overlaps  $c_j$  (see equations (18), (19)) to a good approximation only in terms of the post-quench Hamiltonian eigenstates for sufficiently weak quenches. Thus, we can fully simulate the time-evolution of  $\rho_1(Y_i, t)$  by using only the post-quench Hamiltonian properties obtained in section 4.

In the following, we regard the excitations of the first even  $R_{AB}$ -parity branch as the lowest monopole modes and show that each monopole mode is directly connected to the breathing modulation of a single relative-frame density, if the two components are but weakly coupled. This behaviour changes for increasing  $g_{AB}$ , where each coordinate begins to exhibit an oscillation with more than one frequency. By inspecting the modulations of the variances of each relative-coordinate and taking the excitation amplitudes into account, we show that four (three) breathing modes are excited for  $g_A \neq g_B$  ( $g_A = g_B$ ) in the weakly coupled regime, while only two breathing modes are of relevance in the strongly coupled regime. First, we inspect the component-asymmetric case of figure 1(c) in detail to illustrate some peculiarities of the involved breathing modes, since it contains the most relevant features. Thereafter, we unravel differences to the component-symmetric case of figure 1(b).

### 5.1. Component-asymmetric case

Because of the low amplitude quenching protocol, we will excite four breathing modes simultaneously in the component-asymmetric case ( $g_A = 1, g_B = 2$ ). Three of them stem from the first even  $R_{AB}$ -parity branch of figure 1(c). Remember, however, that the total CM was assumed to be in the ground state to keep the spectrum discernible. One obtains the full energy spectrum by including all CM excitations, meaning duplicating and up-shifting depicted energy curves by  $\Delta E = n$  with  $n \in \mathbb{N}$ . This reveals a fourth mode, namely a double total CM excitation. It features the same parity symmetries and is energetically of the same order as the states from the first even  $R_{AB}$ -parity branch ensuring a considerable overlap with the initial state. The total CM trivially oscillates

<sup>7</sup> In this work, we call coordinates normal if they completely decouple the Hamiltonian, implying the possibility to excite each degree of freedom independently.



with the constant frequency  $\Omega_{CM} = 2$  independent of any interactions  $g_\alpha$  it being a decoupled degree of freedom with the single-particle HO Hamiltonian (equation (5)) [25, 43]. The other three modes, which are excited, are known analytically, when there is no coupling between the components, and we label the corresponding mode frequencies as (see also the labels in figure 1(c)):

- (i)  $|0\rangle|0, 1, 0\rangle \leftrightarrow \Omega_A(g_{AB} = 0) = \mu(g_A, 1) - \mu(g_A, 0)$ ,
- (ii)  $|0\rangle|0, 0, 1\rangle \leftrightarrow \Omega_B(g_{AB} = 0) = \mu(g_B, 1) - \mu(g_B, 0)$ ,
- (iii)  $|0\rangle|2, 0, 0\rangle \leftrightarrow \Omega_{AB}(g_{AB} = 0) = 2$ ,
- (iv)  $|2\rangle|0, 0, 0\rangle \leftrightarrow \Omega_{CM} = 2$ ,

where we have prepended the CM eigenstate  $|n\rangle$  for a complete characterization of the involved states. States of higher order even  $R_{AB}$ -parity branches as well as higher excitations of the CM coordinate are negligible due to small overlaps with the initial state.

In the uncoupled regime  $g_{AB} = 0$ , one can show analytically that each relative-coordinate density oscillates with a single frequency, each corresponding to exactly one eigenstate of the first even  $R_{AB}$ -parity branch (see figures 3(a)–(c)). E.g. for  $\rho_1(R_{AB}, t)$ , the only transition density  $\rho_1^{(0,i)}(R_{AB})$  which survives taking the partial trace is the one corresponding to  $|0\rangle|2, 0, 0\rangle$ , while the contributions from the remaining excited states vanish. This leads to the breathing motion in the  $R_{AB}$  coordinate with a single frequency  $\Omega_{AB}$ . Analogously one can show that  $|0\rangle|0, 1, 0\rangle$  solely induces density modulation in  $\rho_1(r_A)$  with the frequency  $\Omega_A$ , while  $\rho_1(r_B)$  oscillates with  $\Omega_B$  exclusively due to  $|0\rangle|0, 0, 1\rangle$ . Thereby, the relative-frame coordinates render ‘normal coordinates’ in the uncoupled regime, which is also a valid picture for extremely weak couplings.

By introducing a larger coupling between the components one observes that each relative frame density, except for  $\rho_1(R_{CM}, t)$ , begins to oscillate with up to three frequencies simultaneously. So all the modes begin to contribute to the density modulation of each relative coordinate. However, there are some peculiarities we observe, for the visualization of which the densities are not well suited any more. Instead, we will transform the breathing observable to the relative frame and consider the expectation values of individual terms it decomposes into:

$$\sum_{\sigma,i} x_{\sigma,i}^2 = 4R_{CM}^2 + R_{AB}^2 + \frac{1}{2}r_A^2 + \frac{1}{2}r_B^2. \quad (15)$$

The expectation value of each observable with respect to the time-evolved state  $|\Psi(t)\rangle$  is directly related to the respective relative-frame density:

$$\langle \Psi(t) | Y_i^2 | \Psi(t) \rangle = \int dY_i Y_i^2 \rho_1(Y_i, t). \quad (16)$$

Inserting the time-evolution of the relative frame density from equation (14) one finds that the observables decompose into a stationary value and a time-dependent modulation as well. In particular, we are interested in the amplitudes of modulations, when the inter-component coupling is varied, since they determine how many frequencies are of essential relevance for the considered motion. The amplitude of the  $j$ th mode is essentially composed of the overlap  $c_j$  and of the transition element:

$$\langle E_j | Y_i^2 | E_0 \rangle = \int dY_i Y_i^2 \rho_1^{(0,j)}(Y_i). \quad (17)$$

In order to evaluate the overlaps  $c_j = \langle E_j | E_0 \rangle_{\omega_0}$  with  $j \neq 0$  in terms of only the post-quench Hamiltonian eigenstates, we perform a Taylor approximation with respect to the weak quench strength  $\delta\omega = \omega - \omega_0$ , namely  $|E_0\rangle_{\omega_0} \approx |E_0\rangle_{\omega} - \delta\omega \frac{d}{d\omega} |E_0\rangle_{\omega}$  evaluated at  $\omega = 1$ , and arrive at

$$c_j \approx - \left\langle E_j \left| \frac{d}{d\omega} \right| E_0 \right\rangle \delta\omega. \quad (18)$$

Applying the (off-diagonal) Hellmann–Feynman theorem [69], one obtains:

$$\left\langle E_j \left| \frac{d}{d\omega} \right| E_0 \right\rangle = \frac{-\omega \langle E_j | \sum_{i,\sigma} x_{i,\sigma}^2 | E_0 \rangle}{E_j - E_0}. \quad (19)$$

The overlaps are hence connected to the transition elements of each relative-frame breathing observable (equation (15)), weighted with the inverse of the mode frequency, which leads to a damping of contributions from higher order branches. This relation enables us to calculate the amplitude  $A_j$ , with which the  $j$ th mode contributes to the oscillation of the observable  $Y_i^2$ :

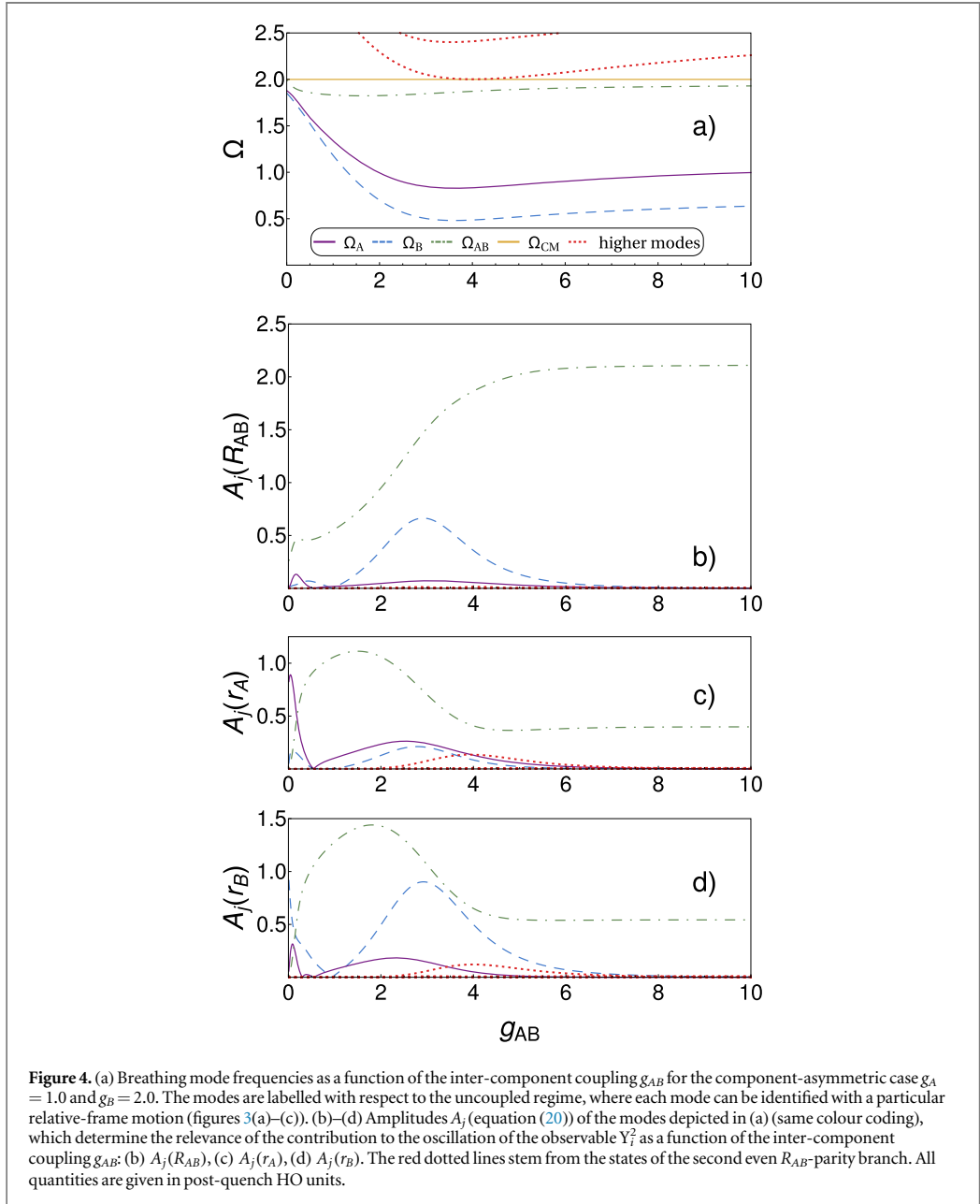
$$A_j(Y_i) = \left| \frac{c_j}{\delta\omega} \langle E_j | Y_i^2 | E_0 \rangle \right|, \quad (20)$$

which may be interpreted as the susceptibility of the  $Y_i^2$  observable for the excitation of the state  $|E_j\rangle$ .

In figure 4(a) we show the values of possible breathing mode frequencies, obtained from the spectrum of figure 1(c).  $\Omega_{\text{CM}} = 2$  does not depend on any interaction strength  $g_{\alpha}$ . In contrast to this,  $\Omega_{AB}$  is degenerate with  $\Omega_{\text{CM}}$  for  $g_{AB} = 0$ , and when increasing  $g_{AB}$ , decreases to a minimum first and then increases with the tendency to asymptotically reach  $\Omega_{\text{CM}}$  again. This behaviour strongly resembles the dependence of the relative-coordinate breathing-mode frequency in the single-component case [43].  $\Omega_A$  and  $\Omega_B$  have qualitatively akin curve shapes, varying much stronger with  $g_{AB}$ . In particular, we note that these frequencies reach values below the frequency of the CM dipole mode being equal to unity.

The breathing mode frequencies discussed above are labelled according to the peculiarity of the uncoupled regime, where each eigenstate from the first even  $R_{AB}$ -parity branch leads to a breathing motion of some specific relative-frame coordinate. Indeed, if we look at the amplitudes  $A_j$  in figures 4(b)–(d) in the decoupled regime ( $g_{AB} = 0$ ), we recognize that the amplitude for the coordinate  $Y_i$  is non-zero only for one mode, namely the one with which  $\rho_1(Y_i, t)$  oscillates in figures 3(a)–(c). When we increase the inter-component coupling, the eigenstates cease to be simple product states in the relative coordinate frame resulting in contamination of each density modulation with the frequencies from the other modes as well, which leads to a three-mode oscillation. Nevertheless, we label the frequencies corresponding to the uncoupled case and follow the states continuously throughout the  $g_{AB}$  variation.

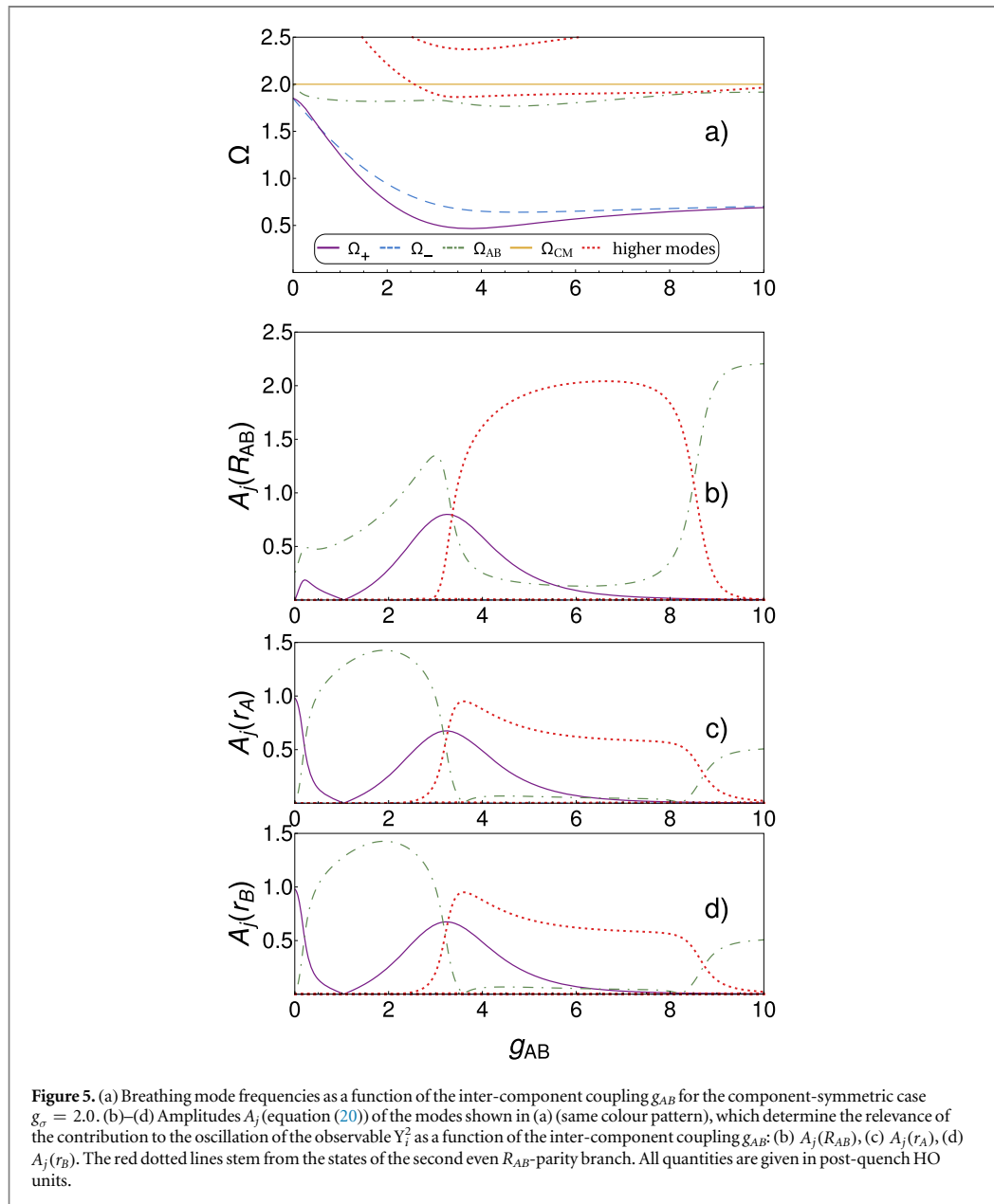
Another peculiarity worth noting arises in the strongly coupled regime: The  $\Omega_{\sigma}$  oscillations become strongly suppressed for all the observables making  $\Omega_{AB}$  and  $\Omega_{\text{CM}}$  the main contributors to the density modulations, which reminds us of the single-component behaviour [43]. Furthermore, the dependence of  $\Omega_{AB}$  on  $g_{AB}$  has striking resemblance to the dependence of  $\Omega_{\text{rel}}$  on  $g$  for the single component gas. In figures 3(d)–(f) we show that all the relative-coordinate densities oscillate with the same frequency  $\Omega_{AB}$ . We highlight that in the CF regime each density peak of the bimodal distribution  $\rho_1(R_{AB}, t)$  does not only breath periodically but also its maximum height position performs dipole-mode like oscillations, see figure 3(d). Our intuitive picture for this effect is as follows: in the CF phase the two species are located on opposite sides of the HO trap and feel a tighter effective trap induced by the other component, which is in accordance to the tighter localization of the  $r_{\sigma}$  coordinates, see figures 2(b) and (c). Upon inducing the quench dynamics by instantly lowering the trap frequency, the two species separate even further. When the turning point is reached, they move back towards the centre of the trap, fail, however, to penetrate each other due to a strong mutual repulsion, which results in dipole-like oscillation of each of the two  $\rho_1(R_{AB}, t)$  density fragments. These dipole oscillations quite likely act as



a driving force for the  $r_\sigma$  coordinates making them to oscillate with the same frequency thereby suppressing  $\Omega_\sigma$  modes.

### 5.2. Component-symmetric case

Now we compare the above results with the component-symmetric case of figure 1(b), where  $g_A = g_B = 2$ . Figure 5(a) depicts the possible breathing-mode frequencies. Here, two main differences arise: first, the  $\Omega_{AB}$  curve features two minima due to two avoided crossings with an eigenstate of the second even  $R_{AB}$ -parity branch. Second, the other two breathing mode frequencies of the relative coordinates are degenerate for  $g_{AB} = 0$ , then separate with increasing  $g_{AB}$  and approach one another asymptotically. Instead of using the labels  $\Omega_A$  and  $\Omega_B$  as in the component-asymmetric case, we label these two modes with  $\Omega_+$  and  $\Omega_-$ , since the corresponding excited eigenstates are symmetric and antisymmetric w.r.t.  $S_r$ , respectively (see figure 1(b)). The latter frequency, however, does not give any contribution to the breathing dynamics, it being symmetry excluded.



The motion of the  $r_A$  and  $r_B$  coordinates is identical due to the imposed component-symmetry and in the uncoupled regime ( $g_{AB} = 0$ ) they both oscillate solely with the  $\Omega_+$  frequency (see figures 5(c) and (d)). Similarly to the component-asymmetric case, we see that when increasing  $g_{AB}$  the  $\Omega_{AB}$  ( $\Omega_+$ ) mode contributes also to the observable  $r_{\sigma}^2$  ( $R_{AB}^2$ ).

However, in the intermediate interaction regime  $3.7 \lesssim g_{AB} \lesssim 8.3$  we observe a strong suppression of the  $\Omega_{AB}$  mode contribution for all observables, which is in stark contrast to the component-asymmetric case. Instead, a state of the second even  $R_{AB}$ -parity branch gains relevance. These two eigenstates actually participate in the avoided crossing exemplarily indicated by an arrow in the spectrum (see figure 1(b)) and thereby exchange their character. According to equation (20) the breathing amplitude is determined by the transition elements (16) as well as the overlap coefficients (18), which in turn depend also on the transition elements due to equations (19) and (15). While the energy denominator of equation (19) does not single out one of the two states participating in the avoided crossing, the values of the individual transition elements strongly depend on the character of the respective eigenstate. Thereby, the energetically slightly lower mode has a large amplitude before the crossing and after the crossing the composition character of states changes such that the higher mode dominates. By further increasing  $g_{AB}$  we observe another exchange of roles, which is attributed to the presence of

a second avoided crossing (see figure 5(a)) such that the strong inter-component coupling regime shows again the absolute dominance of the  $\Omega_{AB}$  mode over the other lowest breathing modes besides  $\Omega_{CM}$ .

## 6. Experimental realization

The few-body Bose–Bose mixture studied here should be observable with existing cold atom techniques. Quantum gas microscopes allow the detection of single particles in a well controlled many-body or few-body system [70, 71] and recent progress also allows for spin-resolved imaging in 1D systems using an expansion in the perpendicular direction [72, 73]. In these set-ups, the single-particle sensitivity relies on pinning the atoms in a deep lattice during imaging and experiments have so far focused on lattice systems. However, bulk systems might be imaged with high spatial resolution by freezing the atomic positions in a lattice before imaging. For fast freezing, this would allow a time-resolved measurement of the breathing dynamics. Moreover, spin order was recently observed in very small fermionic bulk systems via spin-selective spilling to one side of the system [74].

Deterministic preparation of very small samples was demonstrated for fermions via trap spilling [75] and for bosons by cutting out a subsystem of a Mott insulator [76]. The tight transverse confinement for a 1D system can be obtained from a 2D optical lattice, while the axial confinement would come from an additional optical potential, which can be separately controlled to initialize the breathing mode dynamics.

Choosing two hyperfine states of the same atomic species ensures the same mass of the two bosonic species. Possible choices include  ${}^7\text{Li}$ ,  ${}^{39}\text{K}$  or  ${}^{87}\text{Rb}$ . While the former have usable FRs to tune the interaction strengths, the latter allows selective tuning via CIR in a spin-dependent transversal confinement as can be realized for heavier elements. Note that the longitudinal confinement needs to be spin-independent in order to ensure the same longitudinal trap frequencies and trap centres assumed in the calculations. The inter-component interaction strength can be tuned via a transverse spatial separation as obtained e.g. from a magnetic field gradient [77]. In the case of  ${}^7\text{Li}$  and  ${}^{39}\text{K}$ , the inter-component background scattering lengths are negative [14] leading to negative  $g_{AB}$ , but although not reported, inter-component FRs might exist. Alternatively,  $g_{AB}$  might be tuned via a CIR, which selectively changes  $g_{AB}$  at magnetic fields, where the intra-component scattering lengths are very different.

In the following we give concrete numbers for a choice of  ${}^7\text{Li}$ . The density distribution has structures on the scale of the HO unit  $a_{\text{ho}}$  (figure 2). Choosing the trap parameters as in [75] as  $\omega/(2\pi) = 1.5$  kHz and  $\omega_{\perp}/(2\pi) = 15$  kHz, yields  $a_{\text{ho}} = 1$   $\mu\text{m}$ , i.e. larger than a typical optical resolution of 0.8  $\mu\text{m}$ . At the same time, temperatures much lower than  $\hbar\omega/k_B = 72$  nK are state of the art. The breathing dynamics will occur on a time scale of several 100  $\mu\text{s}$ , which is easily experimentally accessible. Choosing a smaller  $\omega$  would make the imaging easier, but would impose stricter requirements on the temperature.

For the observation of the breathing mode dynamics, one would record the positions of all four particles in each experimental image and obtain the widths  $\langle R_{CM}^2 \rangle_t$ ,  $\langle R_{AB}^2 \rangle_t$ ,  $\langle r_{\sigma}^2 \rangle_t$  by averaging the occurring relative coordinates over many single-shots after a fixed hold time  $t$ .

## 7. Discussion and outlook

In this work we have explored a few-body problem of a Bose–Bose mixture with two atoms in each component confined in a quasi-1D HO trapping potential by exact diagonalization. By applying a coordinate transformation to a suitable frame we have constructed a rapidly converging basis consisting of HO and PCF. The latter stem from the analytical solution of the relative part of the two-atom problem [57] and include the information about the intra-species correlations, which renders our basis superior to the common approach of using HO eigenstates as basis states.

We have then explored the behaviour of the low-lying energy spectrum as a function of the inter-species coupling for various fixed values of intra-species interaction strengths. Hereby we have covered the strongly coupled limiting cases of CF, FF and PS, studied also intermediate symmetric and asymmetric values of  $g_A$  and  $g_B$  and related the ground state relative-frame densities of some limiting cases to the known laboratory frame results [40]. We have discussed the evolution of degeneracies and explained appearing (avoided) crossings in terms of the symmetries of the Hamiltonian, which become directly manifest in the chosen relative-coordinate frame.

Finally, the obtained results were used to study the dynamics of the system under a slight component-symmetric quench of the trapping potential. We have derived expressions for the time evolution of the relative-frame densities within the linear response regime and observed that in the uncoupled regime ( $g_{AB} = 0$ ) the density of each relative frame coordinate performs breathing oscillations with a single frequency corresponding to a specific excited state of the first even  $R_{AB}$ -parity branch of the spectrum. The total CM coordinate performs breathing oscillations with the frequency  $\Omega_{CM} = 2$  (HO units). For *asymmetric* choices of  $g_{\sigma}$  values, three

additional monopole modes participate in the dynamics, each of them corresponding to the motion of a particular relative coordinate:  $\Omega_A$  for the relative coordinate of the  $A$  component,  $\Omega_B$  for the relative coordinate of the  $B$  component and  $\Omega_{AB}$  for the relative distance of the CMs of both components. In contrast to this, the *symmetric* case  $g_A = g_B$  leads to only two additional modes because of a symmetry-induced selection rule:  $\Omega_+$  for the relative coordinates of both components and  $\Omega_{AB}$  for the relative distance of the CMs of both components.

For not too strong inter-component coupling, each relative coordinate exhibits multi-mode oscillations and we have explored their relevance for the density modulations by analysing the behaviour of suitably chosen observables as one gradually increases the coupling between the components for symmetric and asymmetric choices of intra-component interactions strengths. Thereby, we have found that for strong couplings, where CF takes place, the  $\Omega_\sigma$  ( $\Omega_+$ ) modes become highly suppressed, leaving only two monopole modes in this regime:  $\Omega_{AB}$  and  $\Omega_{CM}$ . We have observed the same effect for the case of PS (results not shown). Interestingly, the dependence of  $\Omega_{AB}$  on  $g_{AB}$  strongly resembles the behaviour of the relative-coordinate breathing frequency in the single-component case [43]. All in all, we have obtained 2 to 4 monopole modes for the quench dynamics depending on the strength of the inter-component coupling and the symmetry of the intra-species interactions, which is in strong contrast to the single-component case [43] as well as to the MF results, where two low-lying breathing modes can be obtained, namely an in-phase (out-of-phase) mode for a component-symmetric (component-asymmetric) quench [23]. Finally, we have argued that the experimental preparation of the considered few-body mixture and measurement of the predicted effects are in reach by means of state-of-the-art techniques.

This work serves as a useful analysis tool for future few-body experiments. Measurements of the monopole modes can be mapped to the effective interactions within the system such that precise measurements of the scattering lengths or external magnetic fields can be performed. The numerical method used here can be applied to Bose–Fermi and Fermi–Fermi mixtures with two particles in each component simplifying the numerics, because the PCFs have to be replaced by odd HO eigenstates, if a bosonic component is switched to a fermionic one, which significantly accelerates the calculation of integrals. Further, it would be interesting to see how the frequencies and the amplitudes of the monopole modes vary for an increasing number of particles. Exploring the spectrum for negative values of interaction parameters is also a promising direction of future research.

## Acknowledgments

The authors acknowledge fruitful discussions with H-D Meyer, J Schurer, K Keiler and J Chen. Furthermore, the authors thank F Deuretzbacher for providing us helpful insights into the mapping of our system to a spin-chain model being applicable close to the Full Fermionization limit. CW and PS gratefully acknowledge funding by the Deutsche Forschungsgemeinschaft in the framework of the SFB 925 ‘Light induced dynamics and control of correlated quantum systems’. SK and PS gratefully acknowledge support for this work by the excellence cluster ‘The Hamburg Centre for Ultrafast Imaging-Structure, Dynamics and Control of Matter at the Atomic Scale’ of the Deutsche Forschungsgemeinschaft.

## Appendix

In the following, we discuss how to efficiently calculate matrix elements of the coupling operator  $H_1$  from equation (8) with respect to the basis (10). Because of the already mentioned even parity of  $\varphi_i^\sigma$  one can make simple substitutions of the form  $\tilde{r}_\sigma = -r_\sigma$  to show that each delta in the sum of  $H_1$  gives the same contribution, such that after performing an integral over  $R_{AB}$  one obtains:

$$\begin{aligned} \langle a, b, c | H_1 | k, l, m \rangle &= 4 \int dr_A \int dr_B \Phi_a^{AB} \left( \frac{r_A + r_B}{2} \right) \Phi_k^{AB} \left( \frac{r_A + r_B}{2} \right) \\ &\quad \times \varphi_b^A(r_A) \varphi_l^A(r_A) \varphi_c^B(r_B) \varphi_m^B(r_B). \end{aligned} \quad (\text{A1})$$

At this point it is important to notice that the integral vanishes for odd  $(a + k)$  because of the parity symmetries of  $\Phi^{AB}$  and  $\varphi^\sigma$ , which can be seen by transforming to relative and centre-of-mass coordinates  $r = r_A - r_B$ ,  $R = (r_A + r_B)/2$ . In the following, we assume that the quantum numbers for the  $R_{AB}$  coordinate are restricted to  $a, k \in \{1, \dots, n_{AB}\}$  and for the  $r_\sigma$  coordinates to  $b, c, l, m \in \{1, \dots, n_{rel}\}$ . Now our computation strategy consists of three steps:

First, we circumvent evaluating the 2D integral from equation (A1) by viewing the product of the two HO eigenstates  $\Phi_a^{AB} \Phi_k^{AB}$  as a pure, in general not normalized state  $\chi_{a,k}$  depending on the two coordinates  $r_A$  and  $r_B$  and applying the Schmidt decomposition [58] or, equivalently, the so-called POTFIT algorithm [59].

$$\begin{aligned}\chi_{a,k}(r_A, r_B) &\equiv \Phi_a^{AB}\left(\frac{r_A + r_B}{2}\right)\Phi_k^{AB}\left(\frac{r_A + r_B}{2}\right) \\ &\approx \sum_{i=0}^d \lambda_i^{(a,k)} w_i^{A;(a,k)}(r_A) w_i^{B;(a,k)}(r_B).\end{aligned}\quad (\text{A2})$$

Here<sup>8</sup>,  $|\lambda_i^{(a,k)}|^2$  coincides with the  $i$ th eigenvalue of the reduced one-body density matrix corresponding to the degree-of-freedom  $r_\sigma$  and  $w_i^{\sigma;(a,k)}(r_\sigma)$  denotes the corresponding eigenvector, which can be shown to feature a definite parity symmetry. We remark that (i) we may choose  $w_i^{A;(a,k)}(r) = w_i^{B;(a,k)}(r) \equiv w_i^{(a,k)}(r)$  because of  $\chi_{a,k}(r_A, r_B) = \chi_{a,k}(r_B, r_A)$  without loss of generality and that (ii) the decomposition of equation (A2) becomes exact for  $d \rightarrow \infty$ . Having ordered the coefficients  $\lambda_i^{(a,k)}$  in decreasing sequence w.r.t. to their modulus, we choose  $d$  such that only terms with  $|\lambda_i^{(a,k)} / \lambda_0^{(a,k)}| > 10^{-6}$  are taken into account, which results in an accurate approximation to 2D integrals with a relative accuracy of  $10^{-5}$ , valid for all interactions and quantum numbers considered below. We perform this decomposition for all the relevant HO quantum numbers  $(a, k)$ , meaning  $a \leq k \leq n_{AB}$  with  $(a + k)$  even. This procedure is independent of any interactions  $g_\alpha$  and needs to be executed only once.

By inserting equation (A2) into (A1) we obtain the following expression:

$$\begin{aligned}\langle a, b, c | H | k, l, m \rangle &\approx 4 \sum_{i=0}^d \lambda_i^{(a,k)} \int dr_A w_i^{(a,k)}(r_A) \varphi_b^A(r_A) \varphi_l^A(r_A) \\ &\quad \times \int dr_B w_i^{(a,k)}(r_B) \varphi_c^B(r_B) \varphi_m^B(r_B).\end{aligned}\quad (\text{A3})$$

As one can see, the 2D integral is replaced by a sum of products of 1D integrals. In order to greatly overcome the numerical effort for computing a 2D integral  $d$  should be preferably a small number (see below).

The second step consists in the calculation of 1D integrals and here we provide an efficient strategy to circumvent redundant computations. Consider the integral:

$$\int dr w_i^{(a,k)}(r) \varphi_s^\sigma(r) \varphi_t^\sigma(r), \quad (\text{A4})$$

with  $s \leq t \leq n_{\text{rel}}$ . The PCFs are of even parity and thus only even  $w_i^{(a,k)}$  actually contribute allowing to reduce the number of expansion terms in equation (A3) to  $\lfloor d/2 \rfloor$ . Both PCFs  $\varphi_s^\sigma$  and  $\varphi_t^\sigma$  depend on the same interaction strength  $g_\sigma$  meaning that the above integral does not distinguish between the two subsystems such that the index  $\sigma$  can be dropped for the moment. Now we fix the PCFs by specifying the strength of intra-component interaction  $g$  and further we fix the HO quantum numbers  $(a, k)$ , which determine the functions  $w_i^{(a,k)}$ , as well as PCF quantum numbers  $(s, t)$ . We loop over all  $i$  and save the integral values, labelled as  $(g, a, k, s, t)$ . This procedure is performed for a set  $I$  of multiple values of  $g$  we are interested in and for all the relevant quantum number configurations  $a \leq k \leq n_{AB}$  with  $(a + k)$  even and  $s \leq t \leq n_{\text{rel}}$ .

In the last step we calculate the matrix elements from equation (A3). For HO quantum numbers  $(a, k)$  we extract all the expansion coefficients  $\lambda_i^{(a,k)}$ , obtained in the first step, and for the chosen interactions parameters  $(g_A, g_B)$  and PCF quantum numbers  $(b, c, l, m)$  we pick the appropriate integral values corresponding to  $(g = g_A, a, k, s = b, t = l)$  and  $(g = g_B, a, k, s = c, t = m)$ . The advantage of this procedure is that not only symmetric choices of intra-component interaction strengths are accessible, but also an arbitrary asymmetric combination  $(g_A, g_B) \in I \times I$ . Additionally, the proposed scheme can be easily parallelized. However, adding new  $g$  values to the set  $I$  is in general very time-consuming as one needs to calculate a bunch of 1D integrals for all the relevant quantum number configurations.

Now let us analyse quantitatively the speed-up obtained by our algorithm in contrast to the straightforward evaluation of 2D integrals. Since the energy spacing of the PCF modes is approximately twice the energy spacing of the HO modes corresponding to the  $R_{AB}$  motion, we assume  $n_{\text{rel}} = (n_{AB} - 1)/2$  with an odd  $n_{AB}$  to keep the number of even and odd  $R_{AB}$ -parity basis states the same. The number of 1D integrals one needs to compute for each  $g \in I$  in order to construct the  $H_1$  matrix is approximately  $(\bar{d}/64)[(n_{AB} + 1)(n_{AB} + 3)]^2$ , where  $\bar{d}$  is an average number of terms in (A3), as the criterion  $|\lambda_i^{(a,k)} / \lambda_0^{(a,k)}| > 10^{-6}$  requires more terms for larger values of  $a, k$ . The number of 2D integrals amounts to  $(1/256)[(n_{AB} + 1)(n_{AB} + 3)]^3$ . For checking the convergence (see below), we have chosen  $n_{AB} = 21$  and  $n_{\text{rel}} = 10$ , i.e. 2662 basis states. The number of expansion terms varies in the interval  $d \in \{50, \dots, 100\}$  resulting in  $\bar{d} = 75$ . Thus, we need to either evaluate 326 700 1D integrals or 574 992 2D integrals. Not only is the number of 1D integrals smaller, the computation of one 2D integral takes also significantly longer than of one 1D integral, especially for higher quantum numbers. Moreover, in order to build the Hamiltonian matrix for all  $(g_A, g_B) \in I \times I$ , the 2D integrals (A1) would have to be evaluated for the  $n_g(n_g + 1)/2$  distinct combinations  $g_A \leq g_B$ , where  $n_g$  denotes the cardinality of  $I$ , while the 1D integrals (A4) must be calculated only for all  $g \in I$ , i.e.  $n_g$  distinct values, which renders this approach much more efficient.

<sup>8</sup> Note that in contrast to the usual convention we do not require the coefficients  $\lambda_i^{(a,k)}$  to be semi-positive without loss of generality.



For the spectra shown in section 4 we have chosen  $n_{AB} = 17$  and  $n_{\text{rel}} = 8$ , i.e. 1458 basis states. Since we know that basis states of different  $R_{AB}$ -symmetry do not couple, we can split the  $H$  matrix into subspaces of even and odd  $R_{AB}$ -parity, leading to  $(729 \times 729)$ -size matrices for each subspace such that the computational effort for the diagonalization becomes negligible. Since the inter-component coupling  $g_{AB}$  enters the matrix  $H = H_0 + g_{AB}H_1$  to be diagonalized only as a pre-factor, a very fine  $g_{AB}$  scan can be easily performed. We note that for the covered  $g_{AB} \in [0, 10]$  space the convergence check provides us with the relative energy change below 1% for the low-lying energy spectrum.

## References

- [1] Anderson M H, Ensher J R, Matthews M R, Wieman C E and Cornell E A 1995 *Science* **269** 198
- [2] Davis K B, Mewes M-O, Andrews M R, Van Druten N, Durfee D, Kurn D and Ketterle W 1995 *Phys. Rev. Lett.* **75** 3969
- [3] Jin D, Ensher J, Matthews M, Wieman C and Cornell E A 1996 *Phys. Rev. Lett.* **77** 420
- [4] Mewes M-O, Andrews M, Van Druten N, Kurn D, Durfee D, Townsend C and Ketterle W 1996 *Phys. Rev. Lett.* **77** 988
- [5] Stringari S 1996 *Phys. Rev. Lett.* **77** 2360
- [6] Myatt C, Burt E, Christ R, Cornell E A and Wieman C 1997 *Phys. Rev. Lett.* **78** 586
- [7] Hall D, Matthews M, Ensher J, Wieman C and Cornell E A 1998 *Phys. Rev. Lett.* **81** 1539
- [8] Olshanii M 1998 *Phys. Rev. Lett.* **81** 938
- [9] Görlitz A et al 2001 *Phys. Rev. Lett.* **87** 130402
- [10] Moritz H, Stöferle T, Köhl M and Esslinger T 2003 *Phys. Rev. Lett.* **91** 250402
- [11] Ho T-L and Shenoy V 1996 *Phys. Rev. Lett.* **77** 3276
- [12] Esry B, Greene C H, Burke J P Jr and Bohn J L 1997 *Phys. Rev. Lett.* **78** 3594
- [13] Pu H and Bigelow N 1998 *Phys. Rev. Lett.* **80** 1130
- [14] Chin C, Grimm R, Julienne P and Tiesinga E 2010 *Rev. Mod. Phys.* **82** 1225
- [15] Papp S, Pino J and Wieman C 2008 *Phys. Rev. Lett.* **101** 040402
- [16] Tojo S, Taguchi Y, Masuyama Y, Hayashi T, Saito H and Hirano T 2010 *Phys. Rev. A* **82** 033609
- [17] McCarron D, Cho H, Jenkin D, Köpinger M and Cornish S 2011 *Phys. Rev. A* **84** 011603
- [18] Pattinson R, Billam T, Gardiner S, McCarron D, Cho H, Cornish S, Parker N and Proukakis N 2013 *Phys. Rev. A* **87** 013625
- [19] Lee K L, Jørgensen N B, Liu I-K, Wacker L, Arlt J J and Proukakis N P 2016 *Phys. Rev. A* **94** 013602
- [20] Egorov M, Opanchuk B, Drummond P, Hall B, Hannaford P and Sidorov A 2013 *Phys. Rev. A* **87** 053614
- [21] Pu H and Bigelow N 1998 *Phys. Rev. Lett.* **80** 1134
- [22] Gordon D and Savage C 1998 *Phys. Rev. A* **58** 1440
- [23] Morise H and Wadati M 2000 *J. Phys. Soc. Japan* **69** 2463
- [24] Bauch S, Balzer K, Henning C and Bonitz M 2009 *Phys. Rev. B* **80** 054515
- [25] Bauch S, Hochstuhl D, Balzer K and Bonitz M 2010 *J. Phys.: Conf. Ser.* **220** 012013
- [26] Abraham J W, Balzer K, Hochstuhl D and Bonitz M 2012 *Phys. Rev. B* **86** 125112
- [27] Abraham J and Bonitz M 2014 *Contrib. Plasma Phys.* **54** 27
- [28] Menotti C and Stringari S 2002 *Phys. Rev. A* **66** 043610
- [29] Haller E, Gustavsson M, Mark M J, Danzl J G, Hart R, Pupillo G and Nägerl H-C 2009 *Science* **325** 1224
- [30] Fang B, Carleo G, Johnson A and Bouchoule I 2014 *Phys. Rev. Lett.* **113** 035301
- [31] McDonald C, Orlando G, Abraham J, Hochstuhl D, Bonitz M and Brabec T 2013 *Phys. Rev. Lett.* **111** 256801
- [32] Altmeyer A, Riedl S, Kohstall C, Wright M, Geursen R, Bartenstein M, Chin C, Denschlag J H and Grimm R 2007 *Phys. Rev. Lett.* **98** 040401
- [33] Kinoshita T, Wenger T and Weiss D S 2004 *Science* **305** 1125
- [34] Paredes B, Widera A, Murg V, Mandel O, Fölling S, Cirac I, Shlyapnikov G V, Hänsch T W and Bloch I 2004 *Nature* **429** 277
- [35] Girardeau M 1960 *J. Math. Phys.* **1** 516
- [36] Girardeau M D and Minguzzi A 2007 *Phys. Rev. Lett.* **99** 230402
- [37] Zöllner S, Meyer H-D and Schmelcher P 2008 *Phys. Rev. A* **78** 013629
- [38] Hao Y and Chen S 2009 *Eur. Phys. J. D* **51** 261
- [39] Dehkharghani A, Volosniev A, Lindgren J, Rotureau J, Forssén C, Fedorov D, Jensen A and Zinner N 2015 *Sci. Rep.* **5** 10675
- [40] García-March M A, Juliá-Díaz B, Astrakharchik G, Busch T, Boronat J and Polls A 2014 *New J. Phys.* **16** 103004
- [41] García-March M A, Juliá-Díaz B, Astrakharchik G, Boronat J and Polls A 2014 *Phys. Rev. A* **90** 063605
- [42] Zöllner S, Meyer H-D and Schmelcher P 2007 *Phys. Rev. A* **75** 043608
- [43] Schmitz R, Krönke S, Cao L and Schmelcher P 2013 *Phys. Rev. A* **88** 043601
- [44] Tschischik W, Moessner R and Haque M 2013 *Phys. Rev. A* **88** 063636
- [45] Chen X-L, Li Y and Hu H 2015 *Phys. Rev. A* **91** 063631
- [46] Choi S, Dunjko V, Zhang Z and Olshanii M 2015 *Phys. Rev. Lett.* **115** 115302
- [47] Gudyma A I, Astrakharchik G and Zvonarev M B 2015 *Phys. Rev. A* **92** 021601
- [48] Atas Y, Bouchoule I, Gangardt D and Kheruntsyan K 2017 *Phys. Rev. A* **95** 043622
- [49] Koutentakis G M, Mistakidis S I and Schmelcher P 2017 *Phys. Rev. A* **95** 013617
- [50] Szabo A and Ostlund N S 2012 *Modern Quantum Chemistry: Introduction to Advanced Electronic Structure Theory* (Mineola, NY: Dover Publications)
- [51] Echave J and Clary D C 1992 *Chem. Phys. Lett.* **190** 225
- [52] Light J C and Carrington T Jr 2007 *Adv. Chem. Phys.* **114** 263
- [53] Beck M H, Jäckle A, Worth G and Meyer H-D 2000 *Phys. Rep.* **324** 1
- [54] Christensson J, Forssén C, Åberg S and Reimann S M 2009 *Phys. Rev. A* **79** 012707
- [55] Rotureau J 2013 *Eur. Phys. J. D* **67** 153
- [56] Lindgren E, Rotureau J, Forssén C, Volosniev A and Zinner N T 2014 *New J. Phys.* **16** 063003
- [57] Busch T, Englert B-G, Rzażewski K and Wilkens M 1998 *Found. Phys.* **28** 549
- [58] Nielsen M A and Chuang I L 2010 *Quantum Computation and Quantum Information* (Cambridge: Cambridge University Press) p 109
- [59] Jäckle A and Meyer H-D 1996 *J. Chem. Phys.* **104** 7974

- [60] von Neumann J and Wigner E P 1929 *Z. Phys.* **30** 467
- [61] Yukalov V and Girardeau M 2005 *Laser Phys. Lett.* **2** 375
- [62] Deuretzbacher F, Fredenhagen K, Becker D, Bongs K, Sengstock K and Pfannkuche D 2008 *Phys. Rev. Lett.* **100** 160405
- [63] Fang B, Vignolo P, Gattobigio M, Miniatura C and Minguzzi A 2011 *Phys. Rev. A* **84** 023626
- [64] Deuretzbacher F, Becker D, Bjerlin J, Reimann S and Santos L 2014 *Phys. Rev. A* **90** 013611
- [65] Volosniev A G, Petrosyan D, Valiente M, Fedorov D, Jensen A and Zinner N T 2015 *Phys. Rev. A* **91** 023620
- [66] Yang L and Cui X 2016 *Phys. Rev. A* **93** 013617
- [67] Deuretzbacher F, Becker D, Bjerlin J, Reimann S and Santos L 2017 *Phys. Rev. A* **95** 043630
- [68] Deuretzbacher F and Santos L 2017 *Phys. Rev. A* **96** 013629
- [69] Klein D and DeVries P L 1978 *J. Chem. Phys.* **68** 160
- [70] Bakr W S, Peng A, Tai M E, Ma R, Simon J, Gillen J J, Foelling S, Pollet L and Greiner M 2010 *Science* **329** 547
- [71] Sherson J F, Weitenberg C, Endres M, Cheneau M, Bloch I and Kuhr S 2010 *Nature* **467** 68
- [72] Preiss P M, Ma R, Tai M E, Simon J and Greiner M 2015 *Phys. Rev. A* **91** 041602
- [73] Boll M, Hilker T A, Salomon G, Omran A, Nespolo J, Pollet L, Bloch I and Gross C 2016 *Science* **353** 1257
- [74] Murmann S, Deuretzbacher F, Zürn G, Bjerlin J, Reimann S M, Santos L, Lompe T and Jochim S 2015 *Phys. Rev. Lett.* **115** 215301
- [75] Serwane F, Zürn G, Lompe T, Ottenstein T, Wenz A and Jochim S 2011 *Science* **332** 336
- [76] Islam R, Ma R, Preiss P M, Tai M E, Lukin A, Rispoli M and Greiner M 2015 *Nature* **528** 77
- [77] Schachenmayer J, Weld D M, Miyake H, Siviloglou G A, Ketterle W and Daley A J 2015 *Phys. Rev. A* **92** 041602

**Breathing dynamics of the few-body Bose polaron in a species-selective harmonic trap**Maxim Pyzh<sup>1,\*</sup> and Peter Schmelcher<sup>1,2,†</sup><sup>1</sup>*Zentrum für Optische Quantentechnologien, Universität Hamburg, Luruper Chaussee 149, 22761 Hamburg, Germany*<sup>2</sup>*The Hamburg Centre for Ultrafast Imaging, Universität Hamburg, Luruper Chaussee 149, 22761 Hamburg, Germany*

(Received 20 July 2021; accepted 22 March 2022; published 8 April 2022)

We perform an extensive numerical study on the breathing dynamics of a few-body Bose polaron setup in a one-dimensional species-selective harmonic trap. The dynamics is triggered by a quench of the impurity trap. The excitation of the background majority atoms is mediated via the majority-impurity interaction. The breathing spectrum is obtained for different numbers of majority particles, several values of the majority-component interaction strengths, and trap ratios. It is further compared to the breathing spectrum of a particle-balanced few-body Bose-Bose mixture. In particular, for equal postquench traps the employed protocol allows to couple states of different center-of-mass parity in contrast to species-symmetric trap quenches. Among the participating eigenstates we identify one having odd center-of-mass parity and even global parity. The breathing frequency induced by this state is a monotonically decreasing function of the coupling parameter. Importantly, in order to be numerically observable, it requires the entanglement between the species to be taken into account. We demonstrate this by comparing the numerically exact results obtained by means of the multilayer multiconfiguration time-dependent Hartree method for mixtures to the ones of a species mean-field ansatz. The entanglement-sensitive breathing frequency persists also for unequal postquench traps where the center of mass cannot be decoupled. Finally, we analyze the impact of global parity symmetry on the breathing dynamics by initializing a state of odd global parity. We evidence a striking resemblance to the breathing spectrum of the ground state, but find also some additional modes.

DOI: [10.1103/PhysRevA.105.043304](https://doi.org/10.1103/PhysRevA.105.043304)**I. INTRODUCTION**

The polaron concept was introduced quite some time ago by Landau and Pekar [1,2] to describe the motion of an electron in a crystalline material. The notion of an emerging quasiparticle dressed by low-energy excitations of the underlying medium has vastly expanded since its foundation finding broad applications in different areas of physics such as organic semiconductors, polymers, nanowires, quantum dots, and high-temperature superconductors [3–5]. Since the advent of ultracold gases [6,7], a promising experimental platform has emerged allowing to investigate fundamental many-body quantum processes [8] with an exquisite tunability of the underlying interactions and trapping geometries. In particular, the ability to combine different species [9] and the precise control over the number of particles [10] made it possible to experimentally prepare an impurity in a many-body environment of bosons [11–16] or fermions [17–21], leading to what is nowadays termed Bose [22] and Fermi polaron [23,24], respectively. A mapping to the Fröhlich Hamiltonian [25] for the polaron problem can be established while all the Hamiltonian parameters can be addressed individually. The tunability of interactions via Feshbach resonances [26,27] provides access to highly correlated and entangled regimes challenging the theorists to go beyond the weak coupling Fröhlich paradigm [28–34].

The correlations are in particular enhanced in quasi-one-dimensional (1D) systems [35]. A comparatively tight transverse confinement freezes the perpendicular motion of particles and additionally affects the effective 1D interactions known as confinement-induced resonances [36–38]. A prominent example of a strongly correlated 1D system is the Tonks-Girardeau gas [39–41]. In contrast to higher dimensions, where a lower particle density implies weaker correlations, in 1D lower densities lead to stronger interactions. It makes the study of low-density few-body systems of particular interest triggering significant research efforts [42]. At the same time, this represents a great challenge requiring sophisticated numerical techniques able to account for all the relevant correlations [43] when characterizing the static properties or the many-body dynamics, such as the density matrix renormalization group (DMRG) [44] or the multilayer multiconfiguration time-dependent Hartree method for bosons and fermions (ML-MCTDHX) [45]. In species-selective trapping geometries [12,46,47] the inhomogeneity of the medium and the localization length of the impurity impact significantly the degree of correlations [48–50] opening interesting perspectives but requiring also new approaches since the translation symmetry is broken making the well-established technique, the Lee-Low-Pines transformation [51], inapplicable.

In this work, we investigate the low-energy excitations of a few-body Bose polaron trapped harmonically in one spatial dimension. Elementary excitations [52,53] are of fundamental importance to understand the dynamical response of a physical system subject to a weak perturbation in terms of excited eigenstates and respective eigenenergies. Here, we focus on

\*mpyzh@physnet.uni-hamburg.de

†pschmelc@physnet.uni-hamburg.de

the so-called quantum breathing modes. They are characterized by an oscillatory compression and expansion of the one-body density reminiscent of a respiratory movement. On account of their strong sensitivity to the system's parameters such as interactions, trap geometry, and spin statistics, they have been established as a reliable diagnostic tool to access the ground-state properties of a system [54], for precision measurements of the scattering lengths [55] and even as a sensitive test of the equation of state at unitarity [56].

A number of experiments have observed the breathing motion of harmonically or lattice trapped Bose-Einstein condensates (BEC) [55,57–62] and mixtures of bosons and/or fermions [12,17,63–65]. The single-component breathing is theoretically well understood in the many-body case for contact [66–69], power-law [70–72], and dipolar [73] interactions. In a 1D harmonic trap of frequency  $\omega$  at zero temperature, one has identified two breathing modes: (i) center-of-mass breathing of constant frequency  $\Omega_{c.m.} = 2\omega$  and (ii) interaction-sensitive relative motion mode starting at  $\Omega_{rel} = 2\omega$  for an ideal gas (BEC regime), dropping to  $\Omega_{rel} = \sqrt{3}\omega$  at weak repulsive interactions (mean-field Thomas-Fermi regime) and finally saturating back to  $\Omega_{rel} = 2\omega$  in the limit of strong interactions (Tonks-Girardeau regime). The frequency values at intermediate interactions are well approximated via a sum-rule approach [66,67,74–76] and the overall frequency curve features a single minimum between the BEC and TG limits. The curvature in-between those limits and the exact minimum location are quite sensitive to the number of particles and beyond-mean-field effects are often indispensable for a correct quantitative description [77–82].

The breathing dynamics turns out to be even richer for a multicomponent mixture of bosons [83–89], fermions [17,76], and combination of the two [90–93]. Theoretically, up to four breathing frequencies can be extracted from the density width oscillations of both components depending on the interplay between interactions and particle-number imbalance: breathing of the center of mass, the relative motion for each component, and the relative intercomponent motion owing to the particles' distinguishability. The frequencies of the three relative modes behave in a similar fashion as the frequency of the relative mode encountered in the single-component case. To the best of our knowledge, both components have been considered to be equally trapped, allowing for a separation of the center-of-mass motion. In our work, we make use of species-selective trapping potentials to find out (i) how initially different traps would affect the breathing behavior in combination with (ii) how compressing the trap of only one component, the impurity, would impact the breathing motion of the second component, the majority, depending on the intercomponent coupling. For different system parameters, we classify the breathing modes according to their relative amplitude in the Fourier power spectrum obtained by applying a compressed sensing (CS) [94] algorithm to breathing observables evaluated via ML-MCTDHX. Furthermore, we study the role of intercomponent entanglement and parity symmetries on the breathing response. We identify an entanglement-sensitive mode whose frequency is a monotonically decreasing function of the majority-impurity interaction.

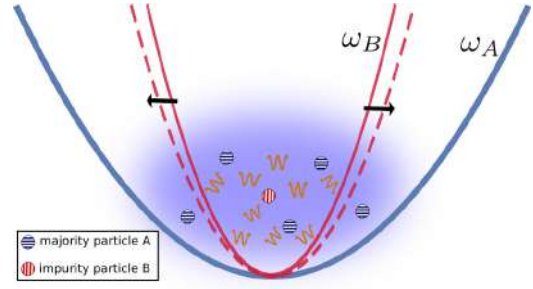


FIG. 1. The impurity (species  $B$  indicated by a red circle with a vertically dashed filling) in a harmonic trap of frequency  $\omega_B$  (red thin solid line) is immersed in a cloud of majority atoms (species  $A$  indicated by a blue blurred ellipse) subject to a different parabolic confinement of frequency  $\omega_A$  (blue broad solid line). The breathing dynamics is initiated by quenching the trap of the impurity (red dashed line) inducing thereby excitations (orange waves) in the composite system via the majority-impurity interaction.

This work is structured as follows. In Sec. II we introduce our setup and Hamiltonian. The numerical approach is discussed in Sec. III A. We use ML-MCTDHX for state initialization, subsequent dynamics, and evaluation of breathing observables. The oscillation frequencies are extracted by means of a CS algorithm outlined in Sec. III B. The results presented in Sec. IV are categorized in four subtopics: an overview of breathing modes in a particle-balanced few-body Bose-Bose mixture [88] (Sec. IV A) for later reference, the breathing spectra in the current Bose polaron setup for different majority-component interactions and particle-number ratio (Sec. IV B), the impact of impurity localization length (Sec. IV C), and, finally, the role of global parity symmetry for the breathing response (Sec. IV D). In Sec. V we provide a summary and draw conclusions in Sec. VI.

## II. SETUP AND HAMILTONIAN

We consider a few-body mixture of two bosonic components (see Fig. 1). A component  $\sigma \in \{A, B\}$  contains  $N_\sigma$  particles of mass  $m_\sigma$ , which experience a quasi-one-dimensional parabolic confinement with trap frequency  $\omega_\sigma$  and interact internally via contact pseudointeraction of strength  $g_\sigma$ . The components are coupled via an interspecies contact interaction of strength  $g_{AB}$ . We assume equal masses and introduce harmonic units of component  $A$  as our natural units, i.e.,  $l_A = \sqrt{\hbar/m\omega_A}$  for length,  $\hbar\omega_A$  for energy and  $1/\omega_A$  for time. The corresponding Hamiltonian reads as follows:

$$\begin{aligned}
 H &= H_A + H_B + H_{AB} \\
 &= \sum_{i=1}^{N_A} \left( -\frac{1}{2} \frac{\partial^2}{\partial x_i^2} + \frac{1}{2} x_i^2 \right) + g_A \sum_{i<j}^{N_A} \delta(x_i - x_j) \\
 &\quad + \sum_{i=1}^{N_B} \left( -\frac{1}{2} \frac{\partial^2}{\partial y_i^2} + \frac{1}{2} \eta^2 y_i^2 \right) + g_B \sum_{i<j}^{N_B} \delta(y_i - y_j) \\
 &\quad + g_{AB} \sum_{i=1}^{N_A} \sum_{j=1}^{N_B} \delta(x_i - y_j), \tag{1}
 \end{aligned}$$

where  $x_i$  ( $y_i$ ) denotes the position of the  $i$ th particle in the  $A$  ( $B$ ) component.

The  $A$  component is referred to as the majority species. It has  $N_A \in \{5, 10\}$  particles. The  $B$  component consists of a single particle,  $N_B = 1$ , and we call it the impurity. The majority component is either noninteracting ( $g_A = 0$ ) or features a weakly attractive or repulsive interaction ( $g_A = \pm 0.5$ ). The majority-impurity coupling covers values from weakly attractive to intermediate repulsive  $g_{AB} \in [-0.5, 2.0]$ . The trap ratio covers cases of equal traps ( $\eta = 1$ ), a “broad” impurity ( $\eta = 0.51$ ) and a “narrow” impurity ( $\eta = 4$ ). The weak-to-intermediate interaction regimes considered here cover most of ground-state density configurations encountered in bosonic mixtures including miscible phase, core-shell separation [49,88,95,96], and composite fermionization [97,98]. The strongly correlated regimes such as full fermionization or the spin-chain configurations [99,100] are computationally challenging and require a fundamentally different treatment than the one employed in this work.

The Hamiltonian (1) possesses a *global reflection symmetry*, corresponding to a map  $x_i \mapsto -x_i$  and  $y_j \mapsto -y_j$  for all  $i, j$ . It implies that the energy eigenstates can be chosen to have a definite global parity, i.e., to be eigenstates of the above operation with eigenvalues  $+1$  (even) or  $-1$  (odd). An eigenstate can be thus classified as being of even or odd global parity. We prepare our system either in the ground state (even global parity in Secs. IV B and IV C) or in the first excited state (odd global parity in Sec. IV D) at  $\eta_0 = 1.05\eta$  of Eq. (1), the *prequench* Hamiltonian. To initiate the breathing dynamics we slightly relax the trap of the impurity from  $\eta_0$  to  $\eta$  and propagate the state with this *postquench* Hamiltonian. The majority species is set in breathing motion indirectly via the coupling to the impurity. Importantly, the two global parity subspaces are not coupled by the trap quench. Thus, an initial state of definite global parity will remain in the corresponding subspace. We can thus investigate the role of global parity on the breathing response.

The breathing motion can be monitored in the one-body densities  $\rho_1^\sigma(z, t)$  as their widths expand and contract periodically in time. Alternatively, one can analyze the time evolution of the corresponding breathing observables  $\langle \hat{O} \rangle_t$  with  $\hat{O} = \sum_i \hat{x}_i^2$  for the majority species and  $\hat{O} = \hat{y}^2$  for the impurity. The reason for equivalence is that the one-body density width, denoted as  $\Delta z$ , can be evaluated via  $\langle \Delta z \rangle^2 = \langle z^2 \rangle - \langle z \rangle^2$ . For an initial state of a definite global parity we have a reflection-symmetric one-body density which yields  $\langle z \rangle = 0$ . The oscillatory motion is usually composed of multiple contributions with amplitudes  $d_n$  and distinct frequencies  $\Omega_n$ , i.e.,  $\langle \hat{O} \rangle_t = \sum_n d_n e^{-i\Omega_n t}$ . Each of the oscillatory contributions in  $\langle \hat{O} \rangle_t$  will be referred to as a *breathing mode* characterized by a distinct frequency. The origin of the breathing modes can be expressed in terms of system’s eigenstates and related eigenenergies as follows. Upon a quench, several eigenstates  $|\psi_n\rangle$  of the postquench Hamiltonian  $H$  with energy  $E_n$  become populated depending on the overlap  $c_n$  with the initial state  $|\Psi(t_0)\rangle$ , i.e.,  $c_n = \langle \psi_n | \Psi(t_0) \rangle$ . The time signal  $\langle \hat{O} \rangle_t = \sum_{n,m} c_m^* c_n \langle \psi_m | \hat{O} | \psi_n \rangle e^{-i\Omega_{n,m} t}$  oscillates with frequencies  $\Omega_{n,m} = E_n - E_m$  for populated eigenstates  $c_n c_m \neq 0$  as long as the transition matrix elements  $\langle \psi_n | \hat{O} | \psi_m \rangle = O_{nm}$  are nonzero. Given a weak perturbation, we expect the lowest-

energy eigenstate of even (odd) global parity  $|\psi_{\text{ref}}\rangle$  to have the largest overlap with the even (odd) global parity initial state  $|\Psi(t_0)\rangle$ , i.e.,  $|c_0|^2 \approx 1$ . For that reason, the major part of frequencies contained in the breathing observable  $\langle \hat{O} \rangle_t$  are energy gaps between any of the populated eigenstates and the reference eigenstate, i.e.,  $\Omega_n = E_n - E_{\text{ref}}$ . Oscillations among any different combination of eigenstates are of minor amplitude, so we do not focus on them by setting a suitable amplitude threshold. For convenience, when we refer to an eigenstate of a breathing mode we mean the eigenstate responsible for this mode while the reference state  $|E_{\text{ref}}\rangle$  is usually clear within the context, unless we state otherwise. In case of “degenerate” energy gaps, i.e., equal energy gaps stemming from different eigenstate pairs, we do not differentiate which pairs actually contribute.

Finally, we would like to emphasize some fine subtleties between the species-asymmetric trap quench protocol employed in this work and the center-of-mass (c.m.) degree of freedom. First, for  $\eta \neq 1$  the c.m. coordinate cannot be decoupled by any linear transformation. This is an important difference to species-symmetric traps at  $\eta = 1$  where the c.m. coordinate provides an exact quantum number of the “free” c.m. harmonic oscillator. This becomes evident after employing a linear transformation to a set of Jacobi coordinates adapted to the Bose polaron problem, namely, relative coordinates of the majority species  $r_j = \frac{1}{j} \sum_i^j x_i - x_{j+1}$  for  $j \in \{1, \dots, N_A - 1\}$ , the global center of mass  $R_{\text{c.m.}} = \frac{1}{(N_A+1)} (\sum_i^{N_A} x_i + y)$ , and the relative coordinate characterizing the distance between the impurity and center of mass of the majority  $R_{AB} = (\frac{1}{N_A} \sum_i^{N_A} x_i) - y$ . Using this representation, the  $R_{\text{c.m.}}$  degree of freedom decouples from the relative coordinates  $r_j$  and  $R_{AB}$  such that  $H = H_{\text{c.m.}} + H_{\text{rel}}$ , where  $H_{\text{c.m.}}$  is a quantum harmonic oscillator of mass  $N_A + 1$  and frequency  $\omega = 1$ , while  $H_{\text{rel}}$  is symmetric under the map  $r_j \mapsto -r_j$  and  $R_{AB} \mapsto -R_{AB}$ . In this alternative relative-frame representation the Hamiltonian features a center-of-mass reflection symmetry, corresponding to a reflection operation  $R_{\text{c.m.}} \mapsto -R_{\text{c.m.}}$ . It implies that eigenstates can be chosen to have a definite c.m. parity, i.e., to be eigenstates of this operation with eigenvalues  $\pm 1$ . We note that it is not equivalent to a global reflection symmetry since the latter applies additionally  $r_j \mapsto -r_j$  and  $R_{AB} \mapsto -R_{AB}$ . In particular, an eigenstate may feature an even global parity, but be of odd c.m. parity and odd relative parity.

Second, we discuss several cases with the postquench Hamiltonian at  $\eta = 1$ , i.e., the corresponding eigenstates  $|\psi_n\rangle$  have a definite c.m. harmonic oscillator quantum number. The initial state, on the other hand, is the ground state of the prequench Hamiltonian at  $\eta_0 = 1.05$ , i.e., it does not have such symmetry. Within the linear response regime, it can be shown that the occupation  $c_n$  of the eigenstate  $|\psi_n\rangle$  is proportional to transition element  $\langle \psi_n | y^2 | \psi_0 \rangle$  induced by the impurity trap quench operator. In particular, as  $y^2$  is composed of a coupling term  $\propto R_{\text{c.m.}} R_{AB}$ , it is allowed for the initial state to be in a superposition of postquench eigenstates with different c.m. parity.

### III. COMPUTATIONAL APPROACH AND ANALYSIS

In this work we use the multilayer multiconfiguration time-dependent Hartree method for mixtures to initialize a system

in its ground state by means of relaxation, i.e., propagation in imaginary time, for the state evolution following a trap quench of the impurity and to evaluate the expectation values of breathing observables for each species as a function of time. We outline the major idea of the method in Sec. III A along with the wave-function ansatz for the system at hand. We then apply a compressed sensing algorithm to retain the frequencies from breathing observables. In view of the fact that CS relies on the sparsity condition in the Fourier space, it is not used as a standard tool for frequency extraction from a time signal. In Sec. III B we discuss advantages of this method in the current application as compared to a straightforward Fourier transformation. In order to be self-contained, we also provide the implementation details.

### A. ML-MCTDHX

To prepare the initial state  $|\Psi(t_0)\rangle$  and to perform the subsequent time evolution  $|\Psi(t)\rangle = e^{-iHt} |\Psi(t_0)\rangle$  with the time-independent Hamiltonian  $H$  from Eq. (1) we employ the *multilayer multiconfiguration time-dependent Hartree method for mixtures* of indistinguishable particles, for short, ML-X [45,101,102]. The core idea behind ML-X is to expand the many-body wave function in a properly symmetrized product state basis, the so-called Fock states, such that the underlying single-particle functions (SPFs) are *time dependent*. These are variationally optimized during the time evolution to provide a more “compact” description compared to Fock states composed of time-independent SPFs. Compact means that in general much less SPFs are required reducing thus the Fock space dimension while retaining a similar degree of accuracy.

As the system evolves, the many-body state travels through different subspaces of the complete Hilbert space. If the Fock basis is fixed, in general a large set of SPFs is required to cover all the relevant subspaces. Many configurations become “actively” populated during the time evolution, though not necessarily all of them at the same time with a fraction staying or becoming inactive. Even when all of Fock states are populated, we may rotate the basis by choosing a different set of SPFs until, eventually, we end up with a more compact representation. Given a truncated Fock space, ML-X rotates the basis vectors such as to find the best possible representation of the exact many-body state at each instant of time. In other words, it looks for the current “active” subspace. Once the truncated variationally evolving Fock space becomes large enough to contain the (major part of) “active” subspace, the representation of  $|\Psi(t)\rangle$  given by ML-X is considered optimal.

The underlying wave-function ansatz for the Bose polaron problem belonging to Eq. (1) is expanded in two layers (multilayer):

$$|\Psi(t)\rangle = \sum_{i=1}^S \sqrt{\lambda_i(t)} |\Psi_i^A(t)\rangle \otimes |\Psi_i^B(t)\rangle, \quad (2)$$

$$|\Psi_i^\sigma(t)\rangle = \sum_{\vec{n}^\sigma | N_\sigma} C_{i,\vec{n}^\sigma}(t) |\vec{n}^\sigma(t)\rangle. \quad (3)$$

In the first step [see Eq. (2)], the majority and impurity degrees of freedom  $x_i$  and  $y$ , respectively, are separated and assigned to  $S \in \mathbb{N}$  time-dependent species wave functions

$|\Psi_i^\sigma(t)\rangle$ . The sum of product form is very convenient as it makes evident the entanglement between the two components. In particular, we use the von Neumann entropy given by  $S_{vN} = -\sum_i \lambda_i \ln(\lambda_i)$  to quantify the degree of entanglement. The time-dependent weights  $\lambda_i(t)$  are normalized  $\sum_i \lambda_i(t) = 1$  and sorted in descending order. A composite system with  $\lambda_i(t) \approx 1$  is considered disentangled. Assuming  $S = 1$  in the expansion is called a species mean-field (SMF) approximation. In the second step [see Eq. (3)], every species wave function belonging to component  $\sigma$  is expanded in the Fock-state basis  $|\vec{n}^\sigma(t)\rangle$  with time-dependent coefficients  $C_{i,\vec{n}^\sigma}(t)$ . The time dependence of number states is meant implicitly through the time dependence of  $s_\sigma \in \mathbb{N}$  underlying SPFs  $\varphi_j^\sigma(t)$  which are represented using a harmonic discrete variable representation (DVR) [103,104]. The DVR is an orthonormal set of eigenfunctions of the position operator, represented by a finite analytical orthonormal basis, called DVR basis. The DVR functions act like a delta function within the finite space and provide analytical expressions for matrix representation of kinetic and position operators making their evaluation very efficient. The notation  $\vec{n}^\sigma | N_\sigma$  denotes particle-number conservation, i.e.,  $\sum_i n_i^\sigma = N_\sigma$ . Finally, by applying the Dirac-Frenkel variational principle [105] the equations of motion for  $\lambda_i$ ,  $C_{i,\vec{n}^\sigma}$ , and  $\varphi_j^\sigma$  are obtained. The convergence of ML-X is controlled via  $S$ ,  $s_\sigma$ , and the number of DVR grid points. We use  $S = s_\sigma = 8$  for  $N_A = 5$  and  $S = s_\sigma = 6$  for  $N_A = 10$ . The DVR grid spans an interval  $[-6, 6]$  and we choose 151 DVR grid points.

### B. Compressed sensing analysis

In this work, we aim to extract frequencies  $\Omega_{n,m} = E_n - E_m$  of system’s excitations where  $E_n$  denotes the eigenenergy of the  $n$ th eigenvector  $|\psi_n\rangle$  of  $H$ . Any physical observable  $\hat{O}$  carries information about excited eigenstates  $\langle \hat{O} \rangle_t = \sum_{n,m} c_m^* c_n \langle \psi_m | \hat{O} | \psi_n \rangle e^{-i\Omega_{n,m}t}$ , as long as the transition matrix elements  $\langle \psi_m | \hat{O} | \psi_n \rangle$  are nonzero and the corresponding eigenstates are initially populated  $c_n c_m \neq 0$  where  $c_n = \langle \psi_n | \Psi(t_0) \rangle$ . We perform a sampling of breathing observables with a uniform rate  $\Delta t$  over an interval  $[0, T]$  containing  $T/\Delta t + 1 = N_t$  points. It gives us a finite time signal  $\mathbf{f} \in \mathbb{R}^{N_t}$  with components  $f_j$  of discrete variable  $t_j \in \mathbb{R}$ , i.e.,  $f_j = f(t_j) = f(\Delta t j)$  with integer index  $j \in [0, N_t - 1] \subset \mathbb{N}_0$ .

A straightforward way to retain the frequencies contained in  $\mathbf{f}$  is to perform a discrete Fourier transformation (DFT), expressed as a linear map  $\mathbf{A}\mathbf{f} = \mathbf{g}$  with a square matrix  $\mathbf{A} \in \mathbb{C}^{N_t \times N_t}$  and signal’s representation in the frequency domain  $\mathbf{g} \in \mathbb{C}^{N_t}$ . The latter is characterized by frequency spacing  $\Delta\omega$  and cutoff frequency  $\omega_{\text{cut}}$ , i.e., it has components  $g_j = g(\omega_j) = g(\Delta\omega j)$  of discrete variable  $\omega_j \in \mathbb{R}$  and for odd (even)  $N_\omega = N_t$  number of points spans an open (closed) interval with end points  $-\omega_{\text{cut}}/2$  and  $\omega_{\text{cut}}/2$ .

The sampling parameters of time and frequency domain are interrelated. Thus, the sampling time  $T$  determines the frequency spacing  $\Delta\omega = 2\pi/T$ , while the sampling rate  $\Delta t$  determines the Nyquist frequency  $\omega_{\text{cut}} = \pi/\Delta t$ . In principle, frequencies can be retained with arbitrary resolution, if sampled long enough, while highly oscillatory components require a finer sampling rate. In practice, there are technical limitations such as generation, storage, and processing of

data. Given a complex system such as ours, data generation becomes a time-consuming factor, making a good resolution in frequency domain out of reach.

In order to overcome this obstacle, some prior information about signal's properties might become useful. Since the system is perturbed weakly, we expect only the low-energy excitations to be of relevance for the underlying dynamics. In particular, we expect  $\mathbf{g}$  to be sparse with major components located in the low-frequency region.

With this prior knowledge, *compressed sensing* (CS) allows to retain the frequencies with a very high resolution while keeping the simulation time with ML-X reasonably small. To this end, we formulate our problem as finding the vector  $\mathbf{g}$  satisfying the inverse DFT condition, i.e.,  $\mathbf{f} = \mathbf{A}^\dagger \mathbf{g}$ . However,  $\mathbf{A}^\dagger \in \mathbb{C}^{N_t \times N_\omega}$  is now a rectangular matrix with  $N_\omega \gg N_t$  and  $\mathbf{g} \in \mathbb{C}^{N_\omega}$  resulting in an underdetermined system of equations. Here,  $\mathbf{A}^\dagger$  is a submatrix of the inverse square DFT matrix  $\mathbf{A}^\dagger \in \mathbb{C}^{N_\omega \times N_\omega}$ , with the last  $N_\omega - N_t$  rows being removed. Importantly, the number of columns  $N_\omega$  and thus the frequency spacing  $\Delta\omega$  can be chosen independently of the simulation time  $T$ . Intuitively, this implies that  $\mathbf{g}$  has been generated by a signal extended over a larger region  $T' > T$  than the current one  $\mathbf{f}$ , though the information contained beyond  $T$  is considered redundant given the priors underlying the evolution.

In order to find a sparse solution to a linear ill-posed inverse problem, we formulate it as  $\ell_1$ -norm penalized least-squares minimization task known as *basis pursuit denoising* (BPDN) [106]:

$$\min_{\mathbf{g}} \frac{1}{2} \|\mathbf{f} - \mathbf{A}^\dagger \mathbf{g}\|_2^2 + \lambda \|\mathbf{g}\|_1, \quad (4)$$

where  $\|\mathbf{x}\|_p = (\sum_i |x_i|^p)^{1/p}$  while the penalty term  $\lambda \geq 0$  controls the tradeoff between the sparsity of the solution and the constraint violation in the presence of noisy signal  $\mathbf{f}$ . We use the least-angle regression (LARS) [107] minimization algorithm to solve Eq. (4) and perform a mean normalization of the signal  $\mathbf{f} \rightarrow \hat{\mathbf{f}} = (\mathbf{f} - \bar{\mathbf{f}})/\|\mathbf{f}\|_1$  beforehand. The employed implementation requires real inputs in Eq. (4). Real  $\mathbf{f}$  implies Hermitian  $\mathbf{g}$  and we use this symmetry to reformulate  $\mathbf{g}$  as a real vector:  $\mathbf{g} \rightarrow \tilde{\mathbf{g}} \in \mathbb{R}^{2N_\omega} = (\text{Re}(\mathbf{g}), \text{Im}(\mathbf{g}))$ . Correspondingly, the inverse Fourier matrix  $\mathbf{A}^\dagger \rightarrow \mathbf{M} \in \mathbb{R}^{N_t \times 2N_\omega} = (\mathbf{C}, \mathbf{D})$  is now composed of two real submatrices  $\mathbf{C} \in \mathbb{R}^{N_t \times N_\omega}$  with components  $c_{i,j} = \cos(\epsilon ij)$  and  $\mathbf{D} \in \mathbb{R}^{N_t \times N_\omega}$  with components  $d_{i,j} = \sin(\epsilon ij)$  where  $\epsilon = \Delta t \Delta \omega$ . The ML-X time-domain parameters are chosen as  $T = 40$  and  $\Delta t = 0.05$ , whereas the CS frequency-domain parameters are  $\omega_{\text{cut}} = 20$  and  $\Delta \omega = 0.01$ .<sup>1</sup> The only noise our signal has is due to floating point numbers and we decide upon the penalty parameter  $\lambda = 10^{-6}$  which displays great performance in terms of accuracy and computation time, which has been tested on a set of randomly generated signals composed of  $\approx 10$ – $20$  frequency components.

As input time signals  $\mathbf{f}$  we use the expectation values of breathing observables  $\sum_i \hat{x}_i^2$  for the majority species and  $\hat{y}^2$  for the impurity evaluated with respect to the dynamical state

$|\Psi(t)\rangle$  obtained by ML-X. We apply the CS algorithm to obtain the corresponding vector  $\tilde{\mathbf{g}}$ . Then, we map  $\tilde{\mathbf{g}}$  back to  $\mathbf{g}$  and convert complex values into amplitudes, i.e.,  $g_j \rightarrow |\text{Re}(g_j) + \text{Im}(g_j)|$ . The final vector we call a Fourier power spectrum and label it as  $X^2(\omega)$  for the majority component and  $Y^2(\omega)$  for the impurity. Finally, for a fixed set of physical parameter values we construct an averaged power spectrum  $\Sigma = (X^2 + Y^2)/2$ . An example is shown in Fig. 2. Each frequency is classified as being of a majority type (red), an impurity type (blue), or of a mixed type depending on the relative weights of  $X^2$  and  $Y^2$  in  $\Sigma$ . These are encoded in subsequent figures (Figs. 7–10 and 13) as a pie chart of two colors for each breathing frequency. Additionally, we use the transparency to indicate the magnitude of participating breathing modes relative to the most relevant mode of amplitude  $\max(\Sigma) = \Sigma_{\text{max}}$  such that faded colors imply less relevant modes. Frequencies with a contribution below  $\Sigma_{\text{max}}/10$  are discarded. This amounts to neglecting (i) low-amplitude oscillations among any two eigenstates not involving the reference eigenstate with the largest population, and (ii) numerically introduced “phantom” peaks which are also of minor amplitude. While the amplitude filtering allows us to focus only on major modes participating in the breathing dynamics, it introduces discontinuities in the subsequent figures (Figs. 7–10 and 13). Namely, it causes some modes, usually of a faint color, to “randomly” appear and disappear with increasing  $g_{AB}$ . The reason is a fluctuation in the population of eigenstates responsible for these modes resulting in mode amplitude fluctuation around the chosen threshold value.

A last remark is in order. Occasionally, the matrix  $\mathbf{M}$  becomes ill conditioned. As a result, the algorithm produces a nonunique solution. Whenever this happens, we obtain either wrong frequencies or correct frequencies but with altered amplitudes. Fortunately, as we monitor the frequency modes continuously as a function of  $g_{AB}$  we are able to differentiate between the two cases. In the first case, we manually remove all frequencies at given  $g_{AB}$ , while in the second case we may encounter isolated absent data points.

#### IV. RESULTS

First, in Sec. IV A we summarize results concerning the breathing dynamics of a single particle, a single-component condensate, two distinguishable particles, and a particle-balanced few-body Bose-Bose mixture. This will provide us with useful insights for the interpretation of breathing modes unraveled in the Bose polaron setup being the subject of Sec. IV B. In Sec. IV C we investigate the impact of the trap ratio  $\eta$  on the breathing spectrum accounting for two cases: a “broad” ( $\eta < 1$ ) and a “narrow” ( $\eta > 1$ ) impurity. Finally, in Sec. IV D we study the breathing response of the first excited state having odd global parity and contrast it to the response of the ground state which is of even global parity.

In the following, when all interactions are zero we employ a notation  $|\vec{n}\rangle = |n_1, n_2, \dots\rangle$  to denote  $n_i$  particles occupying the  $i$ th orbital of a single-particle quantum harmonic oscillator. It is not to be confused with permanents introduced in Sec. III A where the orbitals are variationally optimal at each time instant. We also drop the redundant zeros in the vector tail once all the particles have been accounted for, i.e.,

<sup>1</sup>We remark that similar resolution with DFT can be obtained with  $T \approx 600$ .

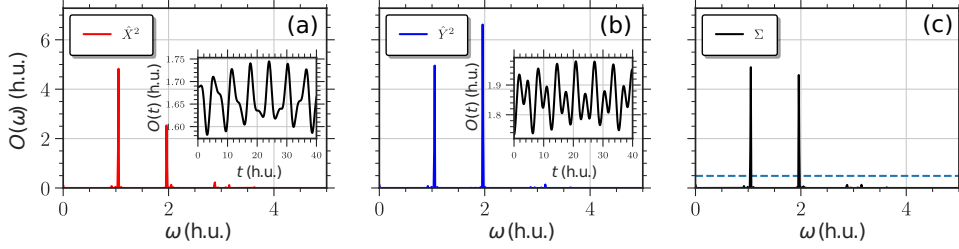


FIG. 2. Fourier power spectrum  $X^2(\omega)$  (a) and  $Y^2(\omega)$  (b) obtained by applying a compressed sensing algorithm to the expectation values of the breathing observables  $\langle \sum_i \hat{x}_i^2 \rangle_t$  and  $\langle \hat{y}^2 \rangle_t$  (insets) evaluated with respect to a dynamical state  $|\Psi(t)\rangle$  obtained by the multiconfiguration time-dependent Hartree method for mixtures. In the averaged power spectrum  $\Sigma(\omega)$  (c) the dashed line indicates a threshold magnitude and only frequencies above it are accounted for in Sec. IV (see text). The physical parameters are  $\eta = 1$ ,  $N_A = 5$ ,  $N_B = 1$ ,  $g_{AB} = 2.0$ ,  $g_A = 0$  (see Sec. II) and the compressing sensing parameters are  $T = 40$ ,  $\Delta t = 0.1$ ,  $\omega_{\text{cut}} = 20$ , and  $\Delta\omega = 0.01$  (see Sec. III B). All quantities are given in harmonic units.

$\sum_i n_i = N$ . The notation  $|\vec{n}^A\rangle \otimes |\vec{n}^B\rangle$  denotes a product state for the two components. Note that for unequal traps ( $\eta \neq 1$ ) the orbitals for each species are different.

For Figs. 7–10 and 13 we did a comparison to results obtained from the ML-X method of lower dimension  $S = s_\sigma = 6$  ( $S = s_\sigma = 4$ ), for  $N_A = 5$  ( $N_A = 10$ ) particles. Instead of displaying the corresponding plots of less converged simulations we put together the most relevant findings for the reader to keep in mind while reading Sec. IV. First, for the values of corresponding frequencies, we evidenced small quantitative discrepancies below  $\pm 0.02$  (in harmonic units), being larger for stronger couplings. Second, we observed that the transparency of the modes (mode amplitude) as well as the ratio of pie slices (species correspondence) for each point maintain their overall qualitative behavior.

### A. Few-body Bose-Bose mixture

The breathing mode frequency of a single particle confined in a parabolic trap of frequency  $\omega$  is known to be  $\Omega = 2\omega$ , corresponding to an excitation by two energy quanta  $|0, 0, 1\rangle$  with respect to the harmonic oscillator basis. An ensemble of  $N$  noninteracting ( $g = 0$ ) bosonic particles introduces an additional eigenstate of the same excitation energy  $2\omega$ , namely, a two-particle excitation  $|N - 2, 2\rangle$  being degenerate with  $|N - 1, 0, 1\rangle$ . For interacting particles, the degeneracy is lifted. The frequency of one mode remains constant for any  $g$  and relates to the c.m. breathing motion. The frequency of the other mode is highly sensitive to a variation of  $g$  and characterizes the relative motion of particles [77, 108]. A mean-field ansatz for the breathing dynamics, being a single-particle picture, is able to recover only the interaction-sensitive breathing frequency, though with quantitative deviations as compared to an exact solution, especially at sizable interactions.

#### 1. 1 + 1 mixture

The Hamiltonian (1) can be solved analytically for  $N_A = 1$  and  $N_B = 1$  at  $\eta = 1$ . To this end, we perform a coordinate transformation to the relative frame composed of the center of mass  $R = (x + y)/2$  and relative  $r = x - y$  coordinates. In

this frame, the two degrees of freedom decouple  $H = H_R + H_r$ .

The first term  $H_R$  is a quantum harmonic oscillator of mass  $m_R = 2$ :

$$H_R = -\frac{\partial^2}{4\partial R^2} + R^2. \quad (5)$$

The solutions  $\Phi_k(R; m_R)$  are the well-known Hermite functions

$$\Phi_k(z; m) = \frac{1}{\sqrt{2^n n!}} \left(\frac{m}{\pi}\right)^{1/4} \exp\left(-\frac{mz^2}{2}\right) H_n(\sqrt{m}z) \quad (6)$$

with  $m$  the particle mass and  $H_n$  the physicists' Hermite polynomials. The corresponding eigenenergies are  $\epsilon_k = k + \frac{1}{2}$ .

The second term  $H_r$  is a quantum harmonic oscillator of mass  $m_r = \frac{1}{2}$  with a delta constraint:

$$H_r = -\frac{\partial^2}{\partial r^2} + \frac{1}{4}r^2 + g\delta(r), \quad (7)$$

where we substituted  $g_{AB} \rightarrow g$  to simplify the notation. The solutions can be classified by parity:

$$\phi_l(r) = \begin{cases} D_{\mu(g, l/2)}(r), & l \text{ even} \\ \Phi_l(r; m_r), & l \text{ odd}. \end{cases} \quad (8)$$

The even parity states are the symmetrized parabolic cylinder functions

$$D_\mu(z) = \sqrt{2^\mu} \exp\left(-\frac{z^2}{4}\right) U\left(-\frac{1}{2}\mu, \frac{1}{2}, \frac{1}{2}z^2\right) \quad (9)$$

with  $U(a, b, z)$  denoting the Tricomi's hypergeometric function and  $\mu(g, l/2)$ ,<sup>2</sup> being a real-valued quantum number obtained by solving a transcendental equation

$$g = -2^{\frac{3}{2}} \frac{\Gamma\left(\frac{1-\mu}{2}\right)}{\Gamma\left(-\frac{\mu}{2}\right)}, \quad (10)$$

which for a fixed  $g$  gives a ladder of solutions and  $l/2$  refers to the index number. The corresponding eigenenergies are  $\epsilon_l = \mu(g, l/2) + \frac{1}{2}$ . The odd parity states vanish at  $r = 0$  and thus

<sup>2</sup> $l < \mu(g, l/2) < l + 1$  for  $0 < g < \infty$ .



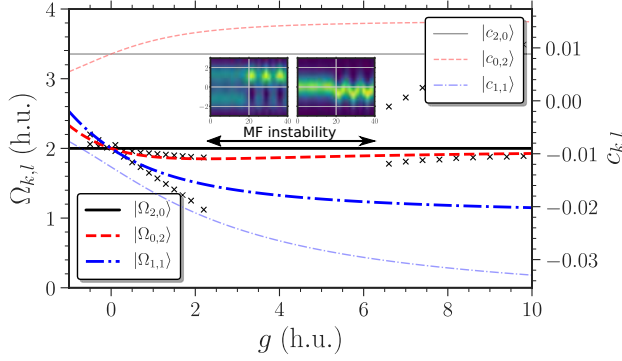


FIG. 3. Breathing mode frequencies (opaque lines)  $\Omega_{k,l} = E_{k,l} - E_{0,0}$  [see Eq. (11)] of two distinguishable particles  $N_A = 1$  and  $N_B = 1$  as a function of the coupling  $g_{AB} \equiv g$  at equal trapping frequency ratio  $\eta = 1$ . Population amplitudes (transparent lines)  $c_{k,l}$  [see Eq. (13)] of eigenstates  $|\psi_{k,l}\rangle$  upon quenching the ground state  $|E_0\rangle_{\eta_0}$  from  $\eta_0 = 1.05$  to  $\eta = 1$ . Crosses stand for frequencies extracted from a laboratory frame mean-field ansatz. Inset: representative example of dynamical symmetry breaking in the one-body densities  $\rho_1(x, t)$  (left) and  $\rho_1(y, t)$  (right) at  $2.5 < g < 6.5$  occurring for a mean-field ansatz. All quantities are given in harmonic units.

do not experience the delta barrier. They are the odd parity Hermite functions  $\Phi_l(r; m_r)$  of mass  $m_r$  and eigenenergy  $\epsilon_l = l + \frac{1}{2}$ .

The two-body eigenstate becomes a product state  $\psi_{k,l}(R, r) = \Phi_k(R; m_R)\phi_l(r)$  with total energy:

$$E_{k,l} = \begin{cases} k + \mu(g, l/2) + 1, & l \text{ even} \\ k + l + 1, & l \text{ odd.} \end{cases} \quad (11)$$

Having analytical expressions for the eigenstates, we proceed with the breathing dynamics induced by releasing the trap of the second particle slightly from  $\eta_0 = 1.05$  to  $\eta = 1$ . The time evolution of the prequench ground state  $|E_0\rangle_{\eta_0}$  can be expressed in terms of postquench eigenstates  $|\psi_{k,l}\rangle$ :

$$|E_0\rangle_{\eta_0} = \sum_{k,l} c_{k,l} e^{-iE_{k,l}t} |\psi_{k,l}\rangle. \quad (12)$$

To find the occupancy of eigenstates  $c_{k,l} = \langle \psi_{k,l} | E_0 \rangle_{\eta_0}$  we perform first-order perturbation theory for the ground state:

$$c_{k,l} = \Delta\eta \frac{\langle \psi_{k,l} | y^2 | \psi_{0,0} \rangle}{\Omega_{k,l}}, \quad (13)$$

with  $\Delta\eta = \eta_0 - \eta$  and  $\Omega_{k,l} = E_{k,l} - E_{0,0}$ . The coupling operator  $y^2 = R^2 - Rr + r^2/4$  can populate states  $|\psi_{2,0}\rangle$  via  $R^2$ ,  $|\psi_{0,2}\rangle$  via  $r^2$ , and  $|\psi_{1,1}\rangle$  via  $Rr$ . All these states are of even global parity,  $|\psi_{2,0}\rangle$  and  $|\psi_{0,2}\rangle$  are of even c.m. parity, and  $|\psi_{1,1}\rangle$  is of odd c.m. parity. They have the same energy gap  $\Omega_{k,l} = 2$  with respect to the ground state at  $g = 0$ . We call them the *first-order* breathing manifold.<sup>3</sup>

<sup>3</sup>The  $n$ th-order breathing manifold has an energy gap  $2n$  with respect to the ground state at  $g = 0$ .

In Fig. 3 we display the energy gaps (opaque curves) as a function of  $g$  (cf. also Fig. 8 in [76]). We concentrate on the three eigenstates from the first breathing manifold. At  $g = 0$  they are degenerate with excitation energy  $\Omega = 2$ . In the laboratory frame, these are a single-particle excitation by two energy quanta in either of the components, i.e.,  $|0, 0, 1\rangle \otimes |1\rangle$  and  $|1\rangle \otimes |0, 0, 1\rangle$ , as well as a two-particle excitation  $|0, 1\rangle \otimes |0, 1\rangle$ . The latter can be thought of as a “correlated” sloshing excitation:  $\langle X \rangle = \langle Y \rangle = 0$  and  $\langle XY \rangle \neq 0$ . Below we will reveal what kind of motion the particles actually undergo.

When the interaction strength  $g$  becomes nonzero, we employ the relative frame. The degenerate manifold splits at finite  $g$ . The frequency of the c.m. mode  $|\psi_{2,0}\rangle$  is independent of interactions  $\Omega_{2,0} = 2$  (black solid opaque line). The relative motion mode  $|\psi_{0,2}\rangle$  features an interaction-sensitive frequency  $\Omega_{0,2} = [\mu(g, 1) - \mu(g, 0)]$  (red dashed opaque line), which displays a single minimum at positive  $g$ , is monotonically decreasing function of  $g$  left of this minimum, and saturates as  $g \rightarrow \infty$ . Curves with such behavior will be abbreviated as *single turning point* (STP) curves. Actually, all mode frequencies will saturate at large positive  $g$  because of contact interaction: the eigenenergies are monotonically increasing functions of  $g$ ,<sup>4</sup> and are bounded from above due to hard-core repulsion.<sup>5</sup> The hybrid “sloshing” mode  $|\psi_{1,1}\rangle$  has a frequency  $\Omega_{1,1} = [2 - \mu(g, 0)]$  (blue dashed-dotted opaque line) which is a monotonically decreasing function of  $g$ . It saturates to a frequency  $\Omega = 1$  at very large positive couplings matching the interaction-independent sloshing (dipole) mode frequency of a single-component condensate in a harmonic trap [52].

Thus, distinguishability allows for an additional breathing mode. A laboratory-frame mean-field ansatz (crosses) predicts two interaction-sensitive breathing frequencies though neither of the exact modes is matched quantitatively for all  $g$ . Importantly, the monotonically decreasing frequency can be matched only at very weak interactions, implying the relevance of entanglement in multicomponent mixtures. There is even a region of interactions  $2.5 < g < 6.5$ , where dynamical symmetry breaking takes place, i.e., the parity symmetry becomes violated after some propagation time (see the inset). It starts right after the low-frequency mean-field mode has reached the value  $\Omega = 1$  around  $g \approx 2.5$ , being the limiting value of the exact mode  $|\psi_{1,1}\rangle$  at  $g = \infty$ .

What kind of motion does each mode induce? In the relative frame, the one-body densities  $\rho_1(R, t)$  and  $\rho_1(r, t)$  undergo the following evolution:

$$\rho_1(R, t) \approx c_{0,0}^2 \rho_1^{(0,0)}(R) + 2 \sum_{k,l} c_{0,0} c_{k,l} \rho_1^{(k,l)}(R) \cos(\Omega_{k,l}t),$$

$$\rho_1(r, t) \approx c_{0,0}^2 \rho_1^{(0,0)}(r) + 2 \sum_{k,l} c_{0,0} c_{k,l} \rho_1^{(k,l)}(r) \cos(\Omega_{k,l}t)$$

with the time-independent background densities  $\rho_1^{(0,0)}(R)$  and  $\rho_1^{(0,0)}(r)$ , modulation densities  $\rho_1^{(k,l)}(R) = \int dr \rho_2^{(k,l)}(R, r)$  and  $\rho_1^{(k,l)}(r) = \int dR \rho_2^{(k,l)}(R, r)$ , where  $\rho_2^{(k,l)}(R, r) =$

<sup>4</sup> $\partial E_j / \partial g_{AB} = \int \rho_2^{AB}(z, z) dz \geq 0$  with  $\rho_2^{AB}(z)$  being the diagonal of the reduced intercomponent two-particle density obtained from the many-body eigenstate  $|E_j(g_{AB})\rangle$ .

<sup>5</sup> $\rho_2^{AB}(z, z) \rightarrow 0$  as  $g_{AB} \rightarrow \infty$ .

$\psi_{0,0}(R, r)\psi_{k,l}(R, r)$ . We neglected terms  $c_{i,j}c_{k,l}$  related to oscillations among the excited states. Inserting the occupied eigenstates we mentioned previously, we get

$$\begin{aligned}\rho_1(R, t) &= c_{0,0}^2 \Phi_0^2(R) + 2c_{0,0}c_{2,0}\Phi_0(R)\Phi_2(R)\cos(2t), \\ \rho_1(r, t) &= c_{0,0}^2 \phi_0^2(r) + 2c_{0,0}c_{0,2}\phi_0(r)\phi_2(r)\cos([\mu(g, 1) \\ &\quad - \mu(g, 0)]t).\end{aligned}$$

Thus,  $\rho_1(R, t)$  performs a constant frequency ( $\Omega_{2,0} = 2$ ) breathing oscillation, while  $\rho_1(r, t)$  undergoes an interaction-dependent single-frequency ( $\Omega_{0,2} = [\mu(g, 1) - \mu(g, 0)]$ ) modulation.

The state  $|\psi_{1,1}\rangle$  and the related frequency ( $\Omega_{1,1} = [2 - \mu(g, 0)]$ ) are not represented in the reduced “one-body” quantities of the relative frame and can be only revealed on the “two-body” level. In particular,  $R$  and  $r$  do not perform a sloshing motion, i.e.,  $\langle R \rangle = \langle r \rangle = 0$  which implies  $\langle x \rangle = \langle y \rangle = 0$ . Instead,  $\langle Rr \rangle = A \cos([2 - \mu(g, 0)]t)$  with amplitude  $A = 2c_{0,0}c_{1,1} \iint dR dr Rr \rho_2^{(1,1)}(R, r)$ .

What is the imprint of the individual oscillatory term  $\rho_2^{(k,l)}(R, r) \cos(\Omega_{k,l}t)$  of the relative frame density matrix  $\rho_2(R, r, t)$  describing the two-particle evolution on the reduced one-particle density  $\rho_1(x, t)$  of the laboratory frame? To this end, we transform  $\rho_2^{(k,l)}(R, r)$  to the laboratory frame and integrate over the coordinate  $y$  to get  $\rho_1^{(k,l)}(x)$ . The corresponding modulations are shown in Fig. 4. Figure 4(a) demonstrates the time-independent background density  $\rho_1^{(0,0)}(x)$ . At negative  $g$  (dotted) it is a narrow Gaussian, which broadens with increasing  $g$  (solid) until it finally splits into a two-hump configuration (dashed) indicating that phase separation has taken place. Figure 4(b) is a density modulation (at  $t = 0$ ) stemming from the c.m. breathing  $\rho_2^{(2,0)}(R, r) \cos(\Omega_{2,0}t)$ . The exact shape is very sensitive to  $g$  variation and in particular to the two-hump structure of the background density at  $g = 8$  where it develops additional nodes. The dotted and solid curves are typical shapes responsible for the breathing motion of a Gaussian background. The dashed curve ( $g = 8$ ) induces breathing for each individual hump of the background density. Figures 4(c) and 4(d) are density modulations (at  $t = 0$ ) stemming from relative motion breathing  $\rho_2^{(0,2)}(R, r) \cos([\mu(g, 1) - \mu(g, 0)]t)$  and hybrid sloshing  $\rho_2^{(1,1)}(R, r) \cos([2 - \mu(g, 0)]t)$ . For a Gaussian background they produce breathing, while for a two-hump profile we expect a simultaneous outwards and inwards sloshing of the two humps. Both the magnitude and functional behavior of the modulations are robust to  $g$  variation. The second particle  $\rho_1(y, t)$  does exactly the same, except  $\rho_1^{(1,1)}(y, t)$  is inverted, i.e., it has a phase shift of  $\pi$ .

To summarize, two distinguishable particles feature an additional breathing mode in contrast to two indistinguishable particles. The responsible eigenstate has even global parity, though it is of odd center-of-mass parity and odd relative parity. It relates to a hybrid sloshing:  $\langle Rr \rangle \neq 0$  while  $\langle R \rangle = \langle r \rangle = 0$ . It induces a breathing oscillation of the one-body densities though they have a relative phase shift of  $\pi$ . The related mode frequency is a monotonically decreasing function of the interparticle interaction  $g$  and a mean-field ansatz fails to capture its functional behavior except for a linear trend at very weak interactions.

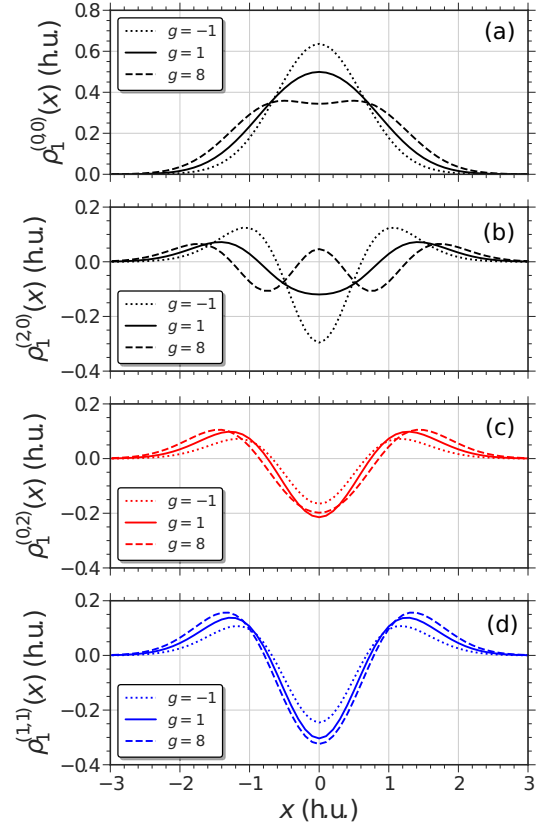


FIG. 4. Decomposition of the one-body density  $\rho_1(x)$ : (a) time-independent background and time-dependent single-frequency modulations  $\rho_1^{(k,l)}(x)$  induced by (b) center-of-mass breathing  $\rho_2^{(2,0)}$ , (c) interparticle distance breathing  $\rho_2^{(0,2)}$ , and (d) hybrid sloshing  $\rho_2^{(1,1)}$  at different interaction strength  $g$ . All quantities are given in harmonic units.

## 2. 2 + 2 mixture

A noninteracting two-component mixture features in total five eigenstates which are two energy quanta above the ground state: two single-particle excitation states  $|N_A - 1, 0, 1\rangle \otimes |N_B\rangle$  and  $|N_A\rangle \otimes |N_B - 1, 0, 1\rangle$ , two states having two indistinguishable particles excited  $|N_A - 2, 2\rangle \otimes |N_B\rangle$  and  $|N_A\rangle \otimes |N_B - 2, 2\rangle$ , and, finally, a state where one particle in each component is excited  $|N_A - 1, 1\rangle \otimes |N_B - 1, 1\rangle$ . The interactions will (partially) break this manifold of degenerate eigenstates. Each of these states, once populated in the initialization step, will induce a breathing oscillation of a characteristic frequency. Together they represent a first-order breathing manifold.<sup>6</sup> To get an insight how the respective frequencies behave depending on the system’s interactions, we briefly summarize and complement the results obtained in [88]. For a few-body fermionic mixture see also [76].

<sup>6</sup>A breathing mode is said to be of  $n$ th order if its frequency can be traced to a value  $2\omega_\sigma n$  when adiabatically tuning all the interactions to zero.

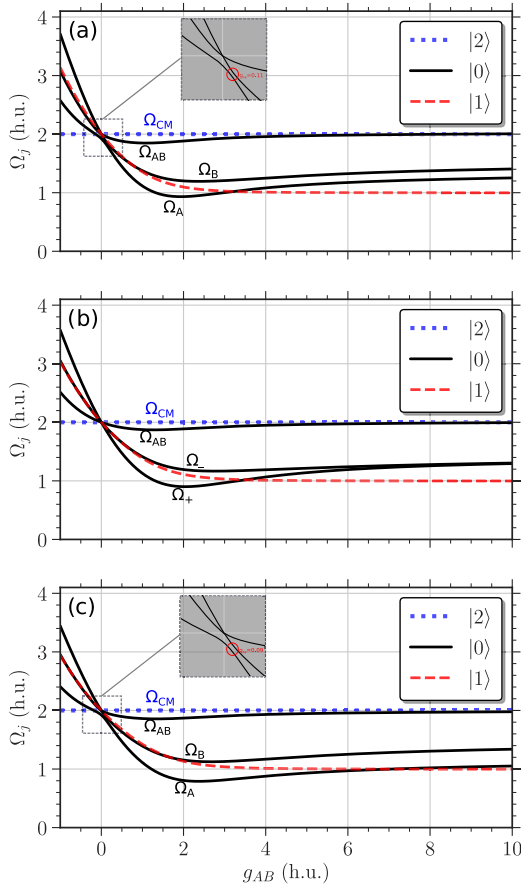


FIG. 5. Energy gaps  $\Omega_j = E_j - E_0$  (with respect to the ground state  $|E_0\rangle$ ) of a few-body bosonic mixture  $N_A = 2$  and  $N_B = 2$  as a function of the intercomponent coupling  $g_{AB}$  at equal trapping frequency ratio  $\eta = 1$ , intracomponent interaction strength  $g_B = 0$  for the second component and (a)  $g_A = -0.5$ , (b)  $g_A = 0$ , (c)  $g_A = 0.5$  for the first component. Whether the corresponding eigenstates are actually excited depends on the quench protocol. Different colors (line styles) refer to the center-of-mass (c.m.) quantum number in the eigenstate  $|E_j\rangle$ . The c.m. is a decoupled degree of freedom in this harmonic confinement. The insets represent a zoom-in on regions with avoided crossings which are indicated by circles and caused by  $g_A \neq g_B$  asymmetry. Curves of different colors (line styles) may only cross. All quantities are given in harmonic units.

In [88], each component consists of two particles trapped within the same parabolic confinement  $\eta = 1$ . Both components experience a sudden but weak trap quench of the same magnitude and the system's response is studied for different intracomponent and intercomponent interaction strengths. Importantly, the c.m. motion decouples while the quench operator prevents transitions among eigenstates possessing different c.m. parity. By performing an exact diagonalization method based on a correlated basis (see [88] for more details)<sup>7</sup> up to four breathing mode frequencies have been identified

<sup>7</sup>It can be applied to bosonic mixtures of  $N_A \leq 2$  and  $N_B \leq 2$  particles subject to contact interactions in a 1D harmonic trap.

and analyzed. These are reproduced in Fig. 5 as a function of the intercomponent coupling  $g_{AB}$  for three different intracomponent interaction values  $g_A$  [Figs. 5(a)–5(c)], assuming  $g_B = 0$ . The curve colors (line styles) encode the c.m. quantum number of the responsible eigenstates  $|E_j\rangle$ , while the reference state  $|E_{\text{ref}}\rangle$  is the ground state  $|E_0\rangle$  of even c.m. parity.

The blue dotted curve is a double excitation of the c.m. harmonic oscillator, the  $\Omega_{\text{c.m.}}$  mode. Thus, it is independent of interactions  $g_A$ ,  $g_B$ , and  $g_{AB}$ . The three black solid curves are interaction-sensitive relative motion modes. They have been labeled  $\Omega_+$ ,  $\Omega_-$  ( $\Omega_A$ ,  $\Omega_B$ ) for species-(anti)symmetric parameter choice, i.e.,  $g_A = g_B$  ( $g_A \neq g_B$ ), and  $\Omega_{AB}$ . All of them are STP curves. The  $\Omega_{AB}$  mode is quite shallow, weakly affected by intracomponent interactions and degenerates with  $\Omega_{\text{c.m.}}$  at strong coupling  $g_{AB}$ . The two lower ones are very sensitive to intracomponent interactions and, depending on the presence of the species-exchange symmetry,<sup>8</sup> they either intersect or experience a bending in the vicinity of avoided crossings [Figs. 5(a) and 5(c) at  $g_{AB} \approx 0$ ].

Thus, for a weak *species-symmetric* trap quench, the system features 2–4 of the above-mentioned breathing frequencies depending on the strength of interaction parameters. For a weak *species-asymmetric* trap quench, all the above-mentioned modes are still energetically accessible plus one extra mode of a comparable frequency. Indeed, based on our discussion on the 1+1 mixture, we anticipate an eigenstate with odd c.m. parity and even global parity to eventually contribute to the dynamics. The corresponding breathing mode frequency is represented by the red dashed curve in Fig. 5. We observe again a monotonous decrease of the mode frequency with increasing coupling  $g_{AB}$  until it energetically separates from one of the relative modes at  $g_{AB} \approx 1$  and, finally, saturates to a value of 1.0 at  $g_{AB} \geq 4$ . Its frequency is barely affected by  $g_\sigma$ . Interestingly, the mode is again invisible to numerical approaches which ignore the entanglement as we evidence by comparing a numerically exact solution to a SMF ansatz.

## B. Few-body Bose polaron

Now we turn our attention to a single impurity  $N_B = 1$  in a few-body majority environment having  $N_A = 5$  or 10 particles. In contrast to [88], here, we initiate the breathing dynamics by relaxing only the  $B$  component, while the  $A$  component is affected indirectly via the intercomponent coupling  $g_{AB}$ . Representative breathing motions in each component can be seen in Fig. 6. At  $\eta = 1$  the c.m. motion still decouples from the relative motions. In particular, the quench operator may mediate between eigenstates of different c.m. parity inducing eventually a special breathing mode caused by population of an eigenstate with odd c.m. parity. Furthermore, there is only one particle in the  $B$  component. Thus, a double excitation state  $|N_A\rangle \otimes |N_B - 2, 2\rangle$  (see Sec. IV A) does not exist and we expect that one of the relative modes (black solid curves in Fig. 5), whose frequency is notably affected by interactions, will not be present.

<sup>8</sup>Corresponding to a map  $x_i \mapsto y_i$  at  $g_A = g_B$ .

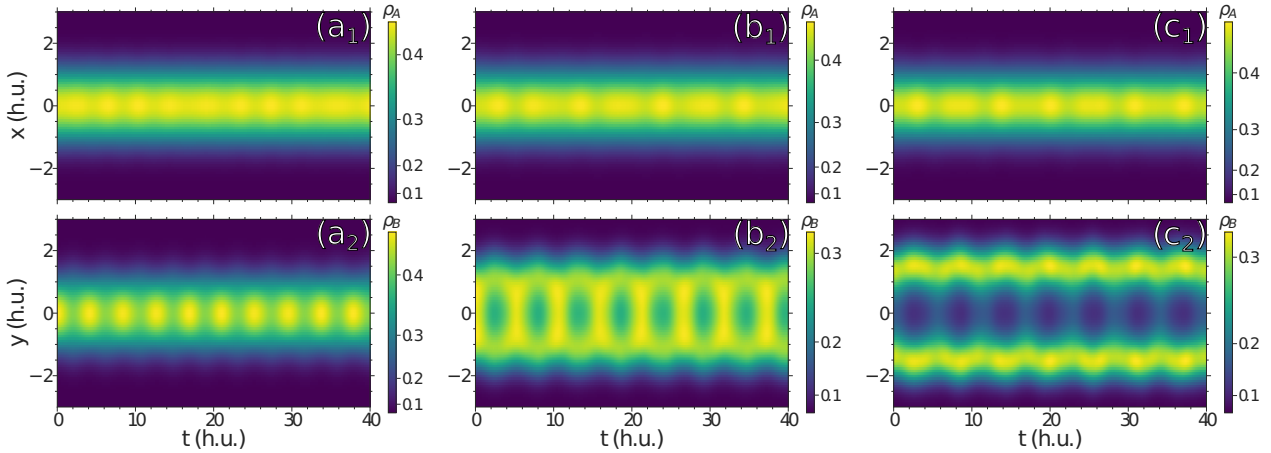


FIG. 6. Breathing oscillations of the one-body densities of the majority component  $\rho_1^A(x)$  (first row) and the impurity  $\rho_1^B(y)$  (second row) at a fixed majority-component interaction  $g_A = 0.5$  for  $N_A = 5$  and  $N_B = 1$  particles initiated by preparation of the ground state of even global parity followed by an abrupt change of the trap ratio from  $\eta = 1.05$  to 1. Columns 1–3 correspond to different intercomponent couplings: (a)  $g_{AB} = 0.5$ , (b)  $g_{AB} = 1.0$ , and (c)  $g_{AB} = 1.5$ . Note that the initial state displays the onset of phase separation in (b) and a pronounced core-shell phase in (c). All quantities are given in harmonic units.

In Figs. 7 and 8 we show the excitation spectrum of the breathing dynamics initialized by quenching the equilibrated system at trap ratio  $\eta = 1.05$  to 1, i.e., partially releasing the trap of the impurity. The majority component consists of  $N_A = 5$  (Fig. 7) or  $N_A = 10$  (Fig. 8) particles subject to several different majority component interactions  $g_A$  [Figs. 7(a)–7(c) and 8(a)–8(c)]. Only frequencies of modes whose contribution is above 10% of the maximum amplitude  $\Sigma_{\max}$  in the averaged power spectrum are shown. Additionally, each frequency data point (full circle) is represented as a pie chart of two different colors and encodes the contribution of the breathing observables to the averaged power spectrum (see Sec. III B): blue color for the impurity  $\hat{y}^2$  and red color for the majority component  $\sum_i \hat{x}_i^2$ . The decomposition into colors tells us whether the respective mode is a single-species mode or whether it is of a mixed character and to what extent. Furthermore, the color intensity indicates the participation of the respective mode in the breathing dynamics as compared to the most relevant mode at fixed  $g_{AB}$  (a more intense color indicates a stronger contribution). Finally, the crosses represent frequencies of modes excited by the same procedure but numerically ignoring the entanglement in the initial state and the subsequent dynamics (SMF approximation).

Let us first focus on Fig. 7(b), the case of a noninteracting majority species ( $g_A = 0$ ). At  $g_{AB} = 0$  only the impurity is excited (blue circle) performing a breathing motion with frequency  $\Omega = 2$  as expected. As one increases the coupling strength ( $g_{AB} > 0$ ), a second mode of decreasing frequency emerges resulting in a beating. This mode has the largest contribution to the ongoing dynamics and is of a mixed type, i.e., it appears both in the majority and impurity breathing observables. For the latter reason it can correspond to the  $\Omega_{AB}$  mode of even c.m. parity or to the hybrid sloshing mode of odd c.m. parity we introduced in the previous section. The quench operator can mediate among eigenstates of different c.m. parity so both are allowed to be populated. Considering limited frequency resolution and the possibility of a quaside-

generacy of the red (dashed) mode with a black (solid) mode observed in Fig. 5, it is likely that the observed mode gets a contribution from both eigenstates. For that reason, no particular eigenstate label can be assigned to it. The frequency of the other mode experiences only a slight variation  $\Omega \approx 2$ . It is represented to a larger extent in the majority component, has a minor amplitude, and is reproduced by a SMF ansatz. Thus, we assign it to the  $\Omega_A$  mode encountered in Sec. IV A (cf. black curves in Fig. 5), though here it is less sensitive to  $g_{AB}$  variation, supposedly due to the particle-number imbalance.

Around  $g_{AB} \approx 0.75$  the lower frequency splits into two branches of comparable significance, resulting altogether in three modes. One of the emerging branches possesses a continuously decreasing frequency with increasing  $g_{AB}$  approaching the value  $\Omega = 1$ . It matches the description of the hybrid sloshing mode which was emphasized in Sec. IV A (cf. red dashed curve in Fig. 5). Interestingly, it is equally represented in both subsystems despite the particle-number imbalance and quench asymmetry. The other frequency branch bends and starts recovering towards  $\Omega = 2$  with increasing  $g_{AB}$  while gradually becoming a pure signature of the impurity motion only (the blue slice dominates at  $g_{AB} = 2$ ). It matches the functional behavior of the  $\Omega_{AB}$  mode (STP curve) mentioned in Sec. IV A (cf. the black solid curves in Fig. 5).

At weak negative coupling ( $g_{AB} < 0$ ) one observes also a beating behavior, although here both frequencies are increasing with decreasing  $g_{AB}$ . The dominant frequency in the power spectrum is more sensitive to the coupling variation, is of a mixed type and reproducible by a SMF ansatz ( $\Omega_{AB}$  mode), while the second is barely affected and primarily represented in the majority component ( $\Omega_A$  mode). Below a certain threshold ( $g_{AB} < -0.4$ ) one observes low-amplitude traces of a third frequency.

We discover several major alternations in the excitation spectrum when the majority component becomes interacting. For weakly attractive ( $g_A = -0.5$ ) majority particles in Fig. 7(a) the coupling-insensitive mode frequency is seem-

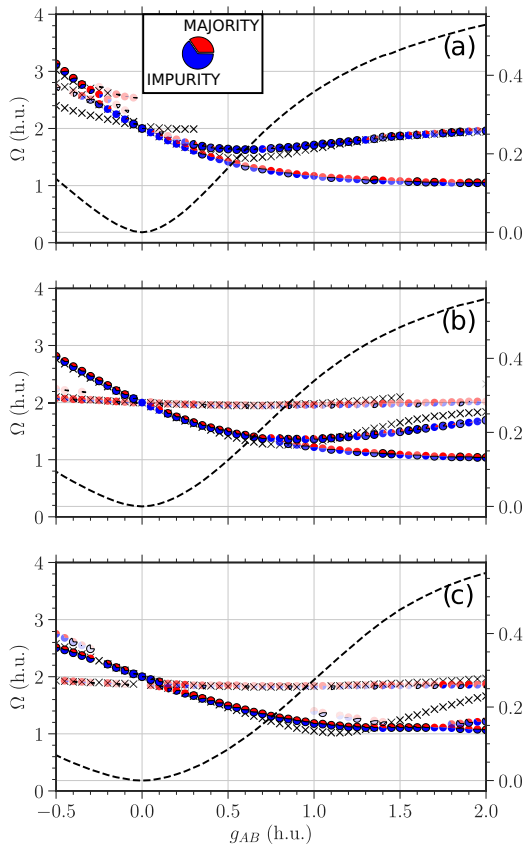


FIG. 7. Frequencies  $\Omega$  of breathing modes excited by quenching the ground state  $|E_0\rangle$  of the Bose polaron for  $N_A = 5$  and  $N_B = 1$ , meaning a change in the trap ratio from  $\eta = 1.05$  to  $1.0$ , shown as a function of the intercomponent coupling  $g_{AB}$  for a fixed majority component interaction (a)  $g_A = -0.5$ , (b)  $g_A = 0$ , and (c)  $g_A = 0.5$ . Each frequency data point (full circle) is divided into two sectors (of different colors) representing the contribution of the breathing observables  $\langle \sum_i \hat{x}_i^2 \rangle_t$  or  $\langle \hat{y}^2 \rangle_t$  to the averaged power spectrum  $\Sigma$  at that frequency (see Sec. III B). The corresponding color intensity indicates the relative strength with respect to the maximum amplitude  $\Sigma_{\max}$  in the averaged power spectrum for fixed  $g_{AB}$  and only modes with contribution above 10% of  $\Sigma_{\max}$  are presented. Crosses stand for frequencies of modes excited within the SMF approximation. Black dashed line indicates the entanglement entropy  $S_{vN}$  of the initial state. All quantities are given in harmonic units.

ingly absent. At positive increasing  $g_{AB}$  the bifurcation of the continuously decaying frequency takes place already for a very weak coupling strength ( $g_{AB} \approx 0.1$ ). It can be related to the fact that the phase separation also takes place at weaker couplings. The character of the excited modes is mostly the same as for  $g_A = 0$ . At negative decreasing  $g_{AB}$  we observe an emerging multifrequency breathing composed of three modes. The lower-frequency mode loses amplitude in favor of higher-frequency modes ( $-0.4 < g_{AB} < -0.1$ ). Then it turns into a single-frequency breathing ( $g_{AB} < -0.4$ ) affecting both components in a similar way.

For weakly repulsive ( $g_A = 0.5$ ) majority particles in Fig. 7(c) the coupling-insensitive mode frequency is still

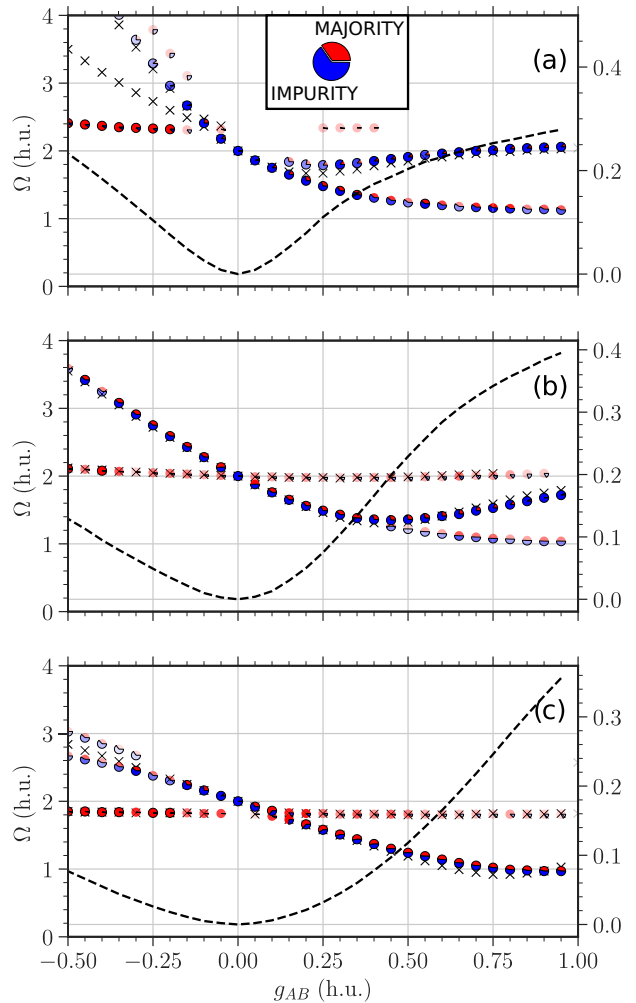


FIG. 8. Same as in Fig. 7 but for  $N_A = 10$ . All quantities are given in harmonic units.

present though energetically shifted downwards to  $\Omega = 1.9$ . The respective mode is weakly represented in the overall dynamics and affects mainly the majority component. The sensitivity to  $g_A$  is yet another indicator that this is the  $\Omega_A$  mode. The point of bifurcation in the lower-frequency branch is located at a stronger coupling  $g_{AB} \approx 1.8$ . Phase separation takes place also at stronger couplings which supports our previous conjecture. At negative  $g_{AB}$  below a certain threshold ( $g_{AB} < -0.3$ ) a third mode is excited. In contrast to  $g_A = 0$ , this additional mode is rather manifested in the impurity breathing and has a larger frequency. In summary, the majority component interaction  $g_A$  determines the coupling value at which the bifurcation takes place as well as the offset of the coupling-insensitive frequency and whether it can be addressed by the current quench protocol.

Next, we double the number of majority component atoms to get an idea of how it affects the excitation spectrum. In the following, we compare the corresponding subfigures of Figs. 7 and 8. We note that at  $N_A = 10$  the interval of the

considered couplings is  $g_{AB} \in [-0.5, 1.0]$  as the convergence is more challenging to achieve beyond  $g_{AB} > 1$ . At  $g_A = 0$  [Fig. 8(b)] the bifurcation point is located at a smaller value of  $g_{AB}$  compared to the  $N_A = 5$  case [see Fig. 7(b)]. Increasing the particle-number imbalance accelerates the phase separation [49]. The coupling-insensitive  $\Omega_A$  mode frequency is barely affected by the particle-number imbalance.

At  $g_A = -0.5$  [Fig. 8(a)] and positive  $g_{AB}$  the minimum of the  $\Omega_{AB}$  frequency mode is shifted to larger frequencies and smaller values of the coupling  $g_{AB}$ . The frequency value recovers back to  $\Omega = 2$  more quickly already at  $g_{AB} \approx 0.75$ . The coupling-insensitive  $\Omega_A$  mode becomes visible at negative  $g_{AB}$  and even dominates the breathing dynamics, although the amplitude decays considerably towards  $g_{AB} = 0$  and there are only minor traces left at positive coupling ( $0.25 < g_{AB} < 0.4$ ). It is certainly present in the breathing dynamics at positive  $g_{AB}$ , but the contribution is not significant enough to overcome the set threshold. The respective frequency is shifted to  $\Omega \approx 2.4$ . At  $g_A = 0.5$  [Fig. 8(c)] the frequency of the coupling-insensitive  $\Omega_A$  mode experiences a slight shift downwards. At negative  $g_{AB}$  it gains amplitude with decreasing  $g_{AB}$  until it becomes a dominant mode below  $g_{AB} \leq -0.25$ . The bifurcation point at positive  $g_{AB}$  is unfortunately not visible within the covered  $g_{AB}$  interval.

Lastly, we want to emphasize the importance of entanglement in our Bose polaron setup. To this end, we neglect it both in the initial state and in the subsequent dynamics (crosses in Figs. 7 and 8). The first striking observation is that in the SMF case, at most *two* frequencies can be extracted. The mode we are missing from the exact simulations is the one whose frequency is a monotonically decreasing function of  $g_{AB}$ , making appearance at finite positive  $g_{AB}$ . We call a mode, which is not reproducible by a SMF ansatz, an entanglement-sensitive mode. It can be assigned to the eigenstate of odd c.m. parity, also called hybrid “sloshing” mode. Regarding the persistent modes, the  $\Omega_A$  mode with coupling-insensitive frequency is overall well captured by the species mean-field ansatz, although it tends to overestimate the frequency for large positive values of  $g_{AB}$ . The  $\Omega_{AB}$  mode, whose frequency is STP function of  $g_{AB}$ , in general is not well matched by SMF ansatz either mispredicting the location [Fig. 7(c)] or the exact value [Fig. 7(a)] of the minimum. Even if both the location and the value of the minimum are well matched [Fig. 7(b)] there is an increasing discrepancy for strong positive  $g_{AB}$ . For a larger particle number (Fig. 8), the consistency between approximated and exact frequencies is much better, though here also we have a mode not reproducible by a SMF ansatz featuring the same functional behavior.

To summarize, we are able to excite up to three breathing modes in the Bose polaron setup by quenching only the impurity. First, there is a coupling-insensitive  $\Omega_A$  majority mode. Its frequency can be manipulated by the particle-number imbalance or the majority component interaction. Second, there is a monotonically decreasing frequency making appearance at finite positive  $g_{AB}$  and converging towards  $\Omega = 1.0$  with increasing  $g_{AB}$ . It cannot be described by the species mean-field ansatz and matches the functional behavior of the hybrid sloshing mode encountered in the 1 + 1 and 2 + 2 mixtures. Third, we have a large-amplitude  $\Omega_{AB}$  mode which is of a

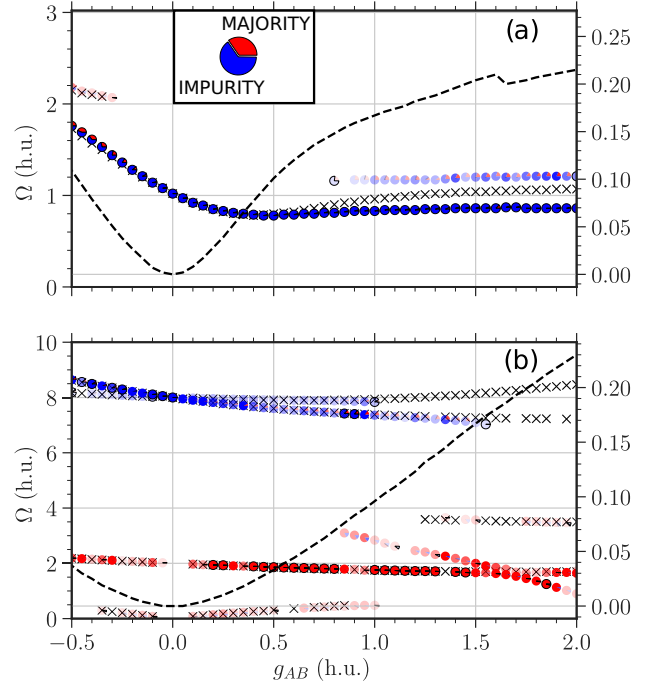


FIG. 9. Frequencies  $\Omega$  of breathing modes for  $N_A = 5$  and  $N_B = 1$  as a function of the intercomponent coupling  $g_{AB}$  at fixed majority component interaction  $g_A = 0$ . The trap ratio is quenched in (a) from  $\eta = 0.536$  to  $0.51$  and in (b) from  $\eta = 4.2$  to  $4$ . Color coding according to Fig. 7. Black dashed line indicates the entanglement entropy  $S_{vN}$  of the initial state. All quantities are given in harmonic units of the majority component.

mixed type. The mode frequency is STP function of  $g_{AB}$  with a minimum being sensitive to  $g_A$  and  $N_A$ .

### C. Impact of the trap

Let us now focus on the impact of the external trap, more specifically we consider a situation where the length scale of the impurity  $l_B = \sqrt{1/\eta}$ , set by the parabolic trap, is either broader ( $l_B = 1.4$ ) or narrower ( $l_B = 0.5$ ) in the postquench system. The quench strength is still 5% of the original trap parameter.

We start with the case of a “broad” impurity  $\eta = 0.51$ . In Figs. 9(a) and 10(a) we show the breathing spectrum for  $N_A = 5$  and 10 majority atoms, respectively. To gain an intuitive picture we set  $g_A = 0$ . For the decoupled case  $g_{AB} = 0$ , the lowest-frequency mode is caused by the eigenstate  $|N_A\rangle \otimes |0, 0, 1\rangle$ , corresponding to a standard breathing of the impurity at frequency  $\Omega = 1.02$ . It is the only mode excited. Once coupled ( $g_{AB} \neq 0$ ), several other eigenstates may become populated leading to additional breathing modes. The states in question can be continuously traced back to the low-energy eigenstates of a decoupled impurity. First, we have the state  $|N_A - 1, 1\rangle \otimes |0, 1\rangle$  corresponding to a hybrid sloshing mode at frequency  $\Omega = 1.51$ . Then follows a quasidegenerate manifold of three modes: two majority component modes at the same frequency  $\Omega = 2$  caused by  $|N_A - 1, 0, 1\rangle \otimes |1\rangle$  and  $|N_A - 2, 2\rangle \otimes |1\rangle$ , and a second order breathing of the

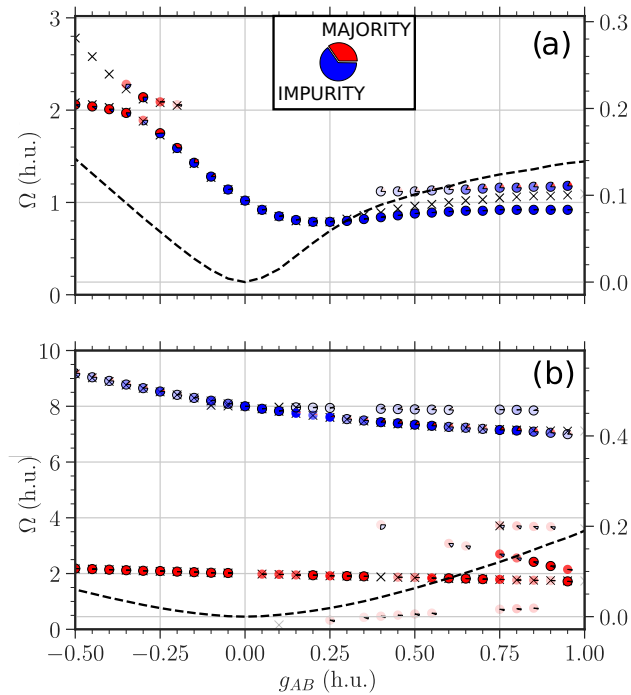


FIG. 10. Same as in Fig. 9 but for  $N_A = 10$ . All quantities are given in harmonic units of the majority component.

impurity at frequency  $\Omega = 2.04$  mediated by  $|N_A\rangle \otimes |0, 0, 0, 1\rangle$ . Any higher-frequency modes are unlikely to be involved.

At weak coupling  $g_{AB}$  there is only one relevant mode excited. It originates from the state  $|N_A\rangle \otimes |0, 0, 1\rangle$  and is barely detectable in the majority component breathing. The corresponding frequency is STP function of  $g_{AB}$  with a minimum at  $g_{AB} \approx 0.5$  for  $N_A = 5$  [Fig. 9(a)] and at  $g_{AB} \approx 0.25$  for  $N_A = 10$  [Fig. 10(a)]. At strong positive  $g_{AB}$ , a beating behavior emerges. The amplitude of the additional mode increases gradually with increasing  $g_{AB}$  while the corresponding frequency  $\Omega \approx 1.2$  is only weakly affected by the intercomponent coupling or the particle number. At negative moderate  $g_{AB}$  there is also a beating. The major amplitude mode, originally being an impurity mode (blue), evolves gradually into the majority component mode (red). The other mode appears just below  $g_{AB} < -0.25$  and affects primarily the majority species.

The SMF fits well the lowest frequency at negative  $g_{AB}$  and at weak positive  $g_{AB}$  until the minimum is reached. Afterwards, it overestimates the frequency having larger deviations at stronger positive  $g_{AB}$ . We witness that SMF is incapable to identify an emerging mode at positive  $g_{AB}$ , though at negative  $g_{AB}$  it does register the beating behavior. It implies that the additional modes entering the dynamics at positive and negative  $g_{AB}$  are of a different character. Based on the insights gained in the previous section, namely, the presence of a breathing mode which is inaccessible to the SMF treatment, we conjecture that the additional mode emerging at positive  $g_{AB}$  stems from the hybrid sloshing mode  $|N_A - 1, 1\rangle \otimes |0, 1\rangle$  at  $g_{AB} = 0$

and  $\Omega = 1.51$ . Its contribution grows as the entanglement becomes stronger.

Next, let us focus on the case of a “narrow” impurity  $\eta = 4$ . The corresponding breathing spectrum is depicted in Fig. 9(b) for  $N_A = 5$  and in Fig. 10(b) for  $N_A = 10$  majority atoms. At  $g_{AB} = 0$  we excite only the standard breathing mode of the impurity at frequency  $\Omega = 8$  caused by the eigenstate  $|N_A\rangle \otimes |0, 0, 1\rangle$ . Considering the amount of available even parity eigenstates with energies up to eight quanta (40 for  $N_A = 5$  and 45 for  $N_A = 10$ ), one might naively think that many modes would be excited at finite  $g_{AB}$ . This is not the case as we count only up to six frequencies. They are well separated from each other and admit a convenient classification: impurity modes (blue) with  $\Omega > 6$  and majority modes (red) with  $\Omega < 4$ .

The impurity features a beating composed of two modes at weak coupling. The gap between the corresponding frequencies grows with increasing  $g_{AB}$ . The one of smaller amplitude vanishes around  $g_{AB} \approx 1.0$ . The contribution of the other mode fades away quickly afterwards until it also disappears. At strong  $g_{AB}$  the impurity motion assimilates the majority component breathing. Both modes are reproducible by SMF ansatz, though SMF overestimates their contribution to the overall dynamics at strong  $g_{AB}$ .

Regarding the majority modes there is one with a nearly constant frequency ( $\Omega \approx 2$ ) entering the dynamics already at weak coupling and making a large contribution to the majority motion across all coupling values. At weak  $g_{AB}$  it is accompanied by an oscillation of a smaller frequency. As the ground state is nondegenerate at  $g_{AB} = 0$ , this frequency corresponds to the gap between the two blue-colored frequencies. It also consistently disappears beyond  $g_{AB} > 1$  along with the impurity modes. The latter are actually replaced by modes of lower frequency. One of them is of particular interest. It appears at  $g_{AB} \approx 1$  for  $N_A = 5$  and at  $g_{AB} \approx 0.5$  for  $N_A = 10$  gaining weight with increasing  $g_{AB}$ . The corresponding frequency is a linearly decreasing function of  $g_{AB}$ . It can be extrapolated to frequency  $\Omega = 5$  at  $g_{AB} = 0$ , matching the energy gap between the ground state  $|N_A\rangle \otimes |1\rangle$  and the hybrid sloshing mode eigenstate  $|N_A - 1, 1\rangle \otimes |0, 1\rangle$ . The entanglement is once again indispensable to account for the respective breathing mode.

To summarize, quenching a broad impurity excites less breathing modes barely affecting the majority motion. Quenching a narrow impurity excites more modes which are energetically well separated: high-frequency impurity-type and low-frequency majority-type modes. In both cases we evidence the presence of an entanglement-sensitive mode. It becomes relevant after some coupling threshold and can be traced back to a hybrid sloshing excitation  $|N_A - 1, 1\rangle \otimes |0, 1\rangle$  at zero coupling.

#### D. Breathing of the first excited state

The Hamiltonian (1) has global reflection symmetry. The eigenstates are therefore separable into two classes of even and odd global parity. The quench operator does not violate that symmetry. Accordingly, an even global parity initial state can be expanded within the subspace of even eigenstates. The odd global parity space of the Hamiltonian has

its own “ground state,” meaning the lowest-energy eigenstate of that subspace. If initialized in such a state, how will each species respond following our quench procedure? Will it be a few-mode breathing within each component, as for the even global parity ground state, or a more complex motion involving many modes? If only a few modes participate, how different are the respective frequencies as compared to the even global parity ground state?

To address the above questions, we start again with the example of a particle-balanced few-body Bose-Bose mixture (see Sec. IV A) at  $\eta = 1$ . There are several major differences regarding the odd global parity subspace. First, in the non-interacting regime the odd global parity “ground state” is twofold degenerate, composed of states where a single particle of either component is excited by one energy quantum:  $|N_A - 1, 1\rangle \otimes |N_B\rangle$  and  $|N_A\rangle \otimes |N_B - 1, 1\rangle$  with respect to harmonic oscillator basis. Once the degeneracy is lifted at finite coupling, the perturbed eigenstates can be distinguished by the c.m. quantum number. Since both states are likely to be populated after the quench, we need to consider each of them as a reference state when evaluating the energy gaps to the neighboring eigenstates. The frequencies of excited modes following a quench of the impurity trap will be contained within the set of these energy gaps. Second, the first-order breathing manifold for odd global parity subspace is composed of three quanta excitations at zero interaction. There are eight of them in total. Half of them are excitations within a single component:  $|N_A - 1, 0, 0, 1\rangle$ ,  $|N_A - 2, 1, 1\rangle$ , and the same for  $B$  species. The other four distribute the three available quanta over both components:  $|N_A - 1, 1\rangle \otimes |N_B - 2, 2\rangle$ ,  $|N_A - 1, 0, 1\rangle \otimes |N_B - 1, 1\rangle$ , and the other way around ( $B \leftrightarrow A$ ).

In Fig. 11 we show the energy gaps between a reference state of even or odd c.m. parity (first or second column, respectively) and energetically closest eigenstates (c.m. quantum number indicated by color) as a function of the intercomponent coupling  $g_{AB}$  for three different intracomponent interaction regimes (rows).

Let us begin with the reference state of even c.m. parity (first column). First, there is a single constant frequency mode  $\Omega = 2$  (blue dotted) for any interaction values. Second, there is a single frequency being a monotonically increasing function of  $g_{AB}$  (green dashed-dotted) and saturating to  $\Omega = 3$  at strong positive  $g_{AB}$ . Third, among the three black solid curves there is one very weakly dependent on the interactions and it recovers to  $\Omega = 2$  at strong positive  $g_{AB}$ , whereas the other two are highly susceptible to interactions and reach values beyond  $\Omega = 3$ . Finally, the lower red dashed curve represents the other reference state of odd c.m. parity. Regarding the frequencies of the remaining three red dashed modes, one of them behaves similar to the green dashed-dotted solid mode, while the other two are highly sensitive to interactions. Some of the crossings seen at  $g_A = 0$  [Fig. 11(b)] among the black solid and red dashed curves become avoided at finite  $g_A$  [Figs. 11(a) and 11(c)] caused by broken-species exchange symmetry. Overall, most frequencies reach values above  $\Omega = 2$  and there is nothing common to the breathing spectrum of the even c.m.-parity ground state (see Fig. 5) except the constant frequency mode.

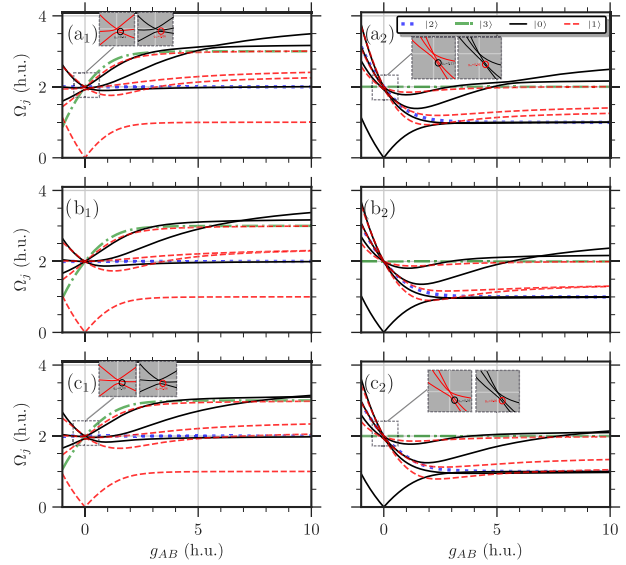


FIG. 11. Energy gaps  $\Omega_j = |E_j - E_{\text{ref}}|$  with respect to lowest-energy reference eigenstates  $|E_{\text{ref}}\rangle$  of odd global parity and even (first column) or odd (second column) c.m. parity in a few-body bosonic mixture  $N_A = N_B = 2$ . The gaps are functions of the intercomponent coupling  $g_{AB}$  at equal trapping frequency ratio  $\eta = 1$ , intracomponent interaction strength  $g_B = 0$  for the second component, and (a)  $g_A = -0.5$ , (b)  $g_A = 0$ , (c)  $g_A = 0.5$  for the first component. Whether the corresponding eigenstates are actually excited depends on the quench protocol. Different colors (line styles) refer to the center-of-mass (c.m.) quantum number in the eigenstate  $|E_j\rangle$ . The c.m. is a decoupled degree of freedom in this harmonic confinement. The insets represent a zoom-in on regions with avoided crossings which are indicated by circles and caused by  $g_A \neq g_B$  asymmetry. Curves of different colors (line styles) may only cross. All quantities are given in harmonic units.

Focusing now on the reference state of odd c.m. parity (second column), we notice that all five frequencies encountered in Fig. 5 have here a corresponding match. The reason is that the reference state is a simple c.m. excitation, being a constant energy shift independent of the interaction strength. Correspondingly, the even global parity ground state and eigenstates responsible for the first-order breathing discussed in Sec. IV A are just spectrally shifted by a common constant. Thus, the corresponding energy gaps remain intact. The four black solid curves are the additional new modes. The lowest one corresponds to the even c.m.-parity reference state of odd global parity. There is one with a monotonically decreasing frequency and two of them are STP functions of  $g_{AB}$  very sensitive to interactions akin to the red dashed mode frequencies. In the Bose polaron setup there are two less “three-quanta” states since the two-particle excitations of the impurity are obviously excluded. However, there is also one more state, namely, a three-particle excitation  $|N_B - 3, 3\rangle$  in the majority component. Thus, the first-order breathing manifold is composed of seven eigenstates in total. Now, we initialize an odd global parity ground state for the subsequent breathing dynamics (see representative examples in Fig. 12 to be compared with Fig. 6) and extract the frequencies of par-



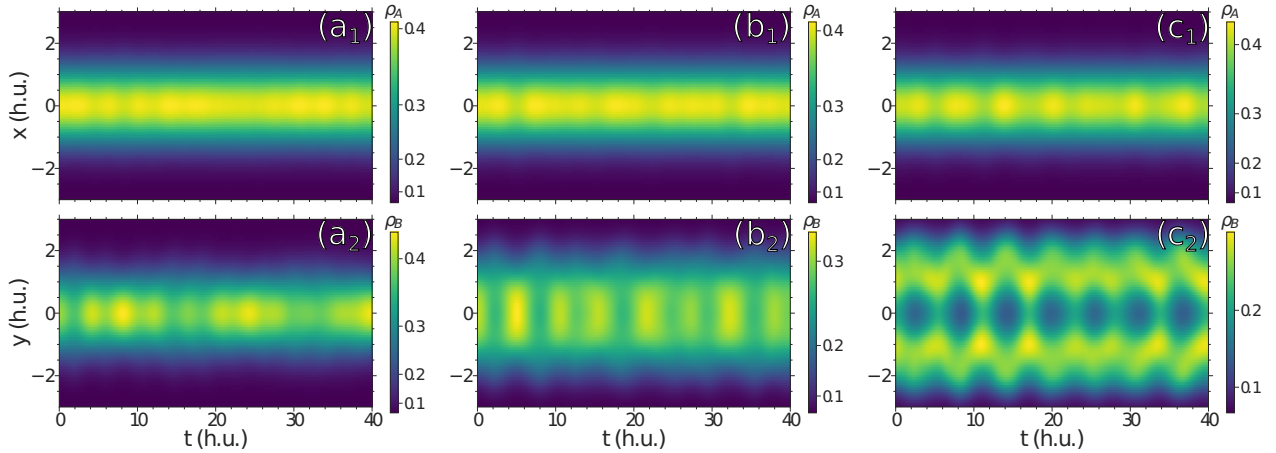


FIG. 12. Breathing oscillations of the one-body densities of the majority component  $\rho_1^A(x)$  (first row) and the impurity  $\rho_1^B(y)$  (second row) at a fixed majority-component interaction  $g_A = 0.5$  for  $N_A = 5$  and  $N_B = 1$  particles initiated by preparation of the first excited state of odd global parity followed by an abrupt change of the trap ratio from  $\eta = 1.05$  to 1. Columns 1–3 correspond to different intercomponent couplings: (a)  $g_{AB} = 0.5$ , (b)  $g_{AB} = 1.0$ , and (c)  $g_{AB} = 1.5$ . All quantities are given in harmonic units.

participating modes shown in Fig. 13. We immediately recognize the frequency pattern from Fig. 7. In particular, we evidence a coupling-insensitive  $\Omega_A$  frequency at  $\Omega \approx 2$ , a monotonically decaying hybrid sloshing mode converging to  $\Omega = 1$  and  $\Omega_{AB}$  mode being an STP function of  $g_{AB}$ . There are, however, several differences. Importantly, both odd global parity reference eigenstates are participating in the dynamics, as indicated by the lowest-frequency curve. They are of opposite c.m. parity. Based on the excitation pattern (cf. Fig. 11) the odd c.m. reference state has a larger contribution than the one of even c.m.. Second, at weak positive  $g_{AB}$  the two odd global parity reference states are dominating the dynamics. The energy gap between them grows with increasing  $g_{AB}$  and approaches its limiting value  $\Omega = 1$ . Meanwhile, there is a gradual transfer of population to the hybrid sloshing eigenstate with a monotonically decaying frequency. Finally, at  $g_A = 0.5$  and positive intermediate  $g_{AB} \approx 1$  as well as at negative  $g_{AB}$  we identify some minor traces of additional modes absent for the even global parity ground state.

To summarize, the breathing response of an odd global parity ground state as compared to the actual ground state of even global parity displays notable differences in the density oscillations but bears strong similarity in the Fourier spectrum. We found an additional low-frequency mode of a mixed type arising from the degeneracy splitting of the odd global parity ground state.

## V. SUMMARY

The breathing dynamics of a few-body Bose polaron in a one-dimensional species-selective parabolic confinement has been investigated in this work by means of the multilayer multiconfiguration time-dependent Hartree method for bosons. The dynamics has been triggered by a weak trap quench of the impurity for different intercomponent couplings  $g_{AB}$  ranging from weak attractive to intermediate repulsive values. The majority motion was affected indirectly via the majority-impurity interaction  $g_{AB}$ . We extracted the frequencies of excited modes

from the breathing observables by using a compressed sensing algorithm. From this we constructed an averaged power spectrum and classified the modes according to their overall contribution to the dynamics. We also determined whether a mode is of majority or impurity type judged by the relative strength of respective observables in the averaged power spectrum. To highlight the importance of entanglement in our setup, we performed the same quench procedure for a species mean-field ansatz, which assumes that a wave function can be written as a single product state of combined majority coordinates and the impurity coordinate.

Different regimes of system parameters have been addressed. The majority component was noninteracting ( $g_A = 0$ ), weakly attractive ( $g_A = -0.5$ ), or weakly repulsive ( $g_A = 0.5$ ) consisting either of  $N_A = 5$  or 10 particles and different ratios of species trapping frequencies including equal localization length ( $\eta = 1$ ), a “broad” impurity ( $\eta = 0.51$ ), and a “narrow” impurity ( $\eta = 4.0$ ) have been taken into account. Finally, we studied the impact of global parity symmetry on the breathing spectrum. To this end, we initialized the system in the first excited state having odd global parity as opposed to the ground state which is even.

For equal traps ( $\eta = 1$ ) we detected up to *three* modes. First, at a weak majority-impurity interaction there is a two-mode beating. One mode is of a majority type. It does a comparatively small contribution to the overall breathing dynamics while its frequency is insensitive to  $g_{AB}$  variations, albeit depending on  $g_A$  and  $N_A$ . It reminds us of the  $\Omega_A$  mode found in a few-body two-component mixture [88], though utterly flattened supposedly due to the particle-number imbalance and the absence of the complementary  $\Omega_B$  mode. Interestingly, it becomes suppressed for a weakly attractive majority species at positive  $g_{AB}$ . The frequency of the second mode decreases monotonically as a function of  $g_{AB}$  until it bifurcates into two distinct frequencies. One of them keeps decreasing and becomes equally represented in both components. Other parameters such as majority-component interaction strength  $g_A$  or the number of majority atoms  $N_A$

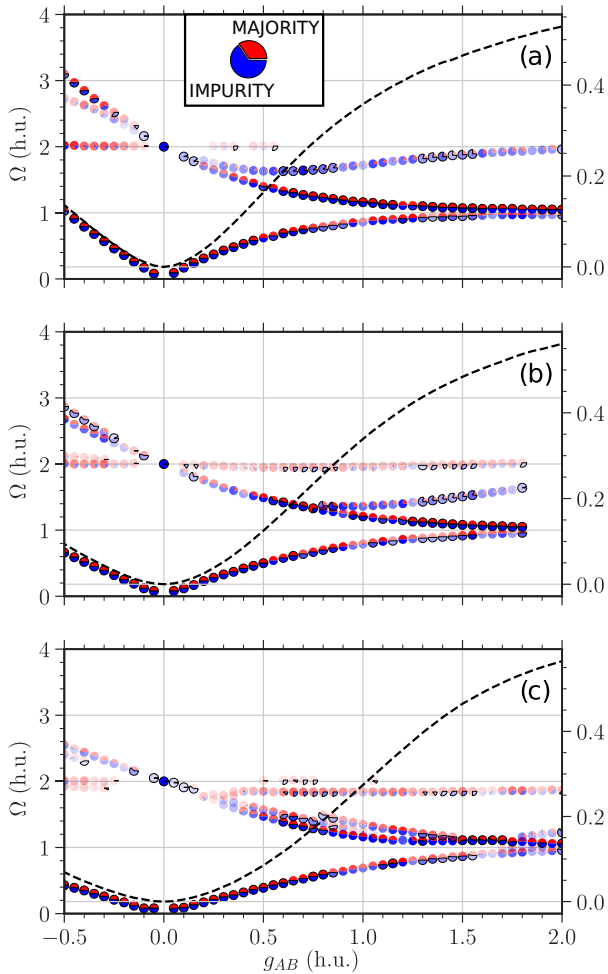


FIG. 13. Frequencies  $\Omega$  of breathing modes excited by quenching the odd global parity ground state  $|E_1\rangle$  of a Bose polaron  $N_A = 5$  and  $N_B = 1$  from a trap ratio  $\eta = 1.05$  to  $1.0$  as a function of the intercomponent coupling  $g_{AB}$  for a fixed majority component interaction (a)  $g_A = -0.5$ , (b)  $g_A = 0$ , and (c)  $g_A = 0.5$ . Color coding as in Fig. 7. Black dashed line indicates the entanglement entropy  $S_{vN}$  of the initial state. All quantities are given in harmonic units.

barely affect this frequency. Why does the frequency behave this way? The corresponding mode is caused by an eigenstate of odd c.m. parity and even global parity. Its eigenenergy is independent of interactions. As the ground-state energy is a monotonically increasing function of  $g_{AB}$  and saturates at hard-core interaction, we obtain a monotonically decreasing energy gap between the two states. Importantly, it cannot be observed for species-symmetric trap quenches and is not a particular feature of the Bose polaron setup but of a two-component mixture in general. Furthermore, the entanglement needs to be taken into account to make the mode numerically visible as we demonstrate by a comparison to a species mean-field ansatz. The other frequency emerging out of the bifurcation bends and saturates back to the noninteracting frequency value with increasing  $g_{AB}$  while dominating the impurity motion. It reminds us of the coupling-sensitive  $\Omega_{AB}$

mode found in a few-body two-component mixture [88], though here it appears to be much more sensitive to system parameters such as  $g_A$  and  $N_A$ .

By broadening the impurity trap ( $\eta = 0.51$ ), only one mode can be excited at weak  $g_{AB}$ . It is of impurity type. The corresponding coupling-sensitive frequency features a minimum at positive  $g_{AB}$  and saturates at large  $g_{AB}$ . With increasing impurity-majority interaction, a beating emerges. At positive  $g_{AB}$  the additional mode is sensitive to the entanglement, while at negative  $g_{AB}$  both frequencies are well matched by the SMF ansatz. For a tightly trapped impurity ( $\eta = 4$ ) up to six frequencies can be observed, though many more modes are in principle available. At weak  $g_{AB}$  we have two impurity-type modes and a single majority-type mode. The two impurity-type modes are of high frequency but are quickly fading away with increasing  $g_{AB}$ . At strong  $g_{AB}$  the impurity oscillations start imitating the majority motion. The lower-frequency majority-type mode has a large contribution to the ongoing dynamics except at very weak  $g_{AB}$ , while the corresponding frequency is rather insensitive to the intercomponent interaction. At finite positive  $g_{AB}$  we evidence the emergence of an entanglement-sensitive mode whose frequency is a monotonically decaying function of  $g_{AB}$ . Thus, the entanglement-sensitive mode is sustained even when the center-of-mass motion cannot be decoupled and, surprisingly, the corresponding frequency maintains its overall qualitative behavior.

Regarding the first excited state of odd global parity as an initial state for the breathing dynamics, we found the corresponding excitation spectrum to bear strong similarity to the one of even global parity ground state. It can be understood as follows. Some of the eigenstates lying in the odd global parity subspace have energies corresponding to the ones of even global parity subspace except for a constant energy shift, which is an integer number (in harmonic units) corresponding to a c.m. excitation. Nevertheless, there are also differences. For a weakly repulsive majority species and at intermediate  $g_{AB}$  we observe several additional modes absent in the ground-state spectrum. This is not surprising since the lowest-energy breathing manifold accessible to the first excited state is larger as compared to the ground state. Importantly, there is a slow-frequency mode equally represented in both components. It is caused by the degeneracy of the first excited state. For that reason, the frequency starts at  $\Omega = 0$  when  $g_{AB} = 0$ . It saturates towards  $\Omega = 1$  with increasing  $g_{AB}$  because the eigenenergy of the first involved state is a monotonically increasing and saturating function of  $g_{AB}$  while the second is independent of  $g_{AB}$ .

## VI. CONCLUSIONS

Overall, the few-body Bose-polaron breathing spectrum has been studied and compared to the one of a particle-balanced Bose-Bose mixture. The species-asymmetric trap quench protocol employed in this work allowed to couple eigenstates of different c.m. parity (at  $\eta = 1$ ) as opposed to a species-symmetric trap quench. We excited a different kind of a breathing mode. The eigenstate responsible for this mode can be traced back to a hybrid sloshing excitation  $|N_A - 1, 1\rangle \otimes |N_B - 1, 1\rangle$  at zero interactions. We gave an

interpretation of the motion induced by this mode for a simple  $1 + 1$  mixture: for a Gaussian background one-body density it induces a breathing motion while for a parity-symmetric two-hump profile we observe a simultaneous outward and inward sloshing motion of the two humps. The mode relies on the presence of entanglement, while its frequency is a monotonically decreasing function of  $g_{AB}$ . This opens the perspective to study the relation between the mode amplitude

and the degree of entanglement, stored in the many-body composite state, adding yet another item into the analysis toolbox of breathing mode diagnostics.

#### ACKNOWLEDGMENT

M.P. gratefully acknowledges a scholarship of the Studienstiftung des deutschen Volkes.

- 
- [1] L. D. Landau, *Phys. Z.* **3**, 664 (1933).  
 [2] S. Pekar, *Sov. Phys.-JETP* **16**, 341 (1946).  
 [3] J. T. Devreese and A. S. Alexandrov, *Rep. Prog. Phys.* **72**, 066501 (2009).  
 [4] A. S. Alexandrov and J. T. Devreese, *Advances in Polaron Physics*, Vol. 159 (Springer, Berlin, 2010)  
 [5] G. D. Mahan, *Many-particle Physics* (Springer, New York, 2013).  
 [6] M. H. Anderson, J. R. Ensher, M. R. Matthews, C. E. Wieman, and E. A. Cornell, *Science* **269**, 198 (1995).  
 [7] K. B. Davis, M.-O. Mewes, M. R. Andrews, N. J. van Druten, D. S. Durfee, D. M. Kurn, and W. Ketterle, *Phys. Rev. Lett.* **75**, 3969 (1995).  
 [8] I. Bloch, J. Dalibard, and W. Zwerger, *Rev. Mod. Phys.* **80**, 885 (2008).  
 [9] C. J. Myatt, E. A. Burt, R. W. Ghrist, E. A. Cornell, and C. E. Wieman, *Phys. Rev. Lett.* **78**, 586 (1997).  
 [10] D. Blume, *Rep. Prog. Phys.* **75**, 046401 (2012).  
 [11] S. Palzer, C. Zipkes, C. Sias, and M. Köhl, *Phys. Rev. Lett.* **103**, 150601 (2009).  
 [12] J. Catani, G. Lamporesi, D. Naik, M. Gring, M. Inguscio, F. Minardi, A. Kantian, and T. Giamarchi, *Phys. Rev. A* **85**, 023623 (2012).  
 [13] T. Fukuhara, A. Kantian, M. Endres, M. Cheneau, P. Schauß, S. Hild, D. Bellem, U. Schollwöck, T. Giamarchi, C. Gross *et al.*, *Nat. Phys.* **9**, 235 (2013).  
 [14] N. Spethmann, F. Kindermann, S. John, C. Weber, D. Meschede, and A. Widera, *Phys. Rev. Lett.* **109**, 235301 (2012).  
 [15] N. B. Jørgensen, L. Wacker, K. T. Skalmstang, M. M. Parish, J. Levinsen, R. S. Christensen, G. M. Bruun, and J. J. Arlt, *Phys. Rev. Lett.* **117**, 055302 (2016).  
 [16] F. Meinert, M. Knap, E. Kirilov, K. Jag-Lauber, M. B. Zvonarev, E. Demler, and H.-C. Nägerl, *Science* **356**, 945 (2017).  
 [17] S. Nascimbène, N. Navon, K. J. Jiang, L. Tarruell, M. Teichmann, J. McKeever, F. Chevy, and C. Salomon, *Phys. Rev. Lett.* **103**, 170402 (2009).  
 [18] A. Schirotzek, C.-H. Wu, A. Sommer, and M. W. Zwierlein, *Phys. Rev. Lett.* **102**, 230402 (2009).  
 [19] M. Koschorreck, D. Pertot, E. Vogt, B. Fröhlich, M. Feld, and M. Köhl, *Nature (London)* **485**, 619 (2012).  
 [20] C. Kohstall, M. Zaccanti, M. Jag, A. Trenkwalder, P. Massignan, G. M. Bruun, F. Schreck, and R. Grimm, *Nature (London)* **485**, 615 (2012).  
 [21] M. Cetina, M. Jag, R. S. Lous, J. T. M. Walraven, R. Grimm, R. S. Christensen, and G. M. Bruun, *Phys. Rev. Lett.* **115**, 135302 (2015).  
 [22] F. Grusdt and E. Demler, *Quantum Matter Ultralow Temp.* **191**, 325 (2015).  
 [23] F. Chevy and C. Mora, *Rep. Prog. Phys.* **73**, 112401 (2010).  
 [24] P. Massignan, M. Zaccanti, and G. M. Bruun, *Rep. Prog. Phys.* **77**, 034401 (2014).  
 [25] H. Fröhlich, *Adv. Phys.* **3**, 325 (1954).  
 [26] C. Chin, R. Grimm, P. Julienne, and E. Tiesinga, *Rev. Mod. Phys.* **82**, 1225 (2010).  
 [27] T. Köhler, K. Góral, and P. S. Julienne, *Rev. Mod. Phys.* **78**, 1311 (2006).  
 [28] A. G. Volosniev and H.-W. Hammer, *Phys. Rev. A* **96**, 031601(R) (2017).  
 [29] F. Grusdt, G. E. Astrakharchik, and E. Demler, *New J. Phys.* **19**, 103035 (2017).  
 [30] F. Grusdt, K. Seetharam, Y. Shchadilova, and E. Demler, *Phys. Rev. A* **97**, 033612 (2018).  
 [31] B. Kain and H. Y. Ling, *Phys. Rev. A* **98**, 033610 (2018).  
 [32] M. Drescher, M. Salmhofer, and T. Enss, *Phys. Rev. A* **99**, 023601 (2019).  
 [33] J. Jäger, R. Barnett, M. Will, and M. Fleischhauer, *Phys. Rev. Research* **2**, 033142 (2020).  
 [34] M. Drescher, M. Salmhofer, and T. Enss, *Phys. Rev. Research* **2**, 032011(R) (2020).  
 [35] T. Giamarchi, *Quantum Physics in One Dimension*, Vol. 121 (Clarendon, Oxford, 2003).  
 [36] M. Olshanii, *Phys. Rev. Lett.* **81**, 938 (1998).  
 [37] T. Bergeman, M. G. Moore, and M. Olshanii, *Phys. Rev. Lett.* **91**, 163201 (2003).  
 [38] E. Haller, M. J. Mark, R. Hart, J. G. Danzl, L. Reichsöllner, V. Melezhik, P. Schmelcher, and H.-C. Nägerl, *Phys. Rev. Lett.* **104**, 153203 (2010).  
 [39] M. Girardeau, *J. Math. Phys.* **1**, 516 (1960).  
 [40] T. Kinoshita, T. Wenger, and D. S. Weiss, *Science* **305**, 1125 (2004).  
 [41] B. Paredes, A. Widera, V. Murg, O. Mandel, S. Fölling, I. Cirac, G. V. Shlyapnikov, T. W. Hänsch, and I. Bloch, *Nature (London)* **429**, 277 (2004).  
 [42] T. Sowiński and M. Á. García-March, *Rep. Prog. Phys.* **82**, 104401 (2019).  
 [43] O. E. Alon, R. Beinke, and L. S. Cederbaum, *arXiv:2101.11615*.  
 [44] U. Schollwöck, *Rev. Mod. Phys.* **77**, 259 (2005).  
 [45] L. Cao, V. Bolsinger, S. Mistakidis, G. Koutentakis, S. Krönke, J. Schurer, and P. Schmelcher, *J. Chem. Phys.* **147**, 044106 (2017).  
 [46] E. Bentine, T. Harte, K. Luksch, A. Barker, J. Mur-Petit, B. Yuen, and C. Foot, *J. Phys. B: At., Mol. Opt. Phys.* **50**, 094002 (2017).

- [47] A. Barker, S. Sunami, D. Garrick, A. Beregi, K. Luksch, E. Bentine, and C. Foot, *J. Phys. B: At., Mol. Opt. Phys.* **53**, 155001 (2020).
- [48] K. Keiler and P. Schmelcher, *Phys. Rev. A* **100**, 043616 (2019).
- [49] M. Pyzh and P. Schmelcher, *Phys. Rev. A* **102**, 023305 (2020).
- [50] M. Pyzh, K. Keiler, S. I. Mistakidis, and P. Schmelcher, *Entropy* **23**, 290 (2021).
- [51] T. Lee, F. Low, and D. Pines, *Phys. Rev.* **90**, 297 (1953).
- [52] F. Dalfovo, S. Giorgini, L. P. Pitaevskii, and S. Stringari, *Rev. Mod. Phys.* **71**, 463 (1999).
- [53] J. Abraham and M. Bonitz, *Contrib. Plasma Phys.* **54**, 27 (2014).
- [54] C. R. McDonald, G. Orlando, J. W. Abraham, D. Hochstuhl, M. Bonitz, and T. Brabec, *Phys. Rev. Lett.* **111**, 256801 (2013).
- [55] H. Moritz, T. Stöferle, M. Köhl, and T. Esslinger, *Phys. Rev. Lett.* **91**, 250402 (2003).
- [56] G. E. Astrakharchik, R. Combescot, X. Leyronas, and S. Stringari, *Phys. Rev. Lett.* **95**, 030404 (2005).
- [57] T. Stöferle, H. Moritz, C. Schori, M. Köhl, and T. Esslinger, *Phys. Rev. Lett.* **92**, 130403 (2004).
- [58] A. Altmeyer, S. Riedl, C. Kohstall, M. J. Wright, R. Geursen, M. Bartenstein, C. Chin, J. H. Denschlag, and R. Grimm, *Phys. Rev. Lett.* **98**, 040401 (2007).
- [59] E. Haller, M. Gustavsson, M. J. Mark, J. G. Danzl, R. Hart, G. Pupillo, and H.-C. Nägerl, *Science* **325**, 1224 (2009).
- [60] B. Fang, G. Carleo, A. Johnson, and I. Bouchoule, *Phys. Rev. Lett.* **113**, 035301 (2014).
- [61] A. Di Carli, C. D. Colquhoun, G. Henderson, S. Flannigan, G.-L. Oppo, A. J. Daley, S. Kuhr, and E. Haller, *Phys. Rev. Lett.* **123**, 123602 (2019).
- [62] D. Luo, Y. Jin, J. H. V. Nguyen, B. A. Malomed, O. V. Marchukov, V. A. Yurovsky, V. Dunjko, M. Olshanii, and R. G. Hulet, *Phys. Rev. Lett.* **125**, 183902 (2020).
- [63] T. H. Johnson, M. Bruderer, Y. Cai, S. R. Clark, W. Bao, and D. Jaksch, *Europhys. Lett.* **98**, 26001 (2012).
- [64] B. Huang, I. Fritsche, R. S. Lous, C. Baroni, J. T. M. Walraven, E. Kirilov, R. Grimm *et al.*, *Phys. Rev. A* **99**, 041602(R) (2019).
- [65] P. T. Grochowski, T. Karpiuk, M. Brewczyk, and K. Rzażewski, *Phys. Rev. Lett.* **125**, 103401 (2020).
- [66] S. Stringari, *Phys. Rev. Lett.* **77**, 2360 (1996).
- [67] C. Menotti and S. Stringari, *Phys. Rev. A* **66**, 043610 (2002).
- [68] A. Minguzzi and D. M. Gangardt, *Phys. Rev. Lett.* **94**, 240404 (2005).
- [69] E. Quinn and M. Haque, *Phys. Rev. A* **90**, 053609 (2014).
- [70] S. Bauch, K. Balzer, C. Henning, and M. Bonitz, *Phys. Rev. B* **80**, 054515 (2009).
- [71] J. W. Abraham, K. Balzer, D. Hochstuhl, and M. Bonitz, *Phys. Rev. B* **86**, 125112 (2012).
- [72] J. W. Abraham, M. Bonitz, C. McDonald, G. Orlando, and T. Brabec, *New J. Phys.* **16**, 013001 (2014).
- [73] S. De Palo, E. Orignac, M. L. Chiofalo, and R. Citro, *Phys. Rev. B* **103**, 115109 (2021).
- [74] S. Stringari, *Phys. Lett. B* **108**, 232 (1982).
- [75] D. Ledesma, A. Romero-Ros, A. Polls, and B. Juliá-Díaz, *Europhys. Lett.* **127**, 56001 (2019).
- [76] A. Rojo-Francàs, A. Polls, and B. Juliá-Díaz, *Mathematics* **8**, 1196 (2020).
- [77] R. Schmitz, S. Krönke, L. Cao, and P. Schmelcher, *Phys. Rev. A* **88**, 043601 (2013).
- [78] T. Keller and T. Fogarty, *Phys. Rev. A* **94**, 063620 (2016).
- [79] A. I. Gudyma, G. E. Astrakharchik, and M. B. Zvonarev, *Phys. Rev. A* **92**, 021601(R) (2015).
- [80] W. Tschischik and M. Haque, *Phys. Rev. A* **91**, 053607 (2015).
- [81] M. Theisen and A. I. Streltsov, *Phys. Rev. A* **94**, 053622 (2016).
- [82] Y. Y. Atas, I. Bouchoule, D. M. Gangardt, and K. V. Kheruntsyan, *Phys. Rev. A* **96**, 041605 (2017).
- [83] B. D. Esry and C. H. Greene, *Phys. Rev. A* **57**, 1265 (1998).
- [84] T. Busch, J. I. Cirac, V. M. Pérez-García, and P. Zoller, *Phys. Rev. A* **56**, 2978 (1997).
- [85] A. Sartori and A. Recati, *Eur. Phys. J. D* **67**, 260 (2013).
- [86] S. Peotta, D. Rossini, M. Polini, F. Minardi, and R. Fazio, *Phys. Rev. Lett.* **110**, 015302 (2013).
- [87] S. Mistakidis, G. Katsimiga, P. Kevrekidis, and P. Schmelcher, *New J. Phys.* **20**, 043052 (2018).
- [88] M. Pyzh, S. Krönke, C. Weitenberg, and P. Schmelcher, *New J. Phys.* **20**, 015006 (2018).
- [89] S. Mistakidis, G. Koutentakis, G. Katsimiga, T. Busch, and P. Schmelcher, *New J. Phys.* **22**, 043007 (2020).
- [90] S. Yip, *Phys. Rev. A* **64**, 023609 (2001).
- [91] P. Siegl, S. I. Mistakidis, and P. Schmelcher, *Phys. Rev. A* **97**, 053626 (2018).
- [92] K. Mukherjee, S. I. Mistakidis, S. Majumder, and P. Schmelcher, *Phys. Rev. A* **102**, 053317 (2020).
- [93] K. M. Mittal, S. I. Mistakidis, P. G. Kevrekidis, and P. Schmelcher, *Phys. Rev. A* **102**, 013302 (2020).
- [94] X. Andrade, J. N. Sanders, and A. Aspuru-Guzik, *Proc. Natl. Acad. Sci. U.S.A.* **109**, 13928 (2012).
- [95] T.-L. Ho and V. B. Shenoy, *Phys. Rev. Lett.* **77**, 3276 (1996).
- [96] H. Pu and N. P. Bigelow, *Phys. Rev. Lett.* **80**, 1130 (1998).
- [97] S. Zöllner, H.-D. Meyer, and P. Schmelcher, *Phys. Rev. A* **78**, 013629 (2008).
- [98] Y. Hao and S. Chen, *Eur. Phys. J. D* **51**, 261 (2009).
- [99] F. Deuretzbacher, D. Becker, J. Bjerlin, S. M. Reimann, and L. Santos, *Phys. Rev. A* **90**, 013611 (2014).
- [100] A. G. Volosniev, D. Petrosyan, M. Valiente, D. V. Fedorov, A. S. Jensen, and N. T. Zinner, *Phys. Rev. A* **91**, 023620 (2015).
- [101] L. Cao, S. Krönke, O. Vendrell, and P. Schmelcher, *J. Chem. Phys.* **139**, 134103 (2013).
- [102] S. Krönke, L. Cao, O. Vendrell, and P. Schmelcher, *New J. Phys.* **15**, 063018 (2013).
- [103] J. Light, I. Hamilton, and J. Lill, *J. Chem. Phys.* **82**, 1400 (1985).
- [104] M. H. Beck, A. Jäckle, G. A. Worth, and H.-D. Meyer, *Phys. Rep.* **324**, 1 (2000).
- [105] A. Raab, *Chem. Phys. Lett.* **319**, 674 (2000).
- [106] E. van den Berg and M. P. Friedlander, *SIAM J. Sci. Comput.* **31**, 890 (2009).
- [107] I. Loris, *Comput. Phys. Commun.* **179**, 895 (2008).
- [108] T. Busch, B.-G. Englert, K. Rzażewski, and M. Wilkens, *Found. Phys.* **28**, 549 (1998).

**Phase separation of a Bose-Bose mixture: Impact of the trap and particle-number imbalance**Maxim Pyzh<sup>1,\*</sup> and Peter Schmelcher<sup>1,2,†</sup><sup>1</sup>*Zentrum für Optische Quantentechnologien, Universität Hamburg, Luruper Chaussee 149, 22761 Hamburg, Germany*<sup>2</sup>*The Hamburg Centre for Ultrafast Imaging, Universität Hamburg, Luruper Chaussee 149, 22761 Hamburg, Germany*

(Received 16 May 2020; accepted 14 July 2020; published 5 August 2020)

We explore a few-body mixture of two bosonic species confined in quasi-one-dimensional parabolic traps of different length scales. The ground-state phase diagrams in the three-dimensional parameter space spanned by the harmonic length scale ratio, interspecies coupling strength, and particle-number ratio are investigated. As a first case study we use the mean-field ansatz (MF) to perform a detailed analysis of the separation mechanism. It allows us to derive a simple and intuitive rule predicting which of the immiscible phases is energetically more favorable at the miscible-immiscible phase boundary. We estimate the critical coupling strength for the miscible-immiscible transition and perform a comparison to correlated many-body results obtained by means of the multilayer multiconfiguration time-dependent Hartree method for bosonic mixtures (ML-X). At a critical ratio of the trap frequencies, determined solely by the particle-number ratio, the deviations between MF and ML-X are very pronounced and can be attributed to a high degree of entanglement between the components. As a result, we evidence the breakdown of the effective one-body picture. Additionally, when many-body correlations play a substantial role, the one-body density is in general not sufficient for deciding upon the phase at hand which we demonstrate exemplarily.

DOI: [10.1103/PhysRevA.102.023305](https://doi.org/10.1103/PhysRevA.102.023305)**I. INTRODUCTION**

Binary mixtures of ultracold gases have been extensively studied over the past years. They represent a unique platform for the investigation of complex interacting many-body quantum systems in a well-controlled environment. In particular, it is experimentally possible to shape the geometry of the trap [1], to reduce the dimensionality of the relevant motion [2,3], to tune the interparticle interactions [4–8], and prepare samples of only a few atoms [9,10]. Numerous experiments have been conducted with different hyperfine states [11–24], different elements [25–38], or different isotopes [39,40] to reveal how the interplay between two condensates impacts their stationary properties and nonequilibrium dynamics. Highlights of these explorations include among others the phase separation between the components and symmetry-breaking phenomena [12,17,36,37,39], the observation of Efimov physics [38], and creation of deeply bound dipolar molecules [28,32,33], as well as dark-bright solitary waves [18,19] and quantum droplets [23,24].

One of the key properties, which makes the multicomponent systems attractive and their physics very rich, is the miscibility, which has significant implications for sympathetic cooling [15,26], coarse-graining dynamics [41–44], and vortex formation [45,46], to name a few. In the very early theoretical investigations a very rich phase space for the ground state of the Bose-Bose mixture has been identified. These investigations [47–52] are based on the one-body densities

obtained from solving the underlying mean-field equations, commonly known as Gross-Pitaevskii equations. In case of a weak intercomponent coupling one finds a miscible phase with a high spatial overlap between the components. For a sufficiently large repulsive coupling there are three types of segregated phases with a rather small overlap. Two of them are core-shell phases with one component being symmetrically surrounded by the other component, whereas the third is an asymmetrical phase, where the rotational or parity symmetry of the underlying trapping potential is broken. Neglecting the kinetic energy (Thomas-Fermi approximation), a simple separation criterion for the miscible-immiscible transition has been derived [53–55]. It depends solely on the intraspecies and interspecies interaction strengths, which are easily adjustable by Feshbach or confinement-induced resonances [4–8].

However, it has been shown that this separation criterion, while valid in homogeneous systems, should be applied with care in inhomogeneous geometries. Thus, in a harmonic confinement, system parameters such as trap frequency, particle numbers, and mass ratio have also an impact on the miscible-immiscible phase boundary [56–60]. The miscibility of a binary mixture of both bosons and fermions has been recently addressed also in other trapping geometries, i.e., in a box [61], double well [62–64], ring lattice [65–67], and combinations thereof [68], as well as the dynamical aspect of phase separation leading to pattern formations [69–72]. From the intuitive point of view, the trap pressure favors miscibility since it costs energy to extend in space. Thus, it requires stronger intercomponent repulsion for the species to separate. However, there are still open questions regarding the impact of different length scales, the characterization of boundaries

\*mpyzh@physnet.uni-hamburg.de

†pschmelc@physnet.uni-hamburg.de

between the immiscible phases, and what type of separation will occur once the critical coupling is reached.

Another relevant topic affecting the critical coupling strength for a transition as well as the resulting type of phase are the interspecies correlations, which generate entanglement between the components and lead to bunching of particles of the same species. Although a mean-field treatment is often justified in experimental setups, a very thorough numerical analysis of one-dimensional (1D) few-body systems has revealed that an asymmetric immiscible phase is one of the two possible configurations of an entangled many-body state, the other one being the mirror image. The one-body densities of this so-called composite fermionization phase [73–77] preserve parity symmetry of the underlying trapping potential and have a high spatial overlap, which is uncharacteristic for an immiscible phase. Nevertheless, the components are indeed separated, which is encoded in the interspecies two-body density matrix. In experiments, the single shots do not represent one-body densities but are projections on one of the two mutually exclusive configurations. An averaging procedure would reveal a parity-preserving density, unless the Hamiltonian itself violates that symmetry, such as not coinciding trap centers of the one-body potentials. Apart from composite fermionization, there are a whole class of so-called spin-chain phases with an even higher degree of entanglement [78–80]. When all interactions in the system become nearly resonant, many states become quasidegenerate and particles, being bosons, gain fermionic features like the Pauli exclusion principle.

Considering the above, our work addresses three different points. First, we characterize the phase diagram in a three-dimensional parameter space spanned by the ratio of the harmonic trap lengths, the interspecies coupling strength, and the particle-number ratio. We switch off intracomponent interactions to reduce the complexity and gain a better understanding of the separation process. A very rich phase diagram is revealed admitting two tricritical points, where three phases may coexist. Second, within the framework of a mean-field approximation, we perform a detailed analysis of the separation mechanism. Equipped with this knowledge we derive a selection rule for phase separation processes and a simple algorithm to estimate the miscible-immiscible phase boundary. Finally, we investigate the deviations of the mean-field picture to a many-body approach. For this we use the multilayer multiconfiguration time-dependent Hartree method for bosonic mixtures [81–83]. We find that in the vicinity of the high-entanglement regime the phase diagram is indeed greatly affected. The symmetry-broken phase is replaced by the composite fermionization, while the onset of symmetry breaking is linked to the degree of entanglement reaching a certain threshold. Furthermore, the location of this beyond-mean-field regime strongly depends on the harmonic length scale ratio and the particle-number ratio. We also find that the one-body density is in general not sufficient to distinguish between a core-shell phase and the composite fermionization.

This work is organized as follows. In Sec. II we introduce our physical setup and in Sec. III our computational approach. Section IV is dedicated to a detailed study of a few-body mixture. Section IV A provides intuitive insights in the framework of the mean-field approximation, while Sec. IV B

focuses on correlation and entanglement effects using multilayer multiconfiguration time-dependent Hartree method for bosonic mixtures. The few-to-many-body transition is subject of Sec. V. Finally, we summarize our findings in Sec. VI.

## II. GENERAL FRAMEWORK

Our system consists of a particle-imbalanced mixture of two distinguishable bosonic components, denoted by  $\sigma \in \{M, I\}$ , with  $N_M$  particles in the majority component and  $N_I$  impurities. All particles are assumed to be of equal mass  $m$  and the intracomponent interactions are assumed to be zero or negligibly small. The majority species interacts with the impurities via  $s$ -wave contact interaction of coupling strength  $g_{MI}$ . The species are confined in separate quasi-1D harmonic traps of different length scales  $a_\sigma = \sqrt{\hbar/m\omega_\sigma}$  with trap frequency  $\omega_\sigma$  and coinciding trap centers. By choosing  $a_M$  and  $\hbar\omega_M$  as length and energy scales we arrive at the rescaled Hamiltonian:

$$\begin{aligned} H &= H_M + H_I + H_{MI} \\ &= \sum_{i=1}^{N_M} \left( -\frac{1}{2} \frac{\partial^2}{\partial x_i^2} + \frac{1}{2} x_i^2 \right) + \sum_{i=1}^{N_I} \left( -\frac{1}{2} \frac{\partial^2}{\partial y_i^2} + \frac{1}{2} \eta^2 y_i^2 \right) \\ &\quad + g_{MI} \sum_{i=1}^{N_M} \sum_{j=1}^{N_I} \delta(x_i - y_j), \end{aligned} \quad (1)$$

where  $x_i$  labels the spatial coordinate of the  $i$ th majority particle,  $y_i$  of the  $i$ th impurity particle, and  $\eta = \omega_I/\omega_M$  denotes the trap frequency ratio.

In this work we focus on the ground-state characterization and consider both attractive and repulsive interactions ranging from weak to intermediate couplings  $g_{MI} \in [-2, 2]$  with the impurity being localized or delocalized with respect to the majority species, i.e.,  $a_I/a_M = \sqrt{1/\eta} \in [0.5, 1.5]$ . We also study the impact of the particle-number ratio  $N_I/N_M$  on the system's properties concentrating on a few-body system.

All the ingredients necessary for the realization of such a Hamiltonian system have been demonstrated experimentally. Mixtures of two-component BECs with the same mass can be prepared with different atomic spin states [11–24]. The 1D geometry can be achieved by strong transversal confinement or by a two-dimensional optical lattice. The interaction strengths are tunable by Feshbach and confinement-induced resonances allowing to vary the coupling strength between the components and to make the intracomponent interactions negligible [4–8]. Species-dependent trapping techniques have been demonstrated [84,85]. Few-body systems are obtainable for fermions via trap spilling [86] and for bosons by cutting out a subsystem of a Mott insulator [87]. High-resolution measurements with single-atom sensitivity have been proposed for nonlattice traps by using a quantum gas microscope [88]. The experimental realization, however, has yet to be demonstrated.

## III. COMPUTATIONAL APPROACH

To find the ground state of our binary mixture, we employ imaginary-time propagation by means of the multilayer multiconfigurational time-dependent Hartree method for atomic mixtures (ML-MCTDHX). For reasons of brevity we call it

ML-X from now on. This multiconfigurational wave-function-based method for efficiently solving the time-dependent Schrödinger equation was first developed for distinguishable degrees of freedom [89] and ML-X is an extension to indistinguishable particles such as bosons or fermions and mixtures thereof [81–83]. ML-X is an *ab initio* method, whose power lies in expanding the wave function in time-dependent basis functions. Let us demonstrate the underlying ansatz for the system at hand:

$$|\Psi(t)\rangle = \sum_{i=1}^S \sqrt{\lambda_i(t)} |\Psi_i^M(t)\rangle \otimes |\Psi_i^I(t)\rangle, \quad (2)$$

$$|\Psi_i^\sigma(t)\rangle = \sum_{\vec{n}^\sigma | N_\sigma} C_{i,\vec{n}^\sigma}(t) |\vec{n}^\sigma(t)\rangle. \quad (3)$$

The time-dependent many-body wave function  $|\Psi(t)\rangle$  has two layers: the so-called species layer (2) and the particle layer (3). In the first step (2) we separate majority and impurity species and assign them to  $S \in \mathbb{N}$  corresponding species wave functions  $|\Psi_i^\sigma(t)\rangle$ . The time-dependent coefficients  $\lambda_i(t)$  are normalized  $\sum_{i=1}^S \lambda_i(t) = 1$  and describe the degree of entanglement between the components. In case  $\exists i \in \{1, \dots, S\} : \lambda_i(t) \approx 1$  the components are said to be disentangled. In the second step (3) each species wave function  $|\Psi_i^\sigma(t)\rangle$ , which depends on  $N_\sigma$  indistinguishable coordinates, is expanded in terms of species-dependent symmetrized product states, also known as permanents or number states  $|\vec{n}^\sigma\rangle = |n_1^\sigma, \dots, n_{s_\sigma}^\sigma\rangle$  admitting  $s_\sigma \in \mathbb{N}$  normalized single-particle functions (SPF)  $|\varphi_j^\sigma(t)\rangle$ . The sum is over all possible configurations  $\vec{n}^\sigma | N_\sigma$  fulfilling the constraint  $\sum_{i=1}^{s_\sigma} n_i^\sigma = N_\sigma$ . The time dependence of number states is meant implicitly through the time dependence of the underlying SPFs. Finally, each SPF is represented on a primitive one-dimensional time-independent grid [90].

When one applies the Dirac-Frenkel variational principle [91] to the above ansatz, one obtains coupled equations of motion for the expansion coefficients  $\lambda_i(t)$ ,  $C_{i,\vec{n}^\sigma}(t)$  and the SPFs  $|\varphi_j^\sigma(t)\rangle$ . This procedure allows to considerably reduce the size of the basis set as compared to choosing time-independent SPFs constituting the number states on the particle layer (3). We note that  $S = 1 \wedge s_\sigma = 1$  is equivalent to solving coupled Gross-Pitaevskii equations. We will show parameter regions, where the mean-field description is valid and regions where it fails as a result of increasing interspecies correlations. These generate entanglement between the components and decrease the degree of condensation of the noninteracting majority atoms.

The results of the ML-X calculations are considered to be converged if two criteria are simultaneously satisfied. First, the expansion coefficients  $\lambda_i$  on the species layer as well as populations of the natural orbitals  $m_i^\sigma$ <sup>1</sup> of species  $\sigma$  on the particle layer feature an exponential decay<sup>2</sup> as a function of the number of orbitals. This ensures that every newly added

orbital or SPF adds a significantly smaller correction to the many-body wave function. Second, the smallest coefficients  $\lambda_S < \epsilon$  and  $m_{s_\sigma}^\sigma < \epsilon$  are below some threshold value  $\epsilon$ . The value of  $\epsilon$  depends in general on the observable of interest and ensures that the least contributing orbital or SPF does only a minor correction to the observable. The ML-X simulations obtained in this work are converged in the above sense with  $\epsilon = 10^{-3}$  unless stated otherwise.

In the following, we will often refer to the one-body density  $\rho_1^\sigma(z)$  of species  $\sigma$ , two-body density matrix  $\rho_2^\sigma(z, z')$  of species  $\sigma$ , and interspecies two-body density matrix  $\rho_2^{MI}(x, y)$  of the many-body density operator  $\hat{\rho} = |\Psi\rangle\langle\Psi|$  defined as

$$\rho_1^\sigma(z) = \langle z | \text{tr}_{N_\sigma \setminus 1} \{ \text{tr}_{N_\sigma} \{ \hat{\rho} \} \} | z \rangle, \quad (4)$$

$$\rho_2^\sigma(z, z') = \langle z, z' | \text{tr}_{N_\sigma \setminus 2} \{ \text{tr}_{N_\sigma} \{ \hat{\rho} \} \} | z, z' \rangle, \quad (5)$$

$$\rho_2^{MI}(x, y) = \langle x, y | \text{tr}_{N_M \setminus 1} \{ \text{tr}_{N_I \setminus 1} \{ \hat{\rho} \} \} | x, y \rangle, \quad (6)$$

where  $N_\sigma \setminus n$  stands for integrating out  $N_\sigma - n$  coordinates of component  $\sigma$  and  $\bar{\sigma} \neq \sigma$ .

#### IV. PHASE SEPARATION: FEW-BODY MIXTURE

We start our analysis with a few-body system consisting of  $N_M = 5$  majority particles with  $N_I \in \{1, 2\}$  impurities. In Sec. V we will discuss cases with larger particle imbalance. Since we aim at the comparison between the mean-field approximation and a many-body approach, we can ensure reasonably converged results only for relatively small system sizes. As we have emphasized previously in Sec. II, such few-body systems are experimentally accessible.

The outline is as follows. First, in Sec. IV A, we obtain the phase diagram within the mean-field approximation. We uncover the mechanism responsible for the phase separation by using an effective description and apply the obtained intuition to derive an estimate for the miscible-immiscible phase boundary. Second, in Sec. IV B, we perform a comparison to the correlated many-body treatment by means of ML-X. Apart from visible changes in the phase diagram we identify the parameter space with a quick buildup of the entanglement reaching large values already for moderate couplings. We then develop an understanding how our intuitive one-body picture is altered due to the presence of entanglement and what implications it has for the ground-state phases, in particular in the parameter space with considerable entanglement.

##### A. Mean-field approach: Basic mechanism of phase separation

For the mean-field description we choose a single species orbital  $S = 1$ , yielding a nonentangled state  $|\Psi(t)\rangle = |\Psi^M(t)\rangle \otimes |\Psi^I(t)\rangle$  on the species layer. On the particle layer a single SPF  $s_\sigma = 1$  is used for each component, meaning that particles of the same species are forced to condense into the same single-particle state  $\varphi^\sigma(z, t)$  and  $|N_\sigma\rangle$  is the only possible number state on the particle level. Thus, our ansatz is  $|\Psi(t)\rangle = |N_M(t)\rangle \otimes |N_I(t)\rangle$  and only  $\varphi^\sigma(z, t)$  are time dependent. As a result of imaginary-time propagation, we end up with the ground-state orbitals  $\varphi_{\text{MF}}^\sigma(z)$ . The interpretation of the mean-field treatment is that each species feels in addition to its own external potential an averaged one-body potential

<sup>1</sup>In the spectral decomposition of the one-body density operator  $\hat{\rho}^\sigma = \sum_{i=1}^{s_\sigma} m_i^\sigma |m_i^\sigma\rangle\langle m_i^\sigma|$  the  $m_i^\sigma$  are called natural populations and  $|m_i^\sigma\rangle$  natural orbitals.

<sup>2</sup> $\lambda_i$  and  $m_i^\sigma$  are sorted by magnitude in descending order.

induced by the other component. To obtain the effective mean-field Hamiltonian  $H_\sigma^{\text{MF}}$  of species  $\sigma$  we need to integrate out the other component  $\bar{\sigma}$ . For convenience, we also subtract the energy offset  $c_{\bar{\sigma}} = \langle N_{\bar{\sigma}} | H_{\bar{\sigma}} | N_{\bar{\sigma}} \rangle$  caused by the one-body energy of component  $\bar{\sigma}$ :

$$\begin{aligned} H_\sigma^{\text{MF}} &= \langle N_{\bar{\sigma}} | H | N_{\bar{\sigma}} \rangle - c_{\bar{\sigma}} \\ &= H_\sigma + N_{\bar{\sigma}} g_{M\bar{\sigma}} \sum_{i=1}^{N_\sigma} \rho_{\text{MF}}^{\bar{\sigma}}(z_i) \\ &= \sum_{i=1}^{N_\sigma} \left( -\frac{1}{2} \frac{\partial^2}{\partial z_i^2} + V_\sigma(z_i) + V_\sigma^{\text{ind}}(z_i) \right) \\ &= \sum_{i=1}^{N_\sigma} \left( -\frac{1}{2} \frac{\partial^2}{\partial z_i^2} + V_\sigma^{\text{eff}}(z_i) \right), \end{aligned} \quad (7)$$

where  $\rho_{\text{MF}}^\sigma(z) = |\varphi_{\text{MF}}^\sigma(z)|^2$  is the one-body density of species  $\sigma$  normalized as  $\int dz \rho_{\text{MF}}^\sigma(z) = 1$ ,  $V_\sigma^{\text{ind}}(z) = N_{\bar{\sigma}} g_{M\bar{\sigma}} \rho_{\text{MF}}^{\bar{\sigma}}(z)$  the induced one-body potential,  $V_\sigma^{\text{eff}}(z) = V_\sigma(z) + V_\sigma^{\text{ind}}(z)$  the effective one-body potential and  $\bar{\sigma} \neq \sigma$ .

To systematically distinguish between different phases, we define the following two functions, applicable also in the more general case of a many-body treatment in Sec. IV B:

$$\Delta_\sigma = \frac{\rho_1^\sigma(z=0)}{\max_z \rho_1^\sigma(z)}, \quad (8)$$

$$d = \left| \int_{-\infty}^{\infty} dz z \rho_1^M(z) - \int_{-\infty}^{\infty} dz z \rho_1^I(z) \right|, \quad (9)$$

with the one-body density  $\rho_1^\sigma(z)$  of component  $\sigma$  (4). Equation (8) compares the one-body density  $\rho_1^\sigma(z)$  at the trap center with its maximum value, while Eq. (9) checks for parity asymmetry, as we will argue below. The above equations are motivated from the literature on binary mixtures and we provide a brief summary on the discovered ground-state phases and some of their properties, which will be relevant in the following discussions.

For weak couplings there is a miscible phase  $M$  with a high spatial overlap of the one-body densities  $\rho_1^\sigma(z)$ . As a result, both components exhibit a Gaussian profile ( $\Delta_\sigma = 1$ ) and occupy the center of their trap ( $d = 0$ ). The state is disentangled and both species are condensed. For negative couplings, i.e., attractive interactions, the phase remains miscible and the widths of the Gaussian densities shrink with decreasing coupling strength. For stronger positive couplings, three different phase separation scenarios are possible. In case the majority species occupies the trap center ( $\Delta_M = 1$ ), pushing the impurities outside in a way that the impurity density forms a shell around the majority density with two parity-symmetric humps ( $\Delta_I < 1$  and  $d = 0$ ), we have a core-shell  $IMI$  phase. When the impurities remain at the trap center instead ( $\Delta_I = 1$ ) with the majority species forming a shell ( $\Delta_M < 1$  and  $d = 0$ ), we have a core-shell  $MIM$  phase. Finally, when both species develop two parity-symmetric humps with a local minimum at the trap center ( $\Delta_\sigma < 1$  and  $d = 0$ ), we have a composite fermionization phase  $CF$ . On the level of one-body densities  $CF$  appears to be miscible owing to the high spatial overlap between the components. However, the deviations to the miscible phase become evident upon investigating the

two-body density matrices (5) and (6). Namely, two particles of the same component can be found either on the left or the right side with respect to trap center, while two particles of different components are always on opposite sides.

While the core-shell phases  $IMI$  and  $MIM$  do not rely on entanglement between the components,  $CF$  is always an entangled many-body state made out of two major species orbitals  $S = 2$  and two major SPFs  $s_\sigma = 2$  on the particle layer. Thus,  $CF$  cannot be obtained within the mean-field approximation. In fact, we observe that once the entanglement of the true many-body state, characterized by the von Neumann entropy (see Sec. IV B), reaches a certain threshold, a collapse to a phase with broken parity symmetry ( $d > 0$ ) will take place in the mean-field picture. We abbreviate this phase with  $SB$  from now on.

The origin of  $SB$  is the onset of a quasidegeneracy between the ground state and the first excited state of the many-body spectrum, which becomes an exact degeneracy in the limit of  $g_{M\bar{\sigma}} \rightarrow \infty$ . Once this limit is reached, any superposition of those two states is also an eigenstate of (1). Since they are of different parity symmetry  $P$  and  $[H, P] = 0$ , it is possible to choose the superposition to be parity symmetric or to break the parity symmetry of (1). It was suggested [73] that the corresponding many-body wave function may be written in terms of number states as  $|\Psi\rangle = c_1 |N_M\rangle_L |0_M\rangle_R \otimes |0_I\rangle_L |N_I\rangle_R + c_2 |0_M\rangle_L |N_M\rangle_R \otimes |N_I\rangle_L |0_I\rangle_R$  with two parity-broken SPFs  $\varphi_j^\sigma(z)$  featuring an asymmetric Gaussian shape with a maximum on the  $j = L$  (left) or  $j = R$  (right) side with respect to the trap center. Within the mean-field approximation, the eigenenergy of the first excited state coincides with the ground-state energy already for a finite coupling  $g_{M\bar{\sigma}}$ . Since mean field does not incorporate entanglement, the state collapses either to  $|N_M\rangle_L \otimes |N_I\rangle_R$  or to  $|N_M\rangle_R \otimes |N_I\rangle_L$ , resulting in a phase with broken parity symmetry.

With this we end our overview over different phases and showcase a compact summary of the phases:

$$\begin{cases} M & : d = 0 \wedge \Delta_M = 1 \wedge \Delta_I = 1, \\ IMI & : d = 0 \wedge \Delta_M = 1 \wedge \Delta_I < 1, \\ MIM & : d = 0 \wedge \Delta_M < 1 \wedge \Delta_I = 1, \\ CF & : d = 0 \wedge \Delta_M < 1 \wedge \Delta_I < 1, \\ SB & : d > 0 \wedge \Delta_M < 1 \wedge \Delta_I < 1. \end{cases} \quad (10)$$

In Fig. 1 we depict the ground-state phases within the mean-field approximation for  $N_B = 5$  with (a)  $N_I = 1$  and (b)  $N_I = 2$  impurities as a function of the intercomponent coupling strength  $g_{M\bar{\sigma}}$  and the impurity localization  $a_I/a_M$ . As expected,  $CF$  is not among the phases in Fig. 1. The transition region on the  $a_I/a_M$  axis, where core shell  $MIM$  is replaced by core shell  $IMI$ , can be tuned by variation of the particle-number ratio such that for  $N_I = N_M$  it lies at  $a_I/a_M = 1$  (not shown), while for increasing particle imbalance  $N_I/N_M < 1$  it is shifted toward a lower  $a_I/a_M$  ratio. This is also the point where the coupling strength  $g_{M\bar{\sigma}}$ , required for the realization of the  $SB$  phase, is the smallest. We will see later in Sec. IV B that the species entropy has here its global maximum. Note that each phase diagram features critical points, where three different phases can coexist (green circles).

Now that we have identified the phases, we are going to shed some light on the mechanism behind the phase separation taking place for different specific coupling strength  $g_{M\bar{\sigma}}$  for



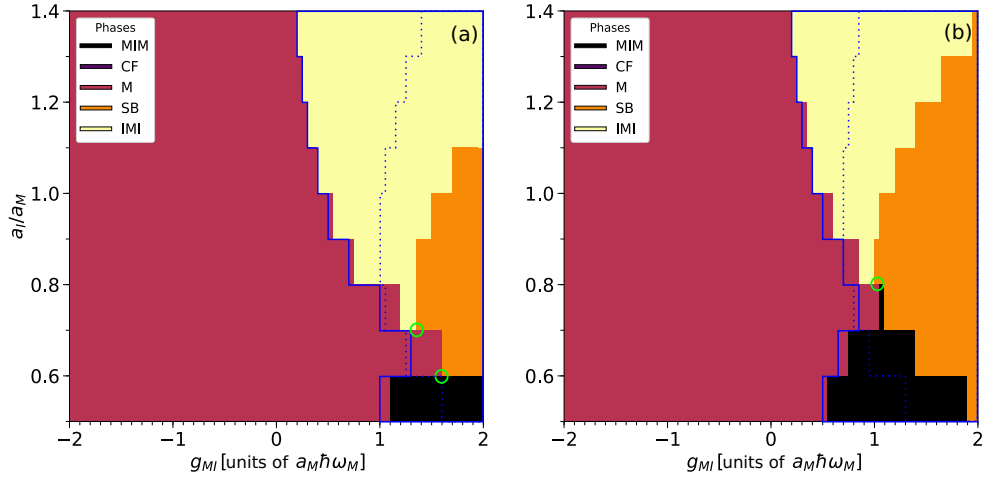


FIG. 1. Mean-field ground-state phase diagram for  $N_B = 5$  majority particles and (a)  $N_I = 1$  or (b)  $N_I = 2$  impurities as a function of the intercomponent coupling strength  $g_{MI}$  and impurity localization  $a_I/a_M = \sqrt{1/\eta}$  with  $\eta = \omega_I/\omega_M$  being the trap frequency ratio and  $a_\sigma = \sqrt{\hbar/m\omega_\sigma}$  the harmonic oscillator length of species  $\sigma$ . The nomenclature of phases is as follows:  $M$  for miscible,  $MIM$  for core shell with impurity at the core,  $IMI$  for core shell with majority at the core,  $CF$  for composite fermionization, and  $SB$  for a phase with broken parity symmetry. The blue solid curve represents the miscible-immiscible phase boundary according to (19). The blue dotted line is an estimate for the  $SB$  phase boundary according to (21). Green circles indicate tricritical points. The coarse structure is due to the finite step size of our data with respect to  $a_I/a_M$ .

a fixed trap ratio  $\eta$ . In particular, we will provide a simple formula, which determines which of the core-shell structures is energetically more favorable. Additionally, we provide an estimate on the miscible-immiscible transition region and on the  $SB$  phase boundary.

Let us make two horizontal cuts across the phase diagram of Fig. 1(b) at  $a_I/a_M = 0.5$  and at  $a_I/a_M = 1.1$ . In Fig. 2 we take a closer look at the variation of the one-body densities  $\rho_{MF}^\sigma$  being part the effective one-body potential  $V_\sigma^{\text{eff}}$  (7) when increasing the coupling strength  $g_{MI}$ . First, let us focus on

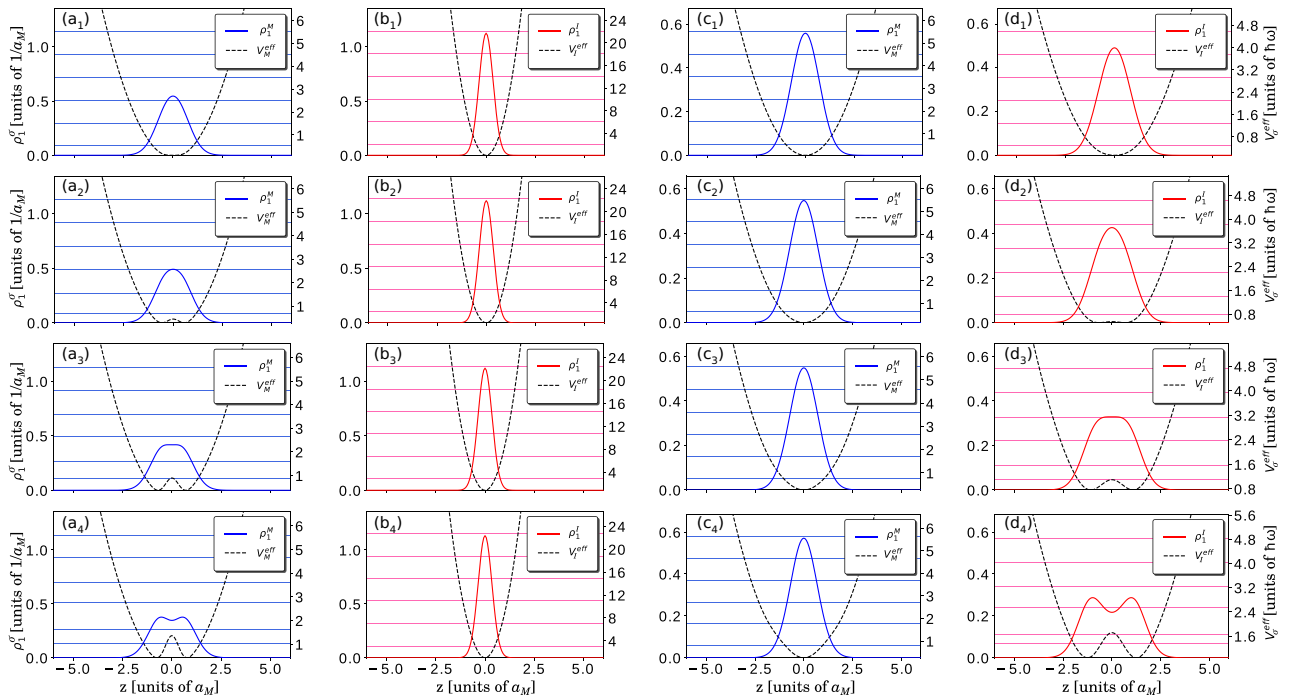


FIG. 2. Ground-state densities  $\rho_{MF}^\sigma(z)$  inside the induced one-body potential  $V_\sigma^{\text{eff}}(z)$  from (7) for  $N_M = 5$ ,  $N_I = 2$  and either  $a_I/a_M = 0.5$  (columns 1 and 2 for majority and impurity species, respectively) or  $a_I/a_M = 1.1$  (columns 3 and 4 for majority and impurity species, respectively). Rows from top to bottom correspond to a variation of the intercomponent coupling  $g_{MI} \in \{0.05, 0.2, 0.4, 0.6\}$ . Horizontal lines depict eigenenergies of (7).

columns 1 and 2, corresponding to  $a_I/a_M = 0.5$ . For very weak coupling (first row), every atom to a good approximation populates the energetically lowest harmonic oscillator orbital of the respective potential  $V_\sigma$ . The induced potential  $V_\sigma^{\text{ind}}$  gains an amplitude linearly with  $g_{MI}$  and with the density profiles being Gaussians of different widths we observe the appearance of a small barrier in  $V_M^{\text{eff}}$  at  $g_{MI} = 0.2$  [Fig. 2(a2)]. This barrier grows with  $g_{MI}$  and at  $g_{MI} = 0.4$  [Fig. 2(a3)] it becomes comparable to the ground-state energy of the effective potential, while the one-body density  $\rho_{\text{MF}}^M$  turns flat at the trap origin. Once the ground-state energy drops below the barrier height, two density humps appear and core shell *MIM* is established [Fig. 2(a4)]. Meanwhile, the effective potential of the impurity  $V_I^{\text{eff}}$  does not show significant deviations from the harmonic case (second column). Especially, the induced part  $V_I^{\text{ind}}$ , being initially also a Gaussian, is not capable to produce a barrier at the trap center. Similar statements can be made for columns 3 and 4, corresponding to  $a_I/a_M = 1.1$ . The only difference is that  $V_I^{\text{eff}}$  develops a barrier instead, whereas  $V_M^{\text{eff}}$  shows only a slight variation, which finally leads to the core-shell *IMI* phase.

Motivated by the above observation, we define an alternative phase classification from an energetical point of view:

$$\begin{cases} M & : E_{0,\sigma}^{\text{MF}} - V_\sigma^{\text{eff}}(0) > 0, \\ IMI & : E_{0,\sigma}^{\text{MF}} - V_M^{\text{eff}}(0) > 0 \wedge E_{0,I}^{\text{MF}} - V_I^{\text{eff}}(0) < 0, \\ MIM & : E_{0,M}^{\text{MF}} - V_M^{\text{eff}}(0) < 0 \wedge E_{0,I}^{\text{MF}} - V_I^{\text{eff}}(0) > 0, \\ SB & : d > 0, \end{cases} \quad (11)$$

where  $E_{0,\sigma}^{\text{MF}}$  is the ground-state energy of (7). As long as the ground-state energy of the effective species Hamiltonian exceeds the effective potential height at the trap center, the species remains at the trap center. Phase diagrams produced this way match exactly the ones shown in Fig. 1.

The interpretation is now as follows. For a very weak coupling, both the majority and the impurity reside in the ground state of the harmonic oscillator. Once the induced potential  $V_\sigma^{\text{ind}}$  of species  $\sigma$  becomes large enough to produce a barrier in  $V_\sigma^{\text{eff}}$ , the corresponding density  $\rho_{\text{MF}}^\sigma$  will start to expand. By growing in width it will prevent the other component  $\bar{\sigma}$  from developing a barrier of its own. When the height of the potential barrier becomes of the same magnitude as the lowest energy of the corresponding effective potential, the species  $\sigma$  splits into two fragments. Then, it starts squeezing the other component  $\bar{\sigma}$  by increasing the effective trap frequency of the renormalized harmonic oscillator  $V_\sigma^{\text{eff}}$ .

The barrier in  $V_\sigma^{\text{eff}}$  appears once the following condition is fulfilled:

$$\exists x_0 \neq 0 : \frac{d}{dx} V_\sigma^{\text{eff}} \Big|_{x_0} = 0. \quad (12)$$

Assuming one-body densities to be unperturbed harmonic oscillator ground states, we obtain the following effective potentials:

$$V_M^{\text{eff}}(z) \approx \frac{1}{2}z^2 + g_{MI}N_I\sqrt{\frac{\eta}{\pi}}e^{-\eta z^2}, \quad (13)$$

$$V_I^{\text{eff}}(z) \approx \frac{1}{2}\eta^2z^2 + g_{MI}N_M\sqrt{\frac{1}{\pi}}e^{-z^2}, \quad (14)$$

and the corresponding barrier conditions

$$\frac{\sqrt{\pi}}{2N_I\sqrt{\eta^3}} \hat{=} g_{MI}^M < g_{MI}, \quad (15)$$

$$\frac{\sqrt{\pi}\eta^2}{2N_M} \hat{=} g_{MI}^I < g_{MI}. \quad (16)$$

For given particle numbers  $N_M$ ,  $N_I$  and trap ratio  $\eta$  either condition (15) or condition (16) will be fulfilled first upon increasing the coupling  $g_{MI}$  and thus either the majority or the impurity will form a shell. We remark that the above criterion for barrier formation is inversely proportional to the particle number of the other component, while the dependence on the trap ratio  $\eta$  for the majority differs substantially from the one for the impurity. Furthermore, for a fixed particle-number ratio there is a critical trap ratio  $\eta_c$ , for which (15) and (16) can be fulfilled simultaneously:

$$\sqrt{1/\eta_c} = \sqrt{N_I/N_M}. \quad (17)$$

Around this critical region we expect that none of the components will occupy the trap center. We summarize our findings in a simple formula, which determines the type of phase separation at the miscible-immiscible phase boundary:

$$\begin{cases} \text{core shell } MIM & : \eta \gg \eta_c, \\ \text{core shell } IMI & : \eta \ll \eta_c, \\ CF \text{ or } SB & : \eta \approx \eta_c. \end{cases} \quad (18)$$

For particle-number ratios discussed in this section, the critical region lies at  $a_I/a_M \approx 0.8$  [Fig. 1(a)] and at  $a_I/a_M \approx 0.9$  [Fig. 1(b)].

Next, we want to find an estimate for the miscible-immiscible phase boundary  $g_{MI}^c$ . To this end, we combine the energetical separation criterion in Eq. (11) with approximate effective potentials from (13) and (14). Specifically, for a given particle number ratio  $N_I/N_M$  we determine the critical trap ratio  $\eta_c$ . Then depending on the choice of  $\eta$  we solve numerically for the ground-state energy of a single particle inside the effective potential (13) or (14). Finally, we compare this energy to the potential height at the trap center:

$$\begin{cases} a_I/a_M < \sqrt{N_I/N_M} & : H_M^{\text{eff}} = -\frac{1}{2}\frac{\partial^2}{\partial x^2} + V_M^{\text{eff}}(x) \begin{cases} E_{0,M}^{\text{eff}} > g_{MI}N_I\sqrt{\frac{\eta}{\pi}} & \Rightarrow M, \\ E_{0,M}^{\text{eff}} < g_{MI}N_I\sqrt{\frac{\eta}{\pi}} & \Rightarrow MIM, \end{cases} \\ a_I/a_M > \sqrt{N_I/N_M} & : H_I^{\text{eff}} = -\frac{1}{2}\frac{\partial^2}{\partial y^2} + V_I^{\text{eff}}(y) \begin{cases} E_{0,I}^{\text{eff}} > g_{MI}N_B\sqrt{\frac{1}{\pi}} & \Rightarrow M, \\ E_{0,I}^{\text{eff}} < g_{MI}N_B\sqrt{\frac{1}{\pi}} & \Rightarrow IMI. \end{cases} \end{cases} \quad (19)$$

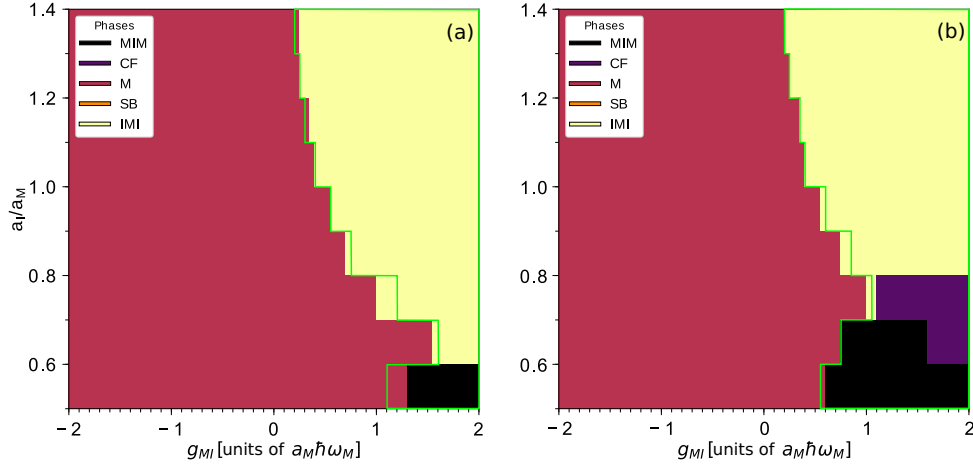


FIG. 3. ML-X ground-state phase diagram for  $N_B = 5$  majority particles and (a)  $N_I = 1$  or (b)  $N_I = 2$  impurities as a function of the intercomponent coupling strength  $g_{MI}$  and impurity localization  $a_I/a_M = \sqrt{1/\eta}$  with  $\eta = \omega_I/\omega_M$  being the trap frequency ratio and  $a_\sigma = \sqrt{\hbar/m\omega_\sigma}$  the harmonic oscillator length of species  $\sigma$ . The nomenclature of phases is as follows:  $M$  for miscible,  $MIM$  for core shell with impurity at the core,  $IMI$  for core shell with majority at the core,  $CF$  for composite fermionization, and  $SB$  for a phase with broken parity symmetry. The green solid curve represents the miscible-immiscible phase boundary based on the mean-field treatment. The coarse structure is due to the finite step size of our data with respect to  $a_I/a_M$ .

The results are plotted as blue solid curves in Fig. 1. We recognize that it performs quite well except for  $\eta \approx \eta_c$ , where it underestimates  $g_{MI}^c$ .

We can also get a rough estimate on the  $SB$  phase boundary  $g_{MI}^{SB}$  by using the following Gaussian ansatz:

$$\varphi^\sigma(z) = \sqrt[4]{\frac{\beta_\sigma}{\pi}} e^{-\frac{\beta_\sigma(z-z_\sigma)^2}{2}}, \quad (20)$$

with the width  $\beta_\sigma$  and the displacement  $z_\sigma$  of component  $\sigma$  being variational parameters. We evaluate the expectation value of (1) and minimize the energy with respect to the above variation parameters. By looking further at the special case when the relative position  $|z_M - z_I|$  becomes zero, one arrives after some algebraic transformations at

$$g_{MI}^{SB} N_I = \frac{\sqrt{\pi}}{2\eta} \sqrt[4]{\frac{\gamma}{1 + \gamma\eta^2}} (1 + \eta^2 \sqrt{\gamma})^{\frac{3}{2}}, \quad (21)$$

with particle-number ratio  $\gamma = N_I/N_M$ . We remark that this equation reduces to Eq. (8) from [60] for  $\eta = 1$ . Although this equation describes well the qualitative behavior of the  $SB$  phase boundary, quantitatively it scales badly when the trap ratio  $\eta$  deviates from  $\eta_c$  (blue dotted line in Fig. 1). There are two possible reasons for this. First, our ansatz incorporates only  $M$  and  $SB$  phases, while ignoring the core-shell phases. Thus, as one draws away from  $\eta_c$  the core-shell parameter region, which lies in-between  $M$  and  $SB$ , grows in size, making the estimate inefficient. The other reason is that the mean-field solution  $\varphi_{MF}^\sigma$  of the  $SB$  phase is rather an asymmetric Gaussian.

Finally, we discuss the limiting cases. When  $\eta \rightarrow \infty$  ( $a_I/a_M \rightarrow 0$ ) the impurity becomes highly localized at  $z = 0$ . It will not be affected by the majority atoms. Meanwhile, the majority species will be subject to an additional delta potential at  $z = 0$  with potential strength  $g_{MI} N_I$ . This analytically solvable one-body problem results in a Weber differential

equation. Upon increasing the delta-potential prefactor  $g_{MI} N_I$ , the initially unperturbed Gaussian solution develops a cusp at the trap center, whose depth tends to zero as the prefactor goes to infinity. When  $\eta \rightarrow 0$  ( $a_I/a_M \rightarrow \infty$ ), we can change our perspective by rescaling the Hamiltonian in impurity harmonic units and argue in a similar way as above.

In the following section, we compare to the results obtained for the corresponding correlated many-body approach of ML-X.

### B. ML-X: Modifications of the phase diagram due to correlations and entanglement

For the total wave function in Eq. (2) we use  $S = 8$  species orbitals and  $s_\sigma = 8$  SPFs for each component. We perform again an imaginary-time propagation of an initially chosen wave function and obtain the ground state of (1). In Fig. 3 we show the resulting ground-state phases based on the selection rules (10) for  $N_B = 5$  and (a)  $N_I = 1$  or (b)  $N_I = 2$ . We remark that the alternative selection scheme defined in Eq. (11) does not apply here, and below we provide an explanation why it fails. The first eye-catching feature is that the  $SB$  phase has completely disappeared, as expected, since it is an artifact of the mean-field treatment. Additionally, we observe the presence of composite fermionization  $CF$  for the case of two impurities in Fig. 3(b). Overall, the transition between the miscible phase and separated phases takes place at a different coupling strength  $g_{MI}^c$  for a fixed trap ratio  $\eta$ .

In order to better understand why the phase diagram is altered this way, we investigate in Figs. 4 and 5 the von Neumann entropy  $S_{vN}$  on the species layer as well as the von Neumann entropy of the majority species  $S_{vN}^M$  and the impurity species  $S_{vN}^I$ .  $S_{vN}$  characterizes the degree of entanglement between the components (entanglement entropy) while  $S_{vN}^{\sigma}$

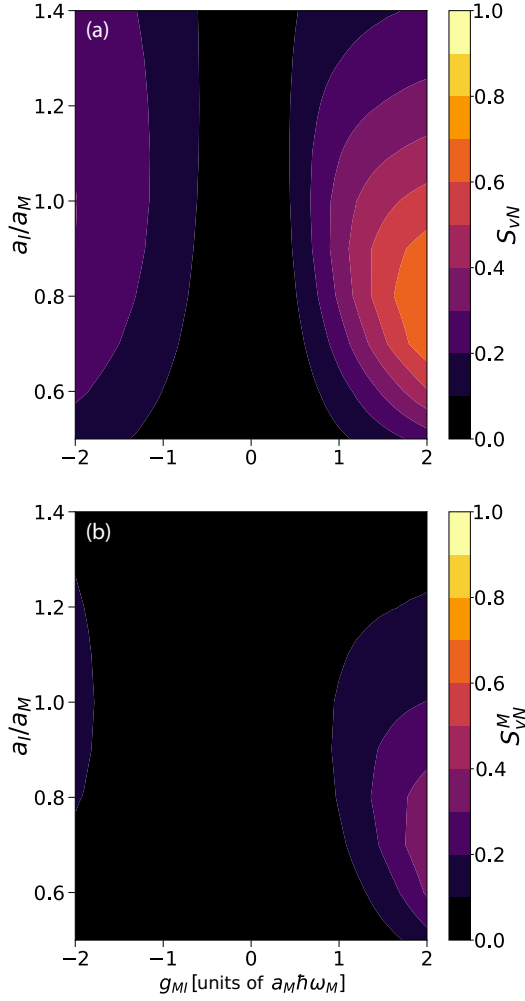


FIG. 4. Ground-state (species) entanglement entropy  $S_{vN}$  (a) from Eq. (22) and the fragmentation entropy  $S_{vN}^M$  from Eq. (23) for the majority (b) for  $N_B = 5$  majority particles and  $N_I = 1$  as a function of the intercomponent coupling strength  $g_M$  and impurity localization  $a_I/a_M = \sqrt{1/\eta}$  with  $\eta = \omega_I/\omega_M$  being the trap frequency ratio and  $a_\sigma = \sqrt{\hbar/m\omega_\sigma}$  the harmonic oscillator length of species  $\sigma$ .

reflects the degree of species fragmentation (fragmentation entropy). The definitions are as follows:

$$S_{vN} = - \sum_{i=1}^S \lambda_i \ln \lambda_i, \quad (22)$$

$$S_{vN}^\sigma = - \sum_{i=1}^{s_\sigma} m_i^\sigma \ln m_i^\sigma \quad \text{with} \quad \hat{\rho}_1^\sigma = \sum_{i=1}^{s_\sigma} m_i^\sigma |m_i^\sigma\rangle \langle m_i^\sigma|, \quad (23)$$

where  $\lambda_i$  are expansion coefficients from (2) and  $m_i^\sigma$  natural populations satisfying  $\sum_{i=1}^{s_\sigma} m_i^\sigma = 1$  and  $|m_i^\sigma\rangle$  natural orbitals of the spectrally decomposed one-body density operator  $\hat{\rho}_1^\sigma$  of species  $\sigma$ . The entanglement entropy is bounded by the equal distribution of orbitals  $S_{vN} \leq \ln(S)$ , whereas for two dominantly occupied orbitals we expect  $S_{vN} \leq \ln(2) \approx 0.7$ . If  $S_{vN} = 0$ , then there is no entanglement between the species

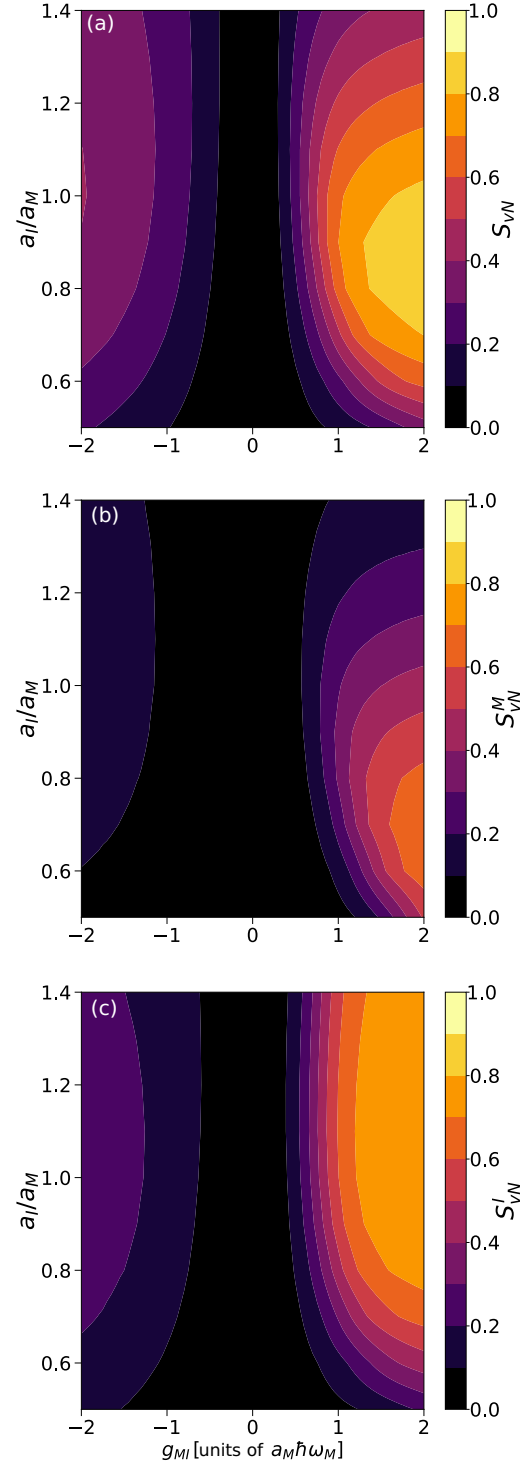


FIG. 5. Ground-state (species) entanglement entropy  $S_{vN}$  from Eq. (22) (a) and the fragmentation entropy  $S_{vN}^\sigma$  from Eq. (23) for the majority (b) and impurity (c) for  $N_B = 5$  majority particles and  $N_I = 2$  impurities as a function of the intercomponent coupling strength  $g_M$  and impurity localization  $a_I/a_M = \sqrt{1/\eta}$  with  $\eta = \omega_I/\omega_M$  being the trap frequency ratio and  $a_\sigma = \sqrt{\hbar/m\omega_\sigma}$  the harmonic oscillator length of species  $\sigma$ .

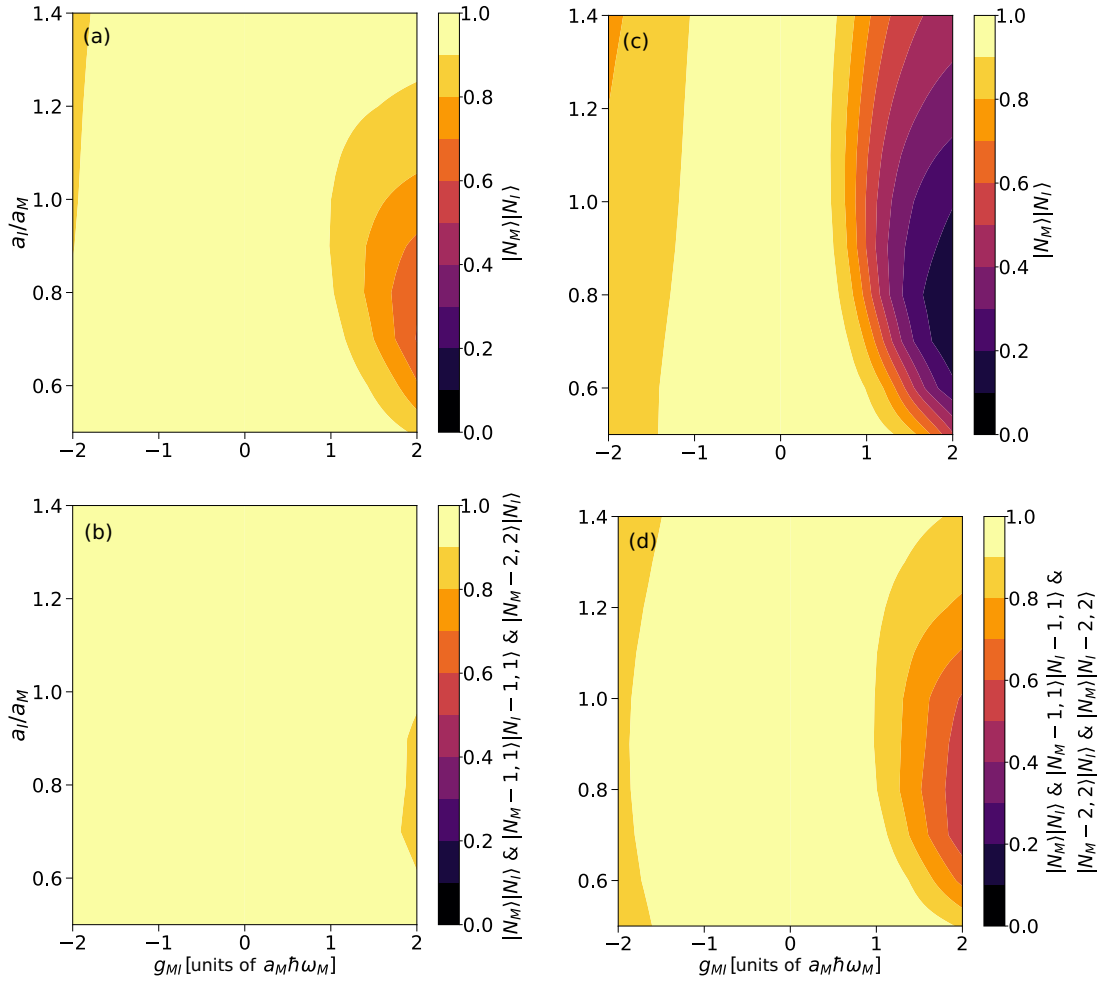


FIG. 6. Projection amplitudes of the many-body ground state on number states  $|\langle \vec{n}^M | \otimes \langle \vec{n}^I | |\Psi\rangle|^2$  for  $N_B = 5$  majority particles and  $N_I = 1$  (first column) or  $N_I = 2$  (second column) impurities as a function of the intercomponent coupling strength  $g_{MI}$  and impurity localization  $a_I/a_M = \sqrt{1/\eta}$  with  $\eta = \omega_I/\omega_M$  being trap frequency ratio and  $a_\sigma = \sqrt{\hbar/m\omega_\sigma}$  the harmonic oscillator length of species  $\sigma$ . The SPFs constituting the permanents are eigenfunctions of the effective Hamiltonian (24). The first row corresponds to the projection on the condensed number state  $|N_B\rangle|N_I\rangle$ , while in the second row one sums over contributions from two-particle excitations  $|N_B - 2, 2\rangle|N_I\rangle$ ,  $|N_B\rangle|N_I - 2, 2\rangle$ , and  $|N_B - 1, 1\rangle|N_I - 1, 1\rangle$ .

and the wave function is a simple product state on the species layer. Similarly, fragmentation entropy  $S_{vN}^\sigma = 0$  means that all particles occupy the same SPF and the species is thus condensed. For parameter values where this is fulfilled, a mean-field treatment is well justified. However, in Figs. 4 and 5 we recognize that for stronger couplings  $g_{MI}$  this is not the case. Particularly, in the vicinity of the critical region  $a_I/a_M \approx \sqrt[3]{N_I/N_M}$  at positive  $g_{MI}$ , identified in the previous section as highly competitive, the entanglement entropy  $S_{vN}$  is very pronounced [Figs. 4(a) and 5(a)]. The fragmentation entropy of the majority species  $S_{vN}^M$  is comparatively weaker and slightly shifted toward a smaller length scale ratio  $a_I/a_M$  at positive  $g_{MI}$  [Figs. 4(b) and 5(b)]. The fragmentation entropy of the impurity species  $S_{vN}^I$  for  $N_I = 1$  (not shown) coincides with the entanglement entropy  $S_{vN}$  [Fig. 4(a)], while for  $N_I = 2$  there are substantial differences [see Fig. 5(c)]. Namely, the impurity shows a higher degree of fragmentation when it is

less confined compared to the majority species and vice versa. In contrast to positive couplings  $g_{MI}$ , for negative couplings the entanglement and species fragmentation build up with a much slower rate. Finally, we emphasize that phase separations like core shell *MIM* or *IMI* are not necessarily related to a high degree of entanglement or species depletion, whereas *CF* is located in the parameter region, where  $S_{vN}$  takes the highest values. Another striking observation is that the onset of the *SB* phase from Fig. 1 is related to the entanglement entropy reaching some threshold value around  $S_{vN} \approx 0.5$  at positive couplings  $g_{MI}$  [compare to Figs. 4(a) and 5(a)].

Now that we have identified the parameter space where deviations from mean field are to be expected, we want to gain a deeper insight into how the effective picture is affected as a result of increasing correlations. For this purpose we define an effective single-body Hamiltonian of species  $\sigma$  similar to the one in Eq. (7), except that we use the exact many-body

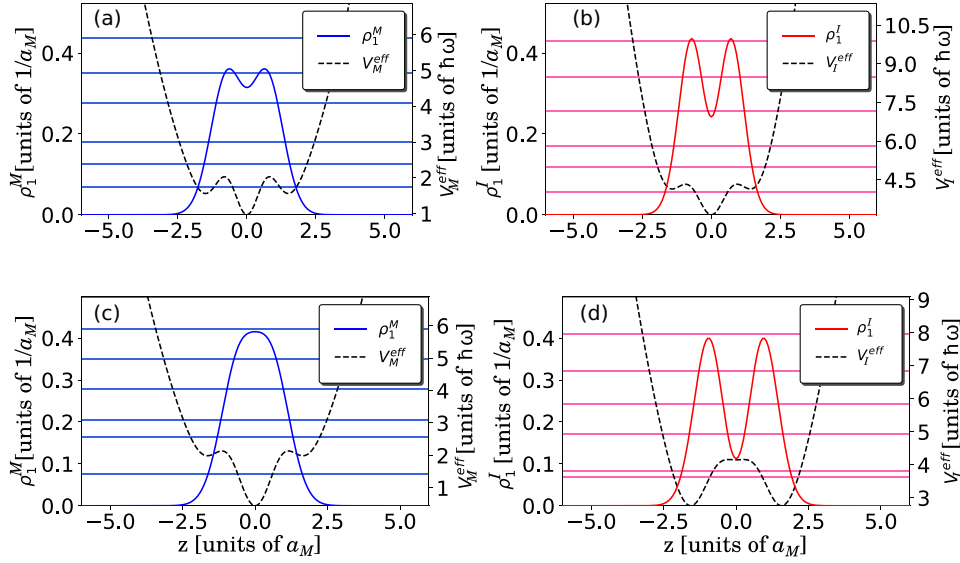


FIG. 7. ML-X ground-state densities  $\rho_1^\sigma(z)$  inside effective one-body potentials  $V_\sigma^{\text{eff}}(z)$  from (24) for  $N_M = 5$ ,  $N_I = 2$ ,  $g_{MI} = 2$ , and  $a_I/a_M = 0.8$  (first row) or  $a_I/a_M = 0.9$  (second row). Horizontal lines are eigenenergies of (24).

densities  $\rho_1^\sigma$  instead of the mean-field densities  $\rho_{\text{MF}}^\sigma$ :

$$H_\sigma^{\text{eff}} = H_\sigma + N_\sigma g_{MI} \sum_{i=1}^{N_\sigma} \rho_1^{\bar{\sigma}}(z_i) \quad \text{with} \quad (24)$$

$$\bar{\sigma} \neq \sigma = \sum_{i=1}^{N_\sigma} \left( -\frac{1}{2} \frac{\partial^2}{\partial z_i^2} + V_\sigma^{\text{eff}}(z_i) \right).$$

Next, we diagonalize (24) and use the obtained eigenfunctions  $\tilde{\varphi}_i^\sigma$  as SPFs for number states  $|\bar{n}^M\rangle \otimes |\bar{n}^I\rangle$  on which we project our many-body ground state  $|\Psi\rangle$ . The reader should distinguish the latter SPFs  $\tilde{\varphi}_i^\sigma$  from the numerical SPFs  $\varphi_i^\sigma$  obtained by improved relaxation which define the permanents contained in our ML-X total wave function. Thus, we decompose our ground state in terms of disentangled product states made out of single permanents. We anticipate that  $|N_M\rangle |N_I\rangle$  represents dominant contribution to  $|\Psi\rangle$ , which should be the case whenever a mean-field approach is valid. From the previous analysis we observed that the entanglement entropy values were mostly  $S_{vN}^\sigma \leq 0.7$ , which suggests two relevant SPFs. Indeed, our many-body state consists of two major orbitals and two major SPFs. Furthermore, taking parity symmetry into account and considering at most two-particle excitations, we conclude that number states  $|N_M - 1, 1\rangle |N_I - 1, 1\rangle$ ,  $|N_M - 2, 2\rangle |N_I\rangle$ , and  $|N_M\rangle |N_I - 2, 2\rangle$  may become of relevance too at stronger couplings. We remark that the one-body density operator of number state  $|N_\sigma - n_2^\sigma, n_2^\sigma\rangle$  with  $n_2^\sigma$  particles in the odd orbital  $\tilde{\varphi}_2^\sigma$  will be a mixed state of one even and one odd orbital, eventually featuring two humps in the corresponding one-body density. Thus, depending on the occupation amplitude of such states, they may either accelerate or slow down the development of humps in  $\rho_1^\sigma(z)$ , thereby quantitatively shifting the critical coupling  $g_{MI}^c$ , at which the mixed phase transforms into one of the species-separated phases.

In Fig. 6 we show the projection on number state  $|N_M\rangle |N_I\rangle$  (first row) and a sum over projections on the above-mentioned

permanents (second row) for  $N_B = 5$  and  $N_I = 1$  (first column) or  $N_I = 2$  (second column). For negative couplings the state  $|N_M\rangle |N_I\rangle$  provides a major contribution and the effective picture holds. Let us focus in the following on positive couplings. In Fig. 6(a) ( $N_I = 1$ ), we observe that the state  $|N_M\rangle |N_I\rangle$  has indeed a major contribution at coupling strength below 1.0. Once interspecies correlations build up with increasing coupling strength, the state  $|N_M - 1, 1\rangle |N_I - 1, 1\rangle$  grows in importance, which corresponds to a simultaneous single-particle excitation within each component. This is mostly pronounced around  $\eta_c$ . Double excitations within the majority species  $|N_M - 2, 2\rangle |N_I\rangle$  are of minor amplitude and rather of relevance for a localized impurity  $a_I/a_M \ll 1$ . All in all, the low-lying excitations of the effective potentials (24) provide a good description [Fig. 6(b)]. In Fig. 6(c) ( $N_I = 2$ ), we observe that the state  $|N_M\rangle |N_I\rangle$  loses its contribution very quickly as one goes deeper into the regime of strong entanglement. Although we are able to get a better understanding for weak entanglement by including two-particle excitations mentioned above, our effective picture clearly does not hold in the parameter region characterized by strong entanglement. There, we may account only for as much as  $\approx 50\%$  of the ground state, even though the one-body density in Eq. (24) incorporates beyond-mean-field corrections. We remark that while it is indeed intuitive that the one-body picture will break at some point as the entanglement becomes stronger, it is not at all obvious to predict the corresponding threshold (trap ratio and coupling strength) where it will happen.

Let us take a closer look at this regime, where the single-particle picture (24) tends to break down. We show in Fig. 7 the one-body densities for  $N_B = 5$  majority particles and  $N_I = 2$  impurities in the strong entanglement region at  $g_{MI} = 2$ . The first row corresponds to the CF phase at  $a_I/a_M = 0.8$ . Here, we recognize immediately why the effective picture fails. The origin of the two humps in the one-body density is counterintuitive considering that they are at the position of local maxima of the effective potential. One would rather

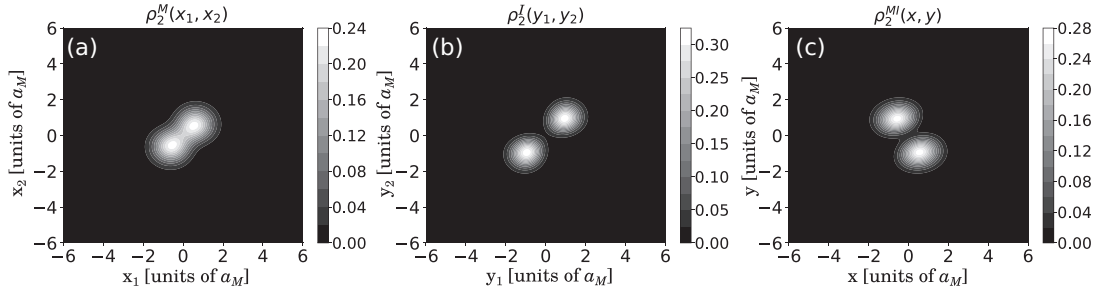


FIG. 8. (a) Majority two-body density matrix  $\rho_2^M(x_1, x_2)$  from Eq. (5). (b) Impurity two-body density matrix  $\rho_2^I(y_1, y_2)$  from Eq. (5). (c) Interspecies two-body density matrix  $\rho_2^{MI}(x, y)$  from Eq. (6) of the ground state for  $N_M = 5$ ,  $N_I = 2$ ,  $g_{MI} = 2$ , and  $a_I/a_M = 0.9$ .

expect a density profile with three peaks at the positions of the potential minima.

The second row ( $a_I/a_M = 0.9$ ) seems at first glance to be an *IMI* phase. The majority is at the core, while the impurity forms a shell. Upon a more detailed investigation we notice that the majority species is broader than it should be inside the squeezed “harmonic” trap. The humps of the impurity also do not coincide with the positions of the minima of the respective effective potential. As a matter of fact, this phase is a latent *CF* phase, which becomes clear when we analyze the corresponding two-body density matrices in Fig. 8. The intraspecies two-body density matrices (5) [Figs. 8(a) and 8(b)] indicate that particles of the same component avoid the trap center and form a cluster either on the right or the left side with respect to trap center. Moreover, the interspecies density matrix (6) [Fig. 8(c)] tells us that the two different clusters of majority and impurity will always be found on opposite sides of the trap with a rather small spatial overlap between them. It allows to diminish the impact of the repulsive energy on the total energy at the cost of paying potential energy. These are clear signatures of the *CF*, which are blurred in the reduced one-body density. We note that the parameter space where ML-X predicts an *IMI* phase, whereas MF produces *SB* phase, we have in fact a latent *CF*, hidden behind a one-body quantity. Thus, in general, the classification of immiscible phases by the one-body density is not sufficient to distinguish *CF* from *IMI* or *MIM*. Nevertheless, sometimes it is still possible to identify *CF* by the one-body density, namely, when it features two reflection-symmetric humps.

Above, we have mentioned that in the literature the *CF* phase was suggested to be a superposition of

two parity-broken mean-field states  $|\Psi\rangle = c_1 |N_M\rangle_L |0_M\rangle_R \otimes |0_I\rangle_L |N_I\rangle_R + c_2 |0_M\rangle_L |N_M\rangle_R \otimes |N_I\rangle_L |0_I\rangle_R$  as a result of the degeneracy onset. Indeed, ML-X has two prominent orbitals on the species layer and two major SPFs on the particle layer. Nevertheless, the other occupied species orbitals and SPFs provide a minor contribution, as we have evidenced in Fig. 5, where the entropies take values beyond  $\ln(2)$ . To provide an illustrative example, we displace the trap centers in Eq. (1) by a small amount to energetically separate the two symmetry-broken configurations. For parameter values for which the *CF* phase is observed, we perform again the improved relaxation to find ground state of the system in order to check whether it is indeed a MF state. It turns out that the majority species and the impurity species are still fragmented states though the degree of depletion is much less compared to the parity-symmetric ground state. The species entropy  $S_{vN}$  is greatly reduced, but still appreciable. The impact of correlations is also visible in Fig. 9. The ground state of the effective potential (24) is different from the one-body density of the many-body ML-X wave function. This is caused by induced attractive interactions mediated by the intercomponent coupling, a beyond-mean-field effect [92].

To conclude our discussion about the high-entanglement regime, we state that the mean-field approach, being an effective one-body model, fails to explain a one-body quantity such as reduced one-body density. Nevertheless, it manages to characterize quite well one of the two possible configurations of the entangled many-body state. The latter is not just a simple superposition of two mean-field states describing two different parity-broken configurations. A thorough analysis showed that on the many-body level the *SB* phase is in fact

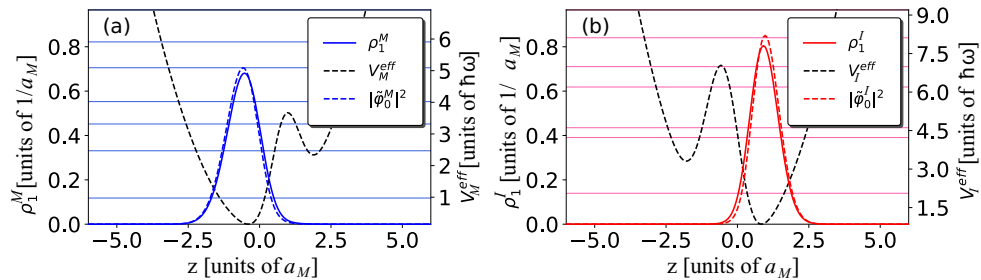


FIG. 9. ML-X parity-broken ground-state densities  $\rho_1^q(z)$  obtained from (1) by slightly displacing centers of harmonic traps in opposite directions for  $N_M = 5$ ,  $N_I = 2$ ,  $g_{MI} = 2$ , and  $a_I/a_M = 0.9$ . Induced one-body potentials  $V_\sigma^{\text{eff}}(z)$  are calculated from (24) and  $\tilde{\varphi}_0^\sigma(z)$  are the corresponding ground states. Horizontal lines are eigenenergies of (24).

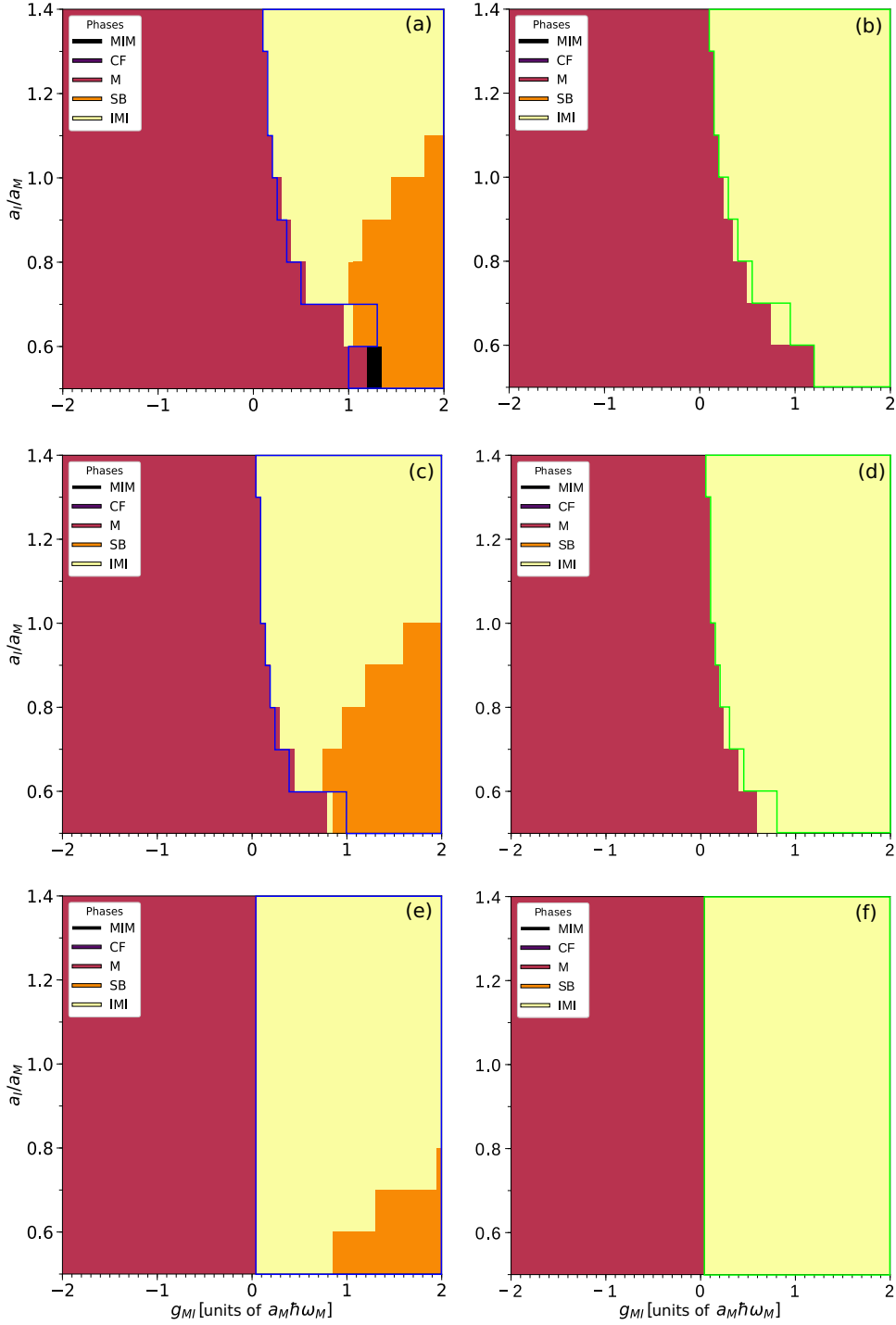


FIG. 10. Mean-field (first column) and ML-X (second column) ground-state phase diagrams for  $N_I = 1$  impurity and  $N_M = 10$  (first row),  $N_M = 20$  (second row), or  $N_M = 1000$  (third row) as a function of the intercomponent coupling strength  $g_M$  and impurity localization  $a_I/a_M = \sqrt{1/\eta}$  with  $\eta = \omega_I/\omega_M$  being the trap frequency ratio and  $a_\sigma = \sqrt{\hbar/m\omega_\sigma}$  the harmonic oscillator length of species  $\sigma$ . The nomenclature of the phases is as follows: *M* for miscible, *MIM* for core shell with impurity at the core, *IMI* for core shell with majority at the core, *CF* for composite fermionization, and *SB* for a phase with broken parity symmetry. The blue solid curve (first column) represents the miscible-immiscible phase boundary according to (19). The green solid curve (second column) is the miscible-immiscible phase boundary based on mean field. The coarse structure is due to the finite step size of our data with respect to  $a_I/a_M$ .



slightly entangled, while each species is partially fragmented. We also evidenced that *CF* completely dominates the highly correlated regime and made a link of its appearance to the onset of *SB* on the mean-field level. Sometimes, *CF* is even camouflaged behind core-shell *IMI* or *MIM* densities, indicating that the one-body density is not enough to distinguish between them.

## V. PHASE SEPARATION: IMPACT OF PARTICLE NUMBERS

When increasing the number of majority atoms  $N_M$ , while keeping  $N_I$  fixed, one might expect two properties based on an intuition for few-body systems. First, the location of the strong entanglement regime will be shifted toward lower values of  $a_I/a_M \approx \sqrt{1/\eta_c} = \sqrt[3]{N_I/N_M}$ . Thus, the *IMI* phase will cover the most part of our parameter space for positive  $g_{MI}$ . Second, at a fixed  $\eta$  the critical coupling  $g_{MI}^c$  for the miscible-immiscible transition will decrease, because according to (16) the majority species will be able to induce a barrier for the impurity species already for a much weaker coupling. The induced barrier of the majority on the other hand will not be affected according to (15).

Indeed, this is what we observe in the phase diagrams depicted in Fig. 10. In the mean field (first column) the location of the *SB* phase relocates from  $\sqrt{1/\eta_c} \approx 0.79$  [ $N_M = 5$ , Fig. 1(a)] to  $\sqrt{1/\eta_c} \approx 0.72$  [ $N_M = 10$ , Fig. 10(a)], then to  $\sqrt{1/\eta_c} \approx 0.65$  [ $N_M = 20$ , Fig. 10(b)] and finally moves outside our parameter space  $\sqrt{1/\eta_c} \approx 0.37$  [ $N_M = 1000$ , Fig. 10(c)]. The blue curve, which estimates the miscible-immiscible transition according to (19) is in good agreement (except for the critical region  $\eta_c$ ) with the mean-field phase boundary. We also recognize that for a fixed trap ratio  $\eta$ , the critical coupling strength  $g_{MI}^c$  decreases with increasing  $N_M$  and at  $N_M = 1000$  a very small  $g_{MI}^c < 0.05$  is sufficient to cause phase separation, which is below our resolution.

We have also performed the corresponding ML-X calculations (second column) with  $S = s_\sigma = 6$  (first row),  $S = s_\sigma = 4$  (second row), and  $S = s_\sigma = 2$  (third row) orbitals. We remark that the latter case might not be converged to the exact solution, which is beyond numerical capabilities to verify. Still, it provides valuable beyond-mean-field corrections. The deviations to the mean field, still clearly visible at  $N_M = 10$ , are most pronounced near  $\eta_c$ . They become less as the particle imbalance is increased until finally at  $N_M = 1000$  the phase diagrams almost coincide except for a small *SB* region. This is mainly attributed to the fact that the strong entanglement regime, where deviations are to be expected, moves outside our parameter space ( $a_I/a_M < 0.5$ ). Furthermore, the deviations may still be there, but on a finer coupling scale  $g_{MI} < 0.05$  according to (15) and (16).

## VI. CONCLUSIONS

In this work we have investigated the phase separation of a quasi-1D inhomogeneous Bose-Bose mixture in a three-dimensional parameter space spanned by the intercomponent

coupling  $g_{MI}$ , harmonic length scale ratio  $a_I/a_M = \sqrt{1/\eta}$ , and the particle-number ratio  $N_I/N_M$ , when the intracomponent couplings  $g_\sigma$  are switched off. Although we have concentrated on the case of equal masses, our results may be easily extended to the more general case of unequal masses. We expect some quantitative changes, but the qualitative picture and the line of argumentation will remain unchanged.

The commonly used separation criterion  $g_{MI} > \sqrt{g_M g_I}$ , which is valid for homogeneous mixtures, would predict a miscible-immiscible transition for any finite coupling  $g_{MI} > 0$ . However, this separation rule does not apply here since we have harmonic traps of different length scales. We have analyzed the mechanism, which leads to phase separation, by using an effective mean-field picture. Within this description each species is subject to an additional induced potential caused by the other component. This potential has initially a Gaussian shape and grows linearly with the coupling strength  $g_{MI}$ . However, it does not immediately trigger a barrier at the center of the harmonic trap. In fact, the species, which first manages to induce a barrier for the other component upon increasing the coupling  $g_{MI}$ , will stay at the center of its parabolic trap. Meanwhile, the other species will split up, once the ground-state energy of the effective potential drops below the barrier height. Thus, we end up with either a core-shell *IMI* or a core-shell *MIM* phase, except for a highly competitive region, where the barrier conditions can be met simultaneously for both components. We have derived a simple rule to predict the type of phase separation, developed a straightforward algorithm to identify the miscible-immiscible phase boundary  $g_{MI}^c$ , and gave a rough estimate on the phase boundary between the segregated phases  $g_{MI}^{SB}$ .

As a next step, we compared mean-field (MF) results to the numerically exact many-body calculations based on multilayer multifactorial time-dependent Hartree method for atomic mixtures (ML-X). It turns out that MF agrees well with ML-X far away from the critical region  $\sqrt{1/\eta_c} = \sqrt[3]{N_I/N_M}$ . At  $\eta_c$  there are considerable quantitative deviations and sometimes the two methods do not even agree on the type of phase separation. This is caused by the growing interparticle correlations, which generate entanglement between the components and increase the degree of species fragmentation. We have seen that symmetry-broken phase (*SB*) is replaced by composite fermionization (*CF*), which is an entangled parity-symmetric ground state. Furthermore, we have linked the onset of *SB* to the fact that the entanglement entropy reaches a certain threshold and saw a clear breakdown of the effective single-particle picture in the strong entanglement region in terms of a corresponding number state analysis. This led to the discovery of a latent *CF* phase in the *IMI* region. The latent *CF* phase has the characteristic one-body density of the *IMI* phase, but a thorough analysis of the two-body densities reveals typical *CF* features. We have argued that at a finite coupling  $g_{MI}$  the *CF* is not a simple superposition of two *SB* states given by mean field.

We have studied the impact of particle-number variations, which confirmed our intuition that  $\eta_c$  and thus the location of the strong entanglement regime can be manipulated as a function of the particle-number ratio. Furthermore, for a

fixed particle-number ratio the critical coupling  $g_{MI}^c$  of the miscible-immiscible transition can be tuned to lower values by increasing the number of particles while keeping the particle-number ratio fixed.

Finally, we remark that an intriguing next step would be to perform a similar study of phase separation at finite intracomponent coupling  $g_\sigma$ . The broadening or shrinking of the density profiles, depending on the sign and strength of  $g_\sigma$ , will definitely modify the barrier conditions (15) and (16).

Another interesting but challenging direction would be the nonequilibrium dynamics by quenching the trap ratio across the phase boundaries.

#### ACKNOWLEDGMENTS

M.P. acknowledges fruitful discussions with K. Keiler and M. Roentgen. M.P. gratefully acknowledges a scholarship of the Studienstiftung des deutschen Volkes.



- 
- [1] R. Grimm, M. Weidemüller, and Y. B. Ovchinnikov, *Adv. At. Mol. Opt. Phys.* **42**, 95 (2000).
- [2] I. Bloch, J. Dalibard, and W. Zwerger, *Rev. Mod. Phys.* **80**, 885 (2008).
- [3] M. A. Cazalilla, R. Citro, T. Giamarchi, E. Orignac, and M. Rigol, *Rev. Mod. Phys.* **83**, 1405 (2011).
- [4] C. Chin, R. Grimm, P. Julienne, and E. Tiesinga, *Rev. Mod. Phys.* **82**, 1225 (2010).
- [5] M. Olshanii, *Phys. Rev. Lett.* **81**, 938 (1998).
- [6] D. S. Petrov, M. Holzmann, and G. V. Shlyapnikov, *Phys. Rev. Lett.* **84**, 2551 (2000).
- [7] T. Bergeman, M. G. Moore, and M. Olshanii, *Phys. Rev. Lett.* **91**, 163201 (2003).
- [8] E. Haller, M. J. Mark, R. Hart, J. G. Danzl, L. Reichsöllner, V. Melezhik, P. Schmelcher, and H.-C. Nägerl, *Phys. Rev. Lett.* **104**, 153203 (2010).
- [9] D. Blume, *Rep. Prog. Phys.* **75**, 046401 (2012).
- [10] T. Sowiński and M. Á. García-March, *Rep. Prog. Phys.* **82**, 104401 (2019).
- [11] C. J. Myatt, E. A. Burt, R. W. Ghrist, E. A. Cornell, and C. E. Wieman, *Phys. Rev. Lett.* **78**, 586 (1997).
- [12] D. S. Hall, M. R. Matthews, J. R. Ensher, C. E. Wieman, and E. A. Cornell, *Phys. Rev. Lett.* **81**, 1539 (1998).
- [13] H.-J. Miesner, D. M. Stamper-Kurn, J. Stenger, S. Inouye, A. P. Chikkatur, and W. Ketterle, *Phys. Rev. Lett.* **82**, 2228 (1999).
- [14] P. Maddaloni, M. Modugno, C. Fort, F. Minardi, and M. Inguscio, *Phys. Rev. Lett.* **85**, 2413 (2000).
- [15] G. Delannoy, S. G. Murdoch, V. Boyer, V. Josse, P. Bouyer, and A. Aspect, *Phys. Rev. A* **63**, 051602(R) (2001).
- [16] K. M. Mertes, J. W. Merrill, R. Carretero-González, D. J. Frantzeskakis, P. G. Kevrekidis, and D. S. Hall, *Phys. Rev. Lett.* **99**, 190402 (2007).
- [17] S. Tojo, Y. Taguchi, Y. Masuyama, T. Hayashi, H. Saito, and T. Hirano, *Phys. Rev. A* **82**, 033609 (2010).
- [18] C. Becker, S. Stellmer, P. Soltan-Panahi, S. Dörscher, M. Baumert, E.-M. Richter, J. Kronjäger, K. Bongs, and K. Sengstock, *Nat. Phys.* **4**, 496 (2008).
- [19] C. Hamner, J. J. Chang, P. Engels, and M. A. Hofer, *Phys. Rev. Lett.* **106**, 065302 (2011).
- [20] E. Nicklas, M. Karl, M. Höfer, A. Johnson, W. Muessel, H. Strobel, J. Tomkovič, T. Gasenzer, and M. K. Oberthaler, *Phys. Rev. Lett.* **115**, 245301 (2015).
- [21] Y. Eto, M. Takahashi, K. Nabeta, R. Okada, M. Kunimi H. Saito, and T. Hirano, *Phys. Rev. A* **93**, 033615 (2016).
- [22] Y. Eto, M. Takahashi, M. Kunimi, H. Saito, and T. Hirano, *New J. Phys.* **18**, 073029 (2016).
- [23] C. Cabrera, L. Tanzi, J. Sanz, B. Naylor, P. Thomas, P. Cheiney, and L. Tarruell, *Science* **359**, 301 (2018).
- [24] G. Semeghini, G. Ferioli, L. Masi, C. Mazzinghi, L. Wolswijk, F. Minardi, M. Modugno, G. Modugno, M. Inguscio, and M. Fattori, *Phys. Rev. Lett.* **120**, 235301 (2018).
- [25] G. Modugno, M. Modugno, F. Riboli, G. Roati, and M. Inguscio, *Phys. Rev. Lett.* **89**, 190404 (2002).
- [26] M. Mudrich, S. Kraft, K. Singer, R. Grimm, A. Mosk, and M. Weidemüller, *Phys. Rev. Lett.* **88**, 253001 (2002).
- [27] G. Thalhammer, G. Barontini, L. De Sarlo, J. Catani, F. Minardi, and M. Inguscio, *Phys. Rev. Lett.* **100**, 210402 (2008).
- [28] K.-K. Ni, S. Ospelkaus, M. De Miranda, A. Pe'Er, B. Neyenhuis, J. Zirbel, S. Kotochigova, P. Julienne, D. Jin, and J. Ye, *Science* **322**, 231 (2008).
- [29] D. J. McCarron, H. W. Cho, D. L. Jenkin, M. P. Köppinger, and S. L. Cornish, *Phys. Rev. A* **84**, 011603(R) (2011).
- [30] A. D. Lercher, T. Takekoshi, M. Debatin, B. Schuster, R. Rameshan, F. Ferlaino, R. Grimm, and H. C. Nägerl, *Eur. Phys. J. D* **65**, 3 (2011).
- [31] B. Pasquiou, A. Bayerle, S. M. Tzanova, S. Stellmer, J. Szczepkowski, M. Parigger, R. Grimm, and F. Schreck, *Phys. Rev. A* **88**, 023601 (2013).
- [32] T. Takekoshi, L. Reichsöllner, A. Schindewolf, J. M. Hutson, C. R. Le Sueur, O. Dulieu, F. Ferlaino, R. Grimm, and H.-C. Nägerl, *Phys. Rev. Lett.* **113**, 205301 (2014).
- [33] P. K. Molony, P. D. Gregory, Z. Ji, B. Lu, M. P. Köppinger, C. R. Le Sueur, C. L. Blackley, J. M. Hutson, and S. L. Cornish, *Phys. Rev. Lett.* **113**, 255301 (2014).
- [34] L. Wacker, N. B. Jørgensen, D. Birkmose, R. Horchani, W. Ertmer, C. Klempt, N. Winter, J. Sherson, and J. J. Arlt, *Phys. Rev. A* **92**, 053602 (2015).
- [35] X. Li, B. Zhu, X. He, F. Wang, M. Guo, Z.-F. Xu, S. Zhang, and D. Wang, *Phys. Rev. Lett.* **114**, 255301 (2015).
- [36] K. L. Lee, N. B. Jørgensen, L. J. Wacker, M. G. Skou, K. T. Skalmstang, J. J. Arlt, and N. P. Proukakis, *New J. Phys.* **20**, 053004 (2018).
- [37] F. Wang, X. Li, D. Xiong, and D. Wang, *J. Phys. B. At. Mol. Phys.* **49**, 015302 (2015).
- [38] G. Barontini, C. Weber, F. Rabatti, J. Catani, G. Thalhammer, M. Inguscio, and F. Minardi, *Phys. Rev. Lett.* **103**, 043201 (2009).
- [39] S. B. Papp, J. M. Pino, and C. E. Wieman, *Phys. Rev. Lett.* **101**, 040402 (2008).
- [40] S. Sugawa, R. Yamazaki, S. Taie, and Y. Takahashi, *Phys. Rev. A* **84**, 011610(R) (2011).
- [41] K. Kasamatsu and M. Tsubota, *Phys. Rev. Lett.* **93**, 100402 (2004).

- [42] S. Ronen, J. L. Bohn, L. E. Halmó, and M. Edwards, *Phys. Rev. A* **78**, 053613 (2008).
- [43] H. Takeuchi, S. Ishino, and M. Tsubota, *Phys. Rev. Lett.* **105**, 205301 (2010).
- [44] J. Hofmann, S. S. Natu, and S. Das Sarma, *Phys. Rev. Lett.* **113**, 095702 (2014).
- [45] K. Kasamatsu, M. Tsubota, and M. Ueda, *Phys. Rev. Lett.* **91**, 150406 (2003).
- [46] P. Mason and A. Aftalion, *Phys. Rev. A* **84**, 033611 (2011).
- [47] T.-L. Ho and V. B. Shenoy, *Phys. Rev. Lett.* **77**, 3276 (1996).
- [48] H. Pu and N. P. Bigelow, *Phys. Rev. Lett.* **80**, 1130 (1998).
- [49] A. A. Svidzinsky and S. T. Chui, *Phys. Rev. A* **67**, 053608 (2003).
- [50] P. Öhberg, *Phys. Rev. A* **59**, 634 (1999).
- [51] M. Trippenbach, K. Góral, K. Rzazewski, B. Malomed, and Y. Band, *J. Phys. B: At. Mol. Phys.* **33**, 4017 (2000).
- [52] A. Alexandrov and V. V. Kabanov, *J. Phys.: Condens. Matter* **14**, L327 (2002).
- [53] E. Timmermans, *Phys. Rev. Lett.* **81**, 5718 (1998).
- [54] P. Ao and S. T. Chui, *Phys. Rev. A* **58**, 4836 (1998).
- [55] B. D. Esry, C. H. Greene, J. P. Burke, Jr., and J. L. Bohn, *Phys. Rev. Lett.* **78**, 3594 (1997).
- [56] R. Navarro, R. Carretero-González, and P. G. Kevrekidis, *Phys. Rev. A* **80**, 023613 (2009).
- [57] L. Wen, W. M. Liu, Y. Cai, J. M. Zhang, and J. Hu, *Phys. Rev. A* **85**, 043602 (2012).
- [58] K. L. Lee, N. B. Jørgensen, I.-K. Liu, L. Wacker, J. J. Arlt, and N. P. Proukakis, *Phys. Rev. A* **94**, 013602 (2016).
- [59] V. Cikojević, L. V. Markić, and J. Boronat, *New J. Phys.* **20**, 085002 (2018).
- [60] L. Wen, H. Guo, Y.-J. Wang, A.-Y. Hu, H. Saito, C.-Q. Dai, and X.-F. Zhang, *Phys. Rev. A* **101**, 033610 (2020).
- [61] B. Parajuli, D. Pećak, and C.-C. Chien, *Phys. Rev. A* **100**, 063623 (2019).
- [62] F. Lingua, A. Richaud, and V. Penna, *Entropy* **20**, 84 (2018).
- [63] G. M. Koutentakis, S. I. Mistakidis, and P. Schmelcher, *New J. Phys.* **22**, 063058 (2020).
- [64] J. Erdmann, S. I. Mistakidis, and P. Schmelcher, *Phys. Rev. A* **99**, 013605 (2019).
- [65] V. Penna and A. Richaud, *Sci. Rep.* **8**, 10242 (2018).
- [66] A. Richaud, A. Zenesini, and V. Penna, *Sci. Rep.* **9**, 6908 (2019).
- [67] K. Keiler and P. Schmelcher, *New J. Phys.* **20**, 103042 (2018).
- [68] K. Keiler, S. I. Mistakidis, and P. Schmelcher, *New J. Phys.* (2020).
- [69] S. Mistakidis, G. Katsimiga, P. Kevrekidis, and P. Schmelcher, *New J. Phys.* **20**, 043052 (2018).
- [70] S. I. Mistakidis, L. Hilbig, and P. Schmelcher, *Phys. Rev. A* **100**, 023620 (2019).
- [71] S. I. Mistakidis, G. C. Katsimiga, G. M. Koutentakis, T. Busch, and P. Schmelcher, *Phys. Rev. Lett.* **122**, 183001 (2019).
- [72] S. Mistakidis, G. Koutentakis, G. Katsimiga, T. Busch, and P. Schmelcher, *New J. Phys.* **22**, 043007 (2020).
- [73] S. Zöllner, H.-D. Meyer, and P. Schmelcher, *Phys. Rev. A* **78**, 013629 (2008).
- [74] Y. J. Hao and S. Chen, *Eur. Phys. J. D* **51**, 261 (2009).
- [75] M. A. García-March, B. Juliá-Díaz, G. Astrakharchik, T. Busch, J. Boronat, and A. Polls, *New J. Phys.* **16**, 103004 (2014).
- [76] A. Dehkharghani, A. Volosniev, J. Lindgren, J. Rotureau, C. Forssén, D. Fedorov, A. Jensen, and N. Zinner, *Sci. Rep.* **5**, 10675 (2015).
- [77] M. Pyzh, S. Krönke, C. Weitenberg, and P. Schmelcher, *New J. Phys.* **20**, 015006 (2018).
- [78] F. Deuretzbacher, D. Becker, J. Bjerlin, S. M. Reimann, and L. Santos, *Phys. Rev. A* **90**, 013611 (2014).
- [79] A. G. Volosniev, D. Petrosyan, M. Valiente, D. V. Fedorov, A. S. Jensen, and N. T. Zinner, *Phys. Rev. A* **91**, 023620 (2015).
- [80] L. Yang and X. Cui, *Phys. Rev. A* **93**, 013617 (2016).
- [81] L. Cao, S. Krönke, O. Vendrell, and P. Schmelcher, *J. Chem. Phys.* **139**, 134103 (2013).
- [82] S. Krönke, L. Cao, O. Vendrell, and P. Schmelcher, *New J. Phys.* **15**, 063018 (2013).
- [83] L. Cao, V. Bolsinger, S. Mistakidis, G. Koutentakis, S. Krönke, J. Schurer, and P. Schmelcher, *J. Chem. Phys.* **147**, 044106 (2017).
- [84] L. J. LeBlanc and J. H. Thywissen, *Phys. Rev. A* **75**, 053612 (2007).
- [85] A. Rubio-Abadal, J.-Y. Choi, J. Zeiher, S. Hollerith, J. Rui, I. Bloch, and C. Gross, *Phys. Rev. X* **9**, 041014 (2019).
- [86] F. Serwane, G. Zürn, T. Lompe, T. Ottenstein, A. Wenz, and S. Jochim, *Science* **332**, 336 (2011).
- [87] R. Islam, R. Ma, P. M. Preiss, M. E. Tai, A. Lukin, M. Rispoli, and M. Greiner, *Nature (London)* **528**, 77 (2015).
- [88] M. Pyzh, S. Krönke, C. Weitenberg, and P. Schmelcher, *New J. Phys.* **21**, 053013 (2019).
- [89] M. H. Beck, A. Jäckle, G. A. Worth, and H.-D. Meyer, *Phys. Rep.* **324**, 1 (2000).
- [90] J. Light, I. Hamilton, and J. Lill, *J. Chem. Phys.* **82**, 1400 (1985).
- [91] A. Raab, *Chem. Phys. Lett.* **319**, 674 (2000).
- [92] J. Chen, J. M. Schurer, and P. Schmelcher, *Phys. Rev. Lett.* **121**, 043401 (2018).



Article

# Entangling Lattice-Trapped Bosons with a Free Impurity: Impact on Stationary and Dynamical Properties

 Maxim Pyzh <sup>1</sup>, Kevin Keiler <sup>1</sup>, Simeon I. Mistakidis <sup>1</sup> and Peter Schmelcher <sup>1,2,\*</sup>

<sup>1</sup> Center for Optical Quantum Technologies, Department of Physics, University of Hamburg, Luruper Chaussee 149, 22761 Hamburg, Germany; mpyzh@physnet.uni-hamburg.de (M.P.); kkeiler@physnet.uni-hamburg.de (K.K.); smistaki@physnet.uni-hamburg.de (S.I.M.)

<sup>2</sup> The Hamburg Centre for Ultrafast Imaging, Universität Hamburg, Luruper Chaussee 149, 22761 Hamburg, Germany

\* Correspondence: mpyzh@physnet.uni-hamburg.de

**Abstract:** We address the interplay of few lattice trapped bosons interacting with an impurity atom in a box potential. For the ground state, a classification is performed based on the fidelity allowing to quantify the susceptibility of the composite system to structural changes due to the intercomponent coupling. We analyze the overall response at the many-body level and contrast it to the single-particle level. By inspecting different entropy measures we capture the degree of entanglement and intraspecies correlations for a wide range of intra- and intercomponent interactions and lattice depths. We also spatially resolve the imprint of the entanglement on the one- and two-body density distributions showcasing that it accelerates the phase separation process or acts against spatial localization for repulsive and attractive intercomponent interactions, respectively. The many-body effects on the tunneling dynamics of the individual components, resulting from their counterflow, are also discussed. The tunneling period of the impurity is very sensitive to the value of the impurity-medium coupling due to its effective dressing by the few-body medium. Our work provides implications for engineering localized structures in correlated impurity settings using species selective optical potentials.

**Keywords:** multi-layer multi-configuration time-dependent Hartree method (ML-MCTDHB); mixtures; impurity; fidelity; entanglement; von Neumann entropy; reduced densities; few-body dynamics



**Citation:** Pyzh, M.; Keiler, K.; Mistakidis, S.I.; Schmelcher, P. Entangling Lattice-Trapped Bosons with a Free Impurity: Impact on Stationary and Dynamical Properties. *Entropy* **2021**, *23*, 290. <https://doi.org/10.3390/e23030290>

Academic Editors: Ofir E. Alon and Axel U.J. Lode

Received: 5 February 2021  
Accepted: 23 February 2021  
Published: 26 February 2021

**Publisher's Note:** MDPI stays neutral with regard to jurisdictional claims in published maps and institutional affiliations.



**Copyright:** © 2021 by the authors. Licensee MDPI, Basel, Switzerland. This article is an open access article distributed under the terms and conditions of the Creative Commons Attribution (CC BY) license (<https://creativecommons.org/licenses/by/4.0/>).

## 1. Introduction

Multicomponent quantum gases can be experimentally studied with a high degree of controllability in the ultracold regime [1,2]. Specifically, two-component mixtures of bosons or fermions can be trapped in various species selective external geometries [3,4]. Few-body ensembles can be realized in particular in one-dimension (1D) [5,6] while the scattering lengths are tunable through Feshbach and confinement induced resonances [7,8]. In 1D bosonic mixtures the adjustability of the intercomponent interactions gives rise to intriguing phenomena such as phase-separation processes [9,10] in the repulsive regime, formation of bound states, e.g., droplet configurations [11,12] for attractive interactions as well as quasiparticle-like states in highly particle imbalanced systems [13,14].

In this latter context, an impurity species is embedded in an environment of the majority species called the medium. The presence of a finite impurity-medium coupling leads to an effective picture where the impurity properties deviate from the bare particle case exhibiting, for instance, an effective mass [15–18] and induced interactions [19–22] mediated by the medium. The resultant states are often called polarons [23,24] and have been experimentally realized mainly in higher-dimensions [25–29] and to a lesser extent in 1D [13,30] using spectroscopic schemes. Since these settings consist of a few-body subsystem they naturally show enhanced correlation properties, especially in 1D, rendering their many-body treatment inevitable. In particular, the emergent impurity-medium

entanglement can lead to spatial undulations of the medium. This mechanism is manifested, for instance, as sound-wave emission [17,31] and collective excitations [32,33] of the host or the formation of a bound state [34–36] between the impurity and atoms of the medium for attractive interspecies interactions.

Another relevant ingredient is the external trapping geometry that the two components experience. Indeed, for harmonically trapped and homogeneous systems remarkable dynamical features of impurity physics include the spontaneous generation of localized patterns [17,37–39], inelastic collisional aspects of driven impurities [40–42] with the surrounding and their relaxation at long timescales [43–45]. On the other hand, when a lattice potential is introduced the situation becomes more complicated giving rise, among others, to doped insulator physics [46,47] and impurity transport [48–50]. Apparently, configuring one component by manipulating its external trap while leaving the other intact, e.g., by using a species selective external potential, it is possible to control the response of the unperturbed component via the impurity-medium interaction [51,52]. For instance, operating in the lowest-band approximation it has been demonstrated that a lattice trapped impurity interacting with a homogeneous host exhibits besides tunneling dynamics [53] also self-trapping events [54,55] and can even undergo Bloch-oscillations [56]. The opposite case, where the medium resides in the lattice, provides an experimental probe of the impurity-medium collision parameters [57] and interaction strength [58].

In this work by considering an impurity in a box potential and a lattice trapped few-body medium we examine how the latter affects the impurity's spatial distribution by means of (de-)localization for different lattice depths and intercomponent interactions. Indeed, a lattice trapped medium can reside either in a superfluid or an insulating-like phase [46], a fact that is expected to crucially impact the impurity's configuration and vice versa [59]. To address the ground state properties and quantum quench dynamics of the above-discussed impurity setting we utilize the multi-layer multi-configuration time-dependent Hartree method for atomic mixtures (ML-MCTDHX) [60–62]. This variational method enables us to account for the relevant correlations of the mixture and operate beyond the lowest-band approximation for the medium.

Focusing on the ground state of the system and in order to testify its overall response for varying intercomponent interactions we determine the fidelity between the coupled and decoupled composite system both at the many-body and the single-particle level. Note that in impurity settings this observable is commonly termed residue [23,24] enabling us to identify, e.g., the polaron formation, while the influence of the impurity-medium entanglement in this observable is still an open issue. It is demonstrated that despite the fact that the total entangled state may strongly deviate from its decoupled configuration, this effect is arguably less pronounced or even diminished at the single-particle level. Furthermore, we showcase that the build-up of impurity-medium entanglement is sensitive to the interplay between the intercomponent interactions and the lattice depth [46]. Interestingly, stronger interactions do not necessarily lead to a larger amount of entanglement, whereas the state of the majority species may undergo substantial structural changes, which remain invisible at the single-particle level. Moreover, we identify the imprint of the background on the impurities and vice versa by relying on one- and two-body density distributions evincing a rich spatial structure of the components with respect to the lattice depth as well as the inter- and intracomponent interactions. In particular, it is argued that for repulsive (attractive) interactions the impurity delocalizes (localizes) around the central lattice site. The delocalization of the impurity is accompanied by its phase-separation with the majority component [63], where the impurity tends to the edges of the box for a superfluid background or exhibits a multi-hump structure for an insulating medium. We further analyze how much the intercomponent correlations are actually involved in the structural changes observed in the spatial probability distributions. To this end we compare density distributions of the numerically exact ground state to the corresponding ones of an approximate non-entangled ground state. We identify that the entanglement-induced

corrections accelerate phase-separation at repulsive couplings and generally slow down spatial localization at attractive interactions.

Finally, we monitor the non-equilibrium dynamics of the mixture. We prepare the system in a phase-separated, i.e., disentangled configuration, and quench the intercomponent interactions to smaller values resulting in the counterflow of the components and thus triggering their tunneling dynamics and the consequent build-up of entanglement. The majority component plays the role of a material barrier for the impurity [50,64] which performs tunneling oscillations whose period depends strongly on the impurity-medium interaction. The many-body nature of the tunneling process of the components is testified by invoking the individual natural orbitals constituting the time-evolved many-body state.

Our presentation is structured as follows. In Section 2, we introduce the impurity setting and in Section 3 we discuss our many-body treatment to tackle its ground state and dynamics. The ground state properties of the delocalized impurity and the lattice trapped medium are addressed in Section 4. We analyze the fidelity between perturbed and unperturbed (reduced) density operators, quantify the degree of entanglement and visualize its impact on single- and two-body density distributions of each species for different intra- and intercomponent interactions and lattice depths. The non-equilibrium dynamics of the mixture following a quench of the impurity-medium coupling to smaller values is discussed in Section 5. We provide a summary of our results and elaborate on future perspectives in Section 6.

## 2. Setup and Hamiltonian

We consider a single impurity particle immersed in a few-body system of ultracold bosons. Both components reside in a quasi-1D geometry ensured by a strong transversal confinement [13]. Along the longitudinal direction the  $N_A$  majority species atoms of mass  $m_A$  are trapped inside a lattice of depth  $V$  with  $l$  sites and length  $L$  with hard-wall boundary conditions. The impurity atom of mass  $m_B$  is subject to a box potential of the same length. The species-dependent trapping has been successfully demonstrated experimentally [3,4]. The inter-particle interactions are of s-wave contact type with  $g_{AA}$  denoting the majority-majority interaction strength and  $g_{AB}$  the majority-impurity coupling. Both may be tuned independently by a combination of Feshbach and confinement induced resonances [7,8]. Furthermore, we assume equal masses  $m_A = m_B$ , which corresponds to a mixture of the same isotope with the particles being distinguishable due to two different hyperfine states [65–70]. By introducing  $R^* = L$  and  $E^* = \hbar^2 / (mL^2)$  as length and energy scales we arrive at the following rescaled many-body Hamiltonian:

$$H = -\frac{1}{2} \frac{\partial^2}{\partial y^2} - \sum_i^{N_A} \left( \frac{1}{2} \frac{\partial^2}{\partial x_i^2} + V \sin^2(\pi l x_i) \right) + g_{AA} \sum_{i < j}^{N_A} \delta(x_i - x_j) + g_{AB} \sum_i^{N_A} \delta(x_i - y), \quad (1)$$

where  $y$  and  $x_i$  denote the spatial coordinates of the impurity and  $i$ th majority atom, respectively.

In this work we primarily focus on the ground state properties of the above many-body Hamiltonian Equation (1) with  $l = 5$  lattice sites and  $N_A = 5$  majority particles. In particular, we are interested in the susceptibility of the composite system to structural changes and the amount of inter-particle correlations it may hold. We cover a parameter space from moderately attractive to repulsive interaction strengths, i.e.,  $g_{AA} \in [-3.0, 3.0] E^* R^*$  and  $g_{AB} \in [-5.0, 5.0] E^* R^*$ , for a range of lattice depths from shallow to deep, namely  $V \in [100, 1000] E^*$ . In the following, we will refer to a lattice as being shallow ( $V < 200$ ), moderately deep ( $V \approx 500$ ) and very deep ( $V > 800$ ). We remark that in recoil units the above parameters translate to  $g_{AA} \in [-0.38, 0.38] E_{rec} x_{rec}$ ,  $g_{AB} \in [-0.64, 0.64] E_{rec} x_{rec}$  and  $V \in [0.81, 8.1] E_{rec}$ . Additionally, we demonstrate how an initially disentangled state prepared in the immiscible regime acquires dynamically a finite amount of entanglement after quenching the intercomponent coupling  $g_{AB}$ , thus triggering a counter-flow tunneling process of the two components.

### 3. Variational Approach

In order to account for effects stemming from inter-particle correlations we rely on the Multi-Layer Multi-Configurational Time-Dependent Hartree Method for atomic mixtures (ML-MCTDHX), for short ML-X [60–62]. This ab-initio method has been successfully applied to solve the time-dependent Schrödinger equation of various experimentally accessible and extensively studied systems. The core idea of this method lies in expanding the many-body wave-function in terms of product states of time-dependent single-particle functions [71,72]. This becomes beneficial, when the number of basis configurations with considerable contribution to the state fluctuates weakly during the time propagation, whereas the configurations themselves do change. Taking a variationally optimal basis at each time-step allows us to cover the high-dimensional Hilbert space at a lower computational cost compared to a time-independent basis.

The wave function ansatz for a given system is decomposed in multiple layers. On the first layer, called top layer, we separate the degrees of freedom of the binary mixture into product states of majority and impurity species functions  $|\Psi_i^\sigma(t)\rangle$  with  $\sigma \in \{A, B\}$  and  $i \in \{1, \dots, S\}$ :

$$|\Psi(t)\rangle = \sum_{i=1}^S \sqrt{\lambda_i(t)} |\Psi_i^A(t)\rangle \otimes |\Psi_i^B(t)\rangle. \quad (2)$$

Here, the time-dependent coefficients  $\lambda_i(t)$ , normalized as  $\sum_{i=1}^S \lambda_i(t) = 1$ , determine the degree of entanglement between the components [73]. The choice of  $S = 1$  results in the so-called species mean-field (SMF) approximation, meaning that no entanglement is assumed between the components [15]. In that case the intercomponent correlations, if present, are neglected and every component is effectively subject to an additional one-body potential induced by the fellow species [50,63]. In this work, we put a special emphasis on the impact of the entanglement on several one- and two-body quantities by comparing the numerically exact ground state to the corresponding SMF approximation.

On the second layer, called species layer, each species function  $|\Psi_i^\sigma(t)\rangle$  is expanded in terms of species-dependent symmetrized product states of single-particle functions (SPFs)  $|\varphi_j^\sigma(t)\rangle$  with  $j \in \{1, \dots, s_\sigma\}$ , accounting for the bosonic nature of our particles and abbreviated as  $|\vec{n}^\sigma\rangle = |n_1^\sigma, \dots, n_{s_\sigma}^\sigma\rangle$ :

$$|\Psi_i^\sigma(t)\rangle = \sum_{\vec{n}^\sigma | N_\sigma} C_{i, \vec{n}^\sigma}(t) |\vec{n}^\sigma(t)\rangle. \quad (3)$$

In this expression, the sum is performed over all configurations  $\vec{n}^\sigma | N_\sigma$  obeying the particle-number constraint  $\sum_{i=1}^{s_\sigma} n_i^\sigma = N_\sigma$ . On the third and final layer, called primitive layer, each SPF is represented on a one-dimensional time-independent grid [74].

The Dirac-Frenkel variational principle [75] is subsequently applied to the above ansatz in order to derive the coupled equations of motion for the expansion coefficients  $\lambda_i(t)$ ,  $C_{i, \vec{n}^\sigma}(t)$  and the SPFs  $|\varphi_j^\sigma(t)\rangle$ . Finally, performing imaginary time-evolution one arrives at the ground state wave-function (4), whereas the real time-propagation allows to study the non-equilibrium dynamics of an arbitrary initial state (5). The results to be presented below have been obtained by using  $(S, s_A, s_B) = (4, 5, 4)$  functions/SPFs on the top/species layers as well as 225 grid points on the primitive layer. We have carefully checked the convergence behavior of our results by comparing to simulations with a larger number of orbitals  $(S, s_A, s_B) = (6, 8, 6)$  and found no significant changes for the quantities of interest.

In the following we will often refer to the reduced  $j$ -body density operators  $\hat{\rho}_j^\sigma$  of species  $\sigma$  and the intercomponent reduced  $(j+k)$ -body density operator  $\hat{\rho}_{j+k}^{\sigma\bar{\sigma}}$  obtained from the many-body density operator  $\hat{\rho} = |\Psi\rangle\langle\Psi|$ :

$$\hat{\rho}_j^\sigma = \text{tr}_{N_\sigma \setminus j} \{ \text{tr}_{N_\sigma} \{ \hat{\rho} \} \}, \quad (4)$$

$$\hat{\rho}_{j+k}^{\sigma\bar{\sigma}} = \text{tr}_{N_\sigma \setminus j} \{ \text{tr}_{N_\sigma \setminus k} \{ \hat{\rho} \} \}, \quad (5)$$



where  $N_\sigma \setminus j$  stands for integrating out  $N_\sigma - j$  coordinates of component  $\sigma$  and  $\bar{\sigma} \neq \sigma$ . Of particular interest are the reduced one-body density operators  $\hat{\rho}_1^A$  and  $\hat{\rho}_1^B$  as well as the reduced two-body intra- and intercomponent density operators  $\hat{\rho}_2^A$  and  $\hat{\rho}_2^{AB}$ , respectively, since they determine the expectation values of various experimentally accessible local one- and two-body observables, such as the average particle position, the inter-atomic distance or the wave-packet width.

#### 4. Impact of Intercomponent Coupling on Ground State Properties

In Section 4.1, we analyze to which extent the many-body wave-function as well as the reduced one-body density operators are modified by the intercomponent interaction. To this end we analyze the fidelity between the interacting and non-interacting (reduced) density operators, which is a measure of their closeness. We find that with increasing absolute value of the interaction strength the system is more robust w.r.t. changes on the one-body as compared to the many-body level. Moreover, each component is affected differently depending on the lattice depth and majority interaction strength.

Subsequently, in Section 4.2 we quantify the degree of entanglement by means of the von Neumann entropy and identify parameter regions with substantial inter-particle correlations. Interestingly, increasing the absolute value of the intercomponent coupling does not always result in stronger entanglement. In fact, there are parameter regions where a strongly interacting ground state becomes almost orthogonal to the non-interacting one and the components remain to a good approximation disentangled.

Finally, we combine insights from Sections 4.1 and 4.2 to identify interesting parameter regimes and perform an in-depth analysis of the underlying physical phenomena in Section 4.3. In particular, we inspect how the spatial representation of density operators is altered and compare those to the corresponding SMF results. The latter allows us to spatially resolve the corrections to the SMF densities induced by the entanglement and interpret its impact as acceleration or deceleration of the undergoing processes, e.g., the phase separation or localization.

##### 4.1. Fidelity for Quantifying the Impact of the Intercomponent Interaction

First, we aim to analyze how the intercomponent coupling  $g_{AB}$  impacts the ground state of non-interacting species (NIS) at  $g_{AB} = 0$ . For this purpose, we evaluate the fidelity [76] of two density operators  $\hat{\rho}$  and  $\hat{\sigma}$  defined as:

$$F(\hat{\rho}, \hat{\sigma}) = \left( \text{tr} \sqrt{\sqrt{\hat{\rho}} \hat{\sigma} \sqrt{\hat{\rho}}} \right)^2 = F(\hat{\sigma}, \hat{\rho}). \quad (6)$$

We start with the fidelity between a NIS many-body density  $\hat{\rho}_0 = |\Psi_0\rangle \langle \Psi_0|$  and a many-body density  $\hat{\rho}_g = |\Psi_g\rangle \langle \Psi_g|$  for some finite coupling  $g_{AB}$  (Figure 1). Since both density operators describe pure states, Equation (6) reduces to  $F_{mb} = |\langle \Psi_0 | \Psi_g \rangle|^2$ . This measure,  $F_{mb}$ , is also known as the polaron residue studied in the context of phonon dressing of an impurity particle immersed in a bath of majority atoms [23,24].

For a weakly interacting ( $g_{AA} = 0.5$ ) majority component Figure 1a we observe that the many-body fidelity at a fixed lattice depth decreases monotonously with the modulus of the coupling strength  $g_{AB}$ . At deep lattices the rate of its reduction is larger, a behavior which is even more pronounced at strong negative  $g_{AB}$ , where the interacting state becomes almost orthogonal to the non-interacting one ( $g_{AB} = -5$  and  $V = 1000$ ). The black dashed line encircles a parameter region of instability where the SMF ansatz collapses to a configuration with broken parity symmetry. For a moderately interacting ( $g_{AA} = 3.0$ ) majority component Figure 1b the many-body fidelity becomes much more stable. Contrarily to Figure 1a the rate of reduction with  $g_{AB}$  is larger at shallow lattices instead. Finally, for a moderately deep ( $V = 500$ ) lattice Figure 1c we observe a peculiar fast decay around  $g_{AA} \approx -1$  starting at  $g_{AB} < -2$ . Additionally, at  $g_{AA} \approx -1$  and positive  $g_{AB}$  there is a small pronounced decay region (black dashed circle), which is absent in the SMF approximation.

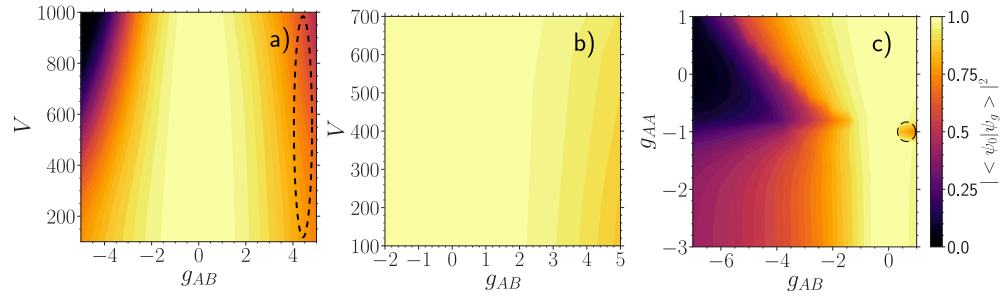


**Figure 1.** Fidelity  $|\langle \Psi_0 | \Psi_g \rangle|^2$  between a many-body state  $|\Psi_0\rangle$  at  $g_{AB} = 0$  and a many-body one  $|\Psi_g\rangle$  at finite  $g_{AB}$ , for (a)  $g_{AA} = 0.5$ , (b)  $g_{AA} = 3.0$  and (c)  $V = 500$  as a function of the majority-impurity coupling  $g_{AB}$  and the lattice depth  $V$  (a,b) or the interaction strength of the majority atoms  $g_{AA}$  (c). All quantities are given in box units with characteristic length  $R^* = L$  and energy  $E^* = \hbar^2/(mL^2)$  with  $L$  denoting the extension of the box trap. Regions encircled by black dashed lines indicate parameter regions with substantial qualitative differences to the SMF ansatz.

Next, we analyze the fidelity between a free impurity described by a pure state  $|\Phi_0\rangle \langle \Phi_0|$  and an entangled one  $\hat{\rho}_1^B$ , in general being a mixed state Figure 2. Equation (6) then simplifies to  $F_1^B = |\langle \Phi_0 | \hat{\rho}_1^B | \Phi_0 \rangle|^2$ . This measure allows to judge to which extent the impurity atom is still a "free" particle of mass  $m_B$ . We emphasize that it should not be confused with a polaron quasi-particle having a renormalized effective mass. We observe that  $F_1^B$  follows overall a similar pattern as the many-body fidelity  $F_{mb}$ , but with a significantly slower decay rate. Though there are some strong qualitative differences, see in particular Figure 2c. Namely, the abrupt decay of  $F_{mb}$  around  $g_{AA} \approx -1$  at negative  $g_{AB}$  Figure 1c is absent in  $F_1^B$  along with the small decay region at positive  $g_{AB}$  (black dashed circle). From this we anticipate that the majority component is responsible for these features in  $F_{mb}$ .

For the above reason, we now investigate the complementary fidelity  $F_1^A = F(\hat{\rho}_1^A(g_{AB} = 0), \hat{\rho}_1^A)$ , i.e., between mixed states characterizing a majority particle in the NIS state  $\hat{\rho}_1^A(g_{AB} = 0)$  and in the interacting state  $\hat{\rho}_1^A$  Figure 3. This quantity captures to which extent a majority particle is still in a mixed state induced solely by the intraspecies interaction strength  $g_{AA}$ . In case of a weak  $g_{AA}$  Figure 3a  $F_1^A$  is notably affected only at deep lattices  $V > 600$  and strong negative coupling  $g_{AB} < -4$ . For large  $g_{AA}$  Figure 3b we observe that the intercomponent correlations are not strong enough to overcome the intraspecies ones, thus barely affecting the mixedness of the NIS majority state, since  $F_1^A \approx 1$  in the whole range  $-2 < g_{AB} < 5$  and  $100 < V < 700$ . In Figure 3c we find evidence that the majority component is indeed responsible for the particular decay patterns observed in the many-body fidelity  $F_{mb}$ , which were absent in  $F_1^B$ . Overall, the majority component demonstrates a higher level of robustness at the single-particle level as compared to the impurity.

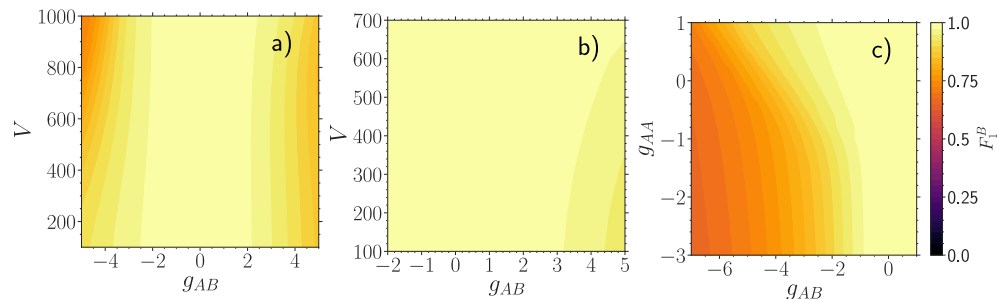


**Figure 2.** Fidelity  $F_1^B = |\langle \Phi_0 | \hat{\rho}_1^B | \Phi_0 \rangle|^2$  between a free impurity particle  $|\Phi_0\rangle$  at  $g_{AB} = 0$  and an entangled one  $\hat{\rho}_1^B$  at finite  $g_{AB}$ , for (a)  $g_{AA} = 0.5$ , (b)  $g_{AA} = 3.0$  and (c)  $V = 500$  and varying majority-impurity coupling  $g_{AB}$  and the lattice depth  $V$  or the interaction strength of the majority atoms  $g_{AA}$ . All quantities are expressed in box units with characteristic length  $R^* = L$  and energy  $E^* = \hbar^2/(mL^2)$  while  $L$  is the extension of the box trap.

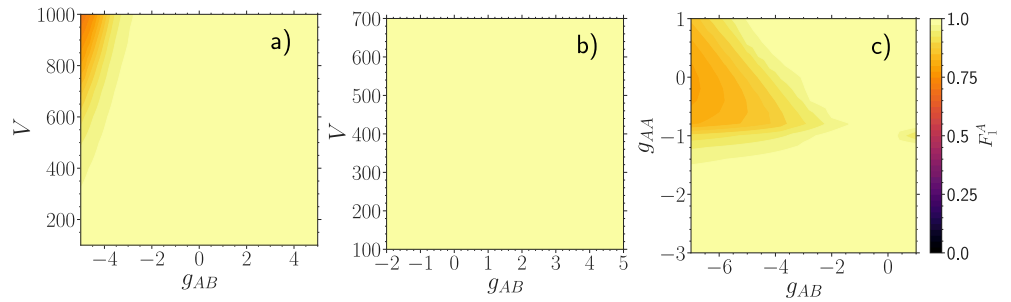


**Figure 3.** Fidelity  $F_1^A = F(\rho_1^A, \hat{\rho}_1^A(g_{AB} = 0))$  between mixed states characterizing a majority particle when the medium is disentangled  $\hat{\rho}_1^A(g_{AB} = 0)$  and entangled  $\hat{\rho}_1^A$  with the impurity atom, for (a)  $g_{AA} = 0.5$ , (b)  $g_{AA} = 3.0$  and (c)  $V = 500$  as a function of the majority-impurity coupling  $g_{AB}$  and the lattice depth  $V$  (a,b) or the interaction strength of the majority atoms  $g_{AA}$  (c). All quantities are provided in box units of characteristic length  $R^* = L$  and energy  $E^* = \hbar^2 / (mL^2)$  with  $L$  being the extension of the box trap.

4.2. Entropy Measures for Quantifying the Degree of Correlations

As we have seen in the previous section, an initially disentangled composite system may be drastically influenced by the intercomponent coupling. However, it is far from obvious to which extent the correlations are actually involved when the ground state undergoes structural changes [77]. For instance, a strongly interacting ground state may in fact just represent a different disentangled state or a state seemingly unaffected by the coupling may feature substantial correlations which guarantee its robustness. To investigate these intriguing possibilities we perform a further classification based on the degree of inter-particle correlations.

To quantify the degree of correlations in our impurity system we use the von Neumann entropy of the reduced density operators [78]. Here, we distinguish between the entanglement entropy  $S_{vN}$  of the reduced density operator  $\hat{\rho}^\sigma$  of species  $\sigma$  [9,46] and the fragmentation entropy  $S_{vN}^\sigma$  of the reduced one-body density operator  $\hat{\rho}_1^\sigma$  of species  $\sigma$  [52,79,80]. The former,  $\hat{\rho}^\sigma$ , is obtained by tracing the density operator  $\hat{\rho}$  of the composite many-body system over one of the species, while the latter,  $\hat{\rho}_1^\sigma$ , by additionally tracing  $\hat{\rho}^\sigma$  over all of the particles of the remaining component except one. In the presence of correlations the resulting reduced density operator will describe a mixed state. The entanglement entropy is caused by intercomponent correlations whereas the fragmentation entropy is primarily a signature of intracomponent ones, though it can be greatly impacted once the intercomponent correlations become dominant. Explicitly, the entanglement and fragmentation entropies are given as:

$$S_{vN} = -\text{tr}(\hat{\rho}^\sigma \ln \hat{\rho}^\sigma) = -\sum_{i=1}^S \lambda_i \ln \lambda_i \quad \text{with } \hat{\rho}^\sigma = \text{tr}_{\bar{\sigma}}(\hat{\rho}) = \sum_{i=1}^S \lambda_i |\Psi_i^\sigma\rangle \langle \Psi_i^\sigma|, \quad (7)$$

$$S_{vN}^\sigma = -\text{tr}(\hat{\rho}_1^\sigma \ln \hat{\rho}_1^\sigma) = -\sum_{i=1}^{s_\sigma} n_i^\sigma \ln n_i^\sigma \quad \text{with } \hat{\rho}_1^\sigma = \text{tr}_{N_\sigma-1}(\hat{\rho}^\sigma) = \sum_{i=1}^{s_\sigma} n_i^\sigma |\Phi_i^\sigma\rangle \langle \Phi_i^\sigma|. \quad (8)$$

In these expressions,  $\lambda_i$  and  $|\Psi_i^\sigma\rangle$  denote the natural populations and natural orbitals of the spectrally decomposed  $\hat{\rho}^\sigma$ , while  $n_i^\sigma$  and  $|\Phi_i^\sigma\rangle$  are the natural populations and natural orbitals of the spectrally decomposed  $\hat{\rho}_1^\sigma$  [60,72]. Furthermore,  $S$  and  $s_\sigma$  are the number of species orbitals and single-particle functions, respectively,  $N_\sigma$  is the number of  $\sigma$  component particles and  $\sigma \neq \bar{\sigma}$ .

In the following, we display the species entanglement  $S_{vN}$  from Equation (7) Figure 4 and the majority fragmentation  $S_{vN}^A$  from Equation (8) Figure 5 as a function of the majority-impurity coupling  $g_{AB}$  and the lattice depth  $V$  or the interaction strength of the majority atoms  $g_{AA}$ . In case the entanglement entropy  $S_{vN}$  is close to zero, the

corresponding subsystems are to a very good approximation disentangled. Thus, making a SMF ansatz in Equation (2) would greatly facilitate numerical calculations while providing quantitatively good results for physical observables. On the other hand, already moderate values of entanglement may have an impact on some physical quantities with measurable differences to the SMF approximation, whereas local peaks may indicate phase transitions [10,81,82]. Regarding the fragmentation entropy of interacting majority atoms  $S_{vN}^A$ , it is highly non-trivial to predict how their intrinsic mixedness, caused by the intra-particle interactions  $g_{AA}$ , can be changed by the intercomponent coupling  $g_{AB}$ .

#### 4.2.1. Weakly Repulsive Interacting Majority Component

For a weakly interacting majority component with  $g_{AA} = 0.5$ , the entanglement entropy  $S_{vN}$  Figure 4a displays two different behaviors depending on the sign of the coupling strength. For positive  $g_{AB}$  it increases gradually with increasing coupling strength  $g_{AB}$ , with the build-up being faster for a deeper lattice [52]. This is related to the onset of phase separation taking place sooner for a deeper lattice with increasing  $g_{AB}$  (see also the discussion in Section 4.3). Turning to negative  $g_{AB}$  the entanglement entropy first grows gradually with decreasing coupling strength  $g_{AB}$ , but then, for larger  $V$  below some threshold value, the entanglement reduces to almost zero ( $g_{AB} < -4$  and  $V > 600$ ). Apart from the above mentioned pattern the overall behavior of  $S_{vN}$  in Figure 4a is very similar to the one observed in the corresponding many-body fidelity Figure 1a.

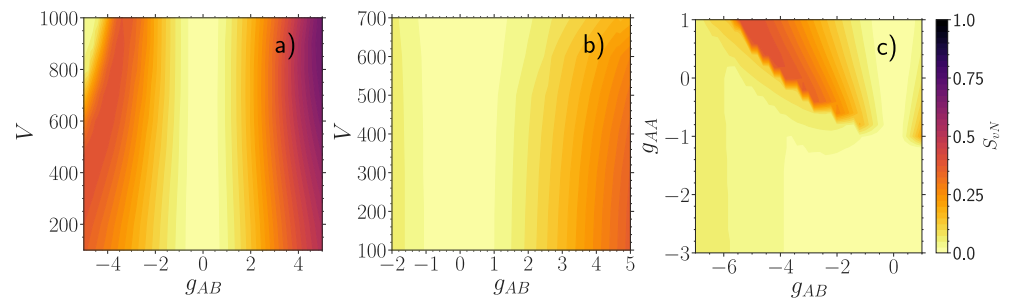


**Figure 4.** Entanglement entropy  $S_{vN}$ , see Equation (7), for (a)  $g_{AA} = 0.5$ , (b)  $g_{AA} = 3.0$  and (c)  $V = 500$  with varying majority-impurity coupling  $g_{AB}$  and the lattice depth  $V$  (a,b) or the interaction strength of the majority atoms  $g_{AA}$  (c). All quantities are given in box units with characteristic length  $R^* = L$  and energy  $E^* = \hbar^2 / (mL^2)$  with  $L$  denoting the extension of the box trap.

The fragmentation entropy of the majority component  $S_{vN}^A$  Figure 5a at  $g_{AB} = 0$  is larger for a deeper lattice. The reason is that the ratio of the intraspecies interaction energy and the single-particle energy of the majority component increases with a larger  $V$  or  $g_{AA}$ . In the limit of an infinitely deep lattice or an infinitely strong intraspecies repulsion we expect full fermionization, meaning that the one-body density operator becomes a mixed state with a uniform distribution of natural orbitals and the fragmentation entropy of the majority component reaches the value  $\ln(N_A) \approx 1.6$ . However, we observe that we are operating far away from that limit, since  $\max S_{vN}^A < 0.4$ .

At positive  $g_{AB}$ , as the entanglement entropy  $S_{vN}$  builds up Figure 4a, the fragmentation entropy  $S_{vN}^A$  of the majority component at  $g_{AB} = 0$  is more robust to variations of  $g_{AB}$  at deeper lattice depths compared to shallow lattices Figure 5a. Once the entanglement becomes strong enough to overcome intracomponent correlations, the fragmentation entropy of the majority atoms starts to increase with a fast rate (e.g.,  $V = 1000$ ,  $g_{AB} > 4$ ). At negative  $g_{AB}$ , if the medium features a small fragmentation entropy at  $g_{AB} = 0$  ( $V < 900$ ), then  $S_{vN}^A$  rises first with decreasing  $g_{AB}$ , reaches a local maximum and finally drops to very small values at a sufficiently strong coupling strength. In contrast, if the fragmentation entropy of the decoupled majority component has already reached a moderate magnitude ( $V > 900$ ), then the initial fragmentation is gradually reduced with decreasing  $g_{AB}$ , until finally both entropies become negligibly small ( $g_{AB} < -4$ ). Once that happens, the resulting

many-body state becomes to a good approximation a disentangled composite state with a condensed majority component.

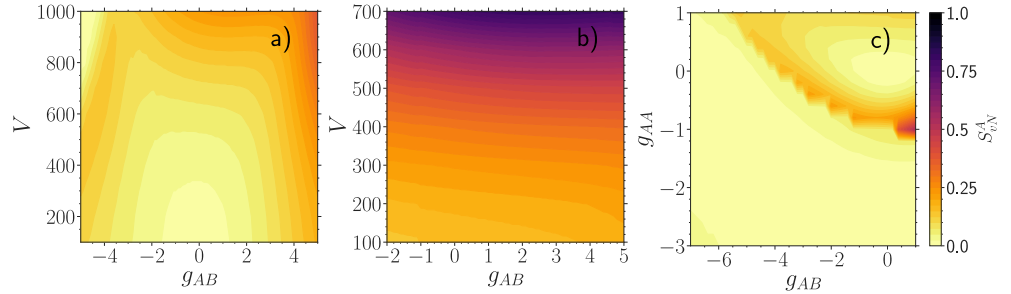


**Figure 5.** Fragmentation entropy  $S_{vN}^A$ , see Equation (8), for (a)  $g_{AA} = 0.5$ , (b)  $g_{AA} = 3.0$  and (c)  $V = 500$  with respect to the majority-impurity coupling  $g_{AB}$  and the lattice depth  $V$  (a,b) or the interaction strength of the majority atoms  $g_{AA}$  (c). All quantities are provided in terms of box units with characteristic length  $R^* = L$  and energy  $E^* = \hbar^2/(mL^2)$  while  $L$  denotes the extension of the box trap.

#### 4.2.2. Moderately Repulsive Interacting Majority Component

The entanglement entropy  $S_{vN}$  of a moderately interacting majority medium at  $g_{AA} = 3.0$  in Figure 4b displays the same qualitative behavior as the many-body fidelity  $F_{mb}$  shown in Figure 1b. Contrary to  $g_{AA} = 0.5$  the entanglement is overall less pronounced and builds up faster at shallow lattice depths instead. Such a comparatively weak entanglement leaves only a minor imprint on the fragmentation of the majority component  $S_{vN}^A$ , see Figure 5b, manifested as a weak dependence on the coupling  $g_{AB}$ . The fragmentation of the majority species is substantial compared to  $g_{AA} = 0.5$  Figure 5a at the same lattice depth. Nevertheless, the fermionization limit is not yet reached, since  $\max S_{vN}^A \approx 0.8$ . The intercomponent correlations are not strong enough to overcome the intraspecies ones in accordance with the robustness of the majority component observed on the one-body level in Figure 3b. From this we expect a rather small impact of entanglement on observables, which depend solely on the majority particle distribution.

#### 4.2.3. Attractively Interacting Majority Component

Finally, we analyze the dependence of the above-described entropy measures on the intraspecies interaction strength  $g_{AA}$  for a moderately deep lattice depth  $V = 500$  Figures 4c and 5c. Since repulsive interactions have been already amply covered, we here concentrate on negative  $g_{AA}$  and  $g_{AB}$ .

As it can be readily seen, there is a parameter sector at  $g_{AB} < 0$  and  $g_{AA} > -1$  containing high values for the entanglement entropy  $S_{vN}$  Figure 4c. This sector displays a similar behavior to  $S_{vN}$  in Figure 4a at negative couplings, namely starting from the decoupled regime, the entanglement grows with decreasing  $g_{AB}$ , only to drastically decrease below some negative threshold value of  $g_{AB}$ . This threshold for  $g_{AB}$  lies at lower values the higher the intracomponent interaction strength  $g_{AA}$  is. We find that this abrupt decay of  $S_{vN}$  coincides with the one observed in the many-body fidelity  $F_{mb}$  Figure 1c. This suggests that the disappearance of intercomponent correlations leads to an increased susceptibility of the system to  $g_{AB}$  variation. The other decay region, present in  $F_{mb}$  at  $g_{AA} \approx -1$  and negative  $g_{AB}$ , is missing in the entanglement entropy  $S_{vN}$ . From this we infer that it can be understood within the SMF picture. Additionally, there is also another much smaller sector characterized by a high entanglement entropy at  $g_{AB} > 0$  and  $g_{AA} \approx -1$ . It is directly related to structural changes observed in  $F_{mb}$  and  $F_1^A$  at the same values Figures 1c and 3c, which would have been absent in the SMF picture. Apart from that, below  $g_{AA} < -1$  the entanglement entropy among the components is either absent or of minor relevance.

Previously, we have mentioned that an isolated majority species, which interacts repulsively ( $g_{AA} > 0$ ), features a higher degree of fragmentation the larger  $g_{AA}$  is. In

the case of attractive interactions ( $g_{AA} < 0$ ), however, the situation is different. Namely, starting from  $g_{AA} = 0$  the fragmentation entropy tends first to increase with decreasing  $g_{AA}$ , but then decreases up to the point of describing approximately a condensed state again see Figure 5c at  $g_{AB} = 0$ . Regarding the impact of the intercomponent coupling  $g_{AB}$  on  $S_{vN}^A$  we observe overall very similar patterns as for the entanglement entropy  $S_{vN}$  Figure 4c. Regions where both entropic measures  $S_{vN}$  and  $S_{vN}^A$  are of small magnitude remind of the corresponding sectors in Figures 4a and 5a at  $V > 800$  and  $g_{AB} < -4$ .

#### 4.3. Single- and Two-Particle Density Distributions

The measures of fidelity and entropy discussed in the previous sections are very useful in identifying parameter regions being substantially impacted and/or highly correlated indicating regimes of high interest for further investigation. However, they do not provide insights into the actually undergoing processes. To get a better understanding we ask for the impact on measurable quantities such as the one-body and two-body density distribution functions, which can be accessed by fluorescence imaging with a quantum gas microscope [83–87].

In the following,  $\rho_1^\sigma(z)$  describes the probability density to find a single particle of species  $\sigma$  at position  $z$ , while  $\rho_2^{\sigma\bar{\sigma}}(z_1, z_2)$  denotes the probability density to simultaneously measure one particle of species  $\sigma$  at position  $z_1$  and another one of the same or different species  $\bar{\sigma}$  at position  $z_2$ . The expectation value of any local observable depending on up to two degrees of freedom can be evaluated as an overlap integral with the appropriate probability density. Since many local observables often depend only on the distance between the particles, i.e.,  $O(z_1, z_2) = O(z_1 - z_2)$ , we replace  $\rho_2^{\sigma\bar{\sigma}}(z_1, z_2)$  by the probability density  $\rho_r^{\sigma\bar{\sigma}}(r)$  to measure two particles belonging to the same or different species at a relative distance  $r$  independent of their individual positions. To this end we perform a coordinate transformation  $R = (z_1 + z_2)/2$  and  $r = z_1 - z_2$  giving the following identity:

$$\int \rho_2^{\sigma\bar{\sigma}}(z_1, z_2) dz_1 dz_2 = \int \rho_r^{\sigma\bar{\sigma}}(r, R) dr dR. \quad (9)$$

Then we define:

$$\rho_r^{\sigma\bar{\sigma}}(r) = \int \rho_2^{\sigma\bar{\sigma}}(r, R) dR. \quad (10)$$

Our first goal here is to investigate how the above mentioned quantities are affected in parameter sectors displaying strong susceptibility to structural changes identified in Section 4.1 and, in particular, whether the density distributions are capable to capture the undergoing changes in the many-body state.

Our second goal is to extract the impact of the entanglement. To this end we compare the above density distributions obtained from the variational ML-X calculations to the ones where the SMF ansatz is assumed. The latter will be distinguished by a tilde sign placed on top of the corresponding quantities. In the following, we shall evince that a large entanglement entropy identified in Section 4.2 has indeed a notable impact, but not always on all of the above mentioned density distributions. Thus, it may enhance or impede the effects coming from the induced SMF potential, such as phase separation and localization, or affect the bunching properties of the majority component.

##### 4.3.1. Weakly Repulsive Interacting Majority Component

For a shallow lattice ( $V = 100$ ) we observe in Figure 6 that the majority component (panel a1) at  $g_{AB} = 0$  occupies mainly the central site (at  $z = 0$ ) and the two intermediate ones (at  $z = \pm 0.2$ ), while  $\rho_r^{AA}$  (panel c1) features an almost Gaussian shape due to weak intraspecies correlations. At moderate positive couplings ( $g_{AB} > 3$ ) both quantities are only slightly affected in accordance with the robustness of  $F_1^A$  in this interaction regime Figure 3a. At moderate negative couplings ( $g_{AB} < -3$ ) both  $\rho_1^A$  and  $\rho_r^{AA}$  shrink with decreasing  $g_{AB}$  indicating an increased bunching tendency of the majority atoms towards the central lattice

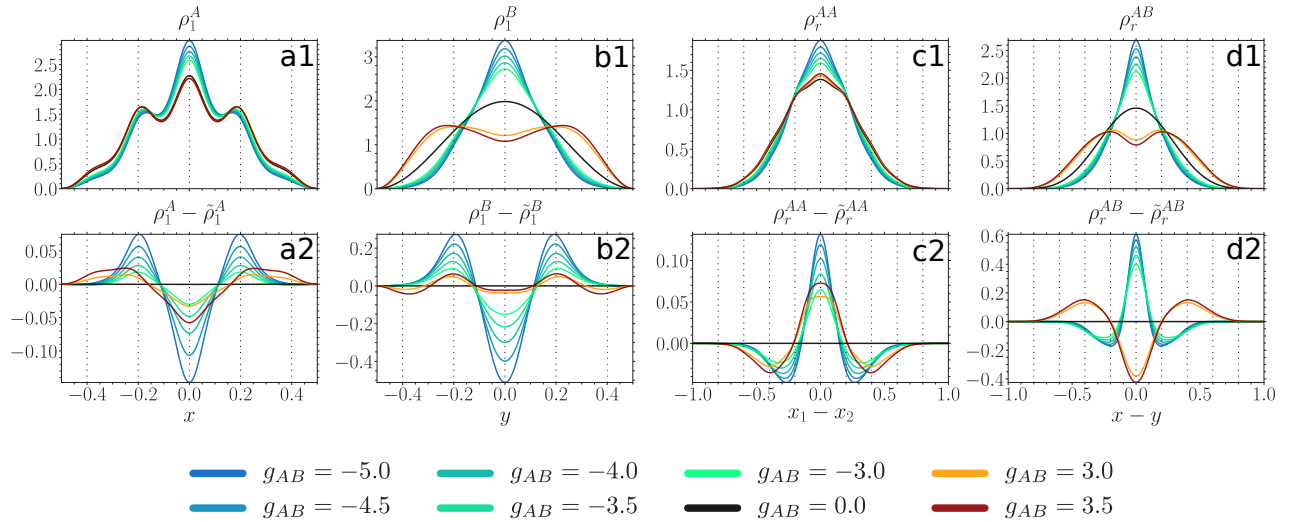


**Figure 6.** Upper panels: one-body probability densities  $\rho_1^A(x)$ ,  $\rho_1^B(y)$  (see Equation (4)) and distance probability distributions  $\rho_r^{AA}(x_1 - x_2)$ ,  $\rho_r^{AB}(x - y)$  (see Equation (10)) at  $g_{AA} = 0.5$ ,  $V = 100$  and for various values of  $g_{AB}$  (see legend). Lower panels: difference between probability densities obtained from the variational ML-X simulations and the SMF ansatz, the latter distinguished by a tilde sign. All quantities are given in box units with characteristic length  $R^* = L$  and energy  $E^* = \hbar^2/(mL^2)$  with  $L$  being the extension of the box trap.

The decoupled impurity particle (panel b1) occupies the ground state of the box potential. At moderate positive couplings it develops two humps and forms a shell around the majority component density, a signature of phase separation [46,63] further confirmed by the appearance of two humps in  $\rho_r^{AB}$  (panel d1). At negative couplings  $\rho_1^B$  and  $\rho_r^{AB}$  shrink with decreasing  $g_{AB}$  accumulating around the trap center. The entanglement favors the process of phase separation at positive couplings and bunching between the two species at negative couplings (panel d2), while slowing down the shrinking of  $\rho_1^B$  at negative coupling (panel b2). We also remark that upon reaching a certain threshold value of  $g_{AB} > 4$ , the SMF solution experiences breaking of parity symmetry, causing substantial differences to the many-body symmetry-preserving solution (not shown).

For a deep lattice ( $V = 1000$ ) in Figure 7 the majority component (panel a1) at  $g_{AB} = 0$  displays an almost uniform distribution over all the lattice sites, while  $\rho_r^{AA}$  (panel c1) features a multi-hump structure due to stronger intraspecies correlations cf. Figure 5a). At moderate positive couplings ( $g_{AB} > 3$ ) the width of  $\rho_1^A$  and  $\rho_r^{AA}$  is only slightly increased, again in accordance with the robustness of  $F_1^A$  Figure 3a. Thus, the majority component, experiencing the presence of a repelling impurity atom, shows a slight enhancement of the already present delocalization over the lattice. At moderate negative couplings ( $g_{AB} < -3$ ) both  $\rho_1^A$  and  $\rho_r^{AA}$  shrink with decreasing  $g_{AB}$  to the extent where all atoms occupy predominantly only the central site ( $g_{AB} < -4$ ). Such a large difference to the non-interacting ground state is in accordance with the observations made in  $F_1^A$  Figure 3a.

The impact of entanglement is structurally different compared to a shallow lattice (panels a2 and c2). At positive couplings, the entanglement greatly increases the probability for the majority atoms to be found at the central site, while decreasing the probability at outer sites ( $z = \pm 0.4$ ) and being indifferent to the intermediate sites (panel a2). Additionally, it favors the bunching of the majority particles at the same or neighboring sites and

disfavors them being more than two sites apart (panel c2). At negative couplings, it acts in a similar way as in the case of shallow lattices, except that for a sufficiently strong coupling strength ( $g_{AB} < -4$ ), where both entropy measures are of small magnitude see Figures 4a and 5a, the SMF ansatz is in good accordance with the many-body solution.

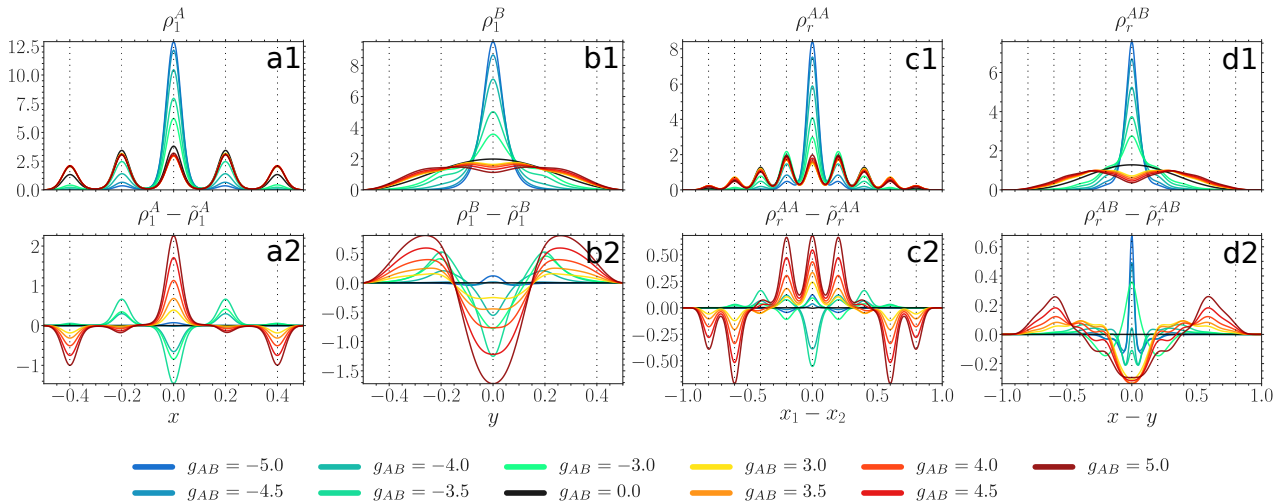


**Figure 7.** Upper panels: one-body probability densities  $\rho_1^A(x)$ ,  $\rho_1^B(y)$  (see Equation (4)) and distance probability distributions  $\rho_r^{AA}(x_1 - x_2)$ ,  $\rho_r^{AB}(x - y)$  (see Equation (10)) at  $g_{AA} = 0.5$ ,  $V = 1000$  and for various values of  $g_{AB}$  (see legend). Lower panels: difference between probability densities obtained from many-body ML-X calculations and SMF ansatz, the latter distinguished by a tilde sign. All quantities are given in box units with characteristic length  $R^* = L$  and energy  $E^* = \hbar^2 / (mL^2)$  with  $L$  denoting the extension of the box trap.

The impurity particle (panel b1) at positive couplings ( $g_{AB} > 3$ ) first develops two humps, but then as the coupling increases, the relative distance between those peaks grows, while the humps themselves become flatter. There is a strong signature of an onset of a four-peak structure at  $g_{AB} = 5$ . This is in accordance with the increasing relative distance between the species (panel d1) and the fact that the majority atoms are distributed uniformly over all the lattice sites in contrast to  $g_{AA} = 0.5$ , where the majority component was occupying mainly the central and the intermediate sites. At negative couplings ( $g_{AB} < -3$ )  $\rho_1^B$  and  $\rho_r^{AB}$  shrink with decreasing  $g_{AB}$ .

The entanglement favors the process where the impurity atom moves from the box center to its boundaries independently of the sign of the coupling (panel b2). At  $g_{AB} < -4.0$  it plays only a minor role, the same as for the majority component. Regarding  $\rho_r^{AB}$ , at positive couplings the entanglement favors the process of phase separation by pushing the impurity particle more than two sites apart from a majority atom (panel d2). At negative couplings it enhances the bunching between the two species, even when the entanglement entropy is very small (e.g., at  $g_{AB} = -5.0$ ).

#### 4.3.2. Moderately Repulsive Interacting Majority Component

Considering our findings regarding fidelity and entropy measures we investigate here only shallow lattices at positive couplings Figure 8, where the structural changes caused by the coupling and the entanglement entropy  $S_{vN}$  may have a sizable impact on density distributions. The decoupled density of the majority component (panel a1) has three pronounced humps at the central ( $z = 0$ ) and intermediate sites ( $z = \pm 0.2$ ). The profile is overall more spread compared to a weakly interacting majority (cf. Figure 6 panel a1). Indeed, it is most beneficial for two particles to occupy neighboring sites (see the two humps in panel c1). The majority component gets only a weak feedback from the presence of a repulsive impurity atom, even at coupling strengths comparable to  $g_{AA}$  in accordance with the robustness of  $F_1^A$  in Figure 3b. The role of the entanglement is also



rather weak, though qualitatively different to  $g_{AA} = 0.5$  in Figure 6. Thus, it increases the probability for the majority particle to be found at the region enclosed between the two intermediate sites, while decreasing the probability to be detected outside of that region (panel a2). Furthermore, it favors particle distances of a half lattice constant ( $a_l = 0.2R^*$ ) (panel c2).

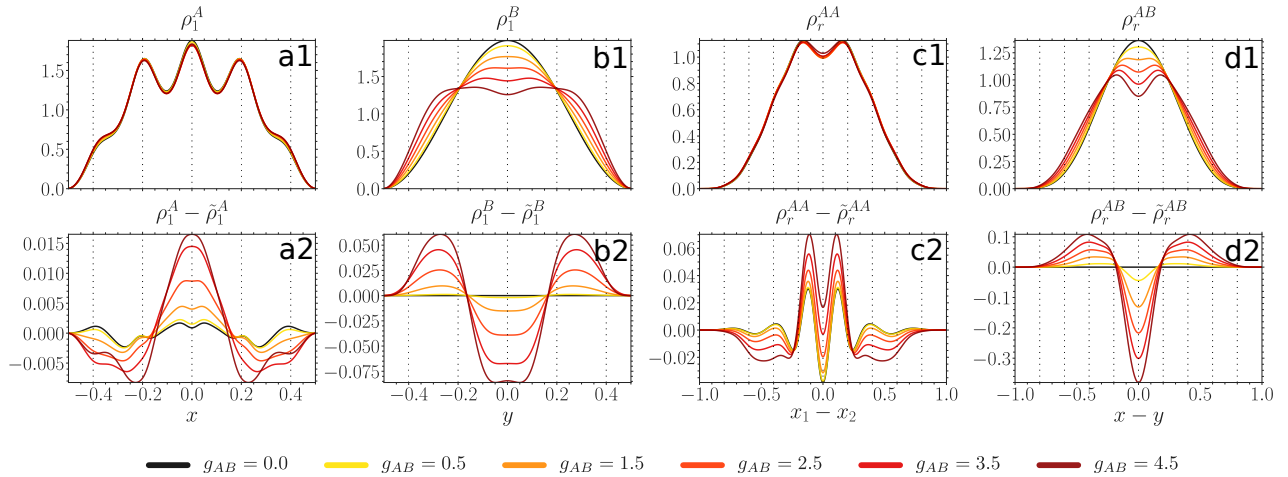


**Figure 8.** Upper panels: one-body probability densities  $\rho_1^A(x)$ ,  $\rho_1^B(y)$  (see Equation (4)) and distance probability distributions  $\rho_r^{AA}(x_1 - x_2)$ ,  $\rho_r^{AB}(x - y)$  (see Equation (10)) at  $g_{AA} = 3.0$ ,  $V = 100$  and for different values of  $g_{AB}$  (see legend). Lower panels: difference between probability densities obtained from the many-body ML-X calculations and SMF ansatz, the latter distinguished by a tilde sign. All quantities are provided in terms of box units with characteristic length  $R^* = L$  and energy  $E^* = \hbar^2 / (mL^2)$  while  $L$  is the extension of the box trap.

The impurity particle (panel b1) experiences phase separation similar to Figure 6 (panel b1), i.e., upon increasing  $g_{AB}$  it develops two humps with a minimum at the trap center. Then, those humps separate and flatten, until finally they would form a four-hump structure with three local minima located at the position of the three peaks in the majority component density (compare to panel a1). The separation between the species is again clearly manifested as two humps in  $\rho_r^{AB}$  with favored distance of a lattice constant ( $a_l = 0.2R^*$ ) (panel d1). The entanglement affects the impurity atom in quite an opposite way when compared to the majority component (panel b2), i.e., it decreases the probability for the impurity atom to be found at the region enclosed between the two intermediate sites, while increasing the probability to lie outside of that region. Additionally, similar to the behavior at weaker  $g_{AA}$  (cf. Figure 6 panel d2), the entanglement accelerates the phase separation process (panel d2).

#### 4.3.3. Attractively Interacting Majority Component

Finally, we concentrate on negative intraspecies interactions  $g_{AA}$ , namely a weak negative  $g_{AA} = -0.4$  at negative  $g_{AB}$  Figure 9, contained in the parameter sector with substantial entanglement entropy Figure 4c.

In Figure 9, a decoupled majority atom where  $g_{AB} = 0$  is localized at the central ( $z = 0$ ) and intermediate ( $z = \pm 0.2$ ) wells (panel a1). Even though the majority atoms are attracted to each other, the probability to be one or even two wells apart is still sizable (panel c1). With decreasing  $g_{AB}$  both  $\rho_1^A$  and  $\rho_r^{AA}$  shrink to a Gaussian. The impact of entanglement is quite different compared to the previously considered cases. Thus, at  $g_{AB} > -4.8$  the entanglement slows down the process of  $\rho_1^A$  localization at the central well (panel a2). The strongest impact is reached around  $g_{AB} \approx -2.4$ , where the entanglement entropy is largest for the given value of intracomponent interaction  $g_{AA} = -0.4$  Figure 4c. Below  $g_{AB} < -4.8$ , as the entanglement entropy suddenly drops, so does the difference to the SMF ansatz. The intercomponent correlations favor clustering of the majority atoms at

$-2.4 < g_{AB} < 0$  and  $g_{AB} < -4.2$ , whereas at  $-4.2 < g_{AB} < -2.4$ , where the entanglement entropy is largest, they inhibit the clustering (panel c2).

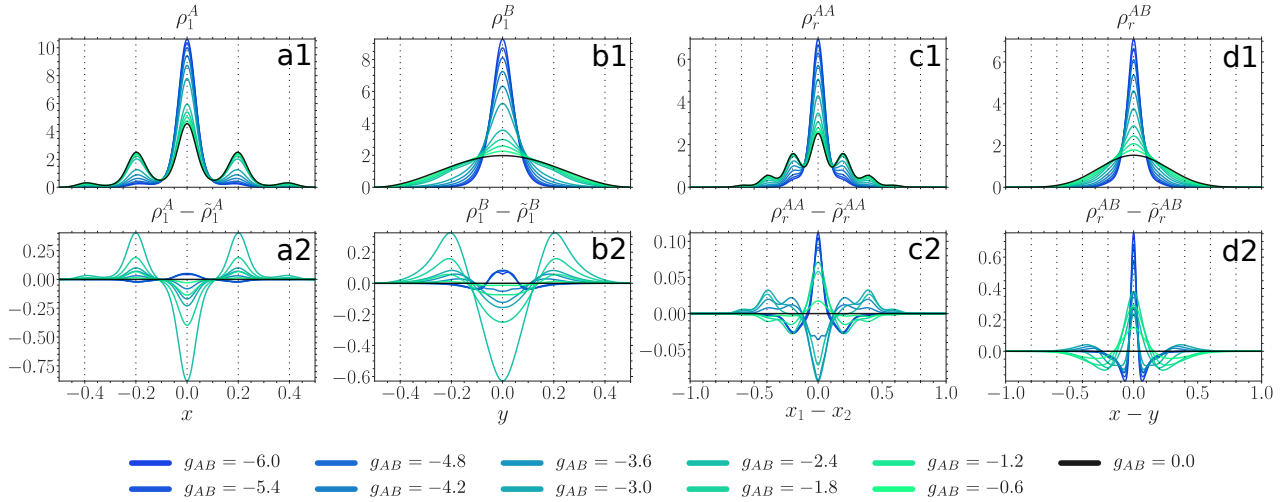


**Figure 9.** Upper panels: one-body probability densities  $\rho_1^A(x)$ ,  $\rho_1^B(y)$  (see Equation (4)) and distance probability distributions  $\rho_r^{AA}(x_1 - x_2)$ ,  $\rho_r^{AB}(x - y)$  (see Equation (10)) at  $g_{AA} = -0.4$ ,  $V = 500$  and for various values of  $g_{AB}$  (see legend). Lower panels: difference between probability densities obtained from the variational ML-X simulations and SMF ansatz, the latter distinguished by a tilde sign. All quantities are expressed in box units of characteristic length  $R^* = L$  and energy  $E^* = \hbar^2/(mL^2)$  while  $L$  being the extension of the box trap.

The impurity density  $\rho_1^B$  shows a similar behavior as the majority component density (panel b1), also in terms of the role of the entanglement (panel b2). The width of  $\rho_r^{AB}$  shrinks with decreasing  $g_{AB}$  (panel d1), while the entanglement enhances the bunching between the two species (panel d2).

## 5. Quench Induced Tunneling Dynamics

Having analyzed in detail the ground state properties of our system, we subsequently study the dynamical response of a single impurity coupled to a lattice trapped species upon quenching the interspecies interaction strength  $g_{AB}$ . To this end we prepare the system in its ground state for  $V = 500$ ,  $g_{AB} = 6.0$  and  $g_{AA} = 0.5$ , leading to the formation of a two-fold degeneracy in the ground state and the two species phase separate [46]. In this sense, the ground state one-body density is given by a superposition state of two parity-symmetry broken configurations, where the density of the first one is depicted in Figure 10a and the second one corresponds to its parity-symmetric (with respect to  $x = 0$ ) counterpart. It is possible to remove this degeneracy in order to select any of the states in the respective degenerate manifold. Technically, this is done by applying a small asymmetry, e.g., a tilt, to the lattice potential, thereby breaking the parity symmetry and energetically favoring one of the above-mentioned states [50].

To trigger the dynamics starting from the initial state configuration illustrated in Figure 10a we quench the interspecies interaction strength to a smaller value. As a representative example of the emergent tunneling dynamics of each species we present the temporal evolution of the corresponding one-body densities in Figure 10c,d following a quench to  $g_{AB} = 4.5$ , while keeping fixed  $V = 500$  and  $g_{AA} = 0.5$ . In this case the impurity performs an oscillatory motion which is reminiscent of the tunneling of a particle in a double-well. This can be attributed to the lifting of the degeneracy for smaller interspecies interaction strengths. For a post-quench value of  $g_{AB} = 4.5$  the initially prepared state has a substantial overlap with the post-quench ground state and the first excited state such that in the course of the dynamics the system will oscillate between those two. This is similar to a single particle in a double-well which is prepared as a superposition of the

first doublet and undergoes a tunneling between the sites. Correspondingly, the majority species will undergo a collective tunneling in the lattice geometry [50,53]. Thus, the probability distribution of a single majority species particle will oscillate between the initial distribution Figure 10a and its parity-symmetric counterpart. Due to the repulsive nature of the interspecies coupling the two species move in opposite directions such that they end up in phase-separated configurations after half a period. Note that the oscillation period, being the energy gap between the two energetically lowest eigenstates of the post-quench Hamiltonian (not shown here), depends on the post-quench  $g_{AB}$ . This can be easily verified by monitoring the temporal evolution of the averaged position of the impurity [13] which is defined as

$$\langle \hat{X}_B \rangle = \int_{-L/2}^{L/2} dx \rho_1^B(x)x. \tag{11}$$

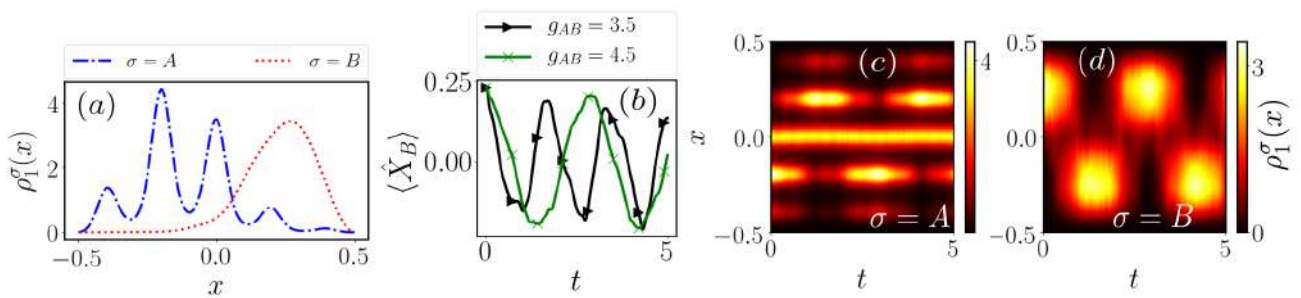


**Figure 10.** (a) One-body density  $\rho_1^\sigma(x)$  of the initial state configuration for  $V = 500$ ,  $g_{AA} = 0.5$  and  $g_{AB} = 6.0$  at  $t = 0$ . Temporal evolution of (b) the averaged position of the impurity  $\langle \hat{X}_B \rangle$  (see Equation (11)), (c) the one-body density of the majority species and (d) the one-body density of the impurity upon quenching the interspecies interaction strength to  $g_{AB} = 4.5$ .

For various post-quench  $g_{AB}$  we find that the impurity will occupy its parity-symmetric counterpart, reflected in the decrease of  $\langle \hat{X}_B \rangle$  towards negative values, while the oscillation decreases with smaller  $g_{AB}$  Figure 10b.

In order to gain insight into beyond mean-field effects we investigate the natural populations  $n_j^\sigma$  (see Equation (8)) which indicate the degree of fragmentation of the subsystem [9,71]. For simplicity here we present the populations of the first two dominantly populated natural orbitals while using six orbitals in the actual calculations. The initial depletion of both subsystems is rather small, i.e.,  $n_1^A \approx 0.996$  and  $n_1^B \approx 0.99$ , such that any decrease of these populations upon quenching  $g_{AB}$  is due to dynamical many-body effects. We find that for both subsystems dominantly two natural orbitals contribute during the dynamics Figure 11c,d, while the ones of the medium are less impacted by the quench. For the natural populations of the impurity signatures of an oscillation can be observed, where  $n_1^B$  initially decreases and revives back towards  $n_1^B \approx 0.99$ , while  $n_2^B$  initially increases and afterwards drops back to nearly zero. In order to attribute the occupation of the additional natural orbital to physical processes, we analyze the spatial distribution of the natural orbitals  $\Phi_j^B(x, t)$  (see Equation (8)) themselves focusing on the impurity Figure 11a,b. In Figure 11a we observe that the first natural orbital corresponds to the oscillatory behavior of the one-body density of the impurity, but lacking the smooth transition between the phase-separated configurations (see Figure 10d). The first natural orbital dominates during the dynamics and we can interpret its behavior as corresponding to the presence of the phase-separated density configurations. Consequently, the second natural orbital Figure 11b, resembling the mirror image of the first one, contributes to deviations from this solution. Due to its structure we can deduce that it is responsible for initiating the transport of the impurity, thereby allowing for the counterflow of the two species. Note that the presence of more than one natural orbital during the dynamics is a clear signature that mean-field theory would not provide an accurate description of the system dynamics.

Hence, the fact that  $|\Phi_2^B\rangle$  is occupied is a manifestation of many-body effects, influencing the motion of both species.

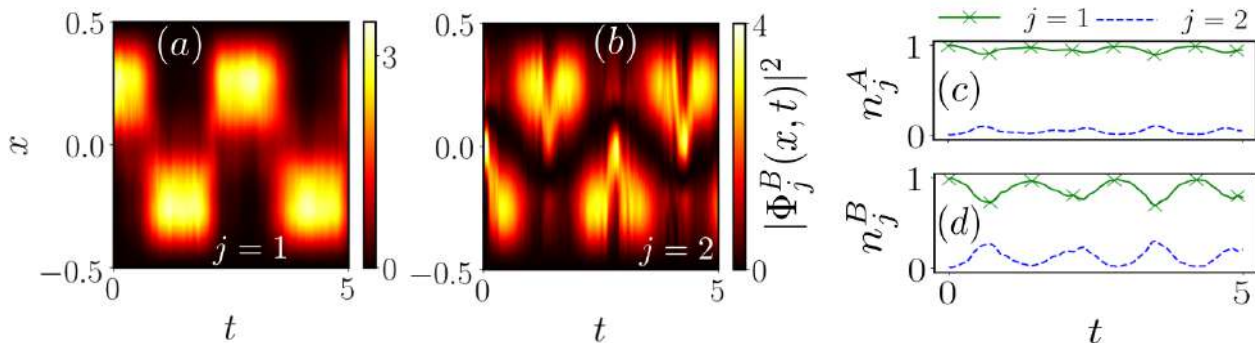


**Figure 11.** Temporal evolution of the density of (a) the first and (b) the second natural orbital  $|\Phi_j^B(x,t)\rangle$  (see Equation (8)) of the impurity and (c), (d) the natural populations  $n_j^\sigma$  of both subsystems upon quenching the interspecies interaction strength  $g_{AB}$  of the ground state in Figure 10a to  $g_{AB} = 4.5$ .

## 6. Summary and Outlook

In this work we analyze the static and dynamical properties of a few-body particle-imbalance bosonic mixture at zero temperature. Importantly, the components are exposed to different one-dimensional external traps where the majority species is subject to a finite lattice potential while the single impurity is trapped in a box of the same extension as the lattice. We study the response of the composite system upon the variation of majority-impurity coupling  $g_{AB}$  and majority component internal parameters being either the lattice depth  $V$  or the majority-majority interaction strength  $g_{AA}$ .

To quantify the response of static properties we employ the fidelity between two density operators describing ground states at zero and a finite intercomponent interaction  $g_{AB}$ . We contrast the response at the many-body to the single-particle level. We observe that the composite system is quite robust to the variation of the intercomponent interaction at strongly repulsive  $g_{AA}$ , while being fragile at strongly attractive  $g_{AB}$  and deep lattices  $V$  as well as when  $g_{AA}$  is weakly attractive and  $g_{AB}$  is strongly attractive. Upon comparison to the fidelities between the corresponding reduced one-body density operators of each component, we not only observe that each species is affected to a much smaller degree, but they also respond differently. Thus, for the impurity atom the deviation from the box ground state increases smoothly with increasing absolute value of  $g_{AB}$ , while the reduced density of the majority component remains very robust to  $g_{AB}$  variations except for the above mentioned parameter regions where the many-body fidelity exhibits significant structural changes in the ground state.

Next, we have been performing a further classification of our system based on entropy measures. Namely, we quantify the amount of entanglement and intraspecies correlations deposited in the binary mixture by evaluating the von Neumann entropy of the respective subsystems. Interestingly, we find that our composite system is only weakly entangled for parameter regions which undergo substantial structural changes. Additionally, we observe that while the entanglement entropy continuously grows with increasing repulsive  $g_{AB}$ , it does not behave the same for attractive  $g_{AB}$ , where it reaches a local maximum at a finite value of  $g_{AB} < 0$ . Another peculiar observation is that the fragmentation entropy of the majority component undergoes a strong variation for parameter regions, where the fidelity measure does not show any evidence of majority particles being affected by the intercomponent interaction. Even though the mixed character of the reduced density of the medium suffers from substantial changes, it remains un-observable on the single-particle level.

To visualize our observations stemming from the fidelity measure we show the one-body density distributions of each component along with the probability distributions

for two particles of the same or different species to be measured at a relative distance from each other. These quantities are usually accessible in state-of-the-art ultracold atom experiments and determine the expectation values of local one- and two-body observables. Indeed, strong deviations appearing in the fidelity at the single-particle level are also clearly visible in the corresponding one-body density. At positive couplings we observe an interspecies phase separation where the impurity is pushed to the box edges, while leaving the majority component intact. At negative couplings both components tend to increase their localization at the central well.

To further quantify our conclusions stemming from the entanglement measure we rely on the difference between the above probability distributions and the corresponding ones when assuming a disentangled state in our calculations. Again, we find strong deviations for parameters displaying high entanglement entropy values. Thus, at positive couplings the entanglement favors the process of phase separation, while at negative couplings it generally, but not always, counteracts the localization of both species.

Quenching the interspecies interaction strength we are able to induce a dynamical process which for the impurity is reminiscent of the tunneling of a single particle in a double well potential. This can be attributed to the lifting of the degeneracy for the corresponding post-quench Hamiltonian as well as the substantial overlap of the initial state configuration with the post-quench ground state and the first excited state. Due to the repulsive interspecies interaction also the majority species will undergo a tunneling in the lattice geometry such that the two species move in opposite directions, ending up in phase-separated configurations after half a period. We identify the presence of two dominant natural orbitals for the impurity species during the dynamics, where the first one corresponds to phase-separated configurations in the respective one-body density, while the second one resembles the mirror image of the first one. The presence of an additional natural orbital emphasizes the many-body character of the dynamics, thereby influencing the motion of the impurity.

There are various promising research directions that are worth pursuing in the future. Indeed, the generalization of our findings for an increasing particle number in the medium or larger lattice potentials as well as the role of the lattice filling factor is desirable. Furthermore, a more elaborated analysis on the possibly emerging impurity-medium bound states or the engineering of droplet-like configurations in such settings at strong intercomponent attractions would be important. Furthermore, it would be intriguing to study the persistence and possible alterations of the identified spatial configurations in the presence of finite temperature which will impact the coherence of the lattice bosons [88–90]. Another perspective is to investigate the relevant radiofrequency spectrum [31,43] in order to capture the emergent polaron properties including their lifetime, residue and effective mass especially in the attractive interaction regimes of bound state formation.

**Author Contributions:** Conceptualization, M.P., K.K. and S.I.M.; Formal analysis, M.P. and K.K.; Investigation, M.P. and K.K.; Project administration, P.S.; Supervision, P.S.; Validation, P.S.; Visualization, M.P., K.K. and S.I.M.; Writing – original draft, M.P. and K.K.; Writing – review & editing, M.P., K.K. and S.I.M.

**Funding:** This research received no external funding.

**Acknowledgments:** M.P. and K.K. gratefully acknowledge a scholarship of the Studienstiftung des deutschen Volkes. S.I.M. gratefully acknowledges financial support in the framework of the Lenz-Ising Award of the Department of Physics of the University of Hamburg.

**Conflicts of Interest:** The authors declare no conflict of interest.

## References

1. Bloch, I.; Dalibard, J.; Zwirger, W. Many-body physics with ultracold gases. *Rev. Mod. Phys.* **2008**, *80*, 885. [[CrossRef](#)]
2. Bloch, I. *Probing and Controlling Strongly Correlated Quantum Many-Body Systems Using Ultracold Quantum Gases*; Cambridge University Press: Cambridge, UK, 2017; p. 253.

3. Fukuhara, T.; Sugawa, S.; Takasu, Y.; Takahashi, Y. All-optical formation of quantum degenerate mixtures. *Phys. Rev. A* **2009**, *79*, 021601. [[CrossRef](#)]
4. Henderson, K.; Ryu, C.; MacCormick, C.; Boshier, M.G. Experimental demonstration of painting arbitrary and dynamic potentials for Bose–Einstein condensates. *New J. Phys.* **2009**, *11*, 043030. [[CrossRef](#)]
5. Serwane, F.; Zürn, G.; Lompe, T.; Ottenstein, T.; Wenz, A.; Jochim, S. Deterministic preparation of a tunable few-fermion system. *Science* **2011**, *332*, 336–338. [[CrossRef](#)] [[PubMed](#)]
6. Schmied, R.; Bancal, J.D.; Allard, B.; Fadel, M.; Scarani, V.; Treutlein, P.; Sangouard, N. Bell correlations in a Bose-Einstein condensate. *Science* **2016**, *352*, 441–444. [[CrossRef](#)]
7. Chin, C.; Grimm, R.; Julienne, P.; Tiesinga, E. Feshbach resonances in ultracold gases. *Rev. Mod. Phys.* **2010**, *82*, 1225. [[CrossRef](#)]
8. Köhler, T.; Góral, K.; Julienne, P.S. Production of cold molecules via magnetically tunable Feshbach resonances. *Rev. Mod. Phys.* **2006**, *78*, 1311. [[CrossRef](#)]
9. Mistakidis, S.I.; Katsimiga, G.C.; Kevrekidis, P.G.; Schmelcher, P. Correlation effects in the quench-induced phase separation dynamics of a two species ultracold quantum gas. *New J. Phys.* **2018**, *20*, 043052. [[CrossRef](#)]
10. Pyzh, M.; Schmelcher, P. Phase separation of a Bose-Bose mixture: Impact of the trap and particle-number imbalance. *Phys. Rev. A* **2020**, *102*, 023305. [[CrossRef](#)]
11. Petrov, D.S.; Astrakharchik, G.E. Ultradilute low-dimensional liquids. *Phys. Rev. Lett.* **2016**, *117*, 100401. [[CrossRef](#)]
12. Parisi, L.; Giorgini, S. Quantum droplets in one-dimensional Bose mixtures: a quantum Monte-Carlo study. *Phys. Rev. A* **2020**, *102*, 023318. [[CrossRef](#)]
13. Catani, J.; Lamporesi, G.; Naik, D.; Gring, M.; Inguscio, M.; Minardi, F.; Kantian, A.; Giamarchi, T. Quantum dynamics of impurities in a one-dimensional Bose gas. *Phys. Rev. A* **2012**, *85*, 023623. [[CrossRef](#)]
14. Meinert, F.; Knap, M.; Kirilov, E.; Jag-Lauber, K.; Zvonarev, M.B.; Demler, E.; Nägerl, H.C. Bloch oscillations in the absence of a lattice. *Science* **2017**, *356*, 945–948. [[CrossRef](#)]
15. Mistakidis, S.I.; Volosniev, A.G.; Zinner, N.T.; Schmelcher, P. Effective approach to impurity dynamics in one-dimensional trapped Bose gases. *Phys. Rev. A* **2019**, *100*, 013619. [[CrossRef](#)]
16. Ardila, L.P.; Giorgini, S. Impurity in a Bose-Einstein condensate: Study of the attractive and repulsive branch using quantum Monte Carlo methods. *Phys. Rev. A* **2015**, *92*, 033612. [[CrossRef](#)]
17. Grusdt, F.; Astrakharchik, G.E.; Demler, E. Bose polarons in ultracold atoms in one dimension: beyond the Fröhlich paradigm. *New J. Phys.* **2017**, *19*, 103035. [[CrossRef](#)]
18. Tajima, H.; Uchino, S. Many Fermi polarons at nonzero temperature. *New J. Phys.* **2018**, *20*, 073048. [[CrossRef](#)]
19. Dehkharghani, A.S.; Volosniev, A.G.; Zinner, N.T. Coalescence of two impurities in a trapped one-dimensional Bose gas. *Phys. Rev. Lett.* **2018**, *121*, 080405. [[CrossRef](#)]
20. Mistakidis, S.I.; Volosniev, A.G.; Schmelcher, P. Induced correlations between impurities in a one-dimensional quenched Bose gas. *Phys. Rev. Res.* **2020**, *2*, 023154. [[CrossRef](#)]
21. Takahashi, J.; Tajima, H.; Nakano, E.; Iida, K. Extracting non-local inter-polaron interactions from collisional dynamics. *arXiv* **2020**, arXiv:2011.07911.
22. Brauneis, F.; Hammer, H.W.; Lemesheko, M.; Volosniev, A.G. Impurities in a one-dimensional Bose gas: The flow equation approach. *arXiv* **2021**, arXiv:2101.10958.
23. Massignan, P.; Zaccanti, M.; Bruun, G.M. Polarons, dressed molecules and itinerant ferromagnetism in ultracold Fermi gases. *Rep. Progr. Phys.* **2014**, *77*, 034401. [[CrossRef](#)]
24. Schmidt, R.; Knap, M.; Ivanov, D.A.; You, J.S.; Cetina, M.; Demler, E. Universal many-body response of heavy impurities coupled to a Fermi sea: a review of recent progress. *Rep. Progr. Phys.* **2018**, *81*, 024401. [[CrossRef](#)]
25. Fukuhara, T.; Kantian, A.; Endres, M.; Cheneau, M.; Schauss, P.; Hild, S.; Bellem, D.; Schollw Ock, U.; Giamarchi, T.; Gross, C.; et al. Quantum dynamics of a mobile spin impurity. *Nat. Phys.* **2013**, *9*, 235–241. [[CrossRef](#)]
26. Yan, Z.Z.; Ni, Y.; Robens, C.; Zwierlein, M.W. Bose polarons near quantum criticality. *Science* **2020**, *368*, 190–194. [[CrossRef](#)] [[PubMed](#)]
27. Scazza, F.; Valtolina, G.; Massignan, P.; Recati, A.; Amico, A.; Burchianti, A.; Fort, C.; Inguscio, M.; Zaccanti, M.; Roati, G. Repulsive Fermi polarons in a resonant mixture of ultracold Li 6 atoms. *Phys. Rev. Lett.* **2017**, *118*, 083602. [[CrossRef](#)] [[PubMed](#)]
28. Jørgensen, N.B.; Wacker, L.; Skalmstang, K.T.; Parish, M.M.; Levinsen, J.; Christensen, R.S.; Bruun, G.M.; Arlt, J.J. Observation of attractive and repulsive polarons in a Bose-Einstein condensate. *Phys. Rev. Lett.* **2016**, *117*, 055302. [[CrossRef](#)]
29. Cetina, M.; Jag, M.; Lous, R.S.; Fritsche, I.; Walraven, J.T.; Grimm, R.; Levinsen, J.; Parish, M.M.; Schmidt, R.; Knap, M.; et al. Ultrafast many-body interferometry of impurities coupled to a Fermi sea. *Science* **2016**, *354*, 96–99. [[CrossRef](#)]
30. Wenz, A.; Zürn, G.; Murmann, S.; Brouzos, I.; Lompe, T.; Jochim, S. From few to many: Observing the formation of a Fermi sea one atom at a time. *Science* **2013**, *342*, 457–460. [[CrossRef](#)]
31. Mistakidis, S.I.; Koutentakis, G.M.; Grusdt, F.; Sadeghpour, H.R.; Schmelcher, P. Radiofrequency spectroscopy of one-dimensional trapped Bose polarons: crossover from the adiabatic to the diabatic regime. *arXiv* **2020**, arXiv:2011.13756.
32. Mistakidis, S.I.; Koutentakis, G.M.; Katsimiga, G.C.; Busch, T.; Schmelcher, P. Many-body quantum dynamics and induced correlations of Bose polarons. *New J. Phys.* **2020**, *22*, 043007. [[CrossRef](#)]
33. Boudjemâa, A.; Guebli, N.; Sekmane, M.; Khelifa-Karfa, S. Breathing modes of repulsive polarons in Bose–Bose mixtures. *J. Phys. Cond. Matt.* **2020**, *32*, 415401. [[CrossRef](#)]

34. Ardila, L.A.P.; Astrakharchik, G.E.; Giorgini, S. Strong coupling Bose polarons in a two-dimensional gas. *Phys. Rev. Res.* **2020**, *2*, 023405. [[CrossRef](#)]
35. Camacho-Guardian, A.; Ardila, L.A.P.; Pohl, T.; Bruun, G.M. Bipolarons in a Bose-Einstein condensate. *Phys. Rev. Lett.* **2018**, *121*, 013401. [[CrossRef](#)] [[PubMed](#)]
36. Mukherjee, K.; Mistakidis, S.I.; Majumder, S.; Schmelcher, P. Induced interactions and quench dynamics of bosonic impurities immersed in a Fermi sea. *Phys. Rev. A* **2020**, *102*, 053317. [[CrossRef](#)]
37. Bougas, G.; Mistakidis, S.I.; Schmelcher, P. Pattern formation of correlated impurities subjected to an impurity-medium interaction pulse. *Phys. Rev. A* **2021**, *103*, 023313. [[CrossRef](#)]
38. Tajima, H.; Takahashi, J.; Nakano, E.; Iida, K. Collisional dynamics of polaronic clouds immersed in a Fermi sea. *Phys. Rev. A* **2020**, *102*, 051302. [[CrossRef](#)]
39. Tonielli, F.; Chakraborty, N.; Grusdt, F.; Marino, J. Ramsey interferometry of non-Hermitian quantum impurities. *Phys. Rev. Res.* **2020**, *2*, 032003. [[CrossRef](#)]
40. Mistakidis, S.I.; Grusdt, F.; Koutentakis, G.M.; Schmelcher, P. Dissipative correlated dynamics of a moving impurity immersed in a Bose-Einstein condensate. *New J. Phys.* **2019**, *21*, 103026. [[CrossRef](#)]
41. Mukherjee, K.; Mistakidis, S.I.; Majumder, S.; Schmelcher, P. Pulse- and continuously driven many-body quantum dynamics of bosonic impurities in a Bose-Einstein condensate. *Phys. Rev. A* **2020**, *101*, 023615. [[CrossRef](#)]
42. Theel, F.; Keiler, K.; Mistakidis, S.I.; Schmelcher, P. Many-body collisional dynamics of impurities injected into a double-well trapped Bose-Einstein condensate. *arXiv* **2020**, arXiv:2009.12147.
43. Mistakidis, S.I.; Katsimiga, G.C.; Koutentakis, G.M.; Busch, T.; Schmelcher, P. Pump-probe spectroscopy of Bose polarons: Dynamical formation and coherence. *Phys. Rev. Res.* **2020**, *2*, 033380. [[CrossRef](#)]
44. Lausch, T.; Widera, A.; Fleischhauer, M. Prethermalization in the cooling dynamics of an impurity in a Bose-Einstein condensate. *Phys. Rev. A* **2018**, *97*, 023621. [[CrossRef](#)]
45. Palzer, S.; Zipkes, C.; Sias, C.; Köhl, M. Quantum transport through a Tonks-Girardeau gas. *Phys. Rev. Lett.* **2009**, *103*, 150601. [[CrossRef](#)]
46. Keiler, K.; Mistakidis, S.I.; Schmelcher, P. Doping a lattice-trapped bosonic species with impurities: From ground state properties to correlated tunneling dynamics. *New J. Phys.* **2020**, *22*, 083003. [[CrossRef](#)]
47. Bohrdt, A.; Grusdt, F.; Knap, M. Dynamical formation of a magnetic polaron in a two-dimensional quantum antiferromagnet. *New J. Phys.* **2020**, *22*, 123023. [[CrossRef](#)]
48. Cai, Z.; Wang, L.; Xie, X.; Wang, Y. Interaction-induced anomalous transport behavior in one-dimensional optical lattices. *Phys. Rev. A* **2010**, *81*, 043602. [[CrossRef](#)]
49. Johnson, T.H.; Clark, S.R.; Bruderer, M.; Jaksch, D. Impurity transport through a strongly interacting bosonic quantum gas. *Phys. Rev. A* **2011**, *84*, 023617. [[CrossRef](#)]
50. Theel, F.; Keiler, K.; Mistakidis, S.I.; Schmelcher, P. Entanglement-assisted tunneling dynamics of impurities in a double well immersed in a bath of lattice trapped bosons. *New J. Phys.* **2020**, *22*, 023027. [[CrossRef](#)]
51. Keiler, K.; Schmelcher, P. State engineering of impurities in a lattice by coupling to a Bose gas. *New J. Phys.* **2018**, *20*, 103042. [[CrossRef](#)]
52. Keiler, K.; Krönke, S.; Schmelcher, P. Correlation induced localization of lattice trapped bosons coupled to a Bose-Einstein condensate. *New J. Phys.* **2018**, *20*, 033030. [[CrossRef](#)]
53. Keiler, K.; Schmelcher, P. Interaction-induced single-impurity tunneling in a binary mixture of trapped ultracold bosons. *Phys. Rev. A* **2019**, *100*, 043616. [[CrossRef](#)]
54. Bruderer, M.; Bao, W.; Jaksch, D. Self-trapping of impurities in Bose-Einstein condensates: Strong attractive and repulsive coupling. *Europhys. Lett.* **2008**, *82*, 30004. [[CrossRef](#)]
55. Yin, T.; Cocks, D.; Hofstetter, W. Polaronic effects in one- and two-band quantum systems. *Phys. Rev. A* **2015**, *92*, 063635. [[CrossRef](#)]
56. Grusdt, F.; Shashi, A.; Abanin, D.; Demler, E. Bloch oscillations of bosonic lattice polarons. *Phys. Rev. A* **2014**, *90*, 063610. [[CrossRef](#)]
57. Weber, C.; John, S.; Spethmann, N.; Meschede, D.; Widera, A. Single Cs atoms as collisional probes in a large Rb magneto-optical trap. *Phys. Rev. A* **2010**, *82*, 042722. [[CrossRef](#)]
58. Will, S.; Best, T.; Braun, S.; Schneider, U.; Bloch, I. Coherent Interaction of a Single Fermion with a Small Bosonic Field. *Phys. Rev. Lett.* **2011**, *106*, 115305. [[CrossRef](#)] [[PubMed](#)]
59. Tajima, H.; Takahashi, J.; Mistakidis, S.I.; Nakano, E.; Iida, K. Polaron problems in ultracold atoms: Role of the medium across different spatial dimensions. *arXiv* **2021**, arXiv:2101.07643.
60. Cao, L.; Bolsinger, V.; Mistakidis, S.; Koutentakis, G.; Krönke, S.; Schurer, J.; Schmelcher, P. A unified ab initio approach to the correlated quantum dynamics of ultracold fermionic and bosonic mixtures. *J. Chem. Phys.* **2017**, *147*, 044106. [[CrossRef](#)] [[PubMed](#)]
61. Cao, L.; Krönke, S.; Vendrell, O.; Schmelcher, P. The multi-layer multi-configuration time-dependent Hartree method for bosons: Theory, implementation, and applications. *J. Chem. Phys.* **2013**, *139*, 134103. [[CrossRef](#)]
62. Krönke, S.; Cao, L.; Vendrell, O.; Schmelcher, P. Non-equilibrium quantum dynamics of ultra-cold atomic mixtures: The multi-layer multi-configuration time-dependent Hartree method for bosons. *New J. Phys.* **2013**, *15*, 063018. [[CrossRef](#)]

63. Mistakidis, S.I.; Katsimiga, G.C.; Koutentakis, G.M.; Busch, T.; Schmelcher, P. Quench dynamics and orthogonality catastrophe of Bose polarons. *Phys. Rev. Lett.* **2019**, *122*, 183001. [[CrossRef](#)]
64. Pflanzner, A.C.; Zöllner, S.; Schmelcher, P. Material-barrier tunnelling in one-dimensional few-boson mixtures. *J. Phys. B At. Mol. Opt. Phys.* **2009**, *42*, 231002. [[CrossRef](#)]
65. Myatt, C.J.; Burt, E.A.; Ghrist, R.W.; Cornell, E.A.; Wieman, C.E. Production of Two Overlapping Bose-Einstein Condensates by Sympathetic Cooling. *Phys. Rev. Lett.* **1997**, *78*, 586–589. [[CrossRef](#)]
66. Hall, D.S.; Matthews, M.R.; Ensher, J.R.; Wieman, C.E.; Cornell, E.A. Dynamics of Component Separation in a Binary Mixture of Bose-Einstein Condensates. *Phys. Rev. Lett.* **1998**, *81*, 1539–1542. [[CrossRef](#)]
67. Miesner, H.J.; Stamper-Kurn, D.M.; Stenger, J.; Inouye, S.; Chikkatur, A.P.; Ketterle, W. Observation of Metastable States in Spinor Bose-Einstein Condensates. *Phys. Rev. Lett.* **1999**, *82*, 2228–2231. [[CrossRef](#)]
68. Maddaloni, P.; Modugno, M.; Fort, C.; Minardi, F.; Inguscio, M. Collective Oscillations of Two Colliding Bose-Einstein Condensates. *Phys. Rev. Lett.* **2000**, *85*, 2413–2417. [[CrossRef](#)]
69. Mertes, K.M.; Merrill, J.W.; Carretero-González, R.; Frantzeskakis, D.J.; Kevrekidis, P.G.; Hall, D.S. Nonequilibrium Dynamics and Superfluid Ring Excitations in Binary Bose-Einstein Condensates. *Phys. Rev. Lett.* **2007**, *99*, 190402. [[CrossRef](#)]
70. Becker, C.; Stellmer, S.; Soltan-Panahi, P.; Dörscher, S.; Baumert, M.; Richter, E.M.; Kronjäger, J.; Bongs, K.; Sengstock, K. Oscillations and interactions of dark and dark-bright solitons in Bose-Einstein condensates. *Nat. Phys.* **2008**, *4*, 496–501. [[CrossRef](#)]
71. Lode, A.U.J.; Lévêque, C.; Madsen, L.B.; Streltsov, A.I.; Alon, O.E. Colloquium: Multiconfigurational time-dependent Hartree approaches for indistinguishable particles. *Rev. Mod. Phys.* **2020**, *92*, 011001. [[CrossRef](#)]
72. Alon, O.E.; Beinke, R.; Cederbaum, L.S. Many-body effects in the excitations and dynamics of trapped Bose-Einstein condensates. *arXiv* **2021**, arXiv:2101.11615.
73. Horodecki, R.; Horodecki, P.; Horodecki, M.; Horodecki, K. Quantum entanglement. *Rev. Mod. Phys.* **2009**, *81*, 865. [[CrossRef](#)]
74. Light, J.; Hamilton, I.; Lill, J. Generalized discrete variable approximation in quantum mechanics. *J. Chem. Phys.* **1985**, *82*, 1400–1409. [[CrossRef](#)]
75. Raab, A. On the Dirac-Frenkel/McLachlan variational principle. *Chem. Phys. Lett.* **2000**, *319*, 674–678. [[CrossRef](#)]
76. Jozsa, R. Fidelity for mixed quantum states. *J. Mod. Opt.* **1994**, *41*, 2315–2323. [[CrossRef](#)]
77. Wang, W.; Penna, V.; Capogrosso-Sansone, B. Inter-species entanglement of Bose-Bose mixtures trapped in optical lattices. *New J. Phys.* **2016**, *18*, 063002. [[CrossRef](#)]
78. Bengtsson, I.; Życzkowski, K. *Geometry of Quantum States: An Introduction to Quantum Entanglement*; Cambridge University Press: Cambridge, UK, 2017.
79. Roy, R.; Gammal, A.; Tsatsos, M.C.; Chatterjee, B.; Chakrabarti, B.; Lode, A.U.J. Phases, many-body entropy measures, and coherence of interacting bosons in optical lattices. *Phys. Rev. A* **2018**, *97*, 043625. [[CrossRef](#)]
80. Bera, S.; Haldar, S.K.; Chakrabarti, B.; Trombettoni, A.; Kota, V.K.B. Relaxation of Shannon entropy for trapped interacting bosons with dipolar interactions. *Eur. Phys. J. D* **2020**, *74*, 1–10. [[CrossRef](#)]
81. Penna, V.; Richaud, A. The phase-separation mechanism of a binary mixture in a ring trimer. *Sci. Rep.* **2018**, *8*, 10242. [[CrossRef](#)]
82. Richaud, A.; Penna, V. Pathway toward the formation of supermixed states in ultracold boson mixtures loaded in ring lattices. *Phys. Rev. A* **2019**, *100*, 013609. [[CrossRef](#)]
83. Bakr, W.S.; Peng, A.; Tai, M.E.; Ma, R.; Simon, J.; Gillen, J.I.; Fölling, S.; Pollet, L.; Greiner, M. Probing the superfluid-to-Mott insulator transition at the single-atom level. *Science* **2010**, *329*, 547–550. [[CrossRef](#)]
84. Sherson, J.F.; Weitenberg, C.; Endres, M.; Cheneau, M.; Bloch, I.; Kuhr, S. Single-atom-resolved fluorescence imaging of an atomic Mott insulator. *Nature* **2010**, *467*, 68–72. [[CrossRef](#)] [[PubMed](#)]
85. Omran, A.; Boll, M.; Hilker, T.A.; Kleinlein, K.; Salomon, G.; Bloch, I.; Gross, C. Microscopic Observation of Pauli Blocking in Degenerate Fermionic Lattice Gases. *Phys. Rev. Lett.* **2015**, *115*, 263001. [[CrossRef](#)] [[PubMed](#)]
86. Hohmann, M.; Kindermann, F.; Lausch, T.; Mayer, D.; Schmidt, F.; Lutz, E.; Widera, A. Individual Tracer Atoms in an Ultracold Dilute Gas. *Phys. Rev. Lett.* **2017**, *118*, 263401. [[CrossRef](#)]
87. Pyzh, M.; Krönke, S.; Weitenberg, C.; Schmelcher, P. Quantum point spread function for imaging trapped few-body systems with a quantum gas microscope. *New J. Phys.* **2019**, *21*, 053013. [[CrossRef](#)]
88. Lingua, F.; Capogrosso-Sansone, B.; Minardi, F.; Penna, V. Thermometry of bosonic mixtures in Optical Lattices via Demixing. *Sci. Rep.* **2017**, *7*, 1–9. [[CrossRef](#)]
89. Suthar, K.; Angom, D. Characteristic temperature for the immiscible-miscible transition of binary condensates in optical lattices. *Phys. Rev. A* **2017**, *95*, 043602. [[CrossRef](#)]
90. Suthar, K.; Angom, D. Optical-lattice-influenced geometry of quasi-two-dimensional binary condensates and quasiparticle spectra. *Phys. Rev. A* **2016**, *93*, 063608. [[CrossRef](#)]





## PAPER

## Quantum point spread function for imaging trapped few-body systems with a quantum gas microscope

## OPEN ACCESS

## RECEIVED

11 February 2019

## REVISED

16 April 2019

## ACCEPTED FOR PUBLICATION

18 April 2019

## PUBLISHED

8 May 2019

Maxim Pyzh<sup>1,4</sup>, Sven Krönke<sup>1</sup>, Christof Weitenberg<sup>2,3</sup> and Peter Schmelcher<sup>1,3</sup><sup>1</sup> Zentrum für Optische Quantentechnologien, Universität Hamburg, Luruper Chaussee 149, D-22761 Hamburg, Germany<sup>2</sup> Institut für Laserphysik, Universität Hamburg, Luruper Chaussee 149, D-22761 Hamburg, Germany<sup>3</sup> The Hamburg Centre for Ultrafast Imaging, Universität Hamburg, Luruper Chaussee 149, D-22761 Hamburg, Germany<sup>4</sup> Author to whom any correspondence should be addressed.E-mail: [mpyzh@physnet.uni-hamburg.de](mailto:mpyzh@physnet.uni-hamburg.de) and [pschmelc@physnet.uni-hamburg.de](mailto:pschmelc@physnet.uni-hamburg.de)**Keywords:** quantum gas microscope, point spread function, few-body systems, one-body density, machine learning, imaging non-lattice systems, high resolutionOriginal content from this work may be used under the terms of the [Creative Commons Attribution 3.0 licence](https://creativecommons.org/licenses/by/3.0/).

Any further distribution of this work must maintain attribution to the author(s) and the title of the work, journal citation and DOI.

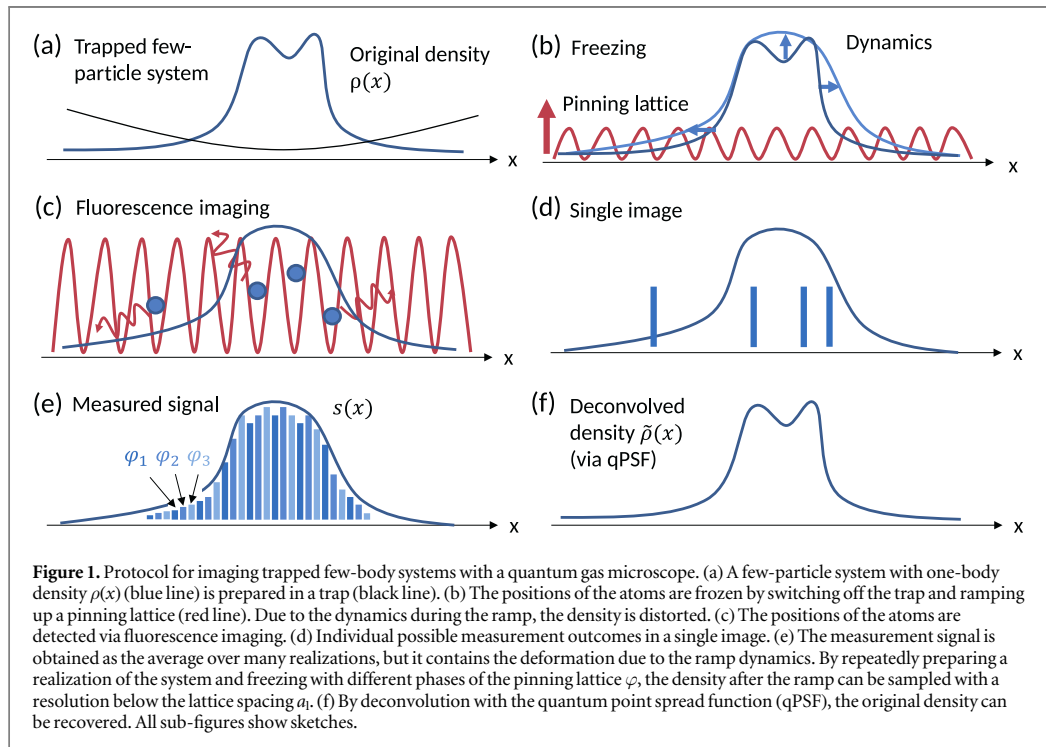
**Abstract**

Quantum gas microscopes, which image the atomic occupations in an optical lattice, have opened a new avenue to the exploration of many-body lattice systems. Imaging trapped systems after freezing the density distribution by ramping up a pinning lattice leads, however, to a distortion of the original density distribution, especially when its structures are on the scale of the pinning lattice spacing. We show that this dynamics can be described by a filter, which we call in analogy to classical optics a quantum point spread function. Using a machine learning approach, we demonstrate via several experimentally relevant setups that a suitable deconvolution allows for the reconstruction of the original density distribution. These findings are both of fundamental interest for the theory of imaging and of immediate importance for current quantum gas experiments.

**1. Introduction**

Imaging with high resolution is a cornerstone for understanding the structure, dynamics and functionality of matter [1–3]. In the field of ultracold atoms, quantum gas microscopes have opened new avenues for studying lattice systems [4–7] and led to remarkable progress and insights, such as density correlations and string order [8], long-range anti-ferromagnetic correlations [9] or entanglement growth [10] in Mott insulators. Naturally, it is of equal interest to study trapped, i.e. *non-lattice systems*, where imaging with single-atom sensitivity is also vital for exploring beyond mean-field physics, i.e. for probing correlation effects [11]. Single-atom resolved imaging in free space has been demonstrated for metastable helium atoms, which can be detected using a multi-channel plate with a typical resolution of 60  $\mu\text{m}$  [12], and recently for lithium atoms using a short fluorescence pulse, where the position spread due to scattering recoils can be reduced to 4  $\mu\text{m}$  [13]. In order to reach sub-micron resolution, the positions of the atoms have to be frozen by ramping up a pinning lattice before the fluorescence imaging and detection of the atoms takes place. Such a capture of atoms in a pinning lattice was demonstrated starting from a larger scale lattice [14] or a larger scale continuous system [15], but freezing and measuring of density structures on the scale of the pinning lattice spacing was so far not considered and achieved.

Alternative schemes to reach sub-lattice resolution of quantum gases, inspired by related imaging techniques in other fields, have been proposed or realized. Stimulated emission depletion microscopy [16], which breaks the diffraction limit set by the imaging wavelength, can be adapted to quantum gases using the position-dependent dark state of a Lambda-system [17–19]. A scanning tunneling microscope could be realized by coupling to a single ion [20] or by using dispersive couplings to a cavity [21]. Momentum mapping in combination with phase retrieval should allow imaging with 1–2 orders of magnitude better than the lattice spacing [22]. Finally, scanning electron microscopy was successfully applied to quantum gases reaching a resolution below 150 nm [23]. However, the combination of sub-micron resolution and single-atom sensitivity has so far only been achieved by fluorescence imaging in a pinning lattice.



Here, we propose to perform repeated measurements with shifted positions of the pinning lattice relative to the trapped physical system, such that a resolution below the lattice spacing becomes possible and we provide an in-depth analysis of this protocol. We show that the density structures on the scale of the lattice spacing will be distorted due to the dynamics taking place during the ramp-up of the pinning lattice. The lattice ramp has to be sufficiently fast to avoid an adiabatic loading of the ground state of the lattice, but sufficiently slow to avoid projections onto very high bands, where the atom positions are not frozen due to large tunneling rates. The proposed scenario is illustrated in figure 1. We show that the distortions during the ramp-up can be captured by a quantum point spread function (qPSF). Using deconvolution techniques, these distortions can be removed, which enhances the resolution of the overall measurement sequence. We find that the deconvolution is both relevant and effective for density structures on the scale of the lattice spacing and provides a sub-wavelength resolution. Our approach and technique suggests itself for immediate applications, because a tight confinement and resulting small structures of the original trapped system allow for strongly interacting quantum systems, while the spacing of the pinning lattice is fixed to typically  $0.5 \mu\text{m}$  by the optical wavelength of the interfering laser beams.

Our work is structured as follows. In section 2 we show that the density measurement outcome of a single particle can be formulated in terms of a convolution of the underlying one-body density matrix with a qPSF. We extend our framework to many-body systems in section 3. In order to remove distortions of the original density caused by our protocol a two-step reconstruction scheme is proposed in section 4, involving a machine learning and a deconvolution step. In section 5, we demonstrate the performance of our approach for several distinct examples and conclude with an outlook in section 5.

## 2. Quantum point spread function

We first derive the qPSF for the measurement of a single particle in the pre-measurement state  $|\phi\rangle^5$  and then extend the concept to many-body systems. For simplicity, we consider only one-dimensional systems, but our framework equally applies to higher spatial dimensions.

The measurement is modeled as a two-step process: the ramp-up of the pinning lattice and the read-out of the state occupations. In the following, we keep the phase offset of the pinning lattice  $\varphi$  fixed and thereafter vary it for resolving fine density structures. During the ramp-up, we assume that all external potentials but the pinning lattice are either switched off or negligible such that the quantum dynamics is governed by the

<sup>5</sup> Our results can be straightforwardly adapted to mixed pre-measurement states.

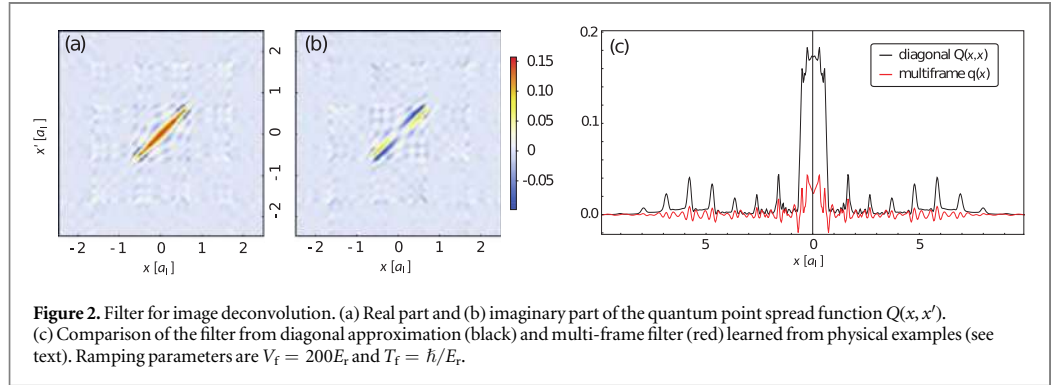


**Figure 2.** Filter for image deconvolution. (a) Real part and (b) imaginary part of the quantum point spread function  $Q(x, x')$ . (c) Comparison of the filter from diagonal approximation (black) and multi-frame filter (red) learned from physical examples (see text). Ramping parameters are  $V_f = 200E_r$  and  $T_f = \hbar/E_r$ .

Hamiltonian

$$\hat{h}_\varphi(t) = \frac{\hat{p}^2}{2m} + V(t) \sin^2(k_1 \hat{x} - \varphi). \quad (1)$$

Here, the lattice depth  $V(t)$  is ramped up from zero to its maximal value  $V_f$  within the time-scale  $T_f$  by using a tanh-like ramping protocol and  $k_1$  denotes the pinning lattice wavenumber corresponding to the lattice spacing  $a_1$ . The lattice sets the recoil energy  $E_r = \hbar^2 k_1^2 / (2m)$  as typical energy scale. Directly after ramping up the lattice, the system is in the state  $\hat{U}_\varphi |\phi\rangle$  with  $\hat{U}_\varphi = \hat{T} \exp(-i/\hbar \int_0^{T_f} d\tau \hat{h}_\varphi(\tau))$  and  $\hat{T}$  denoting the chronological time-ordering operator.

The occupation of the site  $i$  is then read out via fluorescence imaging, which we describe within the established framework of measurement operators  $\hat{R}_{i;\varphi}$  and positive operator-valued measures  $\hat{R}_{i;\varphi}^\dagger \hat{R}_{i;\varphi}$  [24]. Being only interested in the probability for finding the particle at site  $i$  given the phase offset  $\varphi$

$$p_{i;\varphi} = \langle \phi | \hat{U}_\varphi^\dagger \hat{R}_{i;\varphi}^\dagger \hat{R}_{i;\varphi} \hat{U}_\varphi | \phi \rangle, \quad (2)$$

we have to specify the operator  $\hat{R}_{i;\varphi}^\dagger \hat{R}_{i;\varphi}$ . For this purpose, we assume that a particle that ends up in the Wannier state  $|w_{i;\varphi}^\alpha\rangle$  of the pinning lattice Hamiltonian  $\hat{h}_\varphi(T_f)$  after the ramp-up, where  $\alpha$  denotes the band index, is measured with the detection efficiency  $\eta_\alpha \in [0, 1]$ , which can be modeled by

$$\hat{R}_{i;\varphi}^\dagger \hat{R}_{i;\varphi} = \sum_\alpha \eta_\alpha |w_{i;\varphi}^\alpha\rangle \langle w_{i;\varphi}^\alpha|. \quad (3)$$

Here, a high detection efficiency  $\eta_\alpha$  is ensured, if the tunneling rate of the band  $J_\alpha$  is small compared to the imaging time scales. As  $J_\alpha$  increases very rapidly for higher bands  $\alpha$ , we can approximate the efficiencies by a step function, i.e.  $\eta_\alpha = 1$  for a finite number of ‘non-tunneling bands’ and  $\eta_\alpha = 0$  for all higher bands. Then the operator  $\hat{R}_{i;\varphi}^\dagger \hat{R}_{i;\varphi}$  becomes a projector. Atoms in higher bands or continuum states<sup>6</sup> lead to loss and the lattice ramp has to be chosen such that this loss remains small. Deep lattices and not-too-fast ramps keep this loss negligible. Finally, the measurement signal  $s(x)$  is obtained by averaging over the pinning lattice shifts  $\varphi$ .

In order to define the qPSF we consider the analogy to classical optics, where the exact ‘object’ density  $\rho(x)$  becomes blurred in the image plane via the point spread function  $f(x)$  according to the convolution  $s(x) = (f * \rho)(x) = \int dy \rho(y) f(x - y)$ , where  $s(x)$  denotes the signal in the imaging plane. Given this relationship and the precise form of  $f$ , there are various deblurring techniques for (approximately) restoring  $\rho(x)$ . Our aim here is to reformulate the probability  $p_{i;\varphi}$  as a convolution to define qPSF for our imaging protocol. By means of the translation symmetry  $\hat{U}_\varphi^\dagger \hat{R}_{i;\varphi}^\dagger \hat{R}_{i;\varphi} \hat{U}_\varphi = \hat{T}_{ia_1+\varphi}^\dagger \hat{R}_{0;0}^\dagger \hat{R}_{0;0} \hat{T}_{ia_1+\varphi}$  with the translation operator  $\hat{T}_z = \exp(-iz\hat{p}/\hbar)$ , we arrive at our central result:

$$p_{i;\varphi} = \iint dx dy \phi^*(x) Q(z - x, z - y) \phi(y) |_{z=ia_1+\varphi}, \quad (4)$$

where the kernel  $Q(x, y) = \langle -x | \hat{U}_0^\dagger \hat{R}_{0;0}^\dagger \hat{R}_{0;0} \hat{U}_0 | -y \rangle$  describes both the quantum dynamics during the ramp-up of the pinning lattice and the subsequent fluorescence imaging. Thus, we find that the probability of detecting the particle at site  $i$  given the pinning lattice offset  $\varphi$  is provided by the diagonal of the two-dimensional (2D) convolution of  $\phi^*(x)\phi(y)$  with  $Q(x, y)$ , which we therefore name quantum point spread function (see figure 2). Equation (4) moreover shows that the probability  $p_{i;\varphi}$  can be expressed by a continuous function  $s(z)$  evaluated at discrete positions,  $p_{i;\varphi} = s(ia_1 + \varphi)$ . By repeating the experiment for various offsets  $\varphi$  one effectively samples

<sup>6</sup> We note that  $\sum_i \hat{R}_{i;\varphi}^\dagger \hat{R}_{i;\varphi} \neq \mathbf{1}$  due to continuum states and detection efficiencies  $\eta_\alpha < 1$ . Yet our measurement model can be easily extended to a proper positive operator-valued measure by associating the operator  $\mathbf{1} - \sum_i \hat{R}_{i;\varphi}^\dagger \hat{R}_{i;\varphi}$  with the loss measurement outcomes.

this pseudo-probability  $s(z)$ , which shall be called *signal* in the following. For practical calculations, one can spectrally decompose the qPSF and finds that the signal  $s(z)$  equals an incoherent superposition of 1D convolutions of the pre-measurement state with the back-propagated Wannier states  $|\chi_\alpha\rangle = \hat{\pi}\hat{U}_0^\dagger|w_{0;0}^\alpha\rangle$ :

$$s(z) = \sum_\alpha \eta_\alpha \left| \int dx \chi_\alpha^*(z-x) \phi(x) \right|^2, \quad (5)$$

where  $\hat{\pi}$  denotes the parity operator. As a side remark, the quantum dynamics during the ramp is non-adiabatic such that  $\hat{\pi}|\chi_\alpha\rangle$  does not coincide with the corresponding Wannier state of the shallower lattices of the ramp.

### 3. Extension of the qPSF theory to many-body systems

In the following, we extend the qPSF theory to many-body systems by first inspecting the case of distinguishable particles, then discussing single-shot measurements of indistinguishable particles, and finally deriving the relationship between the ensemble average of such single-shot measurements and few-body correlations.

#### 3.1. Single-shot measurements of distinguishable particles

In order to extend the qPSF theory to many-body systems, we make the following assumptions: (i) as in the single-particle case, we assume that all external traps but the pinning lattice are either switched off or negligible during the full measurement protocol. (ii) Moreover, we assume that the inter-atomic interactions are either switched off by means of a Feshbach resonance or negligible during the full measurement protocol. (iii) Finally, we regard the fluorescence imaging of the pinning lattice sites to be a pure one-body process, i.e. neglect few-body effects such as loss via light-induced collisions [4, 5]. The latter approximation is valid, if the pre-measurement atomic density is so low that the likelihood of finding more than one atom in a pinning-lattice site after ramp-up is strongly suppressed.

Under the above assumptions, an  $N$ -body system in the pure<sup>7</sup> pre-measurement state  $|\Psi\rangle$  evolves into the state  $\hat{U}_\varphi^{(1)} \otimes \dots \otimes \hat{U}_\varphi^{(N)} |\Psi\rangle$  during the ramp-up of the pinning lattice with given phase offset  $\varphi$ . Here  $\hat{U}_\varphi^{(\kappa)} = \hat{T} \exp[-i/\hbar \int_0^{T_f} d\tau \hat{h}_\varphi^{(\kappa)}(\tau)]$  denotes the single-particle time-evolution operator acting on the  $\kappa$ th particle.

Since the fluorescence imaging is modeled as a single-particle process, we can directly transfer the positive operator-valued measure for the single-particle case [see equation (3)] to the many-body realm and obtain for the probability to detect the 1st, 2nd, ...,  $N$ th particle in the pinning-lattice site  $i_1, i_2, \dots, i_N$ , respectively:

$$P_\varphi(i_1, \dots, i_N) = \langle \Psi | \hat{M}_{i_1; \varphi}^{(1)} \otimes \dots \otimes \hat{M}_{i_N; \varphi}^{(N)} | \Psi \rangle, \quad (6)$$

where  $\hat{M}_{i; \varphi}^{(\kappa)} \equiv [\hat{U}_\varphi^\dagger \hat{R}_{i; \varphi}^\dagger \hat{R}_{i; \varphi} \hat{U}_\varphi]^{(\kappa)}$  (the bracket  $[...]^{(\kappa)}$  shall indicate that the whole operator acts on the  $\kappa$ th particle). Note that for a fixed phase the probability  $\sum_{\mathbf{i}} P_\varphi(\mathbf{i}) \leq 1$  due to the possibility of detection efficiencies being smaller than one. Making use of the translation symmetry of  $\hat{M}_{i; \varphi}^{(\kappa)}$  as in the single-particle case, we may express equation (6) as

$$P_\varphi(i_1, \dots, i_N) = \int d^N x \, d^N y \, \Psi^*(\mathbf{x}) Q_N(\mathbf{z} - \mathbf{x}, \mathbf{z} - \mathbf{y}) \Psi(\mathbf{y})|_{\mathbf{z}=\mathbf{i} \mathbf{a}_1 + \varphi}, \quad (7)$$

where the spatial positions of the  $N$  particles are abbreviated as  $\mathbf{x} \equiv (x_1, \dots, x_N)$  and the integrals are taken w.r.t. all particle coordinates, i.e.  $d^N x \equiv dx_1 dx_2 \dots dx_N$ . Moreover, the pinning-lattice sites, in which the particles are detected, are abbreviated as  $\mathbf{i} \equiv (i_1, \dots, i_N)$  and  $\Psi(\mathbf{x}) \equiv \langle x_1, \dots, x_N | \Psi \rangle$  refers to the position representation of the  $N$ -body pre-measurement state  $|\Psi\rangle$ . Finally, the  $N$ -body qPSF turns out to be the  $N$ -fold product of the one-body qPSF derived for the single-particle case in the previous section:

$$Q_N(\mathbf{x}, \mathbf{y}) = \prod_{\kappa=1}^N Q(x_\kappa, y_\kappa), \quad (8)$$

where  $Q(x_\kappa, y_\kappa) = \langle -x_\kappa | \hat{M}_{0;0}^{(\kappa)} | -y_\kappa \rangle$ . Thereby, we obtain the  $N$ -particle post-measurement distribution  $P_\varphi(i_1, \dots, i_N)$  for a given pinning lattice phase offset  $\varphi$  by evaluating the signal function

$$S(\mathbf{z}) = \int d^N x \, d^N y \, \Psi^*(\mathbf{x}) Q_N(\mathbf{z} - \mathbf{x}, \mathbf{z} - \mathbf{y}) \Psi(\mathbf{y}) \quad (9)$$

at the discrete positions  $\mathbf{z} = \mathbf{i} \mathbf{a}_1 + \varphi$ , i.e.,  $P_\varphi(\mathbf{i}) = S(\mathbf{i} \mathbf{a}_1 + \varphi)$ . Repeating the  $N$ -body measurement for various phase offsets  $\varphi$  effectively means sampling from the pseudo-probability  $S(\mathbf{z})$ .

<sup>7</sup> The extension to mixed pre-measurement states is straightforward.

### 3.2. Single-shot measurements of indistinguishable particles

Next, we concentrate on the special case of  $N$  indistinguishable particles. In this case, the outcome of a single-shot measurement is a pinning lattice occupation-number histogram  $(n_1, \dots, n_L) \equiv \mathbf{n}$ , where  $n_i$  denotes the number of particles found in the  $i$ th lattice site,  $i = 1, \dots, L$  and  $L$  refers to the number of lattice sites. Here, we have in particular few-body situations in mind, where one can easily probe the full distribution of the  $N$  particles in the pinning lattice.

Obviously, the  $N$ -body qPSF  $Q_N(\mathbf{x}, \mathbf{y})$  remains invariant under simultaneous permutation of the particle labels in both  $\mathbf{x}$  and  $\mathbf{y}$ . Given a system of indistinguishable particles, the probability equation (7) does not depend on the concrete particle labeling but only on how many particles are found in a certain site. Taking this combinatorically into account, one finds for the probability of the histogram  $\mathbf{n}$  for a given phase offset  $\varphi$

$$\bar{P}_\varphi(n_1, \dots, n_L) = \frac{N!}{\prod_{i=1}^L n_i!} P_\varphi(\mathbf{i}_\mathbf{n}), \quad (10)$$

where  $\mathbf{i}_\mathbf{n}$  denotes some  $N$ -dimensional lattice-site index vector, which features  $n_r$ -times the entry  $r$  with  $r = 1, \dots, L$ . We remark that while equation (10) describes the (within the considered measurement model) correct probability of detecting the histogram  $\mathbf{n}$  given the number of particles  $N$  and the phase offset  $\varphi$ , these probabilities do not sum up to unity in general when considering all conceivable histograms  $\mathbf{n}$  with  $N$  particles. In fact, the probability for not detecting all  $N$  particles in the pinning lattice due to the occupation of higher bands with detection efficiencies smaller than unity or continuum states after ramp-up (see equation (3)) reads  $1 - \sum_{\mathbf{n}|N} \bar{P}_\varphi(\mathbf{n})$ , where the sum  $\sum_{\mathbf{n}|N}$  runs over all histograms  $\mathbf{n}$  with  $\sum_{i=1}^L n_i = N$ .

### 3.3. Ensemble averages over single-shot measurements and few-particle correlations

Having taken many single-shot measurements of identical copies of the many-body system, one may evaluate the corresponding ensemble average of certain  $n$ -particle observables. In classical absorption imaging of atomic samples for instance, one obtains the reduced one-body density by averaging the spatial particle number distributions of many single-shot measurements. Density–density correlations can be inferred from absorption images by averaging the product of occupation-number fluctuations at two spatial positions over many single-shot measurements. Here, we stress that in classical absorption imaging the average of an  $n$ -particle quantity over many single-shot measurements is directly connected to the pre-measurement reduced  $n$ -body density matrix, whereas in the case of the quantum gas microscope measurement protocol pursued in this work, this relationship is more complicated in general and shall be derived here.

First, let us derive the probability  $p_\varphi^{(1)}(r)$  to find an atom in the pinning-lattice site  $r$  when averaging over many single-shot measurements with the same phase offset  $\varphi$ , i.e. many different histograms  $\mathbf{n}$  distributed according to  $\bar{P}_\varphi(\mathbf{n})$ . Using equation (10), we find

$$\begin{aligned} p_\varphi^{(1)}(r) &= \sum_{\mathbf{n}|N} \frac{n_r}{N} \bar{P}_\varphi(\mathbf{n}) \\ &= \sum_{\mathbf{n}|N} \frac{(N-1)!}{\prod_{i \neq r} n_i!} \frac{n_r}{n_r!} P_\varphi(\mathbf{i}_\mathbf{n}). \end{aligned} \quad (11)$$

Apparently, only histograms  $\mathbf{n}$  with  $n_r > 0$  contribute to  $p_\varphi^{(1)}(r)$ . Substituting  $\mathbf{n} = \mathbf{m} + \mathbf{e}_r$ , where  $\mathbf{m}$  denotes an arbitrary  $(N-1)$ -particle histogram and  $\mathbf{e}_r$  an occupation number vector with all components zero except for the  $r$ th one being set to unity, one obtains

$$p_\varphi^{(1)}(r) = \sum_{\mathbf{m}|N-1} \frac{(N-1)!}{\prod_i m_i!} P_\varphi(\mathbf{i}_{\mathbf{m}+\mathbf{e}_r}). \quad (12)$$

Next, we rewrite the summation over  $(N-1)$ -particle histograms as a summation over  $N-1$  lattice site indices

$$p_\varphi^{(1)}(r) = \sum_{i_2, \dots, i_{N-1}=1}^L P_\varphi(r, i_2, \dots, i_{N-1}). \quad (13)$$

Abbreviating,  $\hat{K}_\varphi^{(\kappa)} \equiv \sum_{i=1}^L \hat{M}_{i;\varphi}^{(\kappa)}$ , we finally obtain

$$p_\varphi^{(1)}(r) = \langle \Psi | \hat{M}_{r;\varphi}^{(1)} \otimes \hat{K}_\varphi^{(2)} \otimes \dots \otimes \hat{K}_\varphi^{(N)} | \Psi \rangle. \quad (14)$$

Since particles in higher bands or continuum states after the pinning lattice ramp-up are not detected,  $\hat{K}_\varphi^{(\kappa)} \neq \mathbf{1}$  and thus  $p_\varphi^{(1)}(r)$  is *not* given as the expectation value of a one-body observable. So the one-particle quantity  $p_\varphi^{(1)}(r)$  may depend on up to  $N$ -particle corrections and cannot be represented as the trace of a one-particle observable times the pre-measurement reduced one-body density operator in general, which is in contrast to the case of absorption imaging.

Our simulations, however, show that the probability to populate higher bands or continuum states by the pinning lattice ramp-up is negligibly small for suitably chosen experimental settings (see the discussion on the impact of higher bands on the qPSF in Appendix, especially table 1). Under these circumstances,  $\hat{K}_\varphi^{(\kappa)}$  effectively acts as the identity operator on the  $\kappa$ th particle in  $|\Psi\rangle$  and we obtain the relation

$$p_\varphi^{(1)}(r) = \text{tr}(\hat{M}_{r,\varphi}^{(1)} \hat{\rho}_1) = \int dx dy Q(z-x, z-y) \rho_1(x, y)|_{z=r a_1 + \varphi}, \quad (15)$$

where  $\rho_1(x, y) = \langle x | \hat{\rho}_1 | y \rangle$  denotes the position representation of the pre-measurement reduced one-body density operator  $\hat{\rho}_1$ , which one obtains from the pre-measurement many-body state by a partial trace over all but one particle,  $\hat{\rho}_1 = \text{tr}_1(|\Psi\rangle\langle\Psi|)$ .

Similarly, one can derive the corresponding expressions for the ensemble average of an  $n$ -particle quantity with  $n > 1$  over many single-shot measurements. Here, we only explicate this relationship for the case  $n = 2$ , i.e., the probability  $p_\varphi^{(2)}(r_1, r_2)$  to detect a particle at site  $r_1$  and another particle at site  $r_2$  in the ensemble average:

$$p_\varphi^{(2)}(r_1, r_2) = \sum_{\mathbf{n}|N} \frac{n_{r_1} n_{r_2} - \delta_{r_1 r_2}}{N(N-1)} \bar{P}_\varphi(\mathbf{n}). \quad (16)$$

Similar manipulations as above can be applied and one arrives at

$$\begin{aligned} p_\varphi^{(2)}(r_1, r_2) &= \sum_{i_3, \dots, i_N=1}^L P_\varphi(r_1, r_2, i_3, \dots, i_N) \\ &= \langle \Psi | \hat{M}_{r_1, \varphi}^{(1)} \otimes \hat{M}_{r_2, \varphi}^{(2)} \otimes \hat{K}_\varphi^{(3)} \otimes \dots \otimes \hat{K}_\varphi^{(N)} | \Psi \rangle. \end{aligned} \quad (17)$$

If the population of higher bands and continuum states after the pinning-lattice ramp-up may be neglected, we end up with

$$\begin{aligned} p_\varphi^{(2)}(r_1, r_2) &= \text{tr}(\hat{M}_{r_1, \varphi}^{(1)} \otimes \hat{M}_{r_2, \varphi}^{(2)} \hat{\rho}_2) \\ &= \int d^2x d^2y Q_2(\mathbf{z}-\mathbf{x}, \mathbf{z}-\mathbf{y}) \rho_2(\mathbf{x}, \mathbf{y})|_{\mathbf{z}=r a_1 + \varphi}, \end{aligned} \quad (18)$$

where  $\mathbf{r} = (r_1, r_2)$  and  $\rho_2(\mathbf{x}, \mathbf{y})$  denotes the position representation of the pre-measurement reduced two-body density operator  $\hat{\rho}_2$ , which one obtains by a partial trace over all but two particles,  $\hat{\rho}_2 = \text{tr}_2(|\Psi\rangle\langle\Psi|)$ . We remark that sampling of high-order correlations is statistically more intensive. If, however, the system possesses some symmetries, a proper pre-processing of single-shot images [25, 26] will decrease the total experimental effort for accessing higher-order correlations.

## 4. Reconstruction algorithm

Inverting the relationship equation (4) or equation (15) is quite a difficult task: deconvolution in general is an ill-posed problem and, moreover, we have to cope with the intriguing situation that the measurement signal  $s(z)$  constitutes only the diagonal of the 2D convolution  $(Q * \rho_1)(z, z')$ . A scheme for measuring the off-diagonal elements of the reduced one-body density matrix has recently been proposed [27], but the feasibility has yet to be demonstrated. By scanning over different lattice ramps we find for suitably chosen  $V_f$  and  $T_f$  that the real part of the qPSF  $Q(x, x')$  acquires a dominant diagonal pattern with a fast decay of the off-diagonal elements, while the imaginary part is significantly smaller [see figures 2(a), (b)]. This motivates us to express the signal  $s(z)$  as a 1D convolution of the one-body density  $\rho(x) = \rho_1(x, x)$  with some yet unknown 1D filter  $q(x)$ :

$$s(z) \approx \int dx q(z-x) \rho(x) = (q * \rho)(z). \quad (19)$$

However, it is *a priori* not clear, whether such a filter, which is independent of the underlying density, exists and if it does, how to obtain it. Yet, if one has found such a filter, equation (19) allows for applying established deconvolution algorithms for obtaining the pre-measurement density  $\rho(x)$ . Making the most obvious choice by taking the diagonal of the qPSF,  $q(x) = Q(x, x)$ , turns out to be numerically unstable and inaccurate. To compensate for the complexity of the 2D convolution, this diagonal needs to be readjusted. To this end we call upon a machine learning approach.

### 4.1. Step 1: Multi-frame filter

Inspired by the multi-frame deconvolution technique, which is applied, e.g. in astronomy [28], we pursue the following machine learning approach to learn the unknown filter  $q(x)$ . Our training set consists of a small number  $n_t$  of one- and many-body states with known (reduced) one-body density matrix  $\rho_1^{(k)}(x, y)$ ,  $k = 1, \dots, n_t$ . For each training sample, we calculate the corresponding measurement signal  $s^{(k)}(z)$  by the full 2D convolution with the exact qPSF  $Q(x, y)$  (see appendix C). Recall that  $Q(x, y)$  depends only on the ramp parameters and not on the

physical sample. Then we estimate each signal  $s^{(k)}(z)$  as a 1D convolution of the corresponding densities  $\rho^{(k)}(z) = \rho_1^{(k)}(z, z)$  with the same density-independent filter  $q(z)$ :

$$s^{(k)}(z) = (\rho_1^{(k)} * Q)(z, z) \approx (\rho^{(k)} * q)(z). \quad (20)$$

Except for being space invariant<sup>8</sup>, no further priors are imposed on  $q$ , because it has no physical interpretation and is rather a mathematical tool. Thus, while the densities of the training set vary from signal to signal, the same filter  $q$  is common to all signals. Each of them provides additional information on  $q$ , thereby restricting the space of possible solutions.

As to the choice of training samples we create a random selection of five dark soliton samples with different healing lengths  $\xi \in [10, \dots, 40] \times 10^{-8}$  m in a box of length  $L_b \in [3/4, \dots, 10/12] L_l$  with  $L_l$  being the pinning lattice extension as well as a random selection of five harmonic oscillator (HO) samples with trapping frequency  $\omega \in [200, \dots, 800] \times 2\pi$  Hz and excitation level  $n \in \{1, \dots, 10\}$  (see appendix). We explicitly include only uncorrelated states as samples in order to also test the performance of the learned filter  $q$  on signals stemming from unseen densities of correlated many-body states later on.

Then, we define a total loss function  $\mathcal{L}$ , which describes a deviation between the true signals  $s^{(k)}$  and their approximations  $\rho^{(k)} * q$ , a least squares problem:

$$\min_q \mathcal{L}(q) = \min_q \frac{1}{n_t} \sum_{k=1}^{n_t} \int dz |s^{(k)}(z) - (\rho^{(k)} * q)(z)|^2 \approx \min_{\mathbf{q}} \frac{1}{n_t} \sum_{k=1}^{n_t} |\mathbf{s}^{(k)} - \mathbf{A}^{(k)} \mathbf{q}|^2, \quad (21)$$

where in the last step we switch to a numerical grid with  $\mathbf{s}^{(k)}$  and  $\mathbf{q}$  being  $(L \pi / \Delta \phi)$ -dimensional vectors and  $\mathbf{A}^{(k)}$  denoting a  $(L \pi / \Delta \phi \times L \pi / \Delta \phi)$  Toeplitz matrix, which represents a 1D discrete convolution with zero padding and limited support.  $L$  corresponds to the the number of lattice sites and  $\pi / \Delta \phi \in \mathbb{N}$  to the number of grid points per lattice site (sampling rate).

To find the filter  $q$ , that is most likely to have created the observed distortions in the signals, we perform the gradient descent algorithm in batch mode, meaning that we take into account all the frames simultaneously. We find that a small amount of samples is sufficient to obtain a well-performing filter. Thus, we do not need to resort to more memory-efficient optimization algorithms such as stochastic or mini-batch gradient descent.

In each iteration step  $m \in \mathbb{N}_0$  the filter is updated such that we follow a path towards the minimum of  $\mathcal{L}$  by taking a direction of negative gradient  $\nabla \mathcal{L}$ . As initial guess we take the diagonal of the qPSF  $\mathbf{q}_0 = Q(x, x)$  and then iterate

$$\mathbf{q}_{m+1} = \mathbf{q}_m - \beta \nabla \mathcal{L}(\mathbf{q}_m), \quad (22)$$

where the gradient of the loss function reads:

$$\nabla \mathcal{L}(\mathbf{q}_m) = \frac{1}{n_t} \sum_{k=1}^{n_t} 2\mathbf{A}^{(k)T} (\mathbf{A}^{(k)} \mathbf{q}_m - \mathbf{s}^{(k)}). \quad (23)$$

The step size or learning rate  $\beta$  can be optimally calculated (accurate line search) for each iteration step as

$$\begin{aligned} \beta &= \underset{\beta}{\operatorname{argmin}} \mathcal{L}(\mathbf{q}_m - \beta \nabla \mathcal{L}(\mathbf{q}_m)) \\ &= \frac{1}{2} \frac{\sum_k (\mathbf{q}_m^T \mathbf{A}^{(k)T} - \mathbf{s}^{(k)T}) \mathbf{A}^{(k)} \mathbf{A}^{(k)T} (\mathbf{A}^{(k)} \mathbf{q}_m - \mathbf{s}^{(k)})}{\sum_k (\mathbf{q}_m^T \mathbf{A}^{(k)T} - \mathbf{s}^{(k)T}) \mathbf{A}^{(k)} \mathbf{A}^{(k)T} \mathbf{A}^{(k)} \mathbf{A}^{(k)T} (\mathbf{A}^{(k)} \mathbf{q}_m - \mathbf{s}^{(k)})}. \end{aligned} \quad (24)$$

Finally, we iterate until the relative change in the total loss function reaches some threshold. Figure 2(c) depicts one such filter for  $V_f = 200E_r$ ,  $T_f = \hbar/E_r$ ,  $L = 33$  and  $\pi / \Delta \phi = 33$ .

#### 4.2. Step 2: Deconvolution

Now that we know the filter  $q$  we can invert equation (19) for several unseen cases  $s(z)$  to obtain the pre-measurement density  $\rho(x)$ . To this end a large toolbox of deconvolution algorithms exists, but these should be applied with care, since the problem is ill-posed and the best algorithm is usually determined by a comparative study.

During the image acquisition by microscopes in molecular biology [29] or telescopes in astronomy [30] multiple degradation sources can distort the true form of the object: noise, scatter, glare and blur. The blur, caused by the passage of light through the imaging system, leads to a non-random light redistribution and poses a fundamental limitation to the imaging system. The recorded image is usually modeled as a convolution of the object with a filter, also known as point spread function (PSF). There exists a variety of methods to reverse this process and retain the original object, called deblurring or deconvolution algorithms [31]. They can be classified as inverse (Wiener-Deconvolution [32]) or iterative (Van-Cittert [33], Lucy-Richardson [34, 35], Steepest

<sup>8</sup> Space invariance of filter  $q$  implies that the same filter is used for calculating every point of the convolution. Space-variant filter would be altered for different regions of the convolution.

Descent [36]); with prior knowledge of the filter (non-blind deconvolution) or completely unknown (blind deconvolution [37]); imposing priors such as non-negativity and smoothness or without them; modeling potential noise sources or neglecting them; using a single frame or a batch of sampled frames (multi-frame deconvolution [38]).

For our case we require an iterative approach, as these algorithms are more stable and provide a better restoration of degraded resolution, although at the cost of longer computation times. Since we obtained the filter in the previous subsection it should be non-blind. The density we are trying to reconstruct is positive and normalized, so corresponding constraints must be enforced, but otherwise no further priors are necessary to impose. We also neglect all sources of noise<sup>9</sup> and the measurement signal is considered as a single frame.

To deconvolve the signal with the trained filter we apply a slightly modified version of the previously described gradient descent algorithm with line search. Namely, we additionally impose the non-negativity and the normalization constraints by replacing the density by its absolute value normalized to unity in each iteration step (see [39]).

The downside of our reconstruction algorithm lies in the fact that it is not clear to which extent the reconstructed density resembles the original density, when the original one is not known, which is the case in an actual experiment. This is a long standing problem of machine learning and deconvolution algorithms in general. Nevertheless, even in the current state a self-consistency check provides a good measure on the quality of the reconstruction procedure: if the reconstructed density is close to the genuine one, it will reproduce the measured signal with a high fidelity when convolved with the previously learned filter. Although it is only a necessary condition, it lies at the core of the majority of deconvolution algorithms, which are frequently used in many scientific applications, where imaging is involved, ranging from astronomy [28] to biology [29].

## 5. Applications

We showcase the performance of our qPSF approach and reconstruction strategy using four physical example setups (see figure 3): excited harmonic oscillator eigenstates featuring a rapidly oscillating density, two identical bosons with infinite repulsion in a harmonic trap [40], BEC with a soliton excitation and a Fermi polaron inside a box potential. For details on the implementation of these systems see appendix B. The examples are chosen to cover a broad range of different situations: single particle, weakly- and highly-correlated few-body physics confined either in a parabolic or a box trap.

The deconvolution uses a multi-frame filter  $q$  [see figure 2(c)] trained with a random selection of sample densities of the harmonic oscillator example and a dark soliton in a small BEC. We find that applying it to the unknown signals from the two-Boson and Fermi polaron problem yields very good results, emphasizing the power of the method. We stress that we learn the multi-frame filter from single-particle and mean-field cases and then apply it to the unseen situations, which involve correlated many-body states.

The insets in figure 3 show the genuine single-particle density  $\rho(x)$ , the measurement signal  $s(x)$  and the deconvolved signal  $\tilde{\rho}(x)$  for different physical examples. In all cases the structure of the genuine density is washed out in the measurement signals, but almost completely recovered by the reconstruction. In particular, we recover all of the many oscillations for the harmonic oscillator with their full original contrast [figure 3(a)]. Similarly, in the two-Boson example, the deconvolution successfully reproduces the original density although the two humps have almost merged into a single one in the measurement signal [figure 3(c)]. The soliton depth is restored, while the background constant density remains intact [figure 3(b)]. In the Fermi polaron example, both the sharp dip in the center of the trap and the Friedel oscillations around it are fully recovered in the deconvolved signal, although they seemed to be lost in the measurement signal [figure 3(d)]. These examples showcase the power of the reconstruction method using the previously learned filter  $q$ .

To judge on the quality, we introduce a dissimilarity measure between two normalized functions  $g$  and  $h$  as

$$D(g, h) = \frac{1}{2} \|g - h\|_1 = \frac{1}{2} \int dx |g(x) - h(x)|. \quad (25)$$

It takes a value of zero for coinciding functions and increases up to one as the absolute deviation becomes more pronounced. Further, we define the dissimilarity between the measurement signal<sup>10</sup>  $s$  and the genuine density  $\rho$  as  $D_s = D(s, \rho)$  and the dissimilarity between the reconstructed density  $\tilde{\rho}$  and the genuine one as  $D_d = D(\tilde{\rho}, \rho)$ . In figure 3, we show how this dissimilarity depends on the typical structure size  $\sigma$  of the genuine density. For structures that are large compared to the lattice spacing ( $\sigma > 2a_1$ ), the dissimilarity  $D$  is negligible both for the

<sup>9</sup> For practical applications a low-pass filter is applied to smooth out spatial fluctuations in the measurement signal due to the atom shot noise.

<sup>10</sup>  $s(z)$  is in general not exactly normalized due to the small particle losses induced by the chosen modeling of quantum efficiencies. We normalize it to unity for the dissimilarity analysis and the deconvolution procedure.



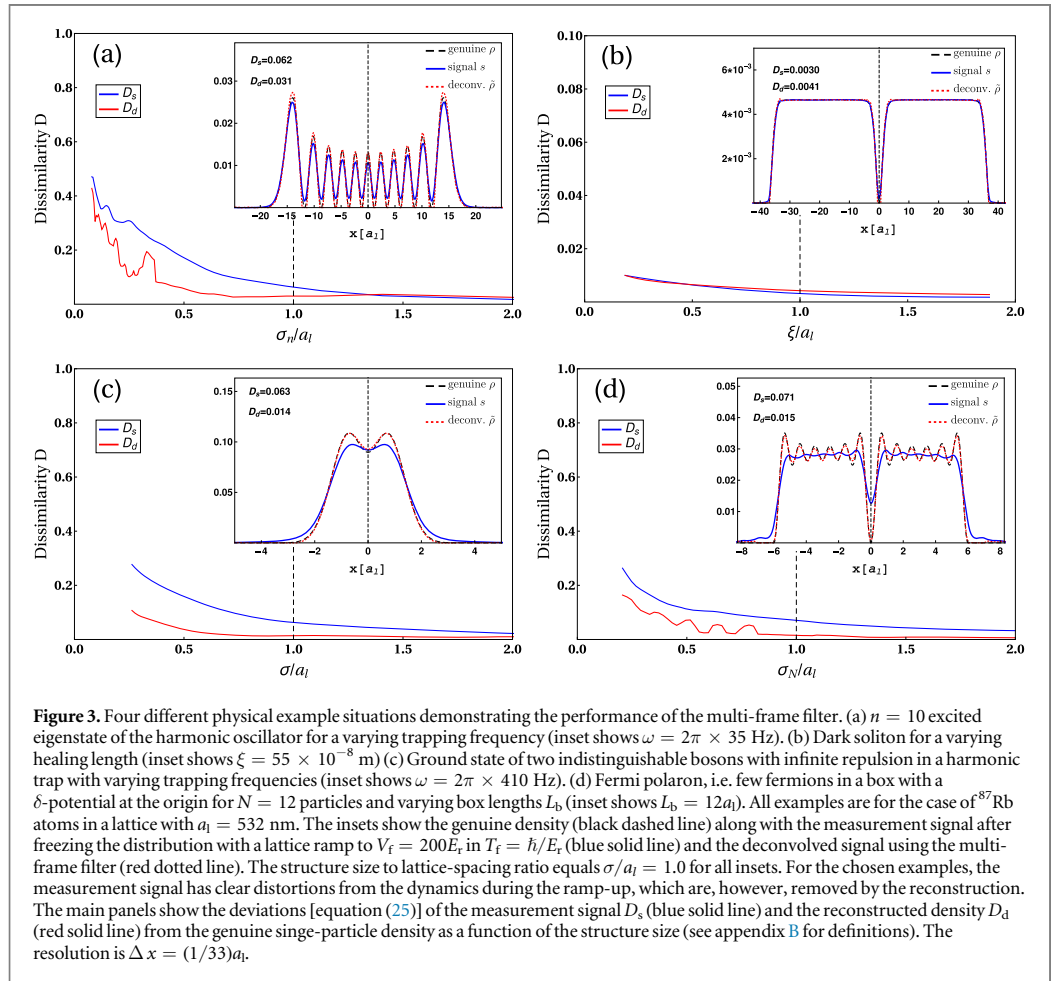


**Figure 3.** Four different physical example situations demonstrating the performance of the multi-frame filter. (a)  $n = 10$  excited eigenstate of the harmonic oscillator for a varying trapping frequency (inset shows  $\omega = 2\pi \times 35$  Hz). (b) Dark soliton for a varying healing length (inset shows  $\xi = 55 \times 10^{-8}$  m) (c) Ground state of two indistinguishable bosons with infinite repulsion in a harmonic trap with varying trapping frequencies (inset shows  $\omega = 2\pi \times 410$  Hz). (d) Fermi polaron, i.e. few fermions in a box with a  $\delta$ -potential at the origin for  $N = 12$  particles and varying box lengths  $L_b$  (inset shows  $L_b = 12a_l$ ). All examples are for the case of  $^{87}\text{Rb}$  atoms in a lattice with  $a_l = 532$  nm. The insets show the genuine density (black dashed line) along with the measurement signal after freezing the distribution with a lattice ramp to  $V_f = 200E_f$  in  $T_f = \hbar/E_f$  (blue solid line) and the deconvolved signal using the multi-frame filter (red dotted line). The structure size to lattice-spacing ratio equals  $\sigma/a_l = 1.0$  for all insets. For the chosen examples, the measurement signal has clear distortions from the dynamics during the ramp-up, which are, however, removed by the reconstruction. The main panels show the deviations [equation (25)] of the measurement signal  $D_s$  (blue solid line) and the reconstructed density  $D_d$  (red solid line) from the genuine single-particle density as a function of the structure size (see appendix B for definitions). The resolution is  $\Delta x = (1/33)a_l$ .

measurement and the deconvolved signal. When the structures are on the scale of the lattice spacing, the measurement signal starts to deviate due to the dynamics during the ramp-up of the pinning lattice. The dissimilarity of the deconvolved signal, however, remains negligible due to the successful deconvolution. Only for structures smaller than about half the lattice spacing ( $\sigma < 0.5a_l$ ), we observe an increase of  $D_d$ , indicating the limitations of the method. Using the deconvolution via the qPSF, we can therefore shift the accessible structure sizes from about  $2a_l$  to about  $0.5a_l$  for bosonic examples and from about  $2a_l$  to about  $1.0a_l$  for the fermionic system, which is a significant improvement that is crucial for many physical examples in quantum gas physics. The reason of fermions being less susceptible to our reconstruction (the humps in  $D_d$  in figure 3(d)) is probably related to the Pauli principle and the incommensurability of the underlying density structure to the lattice constant reminding of the pinning phase transition [41]. The bosons are apparently not affected by this effect [figure 3(c)] due to interactions being switched off right before the pinning procedure starts.

In the above examples we ensured that the results are converged with respect to the grid spacing and assumed the signals to be free from atom shot noise. However, for the experiment it is paramount to know the actual amount of effort involved for a reliable density measurement: for uncorrelated many-body states, we empirically found (see appendix) that the minimum number of the phase shifts amounts to 11, while the minimally required number of single shots per phase offset is approximately  $5 \times 10^3/N$  with  $N$  being the number of particles<sup>11</sup>. Such large numbers of images are feasible with current quantum gas technology, e.g. 20 000 realizations were obtained in [42] and 38 000 realizations in [43]. The effort can be further reduced by realizing an ensemble of 1D systems in a 2D lattice array. Furthermore, due to single-atom sensitivity of the quantum gas microscope one obtains a large signal from each atom during the fluorescence imaging. Thus, the common white noise of classical imaging systems, which makes the deconvolution much more challenging, is absent in our case. After identifying the occupations on the lattice, the images have no further noise.

<sup>11</sup> The signal needs to be preprocessed before the reconstruction algorithm by applying a low-pass filter to smooth out the data.

We remark that our reconstruction scheme with the current filter  $q$  is expected to reliably work only in trap geometries involving a combination of a harmonic trap with a box potential, since the learned filter  $q$  is biased by our training set. The use of prior knowledge is necessary in order to constrain the space of solutions for solving the otherwise ill-posed inverse problem. Although we demonstrated that it generalizes well to correlated situations under the same trapping, another trap geometry requires to learn a different kernel  $q$  with the corresponding training examples. For cold atom systems that we consider here, the trapping potentials can be arbitrarily shaped and are thus completely known within an excellent approximation.

## 6. Outlook

Our work opens the research direction of high-resolution imaging with single-atom sensitivity also for trapped, i.e. non-lattice systems. We propose to apply a pinning lattice for imaging and to sample the reduced one-body density with a resolution below the lattice spacing by performing repeated measurements with shifted positions of the pinning lattice relative to the physically trapped system. We have shown that density distortions resulting from the dynamics during the ramping up of the lattice can be compensated by deconvolution with a trained filter for a wide range of parameters. Our findings are of immediate relevance for ongoing quantum gas microscope experiments. A reliable measurement of small density structures will allow accessing new regimes and imaging of the corresponding physical processes such as the shape of a vortex core taking into account beyond mean-field effects [44] or discrete few-body structures in arbitrary traps. For simplicity, we have focused here on one-dimensional systems, but our framework equally applies to higher spatial dimensions. Further extensions of our work would be the fate of correlation measurements [26], in a single-component ultracold gas as well as mixtures, and blurring effects in the measurement of the dynamics. Another important aspect is the imaging after release from a driven system, e.g. for producing artificial gauge fields [45], where switching off the drive can induce further effects. Releasing from lowest Landau levels yields a self-similar expansion of the wave function [46], which could be used before freezing the distribution.

## Acknowledgments

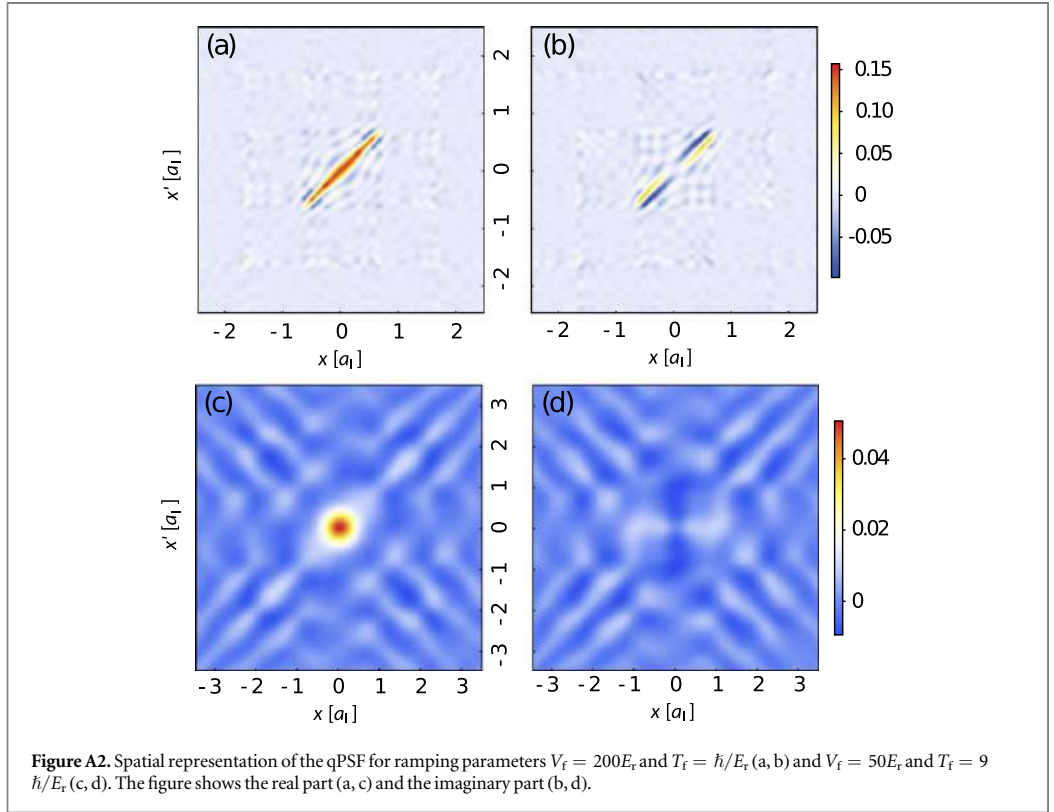
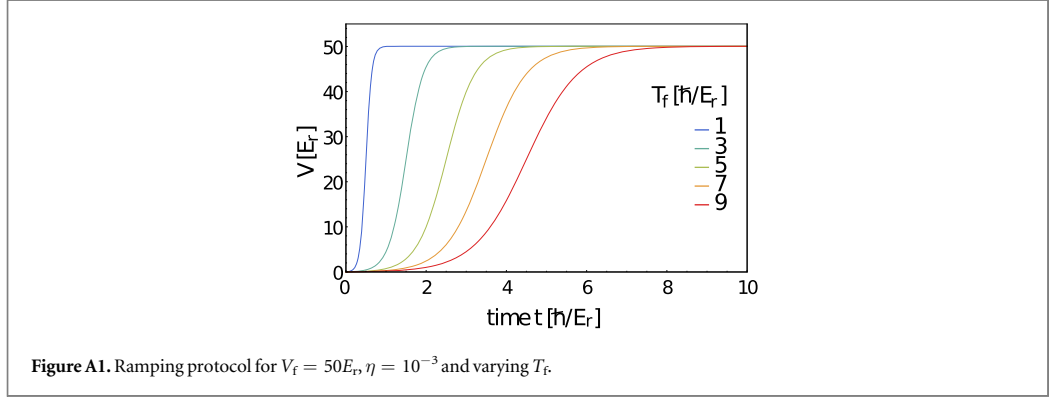
PS and CW gratefully acknowledge funding by the Deutsche Forschungsgemeinschaft in the framework of the SFB 925 ‘Light induced dynamics and control of correlated quantum systems’. SK and MP contributed equally to this work.

## Appendix A. Numerical procedure to obtain the quantum point spread function

According to equation (4) of the main text the qPSF is an operator  $\hat{Q} = \sum_{\alpha} \eta_{\alpha} |\chi_{\alpha}\rangle\langle\chi_{\alpha}|$  with  $|\chi_{\alpha}\rangle = \hat{\pi} \hat{U}_0^{\dagger} |w_{0;0}^{\alpha}\rangle$ . Therefore, we have to calculate the Wannier state  $|w_{0;0}^{\alpha}\rangle$  of the band  $\alpha$  at site  $i = 0$  for the pinning lattice with the final potential depth  $V_f$  and phase offset  $\varphi = 0$  and propagate it with the time-evolution operator  $\hat{U}_0^{\dagger} = \hat{T} \exp(-i/\hbar \int_{T_f}^0 d\tau \hat{h}_0(\tau))$ , which describes the lowering of the pinning lattice from  $V_f$  to zero depth. Finally, the parity operator  $\hat{\pi}$  is applied to reformulate the measurement signal in terms of a convolution.

The Wannier states are obtained by representing the position operator  $\hat{x}$  in the basis of  $\hat{h}_0(T_f)$  and then diagonalizing it. Afterwards, we set a band limit  $\alpha_{\max}$ . Modeling the detection efficiencies  $\eta_{\alpha}$  for energetically high lying bands, however, is more involved as these depend on both the tunneling and fluorescence imaging time scale. The tunneling rates grow exponentially with the band index, such that they can be divided into tunneling and non-tunneling bands within the fluorescence imaging time to a good approximation. For the sake of simplicity, we therefore assume that all (bound) bands lying energetically below  $V_f$  are detected with unit detection efficiency, meaning  $\eta_{\alpha} = 1 \ \forall \ \alpha \leq \alpha_{\max}$ , and  $\eta_{\alpha} = 0$  for the continuum states, since atoms in these states are not pinned during the fluorescence imaging. As a consequence, this model does only give a lower bound on the loss in the measurement signal [equation (C.4)] due to unobserved channels. We use a lattice containing  $L = 99$  sites with 33 grid points to resolve each site, unless stated otherwise, while the potential depth is varied in the range  $V_f \in [50, \dots, 300] E_r$ .

The back-time propagation of relevant Wannier states is performed with the Multi-Layer Multi-Configuration Time-Dependent Hartree for bosons (ML-MCTDHB) approach [47, 48] to obtain  $|\chi_{\alpha}\rangle$ . The ramping times cover  $T_f \in [1, \dots, 9] \hbar/E_r$  and the ramping protocol  $V(t)$  is a logistic function of sigmoid form:



$$V(t) = \frac{V_f}{1 - 2\eta} \left( \frac{1}{1 + \left(\frac{\eta}{1-\eta}\right)^{\frac{2t}{T_f} - 1}} - \eta \right), \quad (\text{A.1})$$

with amplitude  $V_{\max} = V_f/(1 - 2\eta)$ , shift  $t_0 = T_f/2$ , steepness  $\frac{1}{\tau} = \frac{2}{T_f} \ln\left(\frac{1-\eta}{\eta}\right)$  and offset  $V_{\text{off}} = V_{\max} \eta$ . The  $\eta$  parameter ensures that  $V(T_f) = V_f$  does not deviate much from the saturated value  $V_{\max}$ . With  $\eta = 10^{-3}$  fixed,  $T_f$  alone determines the adiabaticity of the ramping protocol (see figure A1).

In the case of an adiabatic preparation of many-body ground states in optical lattices, such as the bosonic Mott insulator, the optimal shape of the ramp function has been extensively discussed [49]. In contrast, for pinning the distribution on the lattice in quantum gas microscopes, simple s-shaped ramps have proven sufficient [4, 5]. We note that in our setting, the dynamics during the ramp will be strongly non-adiabatic in

order to avoid a loading of the ground state of the lattice, but freeze the atoms in their original position. Therefore, we expect that the precise shape of the ramp should not be important.

We show the real and imaginary part of the spatial representation of the qPSF  $Q(x, x') = \langle x | \hat{Q} | x' \rangle$  for a quick ramp  $T_f = \hbar/E_r$  with a deep lattice  $V_f = 200E_r$  and for a slow ramp  $T_f = 9\hbar/E_r$  with a comparatively shallow lattice  $V_f = 50E_r$  (figure A2). In the first case we observe a diagonal pattern in the real part with a fast decay of the off-diagonal, while in the second case the real part displays a Gaussian profile with the imaginary part being suppressed by an order of magnitude. Both cases are rather localized around a small region of approximately  $5a_l$ . The diagonal pattern can be induced and enhanced by choosing deeper lattices, meaning that higher bands are responsible for this effect, although by successively adding bands for the qPSF calculation we found that approximately only the first half of the bands  $\alpha_{\max}$  is responsible for the pattern formation. Going to ramp times beyond  $T_f = 9\hbar/E_r$  requires large lattices with more than  $L = 100$  lattice sites, because the Wannier states, propagated back in time, almost reach the boundaries of the grid.

The qPSF has no direct relation to the classical PSF of the imaging system with finite numerical aperture NA, which is used for the fluorescence imaging after the pinning of the atoms. As long as the NA is large enough to allow for a reconstruction of the lattice occupation (typically  $NA = 0.6-0.8$ ), it drops out of the problem. If one repeats the measurement with varying positions of the pinning lattice with respect to the initial system via the displacement by  $\varphi$ , even the lattice constant  $a_l$  does not pose a fundamental limit to the resolution. In the numerical examples a sampling with resolution  $0.0\bar{3}a_l$  was used and similar relative positioning of  $0.1a_l$  between the pinning lattice and further traps were reported experimentally [50]. The distortion from the dynamics during ramp-up, which is captured by the qPSF and is relevant for structures on the order of  $a_l$ , is therefore the fundamental limitation on the resolution. The reconstruction algorithm described in the main text can then lead to density measurements with a resolution even better than  $a_l$ . We additionally verified that a sampling rate  $0.1a_l$  is enough for a successful reconstruction (see appendix D).

## Appendix B. Examples of application

For the numerical implementation we make use of recoil units  $x_r = 1/k_l$ ,  $E_r = \hbar^2 k_l^2 / (2m)$ ,  $T_r = \hbar/E_r$  with the wavenumber  $k_l = 2\pi/\lambda_l$  of the laser beam of wavelength  $\lambda_l = 1064$  nm to create the lattice potential and  $m$  being the mass of the trapped particles, here  $^{87}\text{Rb}$ . The lattice constant is  $a_l = \lambda_l/2$ .

### B1. Harmonic oscillator (HO) eigenstates

$$\psi_n(x) = \frac{1}{\sqrt{n!2^n}} \frac{1}{\lambda/\pi} \sqrt{\frac{1}{a_{\text{ho}}}} H_n\left(\frac{x}{a_{\text{ho}}}\right) \exp\left(-\frac{x^2}{2a_{\text{ho}}^2}\right), \quad (\text{B.1})$$

where  $a_{\text{ho}} = \sqrt{\frac{\hbar}{m\omega}}$  the harmonic oscillator length,  $\omega$  the frequency of the trap and  $n \in \mathbb{N}_0$  the excitation level. To characterize the structure size of the HO modes with respect to the lattice we consider the variance of the position operator divided by the number of peaks in the density profile  $\sigma_n/a_l$  with  $\sigma_n = \frac{1}{n+1}(\langle \psi_n | x^2 | \psi_n \rangle - \langle \psi_n | x | \psi_n \rangle^2)^{1/2}$ . The HO example is used for training of the filter.

### B2. Dark soliton

We prepare a dark soliton within the mean-field approximation placed in a reflection-symmetric box with an extension  $L_b$  smaller than that of the pinning lattice  $L_l = L a_l$ . We position the soliton in the center of the box and ensure that it is sufficiently separated from the walls:

$$\psi(x) = \begin{cases} -c_1 \tanh\left(\frac{(L_b/2 + x)}{\sqrt{2}\xi}\right) & \text{if } -\frac{L_b}{2} < x < -\frac{L_b}{2} + 10\xi \\ c_2 \tanh\left(\frac{x}{\sqrt{2}\xi}\right) & \text{if } -\frac{L_b}{2} + 10\xi < x < \frac{L_b}{2} - 10\xi, \\ c_3 \tanh\left(\frac{(L_b/2 - x)}{\sqrt{2}\xi}\right) & \text{if } \frac{L_b}{2} - 10\xi < x < \frac{L_b}{2} \end{cases}, \quad (\text{B.2})$$

where the prefactors  $c_i$  are chosen such as to ensure the continuity and the normalization of the wave function,  $\xi = 1/\sqrt{8\pi\bar{\rho}a_{sc}}$  is the healing length of the condensate,  $a_{sc}$  the scattering length and  $\bar{\rho}$  the constant background density. The structure size is chosen as  $\sigma_c/a_l = 2\xi/a_l$ , which is approximately the full-width-at-half-maximum of the soliton profile. The soliton example is used for training of the filter.

### B3. Impurity in a Fermi sea

We put  $N$  spin-polarized fermions in a reflection-symmetric box of length  $L_b < L_1$ . A stationary impurity positioned in the middle of the potential acts as a repulsive delta-potential of infinite strength, inducing a density profile of fermions similar to that of a soliton, but with an oscillatory background. The eigenstates have a defined parity:

$$\psi_j^{\text{even}}(x) = \sqrt{\frac{2}{L_b}} \sin\left(\frac{2\pi j}{L_b}|x|\right), \quad (\text{B.3})$$

$$\psi_j^{\text{odd}}(x) = \sqrt{\frac{2}{L_b}} \sin\left(\frac{2\pi j}{L_b}x\right). \quad (\text{B.4})$$

The density operator for an even number of fermions is then given by a mixed state

$$\hat{\rho}_1 = \frac{1}{N} \left( \sum_{j=1}^{N/2} |\psi_j^{\text{even}}\rangle \langle \psi_j^{\text{even}}| + \sum_{j=1}^{N/2} |\psi_j^{\text{odd}}\rangle \langle \psi_j^{\text{odd}}| \right). \quad (\text{B.5})$$

Here, the structure size is assigned by an average extension of a peak in the one-body density  $\sigma_N/a_1 = (L_b/N)/a_1$ . We observe an oscillatory behaviour of  $D_d$  below  $\sigma_N/a_1 < 1.0$  with a higher oscillation period for an increasing number of fermions (not shown). We believe that the Pauli exclusion principle and the commensurability of the density with respect to the lattice are responsible for this effect.

### B4. Two bosons with infinite repulsion in HO

The highly correlated problem of two bosons trapped in a harmonic trap and interacting with each other via a delta-potential of infinite strength can be solved analytically in the relative frame [40]. By transforming the solution back into the laboratory frame and tracing out one of the coordinates one obtains the following one-body density matrix:

$$\rho_1(x, y) = \frac{b^3}{\pi} e^{-0.5b^2(x^2+y^2)} \begin{cases} g(x, y) & \text{if } x < y \\ g(y, x) & \text{if } y < x \end{cases}, \quad \text{with} \quad (\text{B.6})$$

$$g(x, y) = \sqrt{\pi} \left( xy + \frac{1}{2b^2} \right) (\text{erf}(bx) - \text{erf}(by) + 1) + \frac{y}{b} e^{-b^2x^2} - \frac{x}{b} e^{-b^2y^2} \quad (\text{B.7})$$

and  $b = 1/a_{\text{ho}}$ . The correlated two-body system requires the full 2D convolution to create the signal, which is cumbersome to achieve on a large grid with fine resolution. So we consider very large trapping frequencies and reduce the grid to  $L = 33$  lattice sites. The structure size is defined similar to the HO case:  $\sigma/a_1$  with  $\sigma^2 = \int dx \rho(x) x^2 - \left( \int dx \rho(x) x \right)^2$ .

## Appendix C. Simulation of the measurement signal

In the most general formulation the distorted signal  $s(z)$  can be obtained directly via a 2D convolution of the one-body density matrix  $\rho_1(x, x')$  of the initially prepared system (appendix B) with the kernel  $Q(x, x')$  (appendix A):

$$s(z) = \text{Tr} \{ \hat{T}_z^\dagger \hat{\pi} \hat{Q} \hat{\pi} \hat{T}_z \hat{\rho}_1 \} = (\rho_1 * Q)(z, z) = \iint dx dy \rho_1(x, y) Q(z - x, z - y). \quad (\text{C.1})$$

However, the  $(L \cdot \pi/\Delta\phi) \times (L \cdot \pi/\Delta\phi)$  matrices lead to approximately  $(L \cdot \pi/\Delta\phi)^4$  numerical operations, which renders the direct calculation inefficient for large lattices with fine resolution. One way to circumvent this issue would be to make a smaller support for the density by confining it more tightly and for the filter by defining a cutoff, when the amplitudes drop below a certain value. Here, we just verified that a spacing  $\Delta x = (1/33) a_1$  provides converged signals by doubling the site resolution.

Independently of the above statements we can reduce the numerical effort to  $\propto (L \cdot \pi/\Delta\phi)^2$ , namely for weakly correlated systems the spectrally-decomposed one-body density operator has a finite number of natural populations  $\lambda_\gamma$  with considerable weight:

$$\hat{\rho}_1 = \sum_{\gamma=1}^{\gamma_{\text{max}}} \lambda_\gamma |\phi_\gamma\rangle \langle \phi_\gamma|, \quad (\text{C.2})$$

with  $|\phi_\gamma\rangle$  natural orbitals. Inserting this relation and additionally the expansion of the qPSF into equation (C.1) we obtain the signal as a sum of 1D convolutions of the natural orbitals  $\phi_\gamma$  with the 'band' filters  $\chi_\alpha^*$ :

$$s(z) = \sum_{\gamma=1}^{\gamma_{\max}} \sum_{\alpha=1}^{\alpha_{\max}} \lambda_{\gamma} \eta_{\alpha} |(\chi_{\alpha}^* * \phi_{\gamma})(x)|^2. \quad (\text{C.3})$$

There is another important point worth mentioning, namely the padding. Since we are working with finite systems, a convolved function spans a larger region than the input functions. Thus, we need to provide values for chosen densities outside the grid and padding with zeroes is the most natural choice for trapped systems, while periodic padding would be suitable for ring geometries. Also, we ensure that the distortion of the signal does not reach the boundaries of the grid.

For a given lattice realization, meaning fixed  $V_f$ ,  $T_f$  and phase  $\varphi$ , the signal  $s(z = i \cdot a_1 + \varphi)$  with spatial sampling period  $a_1$  sums up to unity only when  $\eta_{\alpha} = 1 \forall \alpha$ , because  $\hat{R}_{i,\varphi}^{\dagger} \hat{R}_{i,\varphi}$  then forms a positive operator-valued measure. In our case, neglecting continuum states lying energetically above  $V_f$  results in a particle loss  $\Omega$ . In other words,  $\Omega = 1 - \sum_{i=1}^L s(i \cdot a_1 + \varphi)$  is the probability of finding a particle in none of the sites, but in the unobserved channels. Averaging over multiple lattice realizations  $\varphi \in \{0, \dots, \pi\}$  we can estimate the mean particle loss  $\bar{\Omega}$  expected for the given pre-measurement reduced one-body density  $\rho_1$ :

$$\bar{\Omega}(V_f, T_f, \rho_1) = 1 - \frac{1}{\pi} \int_0^{\pi} d\varphi \sum_{i=1}^L s(i \cdot a_1 + \varphi). \quad (\text{C.4})$$

In table 1 we show the average loss  $\bar{\Omega}$  for densities and ramp-up parameters discussed in the main text, which is indeed very small and has a tendency to decrease for larger structures.

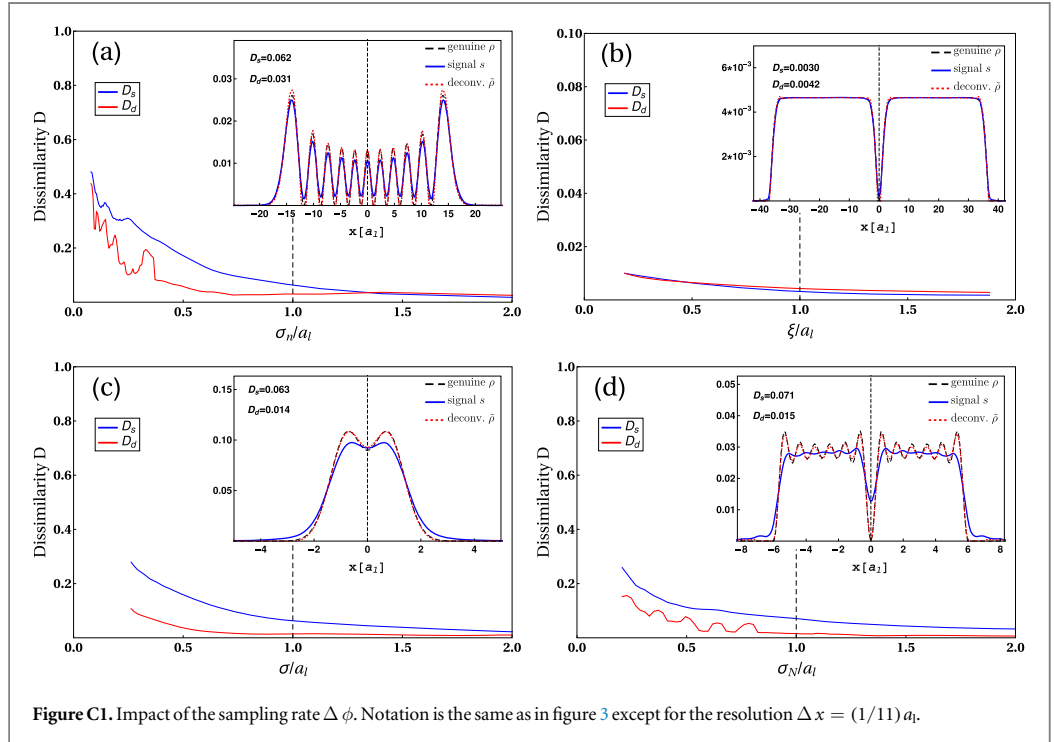


Figure C1. Impact of the sampling rate  $\Delta \phi$ . Notation is the same as in figure 3 except for the resolution  $\Delta x = (1/11) a_1$ .

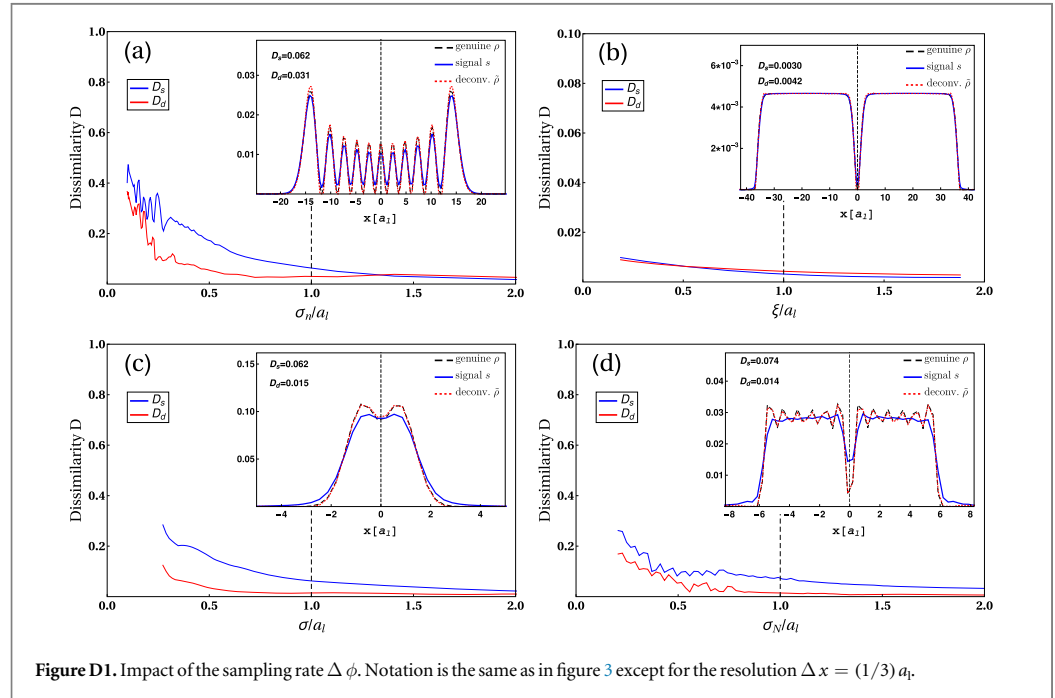
Table 1. Average particle loss  $\bar{\Omega}(V_f, T_f, \rho_1)$  for the densities, discussed in the main text and different structure sizes  $\sigma$  (see appendix B) relative to the lattice spacing. The ramp-up parameters are  $V_f = 200E_r$  and  $T_f = \hbar/E_r$ .

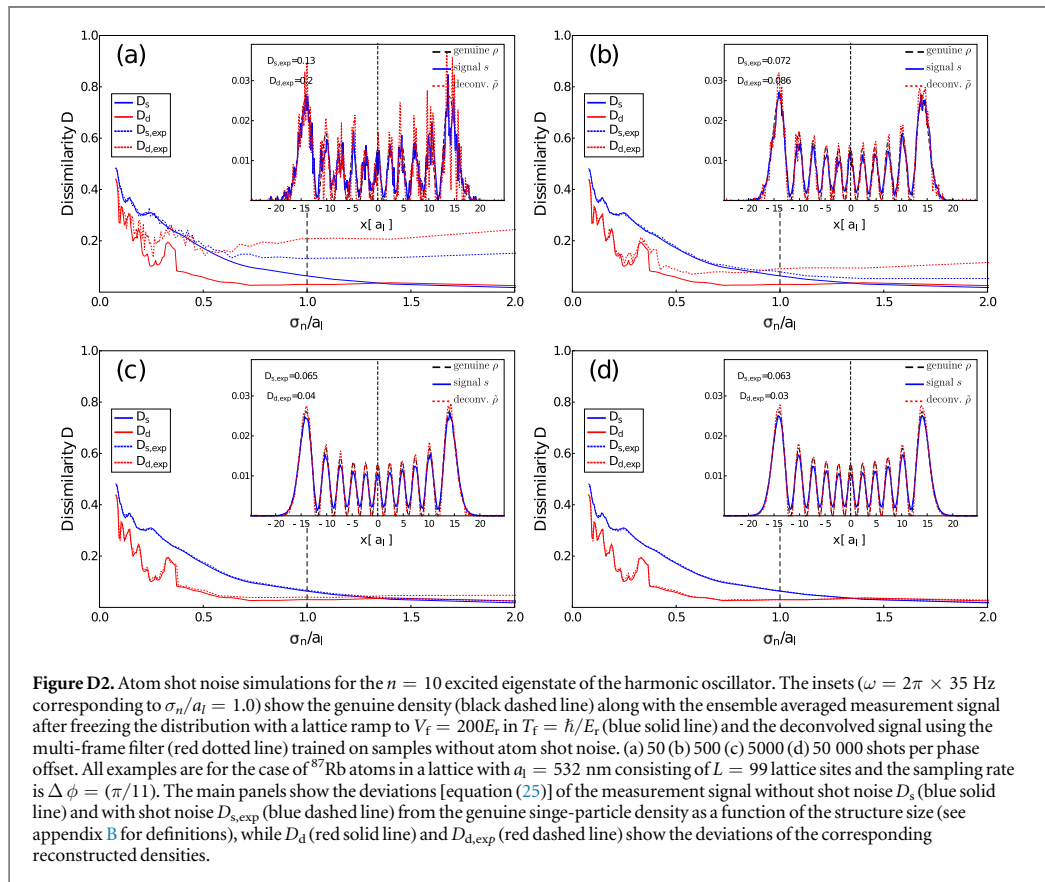
	Structure size $\sigma/a_1$		
	0.5	1.0	2.0
$\rho_1$			
HO $n = 10$	0.030	0.014	0.013
Two-Bosons	0.021	0.015	0.014
Fermi polaron	0.033	0.031	0.017

### Appendix D. Experimental effort

The experimental effort scales linearly with the number of lattice shifts and we study the impact of the sampling rate  $\Delta\phi$  on the quality of the reconstruction. Naively, one would under-sample the signal  $s$  and the filter  $q$ , which we trained on a fine grid with  $\Delta x = (1/33)a_1$ , and apply a deconvolution step from our reconstruction algorithm. However, the procedure does not apply. Instead one needs to learn a different kernel  $q$  for each  $\Delta\phi$  provided a set of correspondingly under-sampled converged signals. By comparing figure 3 to figure C1 we conclude that the quality of the reconstruction does not degrade when the sampling rate is decreased by a factor of three. Reducing the sampling rate by another factor of three (figure D1) provides still a reliable reconstruction for typical structures sizes around  $\sigma/a_1 \approx 1.0$  and above.

Next we consider the robustness of our protocol against atom shot noise. For demonstration we choose the harmonic oscillator example with the sampling rate  $\Delta\phi = \pi/11$ . We simulate the measurement of a single harmonically trapped particle  $n_{\text{shot}}$  times for each phase-offset  $\phi_j$ . The total number of measurements is thus  $11 \cdot n_{\text{shot}}$ . The probability to loose a particle during the measurement is included. Then, we take the ensemble average of the individual measurement signals and spatially smooth out the data with a low-pass filter. Finally, we apply the reconstruction algorithm on the resulting signal with the filter  $q$  trained on signals without shot noise. From figure D2 we estimate the necessary number of single shots to be approximately 5000. More particles would reduce the effort by  $1/N$  if they are uncorrelated, whereas for a correlated few-body system the decrease of the effort with the number of particles is not obvious.





## References

- [1] Binnig G and Rohrer H 1987 *Rev. Mod. Phys.* **59** 615
- [2] Huang B, Bates M and Zhuang X 2009 *Annu. Rev. Biochem.* **78** 993
- [3] Fernandez-Leiro R and Scheres S H 2016 *Nature* **537** 339
- [4] Bakr W S, Peng A, Tai M E, Ma R, Simon J, Gillen J I, Fölling S, Pollet L and Greiner M 2010 *Science* **329** 547
- [5] Sherson J F, Weitenberg C, Endres M, Cheneau M, Bloch I and Kuhr S 2010 *Nature* **467** 68
- [6] Greif D, Parsons M F, Mazurenko A, Chiu C S, Blatt S, Huber F, Ji G and Greiner M 2016 *Science* **351** 953
- [7] Cheuk L W, Nichols M A, Lawrence K R, Okan M, Zhang H and Zwierlein M W 2016 *Phys. Rev. Lett.* **116** 235301
- [8] Endres M *et al* 2011 *Science* **334** 200
- [9] Mazurenko A, Chiu C S, Ji G, Parsons M F, Kanász-Nagy M, Schmidt R, Grusdt F, Demler E, Greif D and Greiner M 2017 *Nature* **545** 462
- [10] Islam R, Ma R, Preiss P M, Eric Tai M, Lukin A, Rispoli M and Greiner M 2015 *Nature* **528** 77
- [11] Wenz A N, Zürn G, Murmann S, Brouzos I, Lompe T and Jochim S 2013 *Science* **342** 457
- [12] Cayla H, Carcy C, Bouton Q, Chang R, Carleo G, Mancini M and Clément D 2018 *Phys. Rev. A* **97** 061609
- [13] Bergschneider A, Klinkhamer V M, Becher J H, Klemm R, Zürn G, Preiss P M and Jochim S 2018 *Phys. Rev. A* **97** 063613
- [14] Omran A, Boll M, Hilker T A, Kleinlein K, Salomon G, Bloch I and Gross C 2015 *Phys. Rev. Lett.* **115** 263001
- [15] Hohmann M, Kindermann F, Lausch T, Mayer D, Schmidt F, Lutz E and Widera A 2017 *Phys. Rev. Lett.* **118** 263401
- [16] Hell S W and Wichmann J 1994 *Opt. Lett.* **19** 780
- [17] Gorshkov A V, Jiang L, Greiner M, Zoller P and Lukin M D 2008 *Phys. Rev. Lett.* **100** 093005
- [18] Subhankar S, Wang Y, Tsui T-C, Rolston S L and Porto J V 2018 *Phys. Rev. X* **9** 021002
- [19] McDonald M, Trisnadi J, Yao K-X and Chin C 2019 *Phys. Rev. X* **9** 021001
- [20] Kollath C, Köhl M and Giamarchi T 2007 *Phys. Rev. A* **76** 063602
- [21] Yang D, Laflamme C, Vasilyev D V, Baranov M A and Zoller P 2018 *Phys. Rev. Lett.* **120** 133601
- [22] Lühmann D-S, Weitenberg C and Sengstock K 2015 *Phys. Rev. X* **5** 031016
- [23] Gericke T, Würtz P, Reitz D, Langen T and Ott H 2008 *Nat. Phys.* **4** 949
- [24] Wiseman H M and Milburn G J 2009 *Quantum measurement and control* (Cambridge: Cambridge University Press)
- [25] Gajda M, Mostowski J, Sowiński T and Załuska-Kotur M 2016 *Europhys. Lett.* **115** 20012
- [26] Schauß P, Cheneau M, Endres M, Fukuhara T, Hild S, Omran A, Pohl T, Gross C, Kuhr S and Bloch I 2012 *Nature* **491** 87
- [27] Ardila L A P, Heyl M and Eckardt A 2018 *Phys. Rev. Lett.* **121** 260401
- [28] Hirsch M, Harmeling S, Sra S and Schölkopf B 2011 *Astron. Astrophys.* **531** A9
- [29] Wallace W, Schaefer L H and Swedlow J R 2001 *Biotechniques* **31** 1076
- [30] Schulz T J 1993 *J. Opt. Soc. Am. A* **10** 1064
- [31] Hansen P C, Nagy J G and O'Leary D P 2006 *Deblurring images: matrices, spectra, and filtering, Vol 3* (Philadelphia, PA: SIAM)



- [32] Wiener N 1949 *Extrapolation, Interpolation, and Smoothing of Stationary Time Series* (New York: Wiley)
- [33] Jansson P A 1996 *Deconvolution of Images and Spectra* (New York: Academic)
- [34] Lucy L B 1974 *Astron. J.* **79** 745
- [35] Richardson W H 1972 *J. Opt. Soc. Am.* **62** 55
- [36] Arfken G B and Weber H J 2013 *Mathematical Methods for Physicists* (New York: Academic) pp 551–98
- [37] Ayers G and Dainty J C 1988 *Opt. Lett.* **13** 547
- [38] Sheppard D G, Hunt B R and Marcellin M W 1998 *J. Opt. Soc. Am. A* **15** 978
- [39] Rosen J B 1960 *J. Soc. Ind. Appl. Math.* **8** 181
- [40] Busch T, Englert B-G, Rzażewski K and Wilkens M 1998 *Found. Phys.* **28** 549
- [41] Haller E, Hart R, Mark M J, Danzl J G, Reichsöllner L, Gustavsson M, Dalmonte M, Pupillo G and Nägerl H-C 2010 *Nature* **466** 597
- [42] Rem B S, Käming N, Tarnowski M, Asteria L, Fläschner N, Becker C, Sengstock K and Weitenberg C 2018 arXiv:1809.05519
- [43] Hilker T A, Salomon G, Grusdt F, Omran A, Boll M, Demler E, Bloch I and Gross C 2017 *Science* **357** 484
- [44] Barberán N, Lewenstein M, Osterloh K and Dagnino D 2006 *Phys. Rev. A* **73** 063623
- [45] Dalibard J, Gerbier F, Juzeliunas G and Öhberg P 2011 *Rev. Mod. Phys.* **83** 1523
- [46] Read N and Cooper N R 2003 *Phys. Rev. A* **68** 035601
- [47] Krönke S, Cao L, Vendrell O and Schmelcher P 2013 *New J. Phys.* **15** 063018
- [48] Cao L, Krönke S, Vendrell O and Schmelcher P 2013 *J. Chem. Phys.* **139** 134103
- [49] Gericke T, Gerbier F, Widera A, Fölling S, Mandel O and Bloch I 2007 *J. Mod. Opt.* **54** 735
- [50] Weitenberg C, Endres M, Sherson J F, Cheneau M, Schauß P, Fukuhara T, Bloch I and Kuhr S 2011 *Nature* **471** 319





Contents lists available at [ScienceDirect](https://www.sciencedirect.com)

## Linear Algebra and its Applications

[www.elsevier.com/locate/laa](http://www.elsevier.com/locate/laa)



# Cospectrality preserving graph modifications and eigenvector properties via walk equivalence of vertices



C.V. Morfonios<sup>a,1</sup>, M. Pyzh<sup>a,1</sup>, M. Röntgen<sup>a,\*,1</sup>, P. Schmelcher<sup>a,b</sup>

<sup>a</sup> Zentrum für Optische Quantentechnologien, Fachbereich Physik, Universität Hamburg, Luruper Chaussee 149, 22761 Hamburg, Germany

<sup>b</sup> The Hamburg Centre for Ultrafast Imaging, Universität Hamburg, Luruper Chaussee 149, 22761 Hamburg, Germany

### ARTICLE INFO

#### Article history:

Received 15 July 2020

Accepted 5 April 2021

Available online 15 April 2021

Submitted by R. Brualdi

#### MSC:

05C50

15A18

05C22

81R40

81V55

#### Keywords:

Cospectrality

Symmetric matrices

Structure of eigenvectors

Matrix powers

Walk equivalence

### ABSTRACT

Originating from spectral graph theory, cospectrality is a powerful generalization of exchange symmetry and can be applied to all real-valued symmetric matrices. Two vertices of an undirected graph with real edge weights are cospectral if and only if the underlying weighted adjacency matrix  $M$  fulfills  $[M^k]_{u,u} = [M^k]_{v,v}$  for all non-negative integer  $k$ , and as a result any eigenvector  $\phi$  of  $M$  has (or, in the presence of degeneracies, can be chosen to have) definite parity on  $u$  and  $v$ . We here show that the powers of a matrix with cospectral vertices induce further local relations on its eigenvectors, and also can be used to design cospectrality preserving modifications. To this end, we introduce the concept of *walk equivalence* of cospectral vertices with respect to *walk multiplets* which are special vertex subsets of a graph. Walk multiplets allow for systematic and flexible modifications of a graph with a given cospectral pair while preserving this cospectrality. The set of modifications includes the addition and removal of both vertices and edges, such that the underlying topology of the graph can be altered. In particular, we prove that any new vertex connected to a walk multiplet by suitable connection weights becomes a so-called unrestricted substitution point (USP), meaning that

\* Corresponding author.

E-mail address: [mroentge@physnet.uni-hamburg.de](mailto:mroentge@physnet.uni-hamburg.de) (M. Röntgen).

<sup>1</sup> These three authors contributed equally.

any arbitrary graph may be connected to it without breaking cospectrality. Also, suitable interconnections between walk multiplets within a graph are shown to preserve the associated cospectrality. Importantly, we demonstrate that the walk equivalence of cospectral vertices  $u, v$  imposes a local structure on every eigenvector  $\phi$  obeying  $\phi_u = \pm\phi_v \neq 0$  (in the case of degeneracies, a specific choice of the eigenvector basis is needed). Our work paves the way for flexibly exploiting hidden structural symmetries in the design of generic complex network-like systems.

© 2021 Elsevier Inc. All rights reserved.

### 1. Introduction

Eigenvalue problems of real symmetric matrices are ubiquitous in many fields of science. Special examples are graph theory in mathematics as well as properties of quantum systems in physics. A first step in dealing with such problems is often based on a symmetry analysis in terms of permutation matrices that commute with the matrix  $H$  at hand. Given a set of such permutation matrices, a symmetry-induced block-diagonalization of  $H$  is possible and powerful statements about the eigenvectors of  $H$  can be made [1,2]. The permutation symmetries of a matrix can be conveniently visualized in the framework of *graphs*. A graph representing a matrix  $H \in \mathbb{R}^{N \times N}$  is a collection of  $N$  vertices connected by edges with weights  $H_{i,j}$ , like the one shown in Fig. 1. Due to this mapping between a matrix and the graph representing it we denote both the graph and the corresponding matrix with the same symbol  $H$ . In this graphical picture, the action of a permutation matrix  $P$  corresponds to permuting the vertices of the graph, along with the ends of the edges connected to them.  $H$  is then transformed to  $H' = PHP^{-1}$ , and if  $P$  and  $H$  commute,  $PH = HP$ , then the graph remains the same after the permutation, i.e.  $H' = H$ . In particular, if  $P$  exchanges two vertices  $u$  and  $v$ , while permuting the remaining vertices arbitrarily, its commutation with  $H$  means that the  $u$ -th and  $v$ -th row of  $H$  coincide,  $H_{u,j} = H_{v,j}$  for all  $j \in \llbracket 1, N \rrbracket \equiv \{1, 2, \dots, N\}$  (and the same for the

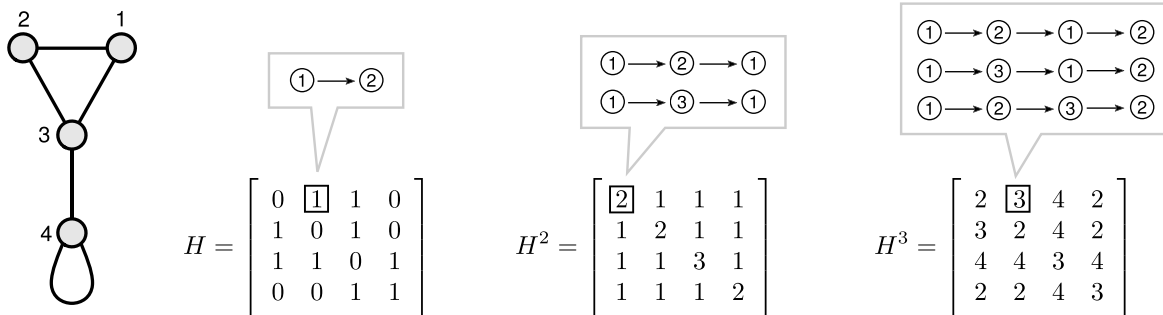


**Fig. 1.** An undirected, unweighted graph with four vertices represented by a  $4 \times 4$  symmetric matrix  $H$ , and the interpretation of its powers  $H^k$  in terms of “walks”: The matrix element  $[H^k]_{i,j}$  counts the number of distinct walks of length  $k$  from vertex  $i$  to  $j$ , as illustrated for  $k = 1, 2, 3$ .

$u$ -th and  $v$ -th column, since  $H$  is symmetric). It can then be shown that the  $u$ -th and  $v$ -th diagonal elements of any non-negative integer power of  $H$  coincide,

$$[H^k]_{u,u} = [H^k]_{v,v} \quad \forall k \in \mathbb{N}, \quad (1)$$

and that any eigenvector  $\phi$  of  $H$  has—or, if degenerate to another eigenvector, can be chosen to have—positive or negative parity on  $u$  and  $v$  [3], that is,

$$\phi_u = \pm \phi_v. \quad (2)$$

The eigenvector components on the remaining vertices, which are generally not pairwise exchanged by  $P$ , may have arbitrary components. Thus Eq. (2) constitutes a *local* parity of the eigenvectors. This property is intricately related to the interpretation of powers of  $H$  in terms of *walks* [4,3], which are sequences of vertices connected by edges, on the corresponding graph. For an unweighted graph (having  $H_{i,j} \in \{0, 1\}$ ), the element  $[H^k]_{i,j}$  counts all possible walks of length  $k$  from vertex  $i$  to  $j$  on the graph. This is illustrated in Fig. 1 for selected walks of length 1, 2, 3. With this interpretation, Eq. (1)—and thereby also Eq. (2)—hold if the graph has an equal number of “closed” walks starting and ending on  $u$  or  $v$ , for any walk length  $k$ . This is the case, e.g., for vertices 1 and 2 in the graph of Fig. 1. For weighted graphs (having  $H_{i,j} \in \mathbb{R}$ ), the interpretation of matrix powers in terms of walks is modified by weighing the walks accordingly (see below), with all corresponding results staying valid.

Interestingly, and in many cases counterintuitively, the local parity of eigenvectors of a graph, Eq. (2), can be achieved even if  $H$  does not commute with any permutation matrix  $P$ , as long as Eq. (1) is fulfilled. Given this condition, the eigenvalue spectra of the two submatrices  $H \setminus u$  and  $H \setminus v$ , obtained from  $H$  by deleting vertex  $u$  or  $v$  from the graph, respectively, coincide, and  $u$  and  $v$  are said to be *cospectral* [3]. Originating from spectral graph theory [5], the results of the study of cospectral vertices have so far been applied to the field of quantum information and quantum computing, but also—under the term *isospectral vertices*—to chemical graph theory [6–8]. In a very recent work [9], cospectral vertices have also been linked to so-called “isospectral reductions”, a concept which allows to transform a given matrix into a smaller version thereof which shares all (or, in special cases, a subset of) the eigenvalues with the original matrix.

Given a graph with cospectral vertices  $u$  and  $v$ , one may ask what kind of changes can be made to it without breaking the cospectrality. One particularly interesting feature that occurs for some graphs is the presence of so-called *unrestricted substitution points* (USPs), which were introduced in Ref. [8]. Given a graph  $H$  with two cospectral vertices  $u$  and  $v$ , a third vertex  $c$  is an USP if and only if one can attach an arbitrary subgraph to  $c$  without breaking the cospectrality of  $u$  and  $v$ . While it is a straightforward task to identify all USPs of a given graph, the origin of these special points has been elusive so far.

In this work we shed new light on this phenomenon by introducing the concept of *walk equivalence* of cospectral vertices  $u, v$  with respect to a vertex subset of a graph. In the

simplest case of an unweighted graph, two vertices  $u$  and  $v$  are walk equivalent relative to a vertex subset if the cumulative number of walks from  $u$  to this subset equals that from  $v$  to this subset, for any walk length. The vertex subset then corresponds to what we call a *walk multiplet* relative to the pair  $u, v$ . The smallest walk multiplets, which we call singlets, consist of a single vertex and are identified with the above mentioned USPs, and we here demonstrate how to create such points in a systematic way. Specifically, we show that a graph can be extended via any of its walk multiplets by connecting it to a new vertex while preserving the cospectrality of the associated vertex pair. This procedure can be repeated any number of times with different walk multiplets. All the newly added vertices turn out to be USPs, thus allowing us to connect arbitrary new graphs exclusively to them without breaking the cospectrality. Additionally, we show that one can also alter the topology of a graph *without extending it* by modifying the interconnections between two or more walk multiplets. This provides a systematic way to construct graphs with cospectral vertices but no permutation symmetry, based on breaking existing symmetries by walk multiplet-induced modifications. The concept of walk equivalence of vertices is further generalized to the case where walks to different subsets of a walk multiplet can be equipped with different weight parameters.

Apart from providing means to modify a graph without breaking the cospectrality, we show that walk multiplets can be used to obtain a substantial understanding of the structure of eigenvectors of general real symmetric matrices with cospectral pairs. In particular, for a suitably chosen eigenbasis, walk multiplets induce linear scaling relations between eigenvector components on the multiplet vertices, in dependence of the local parity—Eq. (2)—of the eigenvector on the cospectral vertex pair associated with the multiplet. As a special case, the eigenvector components vanish on any walk singlet and, by iteration, on any arbitrary new graph connected exclusively to walk singlets. We believe our work will provide valuable insights into the structure of eigenvectors of generic network-like systems and thereby aid in the design of desired properties.

The paper is structured as follows. In Section 2, we first motivate the concept of walk multiplets as a generalization of USPs, before we define them generally in terms of walks on graphs, and proceed discussing their properties. In Section 3, we show how walk multiplets allow for the modification of graphs without breaking vertex cospectrality. In Section 4, we apply the concept to derive relations between the components of eigenvectors on walk multiplet vertices, with vanishing components on walk singlets as a special case. In Section 5, we use walk multiplets to generate graphs that feature cospectral vertices without having any permutation symmetry. We conclude the work in Section 6. In the Appendix we provide the proofs of all theorems.

## 2. Walk multiplets

As the name suggests, the concept of “walk multiplets,” to be developed below, is based on walks along the vertices of a graph. In particular, as illustrated in Fig. 1, the entries of powers  $H^k$  can be interpreted in terms of walks [4] on the corresponding graph

with  $N$  vertices. Indexing the vertices of the graph by  $v_i \in \llbracket 1, N \rrbracket$ , a walk of length  $k$  from vertex  $v_1$  to vertex  $v_{k+1}$  is a sequence

$$\alpha_k(v_1, v_{k+1}) = (v_1, v_2), (v_2, v_3), \dots, (v_k, v_{k+1}) \quad (3)$$

of  $k$  (possibly repeated) edges  $(v_i, v_{i+1})$  corresponding to nonzero matrix elements  $H_{v_i, v_{i+1}}$ . Note that a diagonal element  $H_{n,n}$  corresponds to a “loop” on vertex  $n$ , that is, an edge connecting  $n$  with itself. If the entries of  $H$  are either 0 or 1, that is, the graph is *unweighted*, then the element  $[H^k]_{m,n}$  equals the number of walks from  $m$  to  $n$  on the graph. We leave it like this for now, but will consider walks on general weighted graphs further below. Throughout this work  $H = H^\top \in \mathbb{R}^{N \times N}$  will denote a real symmetric matrix but also the corresponding graph itself, since there is a one-to-one mapping between them for our purposes.

### 2.1. Unrestricted substitution points: the simplest case of walk multiplets

Let us introduce the idea of walk multiplets, starting with some preliminary considerations by inspecting the example graph in Fig. 2(a), adapted from Ref. [8]. As is common in the field of chemical (or molecular) graph theory, this graph is used as a very simple representation of a molecule, with the vertices being atoms of some kind and the edges between them being atom-atom, i.e. molecular, bonds. For simplicity, we consider all bonds to be of the same unit strength, meaning that all edges have the same weight 1, and all atoms to have zero “onsite potential”, so there are no loops on vertices (like the one on vertex 4 in Fig. 1).

While seeming quite common, this graph has some interesting “hidden” properties. First of all, it has cospectral vertices labeled  $u$  and  $v$ . This cospectrality does not stem, though, from a corresponding exchange symmetry (permuting vertices  $u$  and  $v$  with each other). Indeed, without being symmetric under exchange, the cospectral vertices fulfill Eq. (1), that is, the number of closed walks from  $u$  back to  $u$  and from  $v$  back to  $v$  is the same, for any walk length  $k$ . Notably, cospectral vertices go under the name “isospectral points” in molecular graph theory.

A second interesting property of the graph in Fig. 2 is that it has some special vertices, labeled  $c$  and  $r$ , called “unrestricted substitution points” (USPs) [6,8], which were already mentioned in Section 1. Those are vertices to which new vertices or subgraphs may be attached, or which may even be removed completely, without breaking the cospectrality of  $u$  and  $v$ . This is done in Fig. 2(b). Now, let us approach this in terms of walks, and focus on the vertex  $c$  of the example for concreteness. Cospectrality of  $u, v$  is preserved when connecting  $c$  to the arbitrary new graph  $C$ , meaning that the number of closed walks from  $u$  and  $v$  is the same for any walk length also after this modification. All additionally created closed walks from  $u$  or  $v$  which visit the arbitrary subgraph  $C$ , however, necessarily traverse the USP  $c$  on the way. This suggests that the number of walks from  $u$  to  $c$  is the same as from  $v$  to  $c$ , for any walk length—because the possible

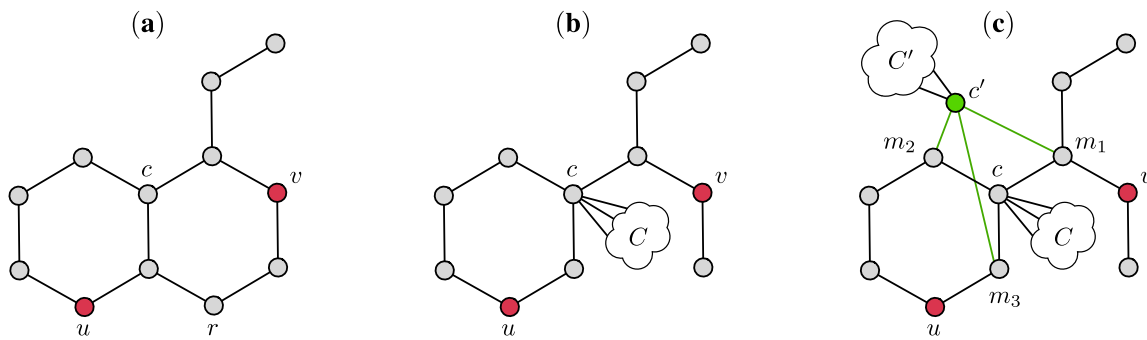


**Fig. 2.** (a) A molecular graph, taken from Ref. [8], which has two cospectral vertices  $u, v$  and two “unrestricted substitution points” (USPs)  $c, r$ . (b) The USPs are vertices which can be connected to any arbitrary graph  $C$  (as done with  $c$ ) or also removed from the graph (as done with  $r$ ), without breaking the cospectrality of  $u, v$ . (c) In the present work we generalize USPs to vertex subsets called “walk multiplets”, an example here being the subset  $\mathbb{M} = \{m_1, m_2, m_3\}$ . We can connect this subset to a new vertex  $c'$ , which we can in turn connect to an arbitrary graph  $C'$ , without breaking the cospectrality of  $u, v$ . The added vertex  $c'$  is a walk “singlet”, which is identified as an USP.

walk segments within  $C$  are evidently the same for walks from  $u$  and from  $v$ . Indeed, this turns out to be exactly the case: A vertex  $c$  of a graph  $H$  with cospectral vertices  $u, v$  is an USP if and only if it fulfills  $[H^\ell]_{u,c} = [H^\ell]_{v,c}$  for any non-negative integer  $\ell$ .

While already offering a great flexibility, USPs do not necessarily occur in all graphs with cospectral pairs. This leads to the question: Are there other possibilities of graph extensions, involving a *set of points* instead of just a single point to which one can connect an arbitrary graph? Imagine, for example, a subset  $\mathbb{M}$  of some graph’s vertex set to which some arbitrary new graph  $C'$  can be connected, by connecting an arbitrary single vertex  $c'$  of  $C'$  to all vertices in  $\mathbb{M}$ , without breaking the cospectrality between two vertices  $u, v$  of the original graph. Such a subset  $\mathbb{M}$ , associated in this way with a cospectral vertex pair, corresponds to what we will call a “walk multiplet” relative to  $u, v$ . An example is illustrated in Fig. 2(c). The key property, in analogy to USPs, is that the cumulative number of walks from  $u$  to all vertices in  $\mathbb{M}$  is the same as from  $v$  to  $\mathbb{M}$ . An USP is then just the simplest case of a walk multiplet consisting of a single vertex, a walk “singlet”.

Below, we will formalize the concept of walk multiplets and describe the various flavors they can assume in general undirected and real-weighted graphs, which correspond to real symmetric matrices. Their value in extending graphs with cospectral vertices will be shown subsequently in Section 3, and their significance for graph eigenvectors will be demonstrated in Section 4. First, we introduce some helpful key notions in the description of walks.

## 2.2. Weighted walks and walk matrices

Let us first extend the correspondence between walks on a graph, defined in Eq. (3), and powers of its matrix  $H$  to a weighted graph, where the entries of  $H$  are arbitrary real numbers. Any walk  $\alpha_k$  from  $v_1$  to  $v_{k+1}$  is then given a weight  $w(\alpha_k)$  equal to



the product of the edge weights  $w(v_i, v_{i+1}) = H_{v_i, v_{i+1}}$  of all edges traversed [10], that is,

$$w(\alpha_k(v_1, v_{k+1})) = w(v_1, v_2)w(v_2, v_3) \cdots w(v_k, v_{k+1}) = \prod_{i=1}^k [H]_{v_i, v_{i+1}}. \tag{4}$$

The entries  $[H^k]_{m,n}$  are then given by the sum over weighted walks as [10]

$$[H^k]_{m,n} = \sum_{\alpha_k} w(\alpha_k(m, n)) \tag{5}$$

where the sum runs over all distinct walks of length  $k$  from  $m$  to  $n$ .

Consider, now, a subset  $\mathbb{M} \subseteq \mathbb{V}$  of the set  $\mathbb{V}$  of the vertices of a graph  $H$ . The *walk matrix* of  $H$  relative to  $\mathbb{M}$  is the matrix [11]  $W_{\mathbb{M}} = [e_{\mathbb{M}}, He_{\mathbb{M}}, \dots, H^{N-1}e_{\mathbb{M}}]$ , whose  $k$ -th column equals the action of  $H^{k-1}$  on the so called *indicator* (or *characteristic*) vector  $e_{\mathbb{M}}$  of  $\mathbb{M}$  with  $[e_{\mathbb{M}}]_m = 1$  for  $m \in \mathbb{M}$  and 0 otherwise. Thus, the element

$$[W_{\mathbb{M}}]_{s,\ell} = \sum_{m \in \mathbb{M}} [H^{\ell-1}]_{s,m} \tag{6}$$

equals the sum over weighted walks [in the sense of Eq. (5)] of length  $\ell - 1 \in \llbracket 0, N - 1 \rrbracket$  from vertex  $s$  to all vertices of  $\mathbb{M}$ .

Below we will use this notion of collective walks to vertex subsets to identify structural properties of graphs and their eigenvectors. It will then be convenient, however, to account also for the case where the walks to different vertices  $m \in \mathbb{M}$ , represented by  $[H^k]_{s,m}$ , are multiplied by some (generally different) factors  $\gamma_m$ . Treating  $W_{\mathbb{M}}$  as the Krylov matrix [12] of  $H$  generated by  $e_{\mathbb{M}}$ , we thus simply replace this generating vector with a *weighted indicator vector*  $e_{\mathbb{M}}^{\gamma}$  having a tuple  $\gamma = (\gamma_m)_{m \in \mathbb{M}}$  of general real values  $\gamma_m$  instead of 1's in its nonzero entries  $m \in \mathbb{M}$ . This extends the common walk matrix to a corresponding “weighted” version which we denote as  $W_{\mathbb{M}}^{\gamma}$ , that is

$$W_{\mathbb{M}}^{\gamma} = [e_{\mathbb{M}}^{\gamma}, He_{\mathbb{M}}^{\gamma}, \dots, H^{N-1}e_{\mathbb{M}}^{\gamma}], \quad \gamma = (\gamma_m)_{m \in \mathbb{M}}, \quad [e_{\mathbb{M}}^{\gamma}]_m = \begin{cases} \gamma_m, & m \in \mathbb{M}, \\ 0, & m \notin \mathbb{M}. \end{cases} \tag{7}$$

For this weighted walk matrix, Eq. (6) is accordingly modified to the more general form

$$[W_{\mathbb{M}}^{\gamma}]_{s,\ell} = \sum_{m \in \mathbb{M}} \gamma_m [H^{\ell-1}]_{s,m}, \quad \ell \in \llbracket 1, N \rrbracket, \tag{8}$$

so that the interpretation of matrix powers in terms of walks is further equipped with weights  $\gamma_m$  for the individual walk destinations  $m$ .

2.3. Walk equivalence of cospectral vertices

Combining the intuition of equal number of walks to vertex subsets in Section 2.1 with the notion of weighted walk matrices in Section 2.2, it now comes natural to define the general case of a walk multiplet. We will then discuss examples of walk multiplets before analyzing their consequences in the next sections.

**Definition 1** (*Walk multiplet*). Let  $H \in \mathbb{R}^{N \times N}$  be a matrix with vertex set  $\mathbb{V}$  and walk matrix  $W_{\mathbb{M}}^\gamma$  relative to a subset  $\mathbb{M} \subseteq \mathbb{V}$  with weighted indicator vector  $e_{\mathbb{M}}^\gamma$  corresponding to the tuple  $\gamma = (\gamma_m)_{m \in \mathbb{M}}$ . If the  $u$ -th and  $v$ -th rows of  $W_{\mathbb{M}}^\gamma$  fulfill

$$[W_{\mathbb{M}}^\gamma]_{u,*} = p[W_{\mathbb{M}}^\gamma]_{v,*} \tag{9}$$

(with  $*$  denoting the range  $\llbracket 1, N \rrbracket$ , i.e. all matrix columns), then  $\mathbb{M}$  corresponds to an **even (odd) walk multiplet** with **parity**  $p = +1$  ( $-1$ ) relative to the two vertices  $u, v$ , denoted as  $\mathbb{M}_{\gamma;u,v}^p$ , and  $u, v$  are **walk equivalent (antiequivalent)** with respect to  $\mathbb{M}_{\gamma;u,v}^p$ .

A walk multiplet  $\mathbb{M}_{\gamma;u,v}^p$  is thus not merely a subset  $\mathbb{M}$ , but this subset equipped with a  $|\mathbb{M}|$ -tuple of weight parameters  $\gamma$  and a parity  $p$ , associated with a given vertex pair  $u, v$ . If all weights  $\gamma_m$  are equal, then  $\mathbb{M}_{\gamma;u,v}^p$  is a *uniform* walk multiplet, and we will first discuss such multiplets. In this case the common weight is obviously a global scaling factor in Eq. (9) and can be set to unity without loss of generality,  $\gamma_m = 1$  for all  $m \in \mathbb{M}$ . We will show cases of *nonuniform* walk multiplets (with unequal  $\gamma_m$  in general) afterwards. Although walk multiplets are generally defined above relative to any pair of vertices  $u, v$ , we will concentrate on multiplets relative to cospectral vertices  $u, v$  from now on. Also, for brevity, we will drop the indication of vertices  $u, v$  in the subscript of  $\mathbb{M}_{\gamma;u,v}^p$  when they are clear from the context. According to their cardinality (the number  $|\mathbb{M}|$  of vertices in  $\mathbb{M}$ ) we call multiplets “singlets”, “doublets”, etc. Note that the same subset  $\mathbb{M}$  can in general correspond simultaneously to different walk multiplets relative to different cospectral vertex pairs or with different tuples  $\gamma$ . We should also point out that the notion of “walk equivalence” of two *graphs* as a whole has been used [13,14], and stress that we here introduce the notion of walk equivalence of two *vertices* with respect to a vertex subset.

Before showing examples of walk multiplets, we note that the condition (9) only incorporates walks of length  $k \in \llbracket 0, N - 1 \rrbracket$  from  $u$  and from  $v$  to  $\mathbb{M}$ ; see Eq. (8). At first sight one might then wonder whether the sum over longer walks ( $k \geq N$ ) to  $\mathbb{M}$  is also equal for  $u$  and  $v$ . This is indeed the case. Due to the Cayley-Hamilton theorem, we have that  $H^N = \sum_{k=0}^{N-1} c_k H^k$  with constant coefficients  $c_k$ , meaning that higher powers  $k > N - 1$  of  $H$  can be written as polynomials in  $H$  of order up to  $N - 1$ . Thus, if Eq. (9) holds, we have that

$$\sum_{m \in \mathbb{M}} \gamma_m [H^k]_{u,m} = p \sum_{m \in \mathbb{M}} \gamma_m [H^k]_{v,m} \quad \forall k \in \mathbb{N}. \tag{10}$$

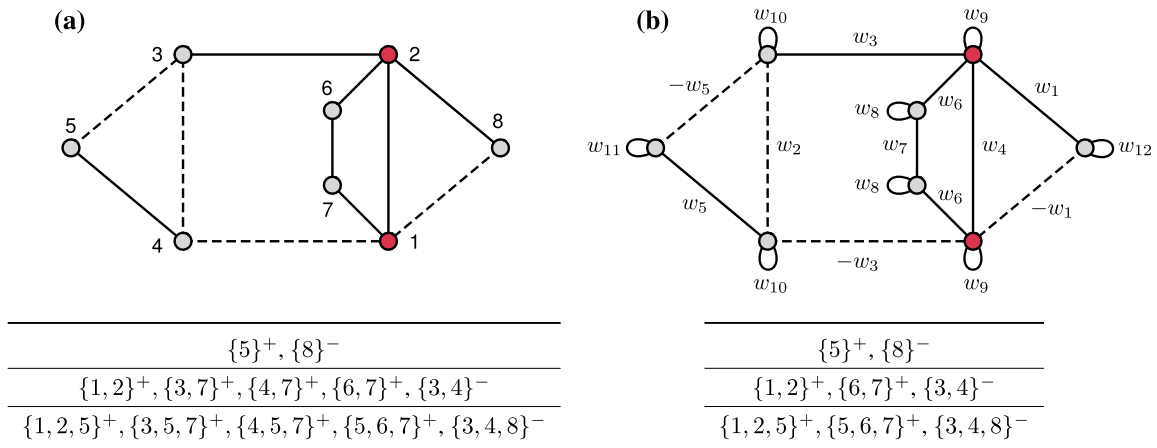


**Fig. 3.** (a) A graph with edge weights +1 (solid lines) and -1 (dashed lines) in which the two vertices 1 and 2 are cospectral (among other cospectral pairs) and (b) the same graph with edges weighted by 12 real parameters  $w_n$  as shown, preserving the cospectrality of  $\{1, 2\}$ . The tables below list all uniform walk singlets, doublets, and triplets (top to bottom) relative to  $\{1, 2\}$ , with superscripts indicating the parity  $p$  of each multiplet; see Example 1.

For an unweighted graph, the notion of walk equivalence of  $u$  and  $v$  with respect to  $\mathbb{M}$  then acquires a simple interpretation: An even uniform walk multiplet ( $\gamma_m = 1$  for all  $m \in \mathbb{M}$ ) corresponds to a vertex subset  $\mathbb{M}$  such that the number of walks from  $u$  to  $\mathbb{M}$  equals the number of walks from  $v$  to  $\mathbb{M}$  (that is, summed over all  $m \in \mathbb{M}$ ) for any walk length  $k$ . Let us now have a look at some uniform walk multiplets in an example graph.

**Example 1.** In the graph depicted in Fig. 3(a), the two vertices  $u = 1, v = 2$  are cospectral. All uniform walk singlets, doublets, and triplets of  $H$  with respect to 1, 2 are given in the table below. We put a superscript  $+(-)$  on each individual multiplet subset to indicate its even (odd) parity  $p$ . Importantly, the vertex cospectrality and multiplet structure of a graph are in general not strictly bound to a specific set of edge weight values. Indeed, one may generally “parametrize” the edge weights, by setting groups of them to the same but arbitrary real value, and still retain the graph’s vertex cospectrality as well as a subset of its walk multiplets. To demonstrate such a parametrization, in Fig. 3(b) the graph of Fig. 3(a) has been weighted by arbitrary real parameters  $w_n$  ( $n = 1, 2, \dots, 12$ ) as shown. The uniform multiplets shown in the table below the graph are present for any choice of the weight parameters  $w_n$ , as does the cospectrality of 1, 2. Note, however, that certain uniform multiplets of the original graph are removed in the parametrized one for arbitrary values  $w_n$  (that is, if there are no further constraints on these values); for example,  $\{3, 7\}^+$  and  $\{4, 7\}^+$ . Other cospectrality-preserving edge weight parameterizations (not shown) may keep different sets of multiplets intact. We note here that the graphs in Fig. 3 were chosen to have a simple geometry to highlight the occurrence of even and odd walk multiplets. Indeed, in this particular case the graph’s matrix  $H$  (for both subfigures of Fig. 3) commutes with the signed permutation

$$H = \begin{bmatrix} 0 & 1 \\ 1 & 0 \end{bmatrix} \oplus \begin{bmatrix} 0 & -1 \\ -1 & 0 \end{bmatrix} \oplus 1 \oplus \begin{bmatrix} 0 & 1 \\ 1 & 0 \end{bmatrix} \oplus -1 \tag{11}$$

with  $\Pi^2 = I$ . This symmetry induces some of the present walk multiplets, e.g. the anti-doublet  $\{3,4\}^-$  relative to  $\{1,2\}$ , since  $[H^k]_{1,3} + [H^k]_{1,4} = [\Pi^2 H^k]_{1,3} + [\Pi^2 H^k]_{1,4} = [\Pi H^k \Pi]_{1,3} + [\Pi H^k \Pi]_{1,4} = -[H^k]_{2,4} - [H^k]_{2,3}$ . In fact, all walk multiplets which are retained after the parametrization in Fig. 3(b) can be seen as a consequence of this symmetry. The remaining ones, that is,  $\{3,7\}^+, \{4,7\}^+, \{3,5,7\}^+, \{4,5,7\}^+$  in Fig. 3(a), cannot be explained by this simple symmetry but rather by a symmetry of the graph’s walk structure—specifically, under row permutation on the graph’s walk matrix, see Eq. (9).

Surely, the graph in Example 1 also features a whole lot of nonuniform multiplets, but we do not show them for simplicity. We have another example dedicated to nonuniform multiplets right below. Apart from that, though, the reader might have noticed that the cospectral pair  $\{1,2\}$  in Fig. 3 itself is included in the list of uniform walk multiplets. This is not a coincidence for this particular graph.

**Remark 1.** A cospectral vertex pair  $\{u, v\}$  is a uniform even walk doublet relative to itself, since  $[H^k]_{u,u} + [H^k]_{u,v} = [H^k]_{v,v} + [H^k]_{v,u}$ , with  $[H^k]_{u,u} = [H^k]_{v,v}$  by Eq. (1) and  $[H^k]_{u,v} = [H^k]_{v,u}$  by the symmetry of  $H = H^T$ . Thus Eq. (10) is fulfilled with  $\mathbb{M} = \{u, v\}$  and  $p = +1$ .

In the next example, we will illustrate the occurrence of nonuniform walk multiplets, where the walks to different destinations  $m$  in the associated subset  $\mathbb{M}$  are *generally weighted differently* by weights  $\gamma_m$ . Usually, however, those weights  $\gamma_m$  are not *all* different from each other, but can be partitioned into groups of equal values. We call the vertex subset of a multiplet with such equal values in the tuple  $\gamma = (\gamma_m)_{m \in \mathbb{M}}$  a *sublet* of the multiplet. In other words, given a nonuniform walk multiplet  $\mathbb{M}_\gamma^p$ , the subset  $\mathbb{M}$  is the union of  $N_s = N_s(\gamma) \leq |\mathbb{M}|$  disjoint sublets  $\mathfrak{m}_\mu$ , that is,

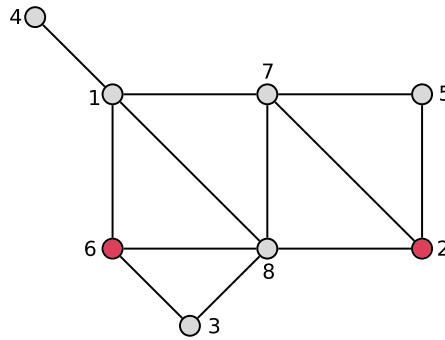
$$\mathbb{M} = \bigcup_{\mu=1}^{N_s} \mathfrak{m}_\mu, \quad \mathfrak{m}_\mu \cap \mathfrak{m}_\nu = \emptyset \quad \forall \mu \neq \nu, \quad \gamma_{m \in \mathfrak{m}_\mu} = \Gamma_\mu \tag{12}$$

such that all weights  $\gamma_m$  with  $m \in \mathfrak{m}_\mu$  have equal value  $\Gamma_\mu$  which we call the “coefficient” of the sublet  $\mathfrak{m}_\mu$ . The expanded form of the multiplet condition, Eq. (10), then becomes

$$\sum_{\mu} \Gamma_\mu \sum_{m \in \mathfrak{m}_\mu} [H^k]_{u,m} = p \sum_{\mu} \Gamma_\mu \sum_{m \in \mathfrak{m}_\mu} [H^k]_{v,m} \quad \forall k \in \mathbb{N}. \tag{13}$$

We indicate the coefficients  $\Gamma_\mu$  as subscripts of vertex sublets within a walk multiplet, as shown in the following example.

**Example 2.** The graph in Fig. 4 has two cospectral vertices  $u = 2$  and  $v = 6$ , with walk multiplets shown in the table for a maximum number of 4 vertices (there are no singlets). As an example of notation, the even nonuniform walk triplet  $\mathbb{M}_\gamma^p = \{(1,5)_a, (4)_{2a}\}^+$




---


$$\{(2, 6)_a\}^+, \{(3, 7)_a\}^+, \{(4)_a, (8)_{-a}\}^+, \{(2)_{-a}, (6)_a\}^-$$


---


$$\{(1, 4)_a, (3)_{-a}\}^+, \{(1)_a, (3)_{-2a}, (5)_{-a}\}^+, \{(1, 8)_a, (3)_{-a}\}^+, \{(1, 5)_a, (4)_{2a}\}^+, \{(1, 4, 7)_a\}^+, \{(1)_a, (5)_{-a}, (7)_{2a}\}^+,$$

$$\{(1, 5)_a, (8)_{2a}\}^+, \{(1, 7, 8)_a\}^+, \{(3, 4, 5)_a\}^+, \{(3, 5, 8)_a\}^+, \{(4, 5)_a, (7)_{-a}\}^+, \{(5, 8)_a, (7)_{-a}\}^+$$


---


$$\{(1)_a, (3)_b, (4)_{2a+b}, (5)_{a+b}\}^+, \{(1, 4)_a, (3)_b, (7)_{a+b}\}^+, \{(1)_a, (3)_{-a}, (4)_b, (8)_{a-b}\}^+, \{(1)_a, (3)_b, (5)_{-a}, (7)_{2a+b}\}^+,$$

$$\{(1)_a, (3)_b, (5)_{a+b}, (8)_{2a+b}\}^+, \{(1, 8)_a, (3)_b, (7)_{a+b}\}^+, \{(1)_a, (4)_b, (5)_{-a+b}, (7)_{2a-b}\}^+, \{(1, 5)_a, (4)_b, (8)_{2a-b}\}^+,$$

$$\{(1, 7)_a, (4)_b, (8)_{a-b}\}^+, \{(1)_a, (5)_b, (7)_{a-b}, (8)_{a+b}\}^+, \{(2, 6)_a, (3, 7)_b\}^+, \{(2, 6)_a, (4)_b, (8)_{-b}\}^+,$$

$$\{(3)_a, (4, 5)_b, (7)_{a-b}\}^+, \{(3, 5)_a, (4)_b, (8)_{a-b}\}^+, \{(3, 7)_a, (4)_b, (8)_{-b}\}^+, \{(3)_a, (5, 8)_b, (7)_{a-b}\}^+,$$

$$\{(4)_a, (5)_b, (7)_{-b}, (8)_{-a+b}\}^+, \{(1, 3)_a, (5, 7)_{-a}\}^-, \{(1, 5)_a, (4, 8)_{-a}\}^-$$


---

**Fig. 4.** An unweighted graph with two cospectral vertices 2, 6, with all existing walk multiplets up to maximal size of four vertices listed in the table below the graph (there are no walk singlets). Each walk multiplet  $\{\dots\}^\pm$  is composed of sublets  $(\dots)_{\Gamma_\mu}$  with coefficients  $\Gamma_\mu \in \mathbb{R}$  which are independent among multiplets (although the same symbols  $a, b$  are used for brevity); see Example 2.

(with  $\gamma = (\gamma_1, \gamma_4, \gamma_5) = (a, 2a, a)$ ) is composed of the sublets  $m_1 = \{1, 5\}$  and  $m_2 = \{4\}$  with coefficients  $\Gamma_1 = a$  and  $\Gamma_2 = 2a$ , respectively, where the parameter  $a$  can take any nonzero value. Note that the values of sublet coefficients (like  $a, b$  in Fig. 4) in different multiplets are *unrelated*. For instance,  $\{(4)_a, (8)_{-a}\}^+$  is an even doublet composed of sublets  $\{4\}$  and  $\{8\}$  with coefficients  $a$  and  $-a$ , independently of the values of  $a$  in the other multiplets in Fig. 4. Similarly,  $\{(1)_a, (3)_b, (4)_{2a+b}, (5)_{a+b}\}^+$  is an even quadruplet composed of the four sublets  $\{1\}, \{3\}, \{4\}, \{5\}$  with corresponding nonzero coefficients  $a, b, 2a + b, a + b$ . If, however, any  $n > 0$  of these coefficients vanish, then the remaining  $4 - n$  sublets with nonzero coefficients constitute a multiplet with  $4 - n$  vertices. For example, if  $b = -a$ , the coefficient of  $\{5\}$  vanishes, and the remaining three sublets form the triplet  $\{(1, 4)_a, (3)_{-a}\}^+$ . Finally, note that any uniform multiplet consists of a single sublet, like, e.g.,  $\{(1, 4, 7)_a\}^+$ . As one can see, the number of nonuniform multiplets is much larger than the number of uniform ones in the present example.

Now, going back to Fig. 3, a closer look at the table there suggests that the union of multiplets of same parity  $p$  form a multiplet; for instance,  $\{8\}^- \cup \{3, 4\}^- = \{3, 4, 8\}^-$ . Indeed, the union of disjoint uniform multiplets of equal parity always forms a new uniform multiplet. In fact, different uniform multiplets may also overlap (that is, have common vertices), and their union is again a multiplet, though a *nonuniform* one. Take, e.g., the three uniform even multiplets  $\{(3, 7)_a\}^+, \{(4, 7)_b\}^+, \{(5)_{a'}\}^+$ , now written with

arbitrary uniform weights  $a, b, a'$ , respectively. Their union forms the nonuniform even multiplet  $\{(3)_a, (4)_b, (5)_{a'}, (7)_{a+b}\}^+$  consisting of four sublets with coefficients  $\Gamma_{1,2,3,4} = a, b, a', a+b$ . Quite generally, any two walk multiplets of equal parity can be merged into a larger multiplet, as expressed by the following remark.

**Remark 2.** It is clear from Eq. (9) that, if  $\mathbb{A}_\gamma^p$  and  $\mathbb{B}_\delta^p$  are two even (odd) walk multiplets with weighted indicator vectors  $e_{\mathbb{A}}^\gamma$  and  $e_{\mathbb{B}}^\delta$ , respectively, then  $\mathbb{C}_\epsilon^p$  with  $\mathbb{C} = \mathbb{A} \cup \mathbb{B}$  is also an even (odd) multiplet with weighted indicator vector  $e_{\mathbb{C}}^\epsilon = e_{\mathbb{A}}^\gamma + e_{\mathbb{B}}^\delta$ .

Note, however, that not all nonuniform multiplets can be decomposed as a union of uniform multiplets. This is easily verified from the table of Fig. 4. For example, the even nonuniform walk quadruplet  $\{(2, 6)_a, (3, 7)_b\}^+$  is the union of the two even uniform doublets  $\{(2, 6)_a\}^+$  and  $\{(3, 7)_b\}^+$ , but none of the walk triplets can be decomposed into smaller multiplets (that is, a doublet and a singlet or two overlapping doublets). On the other hand, the nonuniform quadruplet  $\{(1)_a, (3)_{-a}, (4)_b, (8)_{a-b}\}^+$  is composed of the nonuniform triplet  $\{(1, 4)_a, (3)_{-a}\}$  and doublet  $\{(4)_{a'}, (8)_{-a'}\}$  with  $a' \equiv b - a$ .

### 3. Preserving vertex cospectrality via walk multiplets

Walk multiplets are very valuable for the analysis and understanding of matrices with cospectral vertices  $u$  and  $v$ . As we will show, once (one or more of) the walk multiplets of  $H$  relative to  $u$  and  $v$  are known, one can use this knowledge to *extend* a graph  $H$  by connecting a new vertex (or even arbitrary graphs) to it whilst preserving the cospectrality of  $u$  and  $v$ . This naturally generalizes the notion of USPs to subsets of more than one vertex of a graph. We will also show how to *interconnect* walk multiplets, thereby changing the topology of a given graph, while preserving the associated vertex cospectrality.

In the literature [11], connecting a single vertex to a graph  $H$  via multiple edges of weight 1 results in a graph  $H'$  which is coined a “cone” of  $H$ . To treat general weighted graphs, we will here require cones with weighted edges:

**Definition 2 (Weighted cone).** Let  $G \in \mathbb{R}^{N \times N}$  represent a graph with vertex set  $\mathbb{V} = \{1, 2, \dots, N\}$ . A **weighted cone** of  $G$  over a subset  $\mathbb{M} \subseteq \mathbb{V}$  with weight tuple  $\gamma = (\gamma_m)_{m \in \mathbb{M}}$  is the graph

$$H = \begin{bmatrix} G & e_{\mathbb{M}}^\gamma \\ e_{\mathbb{M}}^{\gamma^\top} & 0 \end{bmatrix}, \tag{14}$$

constructed by connecting a new vertex  $c = N + 1$  (the **tip** of the cone) to  $\mathbb{M}$  with edges of weights  $\gamma_m = H_{m,c} = H_{c,m}$  to the corresponding vertices  $m \in \mathbb{M}$ , where  $e_{\mathbb{M}}^\gamma$  is the weighted indicator vector of Eq. (7) with nonzero entries  $\gamma_m$ .

For instance, the graph in Fig. 3(a) is the weighted cone  $H$  over the vertex subset  $\{1, 2\}$  of the graph  $H \setminus 8$  ( $H$  after removing vertex 8) with weight tuple  $\gamma = (\gamma_1, \gamma_2) = (-1, 1)$ . We can now state one of the main results of this work, which will allow for the systematic extension of graphs with cospectral pairs while keeping the cospectrality:

**Theorem 1** (*Walk singlet extension*). *Let  $G = G^\top \in \mathbb{R}^{N \times N}$  represent an undirected graph with two cospectral vertices  $u, v$ , let  $\mathbb{M}_\gamma^p$  be an even (odd) walk multiplet of  $G$  relative to  $u, v$ , and let  $H$  be a weighted cone of  $G$  over the subset  $\mathbb{M}$  with real weight tuple  $\gamma = (\gamma_m)_{m \in \mathbb{M}}$ . Then*

- (i) *Vertices  $u, v$  are cospectral in  $H$ .*
- (ii) *The tip  $c$  of the cone  $H$  is an even (odd) walk singlet relative to  $u, v$ .*
- (iii) *Any even (odd) walk multiplet in  $G$  is an even (odd) walk multiplet in  $H$ .*

Point (i) of the theorem extends the notion of USPs to vertex subsets for the case of a single new connected vertex  $c$ : the vertex  $c$  is now connected to a subset  $\mathbb{M}$  instead of a single USP of a graph without breaking the associated vertex cospectrality. Further, by point (ii) of the theorem, another new vertex  $c'$  can be connected to  $c$  while preserving cospectrality, just as would be the case if  $c$  were a USP. Point (iii) finally allows *multiple* single new vertices to be connected to different walk multiplets, or to the same walk multiplet. In the case of a USP, however, cospectrality is preserved when connecting a new *arbitrary graph* to the USP, and not only a single new vertex. This is indeed also the case for a walk singlet.

**Corollary 1.** *Let the vertex  $c$  of a graph  $H$  be an even (odd) walk singlet relative to a cospectral pair  $u, v$  in  $H$ , and let  $C$  be a graph connected exclusively to  $c$  via any number of edges with arbitrary weights. Then all vertices of  $C$  are even (odd) walk singlets relative to  $u, v$ .*

We thus see that any walk singlet is a USP, and below (Corollary 3) we will also show that the reverse is true. Now, suppose we have connected some walk singlets to corresponding new subgraphs  $C, C', \dots$ , which then also consist purely of singlets. Those subgraphs may also be *interconnected* among each other in an arbitrary manner, by iteratively interconnecting pairs of singlets, leaving the associated cospectrality intact. In fact, vertex interconnections preserving cospectrality can be generalized to the suitable interconnection of *arbitrary walk multiplets of equal parity*, as ensured by the following theorem.

**Theorem 2** (*Walk multiplet interconnection*). *Let  $G \in \mathbb{R}^{N \times N}$  be a graph with a cospectral pair  $\{u, v\}$  and  $\mathbb{X}_\gamma^p, \mathbb{Y}_\delta^p$  be (in general non-uniform) walk multiplets relative to  $\{u, v\}$  having same parity  $p$  and weight tuples  $\gamma, \delta$ , respectively, with possible subset overlap  $\mathbb{Z} = \mathbb{X} \cap \mathbb{Y} \neq \emptyset$ . Then the cospectrality of  $\{u, v\}$  and any walk multiplet relative to  $\{u, v\}$  with parity  $p$  are preserved in the graph  $H \in \mathbb{R}^{N \times N}$  with elements*

$$H_{x,y} = H_{y,x} = \begin{cases} G_{x,y} + \gamma_x \delta_y & \text{if } x \notin \mathbb{Z} \text{ or } y \notin \mathbb{Z} \\ G_{x,y} + \gamma_x \delta_y + \gamma_y \delta_x & \text{if } x, y \in \mathbb{Z} \end{cases} \quad \forall x \in \mathbb{X}, y \in \mathbb{Y}$$

and  $H_{i,j} = G_{i,j}$  otherwise.

The above theorem, in contrast to the extension of a graph by external vertices in Theorem 1, allows for the internal modification of the graph itself while keeping the cospectrality of a given vertex pair. In particular, the *topology* of the graph may be changed by adding new edges or deleting existing ones. Before showing examples using Theorems 1 and 2, let us also note the following.

**Remark 3.** By Theorem 2, one can interconnect a cospectral pair  $\{u, v\}$  (which corresponds to a walk doublet relative to itself) to itself by setting  $\mathbb{X} = \mathbb{Y} = \{u, v\}$  and adding an edge between  $u, v$  as well as loops on  $u, v$ , all of equal arbitrary weight (added to possible existing edges), while keeping their cospectrality. Then, by Lemma 3.1 of Ref. [15], those loops can be removed, with  $u, v$  still remaining cospectral. In other words, two cospectral vertices  $u, v$  of a graph can be interconnected or disconnected without affecting their cospectrality.

To show Theorems 1 and 2 in action, we will now apply them to the example graphs in Fig. 3(a) and Fig. 4 of the previous section, whose walk multiplet structure has already been analyzed. With the first example, we showcase the cospectrality-preserving extension of a graph; via a uniform walk multiplet, via a combination of overlapping uniform multiplets, and finally by connecting another arbitrary graph to it.

**Example 3.** In Fig. 5(a) we have modified the graph of Fig. 3(a) by connecting a new vertex  $c = 9$  to the even uniform walk doublet  $\{3, 7\}^+$  relative to the cospectral pair  $\{1, 2\}$  with weight  $a$ . In the terminology of Theorem 1, this new graph is the cone  $H$  of the graph in Fig. 3(a),  $G$ , over the subset  $\mathbb{M} = \{3, 7\}$  with a weight tuple  $\gamma = (\gamma_3, \gamma_7) = (a, a)$ . By Theorem 1, vertex  $c$  then forms an even singlet and all even multiplets of the graph  $G$  in Fig. 3(a) are still present in the new graph of Fig. 5(a), as confirmed in the table at the bottom of the figure. Now, in Fig. 5(b) we further connect  $c$  to other vertices in  $H$ , without breaking the cospectrality of  $\{1, 2\}$  or its walk equivalence to any even multiplet. Indeed, by Theorem 2, vertex  $c$  can be connected to the even singlet  $\{5\}^+$  with some weight  $a'$ . We can—again by Theorem 2—additionally connect  $c$ , with weight  $b$ , to the even uniform doublet  $\{4, 7\}^+$  which *overlaps* with the already connected one  $\{3, 7\}^+$ . As a result, the edge  $(c, 7)$  now has weight  $a + b$ . Of course, these successive connections amount to the final graph simply being the weighted cone of the initial one with tip  $c$  over  $\{3, 4, 5, 7\}$  with weight tuple  $\gamma = (\gamma_3, \gamma_4, \gamma_5, \gamma_7) = (a, b, a', a + b)$ . Thus,  $\{(3)_a, (4)_b, (5)_{a'}, (7)_{a+b}\}^+$  is an even nonuniform walk quadruplet; see Remark 2. In Fig. 5(c) we make use of Corollary 1 and connect a whole graph  $C$ , represented by a cloud since it can be just any graph, to the even singlet  $c$  via any number of



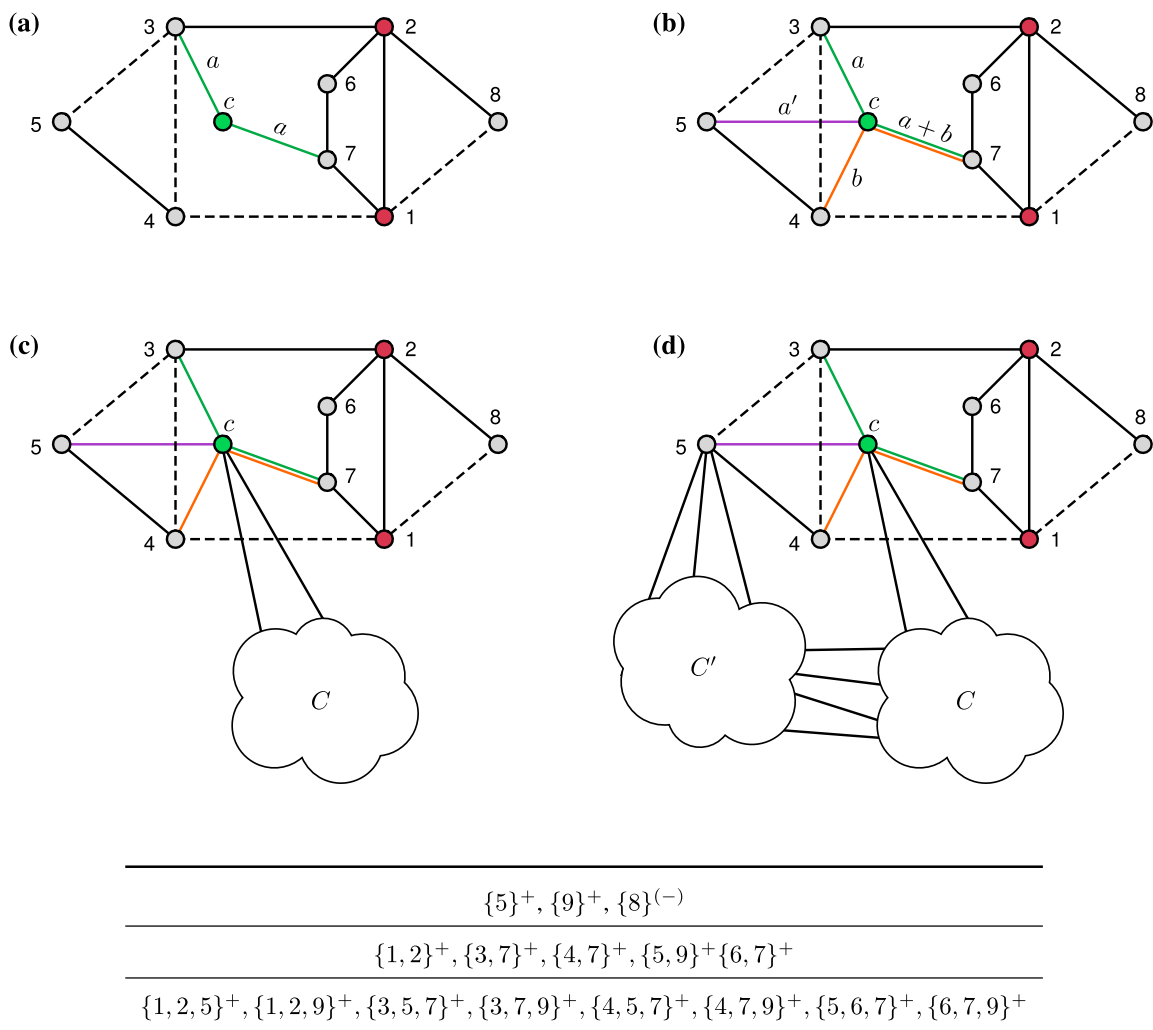


**Fig. 5.** Extension of a graph via walk multiplets, using Corollary 1 and Theorem 2; see Example 3 for details. The graph of Fig. 3(a) is successively extended by (a) connecting a new vertex  $c = 9$  symmetrically to the even uniform walk doublet  $\{3, 7\}^+$  relative to the cospectral pair  $\{1, 2\}$  with weight  $a$ , (b) further connecting  $c$  to the even singlet  $\{5\}^+$  with weight  $a'$  and to the even uniform doublet  $\{4, 7\}^+$  with weight  $b$ , (c) connecting an arbitrary graph  $C$  (cloud) to the even walk singlet  $c$  via any number of edges with arbitrary weights, and (d) connecting another graph  $C'$  to the even walk singlet  $\{5\}^+$  and then  $C'$  to  $C$  in an arbitrary manner, forming a larger arbitrary graph connected to vertices 5 and  $c$ . In all steps, the cospectrality of  $\{1, 2\}$  as well as the uniform walk multiplets listed in the table below (for up to cardinality 3) are preserved. The graph in (b) is the “weighted cone” of the graph in Fig. 3(a) over subset  $\{3, 4, 5, 7\}$  with weight tuple  $\gamma = (\gamma_3, \gamma_4, \gamma_5, \gamma_7) = (a, b, a', a + b)$ . Also,  $\{(3)_a, (4)_b, (5)_{a'}, (7)_{a+b}\}^+$  is an even nonuniform walk quadruplet relative to  $\{1, 2\}$  with the same weight tuple  $\gamma$ .

edges with arbitrary weights—again preserving cospectrality and walk equivalence of  $\{1, 2\}$ . In Fig. 5(d), we have connected another cloud graph  $C'$  to the walk singlet  $\{5\}^+$ . This latter cloud  $C'$  can finally be connected—by Theorem 2—in any arbitrary way to  $C$  into a larger cloud graph, since both  $\{5\}^+$  and  $\{c\}^+$  are even singlets (as are all cloud vertices connected to them). Note that point (iii) of Theorem 1 means that walk multiplets of the original graph  $G$  with parity *opposite* to that of  $\mathbb{M}_\gamma^p$  are *not* necessarily present in the new graph (cone)  $H$ . Indeed, in the present example with  $p = +1$  all but one odd walk multiplet of Fig. 3(a) (the walk singlet  $\{8\}^-$ ) disappeared in Fig. 5(a)–(d).

As we see, using Theorem 1 together with Corollary 1 and Theorem 2, given a graph  $H$  with cospectral vertices  $u, v$  one can: (1) generate walk singlets by connecting new vertices to existing walk multiplets, (2) connect an arbitrary new subgraph to such a singlet, and subsequently (3) even interconnect such subgraphs. In other words, we now see that, starting from a small graph with cospectral vertices  $u$  and  $v$ , one can construct *arbitrarily* complex graphs maintaining this cospectrality, using the concept and rules for the introduced walk multiplets.

Let us here also corroborate the necessity of equal parity of two walk multiplets for their combination to be a multiplet (see Remark 2), by a counterexample. In Fig. 5,  $\{5\}^+$ ,  $\{8\}^-$  are walk singlets of opposite parity relative to the cospectral pair  $\{1, 2\}$ . Assume, now, that these two singlets can be combined into a walk doublet  $\mathbb{C}_\epsilon^p$  relative to  $\{1, 2\}$  with subset  $\mathbb{C} = \{5, 8\}$ , weight tuple  $\epsilon = (a, b)$  and parity  $p = \pm 1$ . Then, by Theorem 1, connecting a new vertex  $c'$  to  $\mathbb{C}$  via edges with weights  $a, b$  would not break the cospectrality. However, this is not the case. Indeed, in the extended graph we would get  $[H^5]_{1,1} = [H^5]_{2,2} - 4ab$ , violating Eq. (1) for  $k = 5$  if  $ab \neq 0$ . This means that only one of the vertices  $\{5\}^+$  and  $\{8\}^-$  may be connected to  $c'$  ( $a = 0$  or  $b = 0$ ) to keep  $\{1, 2\}$  cospectral. In other words, *either* even *or* odd walk multiplets can generally be simultaneously connected to a new vertex while keeping the cospectrality of the associated cospectral pair.

In the following example, we demonstrate how the topology of a graph itself can be modified, i.e. without extending it by new vertices, while preserving a cospectral pair.

**Example 4.** In Fig. 6, we apply Theorem 2 to the graph of Fig. 4, resulting in graphs with the same vertices as in the original graph but with some of them connected differently. Specifically, in Fig. 6(a), we interconnect the even uniform walk doublet  $\{(3, 7)_a\}^+$  with the even nonuniform walk triplet  $\{(1, 5)_b, (4)_{2b}\}^+$  (see list of walk multiplets in Fig. 4). According to Theorem 2,  $\{u, v\} = \{2, 6\}$  remains cospectral if we add the product  $ab$  to the edge weights between each of the vertices 3, 7 of the doublet and vertices 1, 5 of the triplet, and  $2ab$  to the edge weights between 3, 7 and 4, as shown in the figure. Thus, the *new* edges (1, 3), (3, 4), (3, 5), and (4, 7) are created in the resulting graph, so that the graph topology has been modified. Note, though, that the multiplet interconnection procedure comes with a partial restriction on the weights of the new graph. For instance, starting in Fig. 6(a) with an unweighted graph and setting also  $a = b = 1$ , the edges (1, 7), (3, 4), (4, 7), (5, 7) in the new graph have weight 2 (and the rest 1); that is, the new graph cannot be unweighted. In Fig. 6(b), we interconnect  $\{(3, 7)_a\}^+$  with  $\{(4)_b, (8)_{-b}\}^+$ . Starting with the original graph unweighted and setting  $a = b = 1$ , the addition of edge weights according to Theorem 2 *removes* the edges (3, 8) and (7, 8), while adding (3, 4) and (4, 7), with  $\{2, 6\}$  remaining cospectral. This demonstrates how walk multiplet interconnections can be used to disconnect vertices of a graph while preserving the associated cospectrality.

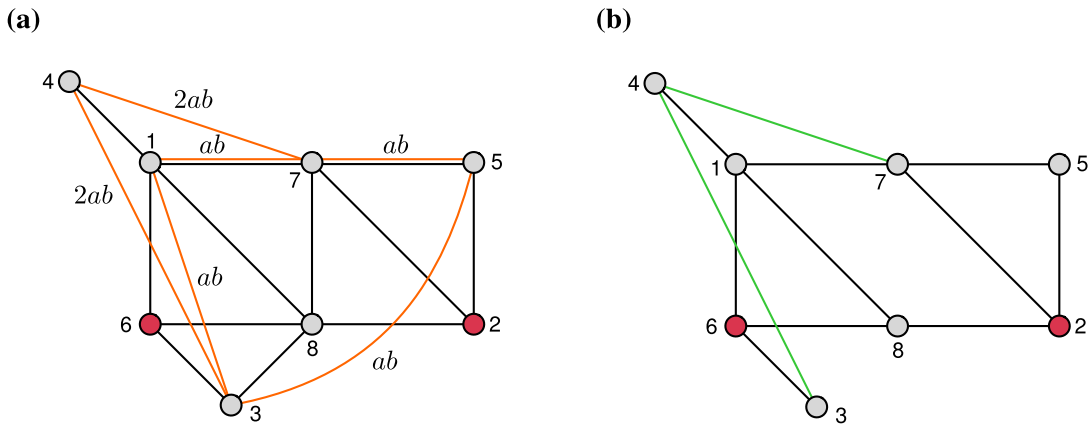


**Fig. 6.** Two modifications of the graph depicted in Fig. 4 which keep the cospectrality of the vertices 2 and 6 while changing the graph topology, using 2; see Example 4. In (a) we interconnect the walk multiplets  $\{(3, 7)_a\}^+$  and  $\{(1, 5)_b, (4)_{2b}\}^+$ , with added edge weights as indicated, and in (b) we interconnect walk multiplets  $\{(3, 7)_a\}^+$  with  $\{(4)_a, (8)_{-a}\}^+$ , starting from the original graph unweighted and setting  $a = 1$ .

By Theorem 1, the cospectrality of a vertex pair is preserved in the weighted cone over a walk multiplet of a graph with the same weight tuple  $\gamma$ , with the tip of the cone then being a walk singlet. We now ask for the reverse: When the cospectrality of  $u, v$  is preserved under a single-vertex addition, is that vertex *necessarily* a walk singlet relative to  $u, v$ ? The affirmative answer is given by the following theorem, which also makes a similar statement for the case of single vertex deletions.

**Theorem 3** (*Preserved cospectrality under single vertex additions or deletions*). *Let  $G$  be a graph with vertex set  $\mathbb{V}$  and with two cospectral vertices  $u, v \in \mathbb{V}$ . Then*

- (i) *The cospectrality of  $u$  and  $v$  is preserved in the cone  $H$  of  $G$  over a subset  $\mathbb{M} \subseteq \mathbb{V}$  with weight tuple  $\gamma = (\gamma_m)_{m \in \mathbb{M}}$  if and only if  $\mathbb{M}_\gamma^c$  is a walk multiplet relative to  $u, v$ .*
- (ii) *The cospectrality of  $u$  and  $v$  is preserved in the graph  $R = G \setminus c$  (obtained from  $G$  by removing the vertex  $c \in \mathbb{V}$ ) if and only if  $c$  is a walk singlet in  $G$  relative to  $u, v$ .*

Recall that the tip of the cone in part (i) is a walk singlet relative to  $u, v$  (by Theorem 1). In part (ii), a walk singlet is removed, without breaking the cospectrality of  $\{u, v\}$ . Thus, the theorem implies that the only way to add a single vertex to a graph, or to remove a single vertex from it, without breaking the cospectrality of two vertices  $u, v$ , is if that vertex is a walk singlet relative to  $u, v$ .

A word of caution, though: Whereas walk *singlets* can safely be removed from a graph without destroying the associated cospectral pair, the same is not true for larger walk multiplets in general. An interesting special case where a multiplet can be removed is when (i) its vertices are pairwise cospectral and (ii) relative to each such cospectral pair its remaining vertices are singlets, as explained in the proof of Theorem 3 in the Appendix. An example of this is the walk anti-doublet  $\{3, 4\}^-$  in Fig. 3(a), whose removal does preserve the cospectrality of the pair  $\{1, 2\}$ .

Combining Theorem 1 with Theorem 3 results in the following conclusion regarding walk singlets.

**Corollary 2.** *A vertex  $c$  of a graph is a walk singlet relative to cospectral vertices  $u, v$  if and only if it is exclusively connected via edges with weight tuple  $\gamma = (\gamma_m)_{m \in \mathbb{M}}$  to a walk multiplet  $\mathbb{M}_\gamma^p$  relative to  $u, v$ .*

Let us now make the link to where we started (in Section 2.1), with the notion of USPs. Recall that an USP is a single vertex to which an arbitrary new graph can be connected, or which can also be removed, without breaking the cospectrality of a vertex pair. While it is clear from Theorem 1 that any walk singlet is an USP, one might ask if also the *reverse* is true, that is, whether any USP is a walk singlet. The removal of a walk singlet is covered by Theorem 3(ii). Regarding the connection of arbitrary graphs, we have the following.

**Corollary 3** (*USPs are singlets*). *If the cospectrality of a vertex pair  $\{u, v\}$  of a graph  $H$  is preserved when connecting an arbitrary graph  $C$  to a single vertex  $c$  of  $H$ , via edges of arbitrary weights, then  $c$  is a walk singlet relative to  $\{u, v\}$ .*

This statement can be easily understood from the above. Indeed, since  $C$  is an arbitrary graph, we can choose it to be a single vertex  $c'$ . If the cospectrality of  $u, v$  is preserved under this addition, then by Theorem 3(i),  $c'$  must then be a walk singlet. But by Corollary 2,  $c$  must be a walk singlet as well. Thus, we have that every USP is a walk singlet.

Before we proceed, let us review the above, starting with a recapitulation of the concept of cospectral vertices. Known in molecular graph theory as “isospectral points”, this concept can be seen as a *generalization* of exchange symmetry [6]. Indeed, any two vertices  $u$  and  $v$  that are exchange symmetric are also cospectral, but the reverse is not necessarily the case. Similar to the case of exchange symmetries, one can then draw powerful conclusions from the presence of cospectral vertices. For example, one can use the presence of cospectral vertices to express the characteristic polynomial of the underlying matrix  $H$  in terms of smaller polynomials [16]. In quantum physics it has been shown [3] that cospectrality of  $u$  and  $v$  is a necessary condition for so-called perfect state transfer between these two vertices, which is important in the realization of quantum computers. In general, if two vertices  $u$  and  $v$  are cospectral, then all eigenvectors have (in the case of degeneracies, can be chosen to have) definite parity on these two vertices [15]. The implications of such local parity depend, of course, on what the underlying matrix  $H$  represents, but can be quite impactful. In network theory [9,17], for example, the local parity of eigenvectors implies that two cospectral vertices have the same “eigenvector centrality”, which is a measure for their importance in the underlying network.

Irrespective of these powerful implications of cospectrality, however, one might object that fulfilling its defining Eq. (1) is rather difficult, especially in larger graphs comprising

thousands of vertices. What we have shown above is that fulfilling Eq. (1) is, on the contrary, *rather easy*: Given a small graph  $G$  with cospectral vertices  $u$  and  $v$ , one can easily embed  $G$  into a (much) larger graph  $G'$  by suitably connecting some vertices of  $G'$  to the walk multipliers of  $u$  and  $v$ . In other words, we have shown that cospectrality does not necessarily rely on *global* fine-tuning. This viewpoint-changing finding, however, is just the implication of a much more important insight. Namely, that the matrix powers of  $H$ —which are used to identify walk multipliers—are a source of detailed information about the underlying graph, as we will demonstrate in the following.

#### 4. Eigenvector components on walk multipliers

Having seen how multipliers can be used to extend a graph whilst keeping the cospectrality of vertices, we now analyze their relation to the eigenvectors of  $H$ . To this end, we first choose the orthonormal eigenvector basis according to the following Lemma.

**Lemma 1** (Lemma 2.5 of [15]). *Let  $H$  be a symmetric matrix, with  $u$  and  $v$  cospectral. Then the eigenvectors  $\{\phi\}$  of  $H$  are (or, in the case of degenerate eigenvalues, can be chosen) as follows. For each eigenvalue  $\lambda$  there is at most one eigenvector  $\phi$  with even local parity on  $u$  and  $v$ , i.e.,  $\phi_u = \phi_v \neq 0$ , and at most one eigenvector  $\phi$  with odd local parity on  $u$  and  $v$ , i.e.,  $\phi_u = -\phi_v \neq 0$ . All remaining eigenvectors for  $\lambda$  fulfill  $\phi_u = \phi_v = 0$ . The even (odd) parity eigenvector can be found by projecting the vector  $e_u \pm e_v$  onto the eigenspace associated with  $\lambda$ .*

**Remark 4.** If the projection of  $e_u \pm e_v$  onto the eigenspace associated with  $\lambda$  yields the zero-vector, then the corresponding even (odd) parity eigenvector does not exist.

With this choice, the components of odd and even parity eigenvectors on a walk multiplier obey the following constraint.

**Theorem 4** (Eigenvector components on walk multipliers). *Let  $H = H^\top \in \mathbb{R}^{N \times N}$  represent a graph with a pair of cospectral vertices  $u, v$ , and let its eigenvectors be chosen according to Lemma 1. Then any eigenvector  $\phi$  of  $H$  with eigenvalue  $\lambda$  and nonzero components of odd (even) parity  $p$  on  $u, v$ ,*

$$\phi_u = p \phi_v \neq 0, \quad p \in \{+1, -1\}, \quad (15)$$

*fulfills*

$$\sum_{m \in \mathbb{M}} \gamma_m \phi_m = 0 \quad (16)$$

*if and only if  $\mathbb{M}_\gamma^{-p}$  is a walk multiplier relative to  $u, v$  with even (odd) parity  $-p$  and weight tuple  $\gamma = (\gamma_m)_{m \in \mathbb{M}}$ .*

**Remark 5.** It is an interesting—and to the best of our present knowledge unanswered—question whether analogous general statements can be made regarding the eigenvector components on walk multiplets relative to a cospectral pair  $\{u, v\}$  for eigenvectors with zero components on  $u, v$ .

Let us take a look at the impact of Theorem 4 in an example. We use a graph we are already familiar with and which has an interesting multiplet structure.

**Example 5.** The graph of Fig. 4 has three eigenvectors  $\phi^\nu$  (labeled by  $\nu = 1, 2, 3$ ) with odd parity on the cospectral pair  $\{2, 6\}$ , given by the columns

$$\begin{bmatrix} -\frac{2}{\sqrt{10}} & \frac{1}{2\sqrt{5}} & -\frac{1}{2\sqrt{5}} \\ -\frac{1}{\sqrt{10}} & -\frac{1}{\sqrt{5}} & \frac{1}{\sqrt{5}} \\ -\frac{1}{\sqrt{10}} & \frac{1}{20}(5 + \sqrt{5}) & \frac{1}{20}(5 - \sqrt{5}) \\ \frac{1}{\sqrt{10}} & \frac{1}{20}(5 - \sqrt{5}) & \frac{1}{20}(5 + \sqrt{5}) \\ 0 & -\frac{1}{2} & -\frac{1}{2} \\ \frac{1}{\sqrt{10}} & \frac{1}{\sqrt{5}} & -\frac{1}{\sqrt{5}} \\ \frac{1}{\sqrt{10}} & \frac{1}{20}(-5 - \sqrt{5}) & \frac{1}{20}(\sqrt{5} - 5) \\ \frac{1}{\sqrt{10}} & \frac{1}{20}(5 - \sqrt{5}) & \frac{1}{20}(5 + \sqrt{5}) \end{bmatrix}.$$

As an example, we apply Theorem 4 for the even walk quadruplet  $\{(1)_a, (3)_b, (4)_{2a+b}, (5)_{a+b}\}^+$  (shown in the table of Fig. 4) relative to  $\{2, 6\}$ . By Eq. (16), each of the above eigenvectors fulfills

$$a\phi_1^\nu + b\phi_3^\nu + (2a + b)\phi_4^\nu + (a + b)\phi_5^\nu = 0; \quad \phi_2^\nu = -\phi_6^\nu \neq 0, \quad \nu = 1, 2, 3, \quad (17)$$

for any values of the parameters  $a, b$ , as the reader may easily verify. Note that the above eigenvectors also have local odd parity on  $\{3, 7\}$ . This is again a result of Eq. (16), since  $\{(3, 7)_a\}^+$  is an even walk doublet relative to the cospectral pair  $\{2, 6\}$ , so that  $\phi_3^\nu + \phi_7^\nu = 0$  for  $\nu = 1, 2, 3$ .

For uniform walk multiplets, and especially singlets, Theorem 4 simplifies: If an even (odd) walk multiplet  $\mathbb{M}_\gamma^p$  relative to  $u, v$  is uniform ( $\gamma_m = \text{const.}$ ), then  $\sum_{m \in \mathbb{M}} \phi_m = 0$  for any eigenvector  $\phi$  with odd (even) parity on  $u, v$ ; in particular,  $\phi$  has zero component on any even (odd) walk singlet. The zero component of an eigenvector  $\phi$  on a vertex  $c$  can be understood as a cancellation of weighted eigenvector components in the eigenvalue equation  $H\phi = \lambda\phi$ , written as  $\sum_{m \neq c} H_{cm}\phi_m = (\lambda - H_{cc})\phi_c$ . If  $\phi_c = 0$ , the sum over components  $\phi_m$  on vertices  $m$  adjacent (i.e. connected by edges) to  $c$ , weighted by the corresponding edge weights, vanishes, i.e.  $\sum_{m \neq c} H_{cm}\phi_m = 0$ . This coincides, though, with Eq. (16) of Theorem 4 for  $H_{cm} = \gamma_m$ . Further, recall that the components of eigenvectors with parity  $p$  on cospectral vertices vanish on walk singlets with opposite parity  $-p$ . In the light of Theorem 1(ii) and Corollary 1, this suggests that walk multiplets may

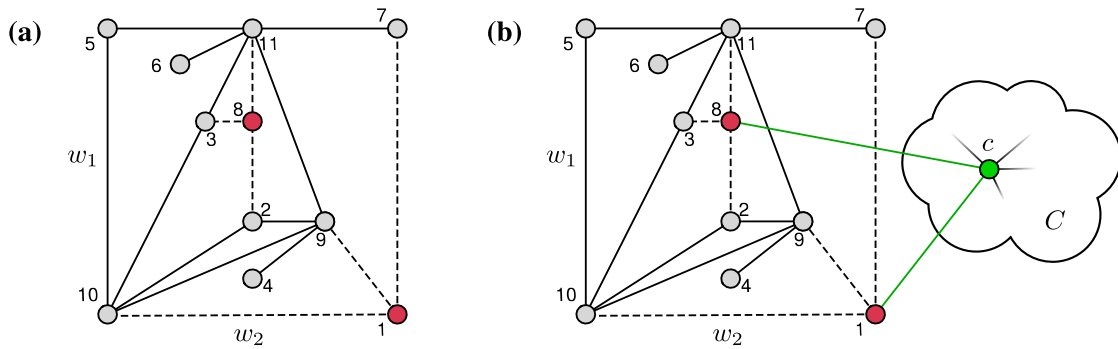


**Fig. 7.** (a) A graph with no walk singlets relative to the only cospectral pair  $\{1, 8\}$  which remains cospectral for any nonzero edge weights  $w_1$  (solid lines) and  $w_2$  (dashed lines). The graph has seven eigenvectors with odd local parity (and nonzero components) on  $\{1, 8\}$ . (b) When connecting an arbitrary graph  $C$  symmetrically via a single vertex  $c$  to the cospectral pair  $\{1, 8\}$ , which is also a uniform even walk doublet  $\{1, 8\}^+$ , then by Corollary 1 all vertices within  $C$  are walk singlets relative to  $\{1, 8\}$ . The original odd parity eigenvectors vanish on all vertices of  $C$ .

be used to construct graphs having eigenvectors with multiple vanishing components, namely on graph extensions consisting only of walk singlets. We demonstrate this in the following example.

**Example 6.** We start with the graph in Fig. 7(a), which has no walk singlets (or any other walk multiplets up to size 5, for that matter) relative to its cospectral pair  $\{1, 8\}$ . The cospectrality of  $\{1, 8\}$  is independent of the values of the weights  $w_1$  and  $w_2$  (indicated by solid and dashed lines), as long as they are nonzero. We can now easily create singlets by symmetrically connecting a new graph  $C$ , depicted by a cloud in Fig. 7(b), to the two cospectral vertices 1, 8 via a single vertex  $c$  of  $C$ . This is ensured by Corollary 1 and Theorem 2, with the cospectral pair here simultaneously representing a walk doublet (see Remark 1). The original graph in Fig. 7(a) has seven eigenvectors with odd parity on  $\{1, 8\}$  for any choice of the edge weights  $w_1, w_2 \neq 0$ . We note that this number can be deduced by applying the methodology of Ref. [18], wherein the so-called “isospectral reduction” is used to split the graph’s characteristic polynomial into smaller pieces, the orders of which are linked to the number of positive and negative parity eigenvectors. Coming back to the example, we note that each of those seven odd parity eigenvectors has vanishing components on all vertices of  $C$  by Corollary 1 and Theorem 4. Of course, depending on the internal structure of the subgraph  $C$ , the total graph may now feature further eigenvectors (not those seven from above) which have zero components on different subgraphs (not  $C$ ).

When the subgraph  $C$  is much larger than the original graph of Fig. 7(a), most of the eigenvector components of the seven odd parity eigenvectors vanish. Eigenvectors with such a property are known as “sparse eigenvectors” [19,20] in engineering or computer science. Such eigenvectors can also be characterized as “compact”, since they have nonzero components only on a strict subset of the vertex set of a graph  $H$ . Indeed, if  $H$  represents a Hamiltonian of a physical system composed of discrete sites (like the atoms

in molecular model of Fig. 2), then eigenstates of  $H$  which are strictly confined to a subset of sites are often referred to as “compact localized states” [21,22] or even “dark states” [23,24] depending on the context. We have here demonstrated how such compact eigenvectors can be generated for a graph featuring cospectral vertices, by extending the graph via walk multiplets. As a perspective for future work, this may be used to design discrete physical setups with compact localized states or, more generally, network systems with some eigenvectors vanishing on desired nodes.

## 5. Generating cospectral vertices without permutation symmetry from highly symmetric graphs

Until now, the existence of cospectral vertices has been assumed to be given, and we now come to the question of how to generate such graphs. One possible method is to start from two graphs  $G_1, G_2$  with the same characteristic polynomial (such graphs can be constructed by means of the so-called “Godsil-McKay-switching” from Ref. [25]), and then search for a graph  $H$  such that  $H \setminus u = G_1$  and  $H \setminus v = G_2$ . The two vertices  $u$  and  $v$  are then guaranteed to be cospectral in  $H$ .

The concept of walk multiplets, as introduced in this work, naturally suggests another scheme for generating graphs with cospectral vertices. Starting from a matrix  $H$  which commutes with a permutation matrix  $P$  which exchanges  $u$  and  $v$  (with arbitrary permutations of the remaining vertices, so that other vertices could be symmetry-related as well), one first identifies the walk multiplets of  $H$  relative to  $\{u, v\}$ . In a second step,  $H$  is changed by either (i) connecting one or more new vertices to (some of) the multiplets having common parity, following Theorem 1, or (ii) interconnecting multiplets by adding edge weights between them, following Theorem 2. Vertices  $u$  and  $v$  remain cospectral under these operations, but the resulting matrix  $H'$  may feature less permutation symmetries than  $H$ . Interestingly,  $H'$  could feature *no permutation symmetry at all*, as we demonstrate in the following examples.

**Example 7.** Fig. 8(a) shows a “ladder” graph with two legs and three rungs. As drawn here, it is symmetric both under a reflection about the horizontal and the vertical axis. As a result of the symmetry about the vertical axis, and among other cospectral pairs, the two central vertices  $u, v$  are cospectral. Moreover, as a result of the combined horizontal and vertical reflection symmetry, the two pairs  $\{d_1, d_2\}$  and  $\{d_1, d_3\}$  correspond to even uniform walk doublets relative to  $\{u, v\}$ . In Fig. 8(b), a new vertex  $c$  is connected to  $\{d_1, d_2\}$  and another new vertex  $c'$  is connected to  $\{d_1, d_3\}$ , with some arbitrary but uniform weights  $a$  and  $b$ , respectively. The extension by  $c$  and  $c'$  breaks the previous reflection symmetries in the resulting graph, which in fact features no permutation symmetries at all. By Theorem 1, however, the vertices  $u, v$  remain cospectral. Note, in particular, that the occurrence of the walk doublet  $\{d_1, d_3\}$  in Fig. 8(a) can be intuitively explained by the graph’s combined reflection symmetry about its vertical and horizontal axes. The symmetry about the horizontal axis is then broken when first adding ver-



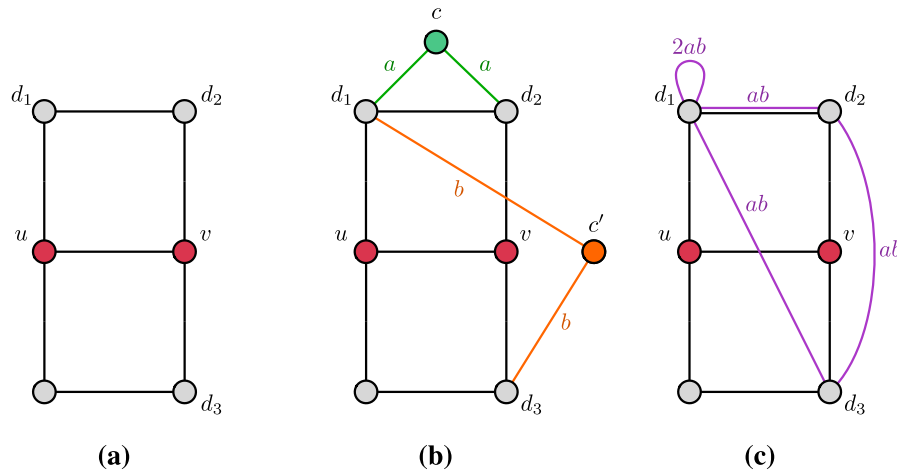


**Fig. 8.** Generation of a weighted graph with cospectral vertices and without any permutation symmetry; see Example 7. (a) A “ladder” graph, reflection symmetric about its vertical and horizontal axes, with cospectral vertices  $u$  and  $v$ , is modified by (b) connecting two new vertices  $c$  and  $c'$  to the uniform walk doublets  $\{d_1, d_2\}^+$  and  $\{d_1, d_3\}^+$  relative to  $\{u, v\}$  with weights  $a$  and  $b$ , respectively, or (c) interconnecting those walk doublets by adding edge weights as shown. In both (a) and (b), the resulting graph has no permutation symmetries, while  $u, v$  remain cospectral, as ensured by Theorems 1 and 2, respectively.

tex  $c$ , so one might intuitively expect also the walk multiplet condition for  $\{d_1, d_3\}$  to be violated. Nevertheless, Theorem 1 guarantees that  $\{d_1, d_3\}$  remains a walk multiplet relative to  $\{u, v\}$ , and so  $c'$  can be further added without breaking cospectrality. An alternative way to generate a graph with cospectral vertices and no permutation symmetries is shown in Fig. 8(c). Here the same original graph is modified by applying Theorem 2: Instead of connecting the two walk doublets  $\{d_1, d_2\}^+$  and  $\{d_1, d_3\}^+$  to added vertices, they are now interconnected to each other. Specifically, the weights  $ab$  are added pairwise to the edges between  $d_1, d_2, d_3$ , and a loop of weight  $2ab$  is added to the overlap  $d_1 = \{d_1, d_2\} \cap \{d_1, d_3\}$ , with  $a$  and  $b$  being arbitrary parameters. Note that, while the vertex set of the graph remains the same, its topology has now changed by the added edges  $(d_1, d_3)$  and  $(d_2, d_3)$ . Again, the pair  $\{u, v\}$  remains cospectral, while the resulting graph has no permutation symmetry.

**Example 8.** Fig. 9(a) shows again a graph which, as visualized, is vertically and horizontally reflection symmetric and has (among others) two cospectral vertices  $u, v$  and two uniform even walk doublets  $\{d_1, d_2\}^+$  and  $\{d_1, d_3\}^+$  relative to  $\{u, v\}$ . We now use Theorem 2 to change the topology of the original graph and subsequently Theorem 1 to further extend it by new vertices, with  $u, v$  remaining cospectral in the final graph where all permutation symmetries are broken. Specifically, in Fig. 9(b) we interconnect the walk doublet  $\{d_1, d_3\}^+$  to the doublet  $\{u, v\}^+$  by uniformly adding edge weights between their vertices (creating new edges if absent) according to Theorem 2. In Fig. 9(c) we proceed by connecting a new vertex  $c$  to the doublet  $\{d_1, d_2\}^+$  and another new vertex  $c'$  first to  $\{d_1, d_3\}^+$  and then to  $\{u, v\}^+$  (equivalent to connecting  $c'$  directly to the walk quadruplet  $\{(d_1, d_3)_a, (u, v)_b\}^+$ ), following Theorem 1. We finally also disconnect  $u$  from  $v$ , which leaves them cospectral according to Remark 3.

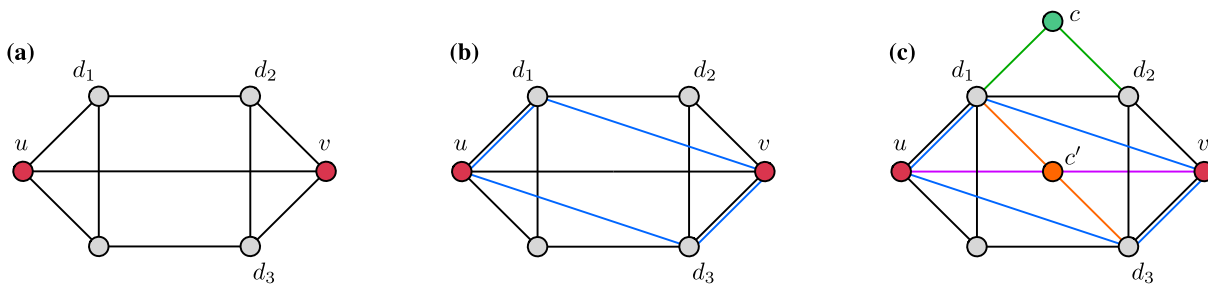


**Fig. 9.** The highly symmetric graph in (a) with (among other pairs) the cospectral vertex pair  $\{u, v\}$  is modified by (b) interconnecting the walk doublets  $\{u, v\}^+$  and  $\{d_1, d_3\}^+$  (according to Theorem 2), and then (c) disconnecting the two cospectral vertices  $u, v$  from each other (Remark 3), connecting a new vertex  $c$  to the walk doublet  $\{d_1, d_2\}^+$ , and another new vertex  $c'$  to the walk quadruplet  $\{(d_1, d_3)_a, (u, v)_b\}^+$  (Theorem 1), resulting in a graph with cospectral vertices  $u, v$  but no permutation symmetries; see Example 8.

The highly symmetric base graphs in Examples 7 and 8 were chosen unweighted and without loops for simplicity. Notably, they could easily be enriched by adding loops on their vertices and weighting the edges such that the indicated cospectral pairs  $\{u, v\}$  are still present (that is, by respecting the reflection symmetries about the vertical and/or horizontal axes). Then, the extensions and interconnections described above could still be performed, creating weighted graphs featuring cospectral pairs without permutation symmetries.

## 6. Conclusions

Cospectral vertices offer the exciting possibility of eigenvectors of a matrix  $H$  having local parity on components corresponding to cospectral vertex pairs, even without the existence of corresponding permutation matrices commuting with  $H$ . Here, we introduced the notion of “walk equivalence” of two cospectral vertices with respect to a vertex subset of a graph represented by a matrix  $H$ . Such subsets, corresponding to what we call “walk multiplets”, provide a simple and generally applicable method of modifying a given graph with cospectral vertices such that the cospectrality is preserved. The definition of walk multiplets is based on the entries of the powers of  $H$  and can be expressed in terms of so-called walk matrices used in graph theory. As we demonstrate here, the concept of walk multiplets generalizes that of “unrestricted substitution points” (USPs), introduced for molecular graphs, to vertex subsets of arbitrary size: Any arbitrary new graph can be connected, via one of its vertices, to all vertices of a walk multiplet relative to a cospectral pair in an existing graph, without breaking the cospectrality. In fact, USPs turn out to coincide with walk “singlets”, that is, multiplets comprised of a single vertex. We further showed how walk multiplets can be used to derive sets of local relations between the components of an eigenvector with certain parity on a given associated cospectral pair. As a special case, the eigenvector components then vanish on any walk singlet as well as on any graph connected exclusively to walk singlets. This relates to the generation of so-called “compact localized states” in artificial physical setups, also known as “sparse eigenvectors” in other areas of science. We also presented a scheme in which we use

walk multiplets to construct a class of graphs having cospectral vertices without any permutation symmetries.

It is important to notice that the analysis performed here applies also to more than two cospectral vertices: For any subset  $\mathbb{S}$  of cospectral vertices, cospectrality is indeed defined *pairwise* for any two vertices  $u, v \in \mathbb{S}$ , and thus the walk multiplet framework applies to any such pair. Our results may thus offer a valuable resource in understanding and manipulating the structure of eigenvectors in an engineered network system via its walk multiplets—that is, by only utilizing the powers of the underlying matrix. In particular, the local eigenvector component relations derived here may be systematically exploited to deduce parametric forms of eigenvectors for generic graphs with cospectral pairs; an investigation left for future work.

Let us finally also hint at a possible connection to recent studies of local symmetries in discrete quantum models, which provide relations between the components of general states in the form of non-local continuity equations [26,27] and may offer advantages for state transfer on quantum networks [18]. In this context, it would be intriguing to explore the possible implications of walk multiplets for the dynamical evolution of wave excitations on general network-like systems.

### Declaration of competing interest

The authors declare no conflict of interest.

### Acknowledgements

M.R. is thankful to the Stiftung der Deutschen Wirtschaft and M.P. is thankful to the Studienstiftung des Deutschen Volkes for financial support in the framework of scholarships.

### Appendix A. Proofs of theorems

We here restate Theorems 1 to 4 together with their proofs.

**Theorem 1** (*Walk singlet extension*). *Let  $G = G^T \in \mathbb{R}^{N \times N}$  represent an undirected graph with two cospectral vertices  $u, v$ , let  $\mathbb{M}_\gamma^p$  be an even (odd) walk multiplet of  $G$  relative to  $u, v$ , and let  $H$  be a weighted cone of  $G$  over the subset  $\mathbb{M}$  with real weight tuple  $\gamma = (\gamma_m)_{m \in \mathbb{M}}$ . Then*

- (i) *Vertices  $u, v$  are cospectral in  $H$ .*
- (ii) *The tip  $c$  of the cone  $H$  is an even (odd) walk singlet relative to  $u, v$ .*
- (iii) *Any even (odd) walk multiplet in  $G$  is an even (odd) walk multiplet in  $H$ .*

**Proof.** We partition any walk of length  $k$  in  $H$  into the walks restricted exclusively to  $G$  and the additionally generated walks in  $H$  visiting the new vertex  $c$ . Then we apply the multiplet condition, Eq. (10), which is valid in the old graph  $G$ . For convenience, we define

$$A_{s;\mathbb{M}}^{(\ell)} \equiv \sum_{m \in \mathbb{M}} \gamma_m [G^\ell]_{sm}, \quad B_{s;\mathbb{M}}^{(\ell)} \equiv \sum_{m \in \mathbb{M}} \gamma_m [H^\ell]_{sm}. \tag{A.1}$$

Then, since  $\mathbb{M}_\gamma^p$  is a walk multiplet relative to  $u, v$  in  $G$ , we have from Eq. (10) that

$$A_{u;\mathbb{M}}^{(k)} = p A_{v;\mathbb{M}}^{(k)} \quad \forall k \in \mathbb{N}, \quad p \in \{+1, -1\}. \tag{A.2}$$

To prove (i), we compute, with walk lengths fulfilling  $\ell + n + r = k - 2$ ,

$$[H^k]_{u,u} = [G^k]_{u,u} + \sum_{\ell,n,r} \sum_{m,m' \in \mathbb{M}} [G^\ell]_{u,m} H_{m,c} [H^n]_{c,c} H_{c,m'} [G^r]_{m',u} \tag{A.3}$$

$$= [G^k]_{u,u} + \sum_{\ell,n,r} \sum_{m,m' \in \mathbb{M}} [G^\ell]_{u,m} \gamma_m [H^n]_{c,c} \gamma_{m'} [G^r]_{m',u} \tag{A.4}$$

$$= [G^k]_{u,u} + \sum_{\ell,n,r} A_{u;\mathbb{M}}^{(\ell)} [H^n]_{c,c} A_{u;\mathbb{M}}^{(r)} \tag{A.5}$$

$$= [G^k]_{v,v} + p^2 \sum_{\ell,n,r} A_{v;\mathbb{M}}^{(\ell)} [H^n]_{c,c} A_{v;\mathbb{M}}^{(r)} \tag{A.6}$$

$$= [H^k]_{v,v}, \tag{A.7}$$

where we used  $p^2 = 1$ , Eq. (A.2), and the cospectrality of  $u, v$  in  $G$ . To prove (ii), we compute, now with  $\ell + n = k - 1$ ,

$$[H^k]_{u,c} = \sum_{\ell,n} \sum_{m \in \mathbb{M}} [G^\ell]_{u,m} H_{m,c} [H^n]_{c,c} = \sum_{\ell,n} \sum_{m \in \mathbb{M}} \gamma_m [G^\ell]_{u,m} [H^n]_{c,c} \tag{A.8}$$

$$= \sum_{\ell,n} A_{u;\mathbb{M}}^{(\ell)} [H^n]_{c,c} \tag{A.9}$$

$$= \sum_{\ell,n} p A_{v;\mathbb{M}}^{(\ell)} [H^n]_{c,c} = p [H^k]_{v,c} \tag{A.10}$$

To prove (iii), we compute, again with  $\ell + n = k - 1$ ,

$$[H^k]_{u,m} = [G^k]_{u,m} + \sum_{\ell,n} \sum_{m' \in \mathbb{M}} [G^\ell]_{u,m'} H_{m',c} [H^n]_{c,m} \tag{A.11}$$

$$= [G^k]_{u,m} + \sum_{\ell,n} A_{u;\mathbb{M}}^{(\ell)} [H^n]_{c,m} \tag{A.12}$$

so that, multiplying by  $\gamma_m$  and summing over  $m \in \mathbb{M}$ , we have

$$B_{u;\mathbb{M}}^{(k)} = A_{u;\mathbb{M}}^{(k)} + \sum_{m \in \mathbb{M}} \gamma_m \sum_{\ell, n} A_{u;\mathbb{M}}^{(\ell)} [H^n]_{c,m} \tag{A.13}$$

$$= p A_{v;\mathbb{M}}^{(k)} + \sum_{m \in \mathbb{M}} \gamma_m \sum_{\ell, n} p A_{v;\mathbb{M}}^{(\ell)} [H^n]_{c,m} \tag{A.14}$$

$$= p \sum_{m \in \mathbb{M}} \gamma_m ([G^k]_{v,m} + \sum_{\ell, n} A_{v;\mathbb{M}}^{(\ell)} [H^n]_{c,m}) = p \sum_{m \in \mathbb{M}} \gamma_m [H^k]_{v,m} = p B_{v;\mathbb{M}}^{(k)} \tag{A.15}$$

Note that, if any arbitrary graph  $C$  is connected exclusively to the added vertex  $c$ , then any vertex  $c'$  of  $C$  is also a walk singlet relative to  $\{u, v\}$ . Indeed, simply replacing  $[H^n]_{cc}$  with  $[H^n]_{cc'}$  in Eqs. (A.8) to (A.10) above leads to  $[H^k]_{u,c'} = p [H^k]_{v,c'}$ , which proves Corollary 1.  $\square$

**Theorem 2** (Walk multiplet interconnection). *Let  $G \in \mathbb{R}^{N \times N}$  be a graph with a cospectral pair  $\{u, v\}$  and  $\mathbb{X}_\gamma^p, \mathbb{Y}_\delta^p$  be (in general non-uniform) walk multiplets relative to  $\{u, v\}$  having same parity  $p$  and weight tuples  $\gamma, \delta$ , respectively, with possible subset overlap  $\mathbb{Z} = \mathbb{X} \cap \mathbb{Y} \neq \emptyset$ . Then the cospectrality of  $\{u, v\}$  and any walk multiplet relative to  $\{u, v\}$  with parity  $p$  are preserved in the graph  $H \in \mathbb{R}^{N \times N}$  with elements*

$$H_{x,y} = H_{y,x} = \begin{cases} G_{x,y} + \gamma_x \delta_y & \text{if } x \notin \mathbb{Z} \text{ or } y \notin \mathbb{Z} \\ G_{x,y} + \gamma_x \delta_y + \gamma_y \delta_x & \text{if } x, y \in \mathbb{Z} \end{cases} \quad \forall x \in \mathbb{X}, y \in \mathbb{Y}$$

and  $H_{i,j} = G_{i,j}$  otherwise.

**Proof.** To prove that the vertices  $u, v$  remain cospectral in the modified graph  $H$  with added edge weights  $H_{x,y} - G_{x,y}$  as described in the theorem, we will partition the walks in the new graph into walk segments such that the multiplet relations, Eq. (9), can be applied for the segments within the old graph  $G$ .

We first express the newly generated closed walks from  $u$  using (i) walks segments in the old graph  $G$  to reach a vertex of one of the multiplets  $\mathbb{X}$  (or  $\mathbb{Y}$ ), (ii) the new edge (that is, the weight added if the edge already existed) to cross to the other multiplet  $\mathbb{Y}$  (or  $\mathbb{X}$ ), and (iii) finally coming back to  $u$  using walks in the new graph  $H$ .

Defining  $\mathbb{M} = \mathbb{X} \setminus \mathbb{Z}, \mathbb{W} = \mathbb{Y} \setminus \mathbb{Z}$ , and with added edge weights  $H_{ij} - G_{ij} = \gamma_i \delta_j$  (resp.  $\gamma_i \delta_j + \gamma_j \delta_i$ ) if  $i, j \in \mathbb{X} \cup \mathbb{Y} \wedge (i \notin \mathbb{Z} \vee j \notin \mathbb{Z})$  (resp.  $i, j \in \mathbb{Z}$ ), we have

$$[H^k]_{u,u} = [G^k]_{u,u} + \sum_{l+n+1=k} \left\{ \sum_{m \in \mathbb{M}, w \in \mathbb{W}} [G^l]_{u,m} \gamma_m \delta_w [H^n]_{w,u} + \sum_{z \in \mathbb{Z}, w \in \mathbb{W}} [G^l]_{u,z} \gamma_z \delta_w [H^n]_{w,u} + \right. \tag{A.16}$$

$$\left. \sum_{w \in \mathbb{W}, m \in \mathbb{M}} [G^l]_{u,w} \delta_w \gamma_m [H^n]_{m,u} + \sum_{z \in \mathbb{Z}, m \in \mathbb{M}} [G^l]_{u,z} \delta_z \gamma_m [H^n]_{m,u} \right. \tag{A.17}$$

$$\sum_{m \in \mathbb{M}, z \in \mathbb{Z}} [G^l]_{u,m} \gamma_m \delta_z [H^n]_{z,u} + \tag{A.18}$$

$$\sum_{w \in \mathbb{W}, z \in \mathbb{Z}} [G^l]_{u,w} \delta_w \gamma_z [H^n]_{z,u} + \tag{A.19}$$

$$\sum_{z' \in \mathbb{Z}, z \in \mathbb{Z}} [G^l]_{u,z'} (\gamma_{z'} \delta_z + \gamma_z \delta_{z'}) [H^n]_{z,u} \}. \tag{A.20}$$

We can now combine sums over subsets as follows:  $\sum_{m \in \mathbb{M}} + \sum_{z \in \mathbb{Z}} = \sum_{x \in \mathbb{X}}$  in (A.16), and the same in (A.18) with the first term  $(\gamma_{z'} \delta_z)$  in (A.20). Similarly,  $\sum_{w \in \mathbb{W}} + \sum_{z \in \mathbb{Z}} = \sum_{y \in \mathbb{Y}}$  in (A.17), and the same in (A.19) with the second term  $(\gamma_z \delta_{z'})$  in (A.20). This yields

$$\begin{aligned} [H^k]_{u,u} &= [G^k]_{u,u} + \sum_{l+n+1=k} \left\{ \sum_{x \in \mathbb{X}, w \in \mathbb{W}} [G^l]_{u,x} \gamma_x \delta_w [H^n]_{w,u} \right. \\ &\quad + \sum_{y \in \mathbb{Y}, m \in \mathbb{M}} [G^l]_{u,y} \delta_y \gamma_m [H^n]_{m,u} \\ &\quad + \sum_{x \in \mathbb{X}, z \in \mathbb{Z}} [G^l]_{u,x} \gamma_x \delta_z [H^n]_{z,u} + \sum_{y \in \mathbb{Y}, z \in \mathbb{Z}} [G^l]_{u,y} \delta_y \gamma_z [H^n]_{z,u} \} \\ &= [G^k]_{u,u} + \sum_{l+n+1=k} \left\{ \sum_{x \in \mathbb{X}, y \in \mathbb{Y}} [G^l]_{u,x} \gamma_x \delta_y [H^n]_{y,u} + \sum_{y \in \mathbb{Y}, x \in \mathbb{X}} [G^l]_{u,y} \delta_y \gamma_x [H^n]_{x,u} \right\}. \end{aligned} \tag{A.21}$$

Next, we account for the walk segments from vertex  $i = x, y$  back to  $u$ , which have a similar form:

$$\begin{aligned} [H^n]_{i,u} &= [G^n]_{i,u} + \sum_{r+s+1=n} \left\{ \sum_{x' \in \mathbb{X}, y' \in \mathbb{Y}} [H^r]_{i,x'} \gamma_{x'} \delta_{y'} [G^s]_{y',u} \right. \\ &\quad + \sum_{y' \in \mathbb{Y}, x' \in \mathbb{X}} [H^r]_{i,y'} \delta_{y'} \gamma_{x'} [G^s]_{x',u} \}. \end{aligned} \tag{A.22}$$

Plugging this into (A.21), after some sorting and combining of terms we arrive at (with  $x, x' \in \mathbb{X}$  and  $y, y' \in \mathbb{Y}$ )

$$\begin{aligned} [H^k]_{u,u} &= [G^k]_{u,u} + 2 \sum_{l+n+1=k} \sum_{x,y} [G^l]_{u,x} \gamma_x \delta_y [G^n]_{y,u} + \\ &\quad \sum_{l+r+s+2=k} \sum_{x,x',y,y'} \left\{ [G^l]_{u,x} \gamma_x \delta_y [H^r]_{y,y'} \delta_{y'} \gamma_{x'} [G^s]_{x',u} + \right. \\ &\quad [G^l]_{u,y} \delta_y \gamma_x [H^r]_{x,x'} \gamma_{x'} \delta_{y'} [G^s]_{y',u} + \\ &\quad \left. 2[G^l]_{u,x} \gamma_x \delta_y [H^r]_{y,x'} \gamma_{x'} \delta_{y'} [G^s]_{y',u} \right\} \end{aligned} \tag{A.23}$$

It is now evident that  $[H^k]_{u,u}$  is equal to  $[H^k]_{v,v}$  by applying cospectrality of  $u, v$  in  $G$  and multiplet conditions for  $\mathbb{X}_\gamma^p, \mathbb{Y}_\delta^p$ .

To prove that any general non-uniform walk multiplet  $\mathbb{Q}_\epsilon^p$  (with weight tuple  $\epsilon$  and of the same parity  $p$  as  $\mathbb{X}_\gamma^p, \mathbb{Y}_\delta^p$ ) in  $G$  is preserved in  $H$ , we evaluate the following expression by using Eq. (A.22):

$$\sum_{q \in \mathbb{Q}} \epsilon_q [H^k]_{u,q} = \sum_{q \in \mathbb{Q}} \epsilon_q \left\{ [G^k]_{u,q} + \sum_{r+s+1=k} \sum_{x \in \mathbb{X}, y \in \mathbb{Y}} [G^s]_{u,x} \gamma_x \delta_y [H^r]_{y,q} + \sum_{r+s+1=k} \sum_{y \in \mathbb{Y}, x \in \mathbb{X}} [G^s]_{u,y} \delta_y \gamma_x [H^r]_{x,q} \right\} \quad (\text{A.24})$$

$$= p \sum_{q \in \mathbb{Q}} \epsilon_q [H^k]_{v,q}, \quad (\text{A.25})$$

where in the last step we applied the multiplet conditions for  $\mathbb{Q}_\epsilon^p, \mathbb{X}_\gamma^p, \mathbb{Y}_\delta^p$ .  $\square$

**Theorem 3** (*Preserved cospectrality under single vertex additions or deletions*). *Let  $G$  be a graph with vertex set  $\mathbb{V}$  and with two cospectral vertices  $u, v \in \mathbb{V}$ . Then*

- (i) *The cospectrality of  $u$  and  $v$  is preserved in the cone  $H$  of  $G$  over a subset  $\mathbb{M} \subseteq \mathbb{V}$  with weight tuple  $\gamma = (\gamma_m)_{m \in \mathbb{M}}$  if and only if  $\mathbb{M}_\gamma^p$  is a walk multiplet relative to  $u, v$ .*
- (ii) *The cospectrality of  $u$  and  $v$  is preserved in the graph  $R = G \setminus c$  (obtained from  $G$  by removing the vertex  $c \in \mathbb{V}$ ) if and only if  $c$  is a walk singlet in  $G$  relative to  $u, v$ .*

**Proof.** We start with part (i) of the theorem. If  $\mathbb{M}_\gamma^p$  is a walk multiplet, then cospectrality of  $\{u, v\}$  is preserved by Theorem 1. For the converse, we assume that  $\{u, v\}$  remain cospectral, that is

$$[H^k]_{u,u} = [H^k]_{v,v} \quad \forall k \in \mathbb{N}, \quad (\text{A.26})$$

where, with  $A_{s;\mathbb{M}}^{(\ell)}$  defined as in Eq. (A.1),

$$[H^k]_{s,s} = [G^k]_{s,s} + \sum_n \sum_{\ell, \ell'} \sum_{m, m' \in \mathbb{M}} [G^\ell]_{s,m} \gamma_m [H^n]_{c,c} \gamma_{m'} [G^{\ell'}]_{m',s} \quad (\text{A.27})$$

$$= [G^k]_{s,s} + \sum_n \sum_{\ell, \ell'} A_{s;\mathbb{M}}^{(\ell)} [H^n]_{c,c} A_{s;\mathbb{M}}^{(\ell')} \quad (\text{A.28})$$

with  $s \in \{u, v\}$ ,  $\ell, \ell' \geq 0$ ,  $n \geq 0$ , and  $\ell + \ell' = k - n - 2$ . We further define

$$D_{\ell, \ell'} \equiv A_{u;\mathbb{M}}^{(\ell)} A_{u;\mathbb{M}}^{(\ell')} - A_{v;\mathbb{M}}^{(\ell)} A_{v;\mathbb{M}}^{(\ell')} = D_{\ell', \ell}, \quad a_n^{(k)} \equiv \sum_{\substack{\ell + \ell' = k - n - 2 \\ \ell, \ell' \geq 0}} D_{\ell, \ell'}. \quad (\text{A.29})$$

Using  $[G^k]_{u,u} = [G^k]_{v,v}$  and substituting the decomposition from Eq. (A.28) into Eq. (A.26) for  $s = u, v$  we arrive at

$$[H^k]_{u,u} - [H^k]_{v,v} = \sum_{n=0}^{k-2} a_n^{(k)} [H^n]_{cc} = 0 \quad \forall k \in \mathbb{N}. \tag{A.30}$$

To prove that  $\mathbb{M}_\gamma^p$  is a multiplet, we must show that (dropping the subscript  $\mathbb{M}$ )

$$A_u^{(\ell)} = p A_v^{(\ell)} \quad \forall \ell \in \mathbb{N}, \quad p \in \{+1, -1\}. \tag{A.31}$$

We prove this by induction. For  $k = 2$  (that is,  $n = 0, \ell = \ell' = 0$ ), Eq. (A.30) yields  $[A_u^{(0)}]^2 = [A_v^{(0)}]^2$  or

$$A_u^{(0)} = p A_v^{(0)}, \tag{A.32}$$

so that Eq. (A.31) is fulfilled in zeroth order  $\ell = 0$ . For the induction step, we assume that Eq. (A.31) is fulfilled up to some arbitrary order  $r$ , that is,

$$A_u^{(\ell)} = p A_v^{(\ell)} \quad \forall \ell \leq r, \tag{A.33}$$

and show that this equation also holds for  $\ell = r + 1$ . To this end, we evaluate Eq. (A.30) for  $k = r + 3$ . For this choice of  $k$ , all but two summands vanish, since the assumption Eq. (A.33) implies that  $D_{\ell,\ell'} = 0$  if  $\ell, \ell' \leq r$ . We thus obtain  $D_{0,r+1} + D_{r+1,0} = 0$ , and since  $D_{0,r+1} = D_{r+1,0}$ , it follows that  $A_u^{(0)} A_u^{(r+1)} = A_v^{(0)} A_v^{(r+1)}$ . Thus, if  $A_u^{(0)} \neq 0$ , due to Eq. (A.32) we get  $A_u^{(r+1)} = p A_v^{(r+1)}$ , as desired.

If  $A_u^{(0)} = 0$ , it follows from Eq. (A.32) that also  $A_v^{(0)} = 0$ , and from Eq. (A.29) we obtain  $D_{0,\ell} = D_{\ell,0} = 0$  for all  $\ell$ . We exploit this fact by evaluating Eq. (A.30) for  $k = r + 4$ , yielding  $D_{1,r+1} = D_{r+1,1} = 0$ . Now, if  $A_u^{(1)} \neq 0$  we again get  $A_u^{(r+1)} = p A_v^{(r+1)}$ , as desired. If  $A_u^{(1)} = 0$ , we proceed to the next higher order  $k = r + 5$ , and so on. In the limiting case where  $A_u^{(\ell)} = 0$  for all  $\ell \leq r$ , we evaluate Eq. (A.30) for  $k = 2(r + 2)$ , which yields  $D_{r+1,r+1} = 0$  and therefore  $A_u^{(r+1)} = p A_v^{(r+1)}$ . This completes the proof of the first part.

For part (ii), we first prove that, if  $c$  is a singlet in  $G$ , then its removal does not break the cospectrality of  $u$  and  $v$ . To this end, we use the fact that

$$[G^k]_{u,u} = [R^k]_{u,u} + \sum_{\ell+n=k} [G^\ell]_{u,c} [G^n]_{c,u} \tag{A.34}$$

$$= [R^k]_{u,u} + \sum_{\ell+n=k} [G^\ell]_{v,c} [G^n]_{c,v} \tag{A.35}$$

and

$$[G^k]_{v,v} = [R^k]_{v,v} + \sum_{\ell+n=k} [G^\ell]_{v,c} [G^n]_{c,v}. \tag{A.36}$$



Since  $u$  and  $v$  are cospectral in  $G$ , it follows that  $[R^k]_{u,u} = [R^k]_{v,v}$  for all  $k$ , so that  $u, v$  are also cospectral in  $R$  if  $c$  is a singlet in  $G$ . For the reverse direction we need to prove that, if the cospectrality of  $u$  and  $v$  is preserved by the removal of a single vertex  $c$ , then this vertex must be a walk singlet. With  $G$  being a cone of  $R$  with tip  $c$ , and demanding  $u, v$  to be cospectral in both  $R$  and  $G$ , combining part (i) of this theorem with Theorem 1 immediately gives that  $c$  must be a singlet in  $G$ .  $\square$

*A.1. Comment: removal of a general multiplet*

Consider removing a walk multiplet  $\mathbb{M}_\gamma^p$  instead of the singlet  $c$ . Then

$$[G^k]_{u,u} = [R^k]_{u,u} + \sum_{\ell+r+n=k} \sum_{m,m' \in \mathbb{M}} [G^\ell]_{u,m} [G^r]_{m,m'} [G^n]_{m',u} \tag{A.37}$$

and cospectrality is preserved in the resulting graph  $R$  only if

$$\sum_{\ell+r+n=k} \sum_{m,m' \in \mathbb{M}} [G^\ell]_{u,m} [G^r]_{m,m'} [G^n]_{m',u} = \sum_{\ell+r+n=k} \sum_{m,m' \in \mathbb{M}} [G^\ell]_{v,m} [G^r]_{m,m'} [G^n]_{m',v} \tag{A.38}$$

for all  $k$ . Thus, cospectrality of a vertex pair in a graph is generally not preserved when removing a multiplet, except if Eq. (A.38) is fulfilled. Assuming a uniform multiplet ( $\gamma_m = 1$  for all  $m \in \mathbb{M}$ ), a special case where this occurs is when all pairs  $\{m, m'\}$  in  $\mathbb{M}$  are cospectral and, for each such pair, all remaining vertices  $m'' \notin \{m, m'\}$  in  $\mathbb{M}$  are singlets relative to  $\{m, m'\}$ . Then  $[G^r]_{m,m'}$  can be factored out of the sums in Eq. (A.38) (taken separately for  $m = m'$  and  $m \neq m'$ ) and equality follows from the multiplet condition Eq. (A.31), for both  $p = \pm 1$ . For a walk quadruplet, e.g., the elements  $[G^r]_{m,m'}$  would have the form

$$[G^r]_{\mathbb{M},\mathbb{M}} = \begin{bmatrix} a_r & b_r & b_r & b_r \\ b_r & a_r & b_r & b_r \\ b_r & b_r & a_r & b_r \\ b_r & b_r & b_r & a_r \end{bmatrix}, \tag{A.39}$$

with the values  $a_r$  and  $b_r$  generally depending on the power  $r$ . For a uniform  $p$ -doublet, this reduces to  $[G^r]_{m,m} = [G^r]_{m',m'}$  and  $[G^r]_{m,m'} = [G^r]_{m',m}$ . This is the case, e.g., for the walk anti-doublet  $\{3, 4\}^-$  in Fig. 3(a) which can be removed without affecting the cospectrality of the pair  $\{1, 2\}$ .

**Theorem 4** (*Eigenvector components on walk multiplets*). *Let  $H = H^\top \in \mathbb{R}^{N \times N}$  represent a graph with a pair of cospectral vertices  $u, v$ , and let its eigenvectors be chosen according to Lemma 1. Then any eigenvector  $\phi$  of  $H$  with eigenvalue  $\lambda$  and nonzero components of odd (even) parity  $p$  on  $u, v$ ,*

$$\phi_u = p \phi_v \neq 0, \quad p \in \{+1, -1\}, \tag{15}$$

fulfills

$$\sum_{m \in \mathbb{M}} \gamma_m \phi_m = 0 \tag{16}$$

if and only if  $\mathbb{M}_\gamma^{-p}$  is a walk multiplet relative to  $u, v$  with even (odd) parity  $-p$  and weight tuple  $\gamma = (\gamma_m)_{m \in \mathbb{M}}$ .

**Proof.** Using the spectral decomposition

$$H = \sum_{\nu=1}^N \lambda_\nu \phi^\nu \phi^{\nu \top} \tag{A.40}$$

of  $H$  in the orthonormal eigenbasis  $\{\phi^\nu\}$ , chosen according to Lemma 1, we have, for  $s \in \{u, v\}$ ,

$$[H^k]_{s,m} = \sum_{\nu=1}^N \lambda_\nu^k \phi_s^\nu \phi_m^\nu = \sum_{\nu \in \mathcal{N}^+} \lambda_\nu^k \phi_s^\nu \phi_m^\nu + \sum_{\nu \in \mathcal{N}^-} \lambda_\nu^k \phi_s^\nu \phi_m^\nu \quad \forall k \in \mathbb{N}, \tag{A.41}$$

where we have collected the labels  $\nu$  of eigenvectors with parity  $\pm 1$  on  $\{u, v\}$  into the set  $\mathcal{N}^\pm$  (the remaining eigenvectors with  $\phi_u^\nu = \phi_v^\nu = 0$  do not appear in the sum). Note that Eq. (A.41) incorporates the spectral decomposition of the identity matrix,  $I_{s,m} = \sum_{\nu=1}^N \phi_s^\nu \phi_m^\nu$  for  $k = 0$ , meaning that  $\lambda_\nu^0 = 1$  even in the case of zero eigenvalues. Next we calculate:

$$[H^k]_{u,m} - p[H^k]_{v,m} = (1 - p) \sum_{\nu \in \mathcal{N}^+} \lambda_\nu^k \phi_u^\nu \phi_m^\nu + (1 + p) \sum_{\nu \in \mathcal{N}^-} \lambda_\nu^k \phi_u^\nu \phi_m^\nu \tag{A.42}$$

$$= 2 \sum_{\nu \in \mathcal{N}^{-p}} \lambda_\nu^k \phi_u^\nu \phi_m^\nu, \tag{A.43}$$

where we used the parity of eigenstates on  $\{u, v\}$ , i.e.  $\phi_u^\nu = \pm \phi_v^\nu$  for  $\nu \in \mathcal{N}^\pm$ , so that the prefactor  $(1 \mp p)$  of the sum over  $\nu \in \mathcal{N}^\pm$  vanishes for  $p = \pm 1$ . Multiplying by  $\gamma_m$  and summing over  $m \in \mathbb{M}$  we obtain

$$B_{u;\mathbb{M}}^{(k)} - p B_{v;\mathbb{M}}^{(k)} = 2 \sum_{\nu \in \mathcal{N}^{-p}} \lambda_\nu^k \phi_u^\nu \sum_{m \in \mathbb{M}} \gamma_m \phi_m^\nu, \tag{A.44}$$

with  $B_{s;\mathbb{M}}^{(k)}$  defined as in Eq. (A.1). It follows that, if Eq. (16) is fulfilled with  $\phi = \phi^\nu$ , for all  $\nu \in \mathcal{N}^{-p}$ , then  $B_{u;\mathbb{M}}^{(k)} = p B_{v;\mathbb{M}}^{(k)}$  for all  $k$  and thus  $\mathbb{M}_\gamma^p$  is a walk multiplet relative to  $\{u, v\}$  with parity  $p$ . Conversely, if  $\mathbb{M}_\gamma^p$  is a multiplet, then the left side of Eq. (A.44)

vanishes for all  $k \in \mathbb{N}$ . For  $k \in \llbracket 0, n_p - 1 \rrbracket$ , where  $n_p \equiv |\mathcal{N}^{-p}|$ , we can write Eq. (A.44) in the matrix form

$$V\vec{c} \equiv \begin{bmatrix} 1 & 1 & \cdots & 1 \\ \lambda_1 & \lambda_2 & \cdots & \lambda_{n_p} \\ \lambda_1^2 & \lambda_2^2 & \cdots & \lambda_{n_p}^2 \\ \vdots & \vdots & \ddots & \vdots \\ \lambda_1^{n_p-1} & \lambda_2^{n_p-1} & \cdots & \lambda_{n_p}^{n_p-1} \end{bmatrix} \begin{bmatrix} c_1 \\ c_2 \\ \vdots \\ c_{n_p} \end{bmatrix} = \begin{bmatrix} 0 \\ 0 \\ \vdots \\ 0 \end{bmatrix}, \quad (\text{A.45})$$

with coefficients  $c_\nu = 2\phi_u^\nu \sum_{m \in \mathbb{M}} \gamma_m \phi_m^\nu$ , where  $V^\top$  is the (square) Vandermonde matrix with  $[V^\top]_{i,j} = \lambda_i^{j-1}$ , yielding

$$\det(V) = \det(V^\top) = \prod_{1 \leq \mu < \nu \leq n_p} (\lambda_\nu - \lambda_\mu). \quad (\text{A.46})$$

Now, our choice of eigenvectors ensures that  $\lambda_\nu \neq \lambda_\mu$  for all  $\nu \neq \mu$  with  $\nu, \mu \in \mathcal{N}^{-p}$ , so that  $\det(V) \neq 0$ . Thus  $V$  is invertible, so that Eq. (A.46) yields  $c_\nu = 0$  for all  $\nu \in \mathcal{N}^{-p}$ , and since  $\phi_u^\nu \neq 0$  we have that  $\sum_{m \in \mathbb{M}} \gamma_m \phi_m^\nu = 0$  for all  $\nu \in \mathcal{N}^{-p}$ , completing the proof.  $\square$

## References

- [1] M.S. Dresselhaus, G. Dresselhaus, A. Jorio, *Group Theory: Application to the Physics of Condensed Matter*, Springer-Verlag, Berlin, Heidelberg, 2008.
- [2] A. Francis, D. Smith, B. Webb, General equitable decompositions for graphs with symmetries, *Linear Algebra Appl.* 577 (2019) 287–316, <https://doi.org/10.1016/j.laa.2019.04.035>.
- [3] C. Godsil, J. Smith, Strongly cospectral vertices, arXiv:1709.07975.
- [4] E. Estrada, P.A. Knight, *A First Course in Network Theory*, Oxford University Press, Oxford, New York, 2015.
- [5] A.J. Schwenk, Almost all trees are cospectral, in: *Proceedings of the Third Annual Arbor Conference*, Academic Press, New York, 1973, pp. 257–307.
- [6] C. Rücker, G. Rücker, Understanding the properties of isospectral points and pairs in graphs: the concept of orthogonal relation, *J. Math. Chem.* 9 (3) (1992) 207–238, <https://doi.org/10.1007/BF01165148>.
- [7] W.C. Herndon, The characteristic polynomial does not uniquely determine molecular topology, *J. Chem. Doc.* 14 (3) (1974) 150–151, <https://doi.org/10.1021/c160054a013>.
- [8] W.C. Herndon, M.L. Ellzey, Isospectral graphs and molecules, *Tetrahedron* 31 (2) (1975) 99–107, [https://doi.org/10.1016/0040-4020\(75\)85002-2](https://doi.org/10.1016/0040-4020(75)85002-2).
- [9] M. Kempton, J. Sinkovic, D. Smith, B. Webb, Characterizing cospectral vertices via isospectral reduction, *Linear Algebra Appl.* 594 (2020) 226–248, <https://doi.org/10.1016/j.laa.2020.02.020>.
- [10] R.A. Brualdi, D. Cvetkovic, *A Combinatorial Approach to Matrix Theory and Its Applications*, CRC Press, 2008.
- [11] C. Godsil, Controllable subsets in graphs, *Ann. Comb.* 16 (4) (2012) 733–744, <https://doi.org/10.1007/s00026-012-0156-3>.
- [12] C.D. Meyer, *Matrix Analysis and Applied Linear Algebra*, Society for Industrial and Applied Mathematics, USA, 2000.
- [13] B.L. Douglas, J.B. Wang, A classical approach to the graph isomorphism problem using quantum walks, *J. Phys. A, Math. Theor.* 41 (7) (2008) 075303, <https://doi.org/10.1088/1751-8113/41/7/075303>.
- [14] F. Liu, J. Siemons, Unlocking the walk matrix of a graph, arXiv:1911.00062.
- [15] O. Eisenberg, M. Kempton, G. Lippner, Pretty good quantum state transfer in asymmetric graphs via potential, *Discrete Math.* 342 (10) (2019) 2821–2833, <https://doi.org/10.1016/j.disc.2018.10.037>.

- [16] M. Röntgen, N.E. Palaiodimopoulos, C.V. Morfonios, I. Brouzos, M. Pyzh, F.K. Diakonou, P. Schmelcher, Designing pretty good state transfer via isospectral reductions, *Phys. Rev. A* 101 (4) (2020) 042304, <https://doi.org/10.1103/PhysRevA.101.042304>.
- [17] D. Smith, B. Webb, Hidden symmetries in real and theoretical networks, *Physica A* 514 (2019) 855–867, <https://doi.org/10.1016/j.physa.2018.09.131>.
- [18] M. Röntgen, N.E. Palaiodimopoulos, C.V. Morfonios, I. Brouzos, M. Pyzh, F.K. Diakonou, P. Schmelcher, Designing pretty good state transfer via isospectral reductions, *Phys. Rev. A* 101 (4) (2020) 042304, <https://doi.org/10.1103/PhysRevA.101.042304>.
- [19] K. Benidis, Y. Sun, P. Babu, D.P. Palomar, Orthogonal sparse PCA and covariance estimation via procrustes reformulation, *IEEE Trans. Signal Process.* 64 (23) (2016) 6211–6226, <https://doi.org/10.1109/TSP.2016.2605073>.
- [20] O. Teke, P.P. Vaidyanathan, Uncertainty principles and sparse eigenvectors of graphs, *IEEE Trans. Signal Process.* 65 (20) (2017) 5406–5420, <https://doi.org/10.1109/TSP.2017.2731299>.
- [21] M. Röntgen, C.V. Morfonios, P. Schmelcher, Compact localized states and flat bands from local symmetry partitioning, *Phys. Rev. B* 97 (3) (2018) 035161, <https://doi.org/10.1103/PhysRevB.97.035161>.
- [22] W. Maimaiti, S. Flach, A. Andreanov, Universal  $d = 1$  flat band generator from compact localized states, *Phys. Rev. B* 99 (12) (2019) 125129, <https://doi.org/10.1103/PhysRevB.99.125129>.
- [23] P.J. Pemberton-Ross, A. Kay, S.G. Schirmer, Quantum control theory for state transformations: dark states and their enlightenment, *Phys. Rev. A* 82 (4) (2010) 042322, <https://doi.org/10.1103/PhysRevA.82.042322>.
- [24] T.P. Le, L. Donati, S. Severini, F. Caruso, How to suppress dark states in quantum networks and bio-engineered structures, *J. Phys. A, Math. Theor.* 51 (36) (2018) 365306, <https://doi.org/10.1088/1751-8121/aad3e6>.
- [25] C.D. Godsil, B.D. McKay, Constructing cospectral graphs, *Aequ. Math.* 25 (1) (1982) 257–268, <https://doi.org/10.1007/BF02189621>.
- [26] C.V. Morfonios, P.A. Kalozoumis, F.K. Diakonou, P. Schmelcher, Nonlocal discrete continuity and invariant currents in locally symmetric effective Schrödinger arrays, *Ann. Phys.* 385 (2017) 623–649, <https://doi.org/10.1016/j.aop.2017.07.019>.
- [27] M. Röntgen, C. Morfonios, F. Diakonou, P. Schmelcher, Non-local currents and the structure of eigenstates in planar discrete systems with local symmetries, *Ann. Phys.* 380 (2017) 135–153, <https://doi.org/10.1016/j.aop.2017.03.011>.

## Latent Symmetry Induced Degeneracies

M. Röntgen<sup>1</sup>, M. Pyzh<sup>1</sup>, C. V. Morfonios<sup>1</sup>, N. E. Palaodimopoulos<sup>2</sup>, F. K. Diakonos<sup>2</sup>, and P. Schmelcher<sup>1,3</sup>

<sup>1</sup>Zentrum für optische Quantentechnologien, Universität Hamburg, Luruper Chaussee 149, 22761 Hamburg, Germany

<sup>2</sup>Department of Physics, University of Athens, 15771 Athens, Greece

<sup>3</sup>The Hamburg Centre for Ultrafast Imaging, Universität Hamburg, Luruper Chaussee 149, 22761 Hamburg, Germany



(Received 26 November 2020; revised 11 February 2021; accepted 31 March 2021; published 3 May 2021)

Degeneracies in the energy spectra of physical systems are commonly considered to be either of accidental character or induced by symmetries of the Hamiltonian. We develop an approach to explain degeneracies by tracing them back to symmetries of an isospectral effective Hamiltonian derived by subsystem partitioning. We provide an intuitive interpretation of such latent symmetries by relating them to corresponding local symmetries in the powers of the underlying Hamiltonian matrix. As an application, we relate the degeneracies induced by the rotation symmetry of a real Hamiltonian to a non-Abelian latent symmetry group. It is demonstrated that the rotational symmetries can be broken in a controlled manner while maintaining the underlying more fundamental latent symmetry. This opens up the perspective of investigating accidental degeneracies in terms of latent symmetries.

DOI: 10.1103/PhysRevLett.126.180601

*Introduction.*—Identifying the origin of spectral degeneracies in quantum systems is of fundamental importance for the understanding and control of their structural and dynamical properties. Degenerate states are at the heart of spectacular phenomena like the Jahn-Teller effect [1] and the quantum Hall effect [2,3] as well as the electromagnetic response of, e.g., atoms or molecules [4,5] in general. In lattice systems designed macroscopic degeneracies can realize flat bands within a variety of setups including optical lattices, photonic waveguide arrays, and superconducting networks [6]. Further, degeneracies in the form of conical intersections of molecular potential energy surfaces play a central role for ultrafast dynamical decay processes [7,8] and are responsible, e.g., for molecular self-repair mechanisms in photobiology [9].

When degeneracies occur in the energy spectrum, the first place to seek their origin is commonly the group of geometrical symmetry operations commuting with the underlying Hamiltonian. Prominent examples for such symmetries are the molecular point group in chemistry or the space group in crystallography. If this group is non-Abelian—that is, if at least two symmetry operations do not commute with each other—it induces degeneracies of multiplicities determined by the dimensions of the group’s irreducible representations. More challenging is the reverse question of assigning degeneracies to a symmetry group with a physical significance [10,11]. A famous example of a physically significant, yet not obvious, symmetry from the early days of quantum theory is the  $SO(4)$  symmetry leading to the conservation of the Runge-Lenz vector in the hydrogen atom [12]. If no such physically meaningful symmetry group can be found, the degeneracy is traditionally called accidental [13]. This often occurs for

systems with several or many degrees of freedom where eigenenergies happen to coincide at some location in the corresponding parameter space, intersections of molecular potential energy surfaces being a typical example [14].

In this work, we promote a different viewpoint on assigning degeneracies to symmetries of the system. Instead of performing a symmetry analysis of the Hamiltonian itself, we do this for the effective Hamiltonian obtained from the original one by reducing it onto a subsystem while retaining the energy spectrum. We note that its core property—the preservation of the energy spectrum—clearly distinguishes this approach from those which analyze the symmetries of an effective model obtained by truncation or a mean-field ansatz. Focusing on generic discrete models, we here show how geometrical symmetries of the isospectrally reduced Hamiltonian induce spectral degeneracies for the original system. Such latent symmetries, as introduced recently in graph theory [15], are generally not apparent in the original system at hand. In fact, as we show here, they are directly linked to corresponding local symmetries, though in all powers of the original Hamiltonian. Navigating through the proposed concepts, visualized by minimalistic examples, we (i) show how non-Abelian latent symmetries are necessarily induced by rotation symmetries of a real Hamiltonian, and (ii) demonstrate that these latent symmetries, along with their induced degeneracies, can be preserved even when breaking the original rotational symmetry. Lastly, we link a special case of latent symmetry to what we call here a generalized exchange symmetry of the Hamiltonian.

*Degeneracies from latent symmetries.*—The concepts and results developed in this work are valid for generic setups described by a finite-dimensional matrix. This matrix can be drawn from a wide range of physical

platforms: It could represent a Bloch Hamiltonian of a tight-binding lattice [16], a molecular Hückel Hamiltonian [17,18], a multiport scattering matrix [19], or very generally the matrix  $H$  occurring in (linearized) dynamical problems [20], such as coupled oscillators [21]. To convey the main ideas in a transparent way, we will illustrate it by means of minimalistic prototypical setups.

In order to reveal the latent symmetries of a general complex matrix  $H$ , we will rely on a dimensional reduction of  $H$  which preserves the eigenvalue spectrum. This *isospectral* reduction is defined as [15,22]

$$\mathcal{R}_S(H, \lambda) = H_{SS} - H_{S\bar{S}}(H_{\bar{S}\bar{S}} - \lambda I)^{-1}H_{\bar{S}S}, \quad (1)$$

whereby  $S$  is a set sites and  $\bar{S}$  denotes the complement set of all other sites of the given setup.  $H_{SS}$  and  $H_{\bar{S}\bar{S}}$  denote the respective Hamiltonians of the sub-systems consisting only of the sites in  $S$  or  $\bar{S}$ .  $H_{\bar{S}S}$  and  $H_{S\bar{S}}$  represent the coupling between the two sub-systems, and  $I$  is the identity matrix. The isospectral reduction  $\mathcal{R}_S(H, \lambda)$  is equivalent to an effective Hamiltonian gained from a subsystem partitioning of  $H$  [23], and its entries are rational functions of the parameter  $\lambda$ .

A Hamiltonian  $H$  is *latently symmetric* if there exists an isospectral reduction  $\mathcal{R}_S(H, \lambda)$  with a symmetry, that is, which commutes with a group of matrices  $\{M\}$  independent of  $\lambda$ . We now demonstrate this concept by means of the simple 6-site Hamiltonian  $H$  depicted in fig. 1(a). This Hamiltonian illustrates the minimal prototype of a system with non-trivial latent symmetry.  $H$  is parametrized by three real coupling parameters  $h_i \neq 0$ ,  $i \in \{1, 2, 3\}$  and two on-site potentials  $v_1, v_2$ . The eigenvalue spectrum of  $H$  contains two doubly degenerate eigenvalues for any choice of these parameters. To explain these degeneracies in terms of latent symmetries of  $H$ , we reduce it by means of Eq. (1) over  $S = \{1, 2, 3\}$ . This yields the symmetric matrix

$$\mathcal{R}_{S=\{1,2,3\}}(H, \lambda) = \begin{pmatrix} a & b & b \\ b & a & b \\ b & b & a \end{pmatrix}, \quad (2)$$

with  $a = v_1 + (h_1^2 + h_2^2/\lambda - v_2)$ ,  $b = (h_1 h_2/\lambda - v_2) + h_3$ . A graphical representation of Eq. (2) is depicted in Fig. 1(b). The graph is highly symmetric and is invariant under six symmetry operations: three rotations and three reflections. These six operations form the so-called dihedral group  $D_3$ , which is non-Abelian.

We now draw a general connection between non-Abelian latent symmetries of a given Hamiltonian  $H$  and its eigenvalue spectrum. To this end, we use the fact that *each* of the so-called ‘‘nonlinear’’ eigenvalues belonging to  $\mathcal{R}_S(H, \lambda)$  in Eq. (2), defined as the solutions  $\lambda_j$  to the nonlinear eigenvalue problem

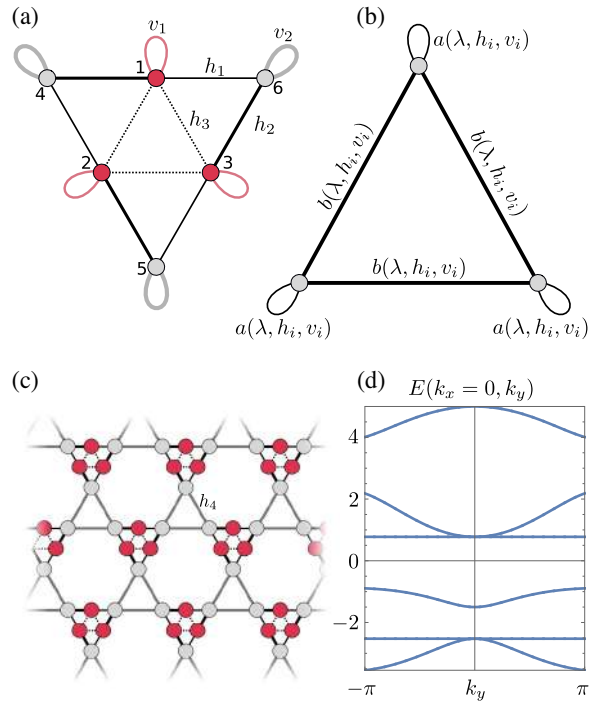


FIG. 1. (a) A six-site Hamiltonian  $H$  which features a non-Abelian  $D_3$  permutation symmetry if  $h_1 = h_2$ , but only an Abelian  $C_3$  permutation symmetry if  $h_1 \neq h_2$ . A line between two different sites  $i, j$  corresponds to a nonvanishing matrix element  $H_{i,j}$ , taking parametric values  $h_1, h_2$ , or  $h_3$  (indicated by different line styles). Loops connecting a site to itself correspond to diagonal matrix elements  $H_{i,i}$  with parametric values  $v_1$  or  $v_2$ . (b) The result of the isospectral reduction of  $H$  over the three red sites  $S = \{1, 2, 3\}$ . The reduced Hamiltonian [Eq. (2)] features a  $D_3$  permutation symmetry for any choice of  $\lambda, h_i$ , or  $v_i$ . (c) A modified kagome lattice with  $H$  as a unit cell. The band structure of this lattice for  $k_x = 0$  is plotted in (d) for  $h_1 = 4/3, h_2 = 5/3, h_3 = 0.7, h_4 = 3/2, v_1 = 0$ .

$$\text{Det}[\mathcal{R}_S(H, \lambda_j) - \lambda_j I] = 0 \quad (3)$$

is also an eigenvalue of  $H$  [22]. Moreover, whenever the eigenvalue spectra of  $H$  and of the subsystem  $H_{\bar{S}\bar{S}}$  do not intersect, the eigenvalue spectra of  $\mathcal{R}_S(H, \lambda)$  and  $H$  coincide [22]. This motivates calling  $\mathcal{R}_S(H, \lambda)$  an ‘‘isospectral reduction.’’ From the above considerations, it is clear that degeneracies in the eigenvalue spectrum of  $\mathcal{R}_S(H, \lambda)$  necessarily correspond to degeneracies in the eigenvalue spectrum of  $H$ . Moreover, and as we show in Sec. I. of the Supplemental Material [24], non-Abelian symmetries of the isospectral reduction  $\mathcal{R}_S(H, \lambda)$  lead to degeneracies in the spectrum of its nonlinear eigenvalues. Thus, non-Abelian latent symmetries of  $H$  necessarily induce degeneracies onto the eigenvalue spectrum of  $H$ . Specifically, lower bounds on the multiplicity of  $H$ ’s eigenvalues are given by dimensions of the irreducible

representations of the underlying non-Abelian symmetry group of  $\mathcal{R}_S(H, \lambda)$ .

We emphasize that the above statements are completely general in the sense that they are valid for all kinds of latent symmetries (not just permutations), and for arbitrary (even non-Hermitian) diagonalizable matrices  $H$ . Irrespective of this applicability to general symmetries, we concentrate on the special case of permutation symmetries throughout this Letter. After all, permutation symmetries are among the easiest to detect—often by bare eye—and thus provide a convenient workhorse for depicting the main features of latent symmetries.

In the above, we have explained the spectral degeneracies of the prototype example Fig. 1(a) in terms of its latent symmetries. This system has been deliberately designed to be as simple as possible in order to convey the main ideas of latent symmetries. The underlying concept is, however, not limited to such basic examples, but can be applied to larger systems, as we demonstrate now. Figure 1(c) shows a lattice built by taking the prototype Hamiltonian  $H$  of Fig. 1(a) as a unit cell. The band structure of this lattice is depicted in Fig. 1(d). At the  $\Gamma$  point, that is, at  $\mathbf{k} = 0$ , the corresponding Bloch-Hamiltonian features the same latent symmetries as  $H$  in Fig. 1(a). This explains the two double degeneracies in the band structure [24]. Interestingly, the lattice further hosts two flat bands, which in general can also be designed through latent symmetries [30].

*Latent  $D_n$  permutation symmetries.*—Let us now examine the symmetries of the prototype example of Fig. 1 in more detail. This setup is invariant under permutations which cyclically permute sets of three sites, graphically represented by rotations of multiples of  $2\pi/3$ . These rotations form the abelian cyclic group of order 3, denoted by  $C_3$ . As we have seen above, the setup also featured a latent  $D_3$  permutation symmetry, and this is no coincidence. Indeed, as we show in the Supplemental Material, every  $C_n$ -permutation symmetric real Hamiltonian  $H$  features a latent  $D_n$  permutation symmetry [24]. As is well known, the dihedral group  $D_n$  is non-Abelian for  $n \geq 3$ , so that the underlying Hamiltonian automatically features degeneracies. This gives an alternative explanation to those degeneracies, which are classically understood in terms of the combination of the Abelian group  $C_{n \geq 3}$  and the real valuedness of  $H$  which corresponds to a time-reversal symmetry of  $H$  [31].

*Latent  $D_n$  symmetries without any permutation symmetries.*—Above we have stated that a  $C_n$  permutation symmetry of a real Hamiltonian is a sufficient condition for a latent  $D_n$  permutation symmetry. However, it is not a necessary condition. Indeed, we demonstrate in the following the versatility of latent symmetries by showing that they can even exist when the underlying Hamiltonian  $H$  has no permutation symmetry at all. Figure 2(a) shows an example of such a Hamiltonian  $H$ , which can also be interpreted as

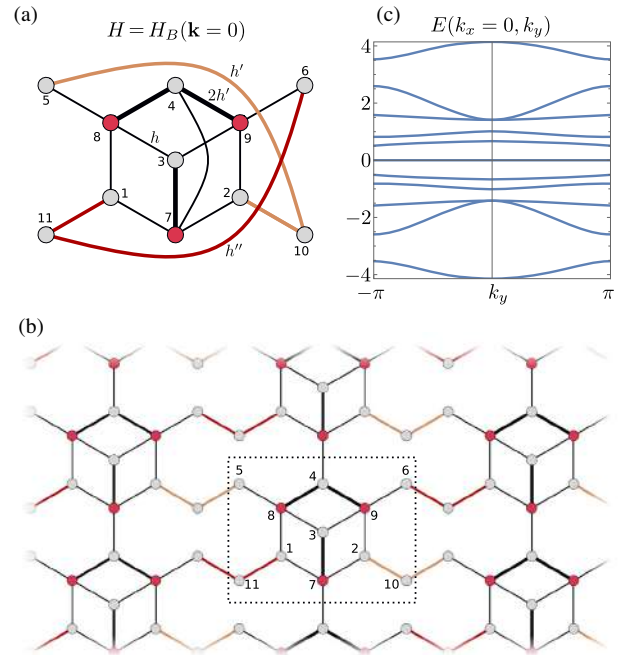


FIG. 2. (a) A Hamiltonian that features no permutation symmetry for  $hh'h'' \neq 0$  and  $h' \neq h''$ . It does, however, feature a latent  $D_3$  permutation symmetry that becomes visible when reducing over  $S = \{7, 8, 9\}$ . (b) A lattice whose Bloch-Hamiltonian  $H_B$  at  $\mathbf{k} = 0$  equals  $H$ . The dotted box shows the lattice unit cell. (c) The band structure of this lattice for  $k_x = 0$ ,  $h = 1$ ,  $h' = 1/2$ ,  $h'' = 3/4$ .

the Bloch Hamiltonian  $H_B(\mathbf{k} = 0)$  of the lattice in Fig. 2(b) at crystal momentum  $\mathbf{k} = 0$ . A detailed derivation of this lattice is shown in Sec. V of the Supplemental Material [24]. For  $hh'h'' \neq 0$  and  $h' \neq h''$ ,  $H$  does not feature any permutation symmetry. However, for any choice of those three hopping parameters, it features a latent  $D_3$  symmetry which becomes visible when reducing  $H$  over the three red sites  $S = \{7, 8, 9\}$ . As a result of this non-Abelian latent symmetry,  $H$  has at least one doubly degenerate eigenvalue pair for any choice of  $h'$  and  $h''$ . We can now understand the two double degeneracies in the band structure [depicted in Fig. 2(c)] of the lattice of Fig. 2(b) at  $k_x = k_y = 0$ : At this point, the Bloch-Hamiltonian is given by  $H$ , so that it features a latent  $D_3$  symmetry and therefore also degeneracies.

Interestingly, when setting  $h' = h''$ ,  $H$  features a  $C_2$  permutation symmetry, graphically corresponding to a reflection about the line connecting the sites 4 and 7. One can thus say that  $h'$  and  $h''$  are control parameters for a symmetry breaking, and since  $H$  features a latent  $D_3$  permutation symmetry for any choice of  $h, h', h''$ , this opens the perspective of investigating and understanding symmetry breaking in terms of latent symmetries. In Sec. III. of the Supplemental Material, we show how latent symmetry preserving modifications (which may break permutation symmetries) can be derived [24].

*Linking latent to local symmetries.*—One might wonder if a latent symmetry leaves some recognizable traces in the original Hamiltonian. This is indeed the case: By expressing  $\mathcal{R}_S(H, \lambda)$  as a power series in  $\lambda$  and subsequently analyzing it order by order, one can show [24] that

$$[\mathcal{R}_S(H, \lambda), M] = 0 \Leftrightarrow [(H^k)_{SS}, M] = 0 \quad \forall k, \quad (4)$$

where  $M$  denotes a symmetry operation. In other words, symmetries of  $\mathcal{R}_S(H, \lambda)$  correspond to local symmetries [32,33] of  $H$  in all matrix powers. In particular,  $H$  itself has to be locally symmetric. Indeed, for our introductory example of Fig. 1(a) and  $S = \{1, 2, 3\}$ , we see that  $H_{SS}$  denotes the inner triangle, which obviously features the same symmetries as the corresponding isospectral reduction  $\mathcal{R}_S(H, \lambda)$  depicted in Fig. 1(b).

Equation (4) can be used to facilitate the search for latent permutation symmetries. To this end, let us assume that we are given a (possibly large) Hamiltonian  $H$  and want to check if it features a latent permutation symmetry as the one depicted in Fig. 1(b). In other words, we look for a set of three sites  $S = \{u, v, w\}$  such that  $\mathcal{R}_S(H, \lambda)$  has the form of Eq. (2). Now, instead of computing and checking all possible isospectral reductions of  $H$  over three sites, we can use Eq. (4) to see that any candidate sites  $u, v, w$  necessarily have to fulfill  $(H^k)_{u,u} = (H^k)_{v,v} = (H^k)_{w,w}$  for all  $k$ . This condition can be augmented by employing the Cayley-Hamilton theorem, which states that any matrix power  $H^{k \geq N}$  ( $N$  being the dimension of  $H$ ) is a polynomial in smaller powers. Thus, by computing the matrix powers  $H, H^2, \dots, H^{N-1}$ —the cost of which grows polynomially with  $N$ —and grouping the sites accordingly, the number of possible candidate sites  $\{u, v, w\}$  can be drastically reduced. In particular, if there is any  $k$  such that  $H^k$  features no three sites with equal on-site potential  $(H^k)_{i,i}$ , a latent symmetry of the kind Eq. (2) is impossible.

*Generalized exchange symmetries.*—Having demonstrated the relation of latent symmetries to symmetries of the subsystem  $H_{SS}$  and to degeneracies of  $H$ , we finally relate a subclass of latent symmetries to symmetries of the original Hamiltonian  $H$ . This subclass consists of latent permutation symmetries of real Hamiltonians. Using graph-theoretical tools [34,35], such Hamiltonians can be shown to necessarily feature what we call here a *generalized exchange symmetry* (GES). A GES is an orthogonal symmetric matrix  $Q^{(i,j)}$  fulfilling  $[Q^{(i,j)}, H] = 0$  and  $(Q^{(i,j)})^2 = I$  and which exchanges the two sites  $i, j$  while acting on the remaining sites as an orthogonal transformation. In the special case when this transformation is a pure permutation,  $Q^{(i,j)}$  becomes a normal exchange symmetry, i.e., it acts on each site either as the identity or as an exchange operator. To provide an impression of the GESs, we explicitly computed—by solving the equations derived from its defining properties— $Q^{(1,2)}$  for the Hamiltonian of Fig. 1(a):

$$Q^{(1,2)} = \begin{pmatrix} 0 & 1 & 0 & 0 & 0 & 0 \\ 1 & 0 & 0 & 0 & 0 & 0 \\ 0 & 0 & 1 & 0 & 0 & 0 \\ 0 & 0 & 0 & \frac{h_1 h_2}{d} & 1 - \frac{h_1^2}{d} & \frac{h_1(h_1 - h_2)}{d} \\ 0 & 0 & 0 & 1 - \frac{h_1^2}{d} & \frac{h_1(h_1 - h_2)}{d} & \frac{h_1 h_2}{d} \\ 0 & 0 & 0 & \frac{h_1(h_1 - h_2)}{d} & \frac{h_1 h_2}{d} & 1 - \frac{h_1^2}{d} \end{pmatrix} \quad (5)$$

with  $d = h_1^2 - h_2 h_1 + h_2^2$ . Note that for the case of  $h_1 = h_2$  the GES  $Q^{(1,2)}$  becomes the ordinary exchange symmetry which permutes (1,2), (5,6), and leaves 3 and 4 invariant, and therefore describes the reflection about the line that connects sites 3 and 4 in Fig. 1. However, in the case where  $h_1 \neq h_2$ , this pure permutation symmetry is broken, whereas the more abstract GES persists. We note that, while the GESs as an abstract symmetry class persists, the *matrix entries* of  $Q^{(1,2)}$  depend on  $h_1$  and  $h_2$ . This is an important difference to the latent  $D_3$  permutation symmetry of  $H$ , whose matrix representation is independent of the values of  $h_i$ .

Finally, let us note that one can use the above insights to prove the existence of degeneracies for real latently  $D_{n \geq 3}$  permutation symmetric Hamiltonians in yet another way [24]. Such Hamiltonians feature more than one GES, and by explicitly constructing them it can be shown that at least two of them do not commute with each other. Since the Hamiltonian  $H$  commutes with both of these GESs, it directly follows that  $H$  has to have at least one degenerate eigenvalue. It remains an open task to classify GESs using group-theoretical tools.

*Conclusions.*—We have provided a theoretical framework which connects non-Abelian latent symmetries of generic discrete models to their spectral degeneracies. For the important class of latent permutation symmetries, our results may allow for a geometrical explanation of apparently accidental degeneracies. Moreover, by identifying latent symmetries as local symmetries of all powers of the Hamiltonian, our results additionally suggest a convenient method for finding these latent symmetries. We further demonstrate that it is possible to break symmetries of an original Hamiltonian while preserving its latent symmetry. This may inspire techniques to modify—or probe—a given system asymmetrically without affecting its degeneracy.

Our considerations apply quite generally to physical systems possessing a discrete representation in terms of a finite-dimensional matrix. This includes, among others, tight-binding models, molecular Hamiltonians in truncated orbital bases, and multiport scattering setups. We therefore envision the applicability of our results in a broad variety of setups, contributing to the better understanding, design, and control of spectral degeneracies beyond conventional symmetries.



M. P. is thankful to the ‘Studienstiftung des deutschen Volkes’ for financial support in the framework of a scholarship. The authors thank G. M. Koutentakis and J. Schirmer for valuable comments on the manuscript.

M. R., M. P., and C. V. M. contributed equally to this work.

- 
- [1] I. Bersuker, *The Jahn-Teller Effect* (Cambridge University Press, Cambridge, England, 2010).
- [2] Z. F. Ezawa, *Quantum Hall Effects: Recent Theoretical and Experimental Developments*, 3rd ed. (World Scientific, Singapore, 2013).
- [3] K. von Klitzing, Quantum Hall effect: Discovery and application, *Annu. Rev. Condens. Matter Phys.* **8**, 13 (2017).
- [4] W. D. Phillips, Nobel Lecture: Laser cooling and trapping of neutral atoms, *Rev. Mod. Phys.* **70**, 721 (1998).
- [5] *The Role of Degenerate States in Chemistry*, edited by M. Baer, G. D. Billing, I. Prigogine, and S. A. Rice, Advances in Chemical Physics Vol. 124 (Wiley-Interscience, New York, 2002).
- [6] D. Leykam, A. Andreanov, and S. Flach, Artificial flat band systems: From lattice models to experiments, *Adv. Phys.* **3**, 1473052 (2018).
- [7] W. Domcke, D. R. Yarkony, and H. Köppel, *Conical Intersections: Electronic Structure, Dynamics and Spectroscopy*, Advanced Series in Physical Chemistry, Vol. 15 (World Scientific, Singapore, 2004).
- [8] H. Köppel, W. Domcke, and L. S. Cederbaum, Multimode molecular dynamics beyond the Born-Oppenheimer approximation, in Advances in Chemical Physics (John Wiley & Sons, Ltd, New York, 1984), Vol. 57, pp. 59–246.
- [9] W. Domcke and D. R. Yarkony, Role of conical intersections in molecular spectroscopy and photoinduced chemical dynamics, *Annu. Rev. Phys. Chem.* **63**, 325 (2012).
- [10] H. V. McIntosh, On accidental degeneracy in classical and quantum mechanics, *Am. J. Phys.* **27**, 620 (1959).
- [11] H. McIntosh, Symmetry and degeneracy, in *Group Theory and Its Applications* (Academic Press, New York, 1971), Vol. 2.
- [12] V. Fock, Zur Theorie des Wasserstoffatoms, *Z. Phys.* **98**, 145 (1935).
- [13] J. von Neumann and E. Wigner, über das Verhalten von Eigenwerten bei adiabatischen Prozessen, *Phys. Z.* **30**, 467 (1929).
- [14] D. R. Yarkony, Diabolical conical intersections, *Rev. Mod. Phys.* **68**, 985 (1996).
- [15] D. Smith and B. Webb, Hidden symmetries in real and theoretical networks, *Physica (Amsterdam)* **514A**, 855 (2019).
- [16] F. Crasto de Lima and G. J. Ferreira, High-degeneracy points protected by site-permutation symmetries, *Phys. Rev. B* **101**, 041107(R) (2020).
- [17] W. C. Herndon and M. L. Ellzey, Isospectral graphs and molecules, *Tetrahedron* **31**, 99 (1975).
- [18] I. N. Levine, *Quantum Chemistry*, 5th ed. (Prentice Hall, New Jersey, NJ, 2000).
- [19] O. Richoux, V. Achilleos, G. Theocharis, I. Brouzos, and F. Diakonou, Multi-functional resonant acoustic wave router, *J. Phys. D* **53**, 235101 (2020).
- [20] O. Galor, *Discrete Dynamical Systems* (Springer-Verlag, Berlin, Heidelberg, 2007).
- [21] E. B. Wilson, J. C. Decius, and P. Cross, *Molecular Vibrations: The Theory of Infrared and Raman Vibrational Spectra*, revised edition ed. (Dover Publ Inc, New York, 1980).
- [22] L. Bunimovich and B. Webb, *Isospectral Transformations: A New Approach to Analyzing Multidimensional Systems and Networks* (Springer, New York, 2014).
- [23] G. Grosso and G. P. Parravicini, *Solid State Physics* (Academic Press, New York, 2013).
- [24] See Supplemental Material at <http://link.aps.org/supplemental/10.1103/PhysRevLett.126.180601> for mathematical details and proofs of the results presented here, which includes also Refs [25–29].
- [25] C. V. Morfonios, M. Pyzh, M. Röntgen, and P. Schmelcher, Cospectrality preserving graph modifications and eigenvector properties via walk equivalence of vertices, *Linear Algebra Appl.* **624**, 53 (2021).
- [26] A. Chan, G. Coutinho, W. Drazen, O. Eisenberg, C. Godsil, G. Lippner, M. Kempton, C. Tamon, and H. Zhan, Fundamentals of fractional revival in graphs, [arXiv:2004.01129](https://arxiv.org/abs/2004.01129).
- [27] O. Eisenberg, M. Kempton, and G. Lippner, Pretty good quantum state transfer in asymmetric graphs via potential, *Discrete Math.* **342**, 2821 (2019).
- [28] G. J. Tee, Eigenvectors of block circulant and alternating circulant matrices, *Res. Lett. Inf. Math. Sci.* **8**, 123 (2005).
- [29] D. Vanderbilt, *Berry Phases in Electronic Structure Theory: Electric Polarization, Orbital Magnetization and Topological Insulators* (Cambridge University Press, Cambridge, England, 2018).
- [30] C. V. Morfonios, M. Röntgen, M. Pyzh, and P. Schmelcher, Flat bands by latent symmetry, [arXiv:2102.12446](https://arxiv.org/abs/2102.12446).
- [31] L. D. Landau, E. M. Lifshitz, and J. Menzies, *Quantum Mechanics: Non-Relativistic Theory*, 3rd ed. (Elsevier Science & Technology, Jordan Hill, United Kingdom, 1981).
- [32] P. A. Kalozoumis, C. Morfonios, F. K. Diakonou, and P. Schmelcher, Invariants of Broken Discrete Symmetries, *Phys. Rev. Lett.* **113**, 050403 (2014).
- [33] P. A. Kalozoumis, C. Morfonios, F. K. Diakonou, and P. Schmelcher, Local symmetries in one-dimensional quantum scattering, *Phys. Rev. A* **87**, 032113 (2013).
- [34] M. Kempton, J. Sinkovic, D. Smith, and B. Webb, Characterizing cospectral vertices via isospectral reduction, *Linear Algebra Appl.* **594**, 226 (2020).
- [35] C. Godsil and J. Smith, Strongly cospectral vertices, [arXiv:1709.07975](https://arxiv.org/abs/1709.07975).

## Supplemental Material

In this supplemental material, mathematical details of the proofs for the results presented in the main text as well as the Bloch-Hamiltonians for the lattices depicted in Figs. 1 and 2 of the main text are included. It is structured as follows. In section I we derive a connection between latent symmetries of  $H$  and degeneracies in its eigenvalue spectrum. Section II relates latent symmetries of  $H$  to local symmetries of  $H$  in all matrix powers. In section III we develop the concept of complement multiplets, which allow one to perturb a Hamiltonian featuring a latent permutation symmetry without breaking this symmetry. In section IV we provide details on the generalized exchange symmetries. Section V shows the derivation of the Bloch Hamiltonians for the lattices of Figs. 1 and 2 of the main text. Section VI contains auxiliary Lemmata used in proofs of Theorems in this Supplemental Material.

Throughout the following,  $\mathbb{L}$  denotes the set of values of  $\lambda$  for which the isospectral reduction  $\mathcal{R}_S(H, \lambda)$  is defined.

### I. THE RELATION BETWEEN THE SYMMETRIES OF THE ISOSPECTRAL REDUCTION AND DEGENERATE EIGENVALUES OF THE HAMILTONIAN

In the main part of this work, it was stated that non-abelian latent symmetries of a Hamiltonian necessarily induce degeneracies onto its eigenvalue spectrum. A key in proving this statement lies in the application of representation theoretical tools to the isospectral reduction, which we shall do in the following

#### Theorem 1: Symmetries of the isospectral reduction and degeneracies of $H$

Let  $\mathcal{R}_S(H, \lambda)$  be the isospectral reduction of the Hamiltonian  $H$  over a set of sites  $S$ , and let  $G$  be a finite group with elements  $\{g\}$  represented by matrices  $\{\Gamma(g)\}$ , and let  $\mathcal{R}_S(H, \lambda)$  commute with all of them, i.e.,  $[\mathcal{R}_S(H, \lambda), \Gamma(g)] = 0 \forall \lambda \in \mathbb{L}, r \in G$ .

Let  $\Gamma$  be decomposed into  $n$  pairwise non-equivalent irreducible representations  $\tilde{\Gamma}_i$  of  $G$  with multiplicities  $a_i \neq 0$  and with dimensions  $d_i$ , that is, there exists an invertible matrix  $A$  such that

$$\Gamma'(g) = A \Gamma(g) A^{-1} = \bigoplus_{i=1}^n \tilde{\Gamma}_i^{\oplus a_i}(g) \forall g \in G \quad (1)$$

where  $\oplus$  denotes the direct sum, and  $M^{\oplus k} = \underbrace{M \oplus \dots \oplus M}_{k\text{-times}}$ . Then for each  $a_i$  the eigenvalue spectrum of  $H$  contains *at least*  $a_i$  eigenvalues that are (individually)  $d_i$ -fold degenerate.

*Proof.*  $\mathcal{R}_S(H, \lambda)$  represents a whole family of matrices parametric in  $\lambda$ . Each matrix in  $\mathcal{R}_S(H, \lambda)$  commutes with the representation  $\Gamma(g)$  of each group element  $g$  of the finite symmetry group  $G$ . Thus, employing Schur's lemma, it is easy to prove that for each  $\lambda \in \mathbb{L}$ ,  $\mathcal{R}_S(H, \lambda)$  is block-diagonalized by the same similarity transformation

$$\mathcal{R}'_S(H, \lambda) = A \mathcal{R}_S(H, \lambda) A^{-1} = \bigoplus_{i=1}^n B_i(\lambda) \quad (2)$$

with  $B_i(\lambda)$  being a  $(a_i d_i)$ -dimensional matrix. Moreover, due to Schur's lemma, each  $B_i(\lambda)$  can be further block-diagonalized by permuting its rows and columns, thereby yielding

$$\mathcal{R}''_S(H, \lambda) = P \mathcal{R}'_S(H, \lambda) P^{-1} = \bigoplus_{i=1}^n b_i^{\oplus d_i}(\lambda) \quad (3)$$

with  $P$  denoting the corresponding permutation matrix, and  $b_i(\lambda)$  a matrix of dimension  $a_i$ .

If we denote by  $\mathbb{W}_\pi$  the set of rational functions  $p(\lambda)/q(\lambda)$  with the numerator degree being less than or equal to the denominator degree, then every matrix element  $(\mathcal{R}_S)_{i,j} \in \mathbb{W}_\pi$  [1]. Moreover, since  $\mathbb{W}_\pi$  is closed under linear transformations,  $(\mathcal{R}''_S)_{i,j} \in \mathbb{W}_\pi$ . This means that every  $a_i$ -dimensional block  $b_i(\lambda)$  of  $\mathcal{R}''_S$ , when being solved for its non-linear eigenvalues via  $\det(\mathcal{R}''_S(H, \lambda) - \lambda I) = 0$ , features *at least*  $a_i$  solutions [1]. Since  $\mathcal{R}''_S$  features  $d_i$  such blocks and since every eigenvalue of  $\mathcal{R}_S(H, \lambda)$  is also an eigenvalue of  $H$  [1], it follows that for each irreducible representation  $\tilde{\Gamma}_i$  of dimension  $d_i$  and multiplicity  $a_i$  the Hamiltonian  $H$  contains at least  $a_i$  eigenvalues that are (individually)  $d_i$ -fold degenerate.  $\square$

## II. THE CONNECTION BETWEEN SYMMETRIES OF THE ISOSPECTRAL REDUCTION AND LOCAL SYMMETRIES OF $H^k$

One of the main results of this work is the relation between latent symmetries of a matrix  $H$  and its local symmetries in every matrix power. This result was given without proof in the main part of this work, and is proven below.

### Theorem 2

Let  $\mathcal{R}_S(H, \lambda)$  denote the isospectral reduction of  $H$  over some set of sites  $S$ , and let  $A \in \mathbb{C}^{|S| \times |S|}$ , where  $|S|$  denotes the number of sites in  $S$ . Then

$$[A, \mathcal{R}_S(H, \lambda)] = 0 \quad \forall \lambda \in \mathbb{L} \quad \Leftrightarrow \quad [A, (H^k)_{S,S}] = 0 \quad \forall k \geq 0, \quad (4)$$

where  $(H^k)_{S,S}$  denotes the submatrix derived from  $H^k$  by taking the rows and columns corresponding to the set  $S$ .

*Proof.* “ $\Rightarrow$ ” can be shown by induction. The initial case  $k = 0$  is trivially fulfilled. The next step is to assume  $[A, (H^k)_{S,S}] = 0$  holds for all  $0 \leq k \leq k'$  and then to show it holds also for  $0 \leq k \leq k' + 1$ . By partitioning the matrix  $H$  into blocks over  $S$  and its complement  $\bar{S}$  the following identity can be shown to hold:

$$(H^k)_{S,S} = (H^{k-1})_{S,S} H_{S,S} + \sum_{m=0}^{k-2} (H^m)_{S,S} H_{S,\bar{S}} (H_{\bar{S},\bar{S}})^{k-2-m} H_{\bar{S},S}. \quad (5)$$

Evaluating the commutator of  $A$  with eq. (5) for  $k = k' + 1$  and applying the induction assumption along with eq. (26) of lemma 3 we get  $[A, (H^{k'+1})_{S,S}] = 0$ , which completes the induction.

“ $\Leftarrow$ ”: First, we evaluate the commutator of  $A$  with eq. (5) and apply the assumption  $[A, (H^k)_{S,S}] = 0 \quad \forall k \geq 0$ .

Next, again by induction we can show that  $[A, H_{S,\bar{S}} (H_{\bar{S},\bar{S}})^l H_{\bar{S},S}] = 0 \quad \forall l \geq 0$ . To prove that  $[A, \mathcal{R}_S(H, \lambda)] = 0$  for all  $\lambda \in \mathbb{L}$  we use the identity eq. (28) for  $\mathcal{R}_S(H, \lambda)$  from lemma 4. Since  $[A, H_{S,S}] = 0$  by assumption and  $[A, H_{S,\bar{S}} (H_{\bar{S},\bar{S}})^n H_{\bar{S},S}] = 0 \quad \forall n \geq 0$  by induction, we have that  $[A, \mathcal{R}_S(H, \lambda)] = 0$  for all  $\lambda \in \mathbb{L}$ .  $\square$

## III. MODIFICATIONS PRESERVING LATENT PERMUTATION SYMMETRIES

Given a Hamiltonian  $H \in \mathbb{C}^{N \times N}$  with a latent permutation symmetry, it is often possible to modify  $H$  while keeping this symmetry. In particular, by analyzing the matrix powers of  $H$ , a large class of such latent-symmetry-preserving modifications can be found, as we derive in the following. We will start by defining what we call complement multiplets.

### Definition 1: Complement multiplet

Let  $S$  be a set of sites of a hermitean Hamiltonian  $H \in \mathbb{C}^{N \times N}$ , that is,  $S \subseteq \{1, \dots, N\}$ , and  $\bar{S}$  denote its complement (i.e., all other sites of  $H$ ). A set  $\mathbb{M}$  of sites of  $H$  with  $\mathbb{M} \subseteq \bar{S}$  forms a complement multiplet with respect to  $S$  if

$$\sum_{m \in \mathbb{M}} (H \bar{H}^k)_{s,m} = c_k \in \mathbb{C} \quad \forall s \in S, k \geq 0. \quad (6)$$

where  $\bar{H}$  is obtained from  $H$  by setting the couplings between  $S$  and  $\bar{S}$  to zero.

Once a (subset of) complement multiplets have been identified, they can be used to modify the Hamiltonian without breaking the underlying latent symmetry, with the procedure and its proof detailed in the following

**Theorem 3**

Let  $S$  be a set of sites of the hermitian Hamiltonian  $\mathring{H} \in \mathbb{C}^{N \times N}$ . If one modifies  $\mathring{H} \rightarrow H \in \mathbb{C}^{(N+1) \times (N+1)}$  by adding a single site  $c$  (with arbitrary on-site potential) and subsequently coupling each complement multiplet  $\mathbb{M}_j$  of  $\mathring{H}$  to the site  $c$  with the coupling  $h_j$ , i.e.,

$$H_{x,c} = H_{c,x}^* = \sum_{x \in \mathbb{M}_j} h_j, \quad (7)$$

with the star denoting complex conjugate, then the isospectral reduction changes as

$$\mathcal{R}_S(H, \lambda) = \mathcal{R}_S(\mathring{H}, \lambda) + a(\lambda)J, \quad (8)$$

with  $a(\lambda)$  being a rational function in  $\lambda$ ,  $J \in \mathbb{R}^{|S| \times |S|}$  is a matrix of ones, and where  $|S|$  denotes the number of sites in the set  $S$ . In particular, if  $S$  is latently permutation symmetric in  $\mathring{H}$ , it remains latently permutation symmetric in  $H$ .

*Proof.* In order to show eq. (8) holds, we evaluate the difference between  $\mathcal{R}_S(H, \lambda)$  and  $\mathcal{R}_S(\mathring{H}, \lambda)$ . To this end, we define  $\tilde{H}$  as the matrix obtained from  $\mathring{H}$  by adding the site  $c$  *without connecting it*, and by lemma 2,  $\mathcal{R}_S(\mathring{H}, \lambda) = \mathcal{R}_S(\tilde{H}, \lambda)$ . Further, we denote  $\bar{S}_c = \bar{S} \cup c$ . Next, for a sufficiently large  $\lambda_0$  and  $|\lambda| > \lambda_0 > 0$ , the matrix inverses occurring in  $\mathcal{R}_S(H, \lambda)$  and  $\mathcal{R}_S(\tilde{H}, \lambda)$  can be simultaneously formulated as convergent Neumann series. Finally, we note that  $H_{S, \bar{S}_c} = \tilde{H}_{S, \bar{S}_c}$  and  $H_{S,c} = \tilde{H}_{S,c} = 0$ . We arrive at:

$$\mathcal{R}_S(H, \lambda) - \mathcal{R}_S(\mathring{H}, \lambda) = \sum_{k=1}^{\infty} H_{S, \bar{S}_c} \left[ \left( H_{\bar{S}_c, \bar{S}_c} \right)^{k-1} - \left( \tilde{H}_{\bar{S}_c, \bar{S}_c} \right)^{k-1} \right] H_{\bar{S}_c, S} t^k \quad (9)$$

$$= \sum_{k=1}^{\infty} \mathring{H}_{S, \bar{S}} \left[ \left( H_{\bar{S}, \bar{S}} \right)^{k-1} - \left( \tilde{H}_{\bar{S}, \bar{S}} \right)^{k-1} \right] \mathring{H}_{\bar{S}, S} t^k \quad (10)$$

where  $t = 1/\lambda$ . In the following, we abbreviate the terms in square brackets of eq. (10) by the matrix  $\Delta_{\bar{S}, \bar{S}}^{(k-1)}$ . We further denote by  $\bar{H}$  and  $\mathring{H}$  the matrices obtained from  $H$  and  $\mathring{H}$ , respectively, by decoupling the set of sites  $S$  from the remaining sites.

Using a graph-theoretical interpretation (see Ref. [2]) the  $(i, j)$ -th matrix element of  $\Delta_{\bar{S}, \bar{S}}^{(k)}$  can be expressed in terms of *walks* in a graph  $\mathbb{G}(\bar{H})$  of length  $k$  starting at site  $\bar{s}_i$ , that is, the  $i$ -th element of  $\bar{S}$ , and ending at site  $\bar{s}_j$  while necessarily visiting the new site  $c$  at least once. This yields

$$\Delta_{\bar{S}, \bar{S}}^{(k)} = \sum_{2+l+m+n=k} \left[ \left( \sum_{x \in \cup_i \mathbb{M}_i} \left( \mathring{H}^l \right)_{\bar{s}, x} H_{x,c} \right) \left( \bar{H}^m \right)_{c,c} \left( \sum_{x \in \cup_i \mathbb{M}_i} H_{c,x} \left( \mathring{H}^n \right)_{x, \bar{s}} \right) \right] \quad (11)$$

Next, we replace  $H_{x,c}$  by eq. (7) and multiply eq. (11) with  $\mathring{H}_{S, \bar{S}}$  on the left and its transpose on the right (compare with eq. (10)):

$$\sum_{2+l+m+n=k} \left[ \left( \sum_i \sum_{x \in \mathbb{M}_i} \mathring{H}_{S, \bar{S}} \left( \mathring{H}^l \right)_{\bar{s}, x} h_i \right) \left( \bar{H}^m \right)_{c,c} \left( \sum_i \sum_{x \in \mathbb{M}_i} h_i^* \left( \mathring{H}^n \right)_{x, \bar{s}} \mathring{H}_{\bar{S}, S} \right) \right] \quad (12)$$

Using eq. (6), we recognize that  $\sum_{x \in \mathbb{M}_i} \mathring{H}_{S, \bar{S}} \left( \mathring{H}^l \right)_{\bar{s}, x} = c_l^{(i)} \bar{\mathbf{1}}_S$  with an all-constant  $|S|$ -dimensional vector  $\bar{\mathbf{1}}_S$ . This means that the matrix in eq. (12) is proportional to all-one matrix  $J$  with a constant pre-factor  $a^{(k)} = \sum_{2+l+m+n=k} \left[ \left( \sum_i h_i c_l^{(i)} \right) \left( \bar{H}^m \right)_{c,c} \left( \sum_i h_i c_n^{(i)*} \right) \right]$ . Inserting this result in eq. (10), we obtain that  $a(\lambda)$  from eq. (8) equals  $\sum_{k=1}^{\infty} a^{(k-1)} \left( \frac{1}{\lambda} \right)^k$  for  $|\lambda| > \lambda_0$ .

Finally, we note that the left-hand side of eq. (10) is a rational function of  $\lambda$ . Since it equals  $a(\lambda)J \forall |\lambda| > \lambda_0$ , by the identity theorem for polynomials it must be equal to  $a(\lambda)J$  also for  $|\lambda| \leq \lambda_0$ ,  $\lambda \in \mathbb{L}$ . Now, since  $J$  commutes with any permutation matrix, each latent symmetry of  $\mathring{H}$  is preserved in  $H$ .  $\square$

#### IV. THE CONNECTION BETWEEN (LATENT) $C_{n>2}$ SYMMETRIES AND DEGENERACIES FOR REAL-SYMMETRIC HAMILTONIANS

In the following, we will present more details on the concept of generalized exchange symmetry (GES). We will then use these to finally prove theorem 5, which states that, for real-valued Hamiltonians, a more than twofold rotational symmetry (that is, a symmetry  $C_{n>2}$ ) necessarily leads to a non-abelian latent  $D_n$  symmetry.

As explained in the main part of this work, each generalized exchange symmetry (GES) is given by a symmetric orthogonal matrix  $Q^{(u,v)}$  which permutes two sites  $u, v$  while acting as an orthogonal transformation on the others. The  $Q^{(u,v)}$  were introduced in Ref. [3], where it has been shown that, for real Hamiltonians,  $Q^{(u,v)}$  exists if and only if  $(H^k)_{u,u} = (H^k)_{v,v}$  for all  $k$ . In this case, the eigenvalue spectra of  $H \setminus u$  and  $H \setminus v$  coincide, and the two sites  $u$  and  $v$  are said to be cospectral [3].

Similar to Ref. [4], we will now explicitly construct  $Q^{(u,v)}$  by means of projectors. To this end, we first choose the eigenstates according to the following

##### Lemma 1: Lemma 2.5 of Ref. [5]

Let  $H$  be a real symmetric matrix, with  $u$  and  $v$  cospectral. Then the eigenstates  $\{|\phi\rangle\}$  of  $H$  are (or, in the case of degenerate eigenvalues, can be chosen) as follows. For each eigenvalue  $\lambda$  there is at most one eigenstate  $|\phi\rangle$  with even local parity on  $u$  and  $v$ , i. e.,  $\langle u|\phi_i^{(+)}\rangle = \langle v|\phi_i^{(+)}\rangle \neq 0$ , and at most one eigenstate  $|\phi\rangle$  with odd local parity on  $u$  and  $v$ , i. e.,  $\langle u|\phi_i^{(-)}\rangle = -\langle v|\phi_i^{(-)}\rangle \neq 0$ . Here,  $|x\rangle$  denotes a vector which possesses the value one at site  $x$  and zeros on all other sites. All remaining eigenstates for  $\lambda$  fulfill  $\langle u|\phi_i^{(0)}\rangle = \langle v|\phi_i^{(0)}\rangle = 0$ . The even (odd) parity eigenstate can be found by projecting the vector  $|u\rangle \pm |v\rangle$  onto the eigenspace associated with  $\lambda$ .

With this choice of the eigenstate basis, we state the following

##### Theorem 4

Let the orthonormal eigenstates  $\{|\phi\rangle\}$  of  $H$  be chosen according to lemma 1, and define the projectors

$$P_+^{(u,v)} = \sum_i |\phi_i^{(+)}\rangle \langle \phi_i^{(+)}|, \quad P_-^{(u,v)} = \sum_i |\phi_i^{(-)}\rangle \langle \phi_i^{(-)}|, \quad P_0^{(u,v)} = \sum_i |\phi_i^{(0)}\rangle \langle \phi_i^{(0)}| \quad (13)$$

Then  $Q^{(u,v)} = P_+^{(u,v)} + P_0^{(u,v)} - P_-^{(u,v)}$  fulfills

$$(Q^{(u,v)})^{-1} = (Q^{(u,v)})^T = Q^{(u,v)}, \quad Q^{(u,v)} |u\rangle = |v\rangle. \quad (14)$$

*Proof.* The property  $(Q^{(u,v)})^{-1} = Q^{(u,v)}$  follows simply from the fact that the projection matrices eq. (13) are idempotent.  $(Q^{(u,v)})^T = Q^{(u,v)}$  follows from the fact that one can choose the eigenvectors of  $H$  to be real-valued, so that the projector onto the eigenspace associated to any eigenvalue is real, thereby rendering also the projection matrices eq. (13) real and therefore also symmetric.

In order to prove that  $Q^{(u,v)} |u\rangle = |v\rangle$ , we use lemma 1 and the orthonormality of eigenstates  $|\phi_i\rangle$  to get  $\langle v|Q^{(u,v)}|u\rangle = (Q^{(u,v)})_{u,v} = \sum_i \langle u|\phi_i\rangle \langle \phi_i|v\rangle = 1$ . Additionally, since  $\sum_i (Q_{u,i}^{(u,v)})^2 = \sum_i (Q_{v,i}^{(u,v)})^2 = 1$  due to the orthogonality of  $Q^{(u,v)}$ , it follows that  $(Q^{(u,v)})_{u,i} = \delta_{i,v}$  and  $(Q^{(u,v)})_{v,i} = \delta_{i,u}$ .  $\square$

With these prerequisites and a good understanding of the concept of GES, we are now finally able to prove the connection between  $C_n$  rotational symmetries of a real Hamiltonian and the necessary emergence of  $D_n$  latent permutation symmetries, explicated in the following

##### Theorem 5

Let  $H \in \mathbb{R}^{N \times N}$  be a real symmetric Hamiltonian that features a latent or non-latent  $C_{n>2}$  permutation symmetry. Then

- $H$  necessarily also features a latent  $D_n$  permutation symmetry and features at least  $\lfloor \frac{n-1}{2} \rfloor$  pairs of doubly degenerate eigenvalues, where  $\lfloor x \rfloor$  rounds  $x$  down to the nearest integer.
- There exist two GESs of  $H$  which do not commute with each other.

*Proof.* • If  $H$  features a (latent or non-latent)  $C_{n>2}$  permutation symmetry, then there is at least one set  $S$  of  $n$  sites and a  $n \times n$  permutation matrix  $P$  fulfilling

$$P^k \neq I \forall 1 \leq k < n, \quad P^n = I, \quad [\mathcal{R}_S(H, \lambda), P] = 0 \forall \lambda \in \mathbb{L} \quad (15)$$

where  $I$  is the identity matrix. Together with the symmetry and real-valuedness of  $H$ , this property implies that the rows and column of  $\mathcal{R}_S(H, \lambda)$  can be permuted such that it is a real symmetric circulant matrix. It is known that such matrices commute with the permutation matrix corresponding to the operation that performs a flip about the anti-diagonal. Together with the cyclic permutations of order  $n$ , this operation generates the dihedral group  $D_n$ , and  $H$  thus features a latent  $D_n$  permutation symmetry.

Next, we note that it is known that the eigenstates of real symmetric circulant matrices are independent of their entries [6], here in particular independent of  $\lambda$ . Using them to diagonalize  $\mathcal{R}_S(H, \lambda)$  one obtains a diagonal  $n \times n$  matrix with entries  $f_j(\lambda) \in \mathbb{W}_\pi$ ,  $j = 1, \dots, n$ , that is, rational functions  $p_j(\lambda)/q_j(\lambda)$  with the numerator degree being less than or equal to the degree of the denominator. The eigenvalues of  $\mathcal{R}_S(H, \lambda)$  are thus given by the sum of the multisets denoting the solutions to  $f_j(\lambda) - \lambda = 0$ . Similar to the proof of theorem 1, it can be shown that each of these equations has at least one solution. Furthermore,  $f_j(\lambda) = f_{n-j}(\lambda)$ , because  $\mathcal{R}_S(H, \lambda)$  is not only circulant but also real-symmetric. Finally, since every eigenvalue of  $\mathcal{R}_S(H, \lambda)$  is contained in the spectrum of  $H$  [1], we conclude that  $H$  has at least  $\lfloor \frac{n-1}{2} \rfloor$  pairs of doubly degenerate eigenvalues.

- From the above and from theorem 2 we have  $[(H^k)_{S,S}, P] = 0$  for all  $k \geq 0$ , i.e.  $(H^k)_{S,S}$  is a real symmetric circulant matrix. In each power  $k$ , the diagonal elements  $(H^k)_{ii} = (H^k)_{jj} \forall i, j$  are pairwise equal, meaning that each pair of sites in  $S$  is cospectral. By Ref. [3], for each such pair there is a GES  $Q^{(i,j)}$  which commutes with  $H$  and theorem 4 applies.

For the sake of simple notation let us now assume that the sites of  $H$  are labeled (if this is not the case, one can easily renumber the sites accordingly) such that  $s_i \rightarrow i$ , with  $P$  permuting the sites in  $S = \{s_1, \dots, s_{|S|}\}$  such that the site  $i < n$  is mapped onto the site  $i + 1$ , and  $n$  onto 1. The fact that  $(H^k)_{S,S}$  is circulant symmetric then implies  $(H^k)_{1,2} = (H^k)_{2,3} \forall k$ . In the terminology of Ref. [2], site 2 is a walk-singlet w.r.t. the cospectral sites 1 and 3. Thus, by Theorem 4 from Ref. [2], the eigenstates of  $H$  [chosen according to lemma 1 for the cospectral pair 1 and 3] with negative parity on cospectral sites vanish on site 2. By combining the projector definition of  $Q^{(1,3)}$  with the completeness relation of eigenstates one can show  $(Q^{(1,3)})_{2,2} = 1$ . Furthermore, since  $Q^{(1,3)}$  is orthogonal, the matrix elements  $(Q^{(1,3)})_{2,j} = \delta_{2,j}$ . On the other hand, site 3 is not necessarily a singlet for the cospectral pair 1 and 2. Specifically, we have

$$Q^{(1,3)} = \left( \begin{array}{ccc|c} 0 & 0 & 1 & 0 \\ 0 & 1 & 0 & 0 \\ 1 & 0 & 0 & 0 \\ \hline & & & A \end{array} \right), \quad Q^{(1,2)} = \left( \begin{array}{cc|c|c} 0 & 1 & 0 & 0 \\ 1 & 0 & 0 & 0 \\ \hline 0 & a & b & \\ \hline 0 & b^T & B & \end{array} \right) \quad (16)$$

where  $A, B \in \mathbb{R}^{(N-3) \times (N-3)}$  and  $b \in \mathbb{R}^{1 \times (N-3)}$ . Since the upper left  $3 \times 3$  block of the commutator of the above two matrices does not vanish, these two matrices do not commute.  $\square$

## V. BAND-STRUCTURE CALCULATIONS

To derive the Bloch-Hamiltonian  $H_B(\mathbf{k}) = H_B(k_x, k_y)$ , we follow the convention of Eq. (2.75) of Ref. [7]. To this end, let  $|m_{\mathbf{R}}\rangle$  denote the state which is completely localized on site  $m$  of the unit cell located at position  $\mathbf{R}$ . For our two-dimensional lattices, the vectors  $\mathbf{R} = A\vec{a}_1 + B\vec{a}_2$ , where  $A, B$  are integers and  $\vec{a}_{1,2}$  are the two primitive vectors describing the lattice. The Bloch-Hamiltonian can then be written as

$$(H_B(\mathbf{k}))_{nm} = \sum_{\mathbf{R}} e^{i\mathbf{k} \cdot \mathbf{R}} \langle m_{\mathbf{0}} | H_L | m_{\mathbf{R}} \rangle \quad (17)$$

where  $H_L$  denotes the Hamiltonian of the infinite lattice.

### A. Bloch-Hamiltonian for the modified Kagome lattice

With  $\vec{a}_1 = (1, 0)^T$ ,  $\vec{a}_2 = (\frac{1}{2}, \frac{\sqrt{3}}{2})^T$ , we obtain the Bloch-Hamiltonian of Fig. 1 (c) of the main text as

$$\begin{pmatrix} 0 & h_3 & h_3 & h_2 & 0 & h_1 \\ h_3 & 0 & h_3 & h_1 & h_2 & 0 \\ h_3 & h_3 & 0 & 0 & h_1 & h_2 \\ h_2 & h_1 & 0 & 0 & h_4 e^{i\left(\frac{\sqrt{3}k_y}{2} - \frac{k_x}{2}\right)} & h_4 e^{-ik_x} \\ 0 & h_2 & h_1 & h_4 e^{-i\left(\frac{\sqrt{3}k_y}{2} - \frac{k_x}{2}\right)} & 0 & h_4 e^{-i\left(\frac{k_x}{2} + \frac{\sqrt{3}k_y}{2}\right)} \\ h_1 & 0 & h_2 & h_4 e^{ik_x} & h_4 e^{i\left(\frac{k_x}{2} + \frac{\sqrt{3}k_y}{2}\right)} & 0 \end{pmatrix}. \quad (18)$$

At  $k_x = k_y = 0$ , the isospectral reduction of the Bloch-Hamiltonian over the sites  $S = \{1, 2, 3\}$  then has the structure

$$\begin{pmatrix} a(\lambda) & b(\lambda) & b(\lambda) \\ b(\lambda) & a(\lambda) & b(\lambda) \\ b(\lambda) & b(\lambda) & a(\lambda) \end{pmatrix}. \quad (19)$$

Thus, the Bloch-Hamiltonian features a latent  $D_3$  permutation symmetry at  $\mathbf{k} = 0$ .

### B. Construction of the Bloch-Hamiltonian belonging to Fig. 2 (b)

Let us here briefly discuss how one could build a lattice from the Hamiltonian depicted in Fig. 2 (a) of the main text. The basic idea is to interpret  $H$  as the Bloch-Hamiltonian  $H_B$  of an extended lattice, evaluated at the  $\Gamma$ -point, that is,  $H = H_B(\mathbf{k} = 0)$ . Out of the many possible ways to achieve this, we here first remove the three curved couplings—the ones between sites (6, 11), (5, 10), and (4, 7)—from  $H$ , and use the resulting system  $H_{UC}$  as the unit cell of a lattice, as depicted in Fig. 2 (b). The corresponding Bloch-Hamiltonian  $H_B(\mathbf{k}) = H_{UC} + H_{IC}(\mathbf{k})$  is the sum of the unit cell Hamiltonian  $H_{UC}$  and a  $\mathbf{k}$ -dependent inter-cell coupling  $H_{IC}(\mathbf{k})$ . The matrix elements of  $H_{IC}(\mathbf{k})$  are obtained by taking an arbitrary reference unit cell,  $A$ . For each site  $i$  in  $A$  that is connected with coupling  $h_{ij}$  to a site  $j$  in an adjacent unit cell  $B$ ,  $(H_{IC}(\mathbf{k}))_{ij} = h_{ij} e^{i\mathbf{k} \cdot \mathbf{R}_{AB}}$  with  $\mathbf{R}_{AB}$  denoting the vector pointing from  $A$  to  $B$ , as one can show by means of eq. (17). At  $\mathbf{k} = 0$ , all complex exponentials in  $H_{IC}(\mathbf{k})$  become unity, and one can design  $H_B(\mathbf{k} = 0) = H$  by suitably connecting the initial unit cell to its neighbors. For the above choice and by choosing  $\vec{a}_1 = (0, 1)^T$ ,  $\vec{a}_2 = (\frac{5}{3} \cos(\pi/6), \frac{1}{2})^T$ , we then obtain the Bloch-Hamiltonian of Fig. 2 (b) of the main text as

$$\begin{pmatrix} \mathbf{0}_{6 \times 6} & \mathbf{C} \\ \mathbf{C}^\dagger & \mathbf{0}_{5 \times 5} \end{pmatrix} \quad (20)$$

with  $\mathbf{0}_{n \times n}$  denoting the  $n \times n$  matrix of zeros, and

$$\mathbf{C} = \begin{pmatrix} h & h & 0 & 0 & h'' \\ h & 0 & h & h' & 0 \\ 2h & h & h & 0 & 0 \\ h e^{ik_y} & 2h & 2h & 0 & 0 \\ h & 0 & h' e^{i\left(\frac{k_y}{2} - \frac{5k_x}{2\sqrt{3}}\right)} & 0 & 0 \\ 0 & 0 & h & 0 & h'' e^{i\left(\frac{5k_x}{2\sqrt{3}} + \frac{k_y}{2}\right)} \end{pmatrix}. \quad (21)$$

For  $k_x = k_y = 0$ , this Hamiltonian equals the one depicted in Fig. 2 (a) of the main text, as intended.

## VI. AUXILIARY LEMMATA

**Lemma 2**

Let  $S$  be a set of sites of  $\mathring{H}$ . If one extends

$$\mathring{H} \rightarrow H = \begin{pmatrix} \mathring{H} & 0 \\ 0 & H' \end{pmatrix} \quad (22)$$

then the isospectral reduction over  $S$  remains unchanged, i.e.,  $\mathcal{R}_S(H, \lambda) = \mathcal{R}_S(\mathring{H}, \lambda)$ .

*Proof.* Follows straightforwardly from the fact that  $(H_{\bar{S}, \bar{S}} - \lambda I)^{-1} = \begin{pmatrix} (H_{\bar{S}_1, \bar{S}_1} - \lambda I)^{-1} & 0 \\ 0 & (H_{\bar{S}_2, \bar{S}_2} - \lambda I)^{-1} \end{pmatrix}$  is block diagonal and  $H_{S, \bar{S}_2} = 0$  with sites  $\bar{S}_1$  from  $\mathring{H}$ ,  $\bar{S}_2$  from  $H'$  and  $\bar{S}_1 \cup \bar{S}_2 = \bar{S}$ .  $\square$

**Lemma 3**

Let the isospectral reduction

$$\mathcal{R}_S(H, \lambda) = H_{S, S} - H_{S, \bar{S}} (H_{\bar{S}, \bar{S}} - \lambda I)^{-1} H_{\bar{S}, S} \quad (23)$$

over some set  $S$  of sites. If  $\mathcal{R}_S(H, \lambda)$  commutes with a  $|S| \times |S|$  matrix  $A$ , that is,  $[A, \mathcal{R}_S(H, \lambda)] = 0 \forall \lambda \in \mathbb{L}$ , then

$$[A, H_{S, S}] = 0 \quad (24)$$

$$\left[ A, H_{S, \bar{S}} (H_{\bar{S}, \bar{S}} - \lambda I)^{-1} H_{\bar{S}, S} \right] = 0 \forall \lambda \in \mathbb{L}. \quad (25)$$

$$\left[ A, H_{S, \bar{S}} (H_{\bar{S}, \bar{S}})^k H_{\bar{S}, S} \right] = 0 \forall k \geq 0. \quad (26)$$

*Proof.* First, eq. (24) follows from  $[A, \mathcal{R}_S(H, \lambda)] = 0$  by evaluating the limit  $\lambda \rightarrow \infty$ . Second, eq. (25) follows from eq. (24) and  $[A, \mathcal{R}_S(H, \lambda)] = 0$ . Last, for a sufficiently large  $\lambda_0$  and  $|\lambda| > \lambda_0 > 0$ , the left-hand side of eq. (25) can be formulated as a convergent power series in  $x = \frac{1}{\lambda}$ :

$$\frac{1}{\lambda_0} \sum_{k=1}^{\infty} c_k x^k = 0 \forall x : 0 < |x| < \frac{1}{\lambda_0} \quad (27)$$

where  $c_k = \left[ A, H_{S, \bar{S}} \left( \frac{H_{\bar{S}, \bar{S}}}{\lambda_0} \right)^{k-1} H_{\bar{S}, S} \right]$ . By the identity theorem for power series it follows that all  $c_k = 0$ , thus proving eq. (26).  $\square$

**Lemma 4**

Let  $\mathcal{R}_S(H, \lambda) = H_{S, S} - H_{S, \bar{S}} (H_{\bar{S}, \bar{S}} - \lambda I)^{-1} H_{\bar{S}, S}$  be the isospectral reduction of  $H$  over a site set  $S$ . Then

$$\mathcal{R}_S(H, \lambda) = H_{S, S} + \sum_{k=1}^{|\bar{S}|} \frac{c_k}{c_0} \sum_{n=0}^{k-1} \binom{k-1}{n} (-\lambda)^{k-1-n} H_{S, \bar{S}} (H_{\bar{S}, \bar{S}})^n H_{\bar{S}, S} \forall \lambda \in \mathbb{L} \quad (28)$$

where  $c_i = c_i(\lambda)$  are the coefficients of the characteristic polynomial of  $H_{\bar{S}, \bar{S}} - \lambda I$ .



*Proof.* For  $\lambda \in \mathbb{L}$  the matrix  $H_{\bar{S}, \bar{S}} - \lambda I := M$  is invertible, with characteristic polynomial  $p_M(\lambda, x) = \sum_{k=0}^{|\bar{S}|} c_k(\lambda) x^k$  and  $c_0 \neq 0$ . From the Cayley-Hamilton theorem one obtains the identity relation  $M^{-1} = -\sum_{k=1}^{|\bar{S}|} \frac{c_k}{c_0} M^{k-1}$ . Inserting this relation into the definition of isospectral reduction and applying the binomial theorem for  $(H_{\bar{S}, \bar{S}} - \lambda I)^{k-1}$  we arrive at eq. (28).  $\square$

- 
- [1] L. Bunimovich and B. Webb, *Isospectral Transformations: A New Approach to Analyzing Multidimensional Systems and Networks* (Springer, New York, NY, United State, 2014).
  - [2] M. Röntgen, M. Pyzh, C. V. Morfonios, and P. Schmelcher, Cospectrality-preserving graph modifications and eigenvector properties via walk equivalence of vertices, (2020), [arXiv:2007.07609](https://arxiv.org/abs/2007.07609).
  - [3] C. Godsil and J. Smith, Strongly Cospectral Vertices, (2017), [arXiv:1709.07975](https://arxiv.org/abs/1709.07975).
  - [4] A. Chan, G. Coutinho, W. Drazen, O. Eisenberg, C. Godsil, G. Lippner, M. Kempton, C. Tamon, and H. Zhan, Fundamentals of fractional revival in graphs, (2020), [arXiv:2004.01129](https://arxiv.org/abs/2004.01129).
  - [5] O. Eisenberg, M. Kempton, and G. Lippner, Pretty good quantum state transfer in asymmetric graphs via potential, *Discrete Math. Algebraic and Extremal Graph Theory*, **342**, 2821 (2019).
  - [6] G. J. Tee, Eigenvectors of block circulant and alternating circulant matrices, *Res. Lett. Inf. Math. Sci.* **8**, 123 (2005).
  - [7] D. Vanderbilt, *Berry Phases in Electronic Structure Theory: Electric Polarization, Orbital Magnetization and Topological Insulators* (Cambridge University Press, Cambridge, 2018).



## SUMMARY AND OUTLOOK

In this chapter we want to give a brief summary of four major topics covered by this thesis: ground state properties and breathing dynamics of binary mixtures (Section 9.1 and Section 9.2, respectively), QGM for non-lattice trapped few-body systems (Section 9.3), and recent concepts from spectral graph theory (Section 9.4). We recount the key findings of our investigations, indicate their implications and potential applications, and suggest directions for future research.

## 9.1 STATIONARY PROPERTIES OF A BOSE MIXTURE

Binary mixtures of ultracold gases are routinely created in modern laboratories all around the world to enrich and challenge our current theoretical understanding of interacting many-body systems. The interaction between two distinct species can greatly impact their stationary properties. Weakly correlated interaction regimes have been thoroughly studied with mean-field techniques and perturbative expansions. Sizeable correlations pose a great challenge for theoretical methods and thus are not yet fully understood. In this regard, we studied beyond-mean-field effects in a few-body binary mixture of bosons subject to a species-selective inhomogeneous trap in  $d$  dimensions. To accomplish this task, we used exact diagonalization and imaginary time propagation with ML-MCTDH-X, an advanced variational method for solving the time-dependent Schrödinger equation.

In [MP1], we obtained the low-energy spectrum of a binary mixture composed of two bosons per species subject to a mutual  $d$  harmonic confinement. Thereby, our work extends and complements the analysis of some previous studies. The distinguishability makes the energy spectrum richer and more complex compared to the single-component case. We represented the Hamiltonian as a matrix using a finite set of basis functions in a relative-coordinates frame and subsequently diagonalized it. This way, we managed to convert sizeable correlations among laboratory-frame coordinates to weak correlations among relative-frame coordinates. The alternative picture greatly accelerates the rate of convergence for exact diagonalization and is particularly suited for parameter regions where the intra-component correlations outweigh the inter-component ones. These insights suggest that an efficient solution of a many-body system might require a coordinate frame transformation, which raises a couple of challenging yet alluring questions. For a given choice of parameter values, does there exist a set of uncorrelated coordinates where the wave function could be described by a mean-field product ansatz? And if so, is there a systematic way for obtaining it? Are there any drawbacks such as an increased complexity of the transformed Hamiltonian?

Another useful insight, which we gained in the course of this study, is the discovery of additional parity-type symmetries in the relative frame, which are otherwise hidden or non-obvious from the laboratory frame perspective. These symmetries were used to classify the eigenstates and proved to be extremely valuable in understanding the breathing response we discuss in Section 9.2. This suggests that an abstract symmetry transformation without any obvious interpretation might become easily interpretable in a different coordinate frame. Are there more useful symmetries than we can see? Moreover, in the context of spectral properties, could it be that some accidental degeneracies are in fact caused by hidden symmetries of such a type? This is a long standing question and by now there have been several precedents where spectral degeneracies, initially believed to be truly accidental, turned out to have a meaningful physical interpretation. In Section 9.4, we discuss yet another class of hidden symmetry, revealed not by a coordinate transformation, but by an effective Hamiltonian obtained via a spectrum-preserving subsystem partitioning.

In [MP3], we studied the miscible-immiscible phase boundary in a Bose polaron problem, i. e., an impurity coupled to a medium of several bosons, subject to a species-selective parabolic confinement. In homogeneous systems, there is a simple criterion which determines this boundary:  $g_{AB}^2 > g_A g_B$ . However, the trap inhomogeneity greatly distorts this rule, e. g., a harmonic trap favours miscibility as it costs energy to expand in space. Together with other species-internal parameters, they determine the spatial overlap region between the two components. Furthermore, there are multiple possibilities to separate, but it is not always a priori clear which configuration would be energetically more favourable.

We derived estimates for the miscible-immiscible phase boundary and a criterion for the type of phase segregation based on arguments derived from the energy competition among the two components to occupy the centre of their trap. When there is a draw, then CF occurs. Otherwise, core-shell PS takes place. In addition, we estimated phase boundaries among separated regimes. We found that a weakly-entangled core-shell PS builds up entanglement upon increasing the strength of the medium-impurity interaction and, eventually, undergoes a transition to CF. However, this process is not visible by inspecting the reduced one-body densities. Instead, one requires inter- and intra-component distance correlators to differentiate among CF and core-shell PS. Thus, our work contributes to a better understanding of the phase-separation mechanism and indicates that reduced one-body densities might be misleading for state classification.

In [MP4], we investigated a different Bose polaron setup, namely a free impurity coupled to a lattice-trapped medium. We quantified the ground-state response to the medium-impurity coupling by evaluating the fidelity between coupled and decoupled many-body states at different lattice depths and intra-medium interaction strengths. The fidelity tells us about the similarity of two states in the Hilbert space. We also looked at the susceptibility of reduced one-body densities to be perturbed by the medium-impurity interaction. We identified parameter regions with sizeable changes on the

many-body level, which are much less pronounced on the level of reduced one-body quantities. Furthermore, while searching for beyond mean-field effects, we found, in addition to the expected phase separation, two further peculiar regimes with a sizeable amount of correlations at the interface of attractive and repulsive interactions. We suspect that they might be analogues of quantum droplets. Finally, we resolved the role of entanglement for spatial density distributions and two-body distance correlators by comparing numerically exact quantities (including entanglement) to the approximate ones obtained using a SMF product ansatz (ignoring entanglement). We found that entanglement-induced corrections favour the process of phase separation at repulsive inter-component couplings and inhibit spatial localization at attractive medium-impurity couplings.

## 9.2 BREATHING DYNAMICS OF A BOSE MIXTURE

Elementary collective excitations dictate the dynamical response of a weakly perturbed physical system and are a valuable source of information comparable to that of spectroscopy. As a part of this thesis, we investigated the quantum breathing of ultracold mixtures in harmonic traps. For a single-species condensate, the breathing mode serves as a reliable diagnostics tool in modern experiments to verify the regime of interactions and to probe several useful stationary properties. Our goal was to study the diversity and utility of breathing modes for binary mixtures.

In [MP1], we analysed the breathing response of a few-body Bose mixture composed of two bosons per species confined in a mutual 1D parabolic trap. We triggered the dynamics by a slight quench of the trap frequency. The dynamics was described in the linear-response regime in terms of eigenstates and -energies obtained by exact diagonalization. We employed a relative-frame coordinate system to define a correlation-adapted product state basis. Specifically, we used the centre-of-mass coordinate  $R_{cm}$ , the relative distances  $r_\sigma$  between two identical particles, and the relative distance  $R_{AB}$  between the two centre-of-masses of the two components. We derived expressions for time evolution of the relative-frame coordinate densities and analysed the amplitudes and frequencies of observed oscillations upon variation of the intra- and inter-component interaction strength parameters.

We identified up to four breathing frequencies depending on the interplay of interactions. At a weak inter-component coupling, we found that each relative-frame coordinate is ‘normal’, in a sense that it performs a single-mode oscillation. We labelled the corresponding frequencies  $\Omega_{cm}$ ,  $\Omega_\sigma$  and  $\Omega_{AB}$ . For equal strength of intra-component interactions, the motion of the two species assimilates. Because of a symmetry-imposed selection rule, instead of two frequencies,  $\Omega_\sigma$ , there is just one,  $\Omega_+$ . At an intermediate inter-component coupling, each relative coordinate (except  $R_{cm}$ ) exhibits multi-mode oscillations. At a strong inter-component coupling, where the mixture becomes immiscible, the frequencies  $\Omega_\sigma$  ( $\Omega_+$ ) are found to be strongly suppressed, such that only two modes,  $\Omega_{cm}$  and  $\Omega_{AB}$ , contribute to the dynamics. Finally, we argued that our results can be verified experi-

mentally by means of state-of-the-art techniques. In addition, we proposed an explicit measurement protocol in [MP5] suitable for this purpose.

In [MP2], we studied the breathing response of a few-body Bose polaron, i. e., an impurity coupled to a medium of several atoms, in a species-selective 1D parabolic trap. As opposed to [MP1], the total number of particles was increased and we made use of the species-selective confinement to quench only the trap of the impurity. The medium was set in motion indirectly via the medium-impurity coupling. Instead of exact diagonalization we used ML-MCTDH-X to simulate the time propagation of the pre-quench many-body ground state with a post-quench Hamiltonian. Then, we evaluated the time evolution of the reduced one-body density for each species,  $\rho_1^\sigma(x, t)$ , and extracted the breathing frequencies and amplitudes from the density width oscillations by a CS algorithm. CS is an alternative to the Fourier transform, particularly suited for time signals which are sparse in the frequency space. It allows for a decent resolution in the frequency domain with a relatively short propagation time (as compared to the Fourier transform), which considerably reduces the amount of computation time with ML-MCTDH-X. We promote this tool for analysing the spectral response of weakly perturbed systems.

We characterized the breathing spectrum as a function of the medium-impurity coupling strength for different numbers of majority atoms and several values of the medium-interaction strength. The modes were classified as being of impurity or majority type. To this end, for each frequency in the common CS spectrum (averaged over the two components), we calculated the corresponding species quota. We could identify all the frequencies from [MP1], except for the internal mode of the second species because it is composed of a single particle. The functional dependence of assigned frequencies on the inter-species coupling strength is substantially altered as compared to the particle-balanced mixture. In addition, we found a qualitatively different mode caused by species-asymmetry of the quench protocol. Its frequency is a monotonically decreasing function of the medium-impurity coupling strength and it emerges after a certain coupling threshold has been reached. Importantly, we linked its appearance to the growth of entanglement between the impurity and the medium. In case of a SMF ansatz, i. e., neglecting all entanglement effects, the frequency does not appear at all in the CS spectrum. Importantly, this mode persists at different values of the trap ratio.

To conclude, our studies serve as a useful analysis tool for future experiments on few-body composite systems. A binary mixture features as many breathing frequencies as there are interaction parameters. Thus, it is in principle possible to map a set of breathing frequencies to a set of interaction parameters. However, there are a couple of issues which make a reliable assignment a challenging task: in some regimes of interactions only a fraction of modes can be excited and there is a further issue of near-degenerate frequencies in several parameter regions. To surpass these limitations, one might think of an alternative quench protocol to excite the damped and symmetry-excluded modes. There is still an open issue regard-

ing the dependence of the breathing response on the number of particles. Considering rapid build-up of correlations with an increasing strength of interactions, it was prohibitive for our method to go beyond ten particles. An interplay between negative and positive interactions is also a promising direction of future research. Relating to the entanglement-sensitive mode, we find it appealing to use it as a probe of bi-partite entanglement in ultracold mixtures. It would add yet another item into the toolbox of breathing mode diagnostics.

### 9.3 QUANTUM GAS MICROSCOPY OF TRAPPED GASES

Imaging is a wide-spread experimental technique to extract information from a physical system. The ability to differentiate individual atoms is of top priority as it allows to probe inter-particle correlations. Recently, QGM has revolutionized the imaging process for lattice-trapped ultracold atoms, offering a sub-micron resolution and single-atom sensitivity. As we are interested to explore beyond mean-field effects in external traps of arbitrary geometry, we studied the applicability of QGM beyond discrete lattice models.

In [MP5], we proposed an imaging protocol to measure the reduced  $n$ -particle density distribution of sparse ultracold samples confined by an external trap of any shape and dimension. As a first step, and because it is of direct relevance for the few-body trapped mixtures we discussed in [MP1–MP4], we considered 1D systems and attempted to access the reduced one-particle density distribution.

Similar to the conventional procedure in QGM, one needs to freeze the position of particles by ramping up a lattice, followed by fluorescence imaging and ensemble averaging over pictures taken. The crucial modification is now as follows: in order to reach a sub-lattice resolution, our idea was to perform ensemble averaging multiple times at several different positions of the pinning lattice relative to the trapped physical system. This way, the recorded one-particle density can, in principle, be oversampled to an arbitrary resolution. However, when the length scale of the system is comparable to the lattice constant, the pre- and post-measurement densities display substantial differences. These imaging artefacts are caused by the non-adiabaticity of the lattice-ramp protocol.

The measurement sequence can be formulated as a 2D convolution of the pre-measurement one-body density matrix with an imaging filter we call the quantum PSF. Since our protocol provides only the diagonal of this convolution, a straightforward deconvolution method is doomed to fail. Instead, we developed a machine-learning-assisted reconstruction procedure to remove the majority of distortions. It is particularly effective when spatial density variations are on the scale of the lattice constant and allows to reach sub-lattice resolution. As for now, the utility of our approach is limited to situations when the shortest period of spatial oscillations in the one-particle density drops below a half of the lattice constant.

Our findings are of fundamental interest for the theory of imaging and of immediate relevance for ongoing QGM experiments. It opens the research direction of high-resolution imaging with single-atom sensitivity also for non-lattice trapped systems. In particular, it is ideally suited for verifying many of the results we obtained in the context of trapped few-body binary mixtures. Further extensions of our work would be to test the feasibility for traps of higher dimension, to attempt the recovery of spatial two-body correlations and to investigate blurring artefacts in a time-evolving system.

#### 9.4 SPECTRAL GRAPH THEORY IN PHYSICS

Matrix eigenvalue problems are ubiquitous in physics and applied sciences. The eigenvalues and -vectors of a matrix are a source of invaluable information. Unfortunately, matrix diagonalization is infamous for unfavourable scaling of the numerical effort with the matrix dimension. Any means allowing to reduce this effort are highly desirable. This is usually done by a symmetry analysis, which can suggest a new set of symmetry-adapted basis functions tailored to obey particular geometrical constraints. However, the more complex a system becomes, the less likely it will feature any of the commonly known symmetries. Are there further tools to learn more about spectral properties of a matrix? We found some useful concepts in spectral graph theory.

In [MP6], we investigated a graph-theoretical concept of cospectral vertex pair. It imposes a parity relation among two particular components of any eigenvector of a graph's matrix, even in the absence of conventional<sup>1</sup> graph symmetries. It has an intuitive interpretation as a symmetry of walks and can be linked to hybrid block-symmetries, with one block being a conventional pair-exchange symmetry and the remainder a general orthogonal matrix. The presence of this peculiar property can be easily inferred by analysing the powers of a graph's matrix and, once confirmed, can be subsequently used for block-diagonalization. We contributed to the study of cospectrality in two ways.

First, we developed a generator of graphs with a cospectral vertex pair. It is a hot topic in spectral graph theory concerned with the following question: when does the spectrum of a graph determines its topology? It is reminiscent of spectroscopy in physics, aimed to infer information about the composition and structure of matter from the spectral data. Biased by our studies on impurities and having in mind symmetry-preserving perturbations, we attempted to couple an additional perturber vertex to a graph having a cospectral vertex pair,  $u$  and  $v$ , without breaking the underlying cospectrality. As an outcome of this study, we identified several subsets of multiple vertices, to which the perturber vertex can be docked. We called them multiplets  $\mathcal{M}$ . In addition, we linked this circumstance to an equality relation  $\sum_{z \in \mathcal{M}} (H^k)_{uz} = \pm \sum_{z \in \mathcal{M}} (H^k)_{vz}$  valid for all matrix powers. In the graph language it means that a multiplet is equally reachable from both  $u$  and  $v$ . The final set of possible modifications include: removal

<sup>1</sup> In discrete mathematics, the term 'conventional symmetry' implies permutations.



and addition of vertices, interconnections among existing multiplets. Thus, multiplets provide building blocks to extend and modify cospectral graphs.

Second, we found that multiplets pose further restrictions on eigenvector components, in addition to parity caused by cospectrality of a vertex pair. As an example, odd parity eigenstates vanish on so-called singlets, i. e., multiplets composed of a single vertex. This work laid the foundation for a flat-band generator we proposed in [MP11]. Using a graph with a cospectral vertex pair as a unit cell, the idea is to interconnect adjacent cells via singlets. As a result, each odd parity eigenstate of a cell becomes a localized eigenstate of the lattice, which leads to macroscopically degenerate flat bands.

In [MP7], we studied another graph-theoretical concept of isospectral reduction. It is a way to shrink the size of a graph to a dedicated subset of vertices  $S$  while preserving (the major part of) the underlying energy spectrum. Physical community is already acquainted with this tool, rather known as the Feshbach-Schur projection method. There, the Hamiltonian  $H$  is bi-partitioned into a subsystem of interest  $S$  coupled to a bath  $\bar{S}$ . One can derive an effective Hamiltonian  $R_S$  governing only the subsystem  $S$  and the impact of the bath  $\bar{S}$  becomes encoded as an additional (energy-dependent) term, called the self-energy. What makes isospectral reduction particularly interesting is that the reduced graph  $\mathcal{G}_S$  might feature symmetries which are not present in the original version  $\mathcal{G}$ . Such symmetries are called *latent*.

We demonstrated that latent symmetries are able to explain the degeneracies of a graph's matrix. To this end, we designed a tight-binding Hamiltonian without permutation symmetries, whose suitably reduced version featured multiple permutation symmetries forming a non-abelian symmetry group. By group-theory arguments,  $R_S$  can be brought into a block-diagonal form and will have duplicate blocks causing structural degeneracies in  $R_S$ . Since the spectrum of  $R_S$  is a sub-multiset of the spectrum of  $H$ , the latter inherits degeneracies from its reduced version. This provides a useful tool to investigate accidental degeneracies in terms of latent symmetries.

As for the future perspective, we aim to apply the above concepts to further physical problems such as vibrational modes in mass-spring systems, principal component analysis of covariance matrices, light- and acoustic-wave transport through a medium and many-body interacting systems such as Heisenberg spin chains or the Bose-Hubbard model. Recently, we have been working on several generalizations of cospectrality such as imposing a scaled-parity or a complex-phase relation among eigenvector components. In [MP9], we established a link between latent and block symmetries of  $H$ :

$$[H, \begin{pmatrix} A & 0 \\ 0 & B \end{pmatrix}] = 0 \quad \Rightarrow \quad [R_S, A] = 0 \quad \text{and} \quad [R_{\bar{S}}, B] = 0,$$

$$[R_S, A] = 0 \quad \Rightarrow \quad \exists B : [H, \begin{pmatrix} A & 0 \\ 0 & B \end{pmatrix}] = 0 \quad \text{and} \quad [R_{\bar{S}}, B] = 0.$$

These relations are very appealing and deserve further investigations.



## BIBLIOGRAPHY

---

- <sup>1</sup>I. Bloch, J. Dalibard, and W. Zwerger, “Many-body physics with ultracold gases,” *Rev. Mod. Phys.* **80**, 885–964 (2008).
- <sup>2</sup>D. Blume, “Few-body physics with ultracold atomic and molecular systems in traps,” *Rep. Prog. Phys.* **75**, 046401 (2012).
- <sup>3</sup>E. Braaten and H.-W. Hammer, “Universality in few-body systems with large scattering length,” *Phys. Rep.* **428**, 259–390 (2006).
- <sup>4</sup>X.-J. Liu, H. Hu, and P. D. Drummond, “Virial Expansion for a Strongly Correlated Fermi Gas,” *Phys. Rev. Lett.* **102**, 160401 (2009).
- <sup>5</sup>I. Brouzos and P. Schmelcher, “Construction of Analytical Many-Body Wave Functions for Correlated Bosons in a Harmonic Trap,” *Phys. Rev. Lett.* **108**, 045301 (2012).
- <sup>6</sup>P. Naidon and S. Endo, “Efimov physics: a review,” *Rep. Prog. Phys.* **80**, 056001 (2017).
- <sup>7</sup>C. H. Greene, P. Giannakeas, and J. Pérez-Ríos, “Universal few-body physics and cluster formation,” *Rev. Mod. Phys.* **89**, 035006 (2017).
- <sup>8</sup>C. J. Pethick and H. Smith, *Bose–Einstein Condensation in Dilute Gases*, 2nd ed. (Cambridge University Press, Cambridge, 2008).
- <sup>9</sup>K. B. Davis et al., “Bose-Einstein Condensation in a Gas of Sodium Atoms,” *Phys. Rev. Lett.* **75**, 3969–3973 (1995).
- <sup>10</sup>M. H. Anderson et al., “Observation of Bose-Einstein Condensation in a Dilute Atomic Vapor,” *Science*, [10.1126/science.269.5221.198](https://doi.org/10.1126/science.269.5221.198) (1995).
- <sup>11</sup>M. Woerdemann, C. Alpmann, M. Esseling, and C. Denz, “Advanced optical trapping by complex beam shaping,” *Laser Photonics Rev.* **7**, 839–854 (2013).
- <sup>12</sup>D. Trypogeorgos, T. Harte, A. Bonnin, and C. Foot, “Precise shaping of laser light by an acousto-optic deflector,” *Opt. Express* **21**, 24837–24846 (2013).
- <sup>13</sup>C. Chin, R. Grimm, P. Julienne, and E. Tiesinga, “Feshbach resonances in ultracold gases,” *Rev. Mod. Phys.* **82**, 1225–1286 (2010).
- <sup>14</sup>F. Serwane et al., “Deterministic Preparation of a Tunable Few-Fermion System,” *Science*, [10.1126/science.1201351](https://doi.org/10.1126/science.1201351) (2011).
- <sup>15</sup>A. N. Wenz et al., “From Few to Many: Observing the Formation of a Fermi Sea One Atom at a Time,” *Science*, [10.1126/science.1240516](https://doi.org/10.1126/science.1240516) (2013).
- <sup>16</sup>S. Murmann et al., “Antiferromagnetic Heisenberg Spin Chain of a Few Cold Atoms in a One-Dimensional Trap,” *Phys. Rev. Lett.* **115**, 215301 (2015).

- <sup>17</sup>S. Murmann et al., “Two Fermions in a Double Well: Exploring a Fundamental Building Block of the Hubbard Model,” *Phys. Rev. Lett.* **114**, 080402 (2015).
- <sup>18</sup>G. Zürn et al., “Fermionization of Two Distinguishable Fermions,” *Phys. Rev. Lett.* **108**, 075303 (2012).
- <sup>19</sup>G. Zürn et al., “Pairing in Few-Fermion Systems with Attractive Interactions,” *Phys. Rev. Lett.* **111**, 175302 (2013).
- <sup>20</sup>H. Ott, “Single atom detection in ultracold quantum gases: a review of current progress,” *Rep. Prog. Phys.* **79**, 054401 (2016).
- <sup>21</sup>C. Gross and W. S. Bakr, “Quantum gas microscopy for single atom and spin detection,” *Nat. Phys.* **17**, 1316–1323 (2021).
- <sup>22</sup>W. S. Bakr et al., “A quantum gas microscope for detecting single atoms in a Hubbard-regime optical lattice,” *Nature* **462**, 74–77 (2009).
- <sup>23</sup>J. F. Sherson et al., “Single-atom-resolved fluorescence imaging of an atomic Mott insulator,” *Nature* **467**, 68–72 (2010).
- <sup>24</sup>E. Haller et al., “Single-atom imaging of fermions in a quantum-gas microscope,” *Nature Phys.* **11**, 738–742 (2015).
- <sup>25</sup>L. W. Cheuk et al., “Quantum-Gas Microscope for Fermionic Atoms,” *Phys. Rev. Lett.* **114**, 193001 (2015).
- <sup>26</sup>G. J. A. Edge et al., “Imaging and addressing of individual fermionic atoms in an optical lattice,” *Phys. Rev. A* **92**, 063406 (2015).
- <sup>27</sup>M. F. Parsons et al., “Site-resolved imaging of fermionic Li 6 in an optical lattice,” *Phys. Rev. Lett.* **114**, 213002 (2015).
- <sup>28</sup>M. Lewenstein, A. Sanpera, and V. Ahufinger, *Ultracold Atoms in Optical Lattices: Simulating quantum many-body systems* (Oxford University Press, Oxford, 2012).
- <sup>29</sup>S. Will et al., “Time-resolved observation of coherent multi-body interactions in quantum phase revivals,” *Nature* **465**, 197–201 (2010).
- <sup>30</sup>P. Cheinet et al., “Counting Atoms Using Interaction Blockade in an Optical Superlattice,” *Phys. Rev. Lett.* **101**, 090404 (2008).
- <sup>31</sup>Y. Miroshnychenko et al., “Inserting Two Atoms into a Single Optical Micropotential,” *Phys. Rev. Lett.* **97**, 243003 (2006).
- <sup>32</sup>X. He, P. Xu, J. Wang, and M. Zhan, “High efficient loading of two atoms into a microscopic optical trap by dynamically reshaping the trap with a spatial light modulator,” *Opt. Express* **18**, 13586–13592 (2010).
- <sup>33</sup>D. Frese et al., “Single Atoms in an Optical Dipole Trap: Towards a Deterministic Source of Cold Atoms,” *Phys. Rev. Lett.* **85**, 3777–3780 (2000).
- <sup>34</sup>R. Bourgain et al., “Evaporative cooling of a small number of atoms in a single-beam microscopic dipole trap,” *Phys. Rev. A* **88**, 023428 (2013).
- <sup>35</sup>T. Giamarchi, *Quantum physics in one dimension*, The international series of monographs on physics 121 (Clarendon ; Oxford University Press, 2004), 424 pp.

- <sup>36</sup>M. A. Cazalilla et al., “One dimensional bosons: From condensed matter systems to ultracold gases,” *Rev. Mod. Phys.* **83**, 1405–1466 (2011).
- <sup>37</sup>X.-W. Guan, M. T. Batchelor, and C. Lee, “Fermi gases in one dimension: From Bethe ansatz to experiments,” *Rev. Mod. Phys.* **85**, 1633–1691 (2013).
- <sup>38</sup>S. Mistakidis et al., “Cold atoms in low dimensions—a laboratory for quantum dynamics,” arXiv preprint arXiv:2202.11071 (2022).
- <sup>39</sup>L. Cao, S. Krönke, O. Vendrell, and P. Schmelcher, “The multi-layer multi-configuration time-dependent Hartree method for bosons: Theory, implementation, and applications,” *J. Chem. Phys.* **139**, 134103 (2013).
- <sup>40</sup>S. Krönke, L. Cao, O. Vendrell, and P. Schmelcher, “Non-equilibrium quantum dynamics of ultra-cold atomic mixtures: the multi-layer multi-configuration time-dependent Hartree method for bosons,” *New J. Phys.* **15**, 063018 (2013).
- <sup>41</sup>L. Cao et al., “A unified ab initio approach to the correlated quantum dynamics of ultracold fermionic and bosonic mixtures,” *J. Chem. Phys.* **147**, 044106 (2017).
- <sup>42</sup>U. Schollwöck, “The density-matrix renormalization group,” *Rev. Mod. Phys.* **77**, 259–315 (2005).
- <sup>43</sup>U. Schollwöck, “The density-matrix renormalization group in the age of matrix product states,” *Ann. Phys.*, January 2011 Special Issue **326**, 96–192 (2011).
- <sup>44</sup>M. L. Wall, “Out-of-Equilibrium Dynamics with Matrix Product States,” in *Quantum Many-Body Physics of Ultracold Molecules in Optical Lattices: Models and Simulation Methods*, edited by M. L. Wall, Springer Theses (Springer International Publishing, Cham, 2015), pp. 177–222.
- <sup>45</sup>N. T. Zinner, “Exploring the few- to many-body crossover using cold atoms in one dimension,” *EPJ Web Conf.* **113**, 01002 (2016).
- <sup>46</sup>T. Sowiński and M. Á. García-March, “One-dimensional mixtures of several ultracold atoms: a review,” *Rep. Prog. Phys.* **82**, 104401 (2019).
- <sup>47</sup>J. Chen, J. M. Schurer, and P. Schmelcher, “Entanglement induced interactions in binary mixtures,” *Phys. Rev. Lett.* **121**, 043401 (2018).
- <sup>48</sup>A. S. Alexandrov and J. T. Devreese, *Advances in polaron physics*, Springer series in solid-state sciences 159 (Springer, 2010), 167 pp.
- <sup>49</sup>Grusdt F. and Demler E., “New theoretical approaches to Bose polarons,” *ENFI* **191**, 325–411 (2016).
- <sup>50</sup>H. Fröhlich, “Electrons in lattice fields,” *Adv. Phys.* **3**, 325–361 (1954).
- <sup>51</sup>M. Olshanij, “Atomic Scattering in the Presence of an External Confinement and a Gas of Impenetrable Bosons,” *Phys. Rev. Lett.* **81**, 938–941 (1998).

- <sup>52</sup>D. S. Petrov, M. Holzmann, and G. V. Shlyapnikov, “Bose-Einstein Condensation in Quasi-2D Trapped Gases,” *Phys. Rev. Lett.* **84**, 2551–2555 (2000).
- <sup>53</sup>T. Bergeman, M. G. Moore, and M. Olshanii, “Atom-Atom Scattering under Cylindrical Harmonic Confinement: Numerical and Analytic Studies of the Confinement Induced Resonance,” *Phys. Rev. Lett.* **91**, 163201 (2003).
- <sup>54</sup>E. Haller et al., “Confinement-Induced Resonances in Low-Dimensional Quantum Systems,” *Phys. Rev. Lett.* **104**, 153203 (2010).
- <sup>55</sup>F. Grusdt, G. E. Astrakharchik, and E. Demler, “Bose polarons in ultracold atoms in one dimension: beyond the Fröhlich paradigm,” *New J. Phys.* **19**, 103035 (2017).
- <sup>56</sup>F. Grusdt, R. Schmidt, Y. E. Shchadilova, and E. Demler, “Strong-coupling Bose polarons in a Bose-Einstein condensate,” *Phys. Rev. A* **96**, 013607 (2017).
- <sup>57</sup>B. Kain and H. Y. Ling, “Analytical study of static beyond-Fröhlich Bose polarons in one dimension,” *Phys. Rev. A* **98**, 033610 (2018).
- <sup>58</sup>C. J. Myatt et al., “Production of Two Overlapping Bose-Einstein Condensates by Sympathetic Cooling,” *Phys. Rev. Lett.* **78**, 586–589 (1997).
- <sup>59</sup>G. Semeghini et al., “Self-Bound Quantum Droplets of Atomic Mixtures in Free Space,” *Phys. Rev. Lett.* **120**, 235301 (2018).
- <sup>60</sup>D. S. Hall et al., “Dynamics of Component Separation in a Binary Mixture of Bose-Einstein Condensates,” *Phys. Rev. Lett.* **81**, 1539–1542 (1998).
- <sup>61</sup>H.-J. Miesner et al., “Observation of Metastable States in Spinor Bose-Einstein Condensates,” *Phys. Rev. Lett.* **82**, 2228–2231 (1999).
- <sup>62</sup>P. Maddaloni et al., “Collective Oscillations of Two Colliding Bose-Einstein Condensates,” *Phys. Rev. Lett.* **85**, 2413–2417 (2000).
- <sup>63</sup>K. M. Mertes et al., “Nonequilibrium Dynamics and Superfluid Ring Excitations in Binary Bose-Einstein Condensates,” *Phys. Rev. Lett.* **99**, 190402 (2007).
- <sup>64</sup>C. Becker et al., “Oscillations and interactions of dark and dark-bright solitons in Bose-Einstein condensates,” *Nature Phys.* **4**, 496–501 (2008).
- <sup>65</sup>C. Hamner, J. J. Chang, P. Engels, and M. A. Hoefer, “Generation of Dark-Bright Soliton Trains in Superfluid-Superfluid Counterflow,” *Phys. Rev. Lett.* **106**, 065302 (2011).
- <sup>66</sup>E. Nicklas et al., “Observation of Scaling in the Dynamics of a Strongly Quenched Quantum Gas,” *Phys. Rev. Lett.* **115**, 245301 (2015).
- <sup>67</sup>C. R. Cabrera et al., “Quantum liquid droplets in a mixture of Bose-Einstein condensates,” *Science*, [10.1126/science.aao5686](https://doi.org/10.1126/science.aao5686) (2018).
- <sup>68</sup>A. Görlitz et al., “Realization of Bose-Einstein Condensates in Lower Dimensions,” *Phys. Rev. Lett.* **87**, 130402 (2001).

- <sup>69</sup>H. Moritz, T. Stöferle, M. Köhl, and T. Esslinger, “Exciting Collective Oscillations in a Trapped 1D Gas,” *Phys. Rev. Lett.* **91**, 250402 (2003).
- <sup>70</sup>T. Kinoshita, T. Wenger, and D. S. Weiss, “Observation of a One-Dimensional Tonks-Girardeau Gas,” *Science*, [10.1126/science.1100700](https://doi.org/10.1126/science.1100700) (2004).
- <sup>71</sup>B. Paredes et al., “Tonks–Girardeau gas of ultracold atoms in an optical lattice,” *Nature* **429**, 277–281 (2004).
- <sup>72</sup>L. J. LeBlanc and J. H. Thywissen, “Species-specific optical lattices,” *Phys. Rev. A* **75**, 053612 (2007).
- <sup>73</sup>A. Rubio-Abadal et al., “Many-Body Delocalization in the Presence of a Quantum Bath,” *Phys. Rev. X* **9**, 041014 (2019).
- <sup>74</sup>R. G. Newton, *Scattering Theory of Waves and Particles* (Springer Science & Business Media, Nov. 2013).
- <sup>75</sup>M. J. Seaton, “Quantum defect theory,” *Rep. Prog. Phys.* **46**, 167–257 (1983).
- <sup>76</sup>D. Blume and C. H. Greene, “Fermi pseudopotential approximation: Two particles under external confinement,” *Phys. Rev. A* **65**, 043613 (2002).
- <sup>77</sup>K. Nho and D. Blume, “Superfluidity of Mesoscopic Bose Gases under Varying Confinements,” *Phys. Rev. Lett.* **95**, 193601 (2005).
- <sup>78</sup>G. E. Astrakharchik and S. Giorgini, “Quantum Monte Carlo study of the three- to one-dimensional crossover for a trapped Bose gas,” *Phys. Rev. A* **66**, 053614 (2002).
- <sup>79</sup>L. A. P. Ardila and S. Giorgini, “Impurity in a Bose-Einstein condensate: Study of the attractive and repulsive branch using quantum Monte Carlo methods,” *Phys. Rev. A* **92**, 033612 (2015).
- <sup>80</sup>M. A. Garcia-March et al., “Sharp crossover from composite fermionization to phase separation in microscopic mixtures of ultracold bosons,” *Phys. Rev. A* **88**, 063604 (2013).
- <sup>81</sup>M. A. García-March et al., “Quantum correlations and spatial localization in one-dimensional ultracold bosonic mixtures,” *New J. Phys.* **16**, 103004 (2014).
- <sup>82</sup>M. A. García-March et al., “Distinguishability, degeneracy, and correlations in three harmonically trapped bosons in one dimension,” *Phys. Rev. A* **90**, 063605 (2014).
- <sup>83</sup>P. Mujal, E. Sarlé, A. Polls, and B. Juliá-Díaz, “Quantum correlations and degeneracy of identical bosons in a two-dimensional harmonic trap,” *Phys. Rev. A* **96**, 043614 (2017).
- <sup>84</sup>J. M. Schurer, A. Negretti, and P. Schmelcher, “Unraveling the Structure of Ultracold Mesoscopic Collinear Molecular Ions,” *Phys. Rev. Lett.* **119**, 063001 (2017).

- <sup>85</sup>J. Broeckhove, L. Lathouwers, E. Kesteloot, and P. Van Leuven, "On the equivalence of time-dependent variational principles," *Chem. Phys. Lett.* **149**, 547–550 (1988).
- <sup>86</sup>M. A. C. Saller and S. Habershon, "Quantum Dynamics with Short-Time Trajectories and Minimal Adaptive Basis Sets," *J. Chem. Theory Comput.* **13**, 3085–3096 (2017).
- <sup>87</sup>D. R. Hartree, "The Wave Mechanics of an Atom with a Non-Coulomb Central Field. Part I. Theory and Methods," *Math. Proc. Camb. Philos. Soc.* **24**, 89–110 (1928).
- <sup>88</sup>V. Fock, "Näherungsmethode zur Lösung des quantenmechanischen Mehrkörperproblems," *Z. Phys.* **61**, 126–148 (1930).
- <sup>89</sup>P. A. Dirac, "Note on Exchange Phenomena in the Thomas Atom," *Math. Proc. Camb. Philos. Soc.* **26**, 376–385 (1930).
- <sup>90</sup>A. McLachlan and M. Ball, "Time-Dependent Hartree-Fock Theory for Molecules," *Rev. Mod. Phys.* **36**, 844 (1964).
- <sup>91</sup>H.-D. Meyer, U. Manthe, and L. S. Cederbaum, "The multi-configurational time-dependent Hartree approach," *Chem. Phys. Lett.* **165**, 73–78 (1990).
- <sup>92</sup>M. H. Beck, A. Jäckle, G. A. Worth, and H.-D. Meyer, "The multiconfiguration time-dependent Hartree (MCTDH) method: a highly efficient algorithm for propagating wavepackets," *Phys. Rep.* **324**, 1–105 (2000).
- <sup>93</sup>O. E. Alon, A. I. Streltsov, and L. S. Cederbaum, "Multiconfigurational time-dependent Hartree method for bosons: Many-body dynamics of bosonic systems," *Phys. Rev. A* **77**, 033613 (2008).
- <sup>94</sup>J. Zanghellini et al., "An MCTDHF approach to multi-electron dynamics in laser fields," *Laser Phys.* **13**, 1064–1068 (2003).
- <sup>95</sup>H.-D. Meyer, F. Gatti, and G. A. Worth, *Multidimensional Quantum Dynamics: MCTDH Theory and Applications* (John Wiley & Sons, Apr. 2009).
- <sup>96</sup>H.-D. Meyer, "Studying molecular quantum dynamics with the multi-configuration time-dependent Hartree method," *Wiley Interdiscip. Rev. Comput. Mol. Sci.* **2**, 351–374 (2012).
- <sup>97</sup>F. Jensen, *Introduction to Computational Chemistry* (John Wiley & Sons, Feb. 2017).
- <sup>98</sup>P. Ring and P. Schuck, *The Nuclear Many-Body Problem* (Springer Science & Business Media, Mar. 2004).
- <sup>99</sup>R. Kosloff and H. Tal-Ezer, "A direct relaxation method for calculating eigenfunctions and eigenvalues of the Schrödinger equation on a grid," *Chem. Phys. Lett.* **127**, 223–230 (1986).
- <sup>100</sup>W. Ritz, "Über eine neue Methode zur Lösung gewisser Variationsprobleme der mathematischen Physik.," **1909**, 1–61 (1909).
- <sup>101</sup>L. P. Pitaevskii, "Vortex lines in an imperfect Bose gas," *Sov. Phys. JETP* **13**, 451–454 (1961).



- <sup>102</sup>E. P. Gross, "Structure of a quantized vortex in boson systems," *Nuovo Cim* **20**, 454-477 (1961).
- <sup>103</sup>E. P. Gross, "Hydrodynamics of a Superfluid Condensate," *J. Math. Phys.* **4**, 195-207 (1963).
- <sup>104</sup>O. Penrose and L. Onsager, "Bose-Einstein Condensation and Liquid Helium," *Phys. Rev.* **104**, 576-584 (1956).
- <sup>105</sup>N. Bogoliubov, "On the theory of superfluidity," *J. Phys.* **11**, 23 (1947).
- <sup>106</sup>C. W. Gardiner, "Particle-number-conserving Bogoliubov method which demonstrates the validity of the time-dependent Gross-Pitaevskii equation for a highly condensed Bose gas," *Phys. Rev. A* **56**, 1414-1423 (1997).
- <sup>107</sup>D. Dagnino, N. Barberán, M. Lewenstein, and J. Dalibard, "Vortex nucleation as a case study of symmetry breaking in quantum systems," *Nature Phys.* **5**, 431-437 (2009).
- <sup>108</sup>L. Tonks, "The Complete Equation of State of One, Two and Three-Dimensional Gases of Hard Elastic Spheres," *Phys. Rev.* **50**, 955-963 (1936).
- <sup>109</sup>M. Girardeau, "Relationship between Systems of Impenetrable Bosons and Fermions in One Dimension," *J. Math. Phys.* **1**, 516-523 (1960).
- <sup>110</sup>M. Greiner et al., "Quantum phase transition from a superfluid to a Mott insulator in a gas of ultracold atoms," *Nature* **415**, 39-44 (2002).
- <sup>111</sup>T. Stöferle et al., "Transition from a Strongly Interacting 1D Superfluid to a Mott Insulator," *Phys. Rev. Lett.* **92**, 130403 (2004).
- <sup>112</sup>L. S. Cederbaum and A. I. Streltsov, "Best mean-field for condensates," *Phys. Rev. A* **318**, 564-569 (2003).
- <sup>113</sup>L. S. Cederbaum and A. I. Streltsov, "Self-consistent fragmented excited states of trapped condensates," *Phys. Rev. A* **70**, 023610 (2004).
- <sup>114</sup>A. I. Streltsov and L. S. Cederbaum, "Properties of fragmented repulsive condensates," *Phys. Rev. A* **71**, 063612 (2005).
- <sup>115</sup>O. E. Alon, A. I. Streltsov, and L. S. Cederbaum, "Zoo of Quantum Phases and Excitations of Cold Bosonic Atoms in Optical Lattices," *Phys. Rev. Lett.* **95**, 030405 (2005).
- <sup>116</sup>O. E. Alon, A. I. Streltsov, and L. S. Cederbaum, "Demixing of Bosonic Mixtures in Optical Lattices from Macroscopic to Microscopic Scales," *Phys. Rev. Lett.* **97**, 230403 (2006).
- <sup>117</sup>O. E. Alon, A. I. Streltsov, and L. S. Cederbaum, "Time-dependent multi-orbital mean-field for fragmented Bose-Einstein condensates," *Phys. Rev. A* **362**, 453-459 (2007).
- <sup>118</sup>L. S. Cederbaum, A. I. Streltsov, Y. B. Band, and O. E. Alon, "Interferences in the Density of Two Bose-Einstein Condensates Consisting of Identical or Different Atoms," *Phys. Rev. Lett.* **98**, 110405 (2007).

- <sup>119</sup>A. I. Streltsov, O. E. Alon, and L. S. Cederbaum, "Role of Excited States in the Splitting of a Trapped Interacting Bose-Einstein Condensate by a Time-Dependent Barrier," *Phys. Rev. Lett.* **99**, 030402 (2007).
- <sup>120</sup>A. I. Streltsov, O. E. Alon, and L. S. Cederbaum, "Formation and Dynamics of Many-Boson Fragmented States in One-Dimensional Attractive Ultracold Gases," *Phys. Rev. Lett.* **100**, 130401 (2008).
- <sup>121</sup>K. Sakmann, A. I. Streltsov, O. E. Alon, and L. S. Cederbaum, "Exact Quantum Dynamics of a Bosonic Josephson Junction," *Phys. Rev. Lett.* **103**, 220601 (2009).
- <sup>122</sup>K. Sakmann, A. I. Streltsov, O. E. Alon, and L. S. Cederbaum, "Quantum dynamics of attractive versus repulsive bosonic Josephson junctions: Bose-Hubbard and full-Hamiltonian results," *Phys. Rev. A* **82**, 013620 (2010).
- <sup>123</sup>A. I. Streltsov, O. E. Alon, and L. S. Cederbaum, "Swift Loss of Coherence of Soliton Trains in Attractive Bose-Einstein Condensates," *Phys. Rev. Lett.* **106**, 240401 (2011).
- <sup>124</sup>A. I. Streltsov, K. Sakmann, O. E. Alon, and L. S. Cederbaum, "Accurate multi-boson long-time dynamics in triple-well periodic traps," *Phys. Rev. A* **83**, 043604 (2011).
- <sup>125</sup>K. Sakmann, A. I. Streltsov, O. E. Alon, and L. S. Cederbaum, "Universality of fragmentation in the Schrödinger dynamics of bosonic Josephson junctions," *Phys. Rev. A* **89**, 023602 (2014).
- <sup>126</sup>H. Wang and M. Thoss, "Multilayer formulation of the multiconfiguration time-dependent Hartree theory," *J. Chem. Phys.* **119**, 1289–1299 (2003).
- <sup>127</sup>U. Manthe, "A multilayer multiconfigurational time-dependent Hartree approach for quantum dynamics on general potential energy surfaces," *J. Chem. Phys.* **128**, 164116 (2008).
- <sup>128</sup>O. E. Alon, A. I. Streltsov, and L. S. Cederbaum, "Multiconfigurational time-dependent Hartree method for mixtures consisting of two types of identical particles," *Phys. Rev. A* **76**, 062501 (2007).
- <sup>129</sup>O. E. Alon, A. I. Streltsov, and L. S. Cederbaum, "Many-body theory for systems with particle conversion: Extending the multiconfigurational time-dependent Hartree method," *Phys. Rev. A* **79**, 022503 (2009).
- <sup>130</sup>O. E. Alon et al., "Recursive formulation of the multiconfigurational time-dependent Hartree method for fermions, bosons and mixtures thereof in terms of one-body density operators," *Chem. Phys.* **401**, 2–14 (2012).
- <sup>131</sup>J. C. Light, I. P. Hamilton, and J. V. Lill, "Generalized discrete variable approximation in quantum mechanics," *J. Chem. Phys.* **82**, 1400–1409 (1985).
- <sup>132</sup>J. C. Light and T. Carrington Jr, "Discrete-variable representations and their utilization," *Adv. Chem. Phys.* **114**, 263–310 (2000).

- <sup>133</sup>G. A. Worth, “Accurate wave packet propagation for large molecular systems: The multiconfiguration time-dependent Hartree (MCTDH) method with selected configurations,” *J. Chem. Phys.* **112**, 8322–8329 (2000).
- <sup>134</sup>F. Köhler et al., “Dynamical pruning of the non-equilibrium quantum dynamics of trapped ultracold bosons,” *J. Chem. Phys.* **151**, 054108 (2019).
- <sup>135</sup>H. Wang and M. Thoss, “Numerically exact quantum dynamics for indistinguishable particles: The multilayer multiconfiguration time-dependent Hartree theory in second quantization representation,” *J. Chem. Phys.* **131**, 024114 (2009).
- <sup>136</sup>H. Bethe, “Zur Theorie der Metalle,” *Z. Physik* **71**, 205–226 (1931).
- <sup>137</sup>M. Gaudin, *The Bethe Wavefunction*, edited by J.-S. Caux (Cambridge University Press, 2014).
- <sup>138</sup>D. S. Petrov, D. M. Gangardt, and G. V. Shlyapnikov, “Low-dimensional trapped gases,” *J. Phys. IV* **116**, 5–44 (2004).
- <sup>139</sup>Bose, “Plancks Gesetz und Lichtquantenhypothese,” *Z. Physik* **26**, 178–181 (1924).
- <sup>140</sup>A. Einstein, “Quantentheorie des einatomigen idealen Gases. Zweite Abhandlung,” in *Albert Einstein: Akademie-Vorträge* (John Wiley & Sons, Ltd, 2005), pp. 245–257.
- <sup>141</sup>E. J. Mueller, T.-L. Ho, M. Ueda, and G. Baym, “Fragmentation of Bose-Einstein condensates,” *Phys. Rev. A* **74**, 033612 (2006).
- <sup>142</sup>E. H. Lieb and W. Liniger, “Exact Analysis of an Interacting Bose Gas. I. The General Solution and the Ground State,” *Phys. Rev.* **130**, 1605–1616 (1963).
- <sup>143</sup>E. H. Lieb, “Exact Analysis of an Interacting Bose Gas. II. The Excitation Spectrum,” *Phys. Rev.* **130**, 1616–1624 (1963).
- <sup>144</sup>V. Dunjko, V. Lorent, and M. Olshanii, “Bosons in cigar-shaped traps: Thomas-Fermi regime, Tonks-Girardeau regime, and in between,” *Phys. Rev. Lett.* **86**, 5413–5416 (2001).
- <sup>145</sup>M. D. Girardeau, E. M. Wright, and J. M. Triscari, “Ground-state properties of a one-dimensional system of hard-core bosons in a harmonic trap,” *Phys. Rev. A* **63**, 033601 (2001).
- <sup>146</sup>P. J. Forrester, N. E. Frankel, T. M. Garoni, and N. S. Witte, “Finite one-dimensional impenetrable Bose systems: Occupation numbers,” *Phys. Rev. A* **67**, 043607 (2003).
- <sup>147</sup>Y. Brun and J. Dubail, “One-particle density matrix of trapped one-dimensional impenetrable bosons from conformal invariance,” *SciPost Phys.* **2**, 012 (2017).
- <sup>148</sup>G. J. Lapeyre, M. D. Girardeau, and E. M. Wright, “Momentum distribution for a one-dimensional trapped gas of hard-core bosons,” *Phys. Rev. A* **66**, 023606 (2002).

- <sup>149</sup>J. B. McGuire, "Study of Exactly Soluble One-Dimensional N-Body Problems," *J. Math. Phys.* **5**, 622–636 (1964).
- <sup>150</sup>E. Tempfli, S. Zöllner, and P. Schmelcher, "Excitations of attractive 1D bosons: binding versus fermionization," *New J. Phys.* **10**, 103021 (2008).
- <sup>151</sup>G. E. Astrakharchik, D. Blume, S. Giorgini, and B. E. Granger, "Quasi-One-Dimensional Bose Gases with a Large Scattering Length," *Phys. Rev. Lett.* **92**, 030402 (2004).
- <sup>152</sup>G. E. Astrakharchik, J. Boronat, J. Casulleras, and S. Giorgini, "Beyond the Tonks-Girardeau Gas: Strongly Correlated Regime in Quasi-One-Dimensional Bose Gases," *Phys. Rev. Lett.* **95**, 190407 (2005).
- <sup>153</sup>E. Haller et al., "Realization of an Excited, Strongly Correlated Quantum Gas Phase," *Science*, [10.1126/science.1175850](https://doi.org/10.1126/science.1175850) (2009).
- <sup>154</sup>P. Ao and S. T. Chui, "Binary Bose-Einstein condensate mixtures in weakly and strongly segregated phases," *Phys. Rev. A* **58**, 4836–4840 (1998).
- <sup>155</sup>T.-L. Ho and V. B. Shenoy, "Binary Mixtures of Bose Condensates of Alkali Atoms," *Phys. Rev. Lett.* **77**, 3276–3279 (1996).
- <sup>156</sup>K. L. Lee et al., "Phase separation and dynamics of two-component Bose-Einstein condensates," *Phys. Rev. A* **94**, 013602 (2016).
- <sup>157</sup>B. D. Esry, C. H. Greene, J. Burke James P., and J. L. Bohn, "Hartree-Fock Theory for Double Condensates," *Phys. Rev. Lett.* **78**, 3594–3597 (1997).
- <sup>158</sup>P. Öhberg and S. Stenholm, "Hartree-Fock treatment of the two-component Bose-Einstein condensate," *Phys. Rev. A* **57**, 1272–1279 (1998).
- <sup>159</sup>H. Pu and N. P. Bigelow, "Properties of Two-Species Bose Condensates," *Phys. Rev. Lett.* **80**, 1130–1133 (1998).
- <sup>160</sup>K. Kasamatsu, Y. Yasui, and M. Tsubota, "Macroscopic quantum tunneling of two-component Bose-Einstein condensates," *Phys. Rev. A* **64**, 053605 (2001).
- <sup>161</sup>R. Navarro, R. Carretero-González, and P. G. Kevrekidis, "Phase separation and dynamics of two-component Bose-Einstein condensates," *Phys. Rev. A* **80**, 023613 (2009).
- <sup>162</sup>R. W. Pattinson et al., "Equilibrium solutions for immiscible two-species Bose-Einstein condensates in perturbed harmonic traps," *Phys. Rev. A* **87**, 013625 (2013).
- <sup>163</sup>S. Zöllner, H.-D. Meyer, and P. Schmelcher, "Composite fermionization of one-dimensional Bose-Bose mixtures," *Phys. Rev. A* **78**, 013629 (2008).
- <sup>164</sup>Y. J. Hao and S. Chen, "Ground-state properties of interacting two-component Bose gases in a one-dimensional harmonic trap," *Eur. Phys. J. D* **51**, 261–266 (2009).
- <sup>165</sup>M. D. Girardeau and A. Minguzzi, "Soluble Models of Strongly Interacting Ultracold Gas Mixtures in Tight Waveguides," *Phys. Rev. Lett.* **99**, 230402 (2007).

- <sup>166</sup>F. Deuretzbacher et al., “Exact Solution of Strongly Interacting Quasi-One-Dimensional Spinor Bose Gases,” *Phys. Rev. Lett.* **100**, 160405 (2008).
- <sup>167</sup>B. Fang et al., “Exact solution for the degenerate ground-state manifold of a strongly interacting one-dimensional Bose-Fermi mixture,” *Phys. Rev. A* **84**, 023626 (2011).
- <sup>168</sup>F. Deuretzbacher et al., “Quantum magnetism without lattices in strongly interacting one-dimensional spinor gases,” *Phys. Rev. A* **90**, 013611 (2014).
- <sup>169</sup>A. G. Volosniev et al., “Engineering the dynamics of effective spin-chain models for strongly interacting atomic gases,” *Phys. Rev. A* **91**, 023620 (2015).
- <sup>170</sup>L. Yang and X. Cui, “Effective spin-chain model for strongly interacting one-dimensional atomic gases with an arbitrary spin,” *Phys. Rev. A* **93**, 013617 (2016).
- <sup>171</sup>F. Deuretzbacher et al., “Spin-chain model for strongly interacting one-dimensional Bose-Fermi mixtures,” *Phys. Rev. A* **95**, 043630 (2017).
- <sup>172</sup>F. Deuretzbacher and L. Santos, “Tuning an effective spin chain of three strongly interacting one-dimensional fermions with the transversal confinement,” *Phys. Rev. A* **96**, 013629 (2017).
- <sup>173</sup>Z.-H. Luo et al., “A new form of liquid matter: Quantum droplets,” *Front. Phys.* **16**, 32201 (2020).
- <sup>174</sup>P. Cheiney et al., “Bright Soliton to Quantum Droplet Transition in a Mixture of Bose-Einstein Condensates,” *Phys. Rev. Lett.* **120**, 135301 (2018).
- <sup>175</sup>D. S. Petrov, “Quantum Mechanical Stabilization of a Collapsing Bose-Bose Mixture,” *Phys. Rev. Lett.* **115**, 155302 (2015).
- <sup>176</sup>M. A. Cazalilla and A. F. Ho, “Instabilities in Binary Mixtures of One-Dimensional Quantum Degenerate Gases,” *Phys. Rev. Lett.* **91**, 150403 (2003).
- <sup>177</sup>D. S. Petrov and G. E. Astrakharchik, “Ultradilute Low-Dimensional Liquids,” *Phys. Rev. Lett.* **117**, 100401 (2016).
- <sup>178</sup>L. Parisi, G. E. Astrakharchik, and S. Giorgini, “Liquid State of One-Dimensional Bose Mixtures: A Quantum Monte Carlo Study,” *Phys. Rev. Lett.* **122**, 105302 (2019).
- <sup>179</sup>E. Tempfli, S. Zöllner, and P. Schmelcher, “Binding between two-component bosons in one dimension,” *New J. Phys.* **11**, 073015 (2009).
- <sup>180</sup>T. Busch, B.-G. Englert, K. Rzazewski, and M. Wilkens, “Two Cold Atoms in a Harmonic Trap,” *Found. Phys.* **28**, 549–559 (1998).
- <sup>181</sup>G. Delannoy et al., “Understanding the production of dual Bose-Einstein condensation with sympathetic cooling,” *Phys. Rev. A* **63**, 051602 (2001).

- <sup>182</sup>M. Mudrich et al., "Sympathetic Cooling with Two Atomic Species in an Optical Trap," *Phys. Rev. Lett.* **88**, 253001 (2002).
- <sup>183</sup>K. Kasamatsu and M. Tsubota, "Multiple Domain Formation Induced by Modulation Instability in Two-Component Bose-Einstein Condensates," *Phys. Rev. Lett.* **93**, 100402 (2004).
- <sup>184</sup>S. Ronen, J. L. Bohn, L. E. Halmo, and M. Edwards, "Dynamical pattern formation during growth of a dual-species Bose-Einstein condensate," *Phys. Rev. A* **78**, 053613 (2008).
- <sup>185</sup>J. Hofmann, S. S. Natu, and S. Das Sarma, "Coarsening Dynamics of Binary Bose Condensates," *Phys. Rev. Lett.* **113**, 095702 (2014).
- <sup>186</sup>K. Kasamatsu, M. Tsubota, and M. Ueda, "Vortex Phase Diagram in Rotating Two-Component Bose-Einstein Condensates," *Phys. Rev. Lett.* **91**, 150406 (2003).
- <sup>187</sup>P. Mason and A. Aftalion, "Classification of the ground states and topological defects in a rotating two-component Bose-Einstein condensate," *Phys. Rev. A* **84**, 033611 (2011).
- <sup>188</sup>K. Keiler, S. I. Mistakidis, and P. Schmelcher, "Doping a lattice-trapped bosonic species with impurities: from ground state properties to correlated tunneling dynamics," *New J. Phys.* **22**, 083003 (2020).
- <sup>189</sup>R. Jozsa, "Fidelity for mixed quantum states," *J. Mod. Opt.* **41**, 2315–2323 (1994).
- <sup>190</sup>M.-O. Mewes et al., "Collective Excitations of a Bose-Einstein Condensate in a Magnetic Trap," *Phys. Rev. Lett.* **77**, 988–991 (1996).
- <sup>191</sup>D. S. Jin et al., "Collective excitations of a Bose-Einstein condensate in a dilute gas," *Phys. Rev. Lett.* **77**, 420–423 (1996).
- <sup>192</sup>F. Chevy et al., "Transverse breathing mode of an elongated Bose-Einstein condensate," *Phys. Rev. Lett.* **88**, 250402 (2002).
- <sup>193</sup>M. Edwards et al., "Collective Excitations of Atomic Bose-Einstein Condensates," *Phys. Rev. Lett.* **77**, 1671–1674 (1996).
- <sup>194</sup>S. Stringari, "Collective Excitations of a Trapped Bose-Condensed Gas," *Phys. Rev. Lett.* **77**, 2360–2363 (1996).
- <sup>195</sup>S. Stringari, "Dynamics of Bose-Einstein condensed gases in highly deformed traps," *Phys. Rev. A* **58**, 2385–2388 (1998).
- <sup>196</sup>L. Pitaevskii and S. Stringari, "Elementary Excitations in Trapped Bose-Einstein Condensed Gases Beyond the Mean-Field Approximation," *Phys. Rev. Lett.* **81**, 4541–4544 (1998).
- <sup>197</sup>F. Dalfovo, S. Giorgini, L. P. Pitaevskii, and S. Stringari, "Theory of Bose-Einstein condensation in trapped gases," *Rev. Mod. Phys.* **71**, 463–512 (1999).
- <sup>198</sup>A. Minguzzi and D. M. Gangardt, "Exact Coherent States of a Harmonically Confined Tonks-Girardeau Gas," *Phys. Rev. Lett.* **94**, 240404 (2005).

- <sup>199</sup>S. E. Pollack et al., “Collective excitation of a Bose-Einstein condensate by modulation of the atomic scattering length,” *Phys. Rev. A* **81**, 053627 (2010).
- <sup>200</sup>S. Choi, V. Dunjko, Z. D. Zhang, and M. Olshanii, “Monopole Excitations of a Harmonically Trapped One-Dimensional Bose Gas from the Ideal Gas to the Tonks-Girardeau Regime,” *Phys. Rev. Lett.* **115**, 115302 (2015).
- <sup>201</sup>M. Bartenstein et al., “Collective Excitations of a Degenerate Gas at the BEC-BCS Crossover,” *Phys. Rev. Lett.* **92**, 203201 (2004).
- <sup>202</sup>G. E. Astrakharchik, R. Combescot, X. Leyronas, and S. Stringari, “Equation of State and Collective Frequencies of a Trapped Fermi Gas Along the BEC-Unitarity Crossover,” *Phys. Rev. Lett.* **95**, 030404 (2005).
- <sup>203</sup>A. Altmeyer et al., “Precision measurements of collective oscillations in the BEC-BCS crossover,” *Phys. Rev. Lett.* **98**, 040401 (2007).
- <sup>204</sup>R. Dubessy et al., “Imaging the collective excitations of an ultracold gas using statistical correlations,” *New J. Phys.* **16**, 122001 (2014).
- <sup>205</sup>B. Fang, G. Carleo, A. Johnson, and I. Bouchoule, “Quench-Induced Breathing Mode of One-Dimensional Bose Gases,” *Phys. Rev. Lett.* **113**, 035301 (2014).
- <sup>206</sup>C. R. McDonald et al., “Theory of the Quantum Breathing Mode in Harmonic Traps and its Use as a Diagnostic Tool,” *Phys. Rev. Lett.* **111**, 256801 (2013).
- <sup>207</sup>M. Egorov et al., “Measurement of s-wave scattering lengths in a two-component Bose-Einstein condensate,” *Phys. Rev. A* **87**, 053614 (2013).
- <sup>208</sup>A. Melzer, M. Klindworth, and A. Piel, “Normal Modes of 2D Finite Clusters in Complex Plasmas,” *Phys. Rev. Lett.* **87**, 115002 (2001).
- <sup>209</sup>J. W. Abraham and M. Bonitz, “Quantum Breathing Mode of Trapped Particles: From Nanoplasmas to Ultracold Gases,” *Contrib. Plasma Phys.* **54**, 27–99 (2014).
- <sup>210</sup>S. Bauch, K. Balzer, C. Henning, and M. Bonitz, “Quantum breathing mode of trapped bosons and fermions at arbitrary coupling,” *Phys. Rev. B* **80**, 054515 (2009).
- <sup>211</sup>J. W. Abraham, K. Balzer, D. Hochstuhl, and M. Bonitz, “Quantum breathing mode of interacting particles in a one-dimensional harmonic trap,” *Phys. Rev. B* **86**, 125112 (2012).
- <sup>212</sup>J. W. Abraham et al., “Quantum breathing mode of trapped systems in one and two dimensions,” *New J. Phys.* **16**, 013001 (2014).
- <sup>213</sup>C. Menotti and S. Stringari, “Collective oscillations of a one-dimensional trapped Bose-Einstein gas,” *Phys. Rev. A* **66**, 043610 (2002).
- <sup>214</sup>R. Schmitz, S. Krönke, L. Cao, and P. Schmelcher, “Quantum breathing dynamics of ultracold bosons in one-dimensional harmonic traps: Unraveling the pathway from few- to many-body systems,” *Phys. Rev. A* **88**, 043601 (2013).

- <sup>215</sup>A. I. Gudyma, G. E. Astrakharchik, and M. B. Zvonarev, “Reentrant behavior of the breathing-mode-oscillation frequency in a one-dimensional Bose gas,” *Phys. Rev. A* **92**, 021601 (2015).
- <sup>216</sup>X.-L. Chen, Y. Li, and H. Hu, “Collective modes of a harmonically trapped one-dimensional Bose gas: the effects of finite particle number and nonzero temperature,” *Phys. Rev. A* **91**, 063631 (2015).
- <sup>217</sup>C. Matthies, S. Zöllner, H.-D. Meyer, and P. Schmelcher, “Quantum dynamics of two bosons in an anharmonic trap: Collective versus internal excitations,” *Phys. Rev. A* **76**, 023602 (2007).
- <sup>218</sup>T. Keller and T. Fogarty, “Probing the out-of-equilibrium dynamics of two interacting atoms,” *Phys. Rev. A* **94**, 063620 (2016).
- <sup>219</sup>D. Ledesma, A. Romero-Ros, A. Polls, and B. Juliá-Díaz, “Dynamic structure function of two interacting atoms in 1D,” *EPL* **127**, 56001 (2019).
- <sup>220</sup>T. Busch, J. I. Cirac, V. M. Pérez-García, and P. Zoller, “Stability and collective excitations of a two-component Bose-Einstein condensed gas: A moment approach,” *Phys. Rev. A* **56**, 2978–2983 (1997).
- <sup>221</sup>B. D. Esry and C. H. Greene, “Low-lying excitations of double Bose-Einstein condensates,” *Phys. Rev. A* **57**, 1265–1271 (1998).
- <sup>222</sup>H. Pu and N. P. Bigelow, “Collective excitations, metastability, and nonlinear response of a trapped two-species Bose-Einstein condensate,” *Phys. Rev. Lett.* **80**, 1134–1137 (1998).
- <sup>223</sup>D. Gordon and C. M. Savage, “Excitation spectrum and instability of a two-species Bose-Einstein condensate,” *Phys. Rev. A* **58**, 1440–1444 (1998).
- <sup>224</sup>H. Morise and M. Wadati, “Phase separation and collective excitations of two-component Bose-Einstein condensates in traps,” *J. Phys. Soc. Jpn.* **69**, 2463–2467 (2000).
- <sup>225</sup>J. Catani et al., “Quantum dynamics of impurities in a one-dimensional Bose gas,” *Phys. Rev. A* **85**, 023623 (2012).
- <sup>226</sup>T. H. Johnson et al., “Breathing oscillations of a trapped impurity in a Bose gas,” *EPL* **98**, 26001 (2012).
- <sup>227</sup>D. Donoho, “Compressed sensing,” *IEEE Trans. Inf. Theory* **52**, 1289–1306 (2006).
- <sup>228</sup>Y. C. Eldar and G. Kutyniok, *Compressed sensing: theory and applications* (Cambridge University Press, Cambridge; New York, 2012).
- <sup>229</sup>W. Ketterle, D. Durfee, and D. Stamper-Kurn, “Making, probing and understanding Bose-Einstein condensates,” in *Bose-Einstein Condensation in Atomic Gases* (IOS Press, 1999), pp. 67–176.
- <sup>230</sup>W. Ketterle and M. W. Zwierlein, “Making, probing and understanding ultracold Fermi gases,” *Riv. Nuovo Cim.* **31**, 247–422 (2008).
- <sup>231</sup>G. Binnig and H. Rohrer, “Scanning tunneling microscopy—from birth to adolescence,” *Rev. Mod. Phys.* **59**, 615–625 (1987).



- <sup>232</sup>B. Huang, M. Bates, and X. Zhuang, "Super-Resolution Fluorescence Microscopy," *Annu. Rev. Biochem.* **78**, 993–1016 (2009).
- <sup>233</sup>A. V. Gorshkov et al., "Coherent Quantum Optical Control with Sub-wavelength Resolution," *Phys. Rev. Lett.* **100**, 093005 (2008).
- <sup>234</sup>M. McDonald, J. Trisnadi, K.-X. Yao, and C. Chin, "Superresolution Microscopy of Cold Atoms in an Optical Lattice," *Phys. Rev. X* **9**, 021001 (2019).
- <sup>235</sup>S. Subhankar et al., "Nanoscale Atomic Density Microscopy," *Phys. Rev. X* **9**, 021002 (2019).
- <sup>236</sup>D. Yang et al., "Quantum scanning microscope for cold atoms," *Phys. Rev. A* **98**, 023852 (2018).
- <sup>237</sup>D. Yang et al., "Theory of a Quantum Scanning Microscope for Cold Atoms," *Phys. Rev. Lett.* **120**, 133601 (2018).
- <sup>238</sup>N. Schlosser, G. Reymond, I. Protsenko, and P. Grangier, "Sub-poissonian loading of single atoms in a microscopic dipole trap," *Nature* **411**, 1024–1027 (2001).
- <sup>239</sup>Y. Miroshnychenko et al., "Continued imaging of the transport of a single neutral atom," *Opt. Express* **11**, 3498–3502 (2003).
- <sup>240</sup>K. D. Nelson, X. Li, and D. S. Weiss, "Imaging single atoms in a three-dimensional array," *Nature Phys.* **3**, 556–560 (2007).
- <sup>241</sup>R. Bücker et al., "Single-particle-sensitive imaging of freely propagating ultracold atoms," *New J. Phys.* **11**, 103039 (2009).
- <sup>242</sup>D. B. Hume et al., "Accurate Atom Counting in Mesoscopic Ensembles," *Phys. Rev. Lett.* **111**, 253001 (2013).
- <sup>243</sup>A. Bergschneider et al., "Spin-resolved single-atom imaging of Li 6 in free space," *Phys. Rev. A* **97**, 063613 (2018).
- <sup>244</sup>T. Gericke et al., "High-resolution scanning electron microscopy of an ultracold quantum gas," *Nature Phys.* **4**, 949–953 (2008).
- <sup>245</sup>P. Würtz et al., "Experimental Demonstration of Single-Site Addressability in a Two-Dimensional Optical Lattice," *Phys. Rev. Lett.* **103**, 080404 (2009).
- <sup>246</sup>W. S. Bakr et al., "Probing the Superfluid-to-Mott Insulator Transition at the Single-Atom Level," *Science* **329**, 547–550 (2010).
- <sup>247</sup>D. Greif et al., "Site-resolved imaging of a fermionic Mott insulator," *Science* **351**, 953–957 (2016).
- <sup>248</sup>A. Lukin et al., "Probing entanglement in a many-body-localized system," *Science* **364**, 256–260 (2019).
- <sup>249</sup>M. Rispoli et al., "Quantum critical behaviour at the many-body localization transition," *Nature* **573**, 385–389 (2019).
- <sup>250</sup>L. W. Cheuk et al., "Observation of spatial charge and spin correlations in the 2D Fermi-Hubbard model," *Science* **353**, 1260–1264 (2016).

- <sup>251</sup>M. F. Parsons et al., "Site-resolved measurement of the spin-correlation function in the Fermi-Hubbard model," *Science* **353**, 1253–1256 (2016).
- <sup>252</sup>M. Boll et al., "Spin- and density-resolved microscopy of antiferromagnetic correlations in Fermi-Hubbard chains," *Science* **353**, 1257–1260 (2016).
- <sup>253</sup>M. Endres et al., "Observation of Correlated Particle-Hole Pairs and String Order in Low-Dimensional Mott Insulators," *Science* **334**, 200–203 (2011).
- <sup>254</sup>T. A. Hilker et al., "Revealing hidden antiferromagnetic correlations in doped Hubbard chains via string correlators," *Science* **357**, 484–487 (2017).
- <sup>255</sup>R. Islam et al., "Measuring entanglement entropy in a quantum many-body system," *Nature* **528**, 77–83 (2015).
- <sup>256</sup>A. M. Kaufman et al., "Quantum thermalization through entanglement in an isolated many-body system," *Science* **353**, 794–800 (2016).
- <sup>257</sup>I. Bloch, "Ultracold quantum gases in optical lattices," *Nature Phys.* **1**, 23–30 (2005).
- <sup>258</sup>M. Greiner and S. Fölling, "Optical lattices," *Nature* **453**, 736–738 (2008).
- <sup>259</sup>R. Grimm, M. Weidemüller, and Y. B. Ovchinnikov, "Optical dipole traps for neutral atoms," in , Vol. 42, *Advances In Atomic, Molecular, and Optical Physics* (Academic Press, 2000), pp. 95–170.
- <sup>260</sup>T. C. Li, H. Kelkar, D. Medellin, and M. G. Raizen, "Real-time control of the periodicity of a standing wave: an optical accordion," *Opt. Express* **16**, 5465–5470 (2008).
- <sup>261</sup>R. A. Williams et al., "Dynamic optical lattices: two-dimensional rotating and accordion lattices for ultracold atoms," *Opt. Express* **16**, 16977–16983 (2008).
- <sup>262</sup>C. Weitenberg, "Single-atom resolved imaging and manipulation in an atomic Mott insulator," PhD thesis (Imu, 2011).
- <sup>263</sup>M. Miranda et al., "Site-resolved imaging of ytterbium atoms in a two-dimensional optical lattice," *Phys. Rev. A* **91**, 063414 (2015).
- <sup>264</sup>M. Miranda, R. Inoue, N. Tambo, and M. Kozuma, "Site-resolved imaging of a bosonic Mott insulator using ytterbium atoms," *Phys. Rev. A* **96**, 043626 (2017).
- <sup>265</sup>A. Omran et al., "Microscopic Observation of Pauli Blocking in Degenerate Fermionic Lattice Gases," *Phys. Rev. Lett.* **115**, 263001 (2015).
- <sup>266</sup>M. Hohmann et al., "Individual Tracer Atoms in an Ultracold Dilute Gas," *Phys. Rev. Lett.* **118**, 263401 (2017).
- <sup>267</sup>W. Wallace, L. H. Schaefer, and J. R. Swedlow, "A workingperson's guide to deconvolution in light microscopy," *BioTechniques* **31**, 1076–1078, 1080, 1082 (2001).

- <sup>268</sup>P. C. Hansen, *Deblurring images: matrices, spectra, and filtering*, Fundamentals of algorithms (SIAM, Society for Industrial and Applied Mathematics, 2006), 130 pp.
- <sup>269</sup>L. A. Peña Ardila, M. Heyl, and A. Eckardt, “Measuring the single-particle density matrix for fermions and hard-core bosons in an optical lattice,” *Phys. Rev. Lett.* **121**, 260401 (2018).
- <sup>270</sup>A. Burkov, *The hundred-page machine learning book* (Andriy Burkov, 2019), 141 pp.
- <sup>271</sup>L. Moroney, *AI and machine learning for coders: a programmer’s guide to artificial intelligence*, First edition, October 2020 (O’Reilly, 2021), 365 pp.
- <sup>272</sup>I. Goodfellow, Y. Bengio, and A. Courville, *Deep learning*, Adaptive computation and machine learning (The MIT Press, 2016), 775 pp.
- <sup>273</sup>S. H. Strogatz, “Exploring complex networks,” *Nature* **410**, 268–276 (2001).
- <sup>274</sup>R. Albert and A.-L. Barabási, “Statistical mechanics of complex networks,” *Rev. Mod. Phys.* **74**, 47–97 (2002).
- <sup>275</sup>S. N. Dorogovtsev and J. F. F. Mendes, “Evolution of networks,” *Adv. Phys.* **51**, 1079–1187 (2002).
- <sup>276</sup>F. R. K. Chung, *Spectral graph theory*, Regional conference series in mathematics no. 92 (Published for the Conference Board of the mathematical sciences by the American Mathematical Society, 1997), 207 pp.
- <sup>277</sup>P. Van Mieghem, *Graph spectra for complex networks* (Cambridge University Press, 2011), 346 pp.
- <sup>278</sup>A. E. Brouwer and W. H. Haemers, *Spectra of graphs* (Springer, 2012).
- <sup>279</sup>A. N. Langville and C. D. Meyer, *Google’s PageRank and beyond: the science of search engine rankings* (Princeton University Press, 2012).
- <sup>280</sup>M. E. J. Newman, *Networks*, Second edition (Oxford University Press, 2018), 780 pp.
- <sup>281</sup>A. Lucas, “Ising formulations of many NP problems,” *Front. Phys.* **2** (2014).
- <sup>282</sup>D. B. West, *Introduction to graph theory*, 2nd ed (Prentice Hall, 2001), 588 pp.
- <sup>283</sup>R. J. Trudeau, *Introduction to graph theory* (Courier Corporation, Apr. 15, 2013), 242 pp.
- <sup>284</sup>E. Estrada and P. A. Knight, *A first course in network theory*, First edition (Oxford University Press, 2015), 254 pp.
- <sup>285</sup>A.-L. Barabási and M. Pósfai, *Network science* (Cambridge University Press, 2016), 456 pp.
- <sup>286</sup>G. D. Battista, P. Eades, R. Tamassia, and I. G. Tollis, “Algorithms for drawing graphs: an annotated bibliography,” *Comput. Geom.* **4**, 235–282 (1994).

- <sup>287</sup>H. C. Purchase, “Metrics for graph drawing aesthetics,” *J. Vis. Lang. Comput.* **13**, 501–516 (2002).
- <sup>288</sup>J. F. K. Schmidt, “Milgram (1967): The Small World Problem,” in *Schlüsselwerke der Netzwerkforschung*, edited by B. Holzer and C. Stegbauer, Netzwerkforschung (Springer Fachmedien, 2019), pp. 407–410.
- <sup>289</sup>B. D. MacArthur, R. J. Sánchez-García, and J. W. Anderson, “Symmetry in complex networks,” *Discrete Appl. Math.* **156**, 3525–3531 (2008).
- <sup>290</sup>B. D. MacArthur and R. J. Sánchez-García, “Spectral characteristics of network redundancy,” *Phys. Rev. E* **80**, 026117 (2009).
- <sup>291</sup>D. Garlaschelli, F. Ruzzenenti, and R. Basosi, “Complex Networks and Symmetry I: A Review,” *Symmetry* **2**, 1683–1709 (2010).
- <sup>292</sup>R. J. Sánchez-García, “Exploiting symmetry in network analysis,” *Commun. Phys.* **3**, 1–15 (2020).
- <sup>293</sup>C. D. Godsil and B. D. McKay, “Constructing cospectral graphs,” *Aeq. Math.* **25**, 257–268 (1982).
- <sup>294</sup>C. Godsil and J. Smith, “Strongly cospectral vertices,” [arXiv:1709.07975 \[math\]](https://arxiv.org/abs/1709.07975) (2017).
- <sup>295</sup>C. Godsil, “State transfer on graphs,” *Discrete Math., Algebraic Graph Theory — A Volume Dedicated to Gert Sabidussi on the Occasion of His 80th Birthday* **312**, 129–147 (2012).
- <sup>296</sup>M. Kac, “Can one hear the shape of a drum?” *Am. Math. Mon.* **73**, 1–23 (1966).
- <sup>297</sup>W. C. Herndon, “The characteristic polynomial does not uniquely determine molecular topology,” *J. Chem. Doc.* **14**, 150–151 (1974).
- <sup>298</sup>W. C. Herndon, “Isospectral molecules,” *Tetrahedron Lett.* **15**, 671–674 (1974).
- <sup>299</sup>W. C. Herndon and M. L. Ellzey, “Isospectral graphs and molecules,” *Tetrahedron* **31**, 99–107 (1975).
- <sup>300</sup>B. Gutkin and U. Smilansky, “Can one hear the shape of a graph?” *J. Phys. A: Math. Gen.* **34**, 6061–6068 (2001).
- <sup>301</sup>E. R. van Dam and W. H. Haemers, “Which graphs are determined by their spectrum?” *Linear Algebra Appl., Combinatorial Matrix Theory Conference (Pohang, 2002)* **373**, 241–272 (2003).
- <sup>302</sup>W. Wang, L. Qiu, and Y. Hu, “Cospectral graphs, GM-switching and regular rational orthogonal matrices of level  $p$ ,” *Linear Algebra Appl.* **563**, 154–177 (2019).
- <sup>303</sup>F. Belardo, M. Brunetti, M. Cavaleri, and A. Donno, “Constructing cospectral signed graphs,” *Linear Multilinear Algebra* **69**, 2717–2732 (2021).
- <sup>304</sup>M. Langberg and D. Vilenchik, “Constructing cospectral graphs via a new form of graph product,” *Linear Multilinear Algebra* **66**, 1838–1852 (2018).

- <sup>305</sup>K. Lorenzen, "Cospectral constructions for several graph matrices using cousin vertices," *Spec. Matrices* **10**, 9–22 (2022).
- <sup>306</sup>S. Dutta and B. Adhikari, "Construction of cospectral graphs," *J. Algebr. Comb.* **52**, 215–235 (2020).
- <sup>307</sup>Y. Ji, S. Gong, and W. Wang, "Constructing cospectral bipartite graphs," *Discrete Math.* **343**, 112020 (2020).
- <sup>308</sup>A. Farrugia, "The Overgraphs of Generalized Cospectral Controllable Graphs," *Electron. J. Comb.*, P1.14–P1.14 (2019).
- <sup>309</sup>M. Röntgen, C. V. Morfonios, and P. Schmelcher, "Compact localized states and flat bands from local symmetry partitioning," *Phys. Rev. B* **97**, 035161 (2018).
- <sup>310</sup>S. Flach et al., "Detangling flat bands into Fano lattices," *EPL* **105**, 30001 (2014).
- <sup>311</sup>L. Bunimovich and B. Webb, *Isospectral transformations: a new approach to analyzing multidimensional systems and networks*, Springer monographs in mathematics (Springer, 2014), 175 pp.
- <sup>312</sup>L. A. Bunimovich and B. Z. Webb, "Isospectral graph transformations, spectral equivalence, and global stability of dynamical networks," *Nonlinearity* **25**, 211–254 (2011).
- <sup>313</sup>P. Duarte and M. J. Torres, "Eigenvectors of isospectral graph transformations," *Linear Algebra Appl.* **474**, 110–123 (2015).
- <sup>314</sup>L. A. Bunimovich and B. Z. Webb, "Restrictions and stability of time-delayed dynamical networks," *Nonlinearity* **26**, 2131–2156 (2013).
- <sup>315</sup>D. Reber and B. Webb, "Intrinsic stability: stability of dynamical networks and switched systems with any type of time-delays," *Nonlinearity* **33**, 2660–2685 (2020).
- <sup>316</sup>L. A. Bunimovich and B. Z. Webb, "Isospectral graph reductions and improved estimates of matrices' spectra," *Linear Algebra Appl.* **437**, 1429–1457 (2012).
- <sup>317</sup>F. G. Vasquez and B. Z. Webb, "Pseudospectra of isospectrally reduced matrices," *Numer. Linear Algebra Appl.* **22**, 145–174 (2015).
- <sup>318</sup>F. Zhang, ed., *The Schur complement and its applications*, Numerical methods and algorithms v. 4 (Springer, 2005), 295 pp.
- <sup>319</sup>V. Bach, J. Fröhlich, and I. M. Sigal, "Renormalization group analysis of spectral problems in quantum field theory," *Adv. Math.* **137**, 205–298 (1998).
- <sup>320</sup>V. Bach, J. Fröhlich, and I. M. Sigal, "Quantum electrodynamics of confined nonrelativistic particles," *Adv. Math.* **137**, 299–395 (1998).
- <sup>321</sup>G. Grosso and G. Pastori Parravicini, *Solid state physics*, Second edition (Academic Press, an imprint of Elsevier, 2014), 857 pp.
- <sup>322</sup>Frobenius, "Ueber lineare Substitutionen und bilineare Formen.," *J. für die Reine und Angew. Math.* **1878**, 1–63 (1878).

- <sup>323</sup>F. R. Chang and H. C. Chen, "The generalized Cayley-Hamilton theorem for standard pencils," *Syst. Control. Lett.* **18**, 179–182 (1992).
- <sup>324</sup>D. Smith and B. Webb, "Hidden symmetries in real and theoretical networks," *Phys. A: Stat. Mech. Appl.* **514**, 855–867 (2019).
- <sup>325</sup>M. Kempton, J. Sinkovic, D. Smith, and B. Webb, "Characterizing cospectral vertices via isospectral reduction," *Linear Algebra Appl.* **594**, 226–248 (2020).
- <sup>326</sup>H. V. McIntosh, "On accidental degeneracy in classical and quantum mechanics," *Am. J. Phys.* **27**, 620–625 (1959).
- <sup>327</sup>H. V. McIntosh, "Symmetry and degeneracy," in *Group theory and its applications*, edited by E. M. Loebl (Academic Press, Jan. 1, 1971), pp. 75–144.
- <sup>328</sup>L. D. Landau, E. M. Lifshitz, TotalBoox, and TBX, *Quantum mechanics* (Elsevier Science, 2013).

*You take the blue pill—the story ends,  
you wake up in your bed and believe whatever you want to believe.  
You take the red pill—you stay in Wonderland,  
and I show you how deep the rabbit hole goes.*  
—Morpheus to Neo, the "Matrix" movie (1999)

## ACKNOWLEDGMENTS

---

It was indeed a long and tough journey though without a doubt it was worth the time. I am extremely grateful to my family, friends and colleagues, who made this time so colourful and enjoyable.

I would like to thank my supervisor, Prof. Dr. Peter Schmelcher, for the given opportunity to do my PhD in his group. In particular, I appreciate his guidance and constant support to freely explore the realms of physics, for providing excellent environment and enjoyable atmosphere where I could feel as at home, for suggesting all the great workshops, which I overly enjoyed, and for offering me the opportunity to organize one at our institute.

I greatly appreciate the financial support provided by the "Studienstiftung des deutschen Volkes", for the informative events and great opportunities. I would like to thank my tutor, Prof. Dr. Harendza Sigrid, who organized entertaining evening Zoom sessions for the Hamburger scholar group in the times of social isolation during the Covid pandemic.

I overly enjoyed daily discussions with former and current members of the group during our lunch time and coffee breaks, journal clubs and ALDI talks, group retreats and occasional group forays after the work.

I thank Malte Röntgen, Dan Bosworth and Fabian Köhler for the valuable feedback to improve the readability of my thesis.

I am indebted to the ML-X elders, Dr. Sven Krönke and Dr. Johannes Schurer, for their patience, altruism and wisdom while teaching me the ways of the Force (how to use the code), and to our current admin, Fabian Köhler, for his constant assistance whenever my ML-X code got spoiled ... for whatever reason ...

I would like to express my thanks to Kevin Keiler, who provided a great company way before I started my PhD, during our Bachelor and Master, which we spent puzzling over exercise sheets, deciphering the lecture notes and having many passionate discussions about the life in Westeros.

I would like to thank my McFit buddy, Alejandro Romero Ros, for suffering with me for several hours per week under inhuman exercises devised by our tyrant trainer Jörg. I wouldn't have made it out alive if it weren't for you!

I am grateful to the local symmetry subgroup, Malte Röntgen and Dr. Christian Morfonios, for revealing to me the MATRIX (obviously, I took the red pill). I will never forget the countless hours we spent in the office, in the WhatsApp and Element, on the weekends and during holidays, while

drawing graphs, concocting crazy theorems and then trying to make sense out of it. In particular, I hold Malte responsible for charging me on a daily basis with his positive energy, for making me addicted to board games and for introducing to me the art of ice tasting. The lawsuit is on its way!

My greatest thanks go to my life companion, Svetlana, for her patient attitude towards my late office hours, sincere love and compassionate care, for sharing and shaping all the great memories in my life.



EIDESSTATTLICHE VERSICHERUNG / DECLARATION  
OF OATH

---

Hiermit versichere ich an Eides statt, die vorliegende Dissertationsschrift selbst verfasst und keine anderen als die angegebenen Hilfsmittel und Quellen benutzt zu haben.

Die eingereichte schriftliche Fassung entspricht der auf dem elektronischen Speichermedium.

Die Dissertation wurde in der vorgelegten oder einer ähnlichen Form nicht schon einmal in einem früheren Promotionsverfahren angenommen oder als ungenügend beurteilt.

*Hamburg, den*

---

Maxim Pyzh